Delft University of Technology

Experimental investigation of ramp-induced shock–boundary-layer interactions in the presence of a sinusoidal roughness strip

Author:
Robert Patrick McCarthy

Experimental investigation of ramp-induced shock–boundary-layer interactions in the presence of a sinusoidal roughness strip

by

Robert Patrick McCarthy

to obtain the degree of Master of Science
at the Delft University of Technology,
to be defended publicly on Thursday December 17, 2020 at 2:00 PM.

Student number:	4743563	
Project duration:	December 1, 2019 – December 17, 2020	
Thesis committee:	Dr. ir. F. F. J. Schrijer,	TU Delft, supervisor
	Dr. ir. B. W. van Oudheusden,	TU Delft
	Dr. F. Avallone,	TU Delft
	L. Laguarda Sanchez,	TU Delft

This thesis is confidential and cannot be made public until December 17, 2020.

TU Delft

Preface

Life is hard. Life is harder if you're dumb. So it goes.

This marks the end of my master's degree. Finally. And as is tradition, I'm going to thank everyone who made this time... memorable.

First is obviously my advisor, Ferry Schrijer, who ensured for the most part I didn't destroy the wind tunnel or damage any of the equipment that he knew of. Faith in my abilities or indifference to my failures? Perhaps we'll never know.

Thank you, Olivia, for helping me move like three times and for showing me the ramen place. A shame you couldn't help the other 11 times I had to move.

I would also like to thank Maaike and Matthias for feeding me and letting me crash on their twin-size inflatable mattress in their storage room when I was homeless. And for letting me live there in exchange for watering their banana plant while they vacationed in Indonesia. I'm sorry I killed your potted angel vine. Maybe next time take me with you ja?

To the approximately ***58*** people I lived with while simultaneously fighting to finish my degree: you made my experience here something I *will absolutely never forget*. Take that how you will, like you took my personal possessions.

To Salvo and Henrique: learning how to barbecue picanha and chicken hearts might actually be the most valuable skill I've acquired in the last three years.

To myself: you're a badass for not giving up. Proud of you.

And finally, I would like to thank my girlfriend. Without your unending and relentless support I would never have made it. I will never forget all our times together and our long phone calls into the night. You made this time bright and enjoyable instead of dark and miserable. Doing this alone would have been unbearable.

Just kidding, I don't have a girlfriend. So it goes.

Robert Patrick McCarthy
Delft, December 2020

Abstract

The goal of this work is to observe and quantify how sinusoidal roughness strips introduce perturbations into a compression ramp shock–boundary-layer interaction system. This is achieved with the Hypersonic Test Facility Delft (HTFD), a hypersonic wind tunnel on the TU Delft campus that utilizes the Ludwieg tube concept to create a low-enthalpy test environment characterized by high velocity and high Mach number. Three test parameters are modified to observe a wide spectrum of results: the Reynolds number, the compression ramp angle, and the sinusoidal strip wavelength (distance between peaks). The ability to vary the Reynolds number, ramp angle, and roughness strip wavelength allows this thesis to explore the effect each parameter has on the overall system. In order to accurately observe the influence of each test parameter on the overall system, this work employs three measurement techniques: schlieren visualization, quantitative infrared thermography (QIRT), and oil flow visualization.

Schlieren visualization, primarily a qualitative technique, is used to visualize and observe the shear layer and shock system upstream of the roughness strip. Though best suited for two-dimensional systems, it nevertheless provides useful information regarding the differences between transitional systems and those that are fully turbulent. The schlieren images illustrate that the incoming boundary layer – and therefore the SBLI system in general – appears to be transitional with just a compression ramp, but begins to destabilize with the addition of a roughness strip and progresses to a fully transitional system. When the model includes a roughness strip and the flow operates at the higher Reynolds number, the strip trips the boundary layer and destabilizes the flow, thereby causing the flow to become fully turbulent. Schlieren images show that the turbulent boundary layer drastically alters the SBLI system, successfully resisting the adverse pressure gradient of the oblique shock at the ramp corner. As a result, the flow neither separates nor forms a circulation region.

Quantitative infrared thermography is used to observe the temperature pattern on the ramp's inclined surface to identify regions of elevated heat flux. This thesis observes stark differences in the temperature patterns from runs that have a roughness strip versus those that lack a strip. Those that lack a strip display bands of elevated heat flux in the spanwise direction with narrower streaks in the streamwise direction. In contrast, the runs that contain a strip display streamwise streaks spaced periodically in the spanwise direction, the wavelength of which closely reflects that of the sinusoidal roughness strip upstream. The flow conditions also allow this thesis to observe the thermal differences between SBLI systems that separate and form a circulation region versus those that remain attached to the ramp corner.

This thesis observes that, in general, surface Stanton number profiles decreases with increasing Reynolds number, increase with increasing ramp angle, and decrease with increasing roughness strip wavelength. However, the latter observation – that of decreasing surface Stanton number with increasing roughness strip wavelength – is less strongly correlated than the prior two observations.

Contents

List of Tables

List of Symbols

α	Ramp angle [∘]
δ	Boundary layer thickness [mm]
δ_{p_k}	Undisturbed laminar boundary layer thickness at peak location [mm]
γ	Ratio of specific heats [–]
λ_δ	Wavelength of sinusoidal roughness element nondimensionalized by the boundary layer thickness (δ): λ/δ [-]
λ_e	Wavelength of sinusoidal roughness element [mm]
μ	Dynamic viscosity [$kg/(m*s)$]
μ	Mach angle (figure 3.7) [∘]
μ_r	Reference dynamic viscosity [$kg/(m*s)$]
ν	Kinematic viscosity [m^2/s]
ρ	Density [kg/m^3]
$\vec{u}$	x-coordinate velocity vector [m/s]
$\vec{v}$	y-coordinate velocity vector [m/s]
$\vec{w}$	z-coordinate velocity vector [m/s]
a	Speed of sound [m/s]
c_h	Stanton number [-]
c_p	Specific heat at constant pressure [$J/(kg*K)$]
d^*	Critical throat diameter [mm]
d_{tube}	Storage tube diameter [mm]
h_e	Height of sinusoidal roughness elements [mm]
L	Length of storage tube [m]
L_s	Separation length
L_u	Upstream interaction length
M_∞	Freestream Mach number [–]
p	Static pressure [Pa]
p_t	Total pressure [Pa]
p_{t_p}	Total pressure as measured by Pitot tube [Pa]
$p_{t_{tube}}$	Total pressure of storage tube [Pa]
R	(Specific) gas constant [$J/(kg*K)$]
S	Sutherland temperature [K]

T Static temperature $[K]$

T_r Reference temperature $[K]$

T_t Total temperature $[K]$

U_∞ Freestream x-coordinate velocity $[m/s]$

V_∞ Freestream y-coordinate velocity $[m/s]$

W_∞ Freestream z-coordinate velocity $[m/s]$

x_r x-coordinate of angled ramp surface (ramp corner at $x_r = 0$) [mm]

$z_{Gaussian}$ Gaussian function of sinusoidal roughness element $[mm]$

$z_{sinusoidal}$ Spanwise function of sinusoidal roughness element (height) $[mm]$

1 Introduction

1.1. Background

Supersonic flight has captivated the imagination of humankind for the better part of 80 years, beginning first with the un-crewed V2 rocket developed by the Axis powers in World War II, and followed shortly thereafter in October 1947 by Chuck Yeager in the Bell X-1 experimental aircraft. Supersonic vehicle development continued throughout the fifties and sixties, culminating in the developments at NASA involving re-entry capsules for the Mercury, Gemini, and Apollo programs. The innovation continued in the post-Apollo spaceflight era in the form of the Space Transportation System (STS), more commonly know as the Space Shuttle.

Now there is renewed interest within the spaceflight community to extend a stronger human presence to low-Earth orbit, the Moon, and to Mars. Some concepts utilize the capsule design used for the Apollo missions, while others, such as the Dream Chaser (figure 1.2) adopt a glide-type design similar to that of the Space Shuttle.

These missions present a number of challenges, perhaps none so dangerously complex as the aerothermodynamic conditions involved when re-entering the atmosphere. During the entire entry-landing-descent phase, entry vehicles experience a variety of extreme high-velocity, high-temperature flow conditions that, if not properly understood or accounted for, can develop flow phenomena along the vehicle's surface that rapidly complicate the vehicle's precarious flight situation. One component of an entry vehicle's design is its control flaps or stabilizers in the form of ramps along its surface. It is in the vicinity of these ramps that one of the aforementioned extreme flow conditions form, which are known as shock–boundary-layer interactions (SBLI). Shock–boundary-layer interactions are an integral component of entry vehicle performance and design, and involve the dynamic coupling of the adverse pressure of a shock and the subsonic nature of a viscous boundary layer ([19]). When these two phenomena interact, they create regions of unpredictable surface pressure and high surface heat transfer, which in turn may rapidly compromise the vehicle's flight performance or structural integrity, condemning it to its destruction. One issue that compounds the wide-ranging effects and complexities of SBLIs is the fact that their behavior is unpredictable, difficult to model, and challenging to study.

In order to avoid future space flight disasters and to better understand the phenomena that occur during re-entry, it is essential to conduct experiments that imitate re-entry flow conditions and to perform tests on the myriad vehicle components. Due to their critical role in the entry-landing-descent phase of space flight, and in the potential danger in their (mis)design, ramp geometries are prime candidates for high-speed wind tunnel testing. They – and the flow phenomena they produce – are therefore the main subject of this master thesis.

1.2. Project Statement

The goal of this thesis is to study and quantify how shock–boundary-layer interactions amplify or dampen prescribed upstream sinusoidal disturbances in Mach 7.5 flow. The research questions naturally follow as, How do compression shock–boundary-layer interactions amplify or decay upstream disturbances? To what extent do sinusoidal roughness strips destabilize the boundary layer? What differences are there between laminar and turbulent upstream boundary layers in propagating disturbances downstream? This thesis answers these questions by using a variety of measurement techniques: schlieren visualization, oil flow visualization, and quantitative infrared thermography (QIRT). The experiments are performed at the Hypersonic Test Facility Delft (HTFD) within the Aerospace Engineering faculty of Delft University of Technology (TU Delft), utilizing hypersonic test facilities that are well-suited to study such phenomena. The broader goal of this thesis is to characterize the amplification effect of the recirculation region on upstream disturbances and to study their effect on the reattachment

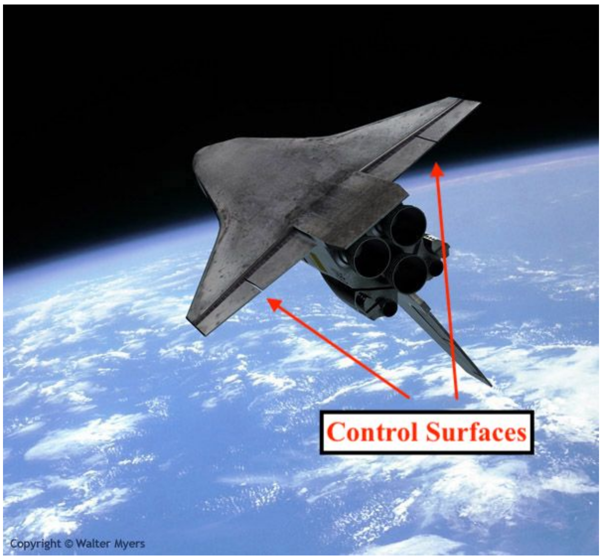

Figure 1.1: Space shuttle with relevant control surfaces.

Figure 1.2: The Dream Chaser – a glide-type re-entry vehicle similar to the space shuttle.

region with particular emphasis on the heating patterns along the ramp surface. The data yield correlations between the wavelength of the sinusoidal roughness strip, the wavelength of the temperature streaks, and the three dimensional nature of the recirculation bubble. These results ultimately provide unique insight into the flow mechanics involved in SBLI re-entry phenomena and thereby contribute to the broader goal of designing safe and reliable entry vehicles.

1.3. Report Outline

Chapter 2 describes general SBLI flow topology. The chapter begins by describing typical features of laminar boundary layers and how they develop over a flat plate. Then, the chapter extends the discussion to turbulent boundary layers, discussing the difference in profile and the general effect of each on the flow at large. The chapter then explores different paths to turbulence and how each path may arise, though the section focuses primarily on the roughness mechanisms used in this thesis. As the SBLIs studied in this thesis are formed by compression corners, the discussion continues with compression ramp interactions, including how they form and general characteristics that determine their structure. The ensuing sections describe the various methods used to characterize the phenomena that occur in SBLIs, including wall pressure and temperature profiles. The chapter concludes by describing typical reattachment behavior and the physics typical of three-dimensional SBLIs.

Chapter 3 describes the test facility used for this thesis, describing its basic features, its ability to simulate hypersonic flow conditions, and characterizing the freestream flow conditions. The chapter also describes the flat plate, ramp, and roughness strip models used in the test facility.

Chapter 4 describes the measurement techniques used to study SBLIs in the HTFD. Section 4.1 describes schlieren visualization, which is used to obtain general flow characteristics such as shock patterns and approximate flow direction. Section 4.2 describes quantitative infrared thermography (QIRT), which is helpful in accurately measuring temperature values on a surface, which can be extrapolated to determine heat transfer into a material body. Section 4.3 describes oil flow visualization, which is useful in detailing regions of recirculation, attachment, and detachment.

Chapter 5 presents SBLI experimental results best suited to discuss the dynamic and evolving flow topology. Section 5.1 describes flat plate QIRT results used to characterize the flat plate boundary layer and validate QIRT measurements against analytical flat plate heat transfer solutions. Section 5.2 follows section 5.1 by describing so-called ‘baseline’ results involving a compression ramp but no roughness strip. The section effectively builds upon the flat plate discussion of section 5.1 by including a ramp. The section focuses on two ramp geometries ($15°$ and $30°$) and the two Reynolds numbers to observe how both a modified ramp angle and modified Reynolds number alters SBLI flow phenomena. Section 5.3 contributes to the discussion by including a sinusoidal roughness strip upstream of the compression ramp. The section limits itself to the lower Reynolds number but explores both aforementioned ramp geometries. The final section of chapter 5 is section 5.4, in which the discussion is extended one step further by studying the strip-ramp conditions of section 5.3 at the higher Reynolds number. The higher Reynolds number destabilizes the flow enough to transition the flow to turbulence after being tripped by the roughness strip.

Section 6 concludes the main body of this document by summarizing the scope, objectives, and results of the overall thesis. Most importantly, it answers the research question: ”to what extent do SBLIs amplify or decay prescribed upstream disturbances?”

Finally, section 7 gives recommendations for future studies involving compression shock–boundary-layer interactions in the presence of a roughness strip.

2
Compression Ramp Flow

We begin to answer the research questions proposed in section 1.2 by describing the flow phenomena characteristic of compression shock–boundary-layer interactions.

2.1. Boundary Layer Flow

Vehicles that spend extended periods of time in hypersonic flight are highly susceptible to the flow's laminar-turbulent behavior, which directly influences skin friction, heat transfer, and the vehicle's overall control and flight performance. It is therefore important to understand the mechanisms that influence hypersonic boundary layers and to be able to predict the effects of transition to turbulence. As such, this section provides a brief overview of the defining characteristics of laminar and turbulent boundary layers, both of which play a central role in the current work.

Figure 2.1 shows typical boundary layer properties over a flat plate, where V_∞ is the freestream velocity, V_w is the velocity at the wall, τ_w is the wall shear stress, and δ is the boundary layer thickness. Typical laminar boundary layers adopt the profile indicated in the left portion of figure 2.1. The no-slip condition at the wall requires that the flow velocity at the wall be zero as an effect of viscosity. Meanwhile, the flow velocity parallel (i.e. tangent) to the wall asymptotically increases as the distance from the wall increases until it achieves the velocity of the free stream. At the wall, the velocity gradient creates shear stress denoted by τ_w, which induces heat transfer into the surface. The greater the velocity gradient, the greater the shear stress and accompanying surface heat transfer. As the flow travels downstream from the leading edge, the decelerating effect of the wall on the flow propagates toward the freestream, resulting in a growing boundary layer whose velocity gradient, shear stress, and surface heat transfer decrease.

Once a laminar boundary layer has transitioned to turbulence, the velocity profile and resulting wall shear change drastically. See section 2.3 for an overview of the different means by which boundary layers may transition from laminar to turbulent. Figure 2.2 presents a comparison of laminar and turbulent boundary layer profiles as they pertain to a supersonic freestream. The figure illustrates a defining characteristic of turbulent flow: the velocity gradient at the wall – and therefore the associated wall shear stress – is far greater than that of the laminar boundary layer [19, 46]. In both subsonic and supersonic flows, the turbulent wall shear imparts greater heat transfer than its laminar counterpart. In hypersonic flows, the heat transfer experienced by the surface can reach extreme levels with

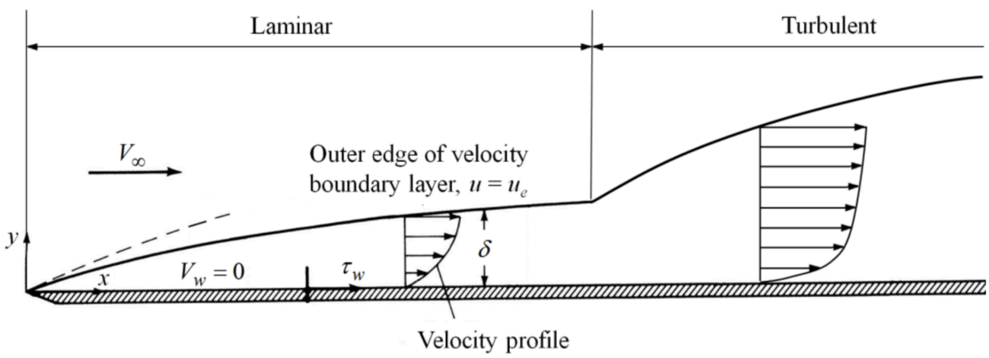

Figure 2.1: Velocity profile and distinguishing features of laminar and turbulent boundary layers over a flat plate at zero angle of attack. Adapted from Ye [60].

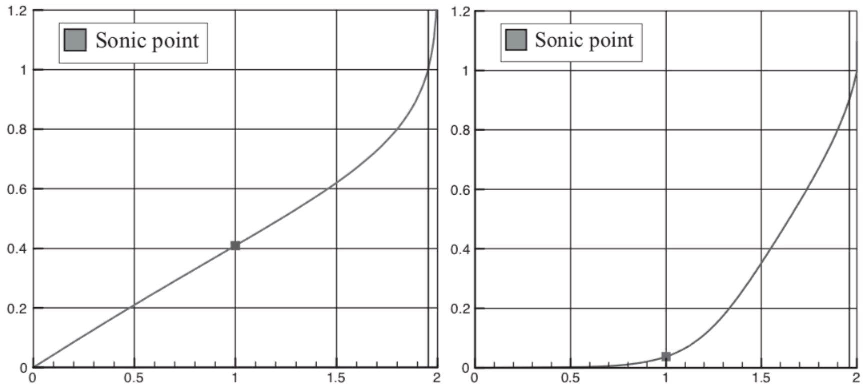

Figure 2.2: Comparison of flat plate laminar and turbulent boundary layer profiles: Mach number distribution. Outer Mach number equal to 2. Adapted from Délery [19].

potentially disastrous consequences. This highlights the importance of understanding instability mechanisms associated with laminar-turbulent transition and accurately predicting their associated effects on the flowfield and nearby surfaces.

One must also note that impinging shocks and their associated adverse pressure gradient are less likely to separate a turbulent boundary layer than one that is laminar. For more information on laminar-turbulent separation in high-speed flows, the reader is directed to section 2.7.

2.2. Reference Temperature Method

The reference temperature method is a method used in hypersonic applications to evaluate boundary layer properties, such as skin friction coefficient c_f, boundary layer thickness δ, and surface heat transfer q. It is based on modifying the equations used in incompressible flow theory to account for compressibility effects. In the reference temperature method, the flow's thermodynamic and transport properties are evaluated at some reference temperature that are indicative of the temperature within the boundary layer.

The first step in deriving the flow's thermodynamic and transport properties is to calculate the reference temperature T^*. As the flow over the flat plate is laminar, these derivations focus on the equations for a laminar boundary layer.

First, calculate the reference temperature T^* for laminar boundary layer:

$$\frac{T^*}{T_e} = 1 + 0.032M_e^2 + 0.58\left(\frac{T_w}{T_e} - 1\right) \tag{2.1}$$

where T_w is the temperature at the wall, given by:

$$\frac{T_w}{T_\infty} = 1 + r\frac{\gamma - 1}{2}M_\infty^2 \tag{2.2}$$

and r is the recovery factor, given as the square root of the Prandtl number:

$$r = \sqrt{Pr} \tag{2.3}$$

The Prandtl number is approximately constant for air under conditions present in the HTFD: $Pr = 0.72$.

The next step is to calculate the reference viscosity μ^* using Sutherland's law:

$$\frac{\mu^*}{\mu_{ref}} = \left(\frac{T^*}{T_{ref}}\right)^{\frac{3}{2}} \frac{T_{ref} + S}{T^* + S} \tag{2.4}$$

where μ_{ref} and T_{ref} are, confusingly, *not* reference values being derived but are reference values *looked up in tables*. (This notation has let to much confusion while writing this thesis...). μ_{ref} is simply the dynamic viscosity of the fluid in question at temperature T_{ref}.

The reference density ρ^* and x-based Reynolds number Re_x may now be calculated:

$$\rho^* = \frac{p_\infty}{RT^*} \tag{2.5}$$

and

$$Re_x = \frac{\rho u_e x}{\mu} \tag{2.6}$$

The reference x-based Reynolds number Re_x^* is calculated as:

$$Re_x^* = \frac{\rho^* u_e x}{\mu^*} = \frac{\rho^* \mu_\infty}{\rho_\infty \mu^*} Re_x \tag{2.7}$$

The boundary layer thickness δ is calculated by employing the incompressible Blasius boundary layer relation at the reference temperature T^*:

$$\delta = \frac{5x}{\sqrt{Re_x^*}} \tag{2.8}$$

The compressible laminar skin friction coefficient $(c_{f,comp})_{lam}$ is calculated as:

$$\left(c_{f,comp}\right)_{lam} = \sqrt{\frac{\rho^* \mu^*}{\rho_\infty \mu_\infty}} \frac{0.664}{\sqrt{Re_x}} \tag{2.9}$$

which is used to calculate the Stanton number using the Reynolds analogy:

$$c_h = \left(c_{f,comp}\right)_{lam} \frac{1}{2} Pr^{-\frac{2}{3}} \tag{2.10}$$

2.3. Paths to Turbulence

Boundary layer transition occurs when the undisturbed laminar boundary layer has a nonlinear response to different types of external disturbances [33]. These disturbances originate in the freestream or any region beyond the boundary layer and may take any number of forms: temperature, sound, entropy, etc. The disturbances propagate into the boundary layer and collectively determine the initial conditions of the disturbance amplitude, phase, and frequency. When the perturbations within the laminar boundary layer amplify to a critical value, the collection of disturbance amplitude, phase, and frequency form an instability wave. Due to the variability of the initial conditions of the disturbance, different forms of instabilities can form.

There are several paths to turbulence identified by Reshotko by which a laminar boundary layer may transition to turbulence [38, 39], shown in figure 2.3. (Fedorov also provides some insight into these mechanisms [21].) Detailed descriptions of the paths to turbulence are beyond the scope of this report. For additional information, the reader is directed to the works of Ye [60], Reshotko [39], and Schneider [47]. The paths are briefly discussed as follows:

- Path A – no transient growth; transition is due to Tollmien-Schlichting, crossflow, or Görtler instabilities

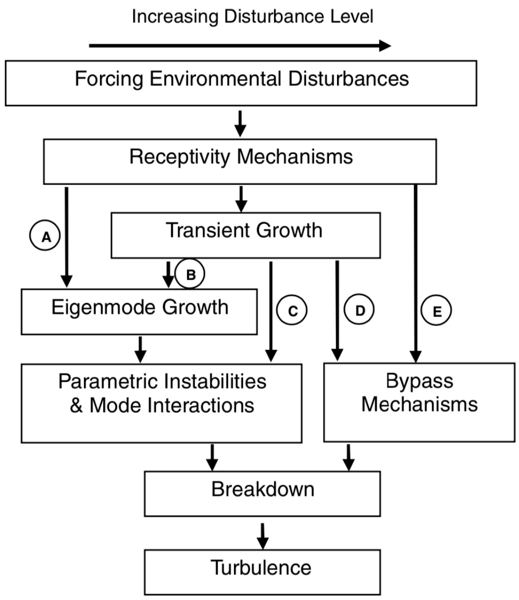

Figure 2.3: Paths to turbulence in boundary layer flow. Adapted from Reshotko [39].

- Path B – some transient growth; provides higher initial amplitude to the eigenmode growth upon crossing into an exponentially unstable region
- Path C – no eigenmode growth; examples include blunt body paradox
- Path D – spectrum of disturbances in boundary layer is full as a result of the transient growth
- Path E – large amplitude forcing, no linear regime

2.4. Roughness

Roughness can affect high-speed transition in several different ways, depending on the freestream flow properties and the instabilities of the smooth wall [47–49]. Roughness in hypersonic flight may have many different effects, depending on the flow properties and the roughness geometry. With regard to turbulence, deformities on the surface of a geometry engaged in hypervelocity flight effectively perturb, trip, or completely obstruct the boundary layer, causing it to break down and transition to turbulence [21, 33]. Roughness may take several forms: sometimes it is distributed over an area, sometimes it is isolated to a single location, and sometimes it may be an elongated step or ramp in the spanwise direction. In general, roughness is characterized as two-dimensional or three-dimensional, and as isolated or distributed.

The methods of transition resulting from two-dimensional roughness elements with constant features in the spanwise direction are well understood [33, 38, 48]. Examples include forward-facing step, backward-facing step, gaps, and wires. Transition with regard to such roughness elements is promoted by Tollmien-Schlichting waves near the separation region downstream of the roughness element. Instabilities of this type generally follow *Path A* in figure 2.3.

2.5. Compression Ramp Interactions

Compression shock–boundary-layer interactions are a particular type of compressible, viscous, supersonic flow phenomena that occur when a shock wave generated by a ramp or control surface converges with a boundary layer. They commonly occur in supersonic flows, particularly when complex geometries are involved, and have immense consequences on flow stability, surface heat flux, and vehicle performance and control [2]. One issue that compounds the wide-ranging effects and complexities of SBLIs is the fact that their behavior is unpredictable, difficult to model, and challenging to study.

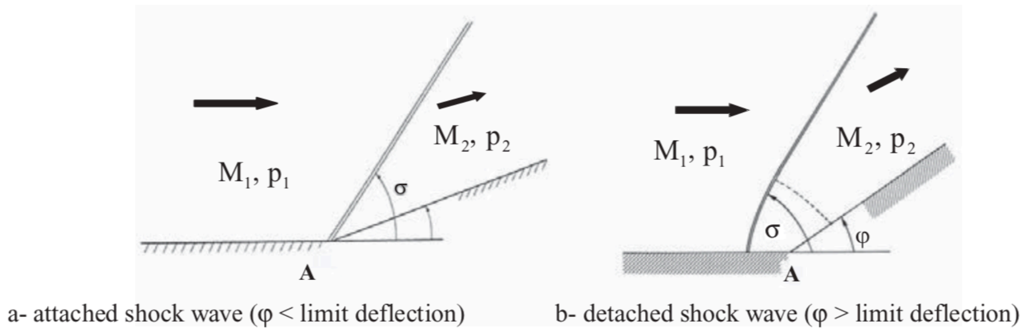

Figure 2.4: Attached (left) and detached (right) compression shock interaction. Figure obtained from Délery [19].

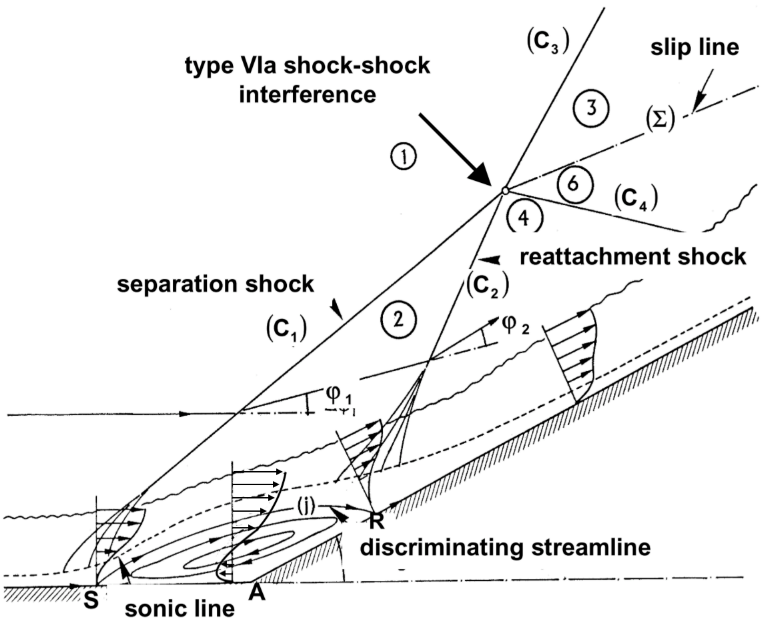

Figure 2.5: Basic structure of compression ramp flow with separation. Figure adapted from Arnal and Délery [2].

In supersonic flow, an inclined surface generates an oblique shock that propagates from the ramp corner into the main body of the flow. At shallow ramp angles and low supersonic Mach numbers, the oblique shock generated by the inclined surface remains attached at the ramp corner (shown in figure 2.4, left) [4]. However, as the ramp angle or Mach number increases, the shock strength (i.e. pressure gradient) increases. When the shock strength reaches a critical value, the shock separates from the ramp corner (figure 2.4, right) and interacts with the incoming boundary layer, thereby forming the basic structure of a compression SBLI. Figure 2.5 shows the typical structure of a compression SBLI while figure 2.6 illustrates various physical features common to compression ramp flow. Figure 2.11 displays a ramp with increasing angle to develop a SBLI.

The unique structure of a shock–boundary-layer interaction is the result of the dynamic coupling between the incoming boundary layer and the oblique compression shock. The momentum and shear forces of the boundary layer acting in the positive streamwise direction are effectively opposed by the adverse pressure of the shock (depicted in figure 2.7). The boundary layer is supersonic at the boundary layer edge and subsonic near the wall, inferring that there is a thin border within the boundary layer where the flow Mach number is equal to 1, termed the sonic line (shown in figure 2.2). In the region where the flow is subsonic, downstream disturbances are able to propagate upstream [2], and the adverse pressure, if great enough, causes the flow to separate and form a recirculation region [19].

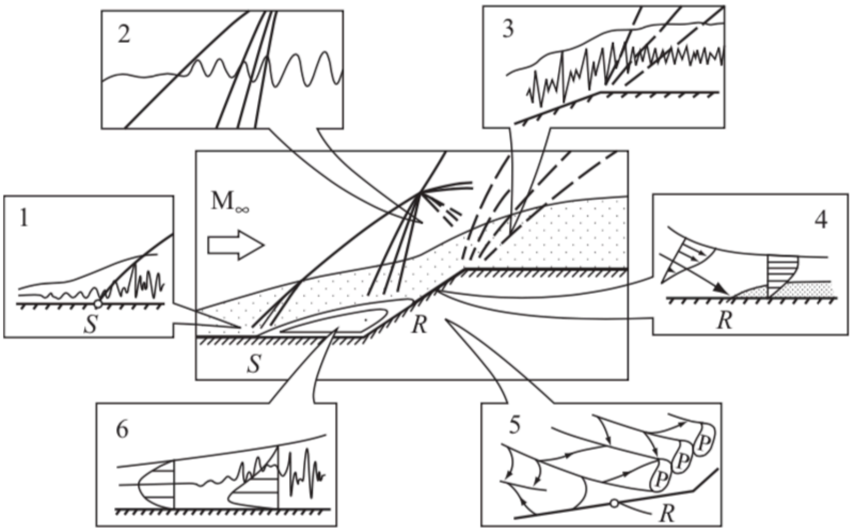

Figure 2.6: Various physical features present in compression-decompression ramp flow: 1.) amplification of disturbances in the boundary layer near the separation point; 2.) amplification of freestream disturbances due to separation and reattachment shocks; 3.) dampening of disturbances due to expansion fans; 4.) reattaching boundary layer at the reattachment location; 5.) Görtler-like vortices near reattachment; 6.) dampening of disturbances in the recirculating flow; figure adapted from Knight and Zheltovodov [28].

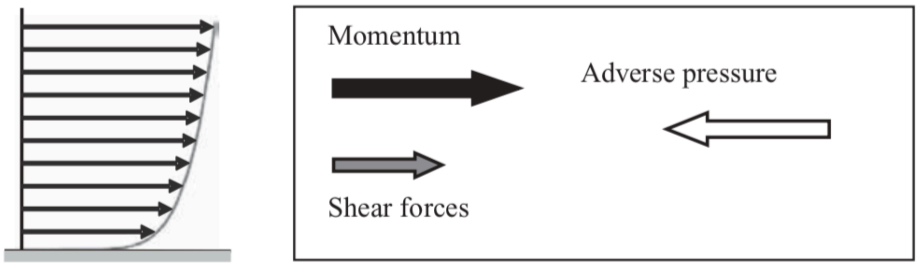

Figure 2.7: Basic illustration of the forces involved in SBLIs, from Délery [19].

The separated flow is bounded and characterized by three distinct flow features: a separation point, a reattachment point, and a dividing streamline [2]. The separation point lies on the surface upstream of the ramp corner and effectively divides the surface between that which experiences positive shear (from a streamwise boundary layer) and that which experiences negative shear (from a negative streamwise boundary layer in the recirculation region). In compression ramp SBLIs, the reattachment point lies on the surface of the ramp and, similar to the separation point, effectively divides the region of the surface that experiences negative shear from that which experiences positive shear. Section 2.8 provides additional insight into the surface skin friction distribution and its relation to separation and reattachment.

The streamline that connects the separation and reattachment points is termed the dividing streamline. The region bounded by the dividing streamline and the wall is effectively the recirculation zone, wherein the flow circulates in the ‘clockwise’ direction (viewed as the gas flowing from left to right). The physics involved in the separation region are further discussed in sections 2.7, 2.8, and 2.9. Reattachment is primarily discussed in sections 2.8, 2.9, and 2.10.

2.6. Free Interaction Theory

The *Free Interaction Theory* is a theory regarding the “free interaction” between the viscous boundary layer and inviscid outer flow resulting in a rise in pressure at the surface during separation [2, 25]. The theory can be helpful to analytically describe the behavior of the separation region for laminar and

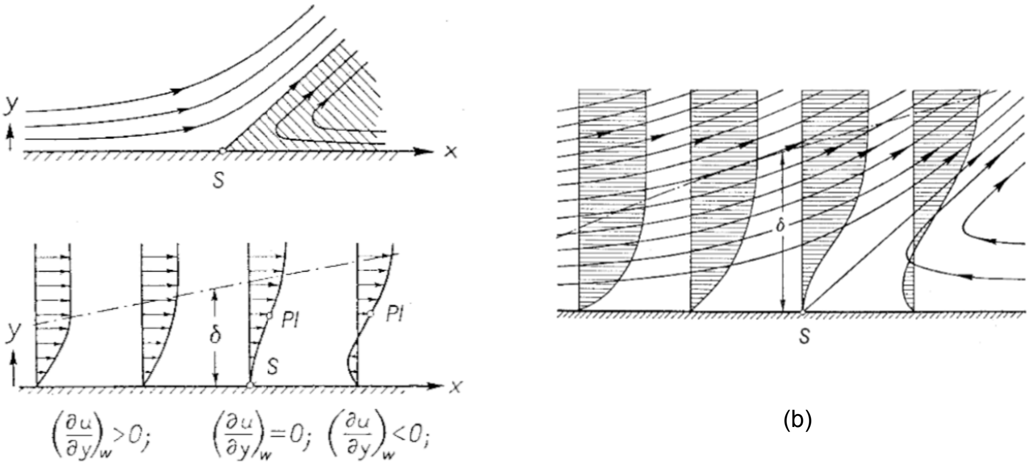

(a)

(b)

Figure 2.8: Top left: laminar flow streamlines near a separation point. Bottom left: laminar boundary layer profile in the vicinity of a separation point (denoted as S). PI denotes point of inflection. Right: boundary layer flow in the vicinity of the separation point. Figures adapted from Schlichting and Gersten [46].

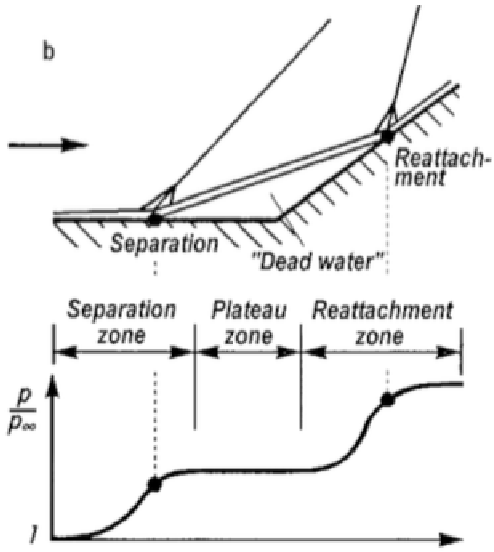

Figure 2.9: Ramp-induced shock–boundary-layer interaction with associated surface pressure distribution. Figure adapted from Schlichting and Gersten [46].

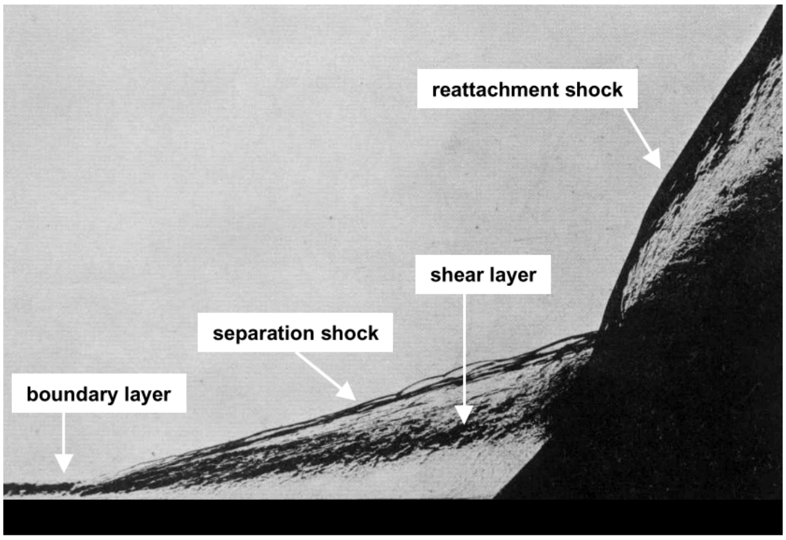

Figure 2.10: Shadowgraph of turbulent ramp flow with separation. Mach number is 9.2. Figure adapted from Arnal and Délery [2].

turbulent flows, which may aid in designing computer simulations or experiments. In addition, it predicts that an increase in compression ramp angle yields increased pressure at reattachment and a greater shear layer length [30]. Figure 2.12, confirms this prediction by illustrating the separation location and pressure rise for a variety of compression ramp angles.

By applying the boundary-layer momentum equation at the wall, integrating in the x-direction, and nondimensionalizing the physical variables present in the equation (along with other steps), one arrives at the following form:

$$\frac{p - p_0}{q_0} \propto \left(C_{f_0}\right)^{-\frac{1}{2}} \left(M_0^2 - 1\right)^{-\frac{1}{4}} \tag{2.11}$$

where p_0, M_0, and C_{f_0} are all evaluated at the the interaction origin x_0 (i.e. $p_0 = p\,(x_0)$), p_0 being the pressure, M_0 being the Mach number, and C_{f_0} being the skin friction coefficient; q_0 is the dynamic pressure of the incoming flow.

Additionally, the extent of streamwise interaction, L, obeys the following relationship:

$$L \propto \delta_0^* \left(C_{f_0}\right)^{-\frac{1}{2}} \left(M_0^2 - 1\right)^{-\frac{1}{4}} \tag{2.12}$$

where δ_0^* is the incoming boundary layer displacement thickness. If the flow is hypersonic, one may derive the following equivalent expression:

$$\frac{L}{\delta_0^*} \propto \frac{\left(M_0 \alpha\right)^2}{\overline{\chi}_0} \tag{2.13}$$

where $\overline{\chi}_0$ is the hypersonic interaction parameter: $\overline{\chi}_0 = M_0^3/\sqrt{R_{x0}}$

Consider equations 2.11, 2.12, and 2.13. We notice that, according to the free interaction theory, the pressure profile and extent of interaction depend only on the flow properties at the location where the interaction begins. Furthermore, the free interaction theory predicts that, with an increase in Reynolds number, the interaction extent increases and the total pressure rise decreases, which is due to the fact that the coefficient of skin friction decreases with increasing Reynolds number. A consequence of these results is that the shock strength required to induce separation is larger at lower Reynolds numbers than at higher Reynolds numbers [2]. This may be observed in laminar flows but not turbulent flows, which may show the opposite trend when the Reynolds number is greater than 10^5. This trend is explained in part by considering the 'composition' of the Reynolds number: inertial flows (i.e. momentum and pressure) vs. viscous forces. The free interaction theory concerns values near the wall where viscous forces dominate, hence why it accurately predicts the trends in interaction extent and total pressure rise

a
b
c
d

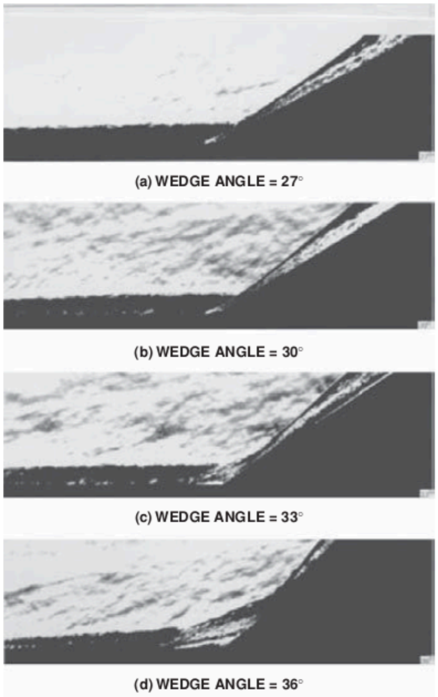

Figure 2.11: Turbulent SBLI at various ramp angles. For the given freestream Mach number ($M_\infty = 8$), separation does not occur until the ramp angle approaches $33°$. Figure adapted from Holden [25].

in low Reynolds number flows. At high Reynolds numbers the inertial terms dominate, which reverses the observed trends in turbulent flows.

2.7. Separation

This section discusses the fundamental characteristics that distinguish laminar and turbulent SBLIs in two-dimensional flows. As the discussions contained in sections 2.5 - 2.6 are quite valid in describing laminar SBLI behavior, the bulk of laminar separation is already covered. Therefore, this section does not elaborate on laminar SBLIs much further. Rather, this section defines additional separation criteria and elaborates on the behavior of *turbulent* SBLIs, whose behavior differ enough from laminar SBLIs to warrant an additional detailed discussion.

It is helpful to establish a means of quantifying and comparing the different physical phenomena present in SBLIs, particularly with regard to the 'size' of the separation zone and to the extent to which the shock influences the flow's upstream behavior. To that end, we define the upstream interaction length L_u as the distance between the *onset of interaction* (often taken to be the location where the wall pressure begins to rise – discussed in section 2.8) and the ramp corner. (The upstream propagation of pressure is due to the subsonic region of the boundary layer discussed in section 2.5 and shown in figure 2.2.) We similarly define the separation length L_S as the distance from the *separation* point to the corner of the ramp [2]. Figure 2.9 shows the distinction between the two lengths – the separation length is measured from the location denoted by "separation", whereas the upstream interaction length is measured from the 'point' where the upstream pressure distribution deviates from unity. The upstream influence length is always greater than the separation length.

Turbulent shock–boundary-layer interactions (TSBLIs) remain particularly challenging to study numerically, largely due to the difficulty in modeling turbulence in the separation region, wherein the turbulence model must accurately reproduce compressibility effects, reverse flow, and shock-turbulence interaction physics [25]. As of the time of writing this thesis, only DNS has had some success in modeling such phenomena, and even those results may be limited in their accuracy.

Turbulent boundary layers display a 'thicker' profile, and have greater momentum. As such, they more strongly resist separation [19, 25] – note the balance of forces in figure 2.7 and the 'shallower' sonic point in figure 2.2 that limits the extent to which perturbations and the gas itself can propagate upstream. Because the subsonic region is so thin, the shock forms well within the boundary layer, which behaves like an inviscid rotational fluid over the majority of its thickness [2, 25]. Figure 2.11 further illustrates a turbulent SBLI's resistance to separation where a larger ramp angle is necessary to induce separation than would be the case for a laminar SBLI. As such, in order to avoid separated flow and the associated SBLI flow physics, it is sometimes desirable to promote turbulent flow where one suspects SBLIs to occur and which one wishes to avoid – despite the fact that turbulent boundary layers themselves exhibit greater wall shear and heat transfer than their laminar counterparts. Additionally, the most relevant characteristics of turbulent SBLIs (i.e. pressure distribution and peak heating) can typically be estimated with experimental results and simple analytical methods.

One must also note that the high Reynolds numbers necessary to develop fully turbulent SBLI regions in hypersonic flows may be difficult to attain in experiments, and that decreasing the Reynolds number encourages the flow to remain laminar throughout the interaction region. The consequences of laminar versus turbulent boundary layer flow therefore extend far beyond simply whether the flow itself exhibits laminar or turbulent behavior: the state of the boundary layer strongly influences whether the flow separates and, by extension, influences the wall pressure, wall shear, and surface temperature profiles in and downstream of the interaction region. Section 2.8 provides additional information regarding the wall pressure and skin friction profiles of laminar and turbulent SBLIs, while section 2.9 does likewise but with regard to the wall temperature profile.

2.8. Wall Pressure and Skin Friction Distribution

This section describes typical wall pressure profiles and skin friction distributions in compression ramp shock–boundary-layer interactions.

In compressible hypersonic flows, particularly those involving complex geometries, the flow is often defined by regions of varying pressure, whether they be due to heating effects, expansion waves, or shocks. The wall pressure distribution likewise exhibits regions of varying pressure with a subtle increase near regions of separation and a large, more drastic increase near regions of reattachment (sometimes with a gradual-to-sharp decrease shortly thereafter). The wall pressure effectively transitions from the pre-shock pressure to the post-shock pressure, but does so gradually rather than instantaneously as is the case for regions away from the wall. As an example, consider figure 2.12 from Arnal and Délery [2], which shows wall pressure distributions in a turbulent Mach 9.22 flow for various ramp angles. We see a 'slight' increase near separation (~ 5 times the reference pressure), a sharp increase near reattachment (many times the value of the reference pressure), and a gradual or sharp decrease shortly thereafter.

The pressure distribution effectively displays the following features:

1. The separation region correlates to a plateau in pressure depicted immediately after the separation region.

2. The plateau reflects the length of separation, which noticeably increases with increasing shock strength.

3. Changing the ramp angle does not change the extent to which the value of pressure itself increases at the separation point. This observation supports the free interaction theory, which states (in section 2.6) that the rise in pressure is a function purely of the conditions *at the separation point*, not of the conditions downstream. The only thing the ramp angle modifies is the shock strength, which increases the separation length.

4. Each distribution curve approaches its unique post-shock inviscid solution value.

Another important value used to evaluate SBLIs is the wall shear stress, which ultimately indicates when separation truly occurs. Figure 2.13 shows the coefficient of friction versus distance from leading edge of several ramp-induced SBLI experiments of varying ramp angle. As is discussed in section 2.5, a shock remains attached to the corner of the ramp until the adverse pressure gradient is great enough to detach the shock and induce separation. Thus, so long as the shock remains attached, no recirculation region forms, and the flow therefore exhibits only positive shear stress and friction

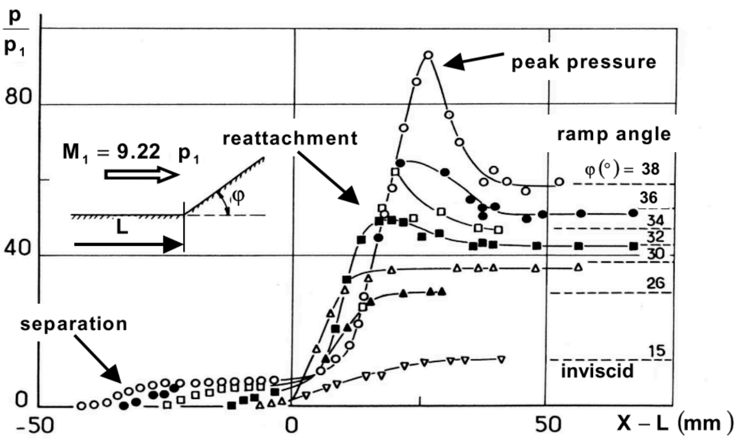

Figure 2.12: Wall pressure distributions for varying ramp angles in turbulent flow. Figure from Arnal and Délery [2].

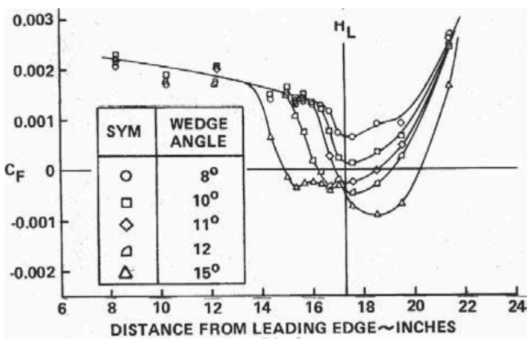

Figure 2.13: Measurements of skin friction in compression ramp SBLI experiments ($M_\infty = 11.7$, $Re/m = 5.2 \times 10^5$). Figure from Holden [24, 25].

coefficient values. In other words, negative shear stress – and thereby negative value of coefficient of friction – denotes separated flow.

Looking at figure 2.13, we see that increasing the ramp angle effectively decreases the skin friction coefficient near the foot of the ramp, which indirectly indicates an increase in shock strength. We also see that a negative coefficient of friction – and hence incipient separation – occurs between 10° and 11°. Above this incipient value, the flow separates [24, 25].

2.9. Wall Temperature Phenomena

The range of low- to high-enthalpic conditions of hypersonic flows affect shock–boundary-layer interactions in several ways. The most import of which with regard to low-enthalpy ramp interactions concerns the shear layer created by the separation region and its impact location on the inclined ramp [2].

In general, colder walls contract the separation length L_S, while hotter walls extend it [18]. This applies for both laminar and turbulent boundary layers. Such observations agree with the free interaction theory (described in section 2.6), which predicts that decreasing the wall temperature increases the coefficient of skin friction and reduces the boundary layer displacement thickness, which therefore contracts the separation length.

The surface heat transfer is typically expressed by the Stanton number [1, 2]:

$$S_t = \frac{q_w}{\rho_e u_e \left(h_r - h_w\right)} \tag{2.14}$$

where q_w is the heat transfer at the wall, ρ_e is the density at the edge of the boundary layer, u_e is

Figure 2.14: Structural damage on the X15 caused by shock-interaction heating. Figure adapted from Holden [25].

the velocity at the edge of the boundary layer, h_r is the recovery enthalpy, and h_w is the enthalpy of the gas at the wall.

The Stanton number may alternatively be expressed by freestream conditions, which is typically the case in hypersonic flows as the boundary layer edge conditions are difficult to measure or predict:

$$c_h = \bar{S}_t = \frac{q_w}{\rho_\infty u_\infty \left(h_{st_\infty} - h_w\right)} \tag{2.15}$$

where ρ_∞ is the freestream density, u_∞ is the freestream velocity, and h_{st_∞} is the freestream stagnation enthalpy. If the flow obeys perfect gas assumptions, the Stanton number can be additionally modified to:

$$c_h = \bar{S}_t = \frac{q_w}{\rho_\infty u_\infty C_p \left(T_{st_\infty} - T_w\right)} \tag{2.16}$$

Extremely high rates of heat transfer occur on ramp SBLIs where the shear layer impinges on the inclined ramp and the region following immediately thereafter (see figure 2.10). This occurs in part due to the following processes: the successively compressed flow (and its corresponding increase in temperature) and the particularly thin boundary layer near the reattachment location combine to transfer excessively high heat loads to the surface of the ramp. In addition, the streamline impinging on the ramp that marks the reattachment location is effectively a stagnation point, which are always regions of high heat transfer due to the flow's deceleration and inherent conversion of kinetic energy to heat. The surface heat transfer near the reattachment location may be several orders of magnitude greater than the stagnation-point heating to the vehicle's leading edge [25]. Shock-interaction heating similar to this type effectively destroyed the pylon support to the ramjet secured underneath the X15 research vehicle, shown in figure 2.14.

Figures 2.15 - 2.17 show Stanton number profiles in laminar, laminar-turbulent, and turbulent SBLIs, respectively. The figures cannot be directly compared as the geometries and flow conditions differ between each, but they nevertheless illustrate the typical heat transfer profile of their respective conditions.

Figure 2.15 shows the heat transfer profile of a laminar SBLI. The heat transfer decreases upstream of the separation point, which is in agreement with viscous interaction theory, before slightly decreasing again immediately following the separation point. The post-separation decrease is typical of laminar SBLIs, as is the rapid increase as the flow nears reattachment. The heat transfer reaches its maximum value shortly after reattachment.

Figure 2.16 illustrates a SBLI characterized by a laminar boundary layer at separation and a turbulent boundary layer at reattachment, as indicated by the decrease in heat transfer near separation (typical of laminar SBLIs). The turbulent flow at reattachment transfers greater amounts of heat to the surface than would be the case for a laminar flow [25].

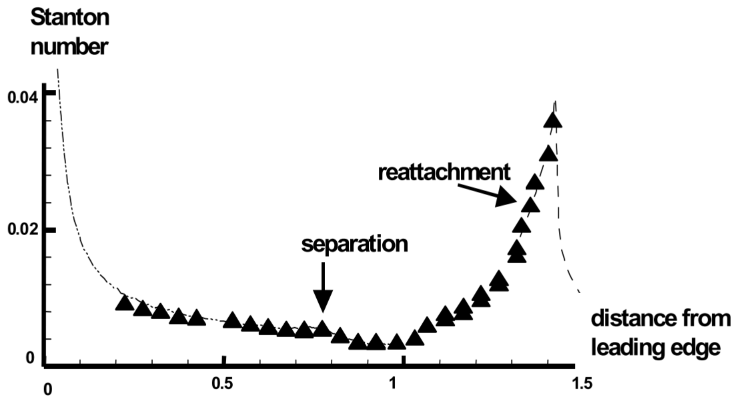

Figure 2.15: Stanton number profile due to a Mach 10, low Re, laminar SBLI on a cylinder-flare model [2, 5, 16]. Figure adopted from Arnal and Délery [2].

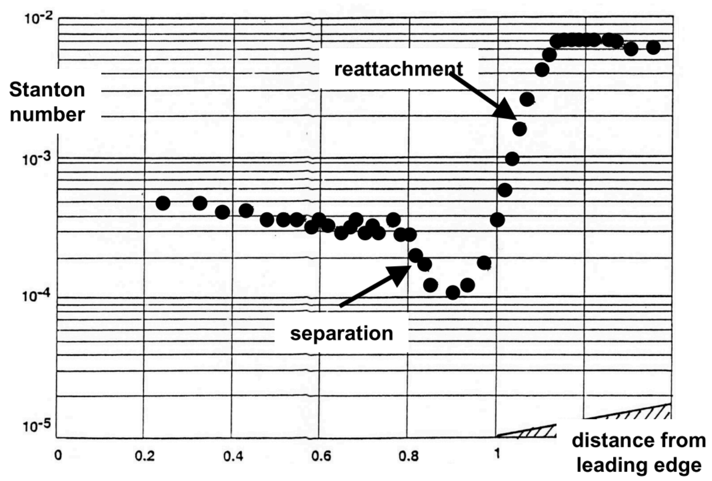

Figure 2.16: Stanton number profile due to a transitional SBLI [2, 17]. Separation occurs due to a 15° ramp mounted on a flat plate with sharp edge; the freestream Mach number is equal to 10, and $T_w/T_r = 0.3$. Figure adopted from Arnal and Délery [2].

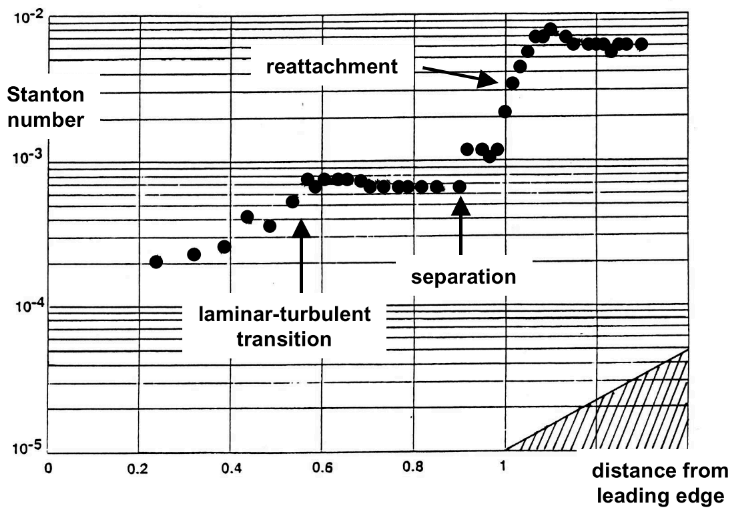

Figure 2.17: Stanton number profile due to a turbulent SBLI [2, 17]. Freestream Mach number is equal to 5; ramp angle is 35°. Figure adopted from Arnal and Délery [2].

Figure 2.17 shows a fully turbulent SBLI at both separation and reattachment. The increase in heat transfer at separation is characteristic of turbulent SBLIs. The increase is attributed to turbulence amplification, wherein large eddies form and promote heat transfer between the high(er)-enthalpy outer flow and the near-wall regions. The location of peak heat transfer is again shortly after reattachment [16, 25].

Of the many complex physical phenomena at play in a SBLI, the most important with regard to a vehicle's structural integrity and thermal protection system is the location and rate of maximum heat transfer. This is commonly the case, regardless of the state of the boundary layer. Current state-of-the-art experimental and modeling methods experience difficulty in this regard, though they continue to improve with the advancement of CFD methods, turbulence models, and enhanced measurement techniques. There are, however, empirical correlations that provide general estimates of the ratio of the peak value of heat transfer to the heat transfer value at the same location with the same flow conditions in absence of any SBLI interaction – "as a function of the total inviscid pressure ratio throughout the interaction" [2]. These correlations are shown in figures 2.18 and 2.19.

2.10. Three-Dimensional Phenomena

This section explores characteristics of three-dimensional compression ramp SBLI phenomena, which may differ greatly from the two-dimensional approach of sections 2.5 - 2.9. Furthermore, this section singles out two main categories of three-dimensional SBLI phenomena to help focus the overall discussion:

- separation in three-dimensional flows
- reattachment in three-dimensional flows

These two categories are obviously not entirely independent of one another, but the physics relevant to each category provide a good starting point to discuss three-dimensional SBLI phenomena. The basic structure of such three-dimensional compression ramp SBLIs is shown in figures 2.20a and 2.20b.

2.10.1. Separation in Three-Dimensional Flow

In two dimensions, the separation bubble is typically defined by a separation point, a reattachment point, and a connecting streamline; the gas flows about a central point located at the center of the circulation region, as illustrated in figure 2.21a.

However, this description is often inadequate for separation in three dimensions [19]. In three dimensions, the separation region is no longer closed (shown in figure 2.21b). Rather, the streamlines

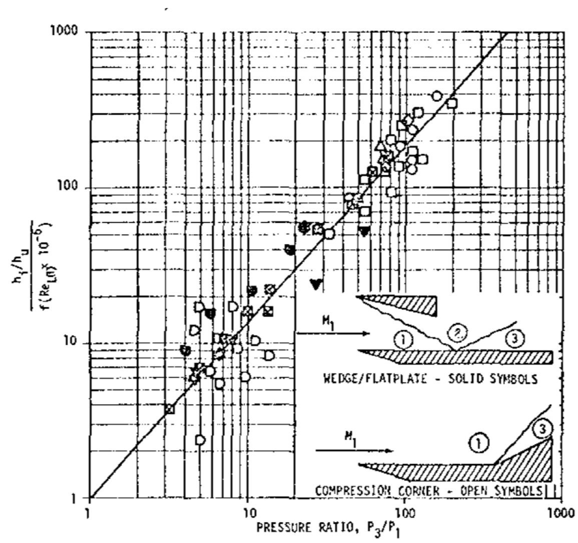

$h_1/h_u = (P_3/P_1)^{1.13} f(Re_{L(1)} \times 10^{-6})$

$f(Re_{L(1)} \times 10^{-6}) = 0.468 (Re_{L(1)} \times 10^{-6})^{1.85}$ WHEN $Re_{L(1)} > 0.5 \times 10^6$

$f(Re_{L(1)} \times 10^{-6}) = 0.13$ WHEN $Re_{L(1)} < 0.5 \times 10^6$

Figure 2.18: Heat transfer correlation for laminar flow [2, 26]. Figure adopted from Hung and Barnett [26].

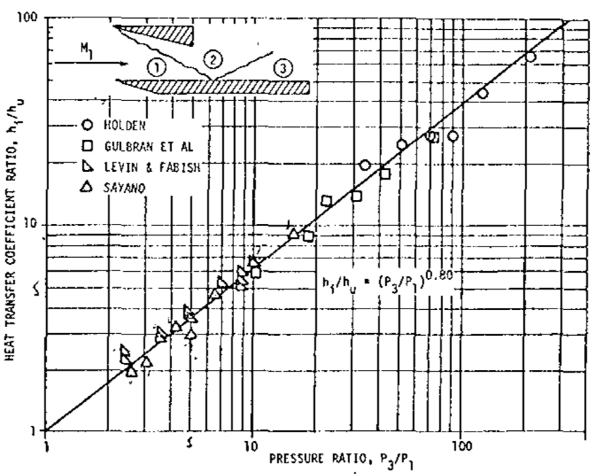

Figure 2.19: Heat transfer correlation for turbulent flow [2, 26]. Figure adopted from Hung and Barnett [26].

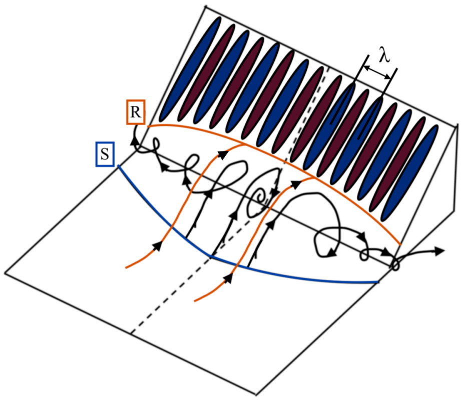

(a)

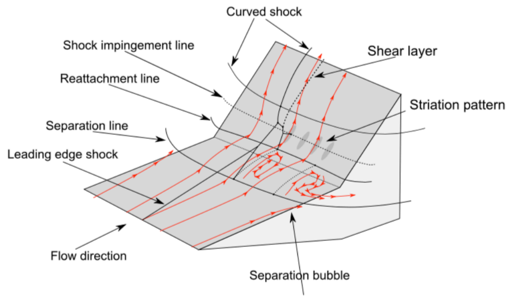

(b)

Figure 2.20: (a): Physical characteristics of steady three-dimensional ramp circulation. **S** denotes separation; **R** denotes reattachment. The maroon and blue streaks represent regions of high- and low-heat transfer to the surface, respectively. λ denotes the periodic wavelength between the regions of surface heat transfer. (b): Physical phenomena of double ramp flows. Figure from Schrijer [51].

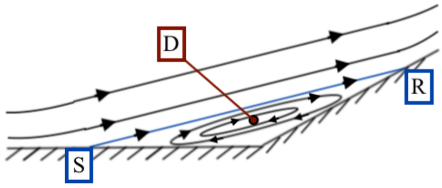

(a) Two-dimensional flow.

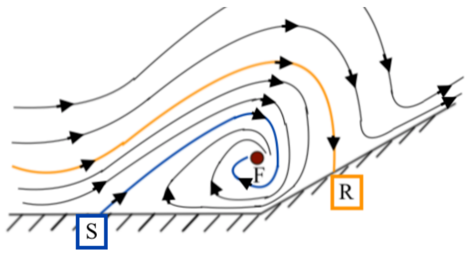

(b) Three-dimensional flow. For orthographic view, see figure 2.20a.

Figure 2.21: Simplified illustrations of two-dimensional and three-dimensional separated flows. **S** denotes the separation point; **R** denotes the reattachment point; **D** denotes the center of the 2D circulation bubble; **F** denotes the focal point of circulation in the 3D bubble.

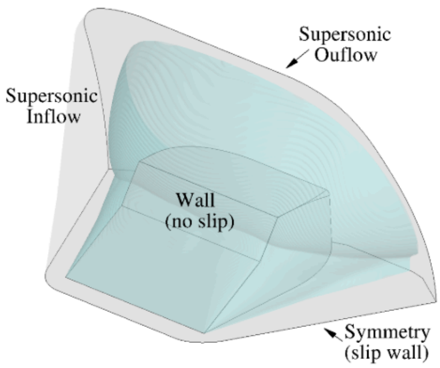

(a) Oblique and bow shock (cyan) demonstrating the gas' ability to flow in the streamwise direction.

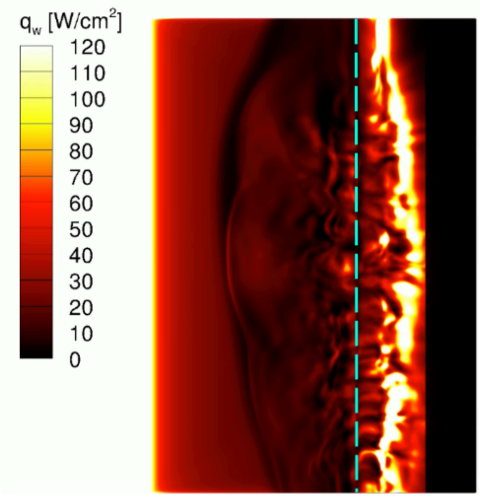

(b) Instantaneous top-down view of surface heat flux. Flow is from left to right. The curved separation line is visible as the dark shade at left with larger separation length near the ramp centerline and smaller separation length near the ramp's lateral edges.

Figure 2.22: DNS of a high-speed double ramp simulation. Figures from Reinert *et al.* [37].

swirl toward a central focal point while simultaneously traveling laterally away from the ramp centerline toward the ramp edge. The streamline connecting the separation point and reattachment point no longer exists. Instead, the streamline originating at the separation point joins the other circulation streamlines in spiraling toward a focal point and escaping laterally toward the ramp edge. Conversely, the streamline that stagnates on the ramp (and hence acts as a reattachment point) originates upstream of the separation point and flows over the separation streamline. Together, figures 2.21a and 2.21b depict the main differences between two-dimensional and three-dimensional separation, while figures 2.20a and 2.20b present orthographic views with an emphasis on the separation, reattachment, and circulating streamlines. Figures 2.20a and 2.20b also show that the gas, in general, flows laterally toward the edge while simultaneously 'spiraling' toward the focal point **F**.

The three-dimensional flow now has the option of escaping in the spanwise direction when confronted with an adverse pressure gradient, e.g. a shock or post-shock region. Figure 2.22a shows the shock profile of a double ramp flow, illustrating the extent to which the flow will diverge in the lateral directions if allowed to do so (i.e. no side walls). The curved separation lines of figure 2.22b depict the curved separation 'line' inherent in three-dimensional ramp flows. The post-shock region near the centerline presents a larger pressure gradient than the post-shock regions near the lateral edges. As such, the gas, once it passes through the leading edge oblique shock, follows the path of least resistance and develops a spanwise velocity profile, traveling toward either lateral edge [37].

The flow 'spilling' off to the sides, termed "spillage", also affects the flow in the circulation region. The reduced cross-sectional area of the circulation region, particularly as the flow nears the edge, indirectly reduces the shock strength and thereby the shock standoff distance. This in turn reduces the separation length [19].

The recirculation region, though generally presented as stable and steady in sections 2.5 - 2.9, often fluctuates with some particular frequency or frequencies [37], which influences the flow's transition to turbulence and shock structure. Furthermore, the circulation region may be so unstable and the fluctuating amplitudes so extreme that the bubble may 'burst' and lose all recognizable SBLI structure before coalescing and reforming a coherent circulation region [37] (see figure 2.23).

Due to a lack of distinct separation or reattachment point, is is necessary to adopt an entirely different approach to describe three-dimensional separation and reattachment locations. The procedure widely adopted by the SBLI community is *critical point theory*, proposed by Legendre [29]. The theory

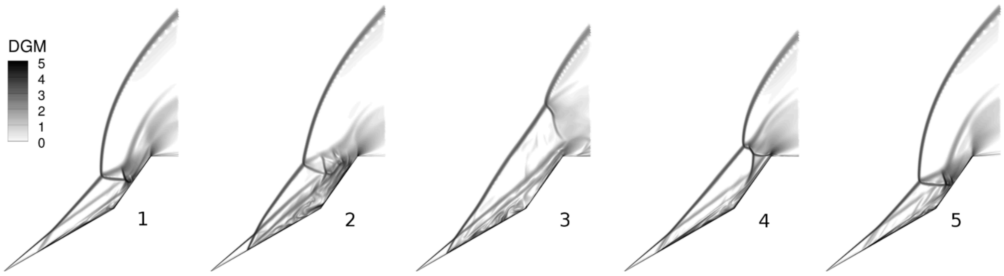

Figure 2.23: DNS time series of a fluctuating double ramp SBLI. Snapshots begin at 6.67 ms and end at 7.19 ms after the flow has set up. $M_\infty = 7.11$, $Re/m = 1.10 \times 10^6$. Figure adapted from Reinert *et al.* [37].

adopts the lines of zero skin friction as the separation and reattachment 'locations', which are essentially locations of stagnant flow on the surface. The point at which the value of the skin friction vanishes is termed a *critical point*, and can be further divided into a *node*, *saddle-point*, or *focus*. Examples of these are presented in figures 2.24 and 2.25. It is essential to identify the flow structure at separation and reattachment, despite the difficulties in doing so. As such, we must recognize the most important and common features of *critical points*:

- The lines of skin friction (and hence the flow at the surface) pass through a *node* (figure 2.24a), which can be further divided into a *separation node* or an *attachment node*.
- If the skin friction at a point is axisymmetric, the node is termed an *isotropic node* (figure 2.24b).
- All skin friction lines adopt a hyperbolic shape around a *saddle point* (figure 2.24c), save for two that run through the *saddle point* directly, which are termed *separators*.
- The flow at the surface may spiral around a *focus* (figure 2.24d), at which the shear lines eventually terminate.
- If the flow is strongly two-dimensional, the spiral around the *focus* may evolve into a *center* (figure 2.24e).

Three-dimensional flows are said to be separated if the lines denoting skin friction form at least one saddle point, through which a separation line passes.

2.10.2. Reattachment in Three-Dimensional Flow

In two dimensions, reattachment is typically presented as being fairly steady and having one single reattachment point. In three-dimensional flows, this is not the case, and reattachment is typically classified by the same critical point theory used to describe three-dimensional separation (section 2.10). As such, this section mainly focuses on the three-dimensional phenomena that occur at reattachment, which are immensely complex, quite numerous, and which strongly interact with one another. Both experiments and numerical simulations experience difficulty accurately observing and explaining reattachment phenomena [10, 22, 40], and this field is a continuously developing area of high-speed research.

The aforementioned experiments and simulations observe periodic streamwise temperature striations in the reattachment and post-reattachment area, often relating to a critical ramp angle or freestream Mach or Reynolds number, shown in figures 2.27 and 2.28b. These streaks are observed over a range of ramp angles, Mach numbers, and surface temperatures [6, 20, 42], and are generally attributed to streamwise vortical structures that arise in the reattachment region due to destabilizing centrifugal forces [22]. These vortical structures are typically identified as Görtler vortices that form when the curved streamlines at reattachment amplify instabilities inherent in the flow. Figure 2.28a illustrates the conditions under which they might form in compression SBLIs. The wavelength of the streaks is typically on the order of two times the thickness of the boundary layer at reattachment [27, 42]. Experiments by de Luca *et al.* [15] and de la Chevalerie *et al.* [14] in Mach 7.1 flow conditions show that the streak wavelength decreases with increasing unit Reynolds number and with decreasing distance from flat-plate leading-edge to ramp corner. Furthermore, Roghelia *et al.* [42] show that increasing

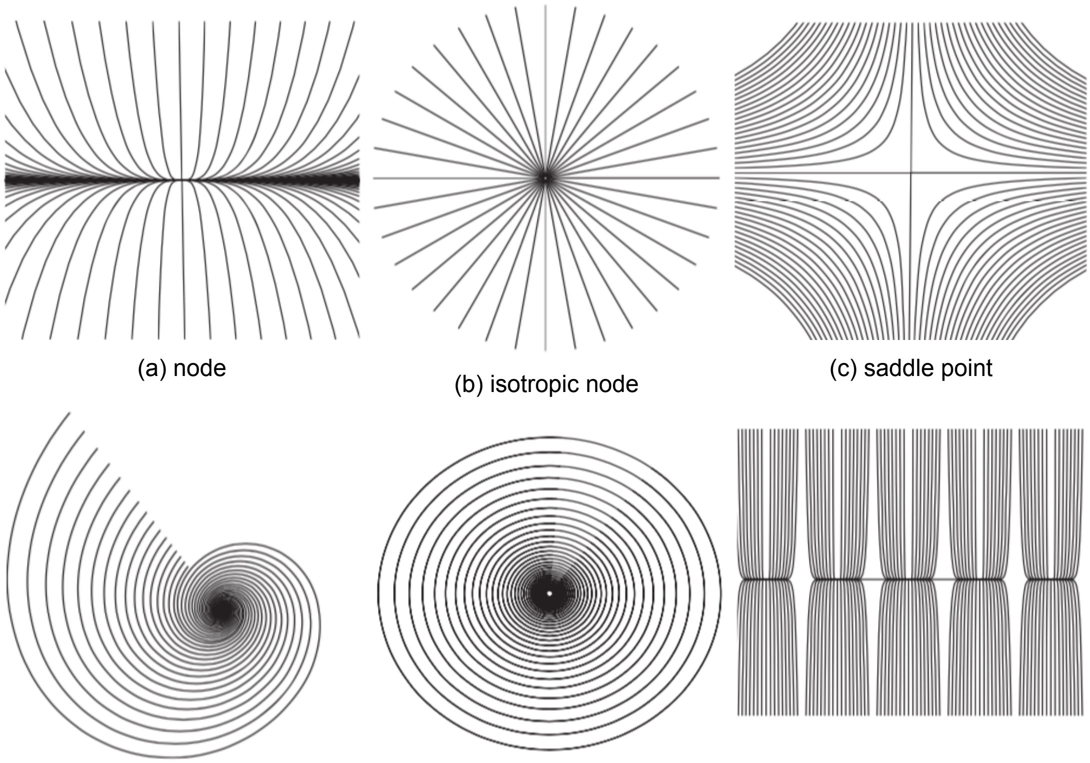

(a) node (b) isotropic node (c) saddle point

(d) focus (e) center (f) saddle-node combination

Figure 2.24: Critical points of surface flow patterns. Figures adapted from Délery [19].

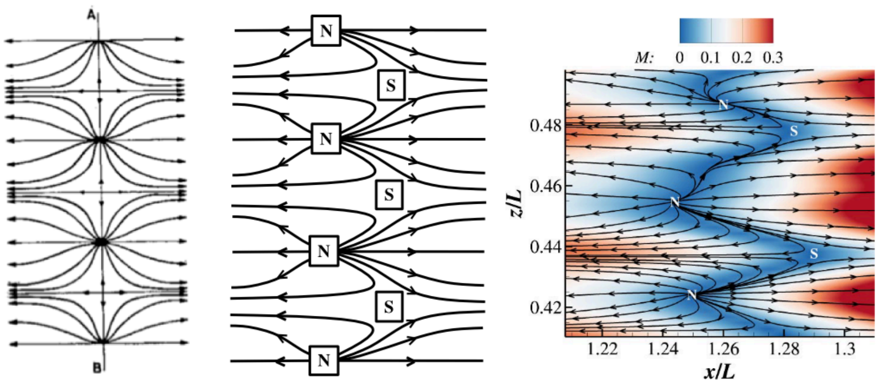

Figure 2.25: Nodes (N) and saddle points (S) at reattachment. Results obtained from DNS. Figure adapted from Cao *et al.* [10].

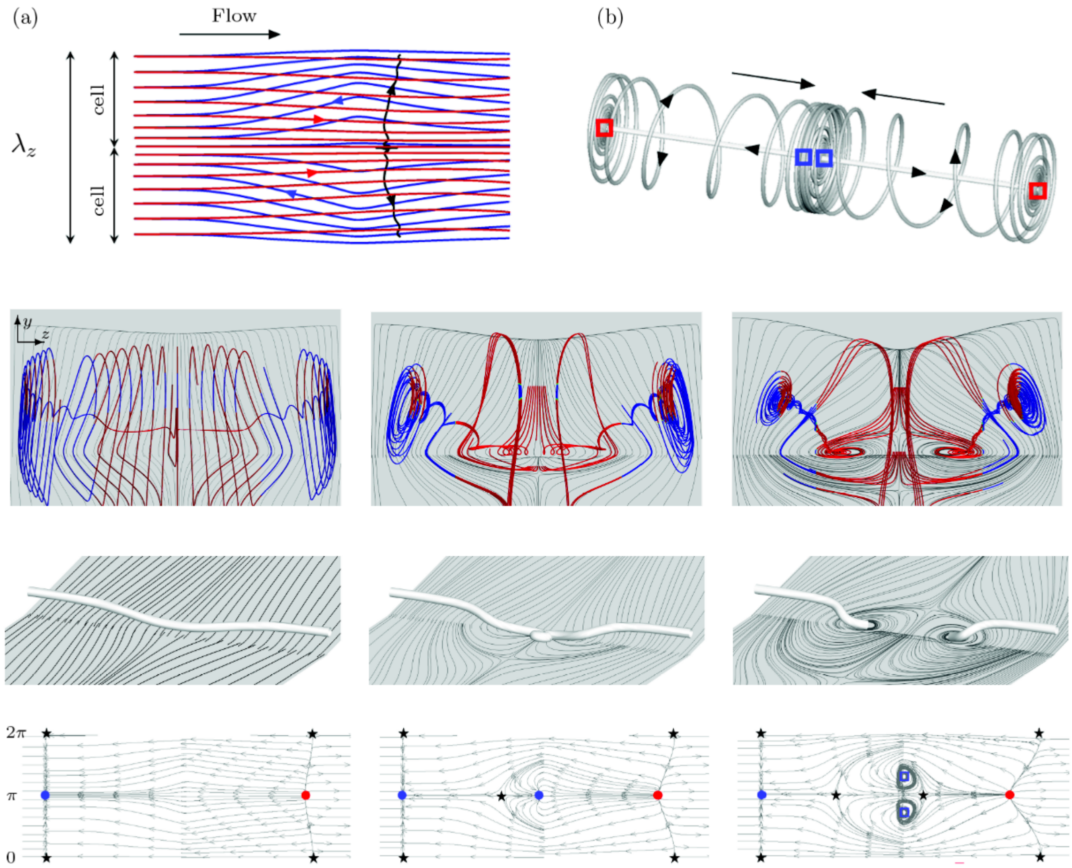

Figure 2.26: Three-dimensional circulation region and its affiliated steady/unsteady vortical structure. Results obtained by DNS. Critical points of wall streamlines: • represents nodes; ⋆ represents saddle points; □ represents foci. Red streamlines are unstable and blue are stable. Figures adapted from Gs *et al.* [22].

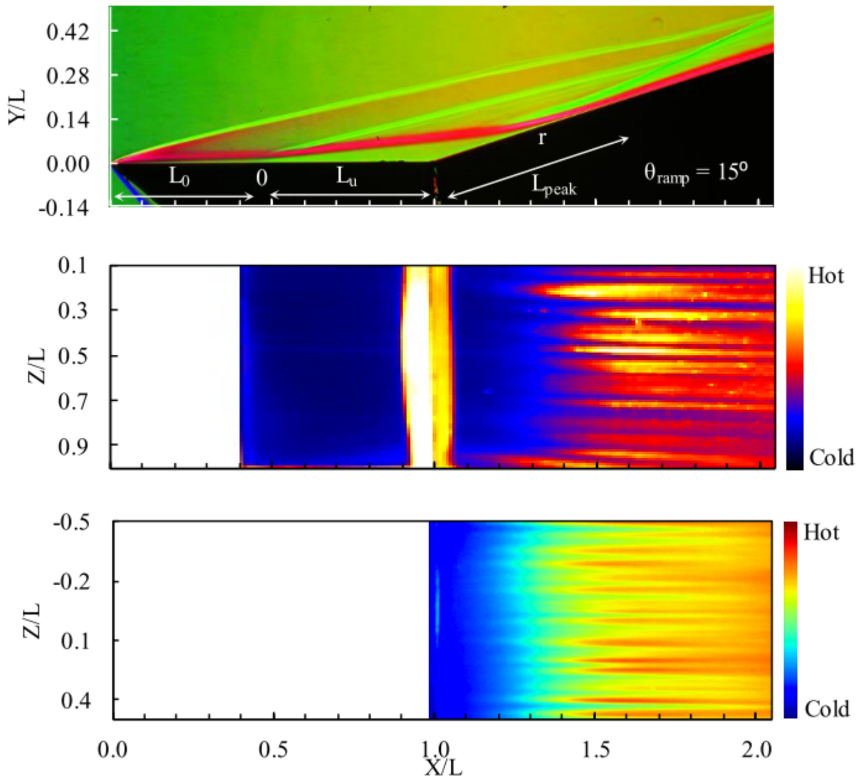

Figure 2.27: Görtler-like signatures induced by hypersonic ramp flow: Top: schlieren image; middle: infrared image; bottom: thermal-sensitive paint image. Figures adapted from Roghelia *et al.* [40].

the flat-plate leading edge radius (i.e. 'blunting' the leading edge) for a Mach 8 15° ramp thickens the boundary layer and therefore increases the streak wavelength. Hence, these studies suggest that the streak wavelength scales with the local boundary layer thickness. And because the streaks are associated with the vortical structures at reattachment, this further suggests that the vortical structures also scale with the local boundary layer thickness.

Upstream roughness also has an effect on the formation of streamwise heat flux patterns. Caljouw [8] conducted Mach 7.5 15°-45° ramp experiments with and without roughness strips near the model leading edge and observed stark differences in the surface streak patterns in the separation zone and at reattachment (figures 2.29a and 2.29b). Figure 2.29c presents infrared thermography results of the flow with roughness. The physical mechanism responsible for the formation of these streaks may be fundamentally different from the results discussed prior due to large ramp angle involved. At such a large angle, the inviscid shock structure changes from Edney type VI to Edney type IV/IVr/V [22].

The connection between the wavelength of the streamwise vortices and the local boundary layer thickness is discussed by Gs *et al.* in their DNS analysis of three-dimensionality in a Mach 5 slender double ramp flow and the growth of spanwise periodic flow structures [22]. They find that the flow is fundamentally three-dimensional, even when undisturbed by upstream perturbations, and that the cause of three-dimensionality is a linear instability present in the nominally two-dimensional recirculation bubble. Furthermore, their analysis suggests that the periodic spanwise streaks in the reattachment area are directly caused by the three-dimensionality in the recirculation region – *not* the centrifugal instability (i.e. Görtler instability or Görtler vortices). They reach this conclusion simply due to the fact that the Görtler instability implies the existence and contribution of upstream perturbations in the formation of Görtler vortices and streaks [23], but their analysis involves a disturbance-free upstream flow. Hence, there are no external disturbances in their flow. In fact, they theorize that the centrifugal instability might also have its origins in the three-dimensionality of the recirculation bubble. However, they also recommend further analysis to better understand the role and influence that such three-dimensionality has on the downstream flow. Results from their work are presented in figure 2.26. For further details,

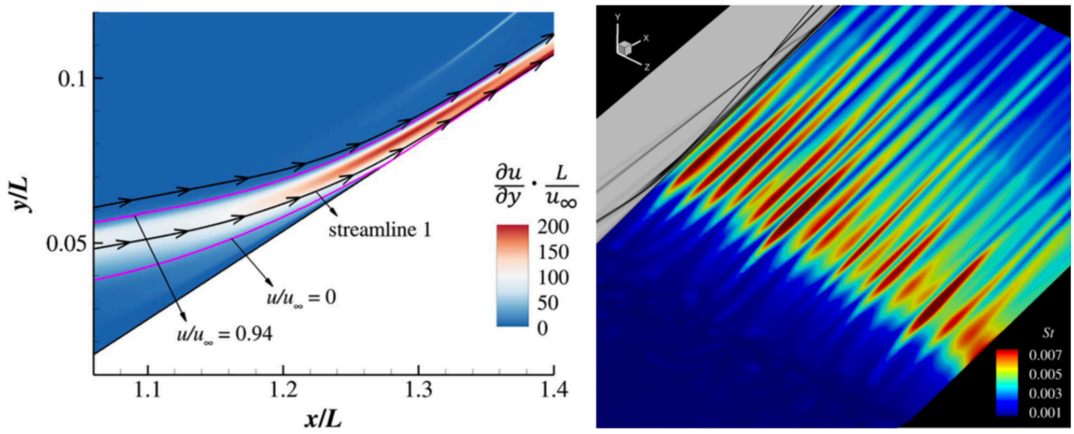

(a) (b)

Figure 2.28: (a) Velocity gradient contours and concave streamlines in the vicinity of a reattaching shear layer. (b) Time-averaged Stanton number distribution in the post-reattachment region. Results obtained with DNS. $M_\infty = 7.7$, $Re_{\infty,L} = 4.2 \times 10^5$, $\theta_{ramp} = 20°$. Images adapted from Cao *et al.*.

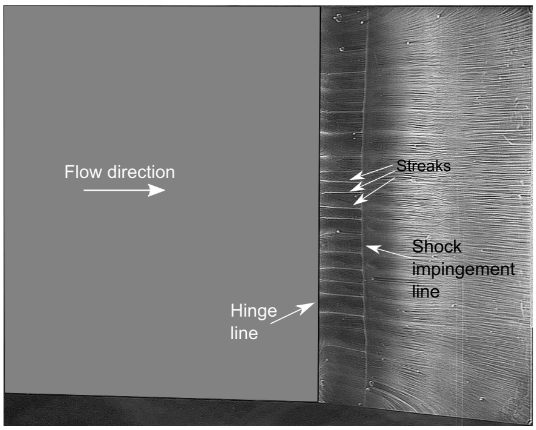

(a) Oil flow visualization on second ramp without roughness strip.

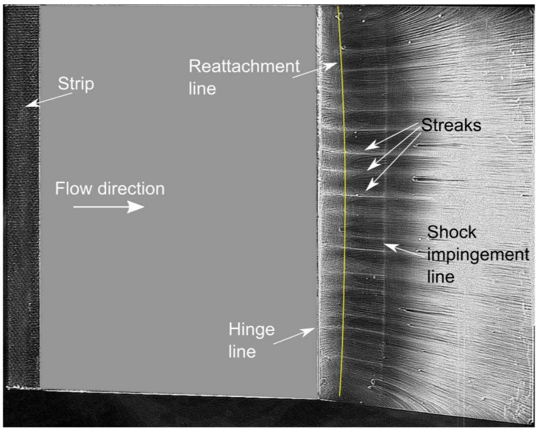

(b) Oil flow visualization on second ramp with roughness strip.

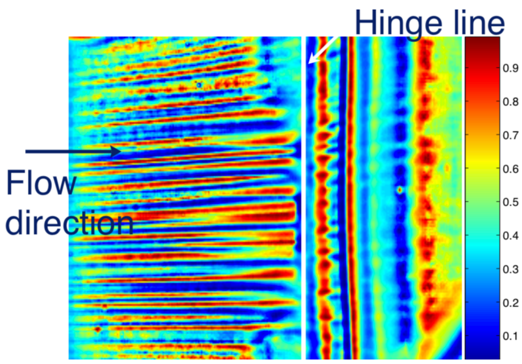

(c) Stanton number without roughness strip.

Figure 2.29: Oil flow and Stanton number visualization of a Mach 7.5, $Re_L = 1.13 \times 10^6$, 15°-45° double ramp flow. Figures adapted from Caljouw [8].

the reader is directed to their work: [22].

It has been theorized that the imperfections in the leading edge are the source of streamwise streaks. But several studies have observed such streaks even with high-quality sharp leading edges. Roghelia *et al.* observed streaks on two different 15° ramp geometries in two different experimental facilities [40]. Matsumura performed experiments on a scramjet forebody geometry and observed regularly spaced streamwise vortices on the compression ramp even with a high-quality edge and an absence of controlled disturbance generators [32]. Zhuang *et al.* [61] employed the nano-tracer planar laser scattering over a 25° compression ramp in a Mach 3 facility and observed Görtler-like vortices not only in the reattachment region but also in the separation area. Furthermore, three dimensional simulations of a cone-flare at Mach 11 carried out by Brown *et al.* [7] suggest that three-dimensionality in the separation zone contributes to the formation of streamwise streaks at reattachment independent of the Görtler instability of the reattaching shear layer.

Therefore, several studies speculate or observe that instabilities present in the separation region are at least partially responsible for the streamwise streaks in the reattachment region, but there remains to be a concerted effort in the high-speed SBLI community to thoroughly investigate this hypothesis.

3
Experimental Setup

This chapter describes the working principle of the HTFD and the flow conditions employed to study compression SBLIs. Section 3.1.1 describes the working principle of the Ludwieg tube concept and the specific dimensions and capabilities of the HTFD itself. Section 3.1.2 extends on the Ludwieg tube working principle and applies those concepts to the HTFD, presenting sample freestream conditions and describing the conditions used for the work in this thesis. Section 3.2 describes the experimental models used to study shock–boundary-layer phenomena in the Hypersonic Test Facility Delft. The setup is loosely composed of three main parts: the flat plate (section 3.2.1), the ramp geometry (section 3.2.2), and the sinusoidal roughness element (section 3.2.3).

3.1. Hypersonic Test Facility Delft (HTFD)

3.1.1. Working Principle

The experimental facility used in this campaign is the Hypersonic Test Facility Delft (HTFD), located within the Aerospace Engineering faculty of TU Delft. The HTFD employs the Ludwieg tube concept to simulate Mach numbers comparable to those experienced in real flight. The Ludwieg tube is a 'cold' hypersonic tunnel concept whereby the gas in question (air, in this case) obeys calorically and thermally perfect gas assumptions, meaning that real gas effects (ionization, nonequilibrium, etc.) are absent.

A Ludwieg tube schematic is presented in figure 3.1. The flow condition at the test section depends on the pressure and temperature of the gas flowing from the storage tube [35]. The air is evacuated from the nozzle and test section while being isolated from the storage tube by a diaphragm. The test gas is pumped from a high-pressure reservoir into the storage tube until specified temperature and pressure values are reached, at which point the diaphragm ruptures and the gas begins to flow through the nozzle. Some facilities heat the storage tube to increase the pressure and achieve greater velocities, temperatures or Reynolds numbers in the test section, which is the case for the HTFD. When the test gas flows through the nozzle, the flow achieves hypersonic conditions. The gas, now at a hypersonic velocity, continues through the test section, through the diffuser, and into the low-pressure chamber. Alternatively, a valve or piston may be used instead of a diaphragm, but the overall procedure is the same. The test ends when the facility achieves equilibrium between the storage tube and low-pressure chamber, at which time the gas stops flowing through the test section. However, the actual test time (pertaining to the desired test conditions) may likely be much shorter. Figure 3.2 shows an overview of the HTFD alongside a view of the test section.

The test for the HTFD begins when the piston located at the nozzle is retracted and the high-pressure air in the storage tube begins to flow into the test section. When the air begins to flow out of the storage tube, an expansion wave propagates 'upstream' until it contacts the wall farthest from the valve. A reflected expansion wave then propagates back toward the valve. When the wave reaches the valve, the flow conditions at the nozzle throat become modified and the test is finished.

A particular feature of the HTFD is the dual nozzle setup (shown in figure 3.3), which allows the facility to simulate a more diverse range of Mach numbers. The first nozzle is termed the throttle nozzle, while the second (optional) nozzle is termed a nozzle insert. The throttle nozzle works with the piston to act as the diaphragm separating the high-pressure air of the storage tube from the vacuum of the test section and vacuum chamber. The contracting cross-sectional area of the throttle nozzle is designed to accelerate the flow to Mach 9, while the various nozzles that can be inserted just downstream have cross-sectional areas that accelerate/decelerate the flow to Mach 6-8. As shown in figure 3.3, the settling chamber in between the two nozzles is necessary to decelerate the flow from Mach 9 to Mach 6-8. Hence, the flow first accelerates to Mach 9, decelerates to a subsonic velocity, and then accelerates to Mach 6-8.

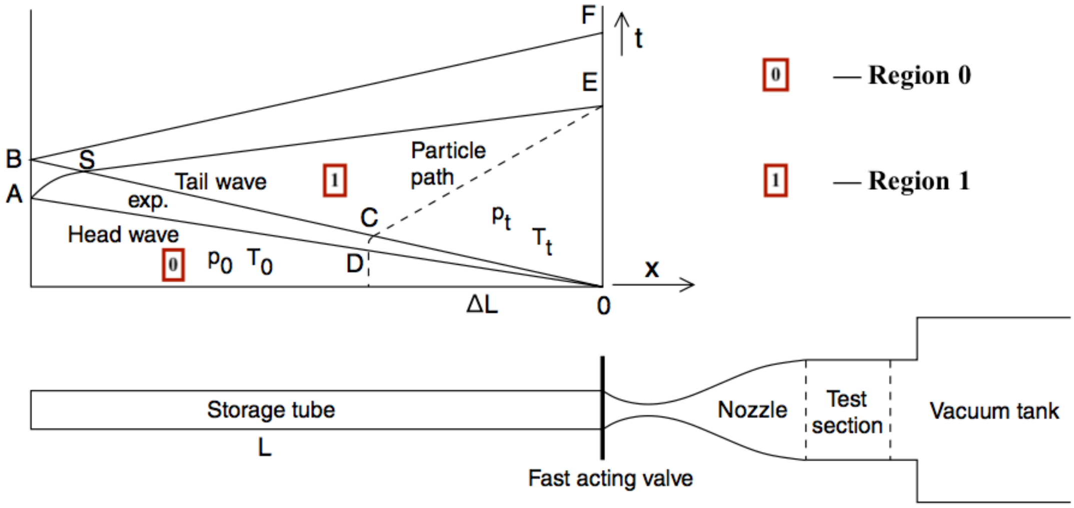

Figure 3.1: Schematic of the Ludwieg tube concept. Figure adapted from Caljouw [8].

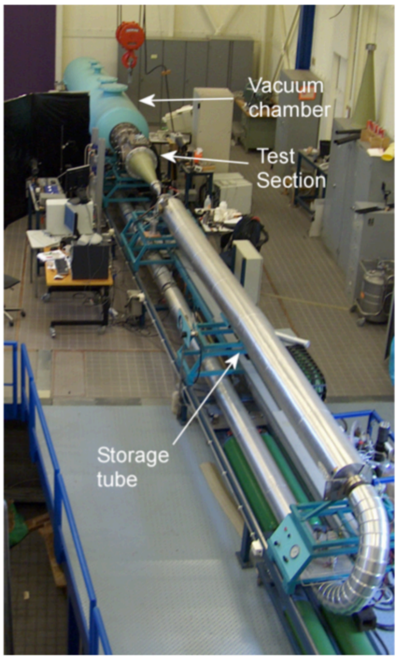

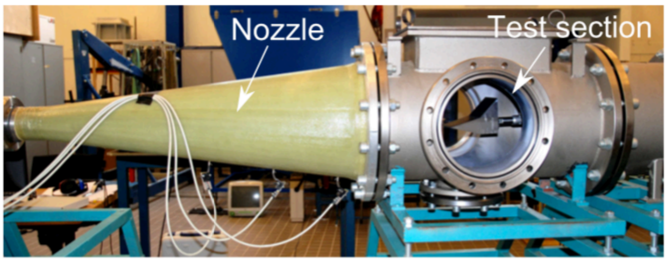

Figure 3.2: Hypersonic Test Facility Delft: overview (left) and test section (right). Figure adapted from Caljouw [8].

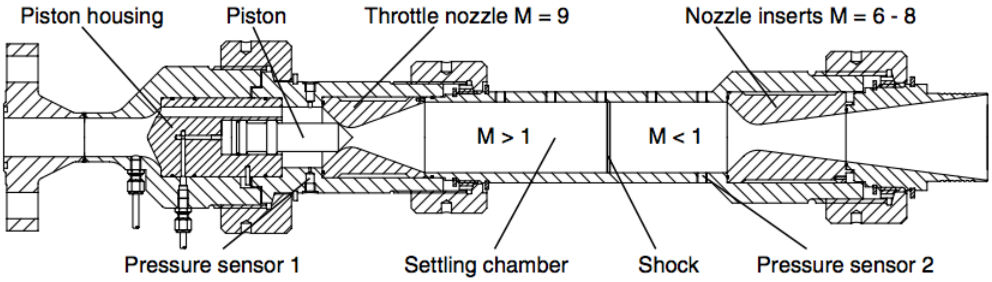

Figure 3.3: HTFD tandem nozzle block. Figure adapted from Ekelschot [20].

Using “simple wave” theory, the flow conditions in the storage tube can be determined. Using the Riemann-invariant theory, the downstream characteristics (AE and BF in figure 3.1) can be described by:

$$u_1 + \frac{2a_1}{\gamma - 1} = \frac{2a_0}{\gamma - 1} \tag{3.1}$$

where the subscript 0 denotes initial storage tube conditions and the subscript 1 denotes post-expansion wave conditions (see figure 3.1). We may rewrite equation 3.1 as:

$$\frac{u_1}{a_0} = \frac{M_1}{1 + \frac{\gamma-1}{2} M_1} \tag{3.2}$$

where M_1 is the post- expansion wave Mach number:

$$M_1 = \frac{u_1}{a_1} \tag{3.3}$$

According to isentropic relations and mass conservation, the Mach number downstream of the expansion wave M_1 is determined by the ratio of the storage tube area to the critical throat area:

$$\left(\frac{d_{tube}}{d^*}\right)^2 = \frac{1}{M_1}\left[\frac{2}{\gamma + 1}\left(1 + \frac{\gamma - 1}{2} M_1^2\right)\right]^{\frac{\gamma+1}{2(\gamma-1)}} \tag{3.4}$$

where $d_{tube} = 48.25mm$ is the diameter of the storage tube, and $d^* = 19.35mm$ is the critical throat diameter. (Here we clarify that the critical throat is the M9 nozzle, depicted in figure 3.3 and table 3.1.)

The total test time is dictated by the time required for the expansion wave to propagate upstream from the retracting piston to the end of the tube and back. A t-x diagram of this principle is shown in figure 3.1. The test time can be calculated by considering the differential equation that holds along the J^+ characteristic with boundary condition $x = -Lt_A = \frac{L}{a_0}$ [51]:

$$\frac{dx}{dt} = u + a = \frac{1}{\gamma + 1}\left(4a_0 + (3 - \gamma)\,\frac{x}{t}\right) \tag{3.5}$$

The time at point (x_s, t_s) is given by:

$$t_1 = t_s - \frac{dt}{dx} x_s = t_s - \frac{x_s}{a_1 + u_1} \tag{3.6}$$

which we write as:

$$t_1 = \frac{L}{a_0}\frac{2}{1+M_1}\left(1+\frac{\gamma-1}{2}M_1\right)^{\frac{\gamma+1}{2(\gamma-1)}} \tag{3.7}$$

Equation 3.7 is the total test time of the HTFD. For the experimental conditions used in this thesis (storage tube pressures of $30\ bar$ and $95\ bar$) the total test time is approximately $100\ ms$. The ratio of pre- and post- expansion wave total pressures is, according to Bannink [3] and Schrijer [51], given as:

$$\frac{p_{t,1}}{p_0} = \left\{\frac{1+\frac{\gamma-1}{2}M_1^2}{\left(1+\frac{\gamma-1}{2}M_1\right)^2}\right\}^{\frac{\gamma}{\gamma-1}} \tag{3.8}$$

which corresponds to a ratio of total temperatures of:

$$\frac{T_{t,1}}{T_0} = \frac{1+\frac{\gamma-1}{2}M_1^2}{\left(1+\frac{\gamma-1}{2}M_1\right)^2} \tag{3.9}$$

3.1.2. Flow Conditions

The freestream conditions at the center of the test section are primarily dictated by the storage tube pressure and the diameter of the second nozzle. The second nozzle used in this thesis is exclusively the M7 nozzle (which, confusingly, produces Mach 7.5 flow in the test section), and the only storage tube total pressures employed are $p_{t_{tube}} = 30\ bar$ and $p_{t_{tube}} = 95\ bar$. For simplicity and validation purposes, the derivations in this chapter are performed at $p_{t_{tube}} = 100\ bar$ (to better compare with earlier work involving the same facility [8, 20, 30, 51]). Table 3.1 provides various nozzle diameters used to attain varying Mach numbers in the HTFD. It is important to note that while the physical diameter of the test section is $350\,mm$, the combination of the expanding flow through the second nozzle and the boundary layer that develops along the nozzle surface results in the flow behaving as if the diameter of the test section were significantly larger than what is physically true [8, 20]. Hence the larger test section diameter used in the subsequent calculations. We employ equation 3.4 and substitute the M7 nozzle diameter and the diameter of the test section from table 3.1 to calculate the freestream Mach number at the center of the test section:

$$\left(\frac{d_{M7}}{d_{\text{test section}_{\text{eff}}}}\right)^2 = \frac{1}{M_\infty}\left[\frac{2}{\gamma+1}\left(1+\frac{\gamma-1}{2}M_\infty^2\right)\right]^{\frac{\gamma+1}{2(\gamma-1)}} \tag{3.10}$$

where from table 3.1 and, considering that for perfect gas conditions, $\gamma_{\text{air}} = 1.4$, equation 3.10 provides a freestream Mach number of:

$$\boxed{M_\infty = 7.518 \approx 7.5} \tag{3.11}$$

For details regarding the boundary layer thickness along the inner surface of the nozzle, the flow expansion rate through the nozzle and test section, and the streamwise distance from the M7 throat to the center of the test section, the reader is referred to the work of Caljouw [8], Ekelschot [20], and Schrijer [51].

M	6	7	8	9	10	11	test section (effective)
$d\ [mm]$	48.0	34.3	25.38	19.35	15.12	12.06	434.81

Table 3.1: HTFD throat diameters. Values from Schrijer and Bannink [50].

The centerline freestream velocity used to correlate freestream values is adopted from PIV measurements presented by Caljouw [8] and Schrijer [51]. Figure 3.4 shows measured freestream velocity values along the test section centerline. At $x = 0\,mm$ in figure 3.4, the freestream velocity is approximately $1033\,m/s$:

$$\boxed{\vec{u} = 1033\,m/s} \tag{3.12}$$

Using the measured centerline freestream velocity and the freestream Mach number from equation 3.11, the we can calculate the static temperature in the test section by the definition of the Mach number and the speed of sound:

$$M = \frac{\vec{u}}{a} \tag{3.13}$$

where

$$a = \sqrt{\gamma RT} = \sqrt{\frac{\gamma p}{\rho}} \tag{3.14}$$

where $\gamma = 1.4$ and $R = 287.058\,J/(kg * K)$.
We substitute equation 3.14 into equation 3.13 to obtain an expression for the static temperature at the center of the test section:

$$T = \frac{\left(\frac{\vec{u}}{M}\right)^2}{\gamma R} \tag{3.15}$$

Substituting $1033\,m/s$ for $\vec{u}$, 7.5 for M, and the previously stated values of γ and R yields:

$$\boxed{T = 47\,K} \tag{3.16}$$

The total temperature is calculated from the energy equation:

$$T_t = T + \frac{|\vec{u}|^2}{2c_p} \tag{3.17}$$

where c_p for air at the specified conditions is approximately: $c_p = 1001\,J/(kg * K)$.
The total temperature of the freestream at the center of the test section is therefore:

$$\boxed{T_t = 579\,K} \tag{3.18}$$

The results derived thus far are summarized in table 3.2.

Velocity	$\lvert V \rvert$	=	$1033\,m/s$
Mach Number	M	=	7.5
Static Temperature	T	=	$47\,K$
Total Temperature	T_t	=	$579\,K$
Total Enthalpy	H_0	=	$0.56\,MJ/kg$

Table 3.2: Freestream conditions for the Mach 7 nozzle setup. Values from Schrijer [51].

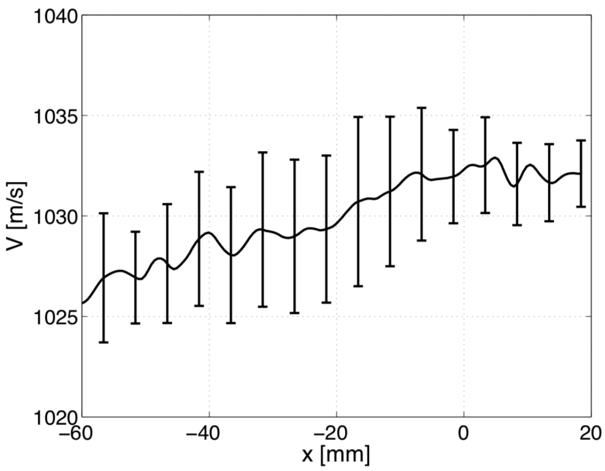

Figure 3.4: Streamwise velocity measurements at the centerline of the test section for the M7 nozzle. Figure adapted from Schrijer [51].

We extend our analysis to consider the total and static pressures of the freestream.

The total pressure of the freestream is inferred from Pitot tube measurements and the previously derived value of the freestream Mach number through the Pitot tube formula employed in supersonic flows:

$$\frac{p_{t_p}}{p_{t_\infty}} = \left[\frac{\gamma + 1}{2\gamma M^2 - (\gamma - 1)}\right]^{\frac{1}{\gamma-1}} \left[\frac{(\gamma + 1)\, M^2}{(\gamma - 1)\, M^2 + 2}\right]^{\frac{\gamma}{\gamma-1}} \tag{3.19}$$

where p_{t_p} is the total pressure as measured by the Pitot tube and p_{t_∞} is the total pressure of the freestream.

The static pressure of the freestream p_s is correlated to the total pressure of the freestream p_{t_∞} through the relation

$$\frac{p_{t_\infty}}{p_s} = \left(1 + \frac{\gamma - 1}{2} M^2\right)^{\frac{\gamma}{\gamma-1}} \tag{3.20}$$

The procedure used to determine p_{t_∞} involves using static pressure taps located along the nozzle wall and Pitot tubes located at the center of the test section (see figure 3.5). The pressure taps and Pitot pressure values are provided by Schrijer [51] (figure 2.14 and table 2.8), which may be substituted into equations 3.19 and 3.20 to yield a freestream total pressure of $27.9\ bar$ (which corresponds to a storage tube pressure of $100\ bar$).

We calculate the speed of sound under these conditions by employing equation 3.3:

$$a = \frac{U_\infty}{M_\infty} = 137.7\ m/s \tag{3.21}$$

The density of the freestream under these conditions may be calculated by employing equation 3.14:

$$\rho = \frac{\gamma p}{a^2} = 0.032\ kg/m^3 \tag{3.22}$$

The dynamic viscosity μ may likewise be determined, albeit using Sutherland's law rather than fundamental physical relations. Sutherland's law, which is used to approximate the dynamic viscosity at a given specific temperature T is:

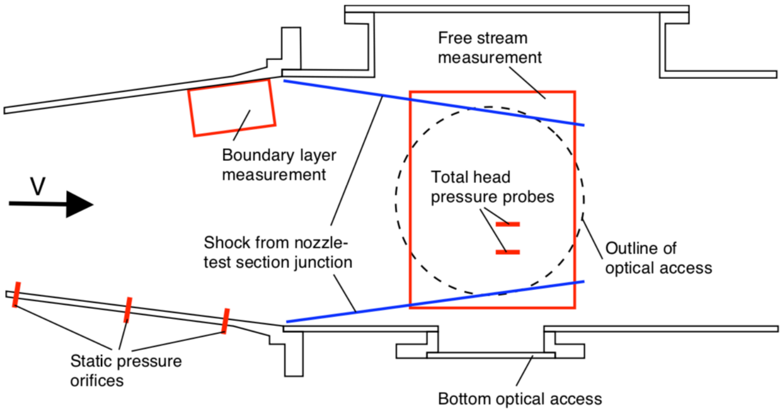

Figure 3.5: HTFD nozzle and test section. Figure adapted from Ekelschot [20].

$$\mu = \mu_r \left(\frac{T}{T_r}\right)\left(\frac{T_r + S}{T + S}\right) \tag{3.23}$$

where μ_r is the reference viscosity at reference temperature T_r. This analysis employs a reference temperature of $T_r = 288\,K$ and a reference viscosity of $\mu_r = 1.789 \times 10^-5\,kg/(m * s)$. The value of S is given as $S = 110\,K$. The (static) temperature at which we wish to evaluate μ is $T = 47\,K$ (from equation 3.16 or table 3.2). We therefore substitute the appropriate values for μ_r, T_r, S, and T into equation 3.23 to calculate μ under the stated conditions:

$$\boxed{\mu = 3.00 \times 10^{-6}\,kg/(m * s)} \tag{3.24}$$

The Reynolds number is defined as:

$$Re = \frac{\rho U_\infty L}{\mu} \tag{3.25}$$

where L is some prescribed length.

To determine the unit Reynolds number at the provided freestream conditions we simply substitute the appropriate values for ρ, U_∞, and μ into equation 3.25:

$$\boxed{Re/m = \frac{\rho U_\infty}{\mu} = 11.05 \times 10^6\,m^{-1}} \tag{3.26}$$

These results are summarized in table 3.3.

Nozzle	M	P_t $[bar]$	T_t $[K]$	$Re/m \times 10^6$ $[m^{-1}]$
M6	6.4	2.8	579	1.61
	6.5	14.3	579	7.90
M7	7.4	5.4	579	2.22
	7.5	28.0	579	11.05
M8	8.4	10.0	579	3.07
	8.5	51.2	579	15.08
M9	9.4	20.0	585	4.65
	9.5	88.0	585	19.70
M10	10.3	20.0	585	3.76
	10.5	88.0	585	15.85

Table 3.3: Freestream total quantities for various nozzles and total pressures. Values from Schrijer [51] and Ekelschot [20].

3.2. Model Setup

This section describes the model(s) used in this thesis to study shock–boundary-layer interactions. The entire model setup is loosely composed of three main parts: a flat plate, a compression ramp, and a sinusoidal roughness strip. Section 3.2.1 discusses the flat plate used to grow the boundary layer while section 3.2.2 discusses the compression ramps used to create the shock–boundary-layer interaction. Section 3.2.3 concludes the discussion by describing the sinusoidal roughness elements used to introduce perturbations into the boundary layer.

3.2.1. Flat Plate

An integral component in studying shock–boundary-layer interactions is, naturally, a boundary layer, which, depending on the flow conditions and setup of the experiment, may maintain its laminar profile or transition to turbulence. This section describes the flat plate used in the experiments to grow the necessary boundary layer as well as some of the considerations necessary to make it suitable for compression ramp shock–boundary-layer interactions. Crucial design factors involved in high-speed wind tunnel tests are therefore how best to grow such a boundary layer, how to control its formation, and how to monitor its behavior during each test. The difference in flow behavior between SBLIs that involve a *laminar* boundary layer versus those involving a *turbulent* boundary layer (described in chapter 2) make these considerations that much more important.

A common method employed by high-speed wind tunnels to grow such a boundary layer is to position a flat plate near the center of the test section. The work described in this thesis employs such a method with the particular consideration that, given the expanding flow in the test section, the plate must be positioned at the y-coordinate of zero y-component velocity. Figures 3.5 and 3.6 illustrate this difficulty.

Figure 3.7 presents a top-down view of the flat plate used in the experiments. The dimensions of the plate are $800\ mm \times 350\ mm$ with a sharp leading edge radius of $50\ \mu m$ to discourage the flow from developing leading edge instabilities [30]. Figures 3.5 and 3.7 additionally show the Mach waves generated by the walls of the tunnel (blue in figure 3.5, orange in figure 3.7), which propagate toward the center of the test section. Lodder [30] calculates μ to be an angle of $\mu \approx 8.3°$ assuming the flow to be at Mach 7.0, where the nozzle meets the test section.

In the context of this thesis, a longer flat plate allows for a thicker boundary layer to develop, which in turn allows the shear layer of the separated region to be larger than would be the case for a thinner boundary layer. The elongated shear layer affords more time for any instabilities in the flow to develop, which renders them (and their effects) stronger and more visible.

Figure 3.8 shows the boundary layer growth along the flat plate calculated using the reference temperature method (discussed in detail by Lodder [30]). The overall goals of the study concern observing SBLI phenomena, which is easier to achieve with a thicker boundary layer. Hence, the ramps are located as far downstream of the flat plate leading edge as possible while still allowing an unobstructed view from the thermal and high-speed cameras. This distance is taken to be $x = 417\ mm$.

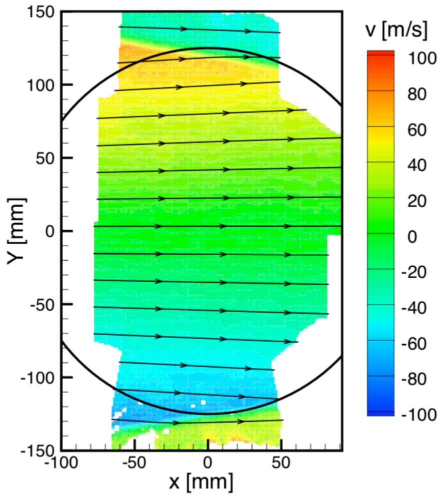

Figure 3.6: Y-component velocity at the center of the test section. Figure adapted from Ekelschot [20].

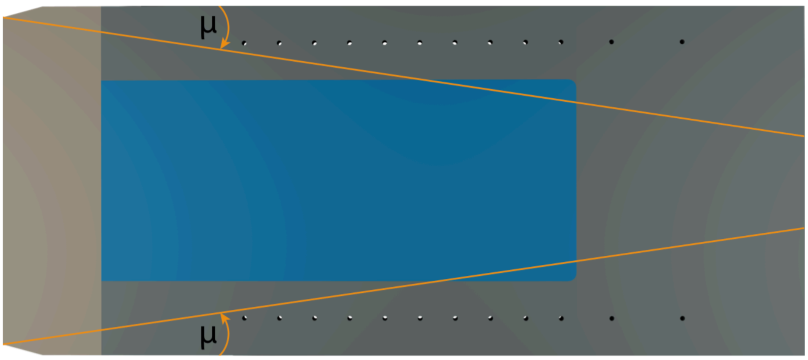

Figure 3.7: Top view of the flat plate used in the experiments. μ depicts the Mach waves created by the walls of the tunnel. Figure adapted from Lodder [30].

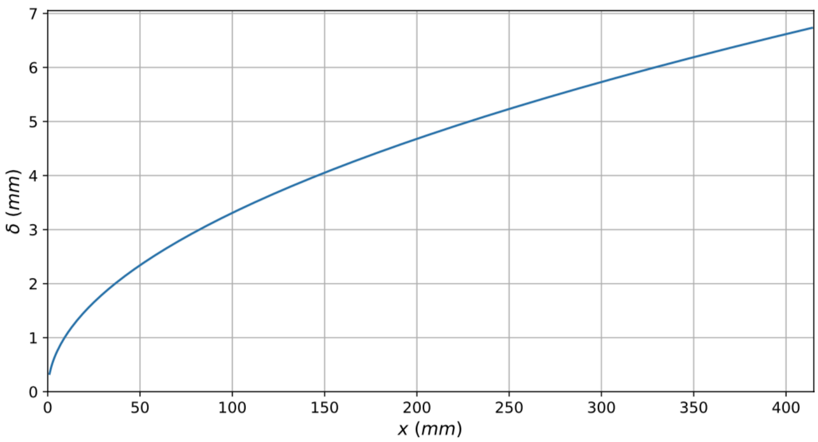

Figure 3.8: Boundary layer growth from the leading edge of the flat plate calculated using the reference temperature method, from Lodder [30].

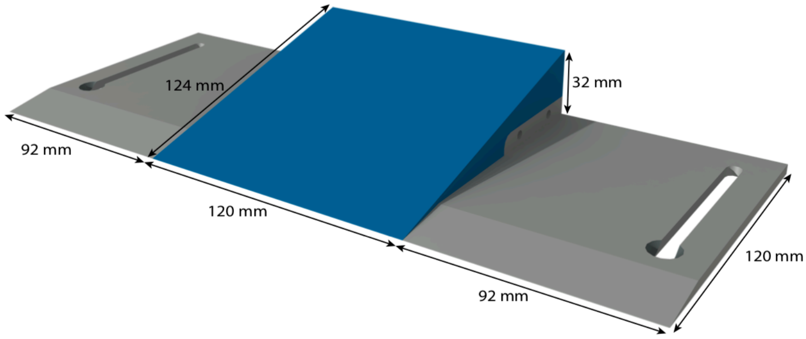

Figure 3.9: Orthogonal view of the 15° compression ramp. Figure adapted from Lodder [30].

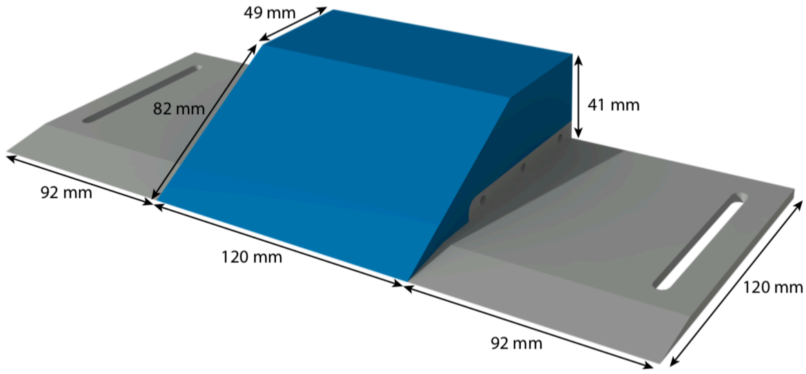

Figure 3.10: Orthogonal view of the 30° compression ramp. Figure adapted from Lodder [30].

3.2.2. Compression Ramps

The compression ramps used in the experiments are characterized by the following ramp angles: 15°, 20°, 25°, and 30°. The corner of each ramp is located $417\ mm$ downstream from the flat plate leading edge and produces a shock emanating from the ramp corner. The strength of the shock – and thereby the strength of the interaction – is dictated by the angle of the ramp: the greater the ramp angle, the greater the strength of the shock. Past studies involving experimental SBLIs typically employ ramp angles within this range to observe distinct yet relatable phenomena that can then be correlated and compared [30, 41, 42, 56].

Figures 3.9 and 3.10 provide example setups of the 15° and 30° ramp geometries, respectively. Ideally the ramps would span the entire width of the flat plate, but startup issues (described by Ekelschot [20]) restrict the total cross-sectional area of any models in the tunnel to a maximum of $130\ cm^2$. In addition, the Mach waves described in section 3.2.1 render a full spanwise model unnecessary. The ramps must also be wide enough to avoid three-dimensional effects, which can strongly influence the ramps if they are too narrow. Therefore, in order to minimize the likelihood of three-dimensional effects and maximize the cross-sectional area of the models, the maximum possible width is adopted for all models (i.e. all models have the same width). For dimensions of all ramps, see the work by Lodder [30].

The flat plate already accounts for $70\ cm^2$ of the cross-sectional limit. Hence, the ramps are limited to a width of $120\ mm$ and a maximum height of $41\ mm$ for a cross-sectional area of $49.2\ cm^2$. The total cross-sectional area of the flat- plate-ramp model is $119.2\ cm^2$, which is just within the limitations of $120\ cm^2$.

3.2.3. Sinusoidal Roughness Elements

Roughness elements themselves in the presence of hypersonic flow are neither novel nor new – isolated and distributed roughness elements in hypersonic flow have been studied since the sixties – but what has yet to be investigated is the presence of *sinusoidal* roughness and its influence on a downstream shock–boundary-layer interaction.

Roughness elements are typically used in real flight conditions to ‘trip’ a boundary layer and induce turbulence. Furthermore, they are generally identified as being either two-dimensional or three-dimensional, and being either isolated or distributed. But in the presence of a shock–boundary-layer interaction, the instabilities introduced into the flow are typically amplified by the nature of the recirculating flow. What makes this difficult to quantify and distinguish is the difficult nature of measuring the flow properties of a shock–boundary-layer itself and the fact that roughness at hypersonic conditions induce shocks that influence the entire flow field.

Recall that the main goal of this thesis is to observe how disturbances amplify or decay in the circulation region of a SBLI, and to additionally quantify their influence on the reattachment region on the ramp. Roughness strips in hypersonic flows are typically introduced to trip the boundary layer and transition the flow to turbulence, but this is not the goal in this thesis. The intention in using the roughness strip is purely to introduce slight disturbances into the flow through the boundary layer and record the results. Additionally, complicated geometries in supersonic flows are notoriously difficult to model correctly in CFD simulations, particularly when sharp edges are involved [9, 11, 19, 36, 55, 57]. The roughness used in this thesis is to be as ‘smooth’ as possible without rough edges or sharp corners, nor is it to be obtrusively large such that transition to turbulence is inevitable. Therefore, this work employs distributed, periodic roughness elements that display sinusoidal peaks in the spanwise direction and a Gaussian distribution in the streamwise direction.

The roughness strips must fulfill the following requirements:

- maximum roughness height must be less than the local boundary layer thickness
- each strip must taper to as fine a point as possible at all four sides to avoid introducing overly large instabilities and to simplify production
- the strips must be one complete piece (i.e. not two halves) to more easily insert and secure them on the model

In order to introduce slight disturbances yet maintain a laminar profile and avoid transitioning to turbulence, the height of the roughness strips should be less than the boundary layer thickness. In addition, they should be placed where the local boundary layer thickness is $1/2$ the thickness of the boundary layer at $417mm$ where the ramp is to be located [14, 15]. To determine the appropriate height and location of the strips, it is helpful to analytically calculate the boundary layer development along the flat plate.

According to figure 3.8, the undisturbed laminar boundary layer thickness at the x location where the corner of the ramps are to be located is approximately $\delta \approx 6.7\ mm$. The x location at which the boundary layer is approximately half of $6.7\ mm$ is $100\ mm$. As such, the strips are located at this x location. In keeping with the requirement that the roughness height should be less than that of the local boundary layer, the height of each strip is taken to be $h_e = 2.7\ mm$ with the height of the sinusoidal function being $2.5mm$ plus an additional thickness of $0.2mm$ to maintain structural integrity of the strips.

Research involving shock–boundary-layer interactions in the presence of sinusoidal disturbances is scarce, particularly when compared to similar work involving non-sinusoidal roughness – both isolated and distributed. The only closely related work identified during the course of this thesis is by Ulrich & Stemmer [58], Muppidi & Mahesh [34], de Luca *et al.* [15], and de la Chevalerie *et al.* [14], the latter two of which are very similar. Ulrich & Stemmer study periodic sinusoidal roughness but do so with direct numerical simulations and at drastically different freestream conditions than what is possible with the HTFD. Muppidi & Mahesh also perform DNS simulations of sinusoidal roughness but do so with the direct intention of transitioning an incoming laminar boundary layer to turbulence through the use of periodically distributed sinusoidal roughness in both the streamwise and spanwise directions. The only experimentally relevant studies of flow conditions similar to those of the HTFD are those of de Luca and de la Chevalerie. As such, the methods used in their work are closely leveraged for the experiments conducted for this thesis.

The choice of wavelength values for the roughness elements is adopted from the work of de Luca *et al.* and de la Chevalerie *et al.*, wherein the authors employ an identical experimental setup and flow conditions to study the effect of sinusoidal perturbations introduced into the flow by a sinusoidal leading edge. The experimental setup involving such a leading edge includes a 15° ramp fixed on flat plate lengths of 30 and $90\,mm$ with freestream Mach number of 7.14 and unit Reynolds number ranging from 7.6×10^6 to 24×10^6. With this setup the authors study the resulting heat flux striations on the surface of the 15° ramp.

The sinusoidal leading edge adopted in the study has a wavelength of $2\,mm$ and an amplitude of $0.5\,mm$. The authors arrive at these values by considering the undisturbed boundary layer thickness of the laminar flat plate at the peak location (δ_{p_k}) such that the ratio λ/δ_{p_k} lies between 1 and 4:

$$1 \leq \frac{\lambda}{\delta_{p_k}} \leq 4 \tag{3.27}$$

where λ is the wavelength of the sine wave.

For the flat plate in the HTFD (from both measurements and analytical calculations), $\delta_{p_k} \approx 4.5 - -7.0\,mm$. Applying the analysis of equation 3.27 to the boundary layer thickness of the laminar flat plate at the peak location ($417\,mm$) yields the expression:

$$1\left(\delta_{p_k}\right) \leq \lambda_e \leq 4\left(\delta_{p_k}\right) \tag{3.28}$$

where λ_e refers to the wavelength of the sinusoidal element.

For $\delta_{p_k} = 4.5\,mm$,

$$4.5\,mm \leq \lambda_e \leq 18.0\,mm \tag{3.29}$$

and for $\delta_{p_k} = 7.0\,mm$,

$$7.0\,mm \leq \lambda_e \leq 28.0\,mm \tag{3.30}$$

Therefore, the full range of candidate λ values for this work is:

$$4.5\,mm \leq \lambda_e \leq 28.0\,mm \tag{3.31}$$

In light of the range of values expressed by equation, 3.31, the following values of λ_e are used to design the sinusoidal roughness strips:

$$\lambda_e = \begin{cases} 6.0\,mm \\ 9.0\,mm \\ 12.0\,mm \\ 15.0\,mm \end{cases} \tag{3.32}$$

The values are incremented periodically by $3mm$ to simplify the design of the strips and the analysis of results.

In order to better compare the end results with respect to a change in strip wavelength, it is often helpful to nondimensionalize the roughness strip height or in this case spanwise wavelength by the local boundary layer thickness. Considering figure 3.8 and the fact that the strips are placed at $x = 100\,mm$, this thesis takes the local boundary layer thickness at $x = 100\,mm$ to be $\delta_{x=100\,mm} = 3.7\,mm$. Dividing the λ_e values of equation set 3.32 by $3.7\,mm$ therefore yields the associated value of λ_δ:

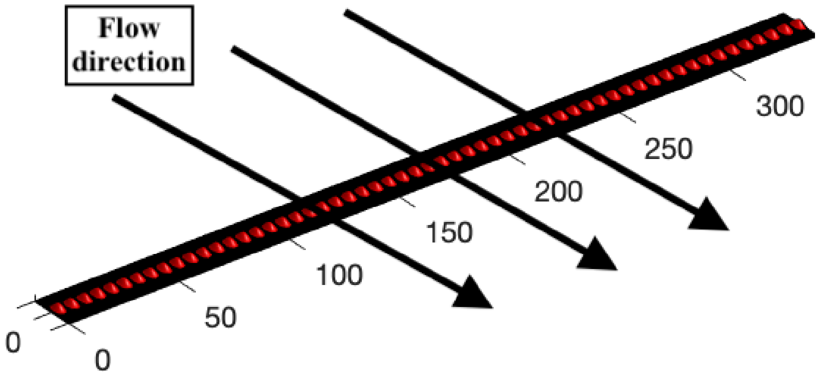

Figure 3.11: Orthogonal view of a sinusoidal roughness strip. The distance between peaks is $6\ mm$.

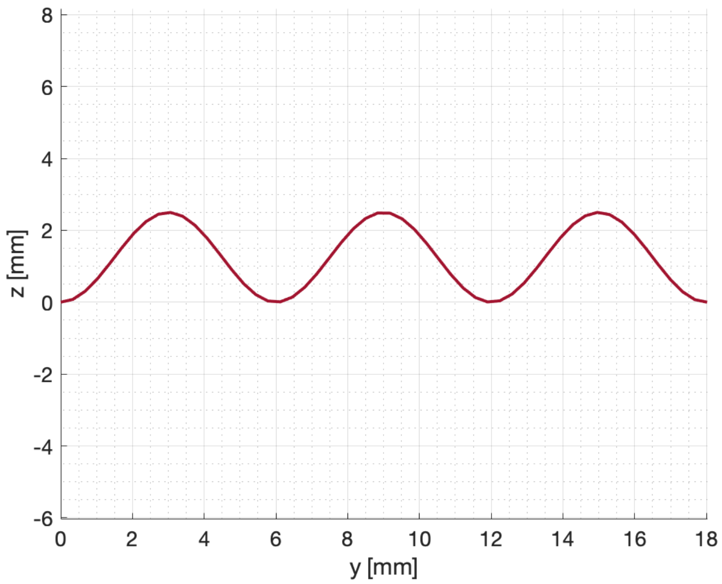

Figure 3.12: Enhanced spanwise view of the $\lambda = 6\,mm$ roughness strip. (The view into the page is in the streamwise direction.)

$$\lambda_\delta = \lambda_e / \delta_{x=100\ mm} = \lambda_e / 3.7\ mm = \begin{cases} 1.8 \\ 2.7 \\ 3.6 \\ 4.5 \end{cases} \tag{3.33}$$

The strips are modeled in the following way: first, the sinusoidal function is calculated for a total length of $350\ mm$ (the width of the flat plate) with the following equation:

$$z_{sinusoidal} = A\,sin(2\pi f y + \phi) + A \tag{3.34}$$

where $A = d/2$, $d = 2.5$ (the amplitude or height of the peak), $f = 1/\lambda_e$, $\phi = -\pi/2$, and y is the independent variable ranging from $0\,mm$ to $350\,mm$. This profile is taken as the maximum height of the roughness strip (at a constant $x = 0$ in figure 3.13), and λ_e is a parameter unique to each strip. This equation effectively adopts the standard sine function, shifts it in the positive z direction, and scales it

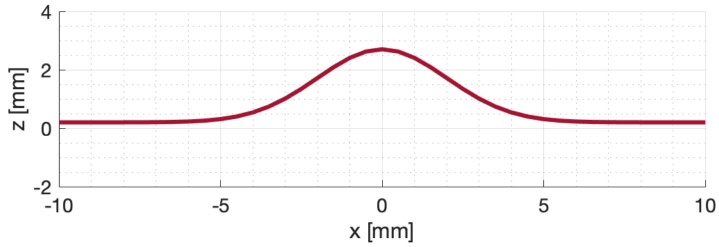

Figure 3.13: Enhanced view of the Gaussian distribution employed for all roughness strips.

to the appropriate roughness height of $2.5\ mm$. The total length of the strip is adjusted to ensure that the far edge tapers to zero. Figure 3.12 shows an enhanced spanwise view of the $\lambda_e = 6\,mm$ profile.

Sharp edges and corners increase the likelihood of the boundary layer 'tripping' and transitioning to turbulence. In order to avoid this situation, a Gaussian distribution is employed in the streamwise direction to 'smooth' the sinusoidal distribution to zero. To calculate the Gaussian distribution, the following equation is used:

$$z_{Gaussian} = z_{sinusoidal} e^{-\frac{1}{2}\left(\frac{x}{c}\right)^2} \tag{3.35}$$

where $z_{sinusoidal}$ is the sinusoidal profile described by equation 3.34, $c = 2.0$, and x is the independent variable ranging from $-10\ mm$ to $10\ mm$. This equation is the fundamental definition of the Gaussian distribution adjusted to adopt the sinusoidal profile as the height of the peak. Figure 3.13 shows the distribution from the maximum height to zero both upstream (negative x direction) and downstream (positive x direction).

Equations 3.34 and 3.35 are employed to calculate the surface points of the strip. After this is complete, a solid structure is formed by extruding the surface downward to the $z = -0.2\ mm$ plane. This is done to ensure the strip has some thickness, otherwise extruding to the $z = 0\ mm$ plane would render the strip structurally unsound both when being constructed and during the test runs. The chosen foundational thickness of $0.2\ mm$ was determined through manufacturing trial-and-error as the thinnest value possible while not compromising the strips' structural integrity. Therefore, the maximum thickness for all roughness strips in this thesis is $2.7\ mm$. Figure 3.11 shows an example 3D model of the $\lambda_e = 6\,mm$ strip.

The construction of the strips is made possible by 3D printing software capable of creating such precise and atypical geometries that traditional manufacturing processes are unable to accomplish. It is this technology that allows such a smooth distribution of the strips' upper surface, particularly when the rest of the structure can be quite fragile.

The 3D printing software is capable of a layer thickness of $0.06\ mm$ and of constructing each strip as a whole. The technology is, in short, precise and accurate enough to meet the requirements of this study. Constructing entire strips avoids the cumbersome prospect of modeling two separate halves and attempting to align them in the tunnel. Preliminary studies consistently demonstrate that the gap between halves – and the methods used to join them – transition the flow to turbulence, therefore rendering the results invalid. The 3D printer produces a smooth finish; any inconsistencies are easily removed with (very fine) sand paper. The strips are secured to the flat plate with $0.03\,mm$ -thick, single-sided tape, which provides additional smoothness to the upper surface and decreases the likelihood of transition.

Table 3.4 summarizes the dimensions and location of each roughness strip:

λ_e $[mm]$	λ_δ [-]	h_e $[mm]$	L_e $[mm]$	x-dimension $[mm]$
6.0	1.8	2.7	100.0	20.0
9.0	2.7	2.7	100.0	20.0
12.0	3.6	2.7	100.0	20.0
15.0	4.5	2.7	100.0	20.0

Table 3.4: Sinusoidal strip dimensions. L_e denotes distance from flat plate leading edge to centerline of strip (corresponds to $x = 0$ in figure 3.13).

3.2.4. Coordinate System

In order to describe and relate the physical phenomena that occur in a SBLI system, it is necessary to adopt a coordinate system that is held constant throughout all measurements and model orientations. Furthermore, if the SBLI involves a compression ramp, it may be additionally beneficial to adopt a co-ordinate system relative to the inclined surface of the ramp. As such, this thesis adopts two coordinate systems: one relative to the flat plate and another relative to the surface of the ramp. The coordinate systems are both centered where the centerline of the flat pate converges with the ramp corner. The coordinate system relative to the flat plate adopts the standard `(x,y,z)` notation, while the system relative to the ramp surface adopts `(s,n,z)` notation. For example, see figures 3.14 and 3.15.

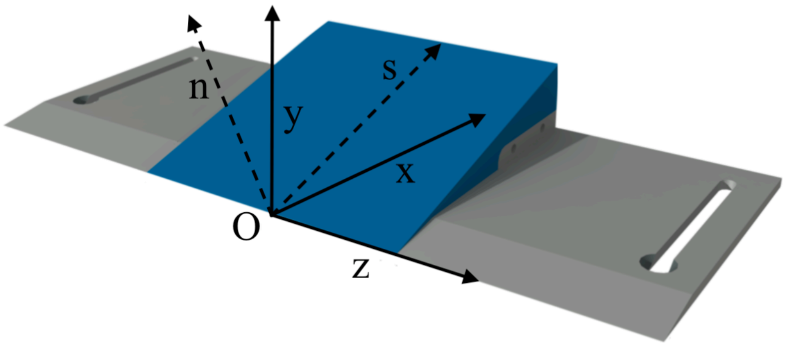

Figure 3.14: Orthogonal view of the 15° compression ramp with coordinate system. Figure adapted from Lodder [30].

Figure 3.15: Profile view of the flat plate and compression ramp with coordinate system. Figure adapted from Lodder [30].

4 Experimental Measurement Techniques

With respect to hypersonic flows, there are a wide variety of measurement techniques that measure different aspects of the flow. In general, they may be distinguished between qualitative vs. quantitative, intrusive vs. non-intrusive, and point vs. field measurements [43–45, 51]. This section focus on three measurement techniques particularly well-suited to study low-enthalpy flows: schlieren visualization, oil flow visualization, and Quantitative Infrared Thermography (QIRT).

4.1. Schlieren

Schlieren visualization is a field measurement technique commonly used in high-speed experiments [53]. It is particularly well suited to visualize shocks, shear layers, and to some extent expansion waves. It is based on light refraction theory through transparent media (e.g. air), in which, when light encounters a region of greater density, the light will refract toward that region. This phenomena is illustrated in figure 4.1.

The index of refraction is the ratio of the speed of light in a vacuum (C_0) and the speed of light in the medium (C):

$$n = \frac{C_0}{C} = 1 - K\rho \tag{4.1}$$

where n is the index of refraction, K is the Gladstone-Dale constant ($K_{air} = 2.24 - 2.33 \times 10^{-4}$), and ρ is the density of the medium.

The extent of refraction is given by Snell's law:

$$n_1 sin\,(\alpha_1) = n_2 sin\,(\alpha_2) \tag{4.2}$$

Light is shone through the facility test section, across the model or region of interest, and directed to a screen or camera system capable of visualizing density gradients (i.e. shocks) [54]. The technique is non-intrusive, provides clear images, and has a fairly simple setup. However, a consequence of the fact that it operates by line-of-sight is that it is typically unsuitable for three-dimensional flows [52]. Furthermore, it is mainly qualitative, providing only 'approximate' locations of shocks and compression regions [51]. Figure 4.2 shows the working principle of the schlieren imaging technique.

Figure 4.3 shows the setup used to conduct schlieren measurements in the HTFD using the f300 lens, while figure 4.4 shows a resulting image of the same setup.

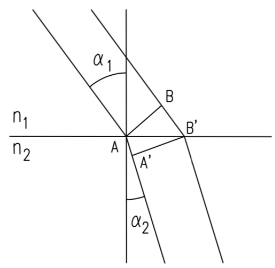

Figure 4.1: Refraction of light rays. n_2 represents the denser region of the gas ($n_2 > n_1$). Figure adapted from Scarano and Sciacchitano [45].

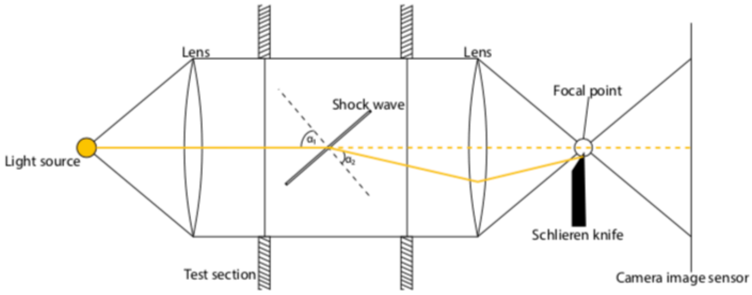

Figure 4.2: Example schlieren setup. Figure adapted from Lodder [30].

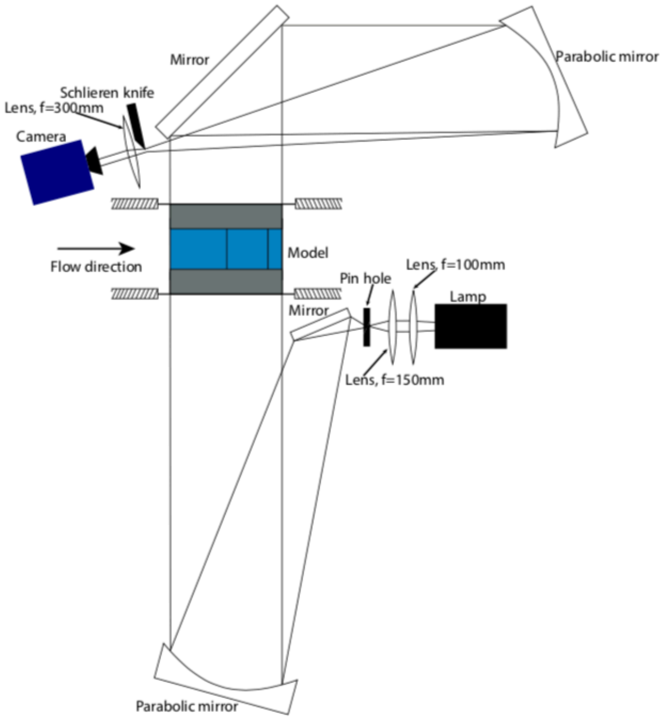

Figure 4.3: Top-down view of the schlieren setup for the HTFD with the f300 lens. Figure adapted from Lodder [30].

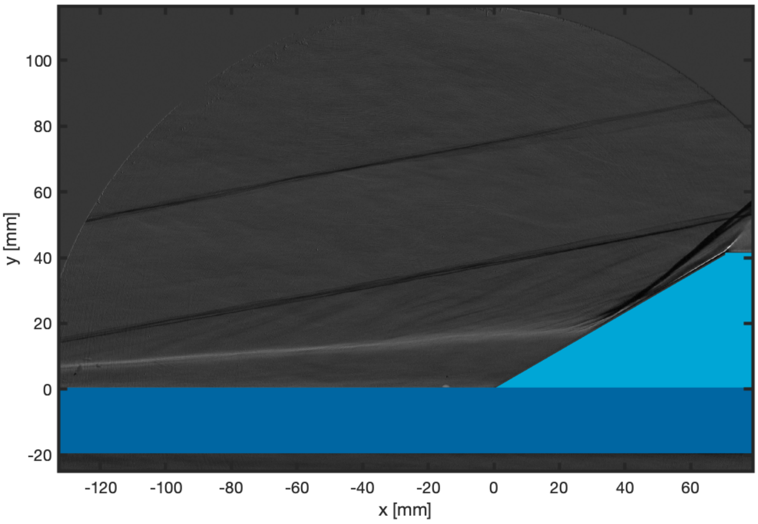

Figure 4.4: Side view of example schlieren image. Dark regions indicate compression (shocks) and white regions indicate expansions. Flow is from left to right.

4.1.1. Uncertainties in Schlieren Measurements

The primary source of uncertainty concerning the schlieren images stems from calibrating the high-speed camera and converting between pixels and millimeters. Two series of schlieren images are captured, each with a different focal length (pixel resolution) and conversion factor. For both types of images, a ruler is placed on the flat plate and the distance between two points on the ruler is recorded in both millimeters and pixels. The conversion factor is simply the distance in millimeters divided by the distance in pixels.

The first set of images is designated by the focal length as `f140`, the calibration ratio for which is determined to be $4.57\ px/mm$. In determining the scaling factor, the maximum amount of error for a distance of $160\ px$ is $3\ px$, yielding an uncertainty of $\approx 2\%$.

The second set of images has a higher resolution and is designated by the focal length as `f300` with a calibration ratio of $9.52\ px/mm$. The maximum amount of error for a distance of $476\ px$ is $4\ px$, yielding an uncertainty of $\approx 1\%$.

4.2. Quantitative Infrared Thermography (QIRT)

Quantitative infrared thermography is a measurement technique that measures a model's surface temperature with infrared-sensing cameras [51]. The model in question should ideally have a low thermal product (ρck, where ρ, c, and k are the material density, specific heat, and thermal conductivity, respectively [31]) so that the increase in surface temperature during run time is maximized for a given heat flux [51]. The change (or difference) in temperature can then be more easily recognized. Additionally, lateral conduction of heat of the model should be low in order to better distinguish surface temperature gradients on the model's surface [8, 20]. As such, the model's conductivity should be low. In order to optimize the signal received by the infrared camera, the material's emissivity should ideally be close to 1.

Figure 4.5 shows a blunted cone-flare model subjected to high-speed flows to study flow separation. The locations of separation and reattachment are identified using QIRT. The model is composed of two materials: metal for the blunted nose; Macrolon for the remainder. The metal nose has high thermal conductivity and low emissivity. As such, it is a poor candidate for QIRT measurements. Macrolon, however, is a polycarbonate with favorable thermal properties – high emissivity and low thermal conductivity – and is a suitable candidate for QIRT measurements [43]. The thermal properties of Macrolon are provided in table 4.1. Figure 4.6 shows the temperature distribution on the model surface during the run. As expected, the metal nose provides poor results, whereas the Macrolon body provides good results, showing regions of separation, circulation, and reattachment.

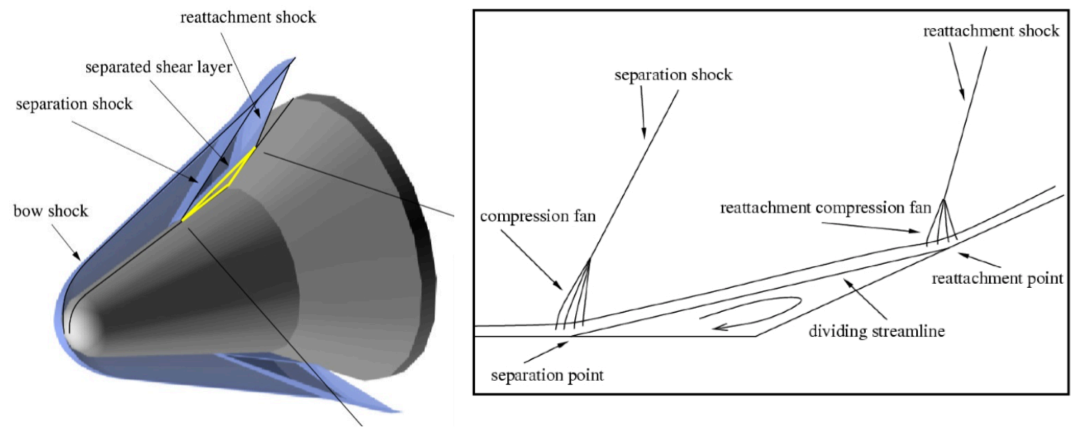

Figure 4.5: Schematic of a blunted nose cone-flare and mechanisms of flow separation and reattachment. Figure adapted from Scarano [44].

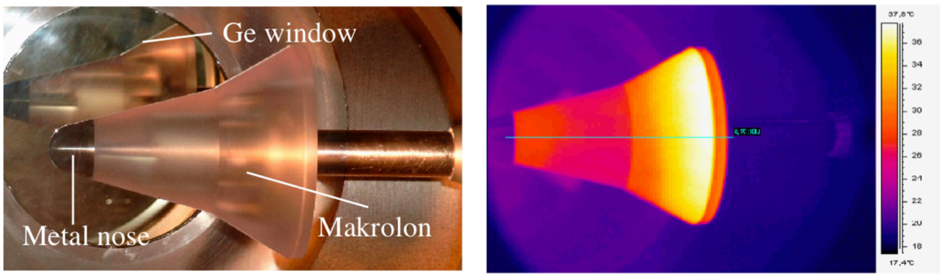

Figure 4.6: Blunted nose cone-flare model (left) and temperature distribution (right). Regions of separation, circulation, and reattachment are visible through differences in temperature. Figure adapted from Scarano [44].

ρ	c	k
1.2×10^3 $[kg/m^3]$	1.17×10^3 $[J/(kg * K)]$	0.2 $[W/(m * K)]$

Table 4.1: Macrolon thermal properties.

The thermal camera used in the experiments is a Cedip Titanium 530L infrared camera, shown in figure 4.7. The following specifications are used:

- Acquisition frequency = 200 Hz
- Integration time = 250 μs
- Spatial resolution = 1.66 px/mm

The camera's quantum detector consists of 320 × 256 Mercury Cadmium Telluride (MCT) individual detectors with spectral response of 7.7 - 9.3 μm. The camera software employs a Non-Uniformity Correction (NUC) procedure that ensures a uniform response from each detector by modifying each detector's gain and offset. If a pixel's value is statistically 'noisy', the software may perform a Bad Pixel Reduction (BPR) procedure that replaces the pixel by a weighted average of the surrounding pixels.

The camera's sensitivity is dictated by the exposure time, which determines the temperature range that can be measured. In experiments that involve particularly high temperatures, such as hypersonic experiments, the temperatures may exceed the limit of the camera's exposure time. Through trial and error, it is determined that an exposure time of 250 μs is adequate to measure the higher temperatures of the experiments. Detailed IR camera schematics are presented by Schrijer [51].

A limitation to infrared cameras is that typical glass windows are opaque in the infrared spectrum, and therefore effectively block the camera from reading the surface temperature of the model. This

Figure 4.7: Cedip Titanium 530L infrared camera.

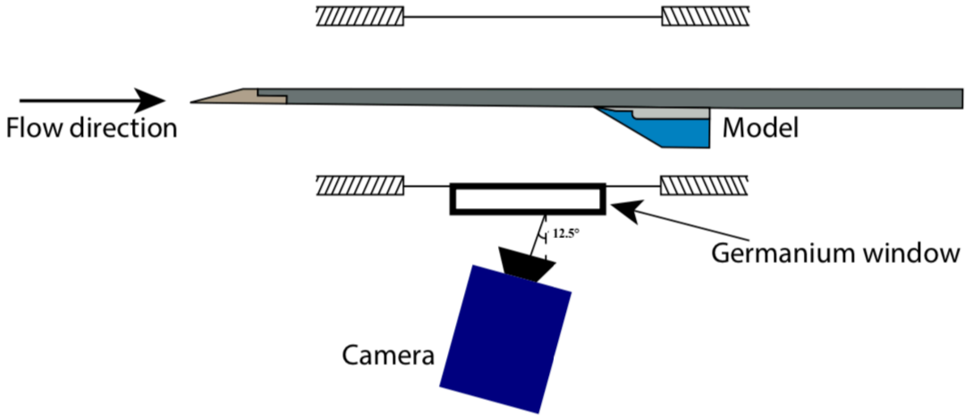

Figure 4.8: QIRT camera setup with respect to tunnel and model. Figure from Lodder [30].

limitation is circumvented by replacing the tunnel's standard glass window with one composed of germanium. In addition, the camera itself emits infrared radiation that reflects off the germanium window back toward the camera lens, so the camera must be positioned at an angle with respect to the window. The angle adopted for this work is 12.5°. The setup employed in the experiments is shown in figure 4.8.

Determining the heat flux imparted into the ramp and flat plate is a multi-step process, at least for the equipment and tools available for this thesis. The general process employed for this work is as follows:

1. Calibrate thermal camera against a black body
2. Obtain polynomial fit to convert between digital levels and temperature
3. Perform experiments
4. Apply Cook and Felderman's method [13] of calculating heat transfer from temperature values
5. Perform flat plate experiments; compare heat flux results to the analytical reference temperature method (RTM)

For detailed discussions on the physics involved in infrared radiation and black bodies, the reader is referred to the work of Voogt [59] and Lodder [30].

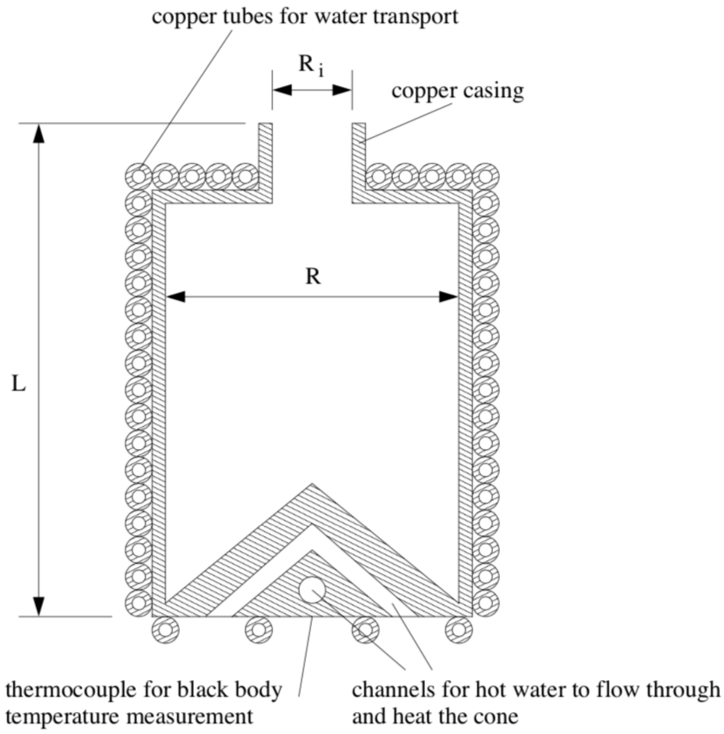

Figure 4.9: Layout of the black body. Figure adapted from Voogt [59].

4.2.1. Calibration Against a Black Body

The thermal camera and settings used in this thesis do not directly read the heat flux or temperature of the surface in question. Instead, the camera reads a digital level, which may then be converted to temperature. Thus, simply performing experiments and measuring digital levels is useless unless one is able to convert those digital levels to temperature. This is achieved using a black body calibration method, wherein the thermal camera is directed onto a surface that emits a minimal amount of thermal radiation (emissivity $\epsilon \approx 0.9$) that is maintained at a specific temperature. Therefore, the digital levels read by the thermal camera directly correlate to the established temperature (measured by separate thermal sensors). The temperature is gradually incremented through a range of temperatures and the digital levels are recorded at each step. Once the calibration procedure is complete, one may apply a polynomial curve fit to the data to derive the relationship between temperature and digital level. Figure 4.9 shows the layout of the black body; figure 4.10 shows the entire setup used for calibration; figure 4.11 shows the results of the black body calibration, the polynomial curve fit of which is:

$$y = \left(-3.571931 \times 10^{-7}\right) x^2 + \left(1.537410 \times 10^{-2}\right) x^1 + \left(-6.214557 \times 10^1\right) x^0 \tag{4.3}$$

In this particular case (and referring to figure 4.11), the x value is the digital level (DL) on the x-axis, and the y value is the temperature (T) on the y-axis:

$$\boxed{T = \left(-3.571931 \times 10^{-7}\right) E^2 + \left(1.537410 \times 10^{-2}\right) E + \left(-6.214557 \times 10^1\right)} \tag{4.4}$$

Therefore, given a particular digital level, one can calculate the corresponding temperature value. Equation 4.4 may be condensed as:

$$\boxed{T = C_1 E^2 + C_2 E + C_3} \tag{4.5}$$

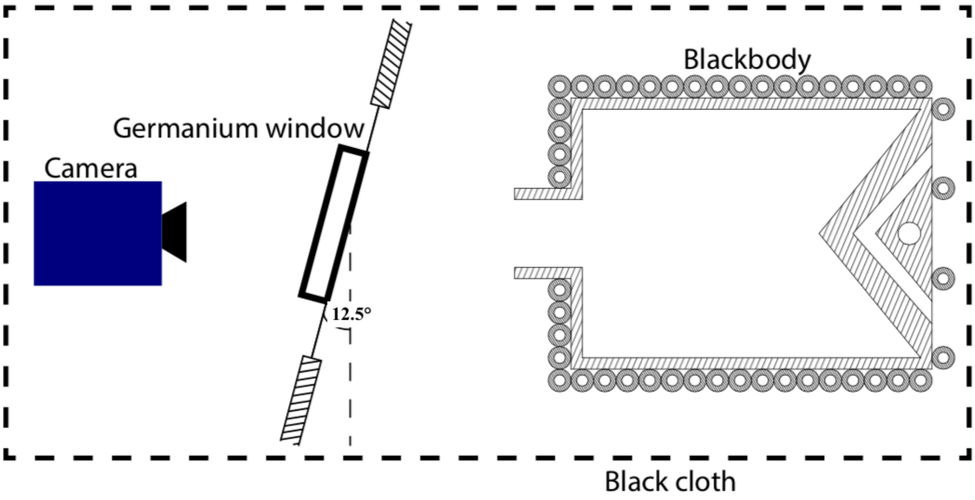

Figure 4.10: Setup used to calibrate the infrared camera. Figure adapted from Lodder [30].

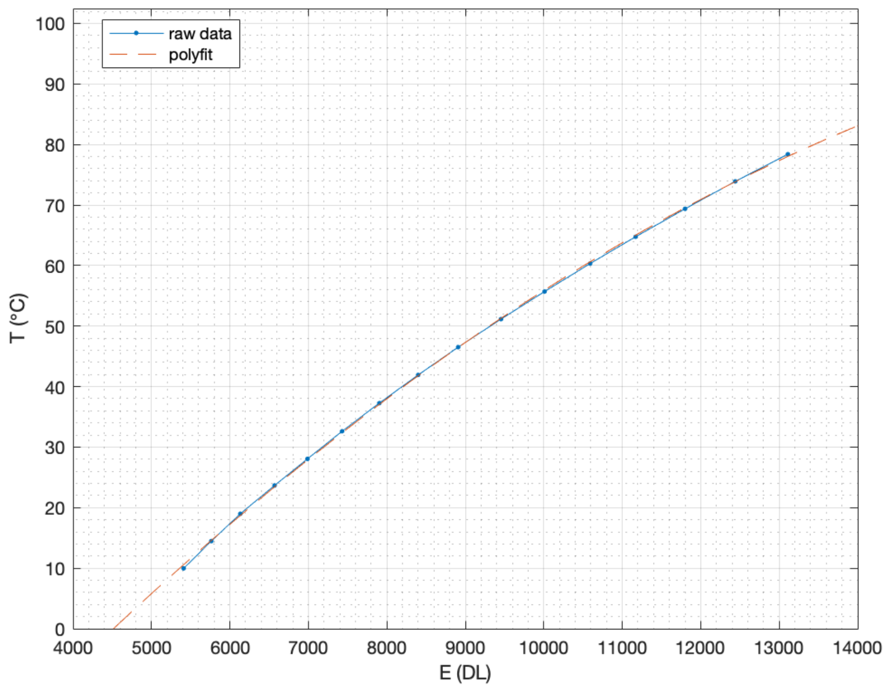

Figure 4.11: Black box calibration curve allowing one to directly convert between digital levels and temperature. The polynomial curvefit allowing this conversion is given in equation 4.4.

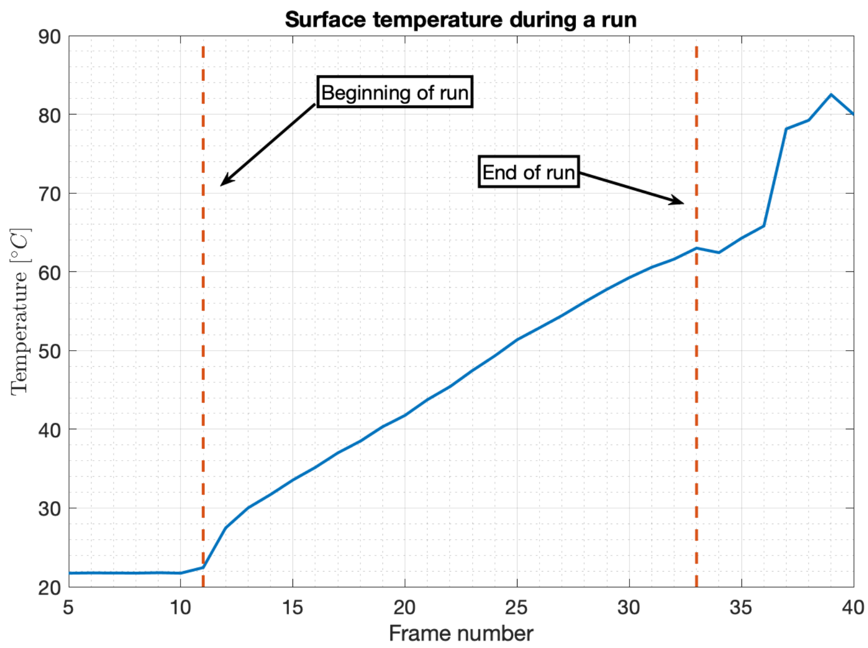

Figure 4.12: Surface temperature during a run. Heat flux calculations are valid along the linear profile within the start and end of the run (e.g. frame 14 - frame 31).

where

C_1	C_2	C_3
-3.571931×10^{-7}	1.537410×10^{-2}	-6.214557×10^{1}

4.2.2. Calculating Heat Flux

Once it is determined how to convert the recorded digital level to temperature, the temperature values recorded over the series of frames must be converted to heat flux. This is achieved by utilizing the numerical expression established by Cook and Felderman [13, 51]:

$$q_s(t_n) = \sqrt{\frac{\rho c k}{\pi}} \left[\frac{\phi(t)}{t} + \sum_{i=1}^{n-1} \left\{ \frac{\phi(t_n) - \phi(t_i)}{\sqrt{t_n - t_i}} - \frac{\phi(t_n) - \phi(t_{i-1})}{\sqrt{t_n - t_{i-1}}} + 2\frac{\phi(t_n) - \phi(t_{i-1})}{\sqrt{t_n - t_i} + \sqrt{t_n - t_{i-1}}} \right\} + \frac{\phi(t_n) - \phi(t_{n-1})}{\sqrt{\Delta t}} \right] \quad (4.6)$$

where $\phi(t)$ is the difference between the temperature at time t and time zero: $\phi(t) = T(t) - T(0)$, n is the total number of (valid) frames, and ρ, c, and k are the thermal properties of Macrolon provided in table 4.1.

During a run with the HTFD, the amount of time recorded by the thermal camera is greater than the total test time of $100\,ms$. It is likely (and indeed preferred) that several frames are captured before and after the run begins to ensure the entire run is recorded. Incorporating *all* recorded image frames into equation 4.6 to calculate the heat flux is yields inaccurate results. Therefore, the beginning and end frames must be specifically selected for each run.

Figure 4.12 shows the recorded temperature (after being converted from digital level using equation 4.4) of a point near the center of the 30° ramp (with strip) during a run. The linear profile marks valid test conditions after the flow has set up and before it finishes. The heat flux for all experiments contained within this thesis is calculated for this linear profile, *not* non-linear segments near the beginning and end of the run.

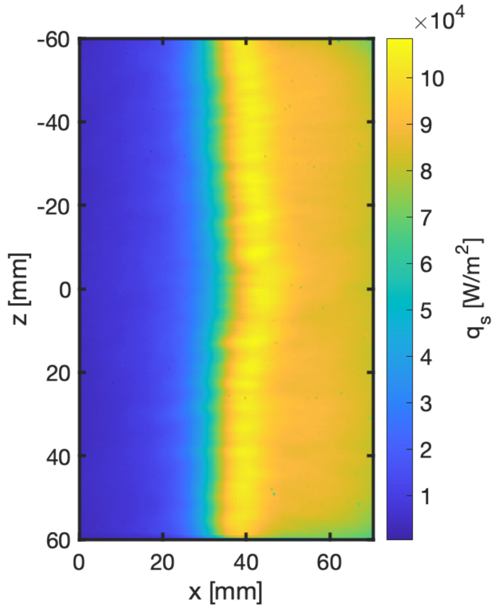

Figure 4.13: Surface heat flux of the $30°$ ramp without strip normal to the flat plate at $M_\infty = 7.5$, $Re = 46.3 \times 10^5$

Calculating the heat flux by itself has its limits in comparing and validating results against the open literature. For example, the *exact cause* of the heat flux may differ between wind tunnels, and therefore a direct comparison may not be entirely sufficient to draw any conclusions about the tunnel conditions or test model. In order to better compare and discuss results, publications often utilize the Stanton number c_h as a measure of heat flux relative to freestream and surface conditions:

$$c_h = \frac{q}{c_p \rho_\infty V_\infty \left(T_t - T_w\right)} \tag{4.7}$$

where q is the (local) heat flux, c_p is the specific heat of air at constant pressure, ρ_∞ is the density of the freestream, V_∞ is the freestream velocity, T_t is the freestream total temperature, and T_w is the (local) temperature of the wall. (Some studies use the adiabatic wall temperature T_{aw} instead of T_t.) For all results contained in this work, $c_p = 1001.0\, J/(kg * K)$, V_∞ and T_t are provided in table 3.22, and ρ_∞ is given in equation 3.2. Figure 4.13 shows an example of calculated surface heat flux while figure 4.14 shows the averaged spanwise surface heat flux. The corresponding mean surface Stanton number profile is calculated using equation 4.7 and given in figure 4.15.

4.2.3. Uncertainties in QIRT Measurements

The infrared measurements are calibrated against the width of the ramp, which is $120\,mm$ for all ramp models. Additionally, the length of the inclined surface in the streamwise direction is also known from the CAD drawings used to design the models themselves. Therefore, the QIRT images are cropped to include only the inclined surface and are then scaled to ensure the ramp width and length adhere to design specifications. When scaling and cropping the images, it is possible the very edges of the inclined surface are removed. Great care is taken to avoid such a scenario, but it is estimated that at most $1\,mm$ could be removed by the cropping procedure. If this occurs at both spanwise ends, then the uncertainty introduced would be $2\,mm$ per $120\,mm$ (the width of each ramp), yielding an uncertainty of $\approx 1.5\%$. The maximum uncertainty in the x direction would involve the ramp with the steepest slope projected normal to the flat plate: the $30°$ ramp. The x distance of the inclined surface of the $30°$ ramp is taken from the design specifications as $71\,mm$. The uncertainty introduced for this model would then be $2\,mm$ per $71\,mm$, yielding an uncertainty of $\approx 3\%$.

An additional source of uncertainty in the QIRT measurements stems from averaging the maximum spanwise mean and maximum spanwise RMS of the Stanton number on the ramp surface. Both the maximum spanwise mean and spanwise RMS are calculated for each of the three runs before being

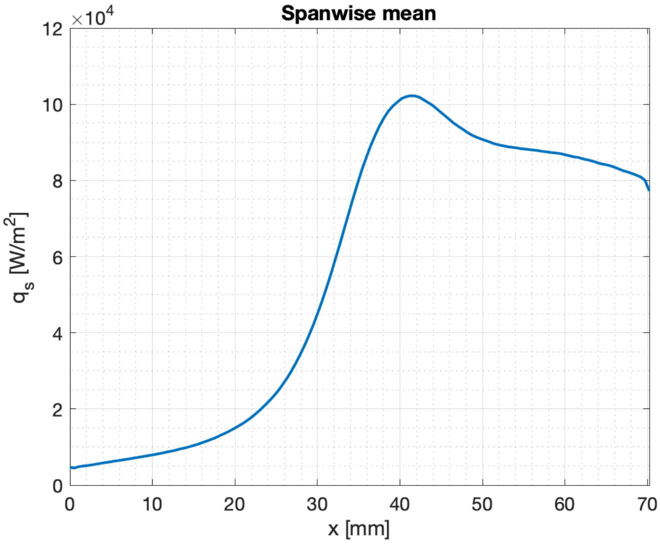

Figure 4.14: Averaged spanwise surface heat flux profile of the 30° ramp without strip normal to the flat plate at $M_\infty = 7.5$, $Re = 46.3 \times 10^5$

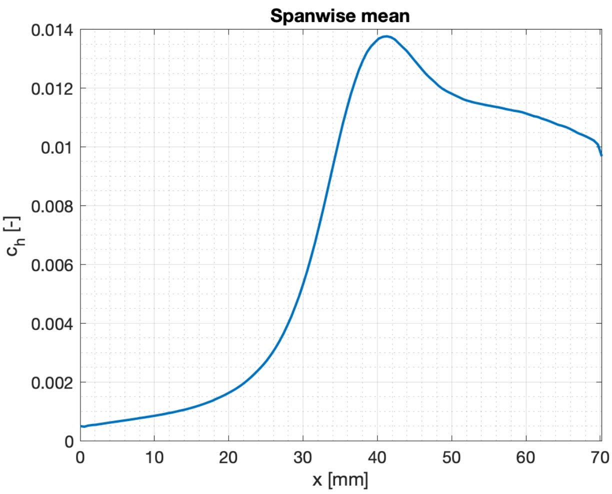

Figure 4.15: Mean spanwise Stanton number profile of the 30° ramp without strip normal to the flat plate at $M_\infty = 7.5$, $Re = 46.3 \times 10^5$

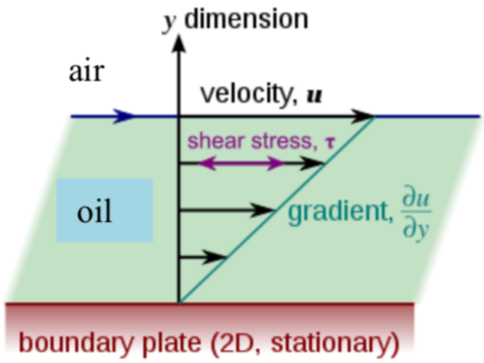

Figure 4.16: Shear gradient of oil flow. Figure adapted from Scarano and Sciacchitano [43].

averaged. The error bars stemming from averaging the three are shown in all maximum spanwise and maximum RMS plots (appendices C and D) except for those containing all results in order not to clutter the plots with too much information.

4.3. Oil Flow

Oil flow visualization is used to distinguish flow direction near the surface of an object. It is particularly adept at identifying regions of stagnation and separation, which makes it a particularly unique measurement technique for hypersonic flows. The working principle is based on the fact that oil has a far greater viscosity – and therefore lower Reynolds number – than air. The advective inertia forces of the oil are dominated by the viscous forces, and the oil follows a linear velocity profile [43]. In effect, it is predominantly acted upon by the shear force exerted by the moving air. The oil flows much slower than the surrounding air, allowing it to follow the flow at the surface, with the additional benefits of conforming to regions of low velocity and retaining its shape for a time after the experiment is complete, thus allowing for improved qualitative data analysis. Figure 4.17 shows an example of a test with oil.

Oil flow visualization typically reveals the following features:

1. Separation lines, which appear as brighter regions due to oil flowing from opposite directions
2. Surface streamlines
3. Steady streamwise vortices, which appear as S-shaped lines
4. Reattachment lines, which appear as brighter regions due to the oil being swept away due to the increased surface shear stress
5. Wall-normal vortices in the wake of bluff bodies, which appear as strong foci due to accumulating oil

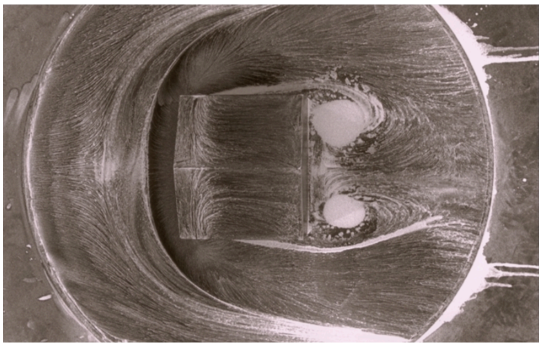

Figure 4.17: Example of oil flow around a model. Figure adapted from Scarano and Sciacchitano [43].

5 Experimental Results

The goal of this thesis is to study and quantify how shock–-boundary-layer interactions (SBLIs) amplify or dampen prescribed upstream disturbances, and how those disturbances influence downstream flow conditions. Thus, this thesis effectively observes the different means by which a laminar shock–boundary-layer interaction may transition to turbulence and what this looks like within the recirculation region and on the surface of the ramp. As described in section 4, this thesis employs three measurement techniques to observe the myriad physical phenomena present in transitional and turbulent SBLIs: schlieren imaging, quantitative infrared thermography (QIRT), and oil flow. This chapter progressively describes the evolution of a SBLI as it transitions from laminar to turbulent.

The discussion begins in section 5.1 with boundary layer flow over the flat plate. The section presents several measurements taken at varying streamwise locations for both freestream conditions and serves to validate the results presented in the remainder of this thesis by comparing measured heat flux signatures with analytical solutions. The Stanton number profile along the centerline of the flat plate strongly indicates that the flow develops and maintains a laminar profile for its entire length.

Section 5.2 analyzes how the flow topology evolves from purely laminar to one that is more transitional when a downstream ramp is installed on the plate. The section also delves deeper into the characteristics of typical SBLI structure using both schlieren images of the circulation region and QIRT measurements along the ramp's inclined surface. The results in this section involve two ramp angles ($15°$ and $30°$), used to observe the influence of increasing the shock strength on a SBLI topology, and two Reynolds numbers (9.2×10^5 and 46.3×10^5) to observe how the the flow's Reynolds number influences the flow's transitional nature and heat flux properties. The goal of this section is to study the flow topology in absence of any upstream perturbance (i.e. roughness strip). As such, this section serves as a 'baseline' against which subsequent results involving upstream perturbations may be compared.

Section 5.3 extends the discussion on the transitional phenomena observed in section 5.2 by introducing a sinusoidal roughness strip into the flow upstream of the compression ramp. The main purpose of the strip is to introduce perturbations into the flow that *do not* transition the flow to turbulence at the lower Reynolds number (9.2×10^5). In this respect, the sinusoidal roughness strip differs from roughness strips typically used in hypersonic research in that traditional strips are generally designed to *intentionally* trip the laminar boundary layer and transition the flow to turbulence, whereas the 'smooth', sinusoidal roughness strips employed in this thesis (at the lower Reynolds number) are not.

The measurement techniques employed in section 5.2 – schlieren imaging and QIRT – are likewise employed in section 5.3 with identical settings and setup. Adhering to identical settings and an identical setup allows one to directly compare the evolving flow topology to the so-called 'baseline' results of section 5.2. Doing so allows one to better quantify how upstream perturbations influence SBLI flow phenomena.

Section 5.4 supplements the discussion by presenting results involving both $15°$ and $30°$ ramp angles with an upstream roughness element at the higher Reynolds number (46.3×10^5). The setup, equipment, settings, and flow conditions (save for the Reynolds number) are identical to those of section 5.3, which allows one to directly observe how the Reynolds number influences SBLI flow topology in the presence of a roughness strip.

The increased Reynolds number in the presence of the roughness strip effectively transitions the boundary layer from laminar to turbulent. This greatly transforms the flow topology and modifies the SBLI structure while still demonstrating how distributed perturbations influence SBLI flow behavior.

In total, this thesis employs four ramp angles and five roughness strip conditions (including no strip at all) to build a comprehensive analysis on the effect of roughness strips on various SBLI conditions. to elucidate the overall discussion, this chapter limits itself to results involving only one specific roughness strip – that with a nondimensional peak-to-peak wavelength of 2.7: $\lambda_\delta = 2.7$. The discussions in

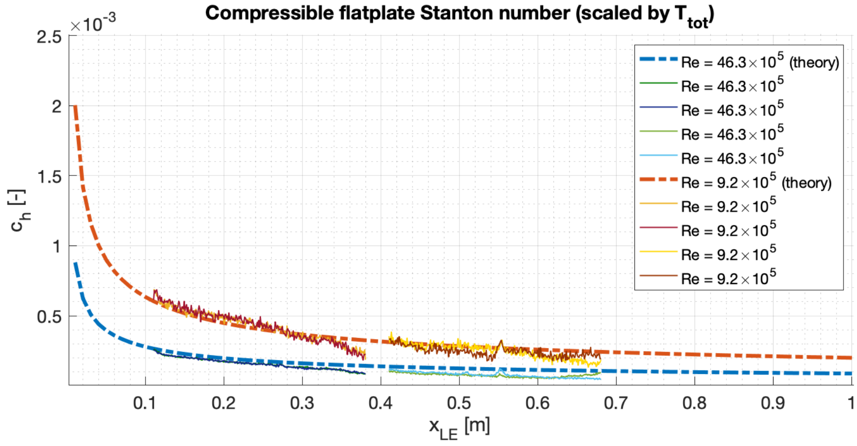

Figure 5.1: Flat plate Stanton number measurements compared to the reference temperature theory

sections 5.3 and 5.4 therefore limit themselves to this strip. For extensive information regarding how the remaining strips influence SBLI flow topology, refer to the appendices.

5.1. Flat Plate Heat Flux

In order to validate any temperature measurements or heat flux calculations obtained in the HTFD, it is helpful to first conduct tests of the flat plate (without ramp or roughness strips) and obtain the Stanton number along the plate's surface from the measured temperature. Then, to properly validate the results, the Stanton number from the flat plate measurements is compared to the analytical Stanton number calculated from the reference temperature method (see section 2.2 and equation 2.10).

Figure 5.1 compares the Stanton number calculated from experiments against the Stanton number calculated using the reference temperature method. The measurements are of the centerline of the plate averaged 10 mm in both the positive and negative spanwise direction. The heat flux is calculated from the temperature measurements with the procedure outlined in section 4.2.2. The results are divided between upstream/downstream measurements and high/low Reynolds number. Both the high and low Reynolds numbers employed in this thesis are represented. Additionally, each condition has two measurements to display the repeatability of the employed setup and procedure. The measurements are distinguished by different colors.

Perhaps the most apparent observation is that the measurements pertaining to the lower Reynolds number (9.2×10^5, orange dotted line) are noticeably more noisy than the measurements conducted at the higher Reynolds number (46.3×10^5, blue dotted line). The reason for this is not known; it may simply be a consequence of imperfections in the flat plate surface or of the camera registering reflections in the window. It is also apparent that the measurements deviate from their trend near the 'tail end' of their line segments (the last $\approx 0.02\ m$ of each line). In addition, the downstream measurements all exhibit a peak or jump near their midpoint. That these occur for both Reynolds numbers and all sets of downstream measurements suggests that the error(s) appears to be more systematic than random given it consistently occurs near the same 'location' within each measurement set. But overall, figure 5.1 displays good agreement between the analytical solutions and measurements. These results give validity to the remaining QIRT measurements in this thesis.

5.2. No Strip

We progress from the flat plate results of section 5.1 by analyzing the effect of adding a compression ramp to the flat plate upper surface. The oblique shock formed by the compression ramp creates an adverse pressure gradient that induces the boundary layer to form an inflection point and, ultimately, causes the flow to develop a circulation region characteristic of shock–boundary-layer interactions. Figures 5.2a and 5.2b show schlieren images of the 15° compression ramp at both the low and high Reynolds numbers. Both figures illustrate the most salient features of SBLIs (described in chapter 2): a shear layer (in white) denoting the upper boundary of the circulation region, and a shock (in dark gray)

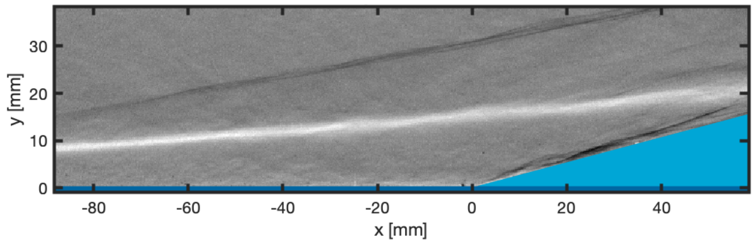

(a) $Re = 9.2 \times 10^5$

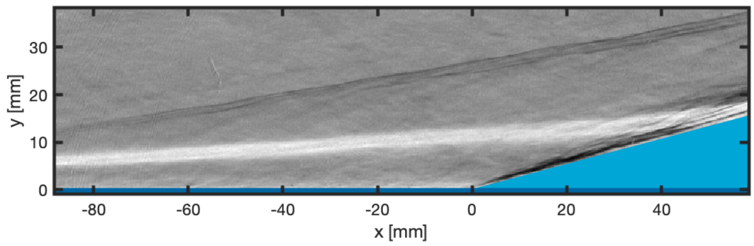

(b) $Re = 46.3 \times 10^5$

Figure 5.2: α = 15°; M_∞ = 7.5; **No roughness strip**, α = 15°

created by the compression formed at the circulation's upstream separation point. The shock formed by the flat plate leading edge is outside the image window in figures 5.2a and 5.2b, but is visible in the images presented in appendix I.

Figures 5.3a and 5.3b show the Stanton number along the compression ramp inclined surface normal to the flat plate at the low and high Reynolds number, respectively. Figure 5.3a corresponds to figure 5.2a while figure 5.3b corresponds to figure 5.2b. The region of greatest Stanton number intensity occurs immediately downstream of the shear layer impingement location.

The shear layer corresponding to the lower Reynolds number barely impacts the inclined ramp, while the shear layer for the larger Reynolds number clearly does. The overall flow topology of figures 5.2a and 5.2b agrees with the assessment developed in section 5.1 that the incoming boundary layer is more likely laminar than turbulent for the simple reason that turbulent boundary layers more strongly resist separation due to a shallow boundary layer profile (see section 2.5 and figure 2.2).

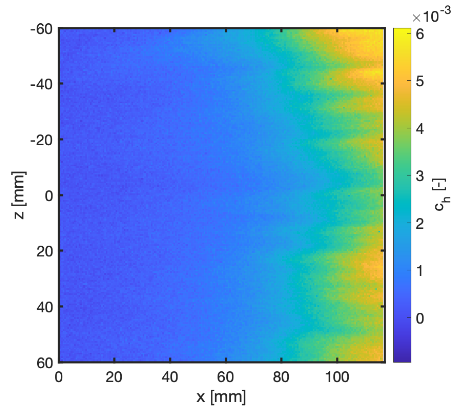

(a) $M_\infty = 7.5$; $Re = 9.2 \times 10^5$

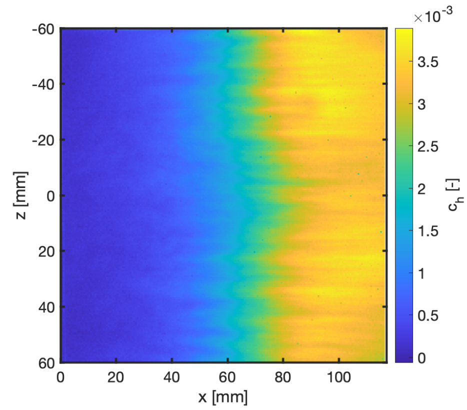

(b) $M_\infty = 7.5$; $Re = 46.3 \times 10^5$

Figure 5.3: **No roughness strip**, α = 15°

To further assess the stability of the shear layer and circulation region, this thesis calculates the root mean square (RMS) of the schlieren contours in the y-direction (normal to the flat plate) over time. In this case, the data set is the two-dimensional array composed of schlieren contour values

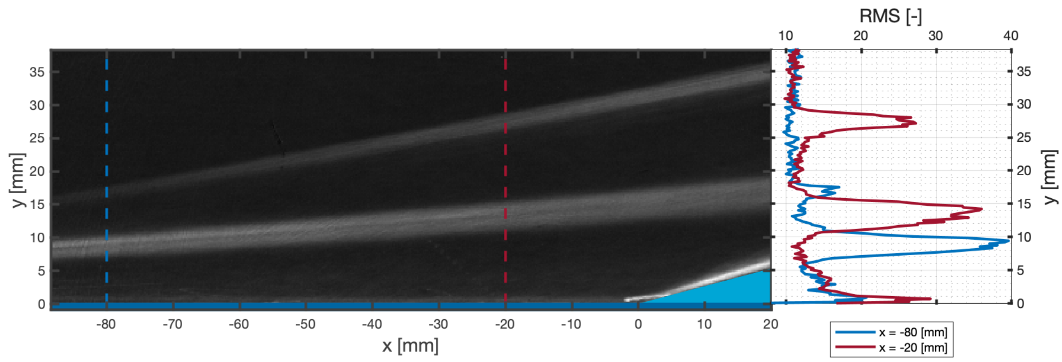

(a) $M_\infty = 7.5$; $Re = 9.2 \times 10^5$

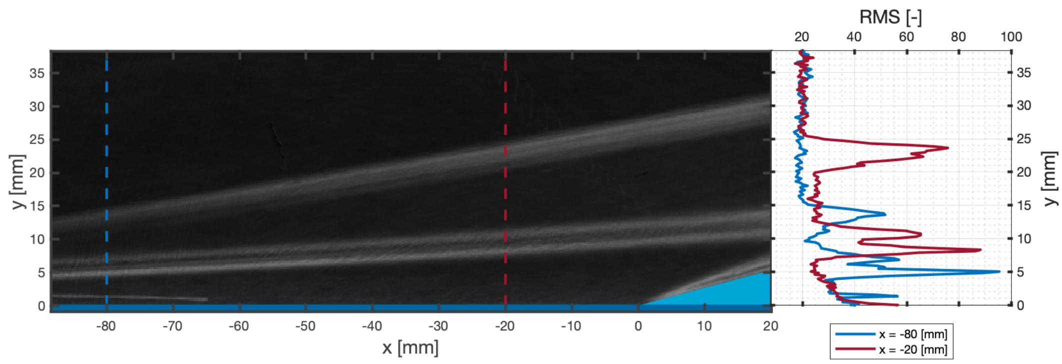

(b) $M_\infty = 7.5$; $Re = 46.3 \times 10^5$

Figure 5.4: **No roughness strip**, α = 15°

in the y-direction over time. In other words, the y-axis is the first dimension, and time is the second. This analysis considers a total of 250 frames ($8.6\ ms$) during the valid test time of $100\ ms$ at $x = [-20, -80]\ mm$. Figures 5.4a and 5.4b show the results of the RMS analysis. The dashed lines on the schlieren image correspond to the solid lines in the plot, blue corresponding to upstream values and maroon corresponding to values farther downstream.

Root mean square values are useful in analyzing SBLIs because they provide insight into the shear layer's behavior. Consider figure set 5.5. A shear layer that is largely steady and laminar attains the RMS profile shown in figure 5.5a, which indicates there is little deviation from the mean and that the flow is steady. However, if the signature begins to fluctuate, the profile begins to widen. If the data fluctuates far enough away from the mean and occupies that 'position' long enough, then the profile may adopt a 'dip' near the peak, as shown in figure 5.5b. With regard to SBLIs, this profile corresponds to a transitional shear layer. Should the data further deviate from the mean but not retain its periodic, oscillatory nature, the resulting profile widens and loses its 'dip' at the peak. Such a profile reflects a turbulent shear layer, and is shown in figure 5.5c.

Looking now at the RMS profiles of figures 5.4a and 5.4b we see that the shear layer at the lower Reynolds number adopts a rather laminar profile, while that of the greater Reynolds number is transitional. Even before introducing a roughness strip to the flow, it is apparent that significant differences exist between low and high Reynolds number conditions, and that boundary layers at higher Reynolds numbers are much more likely to transition to turbulence should they be perturbed. This is important to consider when discussing the results in sections 5.3 and 5.4.

We now focus on the results involving the 30° compression ramp. Figures 5.6 and 5.7 display the same type of measurements as those of the 15° compression ramp, i.e. standard schlieren images and surface Stanton number. The expectation of inclining the compression ramp is that it increases the shock strength of the overall system, increases the scales at which SBLI phenomena occur, and results in increased heat transfer on the ramp surface. Comparing the standard schlieren images –

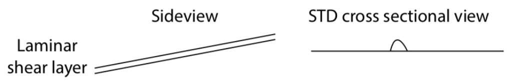

(a) Laminar RMS profile.

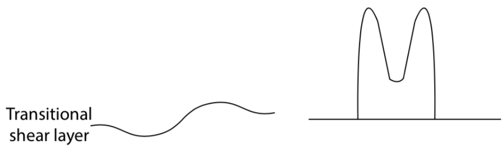

(b) Transitional RMS profile.

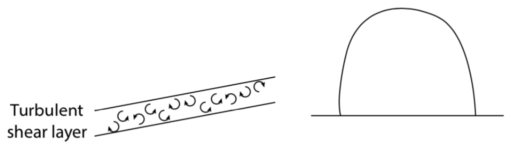

(c) Turbulent RMS profile.

Figure 5.5: Laminar, transitional, and turbulent cross-sectional profiles of shear layers in supersonic flow. Figures adapted from Lodder [30].

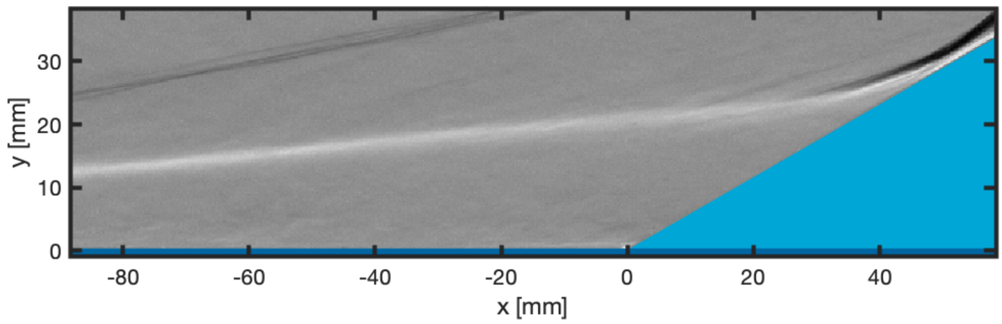

(a) $M_\infty = 7.5$; $Re = 9.2 \times 10^5$

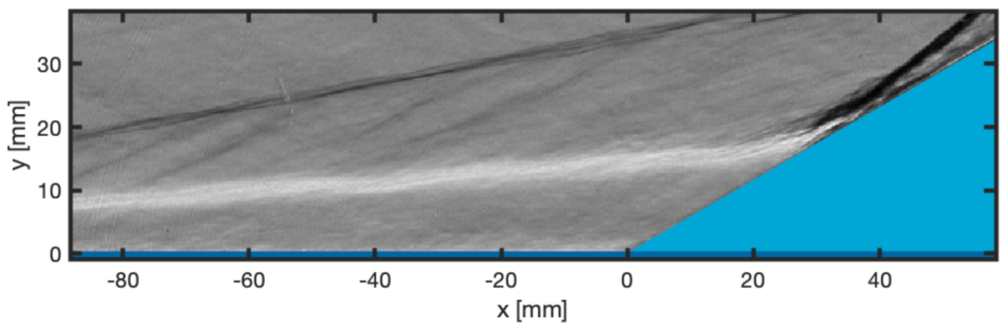

(b) $M_\infty = 7.5$; $Re = 46.3 \times 10^5$

Figure 5.6: **No roughness strip**, $\alpha = 30°$

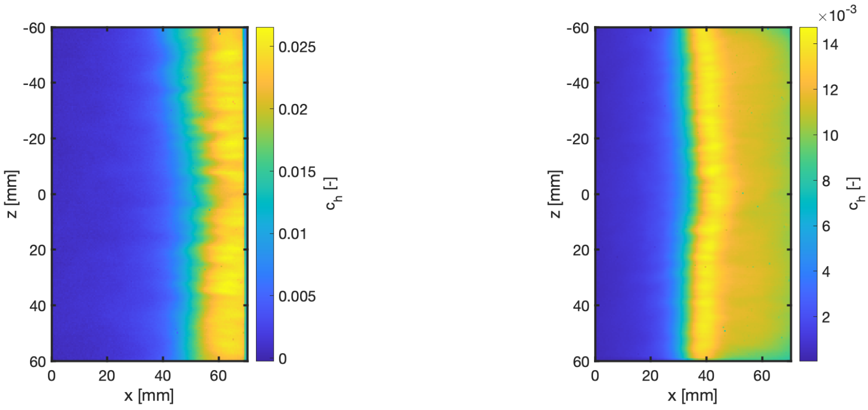

(a) $M_\infty = 7.5$; $Re = 9.2 \times 10^5$ (b) $M_\infty = 7.5$; $Re = 46.3 \times 10^5$

Figure 5.7: **No roughness strip**, $\alpha = 30°$

figures 5.2 and 5.6 – shows that the length scales of the SBLI do indeed increase, and that separation occurs farther upstream when $\alpha = 30°$. Furthermore, comparing figures 5.3 and 5.7 shows that the Stanton number along the ramp surface increases for a larger ramp angle and *decreases with increasing Reynolds number*. Similar observations are reported by Chuvakhov *et al.* [12].

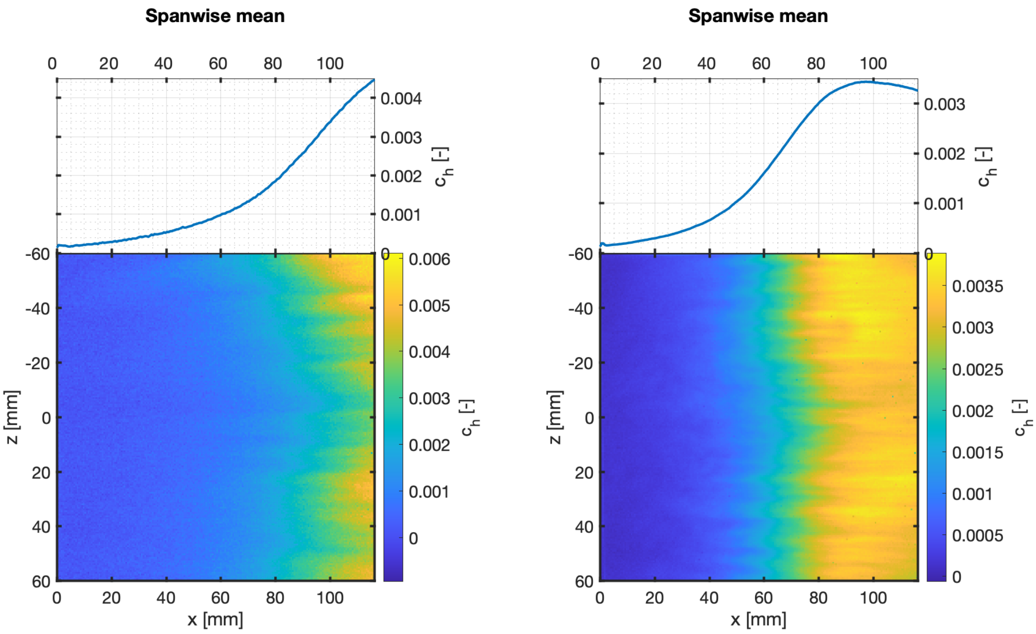

(a) $M_\infty = 7.5$; $Re = 9.2 \times 10^5$ (b) $M_\infty = 7.5$; $Re = 46.3 \times 10^5$

Figure 5.8: **No roughness strip**, $\alpha = 15°$

In discussing and evaluating the thermodynamic properties on a ramp surface, it is helpful to calculate the spanwise mean and spanwise RMS of the Stanton number contour values. Figures 5.8 and 5.9 present the Stanton number contours of figures 5.3 and 5.7, respectively, juxtaposed with the spanwise mean. Two observations present themselves: the maximum spanwise mean decreases with increasing Reynolds number, and the x location of maximum spanwise mean moves upstream with increasing Reynolds number. This assessment agrees with the observations that an increase in Reynolds number shifts the shear layer impingement location upstream, as shown in the schlieren images.

The spanwise Stanton number RMS offers particular insight into the flow behavior near reattach-

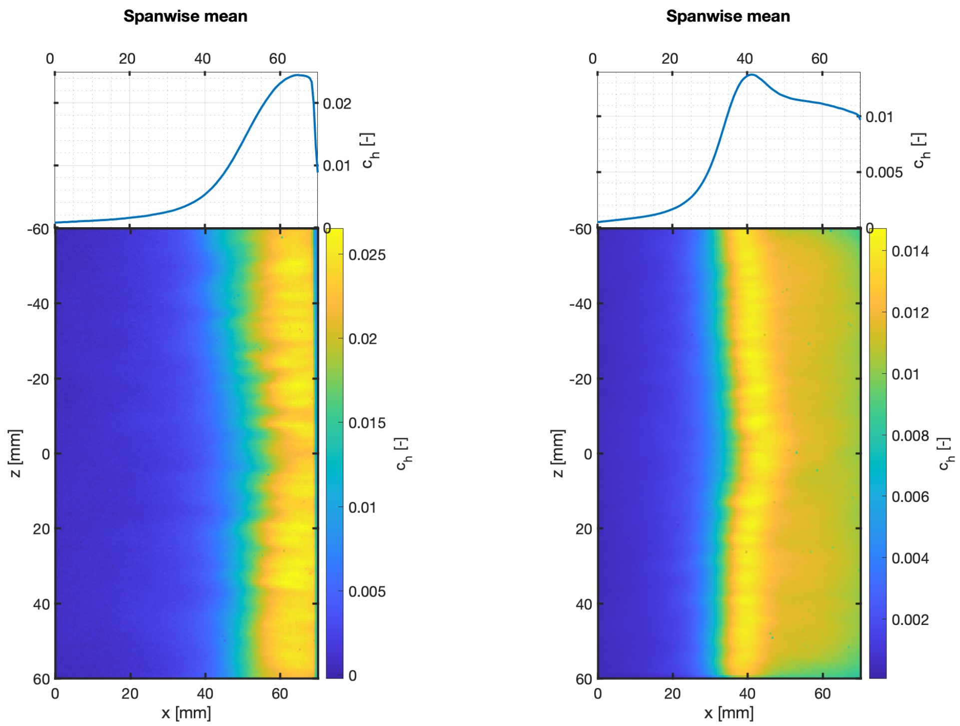

(a) $M_\infty = 7.5$; $Re = 9.2 \times 10^5$ (b) $M_\infty = 7.5$; $Re = 46.3 \times 10^5$

Figure 5.9: **No roughness strip**, $\alpha = 30°$

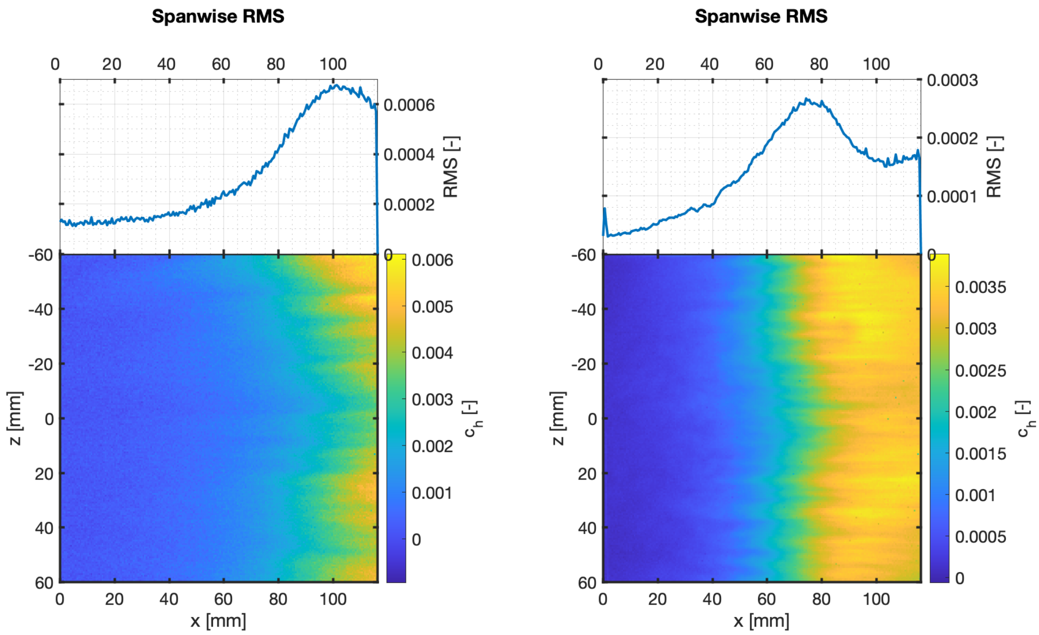

(a) $M_\infty = 7.5$; $Re = 9.2 \times 10^5$ (b) $M_\infty = 7.5$; $Re = 46.3 \times 10^5$

Figure 5.10: **No roughness strip**, $\alpha = 15°$

ment that the mean alone cannot. Its ability to identify areas where there is large deviation from the mean allows it to show regions where temperature striations form from Görtler-like vortices or other three-dimensional effects. Figures 5.10 and 5.11 show such RMS profiles along the surface of the 15°

and 30° ramps, respectively. For both ramp angles, the x location of greatest spanwise variance is upstream of the location of maximum spanwise mean. In fact, it appears that the location of greatest spanwise mean coincides with a dip in spanwise RMS (see $x = 40\,mm$ in figures 5.9b and 5.11b). This suggests that streaks may appear both upstream and downstream of this location. Additionally, this behavior is more pronounced in the results gathered at the greater Reynolds number.

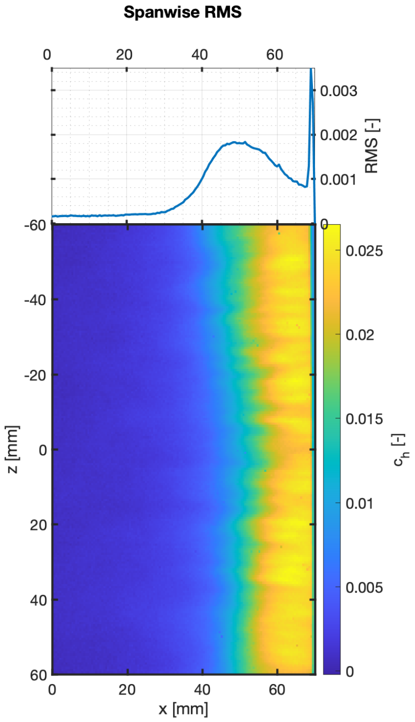

(a) $M_\infty = 7.5$; $Re = 9.2 \times 10^5$

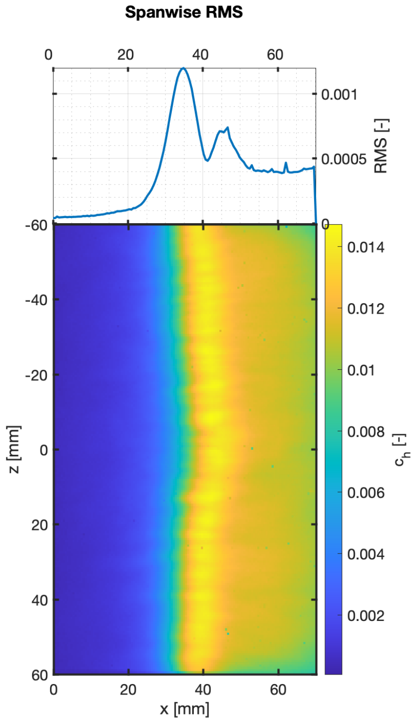

(b) $M_\infty = 7.5$; $Re = 46.3 \times 10^5$

Figure 5.11: **No roughness strip**, $\alpha = 30°$

Figures 5.12a and 5.12b show oil flow results of the 30° ramp surface normal to the flat plate. Both show that the oil is practically undisturbed in the circulation region upstream of reattachment, but that at and downstream of reattachment, streaks form that seem to resemble the temperature streaks shown in figure 5.7. In oil flow measurements, the oil accumulates in regions of relative stagnation, which are visible in white. Conversely, dark regions denote locations where the oil is swept away. (The ramp models are painted black for the oil flow measurements due to the oil being white by nature.) The somewhat periodic white-dark regions suggest periodic rotating and counter-rotating streamwise vortices, simply for the fact that vortices sweep high-momentum flow from regions distant from the wall toward the ramp surface, and vice versa. Furthermore, the streaks are far more visible in 5.12b, which suggests that higher Reynolds number flows are more conducive to the formation of Görtler-like instabilities.

Figures 5.13a and 5.13b supplement the schlieren images of figures 5.6a and 5.6b with RMS calculations over 250 frames at $x = [-80, -20]\ mm$. Recall that the schlieren RMS figures for the 15° ramp at high Reynolds number show that the shear layer exhibits RMS profiles that more strongly reflect transition than at the lower Reynolds number. The results for the 30° ramp resemble those of the 15° ramp with the addition that the transitional profiles (a peak with a 'dip' in the middle) are more clearly defined not just for the shear layer but for the separation shock as well. This suggests that an increase in ramp angle increases the instability of the separated shear layer.

Figure 5.14 presents the maximum spanwise mean Stanton number for the results that lack a roughness strip. This goal of this plot is to summarize the surface heat flux behavior in a succinct and clear manner. Focusing on the $\alpha = 15°$ and 30° results that are relevant to this chapter, they show that an increase in ramp angle results in an increase of the maximum spanwise value and shifts its location in the negative x direction. Furthermore, there is very little uncertainty in the values except for the x loca-

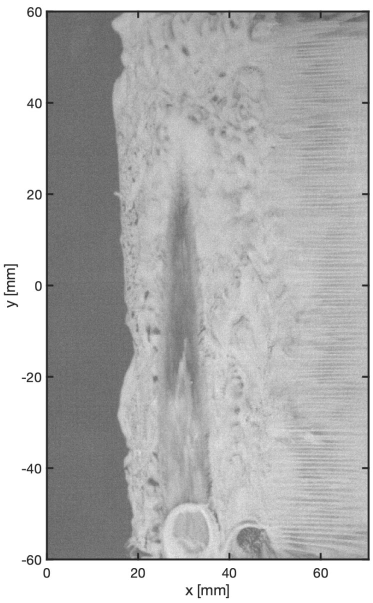

(a) $Re = 9.2 \times 10^5$

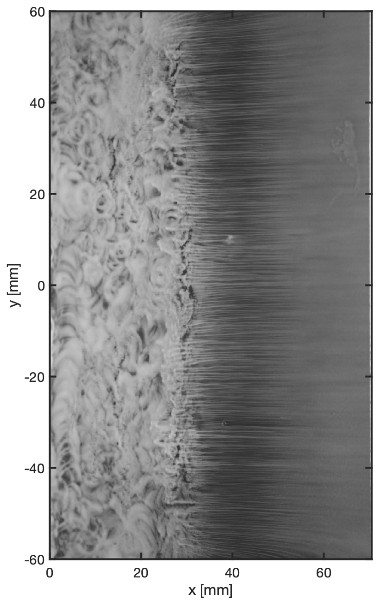

(b) $Re = 46.3 \times 10^5$

Figure 5.12: **Left:** Section between $x = 0\ mm$ and $x = 20\ mm$ is not oiled prior to the run. Section between $x = 20\ mm$ and $x \approx 50\ mm$ is oiled prior to the run but is relatively unaffected. **Right:** Section between $x = 0\ mm$ and $x \approx 30\ mm$ is oiled prior to the run but is relatively unaffected. $\alpha = 30°$.

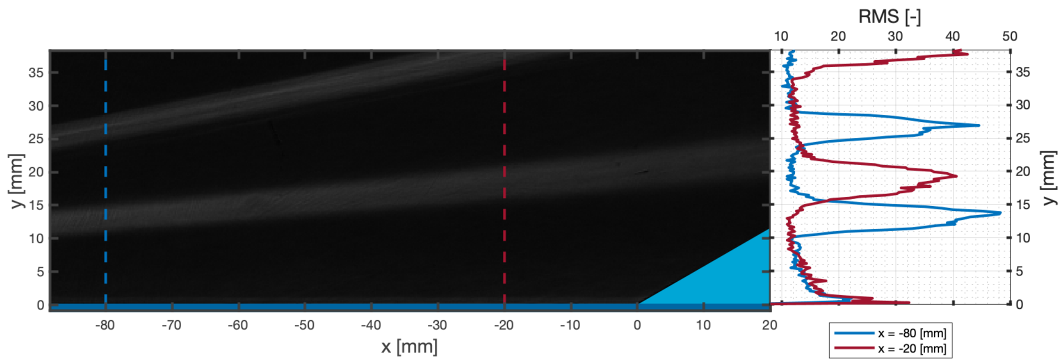

(a) $M_\infty = 7.5$; $Re = 9.2 \times 10^5$

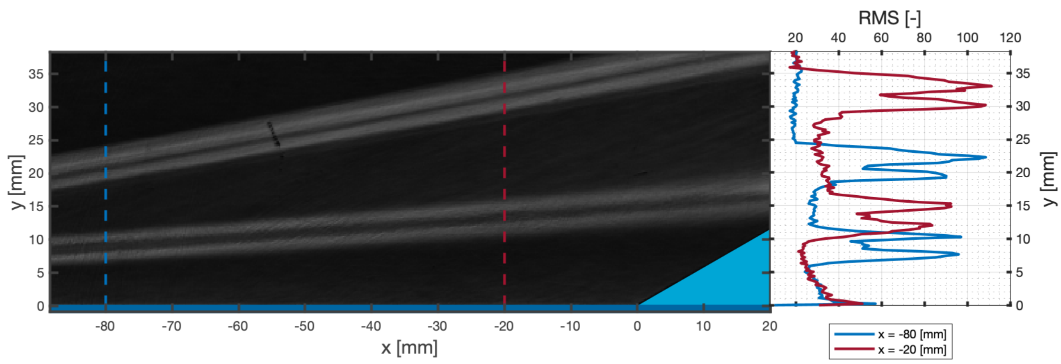

(b) $M_\infty = 7.5$; $Re = 46.3 \times 10^5$

Figure 5.13: **No roughness strip**, $\alpha = 30°$

tion of the 30° ramp at the lower Reynolds number. Additionally, the lower Reynolds number produces a greater maximum spanwise mean than the higher Reynolds number. Similarly, figure 5.15 shows the maximum spanwise RMS, displaying a similar trend to that of figure 5.14: increasing the ramp angle increases the maximum spanwise RMS, while for a given ramp angle, the lower Reynolds number produces a greater value as well. However, at the lower Reynolds number, there is much greater uncertainty between the three runs as one increases the ramp angle. This is particularly apparent for the case of $\alpha = 30°$. However, the error is small enough that the stated trend remains valid.

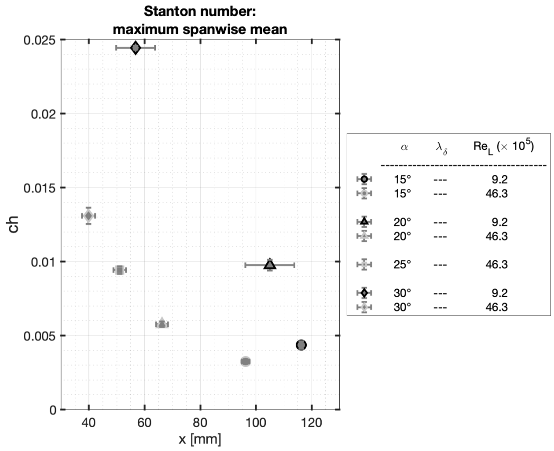

Figure 5.14: **No roughness strip.**

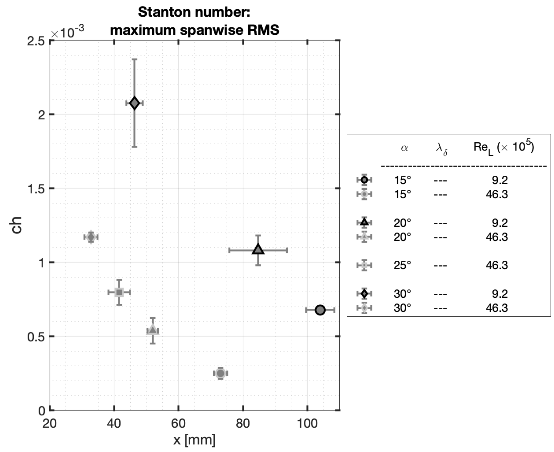

Figure 5.15: **No roughness strip.**

5.3. Sinusoidal Strip, Low Reynolds Number

This section explores transitional phenomena in SBLIs. The results presented in this section build up on the lower Reynolds number results of section 5.2 by introducing a sinusoidal roughness element into the flow upstream of the compression ramp, $100\ mm$ downstream of the flat plate leading edge. The strip employed in this discussion is characterized by its spanwise wavelength nondimensionalized by the local boundary layer thickness as $\lambda_\delta = 2.7$. This section focuses not on the influence of the Reynolds number so much as the influence of ramp angle.

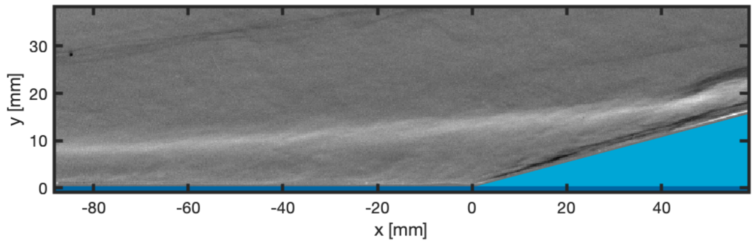

(a) $\alpha = 15°$; $Re = 9.2 \times 10^5$

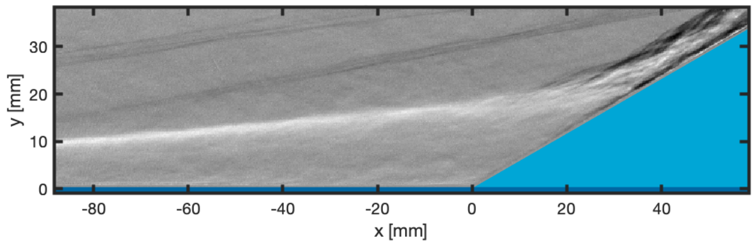

(b) $\alpha = 30°$; $Re = 9.2 \times 10^5$

Figure 5.16: **Nondimensional roughness strip wavelength:** $\lambda_\delta = 2.7$

The discussion begins with figures 5.16a and 5.16b, which show schlieren images of the circulation region involving the 15° and 30° ramps, respectively. It is apparent when comparing figure 5.16a to figure 5.2a, and figure 5.16b to figure 5.6a, that the shear layer and separation shock are not as well defined when under the influence of a roughness strip. The peaks of the strip deflect flow away from the wall, possibly generating shocks, while the gaps between peaks do not. Such behavior is three-dimensional and likely periodic in the spanwise direction. The effect of this is described in the ramp surface heat flux results.

The separation shock in figure 5.16a, while well defined in the cases without a strip, is barely visible, and even then is visible only above the ramp far from its inception near the root of the shear layer. The separation shock for the 30° ramp is better defined, but nevertheless lacks the clarity present in figure 5.6a. The shear layer, too, is not as 'sharp' as in the baseline results. Though clearly present in both figure 5.16b and 5.6a, it appears that the roughness strip influences the flow dynamics within the circulation region, likely because the spanwise periodic regions of alternating perturbed-unperturbed flow (a result of the peaks and valleys of the strip) have different boundary layer profiles – unperturbed flow is more likely to be laminar, and vice versa for perturbed flow. If the boundary layer alternates in profile in the spanwise direction, then different spanwise regions of the flow theoretically interact differently with the adverse pressure gradient of the initial oblique shock formed at the ramp corner. In effect, different regions of the flow theoretically experience different 'sizes' of the circulation region. Thus, the roughness strip introduces three-dimensionality into the flow, which initially manifests itself in the boundary layer profile before being translated into the flow dynamics of the circulation region.

The influence of the roughness strip on the surface heat flux is illustrated in figures 5.17a and 5.17b. It is immediately apparent that the circulation region translates the periodic three-dimensional flow phenomena introduced by the roughness strip through the circulation region and onto the ramp surface. In other words, the perturbations introduced by the roughness strip manifest themselves as temperature striations along the ramp surface. The wavelength of the heat signatures is virtually identical to the wavelength of the roughness strip of $\lambda_\delta = 2.7$ (corresponding to $9\ mm$), with some apparent overspill

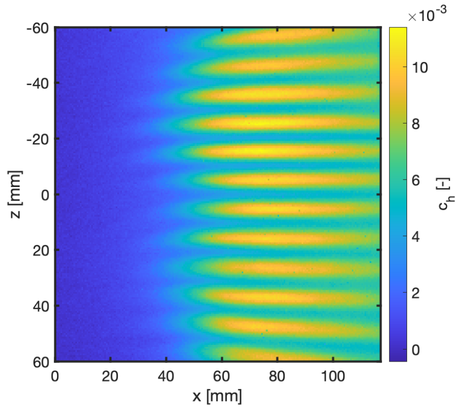

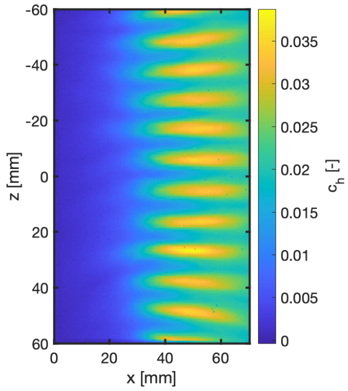

(a) $\alpha = 15°$; $Re = 9.2 \times 10^5$ (b) $\alpha = 30°$; $Re = 9.2 \times 10^5$

Figure 5.17: **Nondimensional roughness strip wavelength:** $\lambda_\delta = 2.7$

near the spanwise edges. Furthermore, the differences between the peaks and valleys of the heat signatures are distinct. The observations made between the baseline results of figures 5.3a and 5.7a also apply here: increasing the ramp angle while maintaining the Reynolds number results in an increase of Stanton number at the ramp surface. However, with a roughness strip upstream of the circulation region, the variation in spanwise Stanton number is, by comparison, extreme.

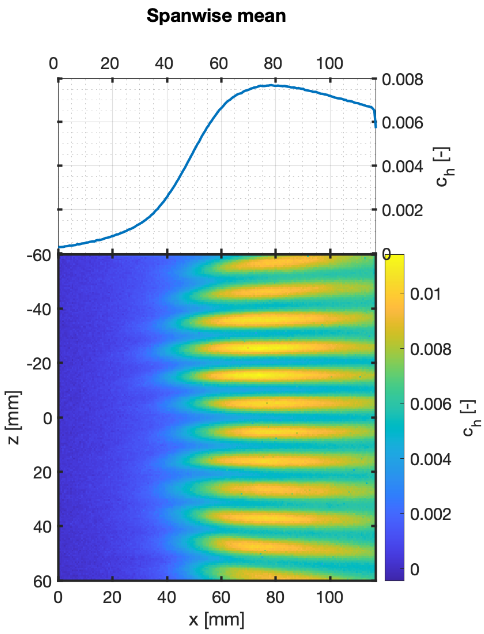

(a) $\alpha = 15°$; $Re = 9.2 \times 10^5$

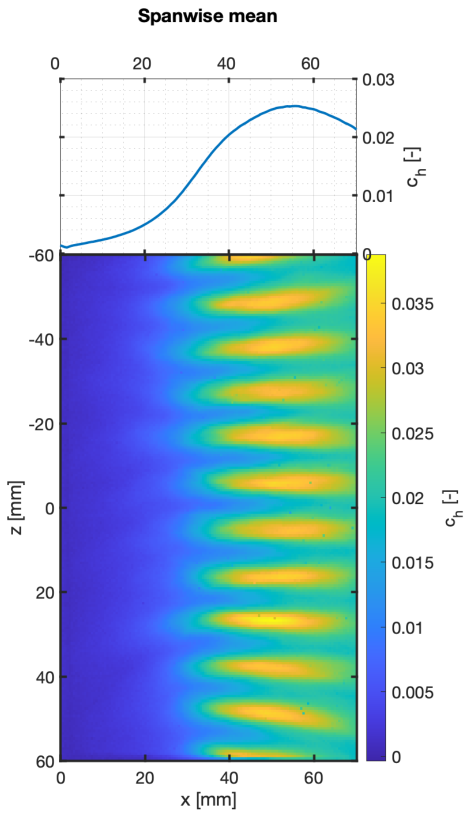

(b) $\alpha = 30°$; $Re = 9.2 \times 10^5$

Figure 5.18: **Nondimensional roughness strip wavelength:** $\lambda_\delta = 2.7$

Figures 5.18a and 5.18b show the spanwise mean profile for both ramps. For the ramp angle of 15°, the maximum occurs at $x = 78\,mm$, which is a noticeable difference from the baseline results of figure

5.8a. A similar observation is made between figures 5.9a and 5.18b, though the effect is less drastic. Such observations, along with their associated schlieren images (figures 5.16a and 5.16b) suggest that in the presence of a roughness strip, at the lower Reynolds number, the shear layer impacts the compression ramp farther upstream than when a roughness strip is absent – for both ramp angles. This suggests that the strip ‘shrinks’ the circulation region, which further supports the possibility that the strip contributes to destabilizing the flow, possibly thickening the boundary layer and thereby causing the boundary layer to resist the adverse pressure gradient formed by the ramp corner.

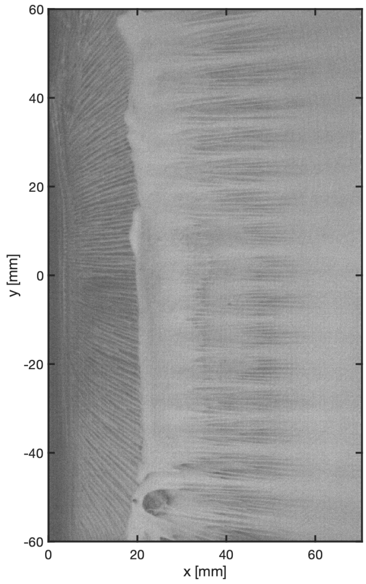

Figure 5.19: $Re = 9.2 \times 10^5$, $\alpha = 30°$. Region of $x < 20\ mm$ shows oil residue from earlier runs and should be ignored.

Figure 5.19 shows oil flow results of the ramp surface normal to the flat plate. The image shows the clear imprint of the roughness strip observed in figure 5.17b, in which darker regions correspond to regions of higher temperature. This further supports the theory that some form of vortices are present in the flow that sweep high momentum flow toward the wall and low momentum flow away. Interestingly, the smaller streaks are still present, though they seem less defined than those in figure 5.17b.

To further analyze the behavior of the circulation region, we again consider the RMS of the shear layer, see for example figures 5.20a and 5.20b. The RMS is calculated at $x = [-80, -20]\ mm$; profiles are on the right. Reflecting on figure 5.5, it appears that the shear layer in both figures 5.20a and 5.20b are primarily transitional. However, the profiles lack any distinct valleys near their maximum, as depicted in figure 5.5b and seen in figure 5.13b. Still, there does appear to be some degree of inflection near the peaks for both profiles. The distinction between transitional and turbulent RMS profiles is further explored in section 5.4.

To conclude the analysis of transitional results, consider the spanwise RMS profile of the Stanton number in figures 5.21a and 5.21b. As before, the RMS is a measure of the deviation from the mean, which means that the x-location where the spanwise RMS is maximum is the x location where there is the greatest amount of variation in spanwise Stanton number – $\approx 72.5mm$ for figure 5.21a and $\approx 45mm$ for figure 5.21b. The x location for the associated baseline results – figure 5.10a for the 15° ramp and figure 5.11a for the 30° ramp – show that the spanwise maximum RMS occurs at approximately the same location, though the shear layer for the 15° ramp does not appear to fully impact the compression ramp.

Figure 5.22 displays the Stanton number maximum spanwise mean, showing very consistent trends for all results of $\lambda_\delta = 2.7$, $Re = 9.2 \times 10^5$. Namely, increasing the ramp angle increases the value of the maximum spanwise mean while shifting the location of the maximum upstream toward the ramp corner. Increasing the ramp angle from 15° to 30° increases the c_h value from 0.0075 to 0.025 – a multiple of 3.33, while the x location shifts from $\approx 82\ mm$ to $\approx 55\ mm$.

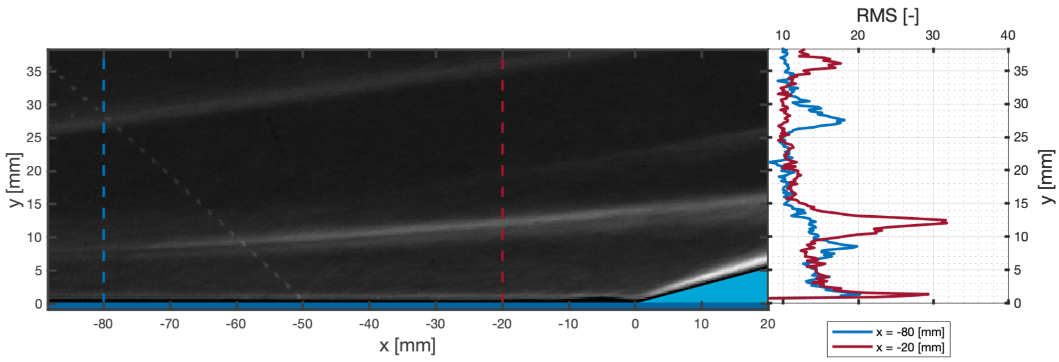

(a) $\alpha = 15°$; $Re = 9.2 \times 10^5$

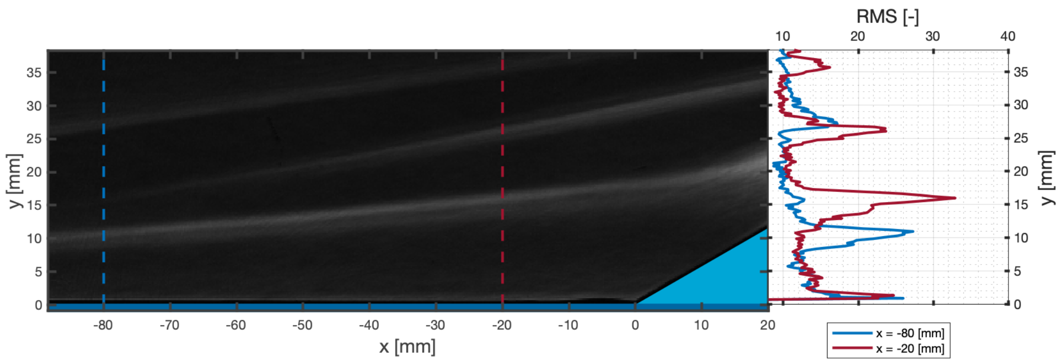

(b) $\alpha = 30°$; $Re = 9.2 \times 10^5$

Figure 5.20: **Nondimensional roughness strip wavelength:** $\lambda_\delta = 2.7$

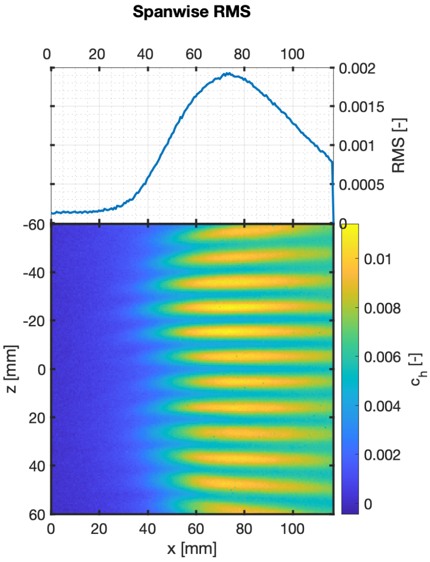

(a) $\alpha = 15°$; $Re = 9.2 \times 10^5$

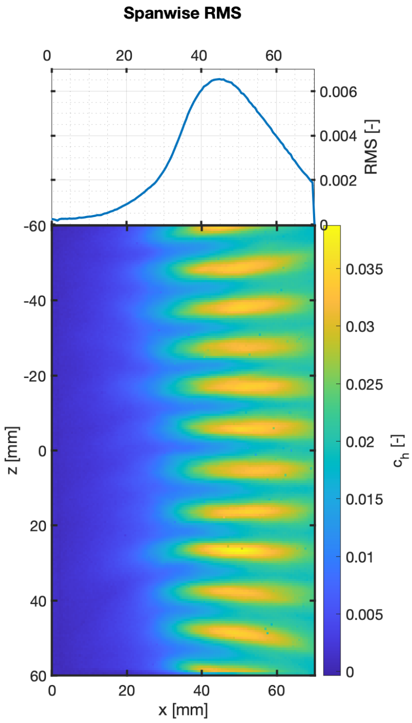

(b) $\alpha = 30°$; $Re = 9.2 \times 10^5$

Figure 5.21: **Nondimensional roughness strip wavelength:** $\lambda_\delta = 2.7$

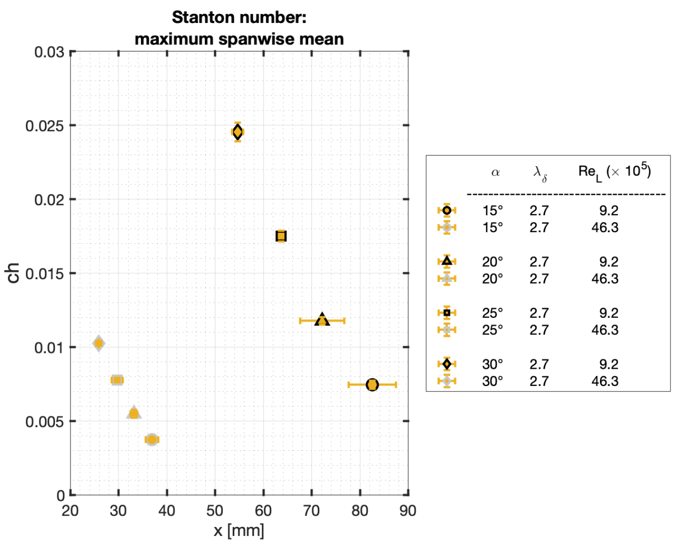

Figure 5.22: **Nondimensional roughness strip wavelength:** $\lambda_\delta = 2.7$

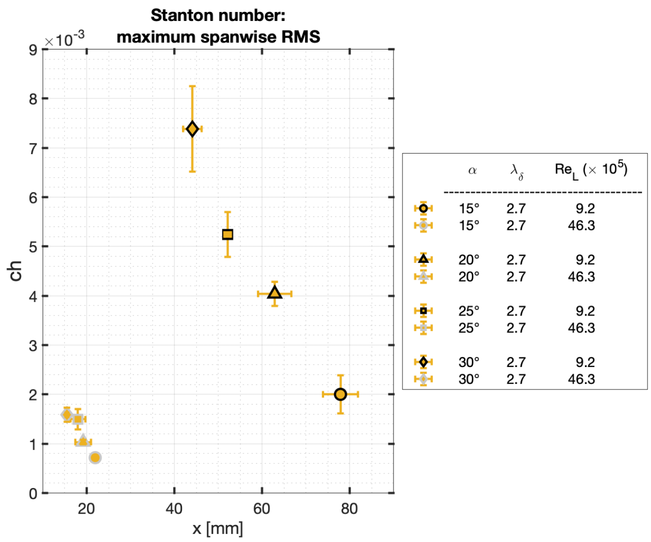

Figure 5.23: **Nondimensional roughness strip wavelength:** $\lambda_\delta = 2.7$

5.4. Sinusoidal Strip, High Reynolds Number

This section explores the behavior of the shock–boundary-layer interaction at the higher Reynolds number when subjected to an upstream roughness element. The results presented in this section share the exact same setup and freestream conditions as those of section 5.3 – except for the Reynolds number, which is at the larger value ($Re = 46.3 \times 10^5$).

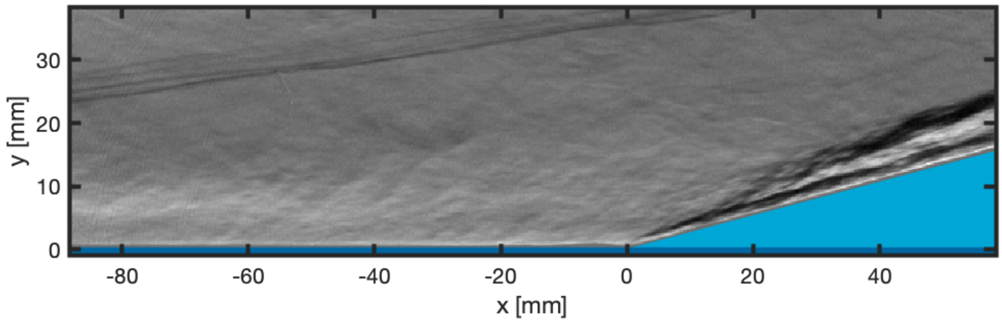

(a) $M_\infty = 7.5$; $\alpha = 15°$; $Re = 46.3 \times 10^5$

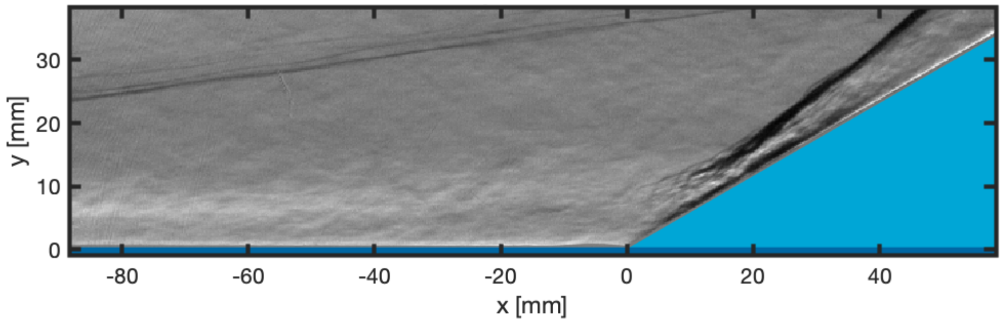

(b) $M_\infty = 7.5$; $\alpha = 30°$; $Re = 46.3 \times 10^5$

Figure 5.24: **Nondimensional roughness strip wavelength:** $\lambda_\delta = 2.7$

Figures 5.24a and 5.24b show schlieren images of the 15° and 30° ramps, respectively. The contrast in flow topology from the results of section 5.3 (figures 5.16a and 5.16b) is immediately apparent: there is a distinct shear layer and separation shock in the low Reynolds number results, but none for the experiments conducted at the high Reynolds number. The boundary layer appears to be completely turbulent. Evidently the difference in Reynolds number from 9.2×10^5 to 46.3×10^5 is great enough to transition the boundary layer to turbulence when encountering the roughness strip. (Note that the shock in the upper left hand corner of figures 5.24a and 5.24b is from the compression occurring at the trailing edge of the roughness strip.) The turbulent boundary layer is apparently shallow enough and with enough momentum to resist the adverse pressure gradient of the oblique shock at the ramp corner, thereby avoiding separation and ensuring the oblique shock remains attached. A separated SBLI system does not form for either ramp – or for *any* run involving a roughness strip at high Reynolds number.

Figures 5.25a and 5.25b show the RMS upstream of the oblique shock. Both exhibit a fully turbulent boundary layer, which is reflected in the RMS profiles near the wall. The profiles of the boundary layer are wider than those of laminar or transitional SBLI characteristics and lack a distinct valley in the peak.

Figures 5.26a and 5.26b show the familiar Stanton number contours on each ramp surface. The lack of a circulation region is immediately apparent. The most obvious difference between these results and those at a lower Reynolds number in section 5.3 is that the striations occur farther upstream, beginning at the ramp corner. The reason for this is due to the fact that the flow never experiences separation, and a circulation region never forms. Instead, the roughness strip trips the boundary layer while simultaneously introducing the sinusoidal perturbations into the flow. There is essentially nothing deflecting the perturbations away from the wall, and thus they advect with the flow along the surface until they encounter the compression ramp. Additionally, the turbulent interaction disperses the heat

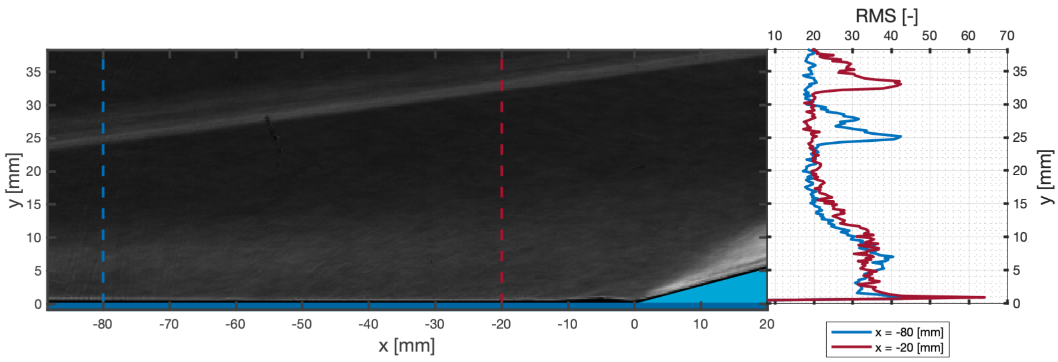

(a) $M_\infty = 7.5$; $\alpha = 15°$; $Re = 46.3 \times 10^5$

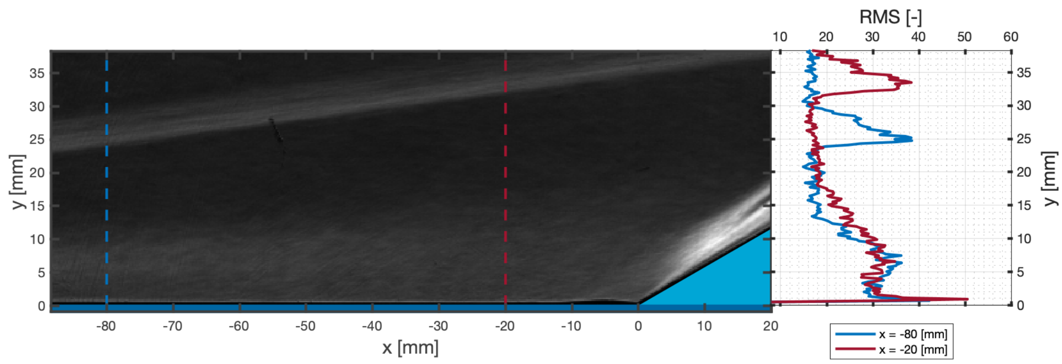

(b) $M_\infty = 7.5$; $\alpha = 30°$; $Re = 46.3 \times 10^5$

Figure 5.25: **Nondimensional roughness strip wavelength:** $\lambda_\delta = 2.7$

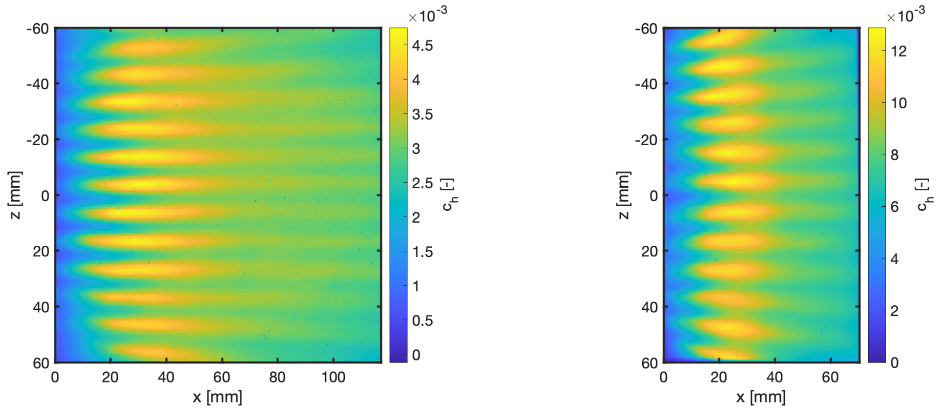

(a) $M_\infty = 7.5$; $\alpha = 15°$; $Re = 46.3 \times 10^5$ (b) $M_\infty = 7.5$; $\alpha = 30°$; $Re = 46.3 \times 10^5$

Figure 5.26: **Nondimensional roughness strip wavelength:** $\lambda_\delta = 2.7$

flux in the spanwise direction, diminishing the regions of low temperature that are so clearly present in figures 5.17a and 5.17b. In general, the 30° ramp exhibits greater Stanton number values than the 15° ramp. To help clarify and quantify this difference, consider the spanwise mean of the two cases in figures 5.27a and 5.27b. The two ramps exhibit similar profiles with a steady increase to the maximum before gradually decreasing to the flow ramp edge. Though the two ramps exhibit similar profiles, the magnitude is vastly different. Noticeably, the maximum of the 15° ramp never even reaches the minimum of the 30°, matching the trend observed in the baseline and transitional results. Figures 5.28a and 5.28b show the spanwise Stanton number RMS for the 15° and 30° ramps, respectively. The two ramps show similar profiles, reaching a maximum near $x = 20\,mm$ for each before decreasing to a plateau at the 'tail end' of the spanwise band of elevated values. These profiles suggest that the temperature difference between the high and low streaks remains relatively constant for the remaining ramp surface. Figure 5.22 shows the relationship between the maximum spanwise mean and ramp angle (as well as x location of the maximum). The turbulent results involving the $\lambda_\delta = 2.7$ roughness strip are denoted with a gray marker edge at bottom left. The trend appears to be remarkably consistent with the values displaying little if any error. It also appears that increasing the ramp angle in a turbulent flow does not significantly increase the maximum spanwise mean of the Stanton number when compared to results that are laminar and undergo circulation (upper right of figure 5.22).

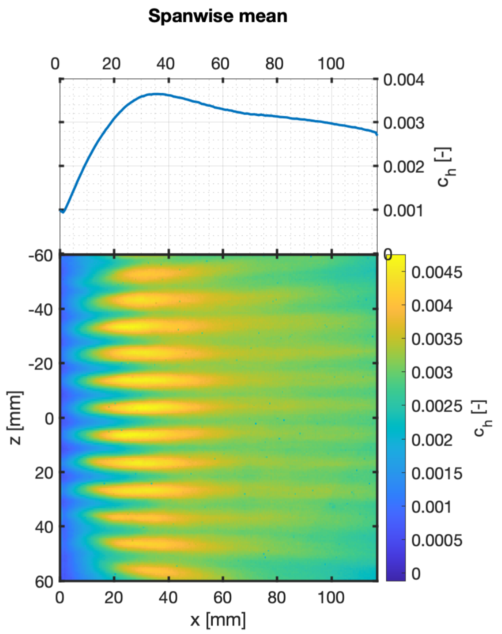

(a) $M_\infty = 7.5$; $\alpha = 15°$; $Re = 46.3 \times 10^5$

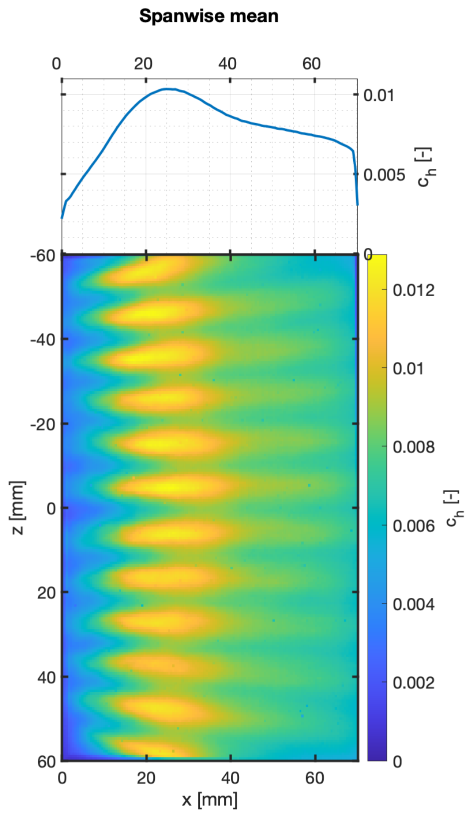

(b) $M_\infty = 7.5$; $\alpha = 30°$; $Re = 46.3 \times 10^5$

Figure 5.27: **Nondimensional roughness strip wavelength:** $\lambda_\delta = 2.7$

Continuing to the turbulent results of the maximum spanwise RMS in figure 5.23, it is apparent that there is little difference between the turbulent results when compared to the laminar results. The trend appears to be that the maximum spanwise RMS increases and shifts slightly toward the negative x direction with increasing ramp angle. But, again, the difference is small.

Figure 5.29 shows oil flow results of the 30° ramp. The effect a turbulent SBLI has on the ramp surface is quite clear and again agrees with the corresponding heat flux results (figure 5.26b). The streaks that are so visible in the baseline and transitional images are less distinct but nevertheless present. However, it is difficult to distinguish the imprint of the roughness strip. This is due to the diffusive and 'smearing' effect of turbulence on the flow properties. The effect of turbulence is also apparent in the region downstream of $x \approx 20\,mm$. The oil is completely smeared, which is in contrast to the baseline and transitional results but also agrees with the heat signatures of figure 5.26b.

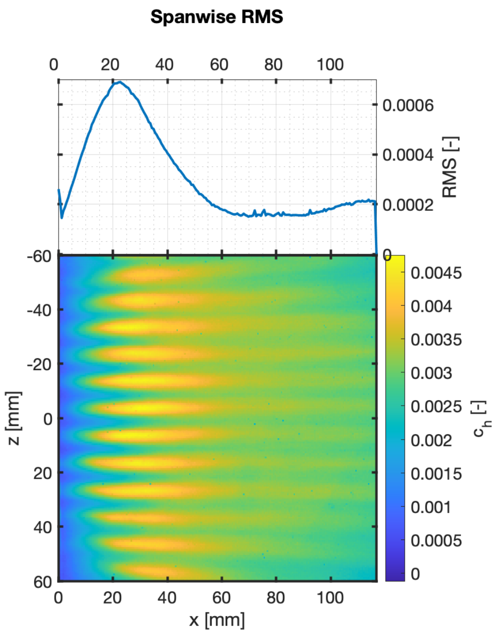

(a) $M_\infty = 7.5$; $\alpha = 15°$; $Re = 46.3 \times 10^5$

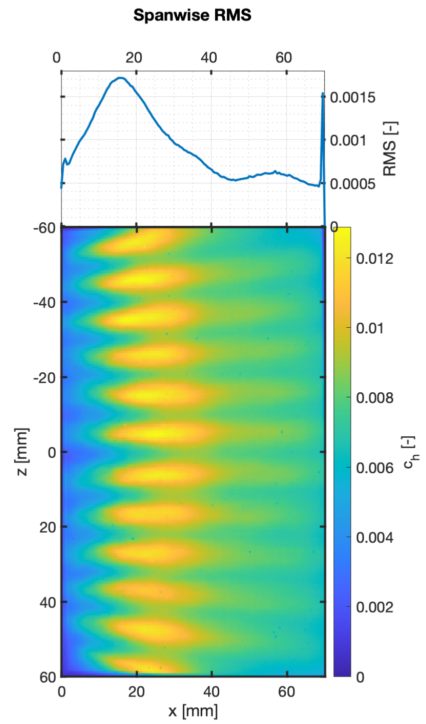

(b) $M_\infty = 7.5$; $\alpha = 30°$; $Re = 46.3 \times 10^5$

Figure 5.28: **Nondimensional roughness strip wavelength:** $\lambda_\delta = 2.7$

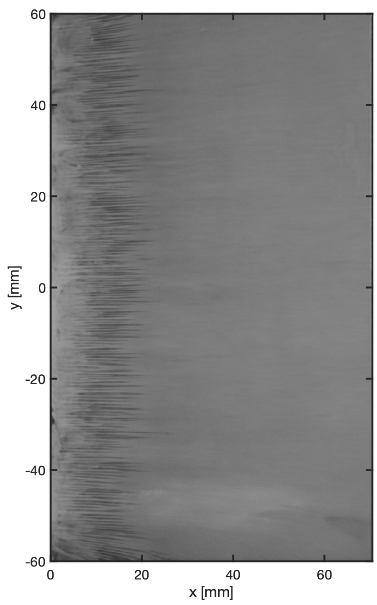

Figure 5.29: $Re = 46.3 \times 10^5$, $\alpha = 30°$

6 Conclusions

The flow phenomena involved in high-speed flight and atmospheric re-entry represent some of the most extreme and perilous flow conditions achieved by human kind. Among the myriad phenomena that occur in the low-enthalpy regime are shock–boundary-layer interactions, which involve the interplay between relatively inviscid shocks and viscous boundary layers. SBLIs often create flow conditions that exacerbate the naturally extreme aerothermal conditions inherent in hypersonic flow, and may amplify instabilities that further destabilize the flow's integrity. Shock–boundary-layer interactions, when present, dramatically alter the flow both near and far from the wall, potentially developing pressure and heat transfer conditions so extreme that the vehicle suffers catastrophic damage or loses control. An additional factor compounding the severity of SBLI effects is that SBLI inception – i.e. where, when, why, and how they form – can be particularly difficult to predict.

An additional factor that strongly dictates SBLI behavior is the state of the boundary later at separation. Laminar and turbulent boundary layers influence the flow in drastically different ways, the most notable of which may well be that turbulent boundary layers are more difficult to separate than laminar boundary layers. This means that, under identical flow conditions (i.e. identical freestream velocity, Mach number, total temperature, etc.), the extent to which the flow separates is due exclusively to the state of the boundary layer. To this extent, it may sometimes be desirable to induce turbulence upstream of a compression ramp or oblique interacting shock to prevent separation altogether, which in turn either mitigates or even prevents the extreme pressure and surface heat transfer conditions that are prone to damaging the vehicle's surface.

This research questions proposed this thesis, How do shock–boundary-layer interactions amplify or dampen prescribed upstream sinusoidal perturbations? To what extent do sinusoidal roughness strips destabilize the boundary layer? What differences are there between laminar and turbulent upstream boundary layers in propagating disturbances downstream? These questions are answered by performing experiments of sinusoidal roughness strips in Mach 7.5 flow over flat- plate-compression -ramp models. Of particular interest is how the state of the boundary layer generated by the flat plate influences the shock–boundary-layer system in general, including flow characteristics and surface effects. The test facility used to conduct the experiments is the Hypersonic Test Facility Delft (HTFD) located within the Aerospace Engineering faculty at the Technological University Delft (TU Delft). The facility operates in the low-enthalpy regime under the Ludwieg tube principle, which employs large pressure differences and fast-acting valves to create high-velocity, high-Mach -number flow. In all, this thesis explores combinations of freestream Reynolds number (9.2×10^5 and 46.3×10^5), compression ramp angle ($\alpha = [-, 15°, 20°, 25°, \text{and } 30°]$), and nondimensional roughness strip wavelength ($\lambda_\delta = [-, 1.8, 2.7, 3.6, 4.5]$).

To study the SBLI features that arise due to the flat- plate-ramp model, this thesis uses three measurement techniques well suited to study low-enthalpy SBLI flow phenomena: schlieren visualization, quantitative infrared thermography (QIRT), and oil flow visualization. Schlieren visualization is used to visualize the shocks and shear layer, while quantitative infrared thermography is used to measure the temperature on the ramp surface, which is then used to calculate the heat transfer. Oil flow is used to visualize the flow direction along the surface of the ramp, and is particularly adept at identifying regions of stagnation and separation. These measurement techniques provide multiple perspectives on the flow phenomena inherent in the SBLIs studied in this work.

The experimental results presented in the main body of this work are largely characterized based on the state of the upstream boundary layer and its effect on the circulation region. In general, the results are discussed in order of decreasing boundary layer stability, beginning with a flat plate laminar boundary layer before ultimately progressing to fully turbulent shock–boundary-layer interactions.

To combat the wealth of data collected for this thesis and elucidate the overall discussion, the only roughness strip discussed is the strip characterized by the nondimensional wavelength of $\lambda_\delta = 2.7$. In addition, the ramp angles discussed are $15°$ and $30°$ to illustrate the contrast in results between the shallowest ramp and the steepest. Both Reynolds numbers are explored to discuss the influence of the Reynolds number on shock–boundary-layer interactions, as well as to investigate the influence of laminar and turbulent upstream boundary layers on shock–boundary-layer flow topology.

For the experiments that lack a strip, schlieren results show that the flow separates from the ramp corner and forms a circulation region distinguished by a separation shock, shear layer, and reattachment on the ramp. Root mean square calculations of the schlieren images indicate that the shear layer is transitional, particularly at the higher Reynolds number. Meanwhile, QIRT results show that the impact of the shear layer on the ramp surface results in an increase in heat flux immediately downstream of reattachment along the entire span of the ramp. In addition, an increase in Reynolds number generally results in a decrease in surface heat flux, indicated by a decrease in the maximum spanwise mean Stanton number. Furthermore, with increasing Reynolds number, the location of maximum heat flux shifts upstream toward the ramp corner. These findings agree with results presented in the open literature [30, 41, 42].

For the second category of results, the Reynolds number is kept constant at the lower of the two values (9.2×10^5) and a roughness strip is used, which is characterized by a nondimensional wavelength of $\lambda_\delta = 2.7$. The results show that the flow separates and forms a circulation region, but that the separation shock and shear layer are less clearly defined when compared to the results that lack a strip. Nevertheless, despite the comparative lack of clarity, the RMS of the shear layer is distinguished and indicates that the shear layer is transitional. It is additionally determined that an increase in ramp angle increases the heat flux on the ramp surface, as indicated by the maximum spanwise mean Stanton number. Furthermore, increasing the ramp angle shifts the location of the maximum spanwise mean Stanton number upstream. This trend agrees with the the results that lack a strip.

The final category of results explored in this thesis involve those with a roughness strip at the the higher of the two Reynolds number values (46.3×10^5). The flow field is dramatically different from that of the previous results – schlieren images indicate that the flow is fully turbulent and lacks any recirculation region at all, with the flow interacting with the ramp to form an oblique shock propagating from the ramp's corner. The heat flux results on the ramp surface imitate the trends shown by the previous results: an increase in ramp angle increases the Stanton number across the entire ramp surface and shifts the location of the maximum upstream. However, the amount by which the Stanton number increases and shifts upstream is comparatively less than when the flow is transitional.

7
Recommendations

This chapter provides recommendations for future studies involving compression shock–boundary-layer interactions in the presence of a sinusoidal roughness strip.

One of the more obvious conclusions of this thesis is that the roughness strip trips the boundary layer at the higher Reynolds number (46.3×10^5), transitions the flow to turbulence, and ultimately prevents the flow from separating and forming a circulation region. Considering the fact that the main goal of this thesis is to observe and quantify how perturbations propagate ‘through’ the SBLI system and manifest themselves on the ramp surface, a lack of circulation region and the diffusive nature of turbulence effectively render it difficult to study these effects. Furthermore, the turbulent results differ little from one another, both with regard to the schlieren images and the heat flux results. As such, the first recommendation of this thesis is to avoid tripping the boundary layer so as to avoid turbulent SBLIs. This may be achieved in three ways: decreasing the Reynolds number, decreasing the height of the roughness strip, and positioning the strip farther downstream so as to be smaller with respect to the boundary layer thickness. Of these three, the latter is recommended simply because it is simplest and likely most effective. Doing so allows the tunnel to operate at a range of Reynolds numbers if desired, thereby obtaining stronger correlations between Reynolds number and transitional/turbulent signatures in the shear layer and on the ramp surface.

An additional recommendation is to avoid using so many roughness strips (i.e. employ only one or two roughness strip wavelengths). In the author’s opinion, it is much more worthwhile to alter the ramp angle or Reynolds number while maintaining one or two roughness strips rather than working with many strips. Doing so likely yields stronger correlations between the various conditions and setup, and additionally benefits from the fact that it is much more difficult to remove and replace a strip than it is to remove and replace a ramp or modify the Reynolds number. Furthermore, several strips were destroyed in the making of this thesis, much to the author’s dismay. Several copies of few strips is preferable to few copies of many strips.

The results primarily focus on the reattachment region rather than the separation point. This is largely due to the fact that the separation location is frequently outside the camera’s frame of view or beyond the tunnel’s window. If one wished to study the separation location it is advisable to relocate the ramp farther downstream so as to position the separation location closer to the middle of the test section.

The oil flow results are rather uninformative compared to the heat flux results. Additionally, oil flow measurements are cumbersome and tedious to set up, not to mention very messy. As such, the author recommends avoiding oil flow measurements at all.

The behavior of the shear layer and the possible presence of Görtler vortices suggests that PIV measurements may be particularly valuable in providing further insight into the behavior of SBLI phenomena. Though the setup may be difficult to achieve, tomographic PIV is most strongly recommended.

A

QIRT Images: Normal to Flat Plate Surface

This appendix chapter presents all valid Stanton number (c_h) surface results for all strip-ramp combinations. Each pair of images represents both the low and high freestream Re conditions (see table 3.3) pertaining to a particular strip. The low and high Reynolds number values are 9.2×10^5 and 46.3×10^5 based on the distance from the flat plate leading edge to the corner of the ramp ($417\ mm$). The analogous unit Reynolds number for each, respectively, is provided in the M7 row in table 3.3. The freestream Mach number is 7.5 for all results. All images are projections normal to the flat plate surface. Images that either do not exist or are corrupted are absent and are replaced with square boxes enclosing a diagonal strike.

The images adhere to the following specifications:

- Frame rate: $200\ Hz$
- Integration time: $250\ \mu s$
- Spatial resolution: $1.66\ px/mm$

A.1. Ramp angle of 15°

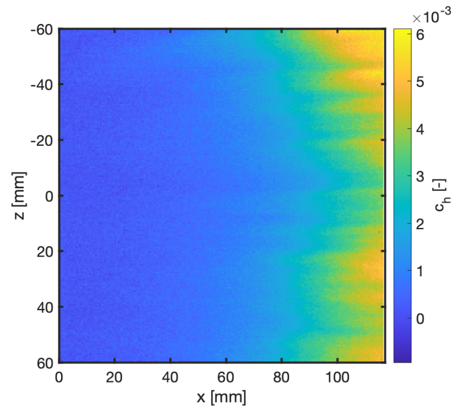

(a) $M_\infty = 7.5$; $Re = 9.2 \times 10^5$

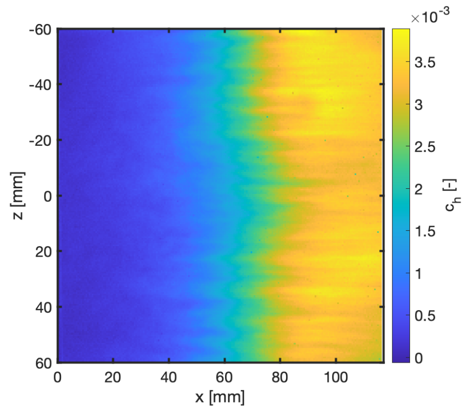

(b) $M_\infty = 7.5$; $Re = 46.3 \times 10^5$

Figure A.1: **No roughness strip.**

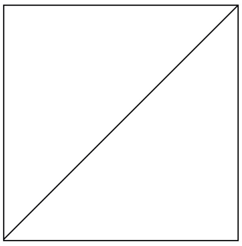

(a) $M_\infty = 7.5$; $Re = 9.2 \times 10^5$

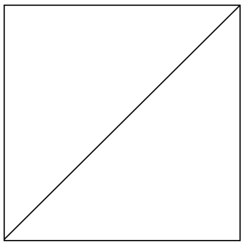

(b) $M_\infty = 7.5$; $Re = 46.3 \times 10^5$

Figure A.2: **Nondimensional roughness strip wavelength:** $\lambda_\delta = 1.8$

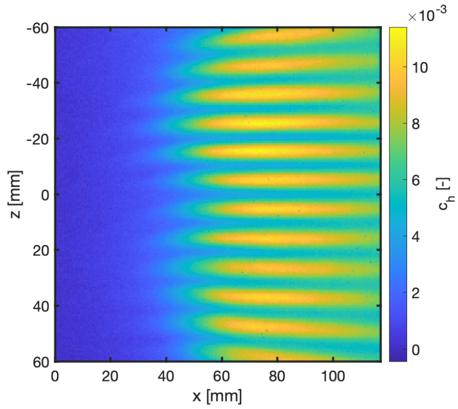

(a) $M_\infty = 7.5$; $Re = 9.2 \times 10^5$

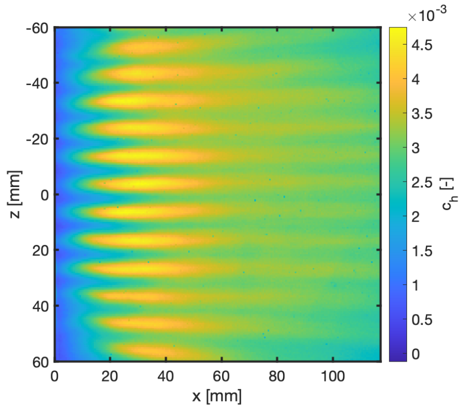

(b) $M_\infty = 7.5$; $Re = 46.3 \times 10^5$

Figure A.3: **Nondimensional roughness strip wavelength:** $\lambda_\delta = 2.7$

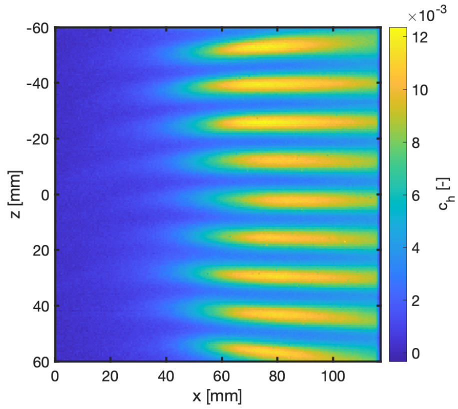

(a) $M_\infty = 7.5$; $Re = 9.2 \times 10^5$

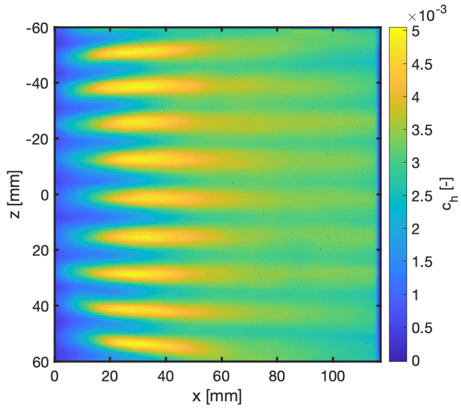

(b) $M_\infty = 7.5$; $Re = 46.3 \times 10^5$

Figure A.4: **Nondimensional roughness strip wavelength:** $\lambda_\delta = 3.6$

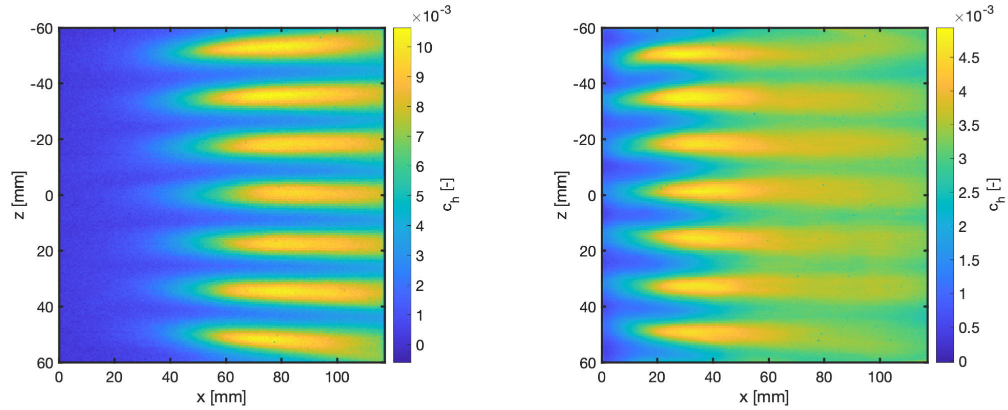

(a) $M_\infty = 7.5$; $Re = 9.2 \times 10^5$

(b) $M_\infty = 7.5$; $Re = 46.3 \times 10^5$

Figure A.5: **Nondimensional roughness strip wavelength:** $\lambda_\delta = 4.5$

A.2. Ramp angle of $20°$

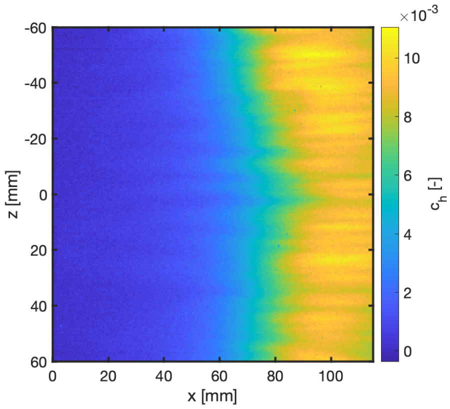

(a) $M_\infty = 7.5$; $Re = 9.2 \times 10^5$

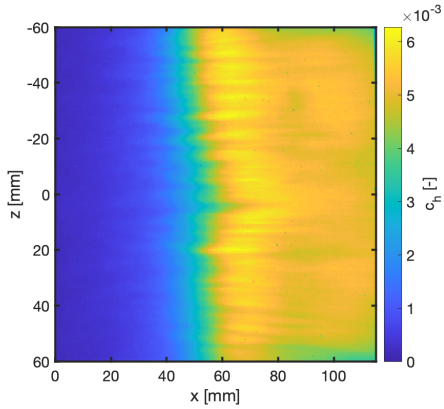

(b) $M_\infty = 7.5$; $Re = 46.3 \times 10^5$

Figure A.6: **No roughness strip.**

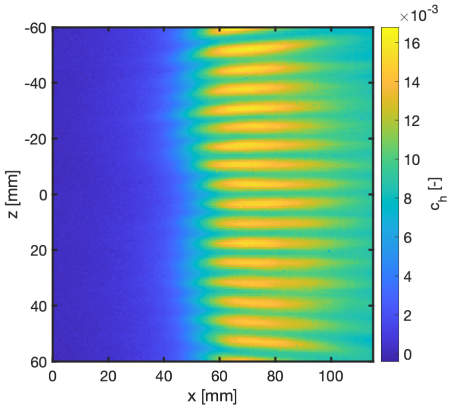

(a) $M_\infty = 7.5$; $Re = 9.2 \times 10^5$

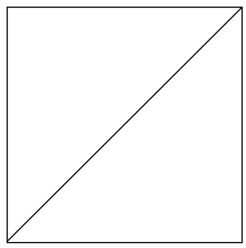

(b) $M_\infty = 7.5$; $Re = 46.3 \times 10^5$

Figure A.7: **Nondimensional roughness strip wavelength:** $\lambda_\delta = 1.8$

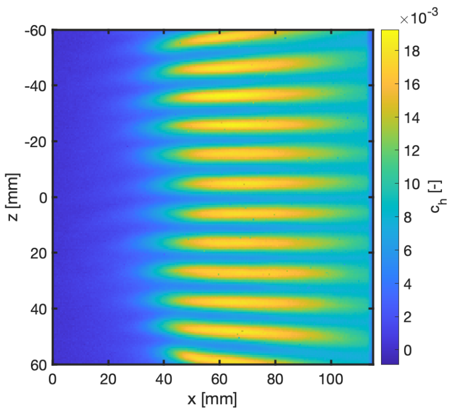

(a) $M_\infty = 7.5$; $Re = 9.2 \times 10^5$

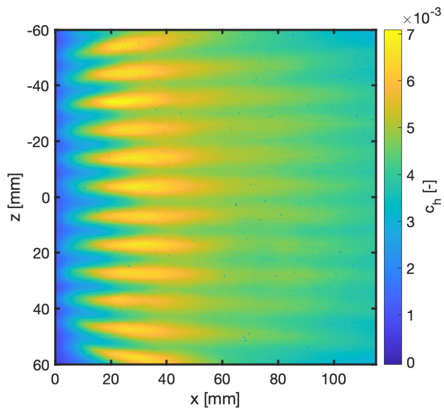

(b) $M_\infty = 7.5$; $Re = 46.3 \times 10^5$

Figure A.8: **Nondimensional roughness strip wavelength:** $\lambda_\delta = 2.7$

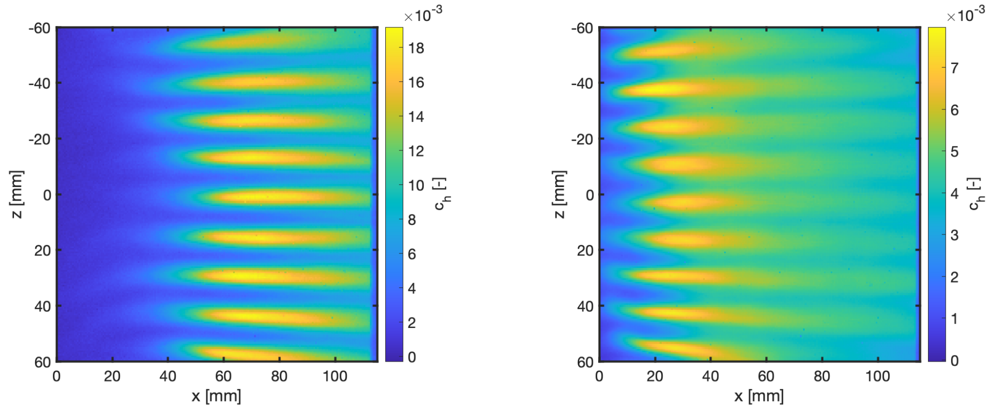

(a) $M_\infty = 7.5$; $Re = 9.2 \times 10^5$

(b) $M_\infty = 7.5$; $Re = 46.3 \times 10^5$

Figure A.9: **Nondimensional roughness strip wavelength:** $\lambda_\delta = 3.6$

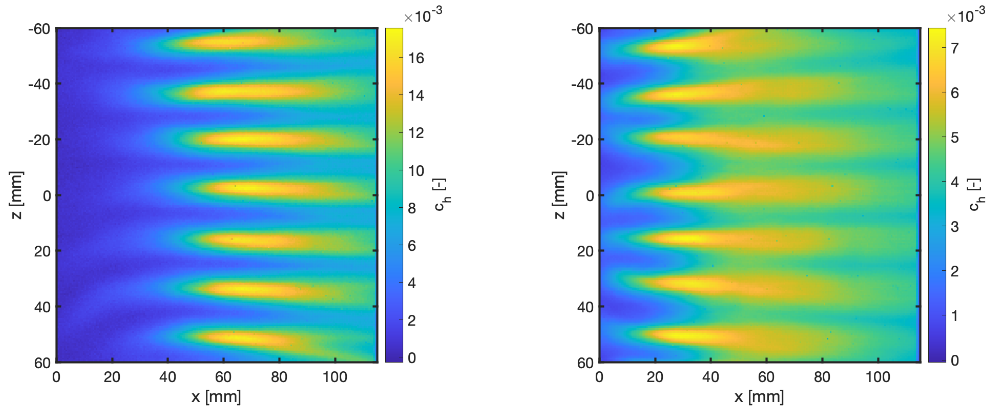

(a) $M_\infty = 7.5$; $Re = 9.2 \times 10^5$

(b) $M_\infty = 7.5$; $Re = 46.3 \times 10^5$

Figure A.10: **Nondimensional roughness strip wavelength:** $\lambda_\delta = 4.5$

A.3. Ramp angle of 25°

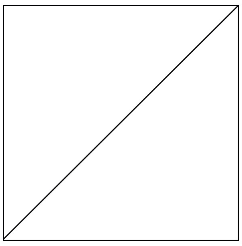

(a) $M_\infty = 7.5$; $Re = 9.2 \times 10^5$

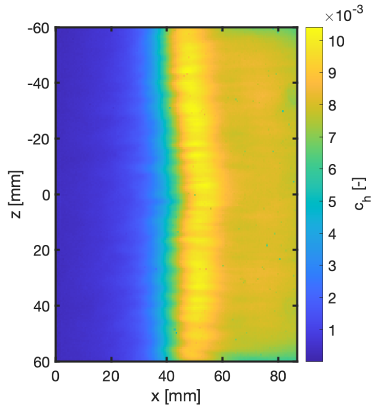

(b) $M_\infty = 7.5$; $Re = 46.3 \times 10^5$

Figure A.11: **No roughness strip.**

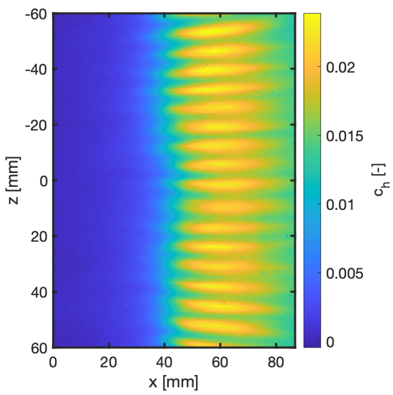

(a) $M_\infty = 7.5$; $Re = 9.2 \times 10^5$

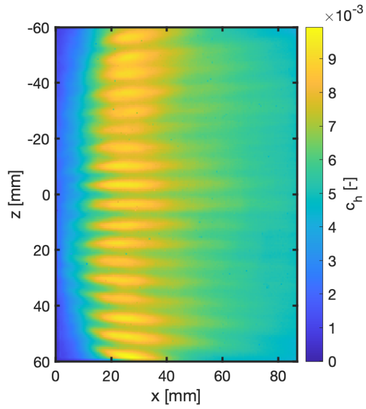

(b) $M_\infty = 7.5$; $Re = 46.3 \times 10^5$

Figure A.12: **Nondimensional roughness strip wavelength:** $\lambda_\delta = 1.8$

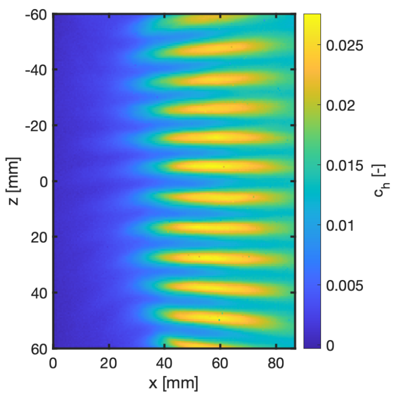

(a) $M_\infty = 7.5$; $Re = 9.2 \times 10^5$

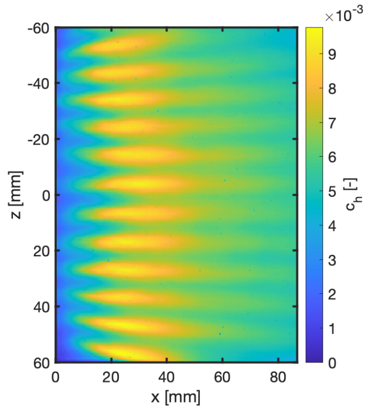

(b) $M_\infty = 7.5$; $Re = 46.3 \times 10^5$

Figure A.13: **Nondimensional roughness strip wavelength:** $\lambda_\delta = 2.7$

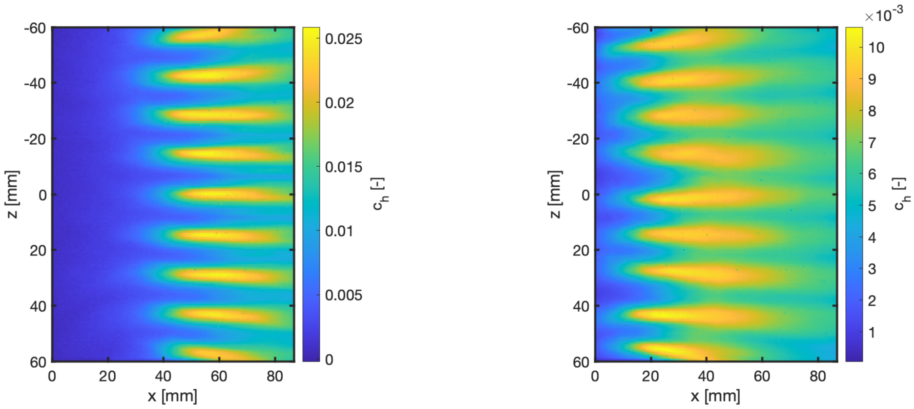

(a) $M_\infty = 7.5$; $Re = 9.2 \times 10^5$

(b) $M_\infty = 7.5$; $Re = 46.3 \times 10^5$

Figure A.14: **Nondimensional roughness strip wavelength:** $\lambda_\delta = 3.6$

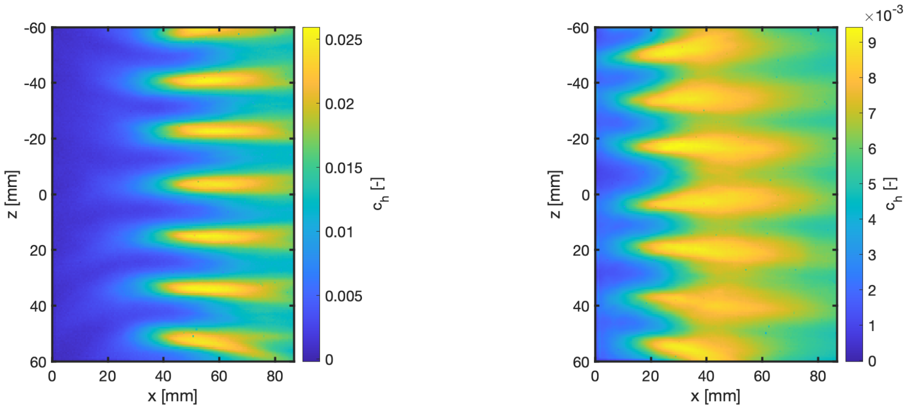

(a) $M_\infty = 7.5$; $Re = 9.2 \times 10^5$

(b) $M_\infty = 7.5$; $Re = 46.3 \times 10^5$

Figure A.15: **Nondimensional roughness strip wavelength:** $\lambda_\delta = 4.5$

A.4. Ramp angle of $30°$

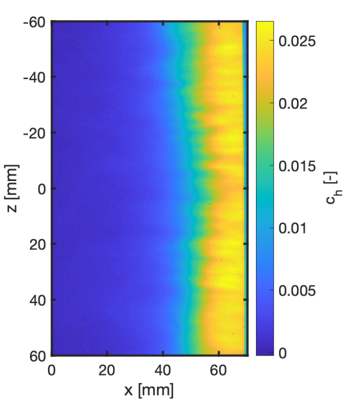

(a) $M_\infty = 7.5$; $Re = 9.2 \times 10^5$

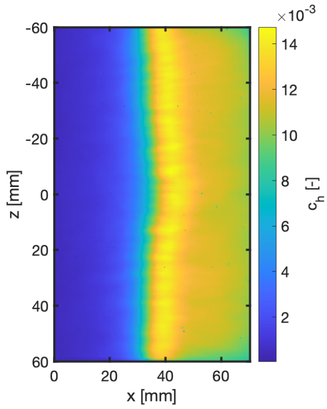

(b) $M_\infty = 7.5$; $Re = 46.3 \times 10^5$

Figure A.16: **No roughness strip.**

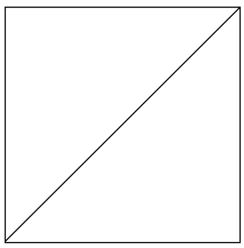

(a) $M_\infty = 7.5$; $Re = 9.2 \times 10^5$

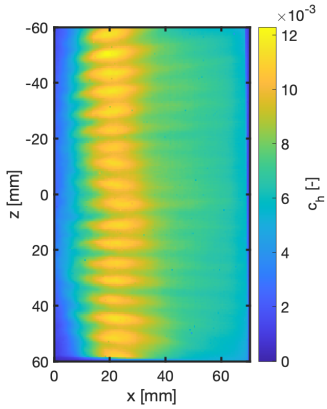

(b) $M_\infty = 7.5$; $Re = 46.3 \times 10^5$

Figure A.17: **Nondimensional roughness strip wavelength:** $\lambda_\delta = 1.8$

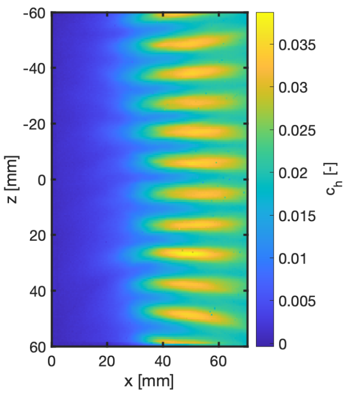

(a) $M_\infty = 7.5$; $Re = 9.2 \times 10^5$

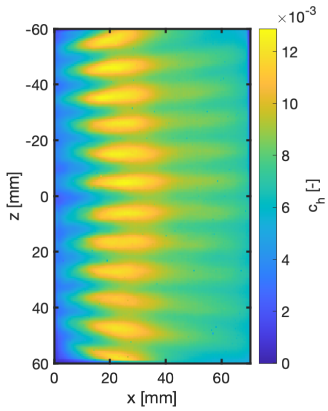

(b) $M_\infty = 7.5$; $Re = 46.3 \times 10^5$

Figure A.18: **Nondimensional roughness strip wavelength:** $\lambda_\delta = 2.7$

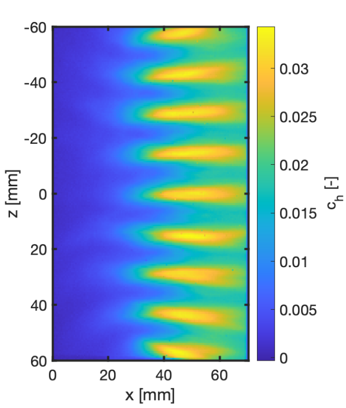

(a) $M_\infty = 7.5$; $Re = 9.2 \times 10^5$

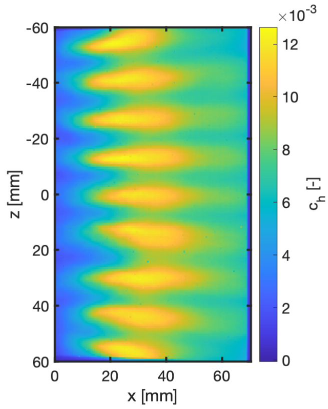

(b) $M_\infty = 7.5$; $Re = 46.3 \times 10^5$

Figure A.19: **Nondimensional roughness strip wavelength:** $\lambda_\delta = 3.6$

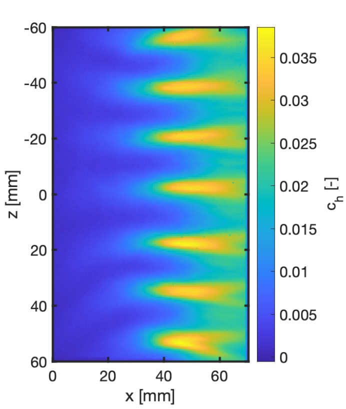

(a) $M_\infty = 7.5$; $Re = 9.2 \times 10^5$

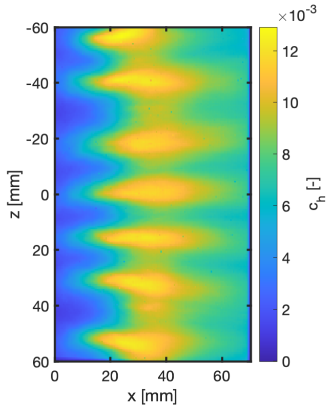

(b) $M_\infty = 7.5$; $Re = 46.3 \times 10^5$

Figure A.20: **Nondimensional roughness strip wavelength:** $\lambda_\delta = 4.5$

B

QIRT Images: Normal to Ramp Surface

This appendix presents all valid Stanton number (c_h) surface results for all strip-ramp combinations. Each pair of images represents both the low and high freestream Re conditions (see table 3.3) pertaining to a particular strip. The low and high Reynolds number values are 9.2×10^5 and 46.3×10^5 based on the distance from the flat plate leading edge to the corner of the ramp ($417\ mm$). The analogous unit Reynolds number for each, respectively, is provided in the M7 row in table 3.3. The freestream Mach number is 7.5 for all results. All images are projections normal to the ramp surface. Images that either do not exist or are corrupted are absent and are replaced with square boxes enclosing a diagonal strike.

The images adhere to the following specifications:

- Frame rate: $200\ Hz$
- Integration time: $250\ \mu s$
- Spatial resolution: $1.66\ px/mm$

B.1. Ramp angle of $15°$

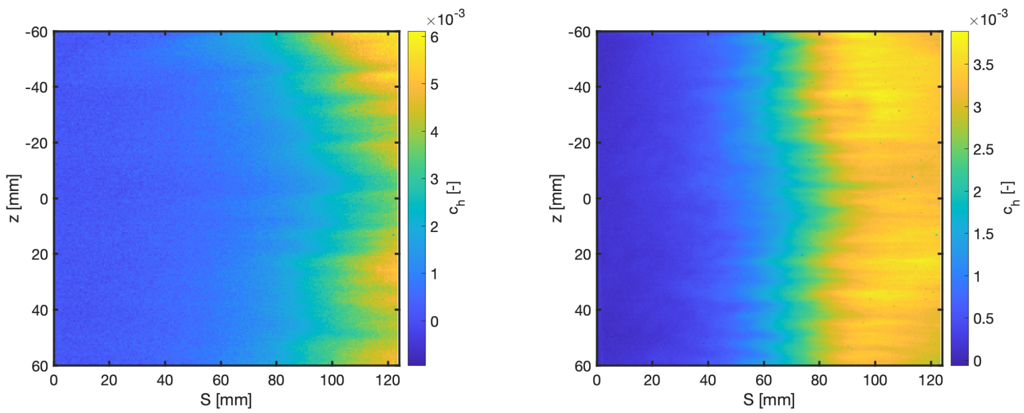

(a) $M_\infty = 7.5$; $Re = 9.2 \times 10^5$

(b) $M_\infty = 7.5$; $Re = 46.3 \times 10^5$

Figure B.1: **No roughness strip.**

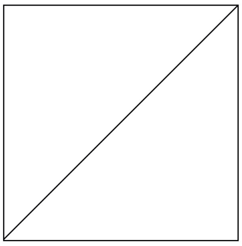

(a) $M_\infty = 7.5$; $Re = 9.2 \times 10^5$

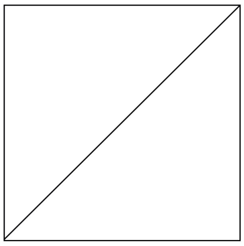

(b) $M_\infty = 7.5$; $Re = 46.3 \times 10^5$

Figure B.2: **Nondimensional roughness strip wavelength:** $\lambda_\delta = 1.8$

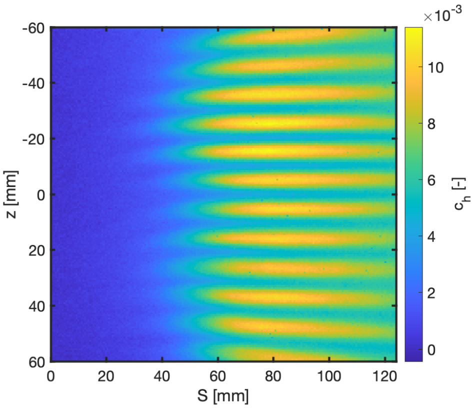

(a) $M_\infty = 7.5$; $Re = 9.2 \times 10^5$

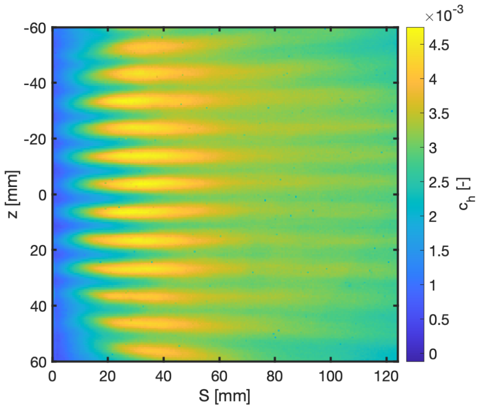

(b) $M_\infty = 7.5$; $Re = 46.3 \times 10^5$

Figure B.3: **Nondimensional roughness strip wavelength:** $\lambda_\delta = 2.7$

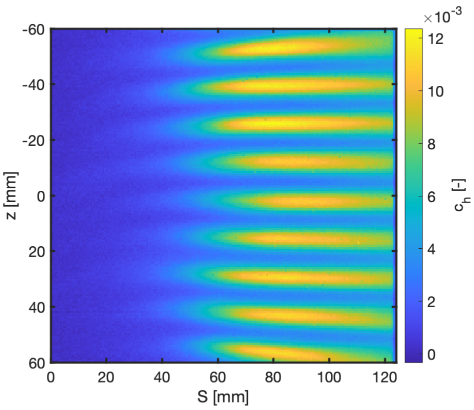

(a) $M_\infty = 7.5$; $Re = 9.2 \times 10^5$

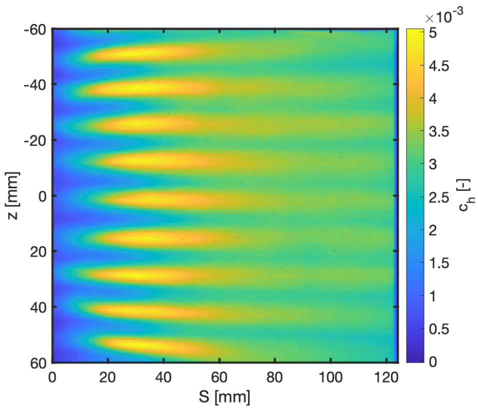

(b) $M_\infty = 7.5$; $Re = 46.3 \times 10^5$

Figure B.4: **Nondimensional roughness strip wavelength:** $\lambda_\delta = 3.6$

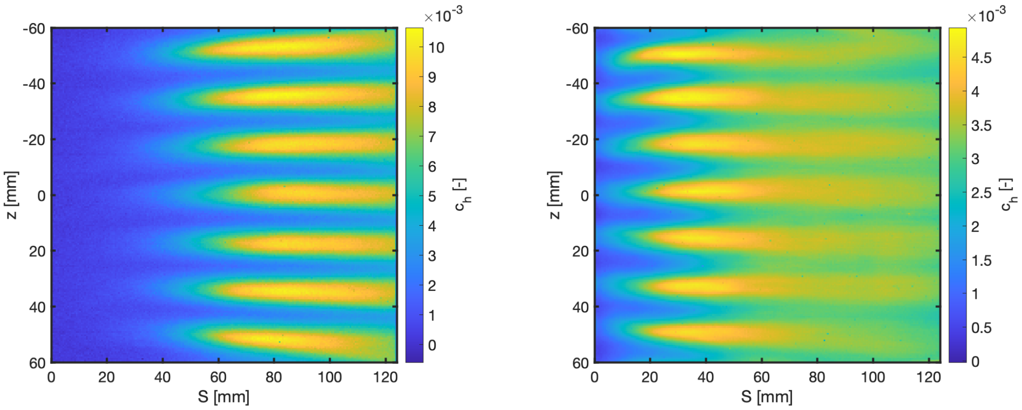

(a) $M_\infty = 7.5$; $Re = 9.2 \times 10^5$ (b) $M_\infty = 7.5$; $Re = 46.3 \times 10^5$

Figure B.5: **Nondimensional roughness strip wavelength:** $\lambda_\delta = 4.5$

B.2. Ramp angle of 20°

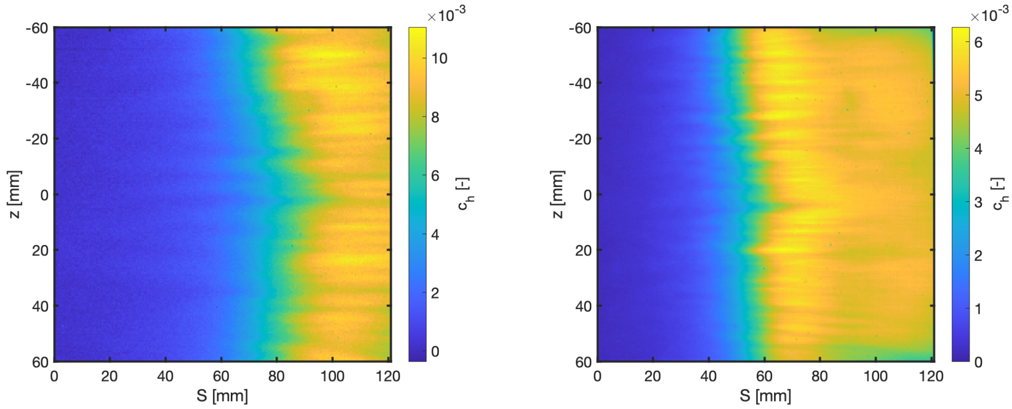

(a) $M_\infty = 7.5$; $Re = 9.2 \times 10^5$ (b) $M_\infty = 7.5$; $Re = 46.3 \times 10^5$

Figure B.6: **No roughness strip.**

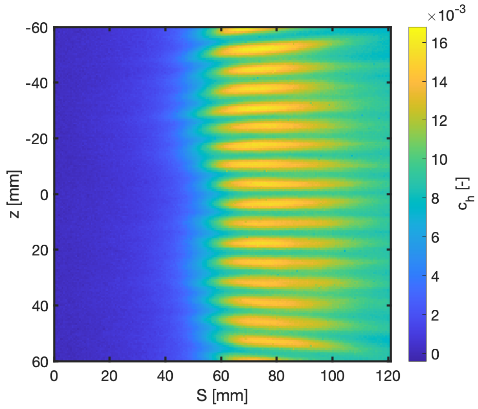

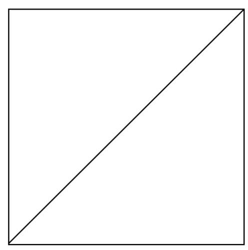

(b) $M_\infty = 7.5$; $Re = 46.3 \times 10^5$

(a) $M_\infty = 7.5$; $Re = 9.2 \times 10^5$

Figure B.7: **Nondimensional roughness strip wavelength:** $\lambda_\delta = 1.8$

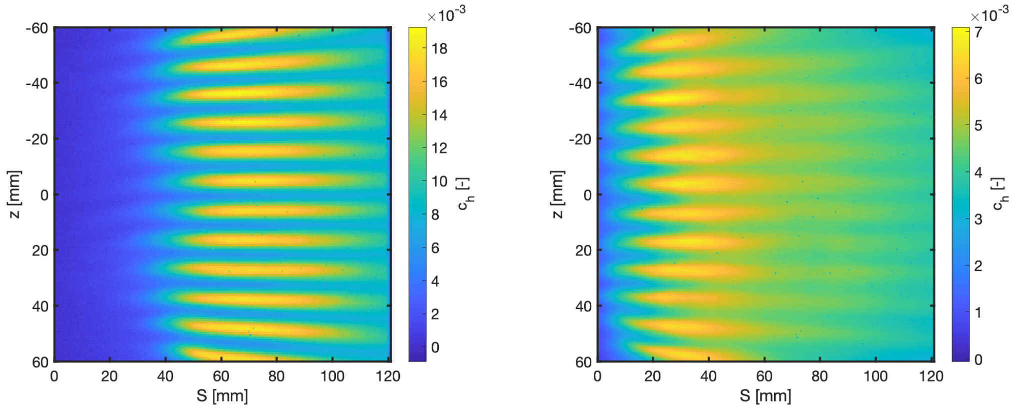

(a) $M_\infty = 7.5$; $Re = 9.2 \times 10^5$ (b) $M_\infty = 7.5$; $Re = 46.3 \times 10^5$

Figure B.8: **Nondimensional roughness strip wavelength:** $\lambda_\delta = 2.7$

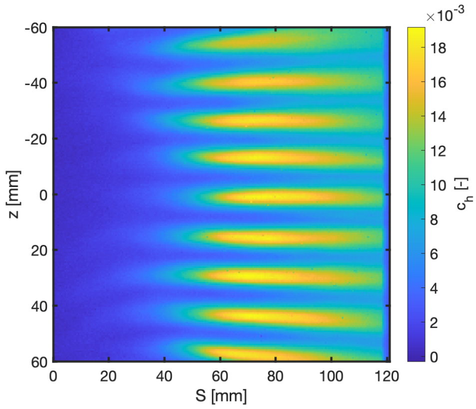

(a) $M_\infty = 7.5$; $Re = 9.2 \times 10^5$

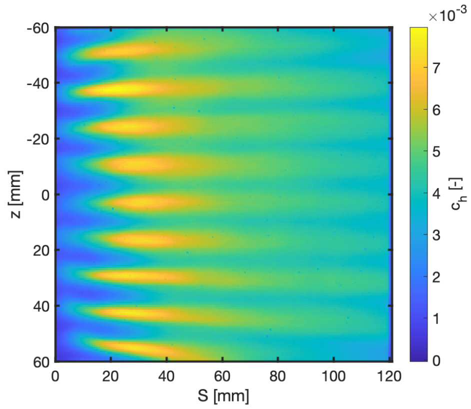

(b) $M_\infty = 7.5$; $Re = 46.3 \times 10^5$

Figure B.9: **Nondimensional roughness strip wavelength:** $\lambda_\delta = 3.6$

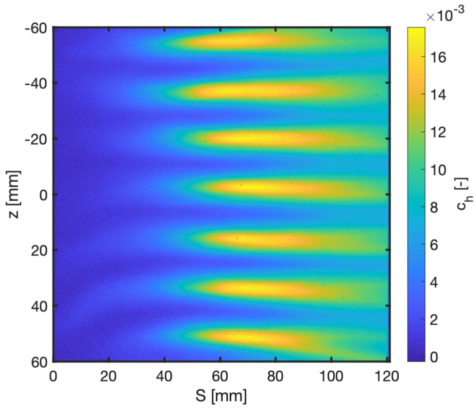

(a) $M_\infty = 7.5$; $Re = 9.2 \times 10^5$

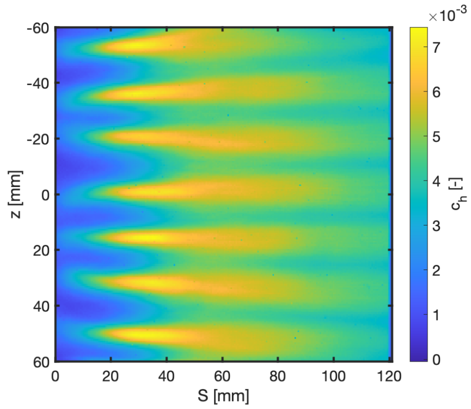

(b) $M_\infty = 7.5$; $Re = 46.3 \times 10^5$

Figure B.10: **Nondimensional roughness strip wavelength:** $\lambda_\delta = 4.5$

B.3. Ramp angle of $25°$

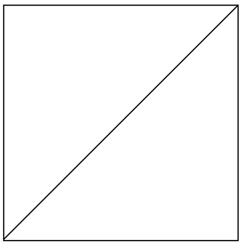

(a) $M_\infty = 7.5$; $Re = 9.2 \times 10^5$

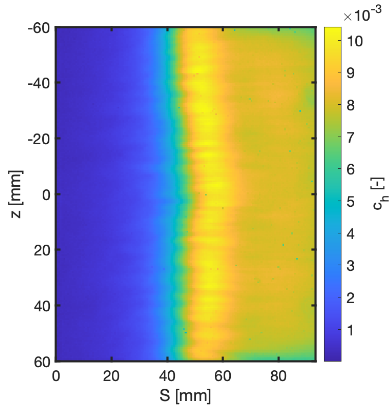

(b) $M_\infty = 7.5$; $Re = 46.3 \times 10^5$

Figure B.11: **No roughness strip.**

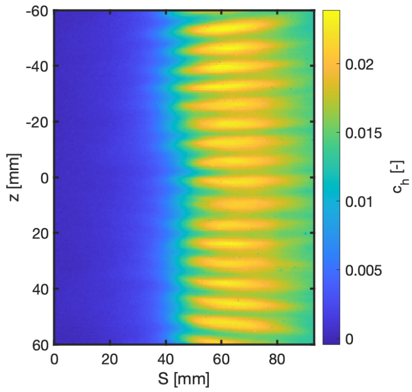

(a) $M_\infty = 7.5$; $Re = 9.2 \times 10^5$

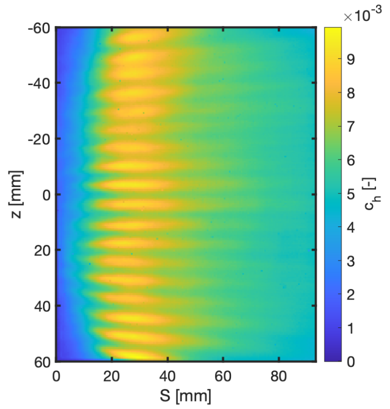

(b) $M_\infty = 7.5$; $Re = 46.3 \times 10^5$

Figure B.12: **Nondimensional roughness strip wavelength:** $\lambda_\delta = 1.8$

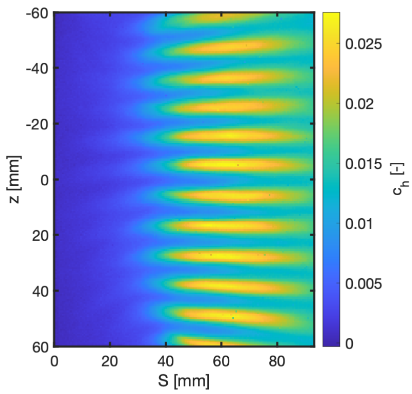

(a) $M_\infty = 7.5$; $Re = 9.2 \times 10^5$

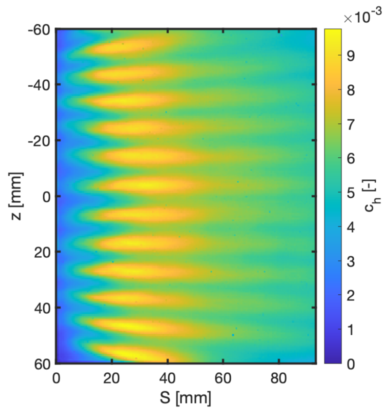

(b) $M_\infty = 7.5$; $Re = 46.3 \times 10^5$

Figure B.13: **Nondimensional roughness strip wavelength:** $\lambda_\delta = 2.7$

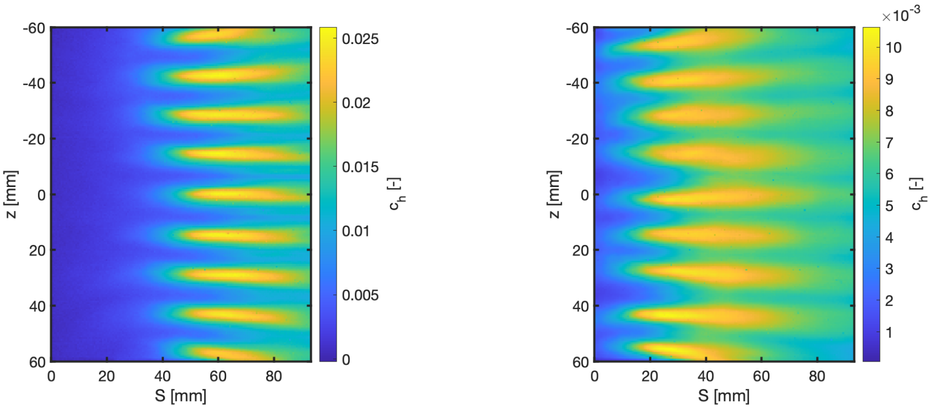

(a) $M_\infty = 7.5$; $Re = 9.2 \times 10^5$ (b) $M_\infty = 7.5$; $Re = 46.3 \times 10^5$

Figure B.14: **Nondimensional roughness strip wavelength:** $\lambda_\delta = 3.6$

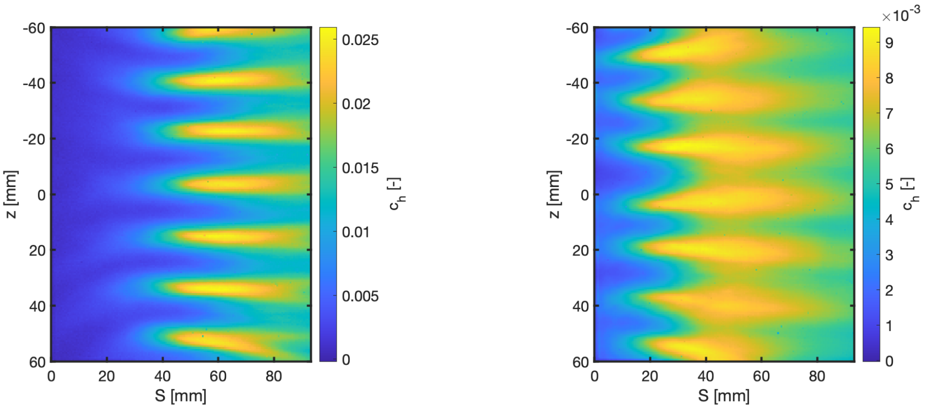

(a) $M_\infty = 7.5$; $Re = 9.2 \times 10^5$ (b) $M_\infty = 7.5$; $Re = 46.3 \times 10^5$

Figure B.15: **Nondimensional roughness strip wavelength:** $\lambda_\delta = 4.5$

B.4. Ramp angle of 30°

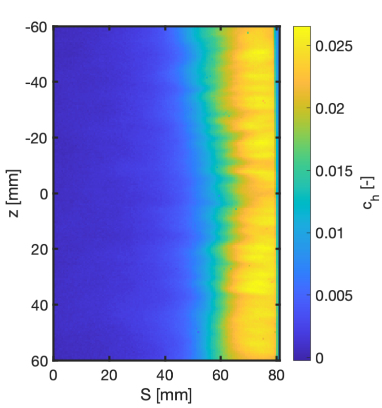

(a) $M_\infty = 7.5$; $Re = 9.2 \times 10^5$

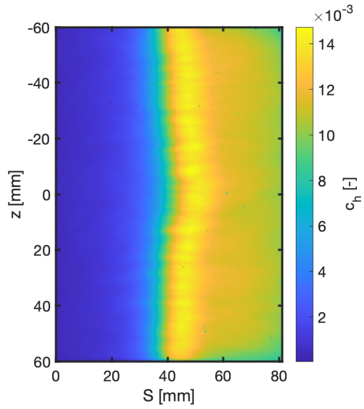

(b) $M_\infty = 7.5$; $Re = 46.3 \times 10^5$

Figure B.16: **No roughness strip.**

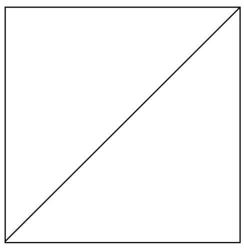

(a) $M_\infty = 7.5$; $Re = 9.2 \times 10^5$

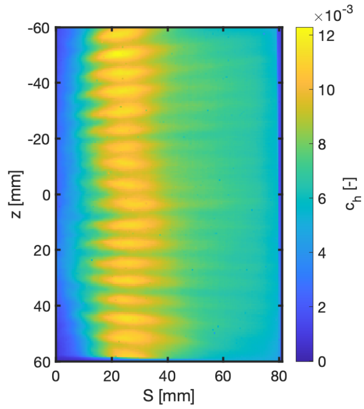

(b) $M_\infty = 7.5$; $Re = 46.3 \times 10^5$

Figure B.17: **Nondimensional roughness strip wavelength:** $\lambda_\delta = 1.8$

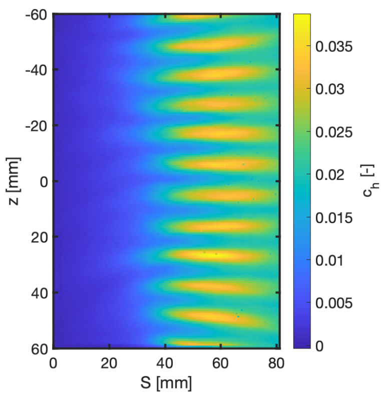

(a) $M_\infty = 7.5$; $Re = 9.2 \times 10^5$

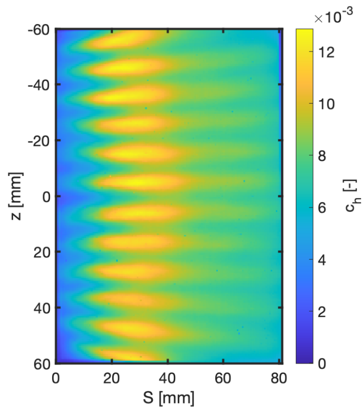

(b) $M_\infty = 7.5$; $Re = 46.3 \times 10^5$

Figure B.18: **Nondimensional roughness strip wavelength:** $\lambda_\delta = 2.7$

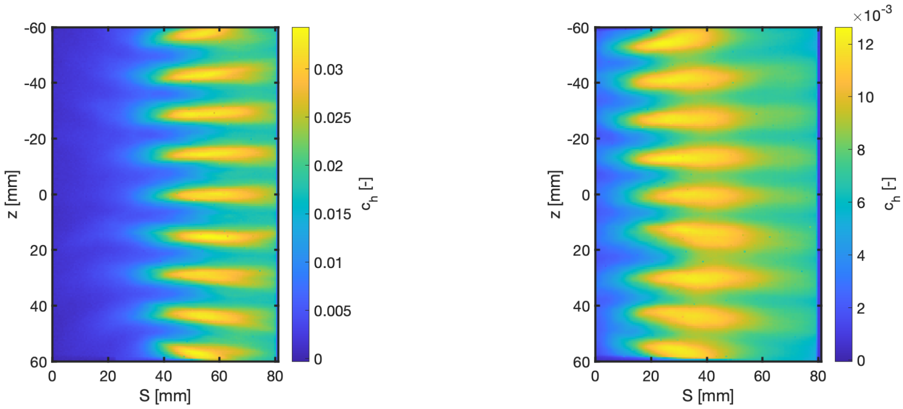

(a) $M_\infty = 7.5$; $Re = 9.2 \times 10^5$ (b) $M_\infty = 7.5$; $Re = 46.3 \times 10^5$

Figure B.19: **Nondimensional roughness strip wavelength:** $\lambda_\delta = 3.6$

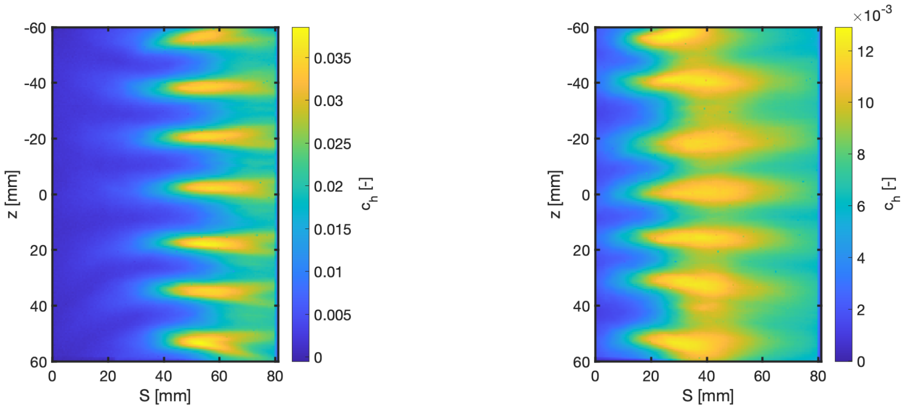

(a) $M_\infty = 7.5$; $Re = 9.2 \times 10^5$ (b) $M_\infty = 7.5$; $Re = 46.3 \times 10^5$

Figure B.20: **Nondimensional roughness strip wavelength:** $\lambda_\delta = 4.5$

C

QIRT Images: Spanwise Mean and Root Mean Square (RMS) Profiles – Normal to Flat Plate

The images adhere to the following specifications:

- Frame rate: $200\ Hz$
- Integration time: $250\ \mu s$
- Spatial resolution: $1.66\ px/mm$

C.1. Mean Results

C.1.1. Ramp angle of $15°$

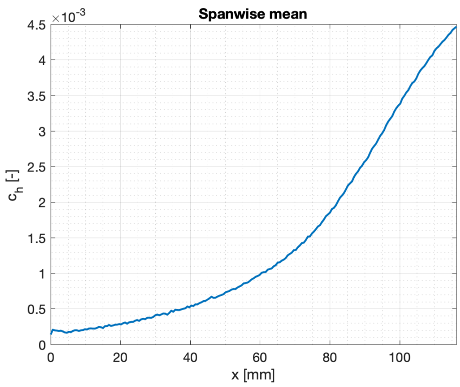

(a) $M_\infty = 7.5$; $Re = 9.2 \times 10^5$

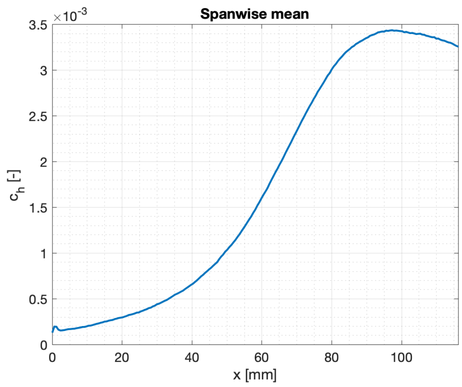

(b) $M_\infty = 7.5$; $Re = 46.3 \times 10^5$

Figure C.1: **No roughness strip.**

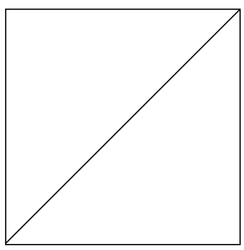

(a) $M_\infty = 7.5$; $Re = 9.2 \times 10^5$

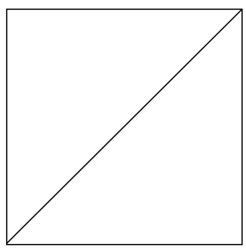

(b) $M_\infty = 7.5$; $Re = 46.3 \times 10^5$

Figure C.2: **Nondimensional roughness strip wavelength:** $\lambda_\delta = 1.8$

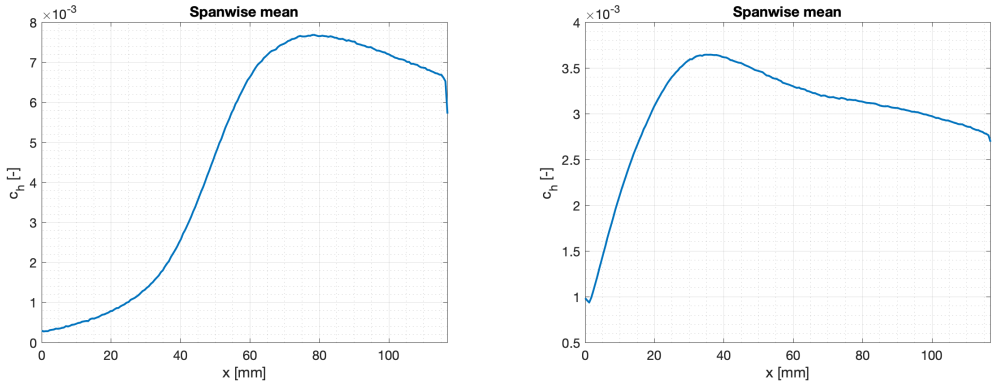

(a) $M_\infty = 7.5$; $Re = 9.2 \times 10^5$ (b) $M_\infty = 7.5$; $Re = 46.3 \times 10^5$

Figure C.3: **Nondimensional roughness strip wavelength:** $\lambda_\delta = 2.7$

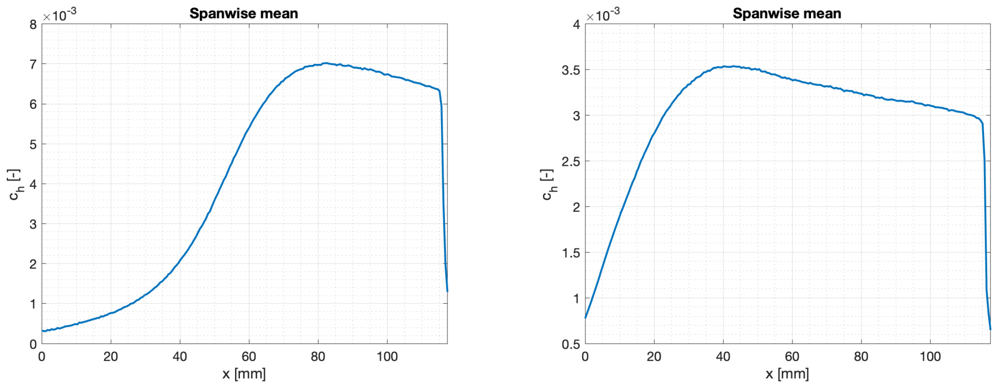

(a) $M_\infty = 7.5$; $Re = 9.2 \times 10^5$ (b) $M_\infty = 7.5$; $Re = 46.3 \times 10^5$

Figure C.4: **Nondimensional roughness strip wavelength:** $\lambda_\delta = 3.6$

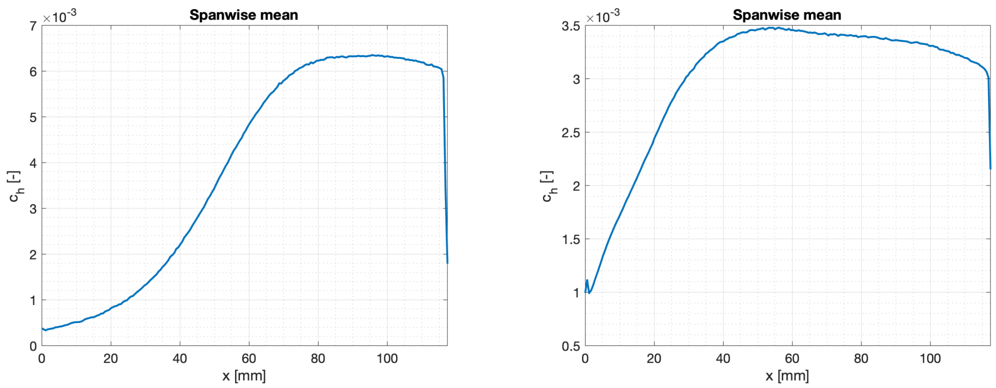

(a) $M_\infty = 7.5$; $Re = 9.2 \times 10^5$ (b) $M_\infty = 7.5$; $Re = 46.3 \times 10^5$

Figure C.5: **Nondimensional roughness strip wavelength:** $\lambda_\delta = 4.5$

C.1.2. Ramp angle of 20°

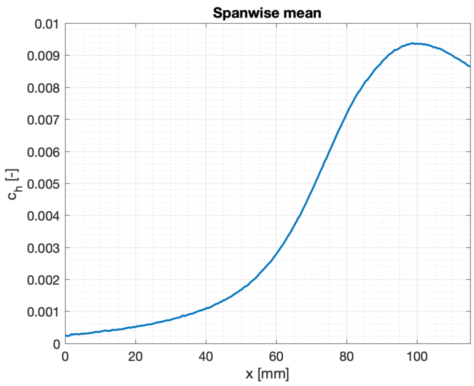

(a) $M_\infty = 7.5$; $Re = 9.2 \times 10^5$

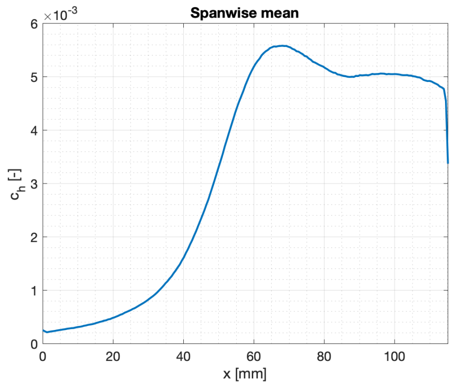

(b) $M_\infty = 7.5$; $Re = 46.3 \times 10^5$

Figure C.6: **No roughness strip.**

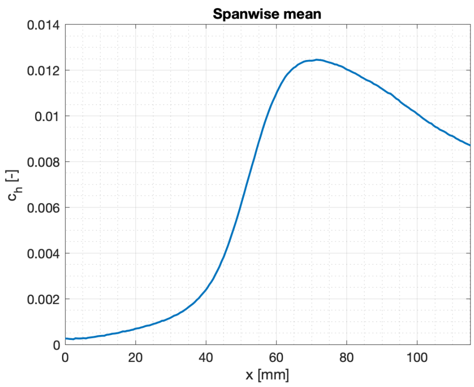

(a) $M_\infty = 7.5$; $Re = 9.2 \times 10^5$

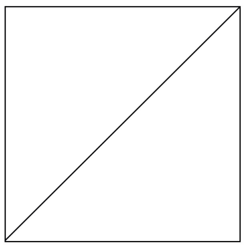

(b) $M_\infty = 7.5$; $Re = 46.3 \times 10^5$

Figure C.7: **Nondimensional roughness strip wavelength:** $\lambda_\delta = 1.8$

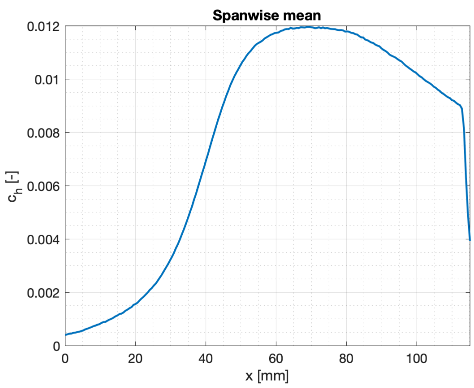

(a) $M_\infty = 7.5$; $Re = 9.2 \times 10^5$

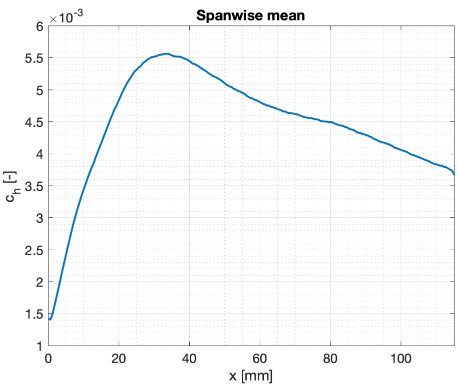

(b) $M_\infty = 7.5$; $Re = 46.3 \times 10^5$

Figure C.8: **Nondimensional roughness strip wavelength:** $\lambda_\delta = 2.7$

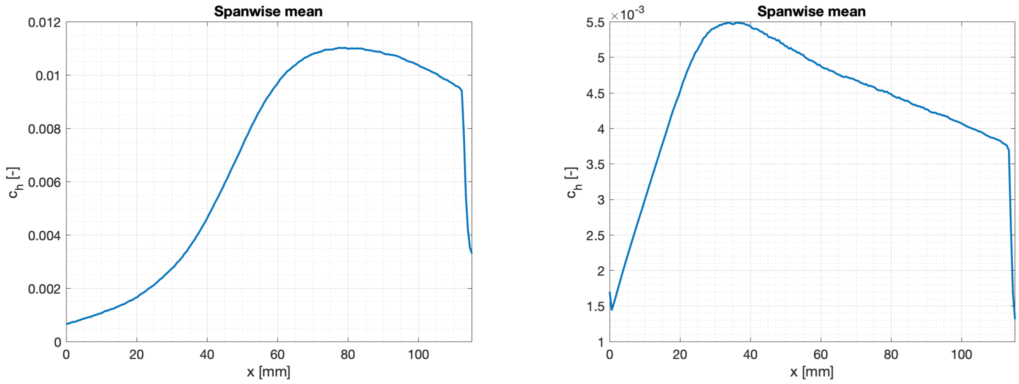

(a) $M_\infty = 7.5$; $Re = 9.2 \times 10^5$ (b) $M_\infty = 7.5$; $Re = 46.3 \times 10^5$

Figure C.9: **Nondimensional roughness strip wavelength:** $\lambda_\delta = 3.6$

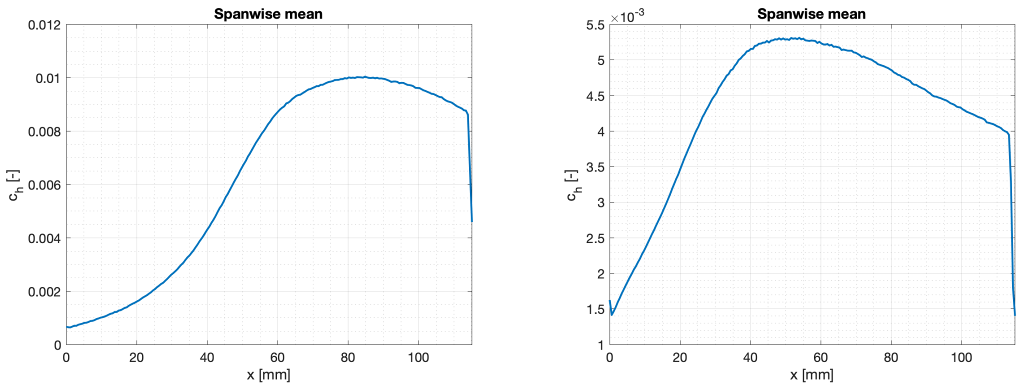

(a) $M_\infty = 7.5$; $Re = 9.2 \times 10^5$ (b) $M_\infty = 7.5$; $Re = 46.3 \times 10^5$

Figure C.10: **Nondimensional roughness strip wavelength:** $\lambda_\delta = 4.5$

C.1.3. Ramp angle of 25°

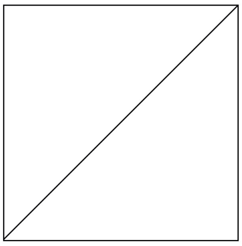

(a) $M_\infty = 7.5$; $Re = 9.2 \times 10^5$

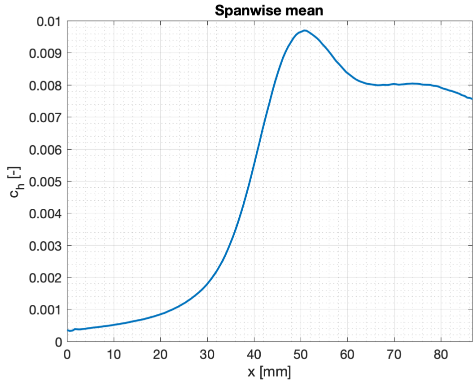

(b) $M_\infty = 7.5$; $Re = 46.3 \times 10^5$

Figure C.11: **No roughness strip.**

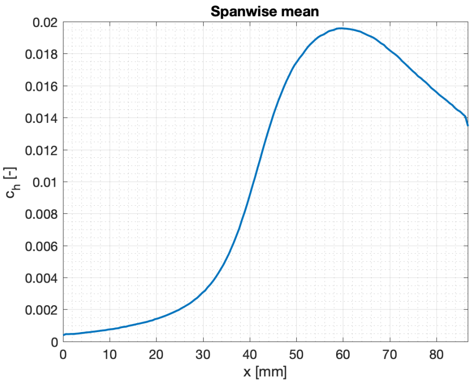

(a) $M_\infty = 7.5$; $Re = 9.2 \times 10^5$

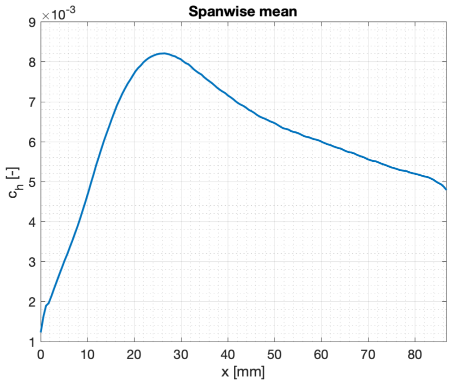

(b) $M_\infty = 7.5$; $Re = 46.3 \times 10^5$

Figure C.12: **Nondimensional roughness strip wavelength:** $\lambda_\delta = 1.8$

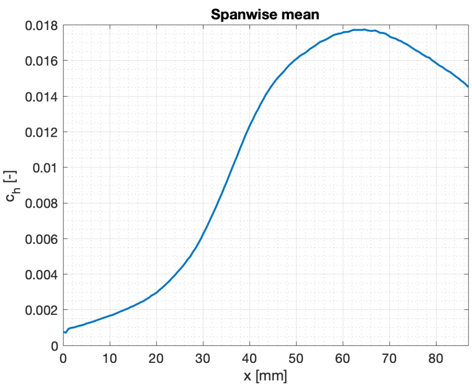

(a) $M_\infty = 7.5$; $Re = 9.2 \times 10^5$

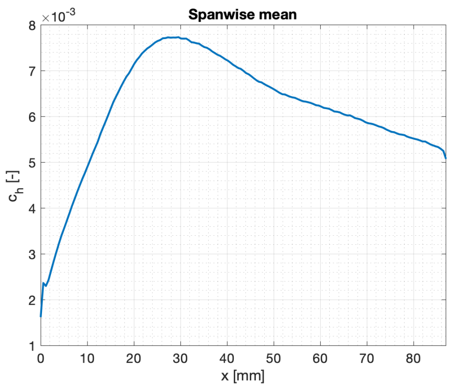

(b) $M_\infty = 7.5$; $Re = 46.3 \times 10^5$

Figure C.13: **Nondimensional roughness strip wavelength:** $\lambda_\delta = 2.7$

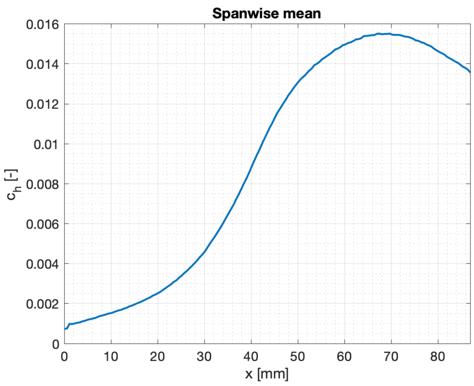

(a) $M_\infty = 7.5$; $Re = 9.2 \times 10^5$

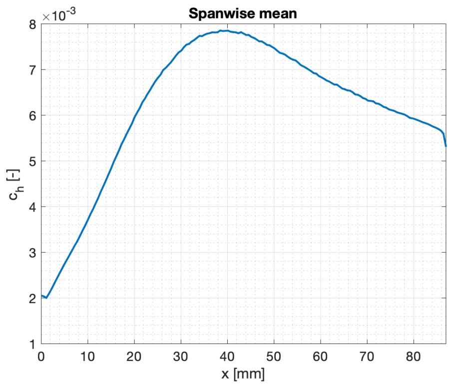

(b) $M_\infty = 7.5$; $Re = 46.3 \times 10^5$

Figure C.14: **Nondimensional roughness strip wavelength:** $\lambda_\delta = 3.6$

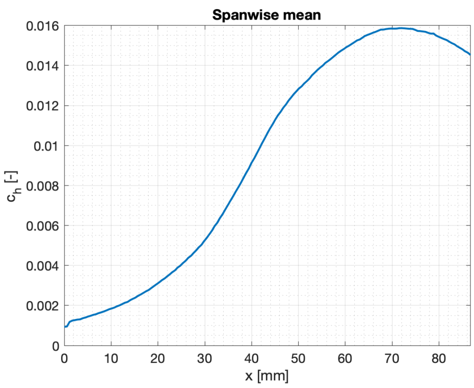

(a) $M_\infty = 7.5$; $Re = 9.2 \times 10^5$

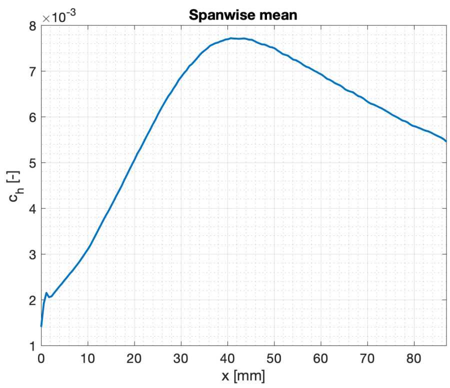

(b) $M_\infty = 7.5$; $Re = 46.3 \times 10^5$

Figure C.15: **Nondimensional roughness strip wavelength:** $\lambda_\delta = 4.5$

C.1.4. Ramp angle of $30°$

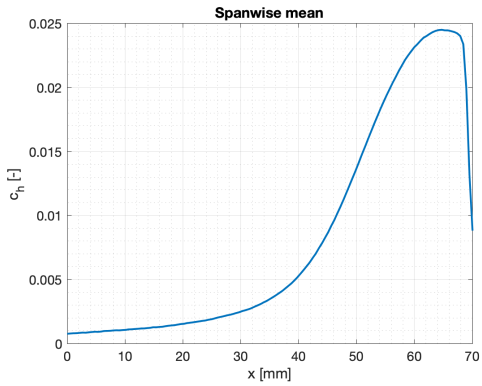

(a) $M_\infty = 7.5$; $Re = 9.2 \times 10^5$

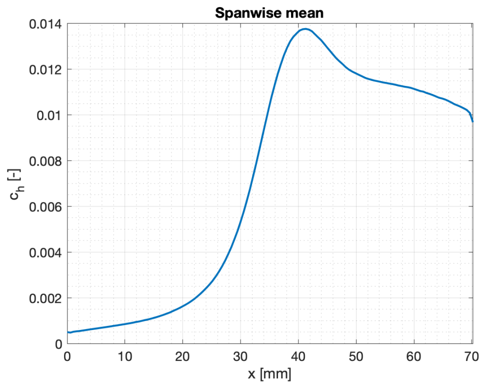

(b) $M_\infty = 7.5$; $Re = 46.3 \times 10^5$

Figure C.16: **No roughness strip.**

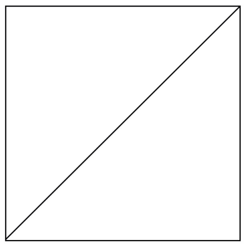

(a) $M_\infty = 7.5$; $Re = 9.2 \times 10^5$

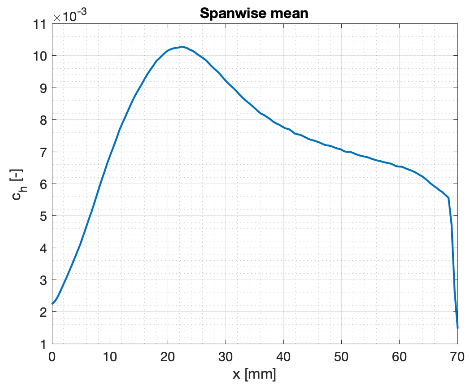

(b) $M_\infty = 7.5$; $Re = 46.3 \times 10^5$

Figure C.17: **Nondimensional roughness strip wavelength:** $\lambda_\delta = 1.8$

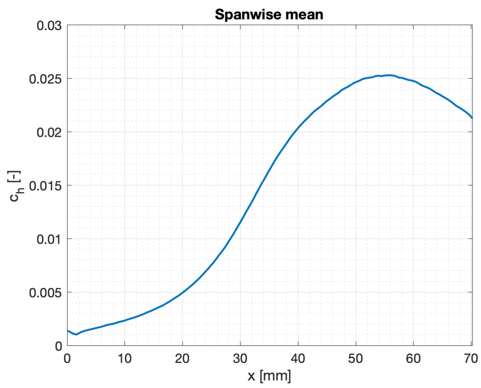

(a) $M_\infty = 7.5$; $Re = 9.2 \times 10^5$

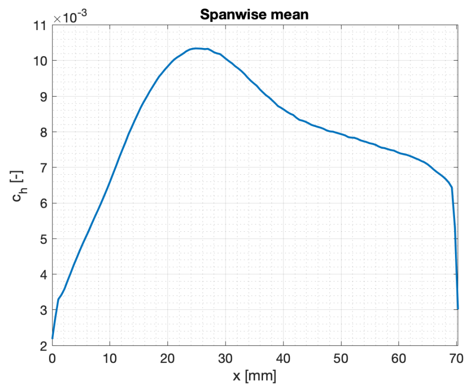

(b) $M_\infty = 7.5$; $Re = 46.3 \times 10^5$

Figure C.18: **Nondimensional roughness strip wavelength:** $\lambda_\delta = 2.7$

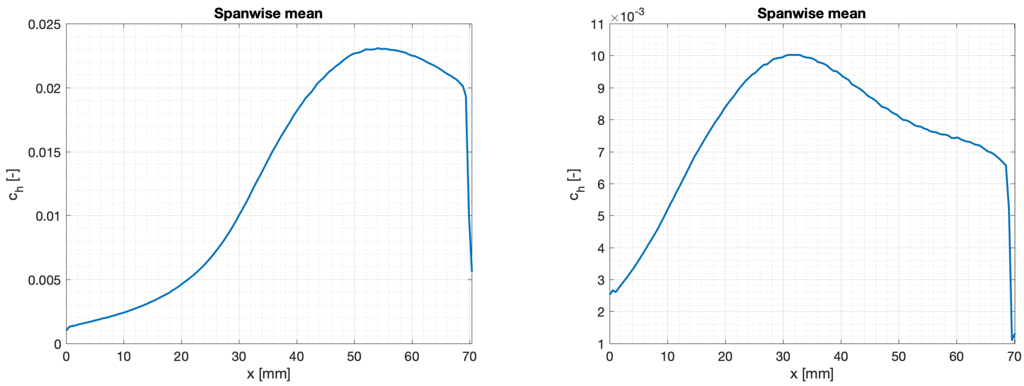

(a) $M_\infty = 7.5$; $Re = 9.2 \times 10^5$ (b) $M_\infty = 7.5$; $Re = 46.3 \times 10^5$

Figure C.19: **Nondimensional roughness strip wavelength:** $\lambda_\delta = 3.6$

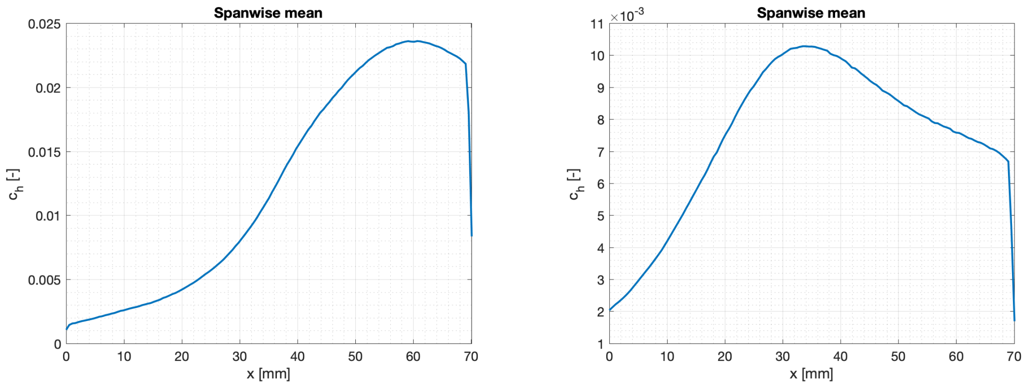

(a) $M_\infty = 7.5$; $Re = 9.2 \times 10^5$ (b) $M_\infty = 7.5$; $Re = 46.3 \times 10^5$

Figure C.20: **Nondimensional roughness strip wavelength:** $\lambda_\delta = 4.5$

C.2. RMS Results

C.2.1. Ramp angle of $15°$

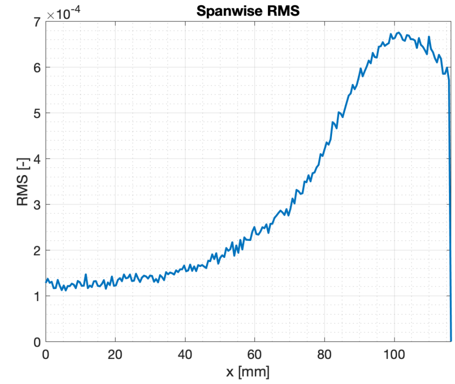

(a) $M_\infty = 7.5$; $Re = 9.2 \times 10^5$

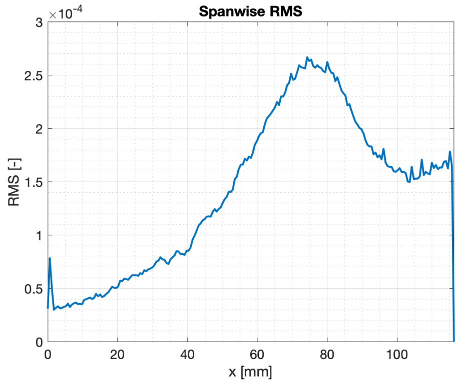

(b) $M_\infty = 7.5$; $Re = 46.3 \times 10^5$

Figure C.21: **No roughness strip.**

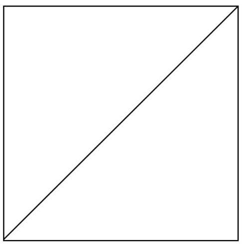

(a) $M_\infty = 7.5$; $Re = 9.2 \times 10^5$

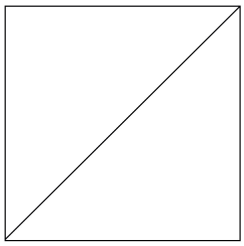

(b) $M_\infty = 7.5$; $Re = 46.3 \times 10^5$

Figure C.22: **Nondimensional roughness strip wavelength:** $\lambda_\delta = 1.8$

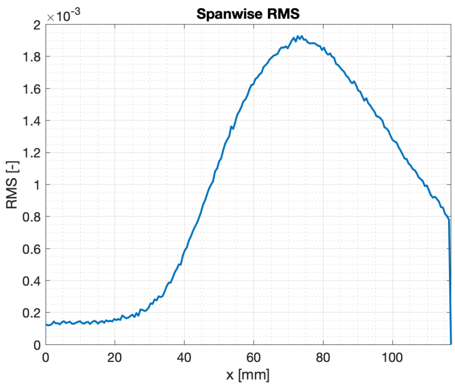

(a) $M_\infty = 7.5$; $Re = 9.2 \times 10^5$

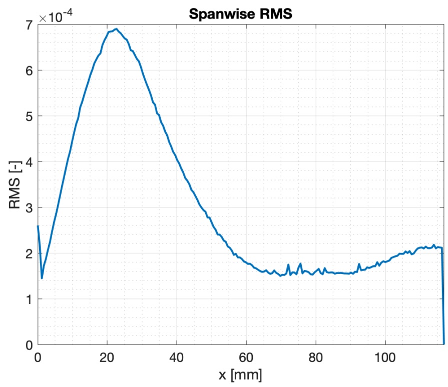

(b) $M_\infty = 7.5$; $Re = 46.3 \times 10^5$

Figure C.23: **Nondimensional roughness strip wavelength:** $\lambda_\delta = 2.7$

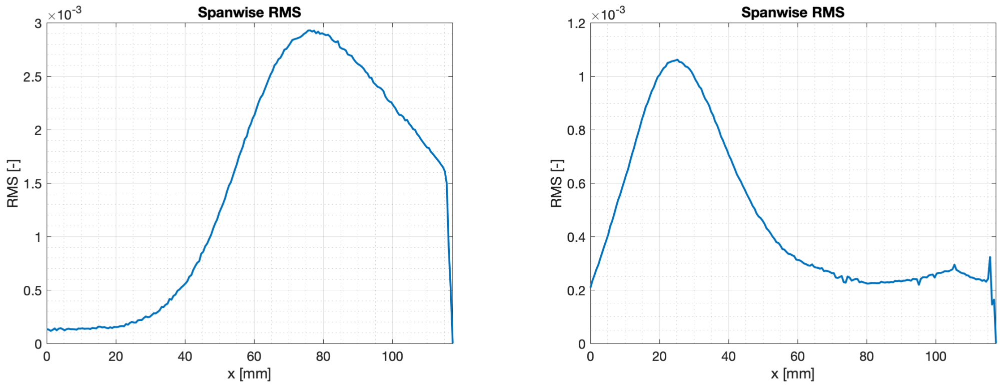

(a) $M_\infty = 7.5$; $Re = 9.2 \times 10^5$

(b) $M_\infty = 7.5$; $Re = 46.3 \times 10^5$

Figure C.24: **Nondimensional roughness strip wavelength:** $\lambda_\delta = 3.6$

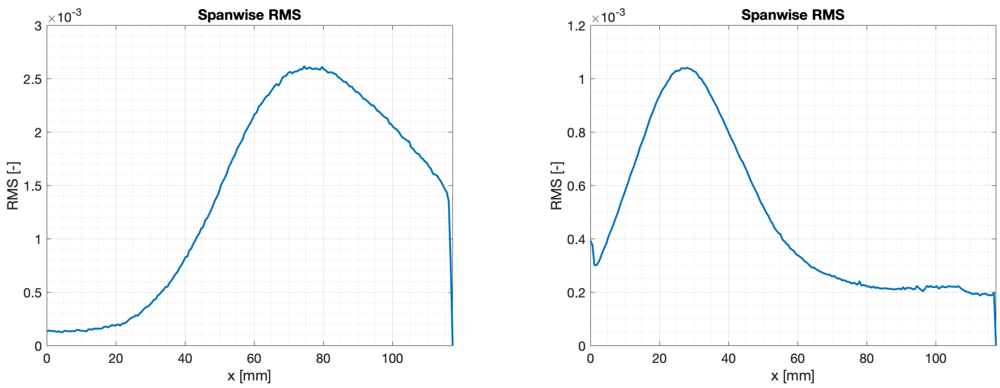

(a) $M_\infty = 7.5$; $Re = 9.2 \times 10^5$

(b) $M_\infty = 7.5$; $Re = 46.3 \times 10^5$

Figure C.25: **Nondimensional roughness strip wavelength:** $\lambda_\delta = 4.5$

C.2.2. Ramp angle of $20°$

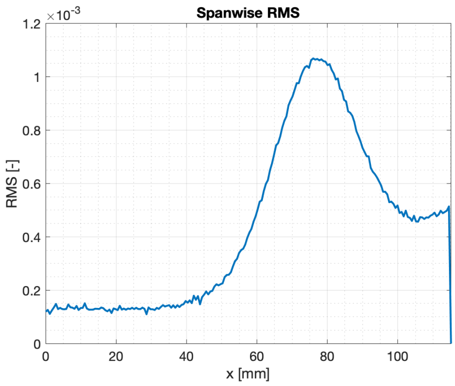

(a) $M_\infty = 7.5$; $Re = 9.2 \times 10^5$

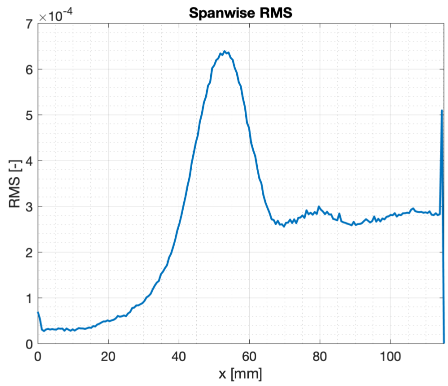

(b) $M_\infty = 7.5$; $Re = 46.3 \times 10^5$

Figure C.26: **No roughness strip.**

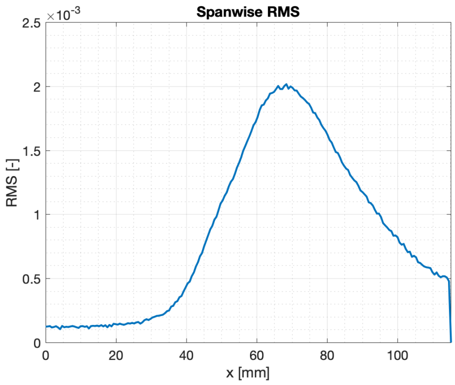

(a) $M_\infty = 7.5$; $Re = 9.2 \times 10^5$

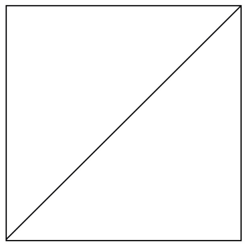

(b) $M_\infty = 7.5$; $Re = 46.3 \times 10^5$

Figure C.27: **Nondimensional roughness strip wavelength:** $\lambda_\delta = 1.8$

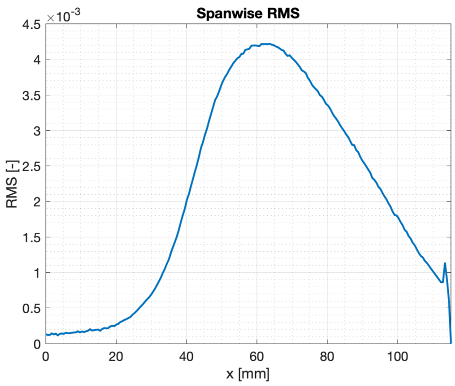

(a) $M_\infty = 7.5$; $Re = 9.2 \times 10^5$

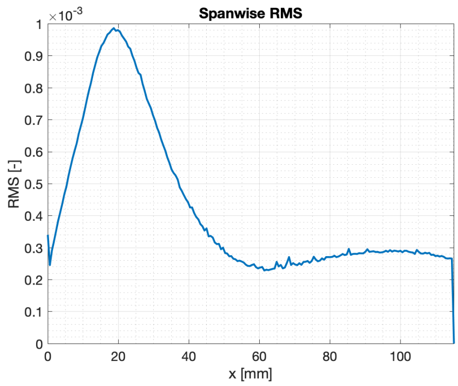

(b) $M_\infty = 7.5$; $Re = 46.3 \times 10^5$

Figure C.28: **Nondimensional roughness strip wavelength:** $\lambda_\delta = 2.7$

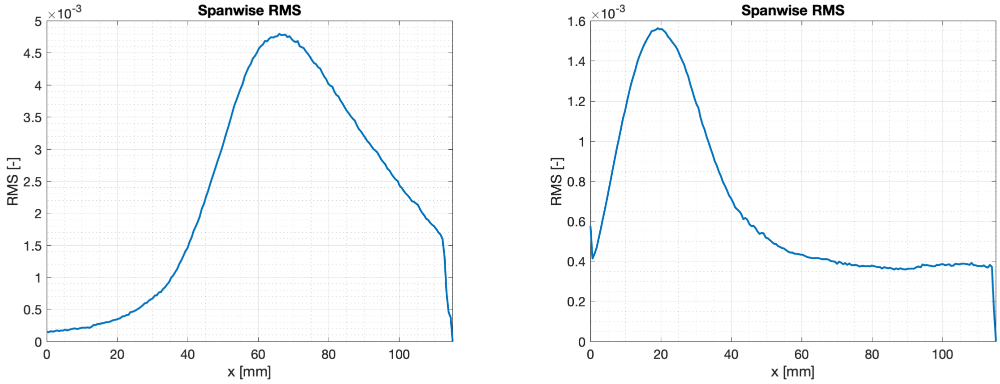

(a) $M_\infty = 7.5$; $Re = 9.2 \times 10^5$ (b) $M_\infty = 7.5$; $Re = 46.3 \times 10^5$

Figure C.29: **Nondimensional roughness strip wavelength:** $\lambda_\delta = 3.6$

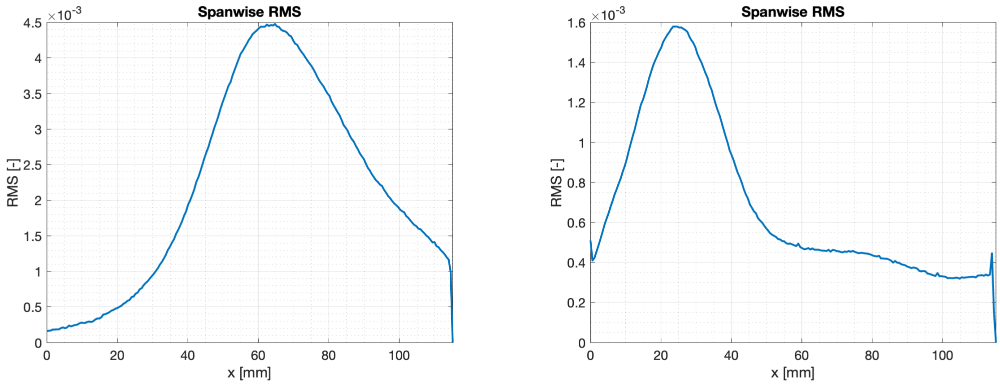

(a) $M_\infty = 7.5$; $Re = 9.2 \times 10^5$ (b) $M_\infty = 7.5$; $Re = 46.3 \times 10^5$

Figure C.30: **Nondimensional roughness strip wavelength:** $\lambda_\delta = 4.5$

C.2.3. Ramp angle of 25°

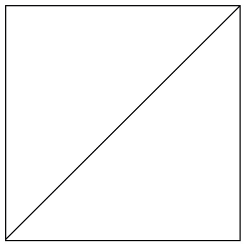

(a) M_∞ = 7.5; Re = 9.2 × 10^5

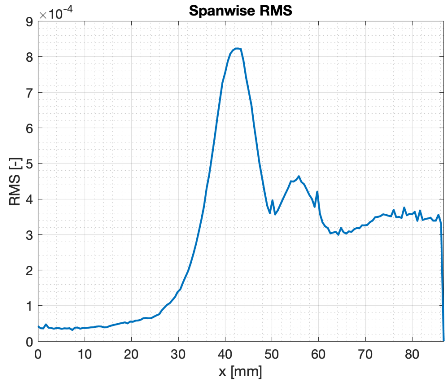

(b) M_∞ = 7.5; Re = 46.3 × 10^5

Figure C.31: **No roughness strip.**

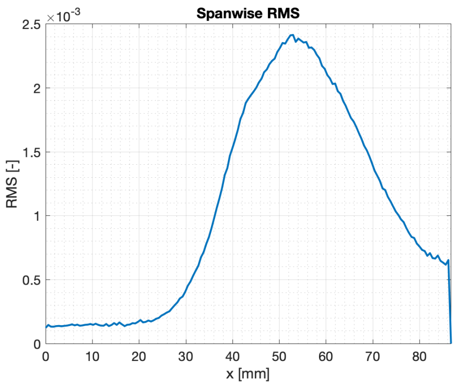

(a) M_∞ = 7.5; Re = 9.2 × 10^5

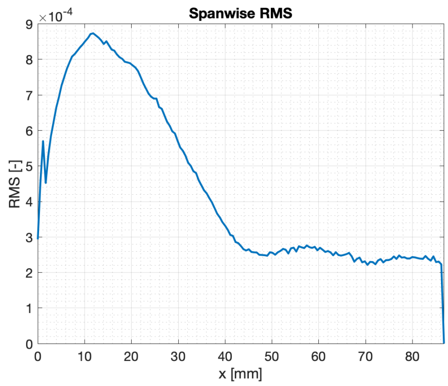

(b) M_∞ = 7.5; Re = 46.3 × 10^5

Figure C.32: **Nondimensional roughness strip wavelength:** λ_δ = 1.8

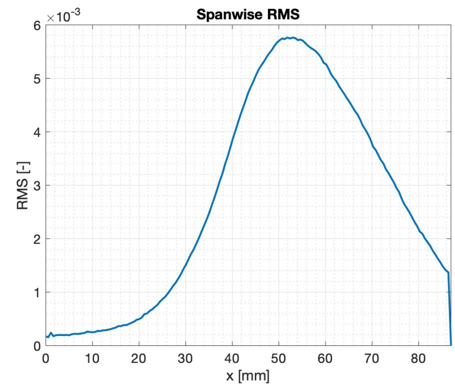

(a) M_∞ = 7.5; Re = 9.2 × 10^5

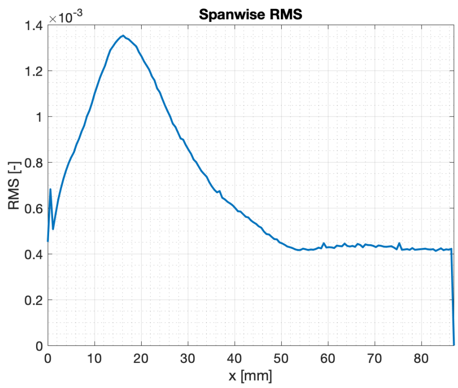

(b) M_∞ = 7.5; Re = 46.3 × 10^5

Figure C.33: **Nondimensional roughness strip wavelength:** λ_δ = 2.7

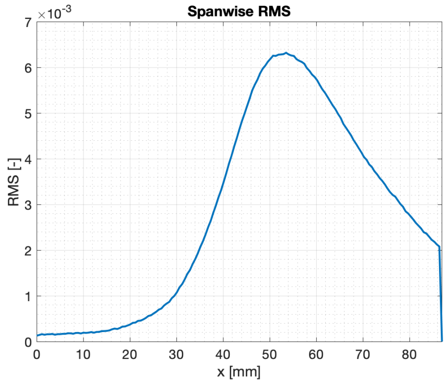

(a) $M_\infty = 7.5$; $Re = 9.2 \times 10^5$

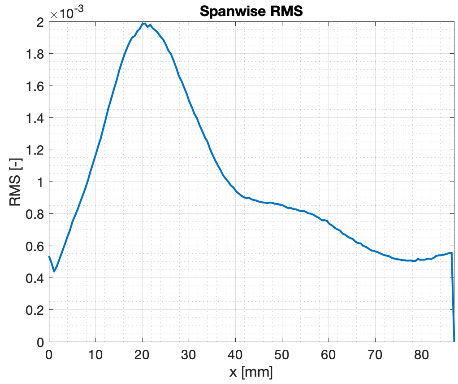

(b) $M_\infty = 7.5$; $Re = 46.3 \times 10^5$

Figure C.34: **Nondimensional roughness strip wavelength:** $\lambda_\delta = 3.6$

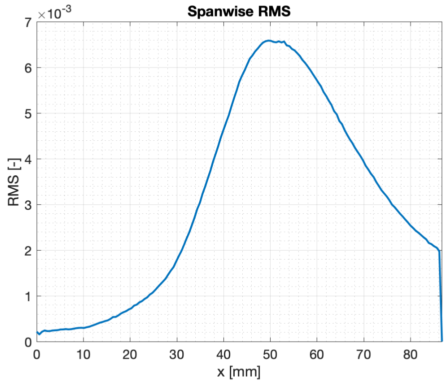

(a) $M_\infty = 7.5$; $Re = 9.2 \times 10^5$

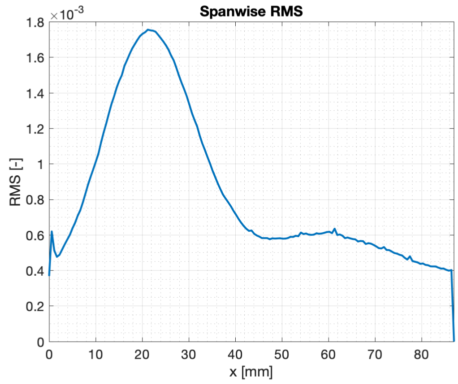

(b) $M_\infty = 7.5$; $Re = 46.3 \times 10^5$

Figure C.35: **Nondimensional roughness strip wavelength:** $\lambda_\delta = 4.5$

C.2.4. Ramp angle of $30°$

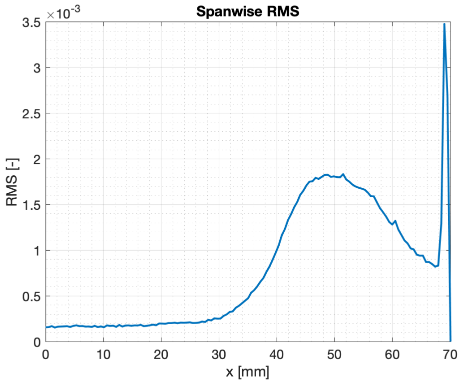

(a) $M_\infty = 7.5$; $Re = 9.2 \times 10^5$

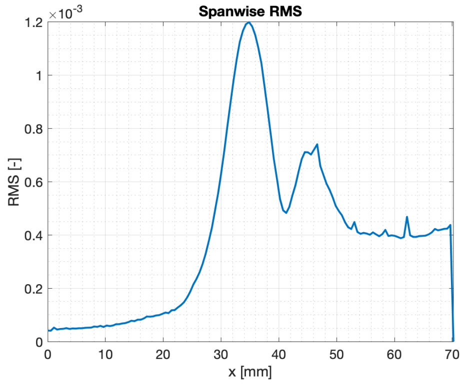

(b) $M_\infty = 7.5$; $Re = 46.3 \times 10^5$

Figure C.36: **No roughness strip.**

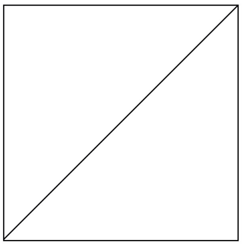

(a) $M_\infty = 7.5$; $Re = 9.2 \times 10^5$

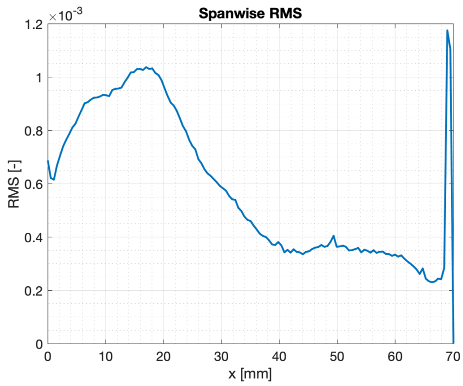

(b) $M_\infty = 7.5$; $Re = 46.3 \times 10^5$

Figure C.37: **Nondimensional roughness strip wavelength:** $\lambda_\delta = 1.8$

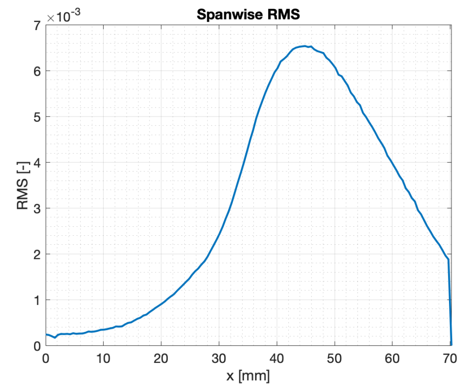

(a) $M_\infty = 7.5$; $Re = 9.2 \times 10^5$

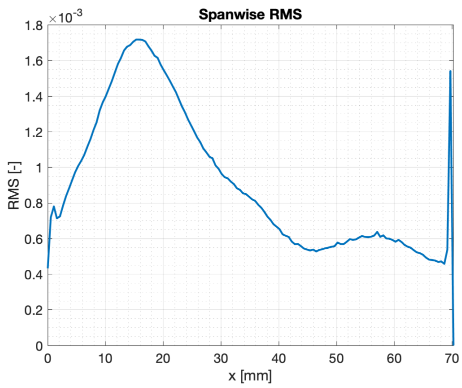

(b) $M_\infty = 7.5$; $Re = 46.3 \times 10^5$

Figure C.38: **Nondimensional roughness strip wavelength:** $\lambda_\delta = 2.7$

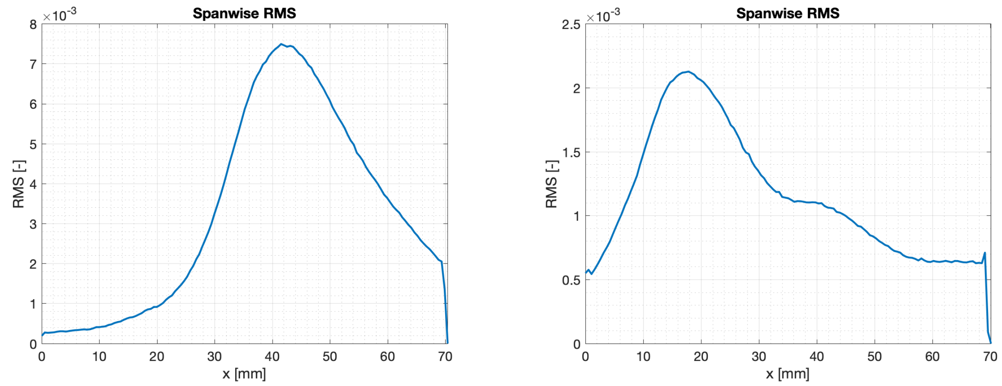

(a) $M_{\infty} = 7.5$; $Re = 9.2 \times 10^{5}$ (b) $M_{\infty} = 7.5$; $Re = 46.3 \times 10^{5}$

Figure C.39: **Nondimensional roughness strip wavelength:** $\lambda_{\delta} = 3.6$

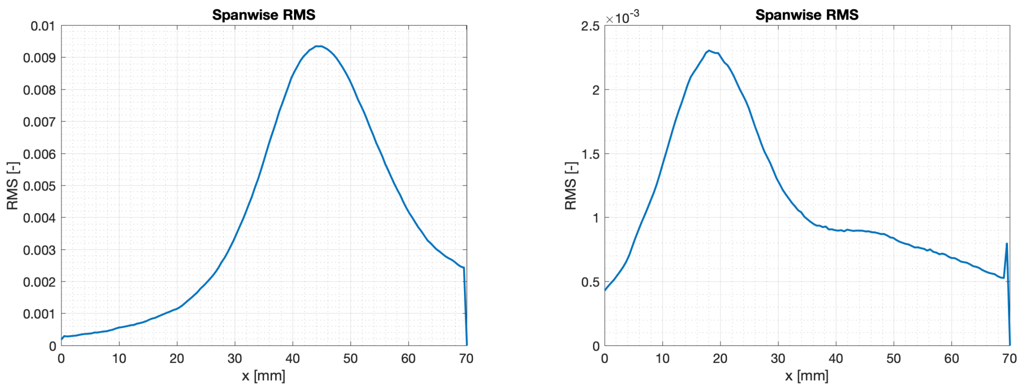

(a) $M_{\infty} = 7.5$; $Re = 9.2 \times 10^{5}$ (b) $M_{\infty} = 7.5$; $Re = 46.3 \times 10^{5}$

Figure C.40: **Nondimensional roughness strip wavelength:** $\lambda_{\delta} = 4.5$

D
QIRT Images: Spanwise Mean and Root Mean Square (RMS) Profiles – Normal to Ramp Surface

The images adhere to the following specifications:

- Frame rate: $200\ Hz$
- Integration time: $250\ \mu s$
- Spatial resolution: $1.66\ px/mm$

D.1. Mean Results

D.1.1. Ramp angle of $15°$

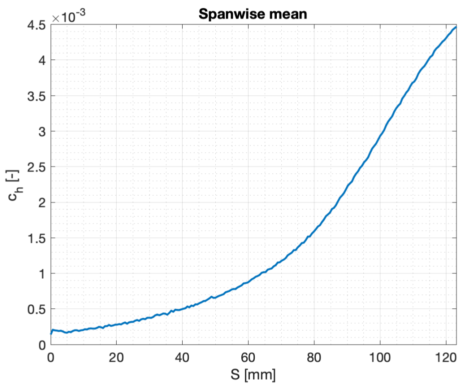

(a) $M_\infty = 7.5$; $Re = 9.2 \times 10^5$

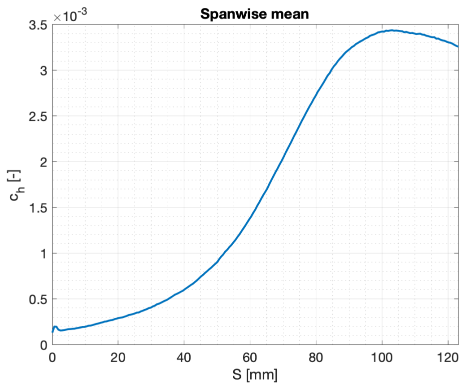

(b) $M_\infty = 7.5$; $Re = 46.3 \times 10^5$

Figure D.1: **No roughness strip.**

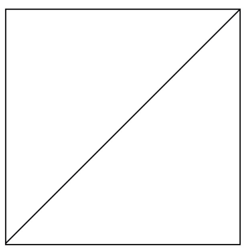

(a) $M_\infty = 7.5$; $Re = 9.2 \times 10^5$

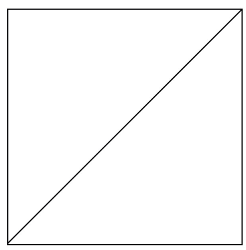

(b) $M_\infty = 7.5$; $Re = 46.3 \times 10^5$

Figure D.2: **Nondimensional roughness strip wavelength:** $\lambda_\delta = 1.8$

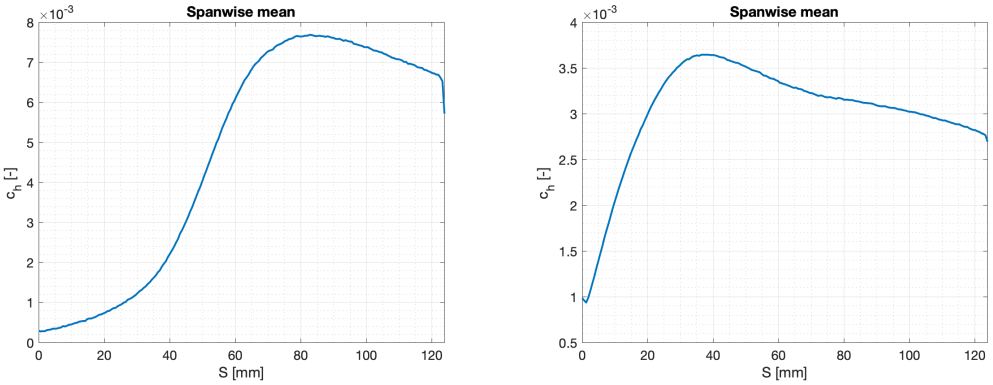

(a) $M_\infty = 7.5$; $Re = 9.2 \times 10^5$ (b) $M_\infty = 7.5$; $Re = 46.3 \times 10^5$

Figure D.3: **Nondimensional roughness strip wavelength:** $\lambda_\delta = 2.7$

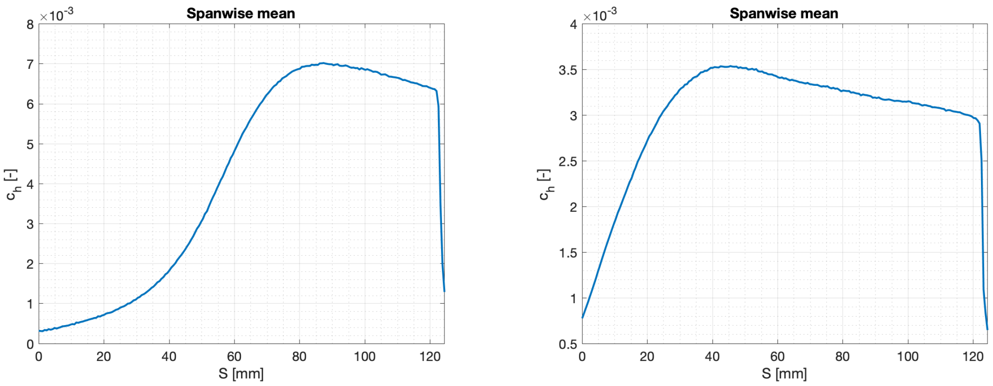

(a) $M_\infty = 7.5$; $Re = 9.2 \times 10^5$ (b) $M_\infty = 7.5$; $Re = 46.3 \times 10^5$

Figure D.4: **Nondimensional roughness strip wavelength:** $\lambda_\delta = 3.6$

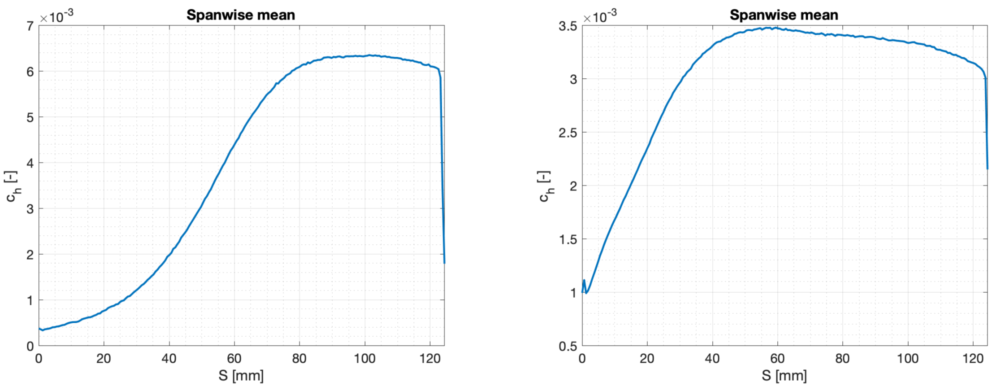

(a) $M_\infty = 7.5$; $Re = 9.2 \times 10^5$ (b) $M_\infty = 7.5$; $Re = 46.3 \times 10^5$

Figure D.5: **Nondimensional roughness strip wavelength:** $\lambda_\delta = 4.5$

D.1.2. Ramp angle of 20°

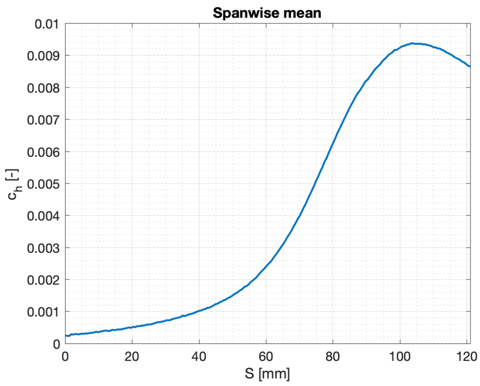

(a) $M_\infty = 7.5$; $Re = 9.2 \times 10^5$

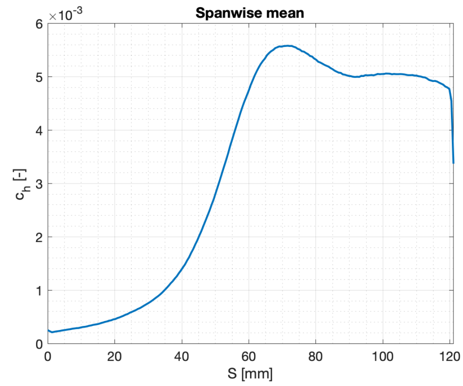

(b) $M_\infty = 7.5$; $Re = 46.3 \times 10^5$

Figure D.6: **No roughness strip.**

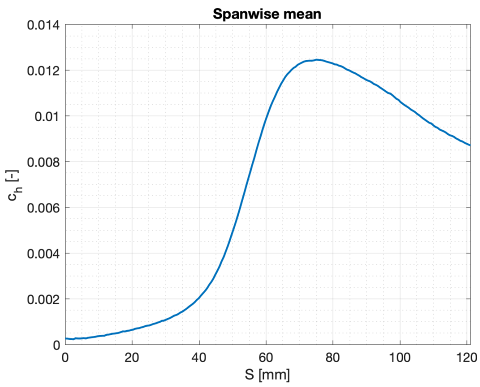

(a) $M_\infty = 7.5$; $Re = 9.2 \times 10^5$

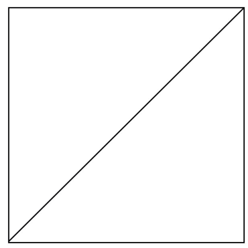

(b) $M_\infty = 7.5$; $Re = 46.3 \times 10^5$

Figure D.7: **Nondimensional roughness strip wavelength:** $\lambda_\delta = 1.8$

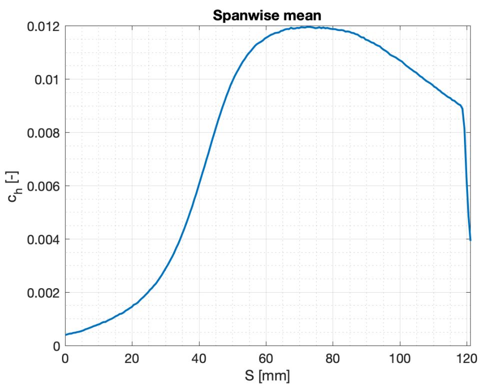

(a) $M_\infty = 7.5$; $Re = 9.2 \times 10^5$

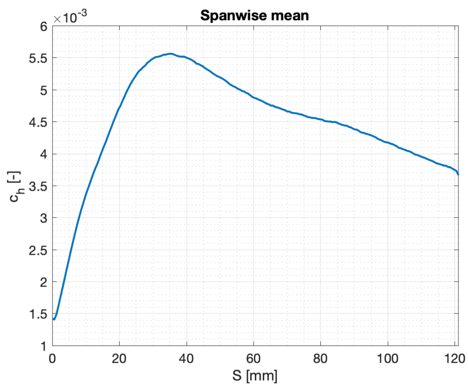

(b) $M_\infty = 7.5$; $Re = 46.3 \times 10^5$

Figure D.8: **Nondimensional roughness strip wavelength:** $\lambda_\delta = 2.7$

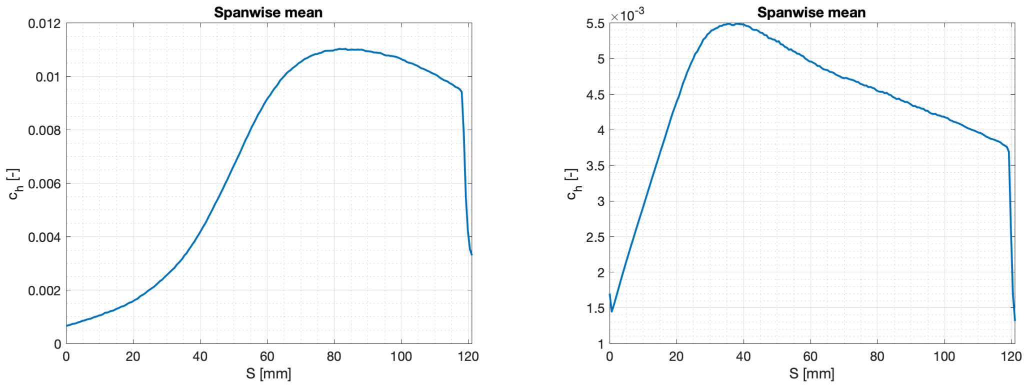

(a) $M_\infty = 7.5$; $Re = 9.2 \times 10^5$

(b) $M_\infty = 7.5$; $Re = 46.3 \times 10^5$

Figure D.9: **Nondimensional roughness strip wavelength:** $\lambda_\delta = 3.6$

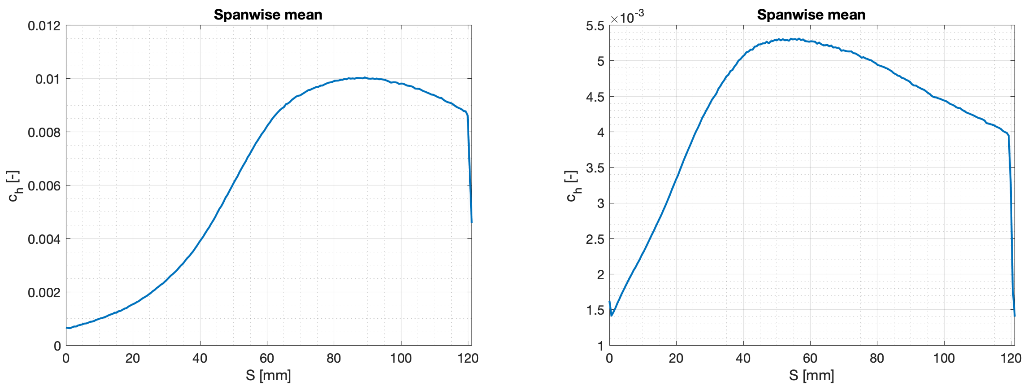

(a) $M_\infty = 7.5$; $Re = 9.2 \times 10^5$

(b) $M_\infty = 7.5$; $Re = 46.3 \times 10^5$

Figure D.10: **Nondimensional roughness strip wavelength:** $\lambda_\delta = 4.5$

D.1.3. Ramp angle of $25°$

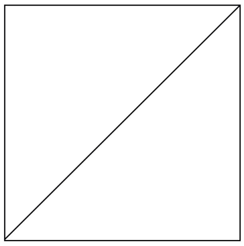

(a) $M_\infty = 7.5$; $Re = 9.2 \times 10^5$

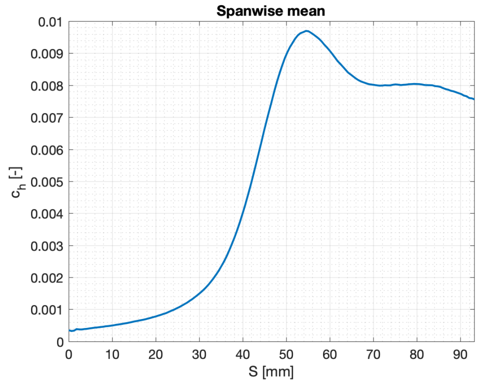

(b) $M_\infty = 7.5$; $Re = 46.3 \times 10^5$

Figure D.11: **No roughness strip.**

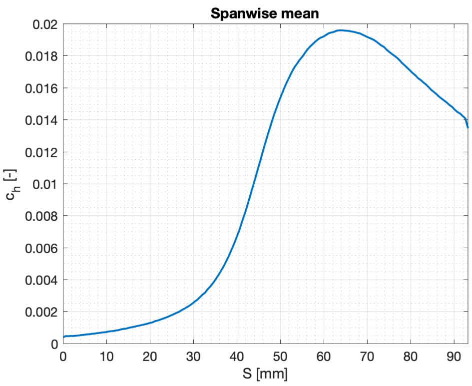

(a) $M_\infty = 7.5$; $Re = 9.2 \times 10^5$

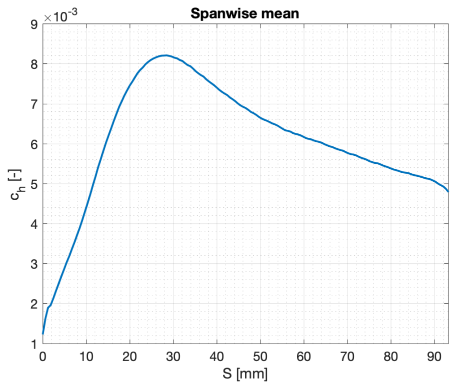

(b) $M_\infty = 7.5$; $Re = 46.3 \times 10^5$

Figure D.12: **Nondimensional roughness strip wavelength:** $\lambda_\delta = 1.8$

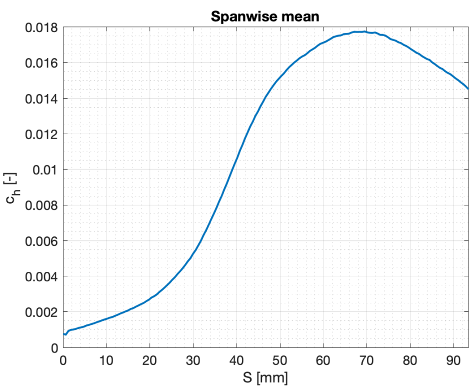

(a) $M_\infty = 7.5$; $Re = 9.2 \times 10^5$

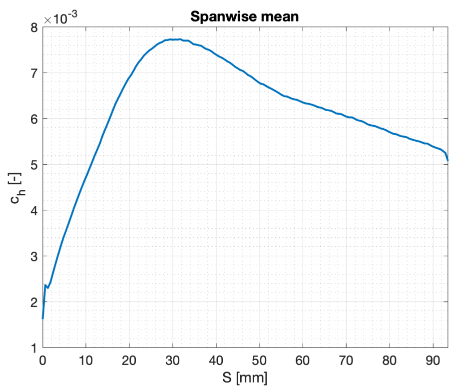

(b) $M_\infty = 7.5$; $Re = 46.3 \times 10^5$

Figure D.13: **Nondimensional roughness strip wavelength:** $\lambda_\delta = 2.7$

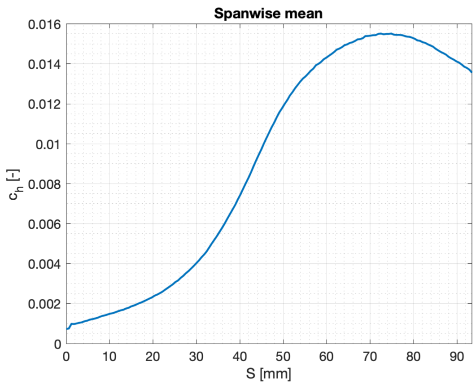

(a) $M_\infty = 7.5$; $Re = 9.2 \times 10^5$

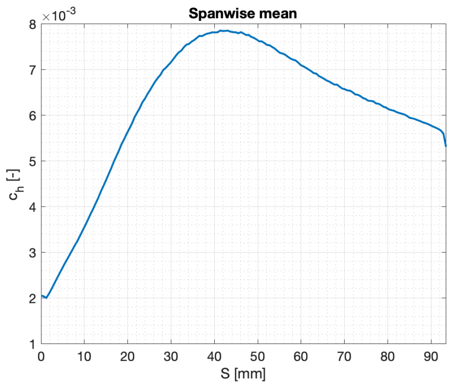

(b) $M_\infty = 7.5$; $Re = 46.3 \times 10^5$

Figure D.14: **Nondimensional roughness strip wavelength:** $\lambda_\delta = 3.6$

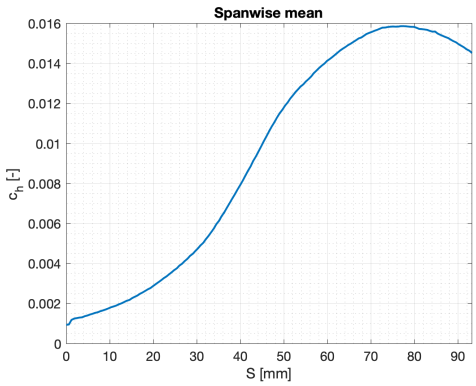

(a) $M_\infty = 7.5$; $Re = 9.2 \times 10^5$

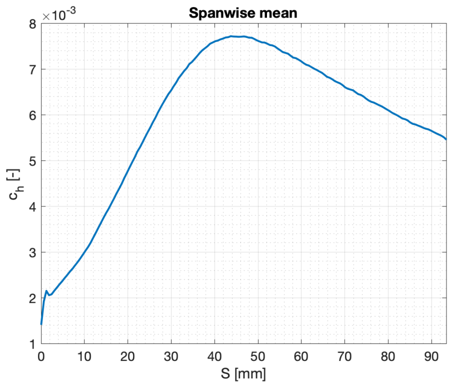

(b) $M_\infty = 7.5$; $Re = 46.3 \times 10^5$

Figure D.15: **Nondimensional roughness strip wavelength:** $\lambda_\delta = 4.5$

D.1.4. Ramp angle of $30°$

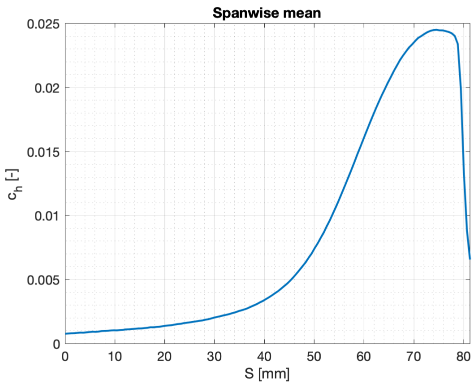

(a) $M_\infty = 7.5$; $Re = 9.2 \times 10^5$

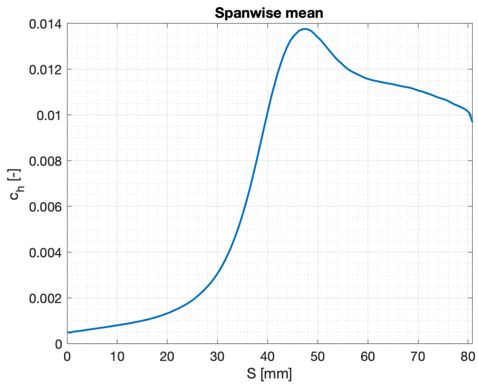

(b) $M_\infty = 7.5$; $Re = 46.3 \times 10^5$

Figure D.16: **No roughness strip.**

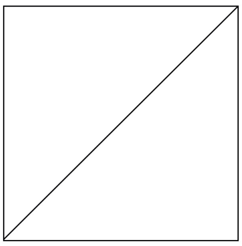

(a) $M_\infty = 7.5$; $Re = 9.2 \times 10^5$

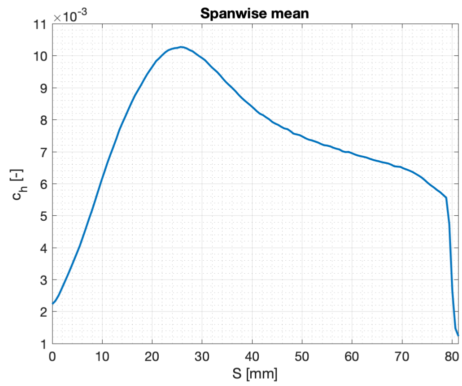

(b) $M_\infty = 7.5$; $Re = 46.3 \times 10^5$

Figure D.17: **Nondimensional roughness strip wavelength:** $\lambda_\delta = 1.8$

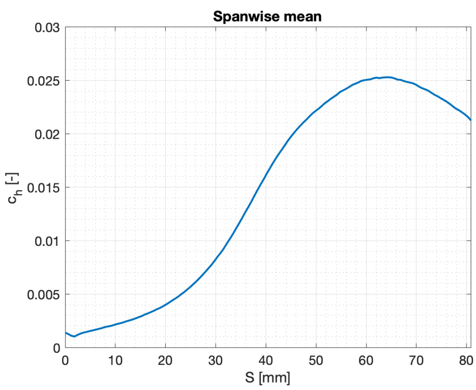

(a) $M_\infty = 7.5$; $Re = 9.2 \times 10^5$

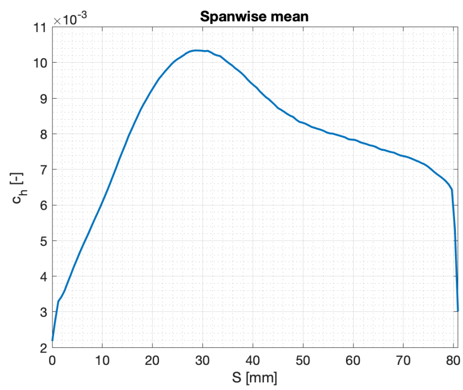

(b) $M_\infty = 7.5$; $Re = 46.3 \times 10^5$

Figure D.18: **Nondimensional roughness strip wavelength:** $\lambda_\delta = 2.7$

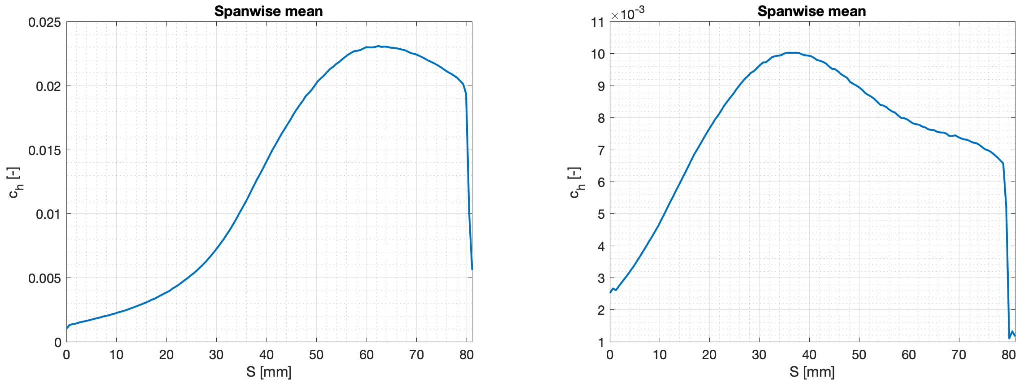

(a) $M_\infty = 7.5$; $Re = 9.2 \times 10^5$ (b) $M_\infty = 7.5$; $Re = 46.3 \times 10^5$

Figure D.19: **Nondimensional roughness strip wavelength:** $\lambda_\delta = 3.6$

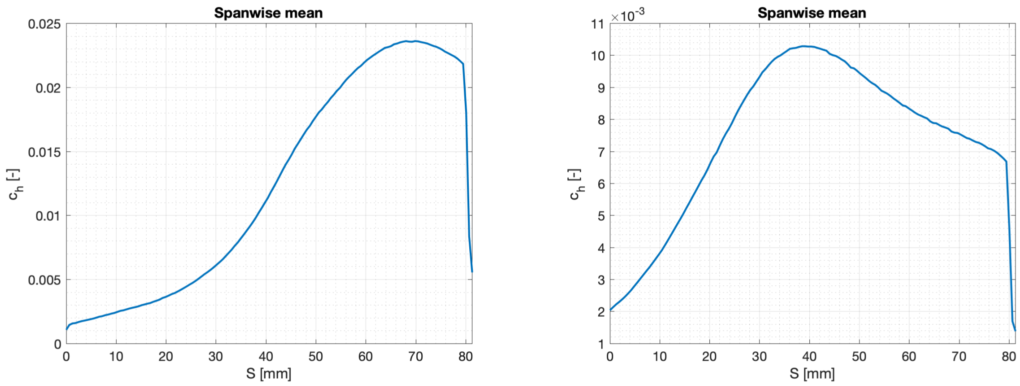

(a) $M_\infty = 7.5$; $Re = 9.2 \times 10^5$ (b) $M_\infty = 7.5$; $Re = 46.3 \times 10^5$

Figure D.20: **Nondimensional roughness strip wavelength:** $\lambda_\delta = 4.5$

D.2. RMS Results

D.2.1. Ramp angle of $15°$

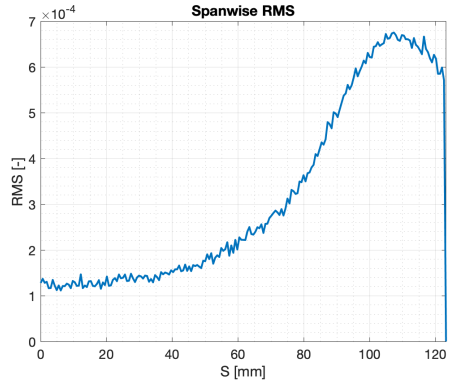

(a) $M_\infty = 7.5$; $Re = 9.2 \times 10^5$

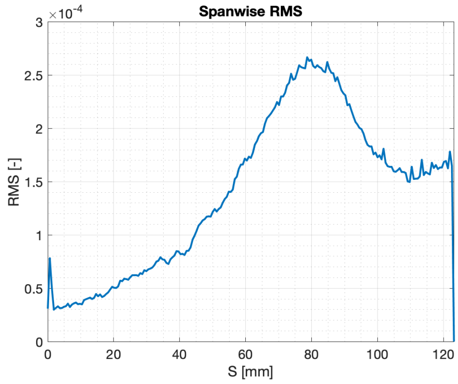

(b) $M_\infty = 7.5$; $Re = 46.3 \times 10^5$

Figure D.21: **No roughness strip.**

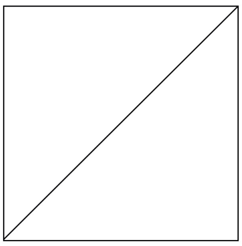

(a) $M_\infty = 7.5$; $Re = 9.2 \times 10^5$

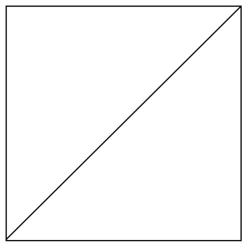

(b) $M_\infty = 7.5$; $Re = 46.3 \times 10^5$

Figure D.22: **Nondimensional roughness strip wavelength:** $\lambda_\delta = 1.8$

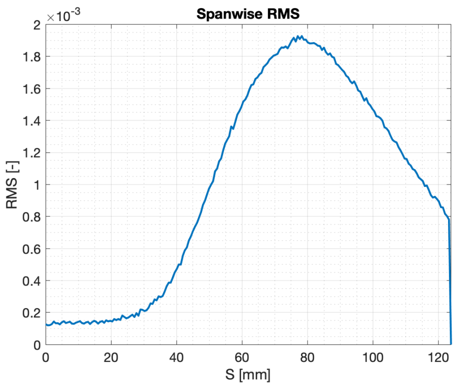

(a) $M_\infty = 7.5$; $Re = 9.2 \times 10^5$

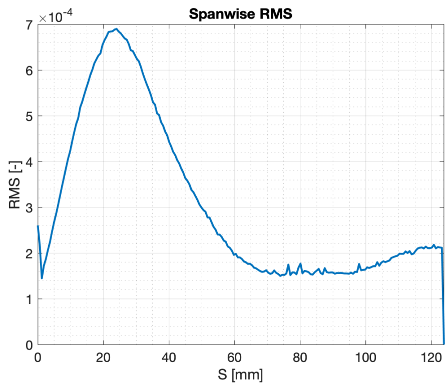

(b) $M_\infty = 7.5$; $Re = 46.3 \times 10^5$

Figure D.23: **Nondimensional roughness strip wavelength:** $\lambda_\delta = 2.7$

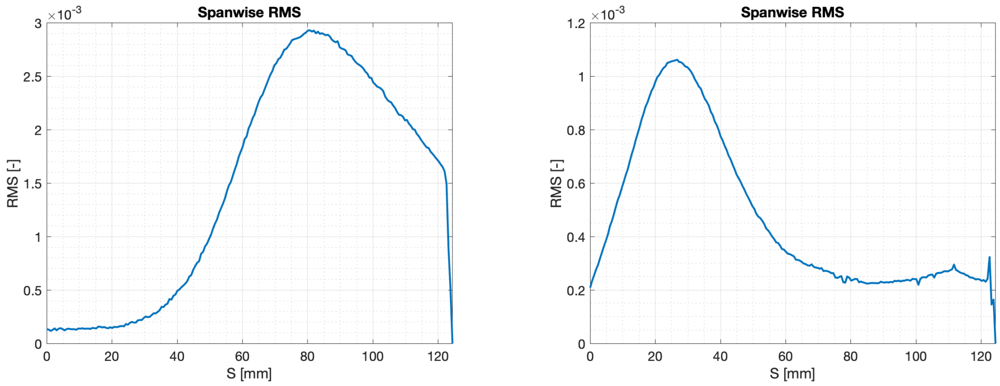

(a) $M_\infty = 7.5$; $Re = 9.2 \times 10^5$ (b) $M_\infty = 7.5$; $Re = 46.3 \times 10^5$

Figure D.24: **Nondimensional roughness strip wavelength:** $\lambda_\delta = 3.6$

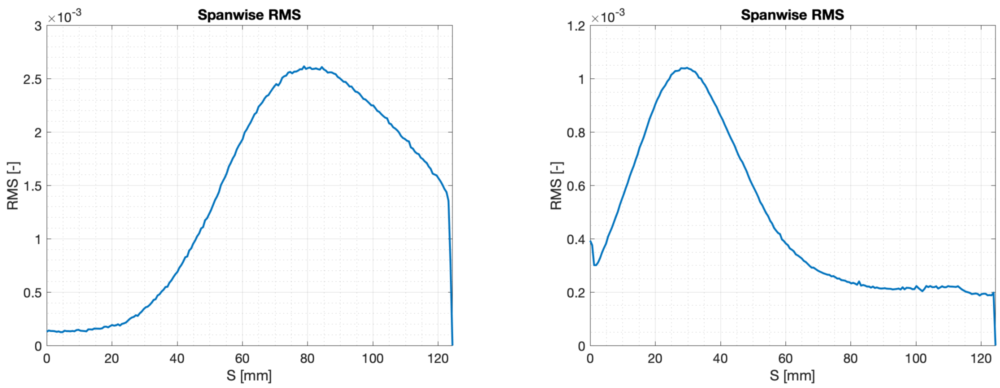

(a) $M_\infty = 7.5$; $Re = 9.2 \times 10^5$ (b) $M_\infty = 7.5$; $Re = 46.3 \times 10^5$

Figure D.25: **Nondimensional roughness strip wavelength:** $\lambda_\delta = 4.5$

D.2.2. Ramp angle of 20°

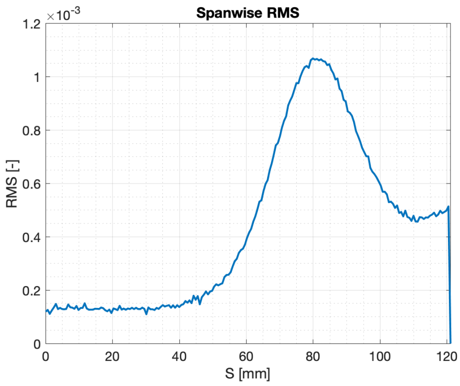

(a) $M_\infty = 7.5$; $Re = 9.2 \times 10^5$

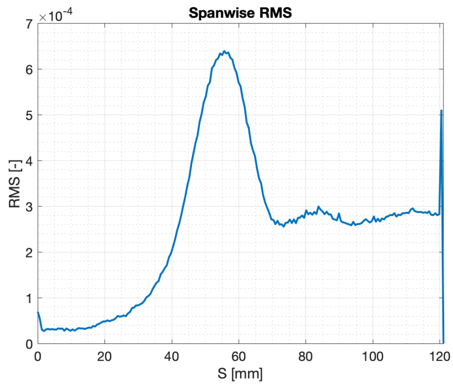

(b) $M_\infty = 7.5$; $Re = 46.3 \times 10^5$

Figure D.26: **No roughness strip.**

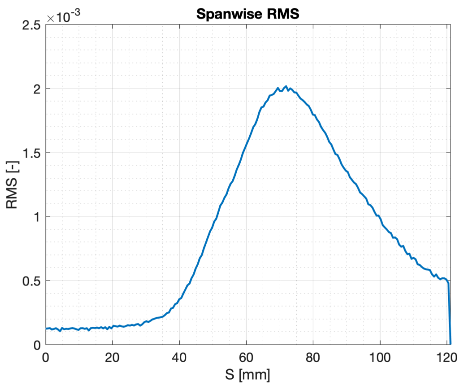

(a) $M_\infty = 7.5$; $Re = 9.2 \times 10^5$

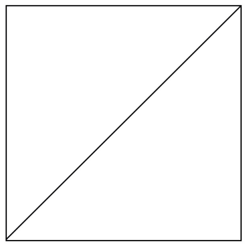

(b) $M_\infty = 7.5$; $Re = 46.3 \times 10^5$

Figure D.27: **Nondimensional roughness strip wavelength:** $\lambda_\delta = 1.8$

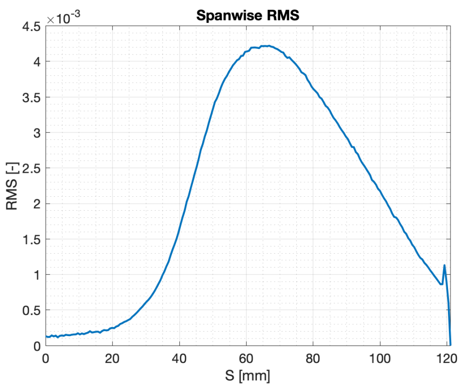

(a) $M_\infty = 7.5$; $Re = 9.2 \times 10^5$

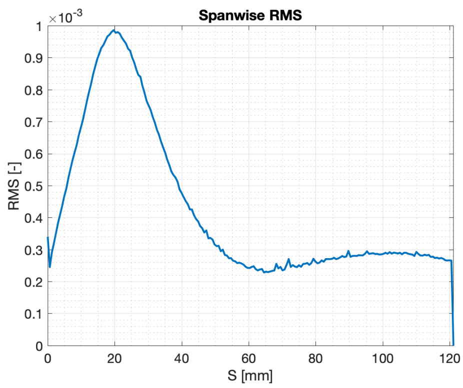

(b) $M_\infty = 7.5$; $Re = 46.3 \times 10^5$

Figure D.28: **Nondimensional roughness strip wavelength:** $\lambda_\delta = 2.7$

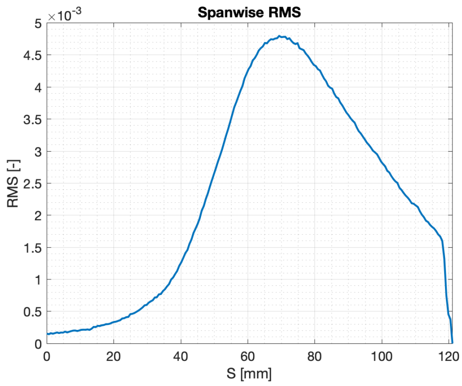

(a) $M_\infty = 7.5$; $Re = 9.2 \times 10^5$

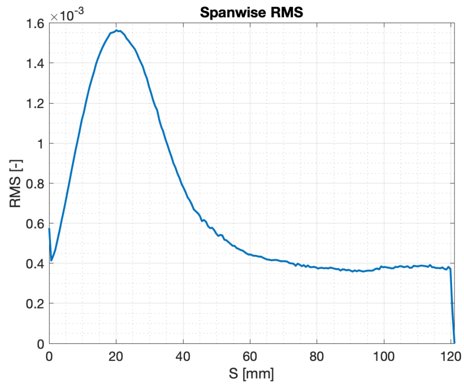

(b) $M_\infty = 7.5$; $Re = 46.3 \times 10^5$

Figure D.29: **Nondimensional roughness strip wavelength:** $\lambda_\delta = 3.6$

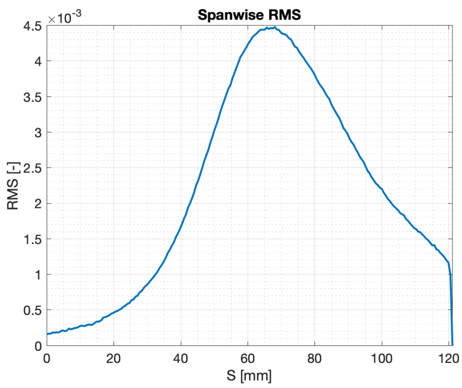

(a) $M_\infty = 7.5$; $Re = 9.2 \times 10^5$

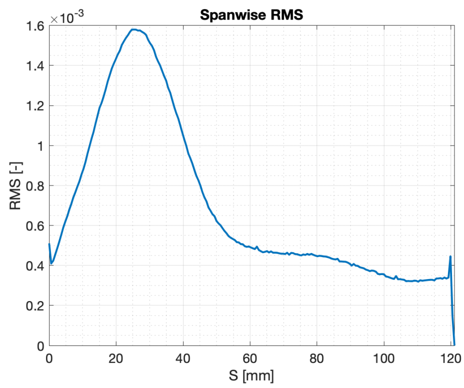

(b) $M_\infty = 7.5$; $Re = 46.3 \times 10^5$

Figure D.30: **Nondimensional roughness strip wavelength:** $\lambda_\delta = 4.5$

D.2.3. Ramp angle of $25°$

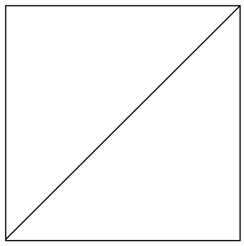

(a) $M_\infty = 7.5$; $Re = 9.2 \times 10^5$

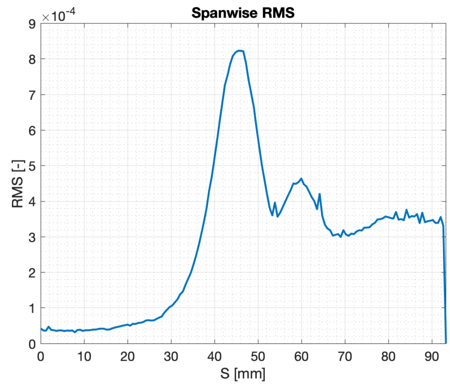

(b) $M_\infty = 7.5$; $Re = 46.3 \times 10^5$

Figure D.31: **No roughness strip.**

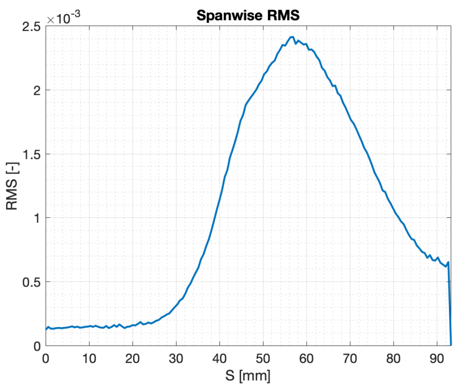

(a) $M_\infty = 7.5$; $Re = 9.2 \times 10^5$

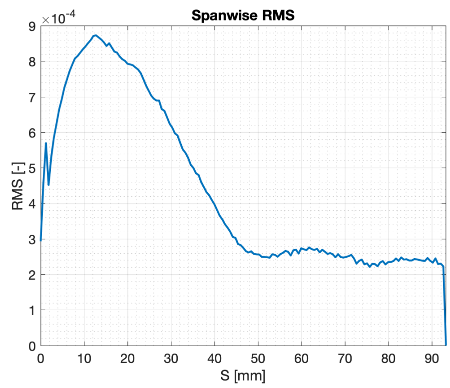

(b) $M_\infty = 7.5$; $Re = 46.3 \times 10^5$

Figure D.32: **Nondimensional roughness strip wavelength:** $\lambda_\delta = 1.8$

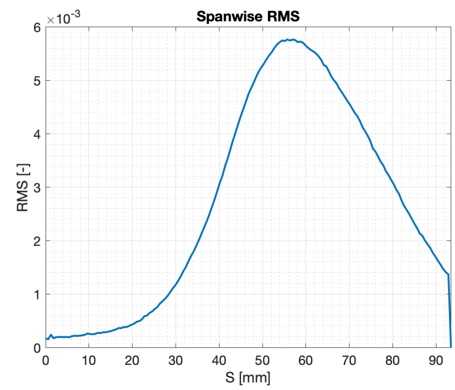

(a) $M_\infty = 7.5$; $Re = 9.2 \times 10^5$

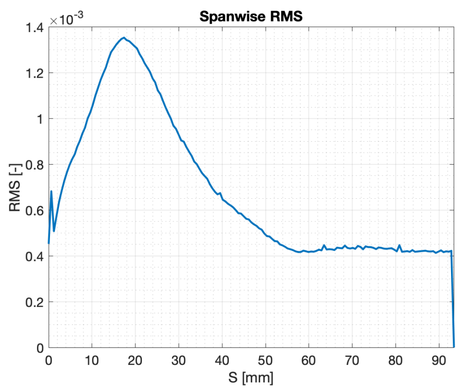

(b) $M_\infty = 7.5$; $Re = 46.3 \times 10^5$

Figure D.33: **Nondimensional roughness strip wavelength:** $\lambda_\delta = 2.7$

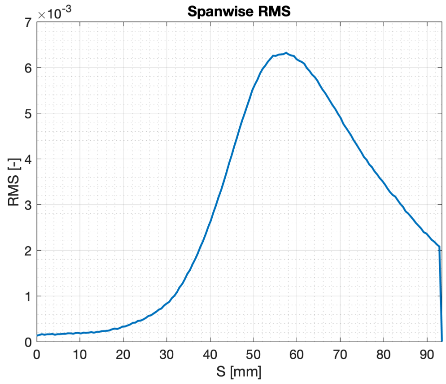

(a) $M_\infty = 7.5$; $Re = 9.2 \times 10^5$

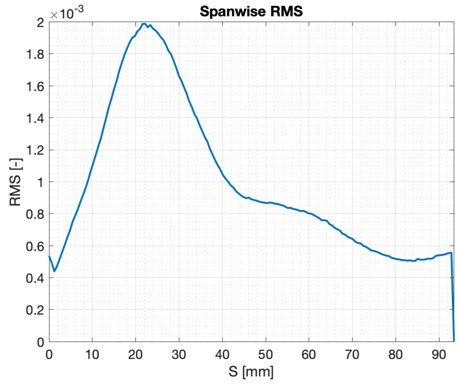

(b) $M_\infty = 7.5$; $Re = 46.3 \times 10^5$

Figure D.34: **Nondimensional roughness strip wavelength:** $\lambda_\delta = 3.6$

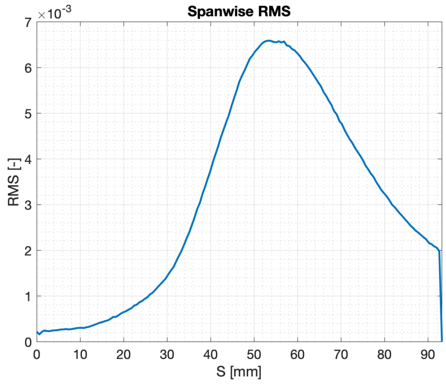

(a) $M_\infty = 7.5$; $Re = 9.2 \times 10^5$

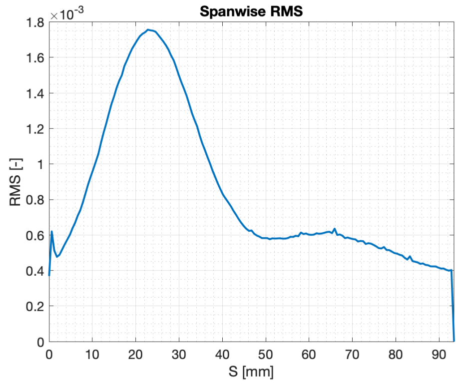

(b) $M_\infty = 7.5$; $Re = 46.3 \times 10^5$

Figure D.35: **Nondimensional roughness strip wavelength:** $\lambda_\delta = 4.5$

D.2.4. Ramp angle of 30°

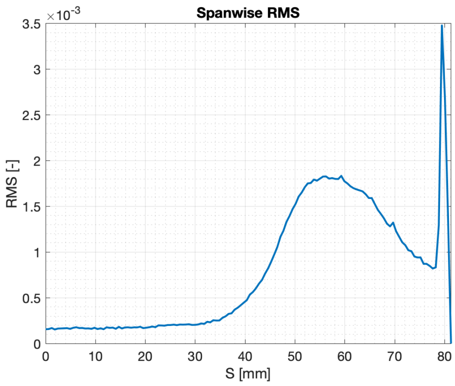

(a) $M_\infty = 7.5$; $Re = 9.2 \times 10^5$

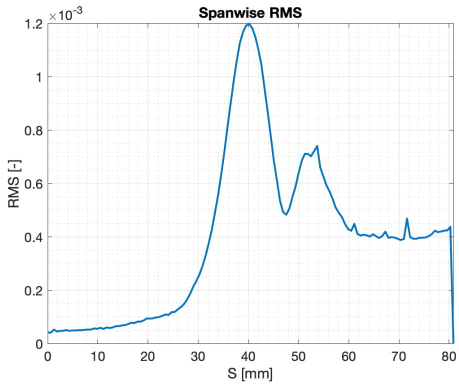

(b) $M_\infty = 7.5$; $Re = 46.3 \times 10^5$

Figure D.36: **No roughness strip.**

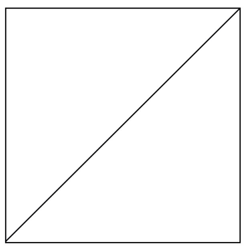

(a) $M_\infty = 7.5$; $Re = 9.2 \times 10^5$

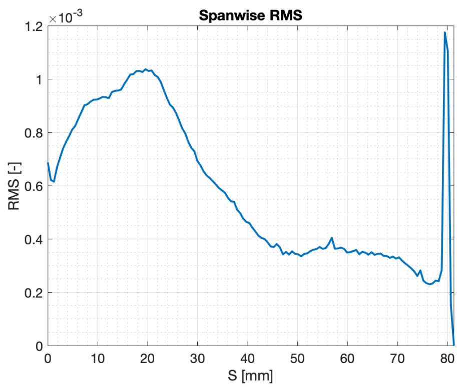

(b) $M_\infty = 7.5$; $Re = 46.3 \times 10^5$

Figure D.37: **Nondimensional roughness strip wavelength:** $\lambda_\delta = 1.8$

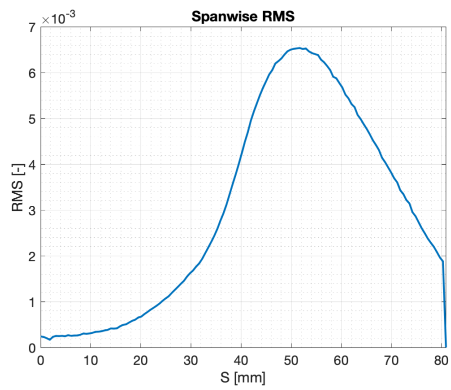

(a) $M_\infty = 7.5$; $Re = 9.2 \times 10^5$

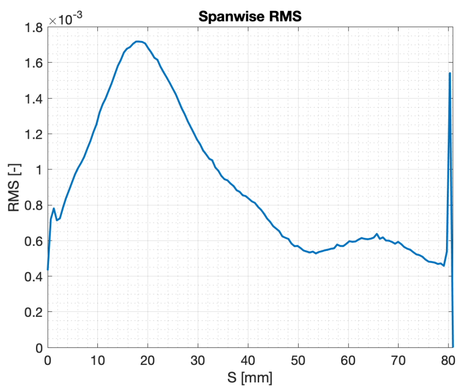

(b) $M_\infty = 7.5$; $Re = 46.3 \times 10^5$

Figure D.38: **Nondimensional roughness strip wavelength:** $\lambda_\delta = 2.7$

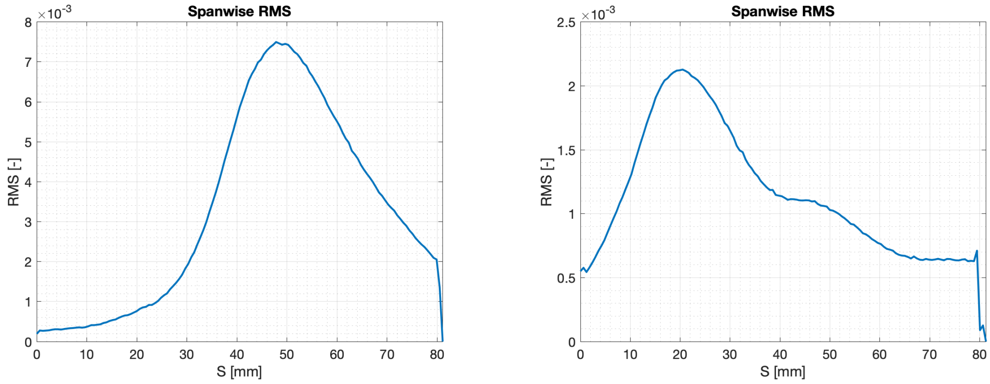

(a) $M_\infty = 7.5$; $Re = 9.2 \times 10^5$ (b) $M_\infty = 7.5$; $Re = 46.3 \times 10^5$

Figure D.39: **Nondimensional roughness strip wavelength:** $\lambda_\delta = 3.6$

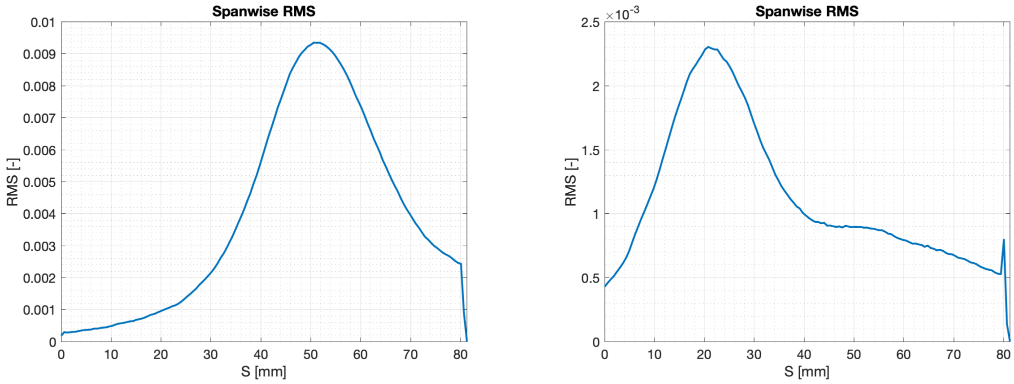

(a) $M_\infty = 7.5$; $Re = 9.2 \times 10^5$ (b) $M_\infty = 7.5$; $Re = 46.3 \times 10^5$

Figure D.40: **Nondimensional roughness strip wavelength:** $\lambda_\delta = 4.5$

E

QIRT Images: Image-Plot Comparison – Normal to Flat Plate

The images adhere to the following specifications:

- Frame rate: $200\ Hz$
- Integration time: $250\ \mu s$
- Spatial resolution: $1.66\ px/mm$

E.1. Mean Results

E.1.1. Ramp angle of $15°$

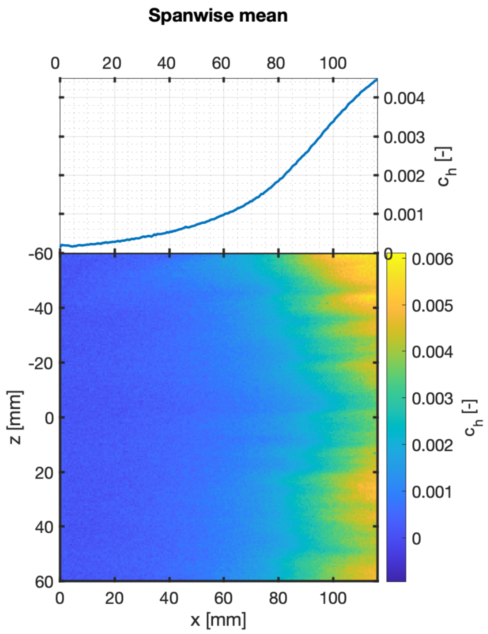

(a) $M_\infty = 7.5$; $Re = 9.2 \times 10^5$

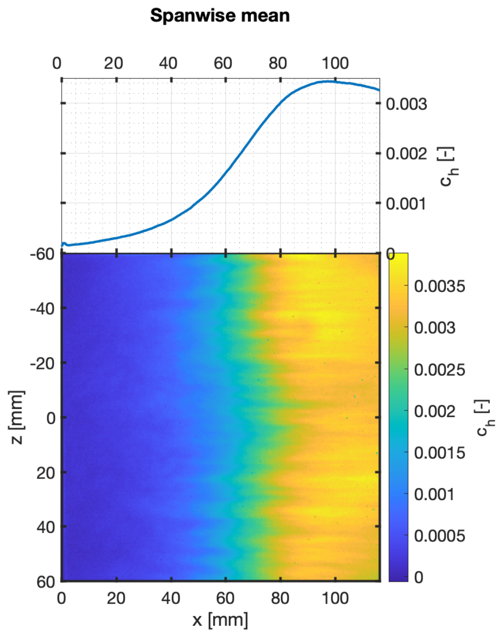

(b) $M_\infty = 7.5$; $Re = 46.3 \times 10^5$

Figure E.1: **No roughness strip.**

(a) $M_\infty = 7.5$; $Re = 9.2 \times 10^5$ (b) $M_\infty = 7.5$; $Re = 46.3 \times 10^5$

Figure E.2: **Nondimensional roughness strip wavelength:** $\lambda_\delta = 1.8$

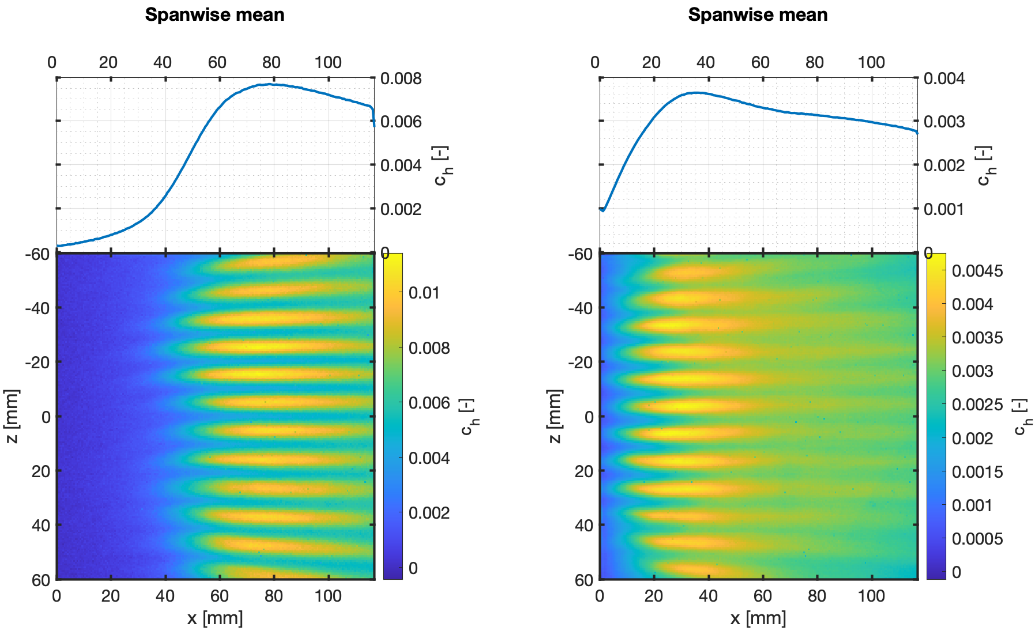

(a) $M_\infty = 7.5$; $Re = 9.2 \times 10^5$ (b) $M_\infty = 7.5$; $Re = 46.3 \times 10^5$

Figure E.3: **Nondimensional roughness strip wavelength:** $\lambda_\delta = 2.7$

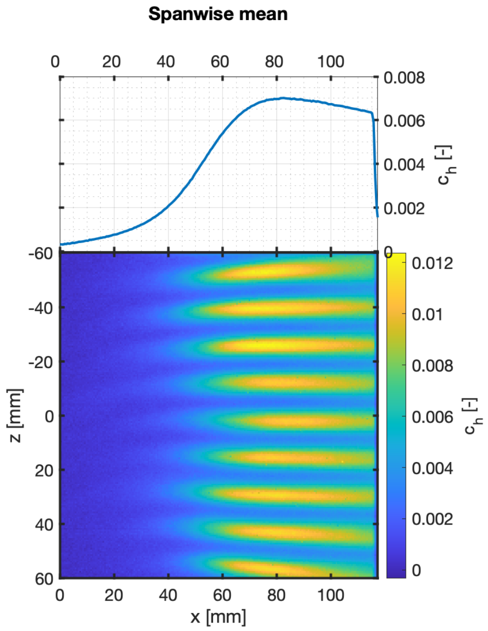

(a) $M_\infty = 7.5$; $Re = 9.2 \times 10^5$

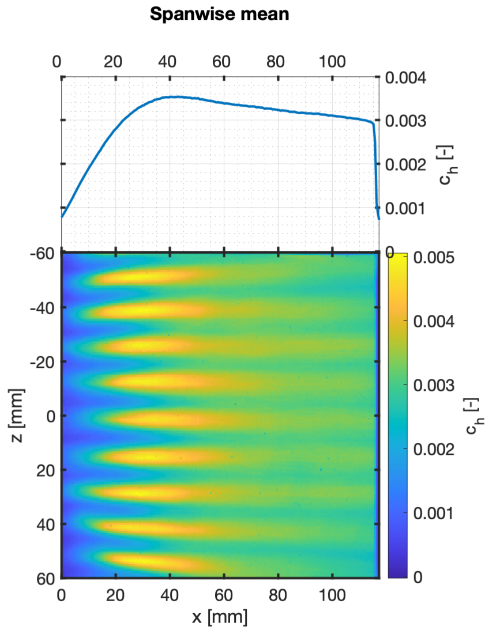

(b) $M_\infty = 7.5$; $Re = 46.3 \times 10^5$

Figure E.4: **Nondimensional roughness strip wavelength:** $\lambda_\delta = 3.6$

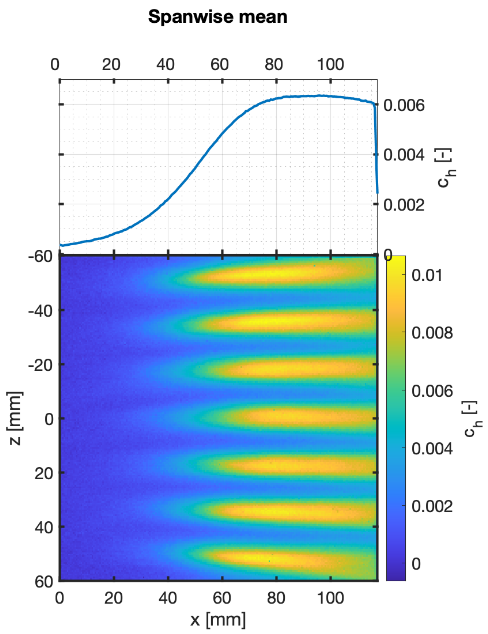

(a) $M_\infty = 7.5$; $Re = 9.2 \times 10^5$

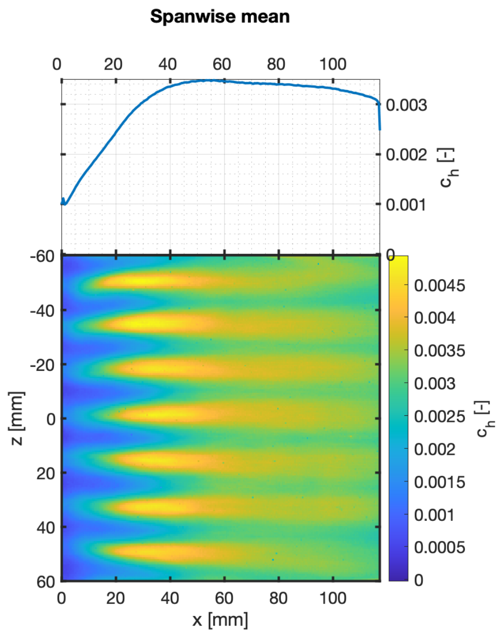

(b) $M_\infty = 7.5$; $Re = 46.3 \times 10^5$

Figure E.5: **Nondimensional roughness strip wavelength:** $\lambda_\delta = 4.5$

E.1.2. Ramp angle of 20°

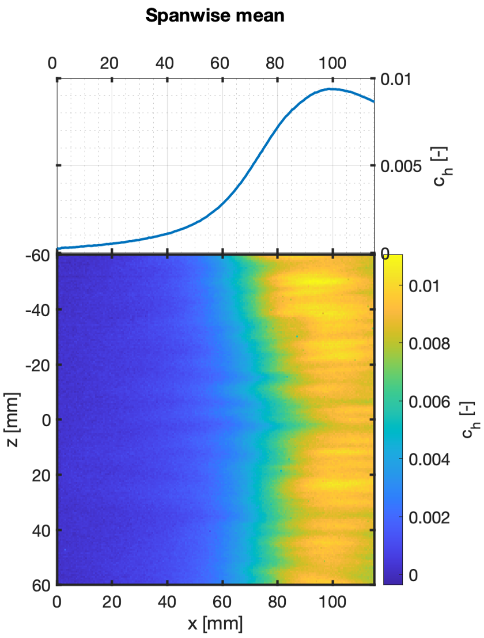

(a) $M_\infty = 7.5$; $Re = 9.2 \times 10^5$

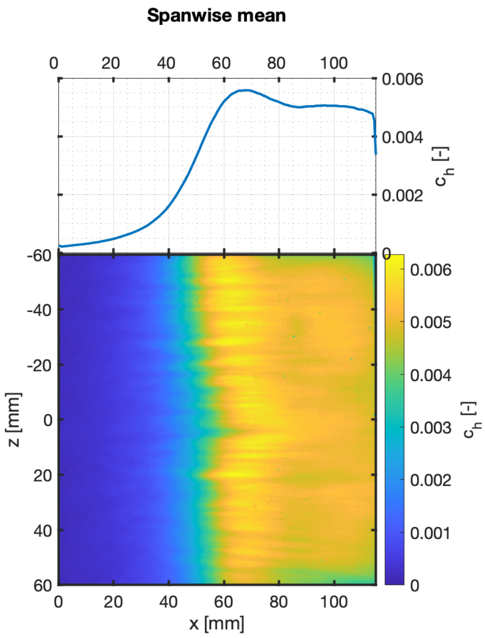

(b) $M_\infty = 7.5$; $Re = 46.3 \times 10^5$

Figure E.6: **No roughness strip.**

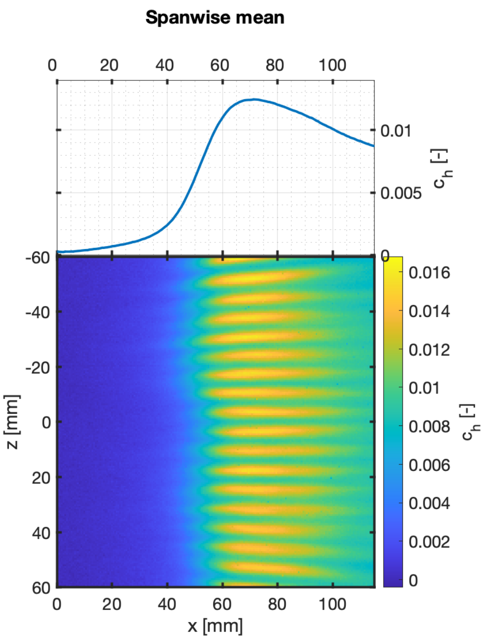

(a) $M_\infty = 7.5$; $Re = 9.2 \times 10^5$

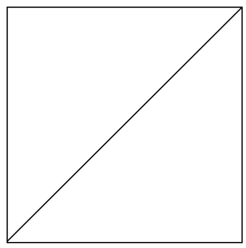

(b) $M_\infty = 7.5$; $Re = 46.3 \times 10^5$

Figure E.7: **Nondimensional roughness strip wavelength:** $\lambda_\delta = 1.8$

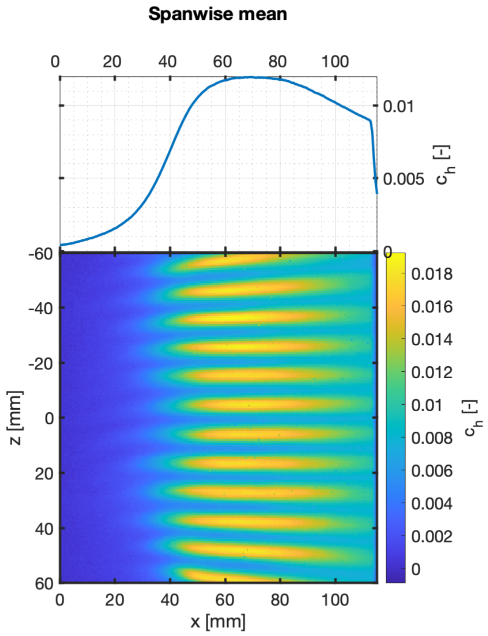

(a) $M_\infty = 7.5$; $Re = 9.2 \times 10^5$

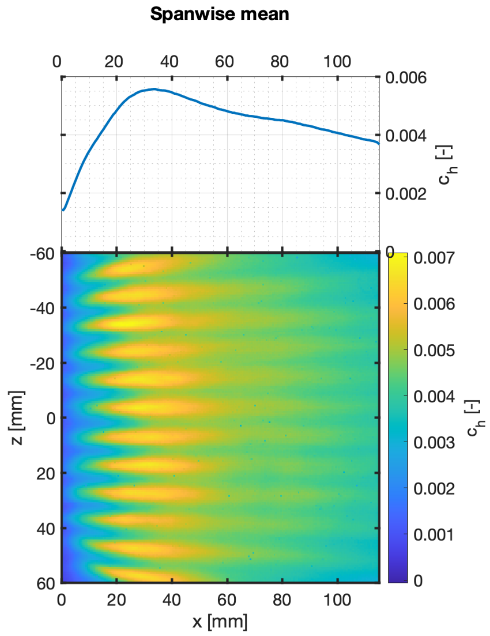

(b) $M_\infty = 7.5$; $Re = 46.3 \times 10^5$

Figure E.8: **Nondimensional roughness strip wavelength:** $\lambda_\delta = 2.7$

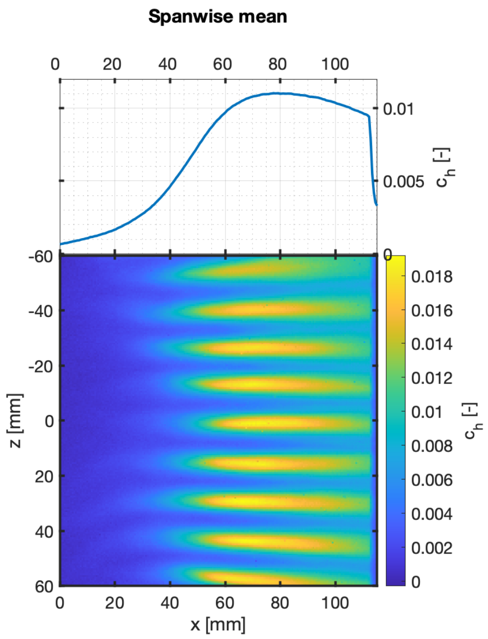

(a) $M_\infty = 7.5$; $Re = 9.2 \times 10^5$

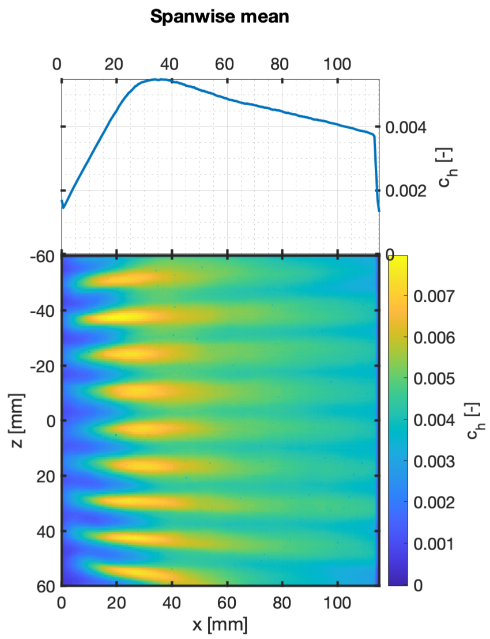

(b) $M_\infty = 7.5$; $Re = 46.3 \times 10^5$

Figure E.9: **Nondimensional roughness strip wavelength:** $\lambda_\delta = 3.6$

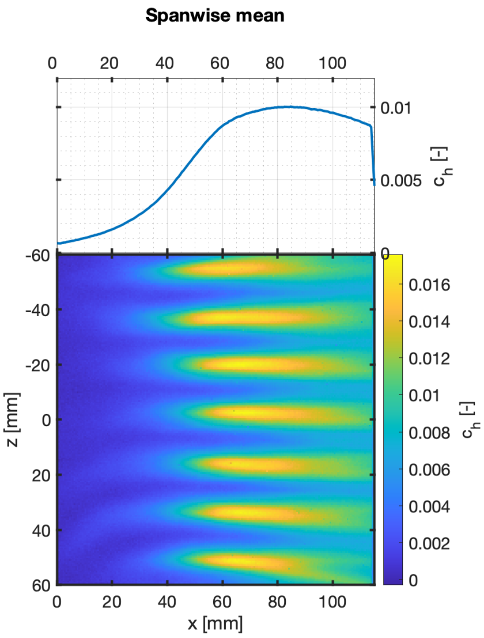

(a) $M_\infty = 7.5$; $Re = 9.2 \times 10^5$

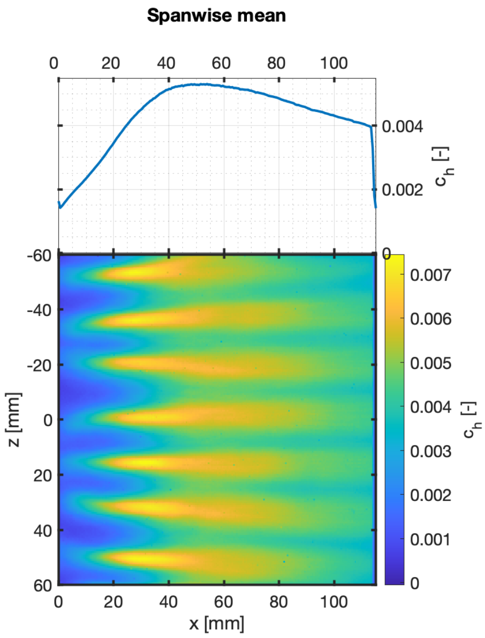

(b) $M_\infty = 7.5$; $Re = 46.3 \times 10^5$

Figure E.10: **Nondimensional roughness strip wavelength:** $\lambda_\delta = 4.5$

E.1.3. Ramp angle of 25°

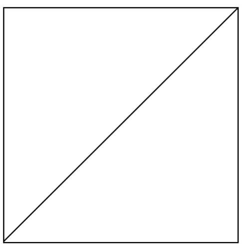

(a) $M_\infty = 7.5$; $Re = 9.2 \times 10^5$

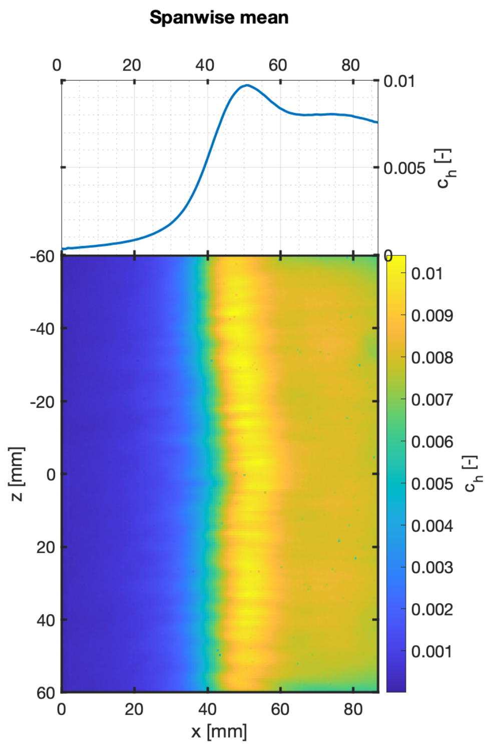

(b) $M_\infty = 7.5$; $Re = 46.3 \times 10^5$

Figure E.11: **No roughness strip.**

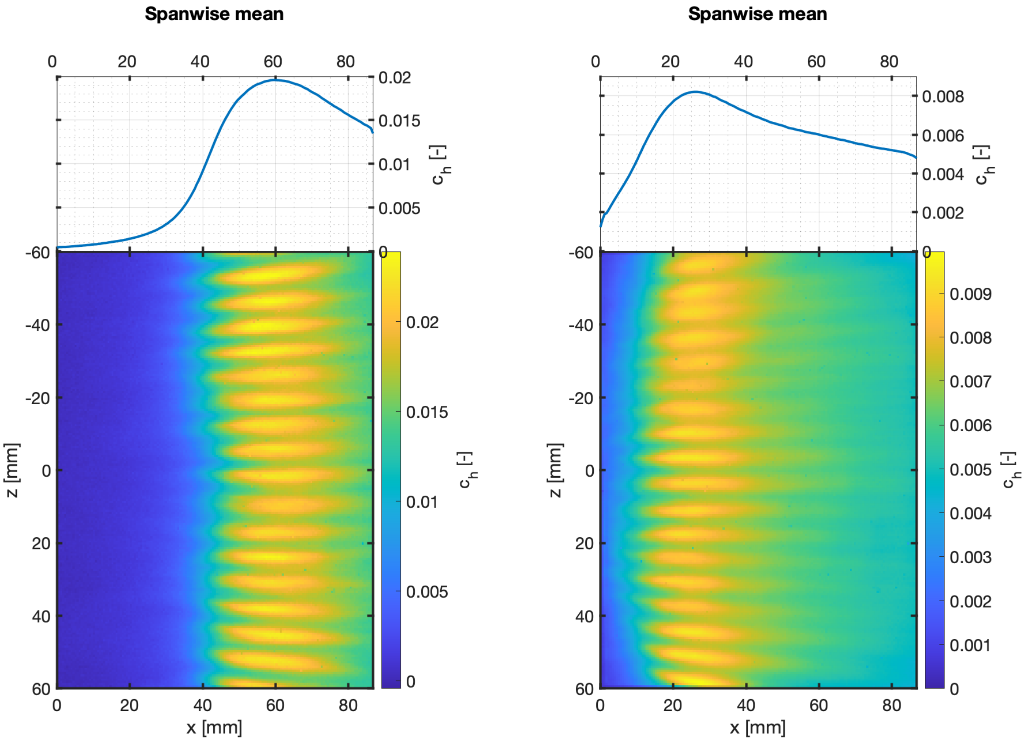

(a) $M_\infty = 7.5$; $Re = 9.2 \times 10^5$ (b) $M_\infty = 7.5$; $Re = 46.3 \times 10^5$

Figure E.12: **Nondimensional roughness strip wavelength:** $\lambda_\delta = 1.8$

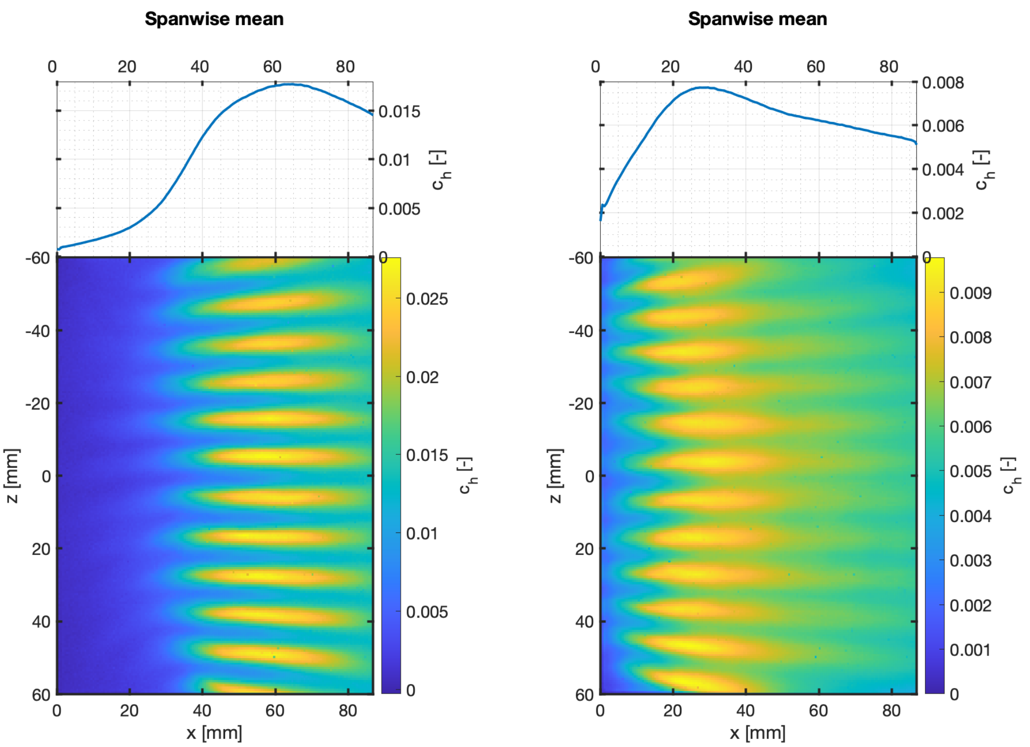

(a) $M_\infty = 7.5$; $Re = 9.2 \times 10^5$ (b) $M_\infty = 7.5$; $Re = 46.3 \times 10^5$

Figure E.13: **Nondimensional roughness strip wavelength:** $\lambda_\delta = 2.7$

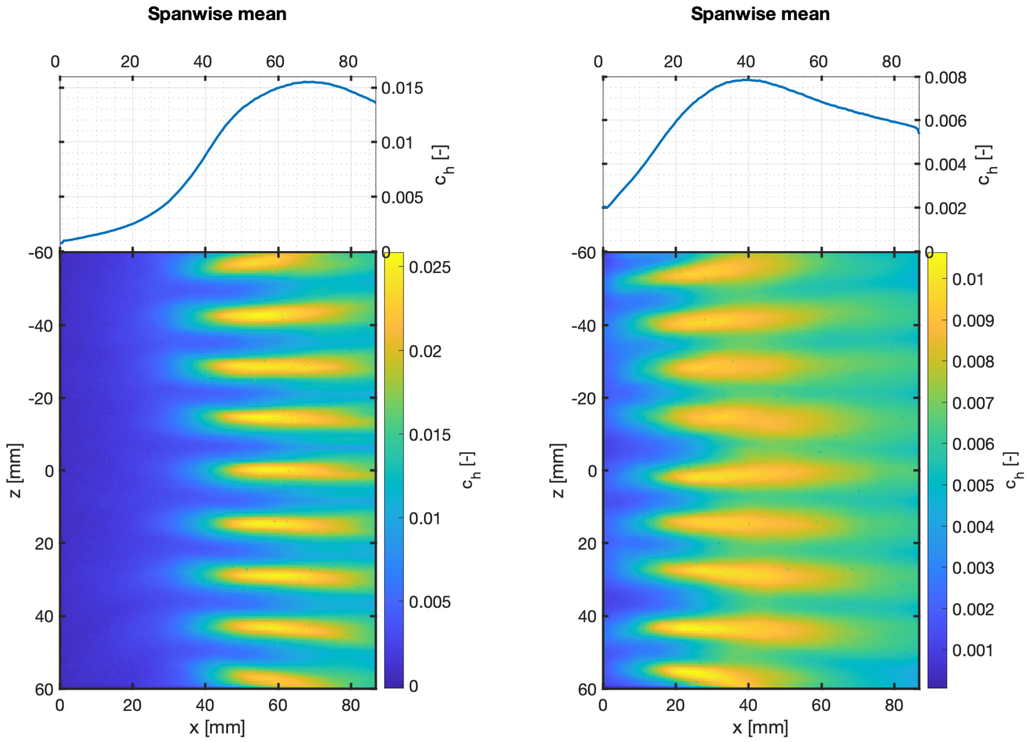

(a) $M_\infty = 7.5$; $Re = 9.2 \times 10^5$ (b) $M_\infty = 7.5$; $Re = 46.3 \times 10^5$

Figure E.14: **Nondimensional roughness strip wavelength:** $\lambda_\delta = 3.6$

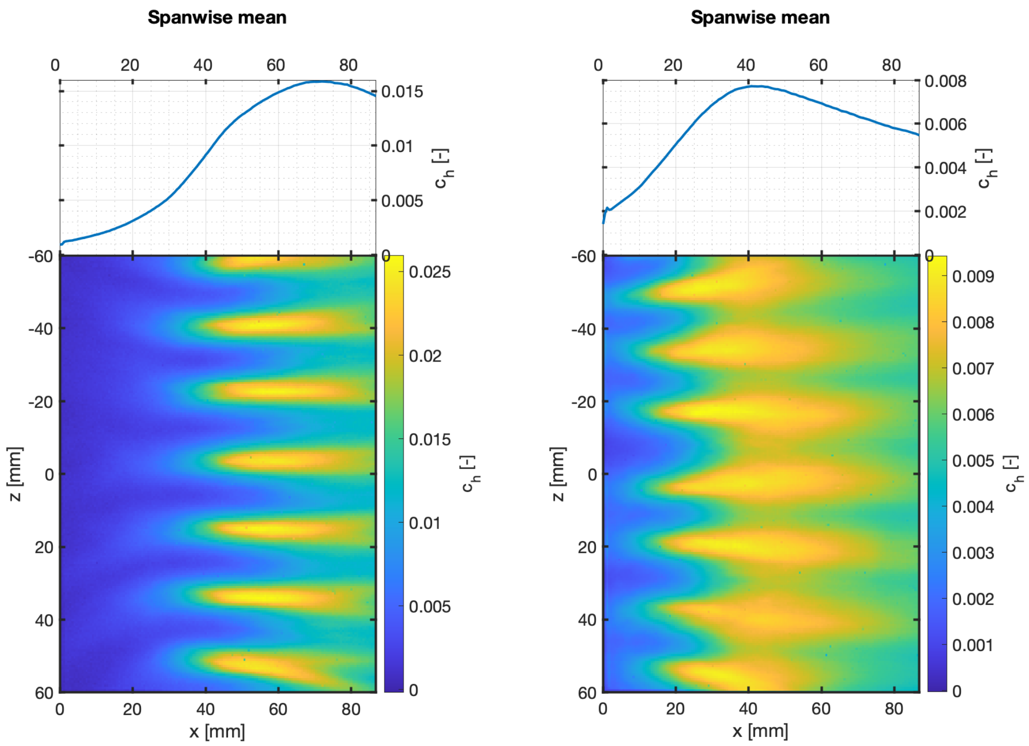

(a) $M_\infty = 7.5$; $Re = 9.2 \times 10^5$ (b) $M_\infty = 7.5$; $Re = 46.3 \times 10^5$

Figure E.15: **Nondimensional roughness strip wavelength:** $\lambda_\delta = 4.5$

E.1.4. Ramp angle of 30°

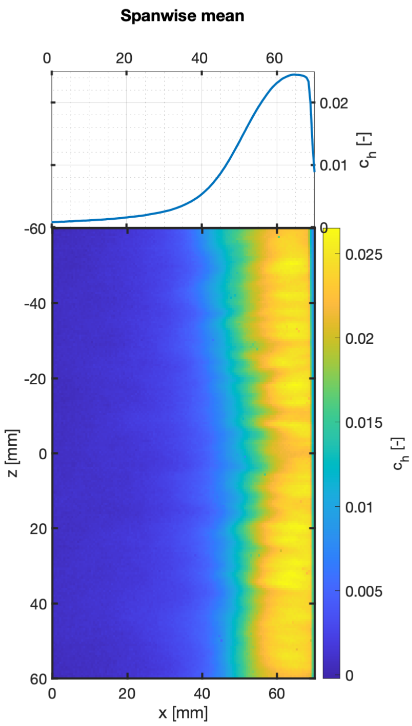

(a) $M_\infty = 7.5$; $Re = 9.2 \times 10^5$

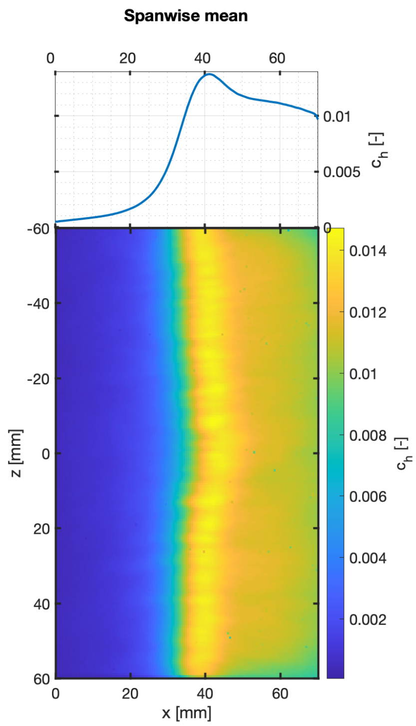

(b) $M_\infty = 7.5$; $Re = 46.3 \times 10^5$

Figure E.16: **No roughness strip.**

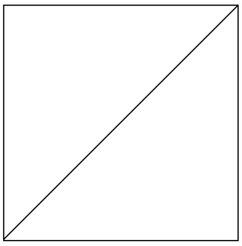

(a) $M_\infty = 7.5$; $Re = 9.2 \times 10^5$

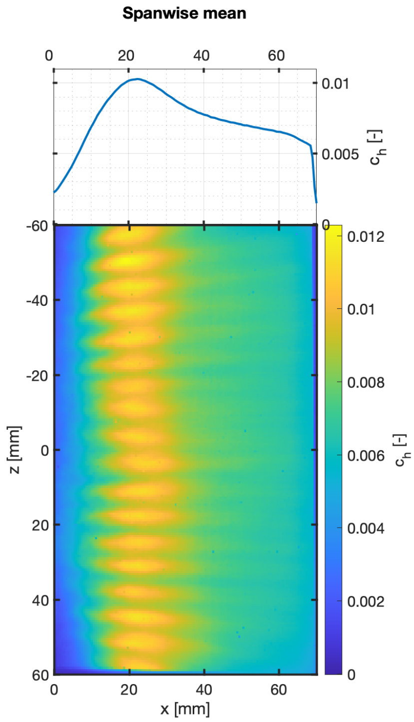

(b) $M_\infty = 7.5$; $Re = 46.3 \times 10^5$

Figure E.17: **Nondimensional roughness strip wavelength:** $\lambda_\delta = 1.8$

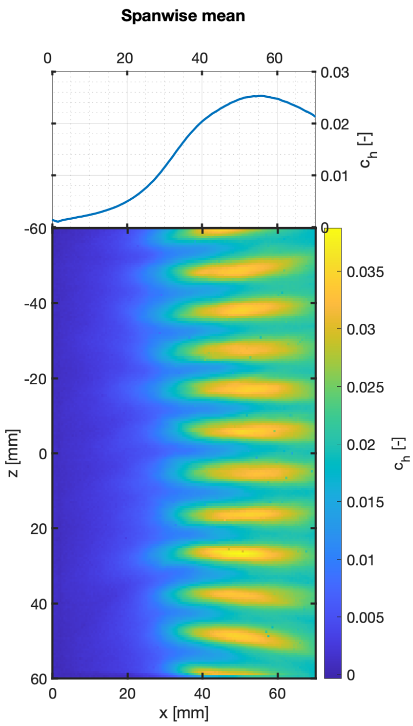

(a) $M_\infty = 7.5$; $Re = 9.2 \times 10^5$

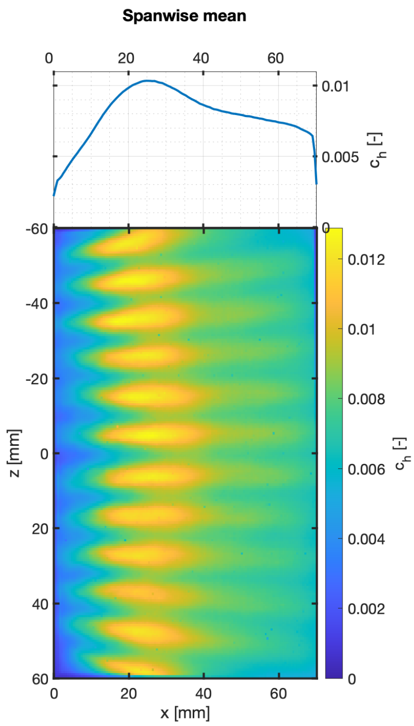

(b) $M_\infty = 7.5$; $Re = 46.3 \times 10^5$

Figure E.18: **Nondimensional roughness strip wavelength:** $\lambda_\delta = 2.7$

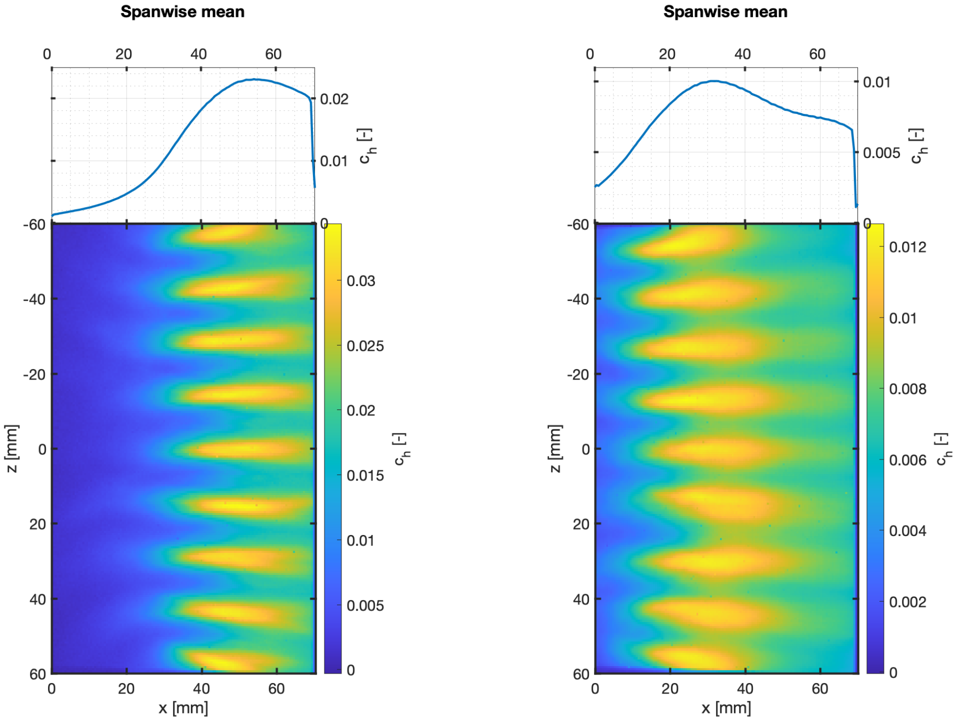

(a) $M_\infty = 7.5$; $Re = 9.2 \times 10^5$

(b) $M_\infty = 7.5$; $Re = 46.3 \times 10^5$

Figure E.19: **Nondimensional roughness strip wavelength:** $\lambda_\delta = 3.6$

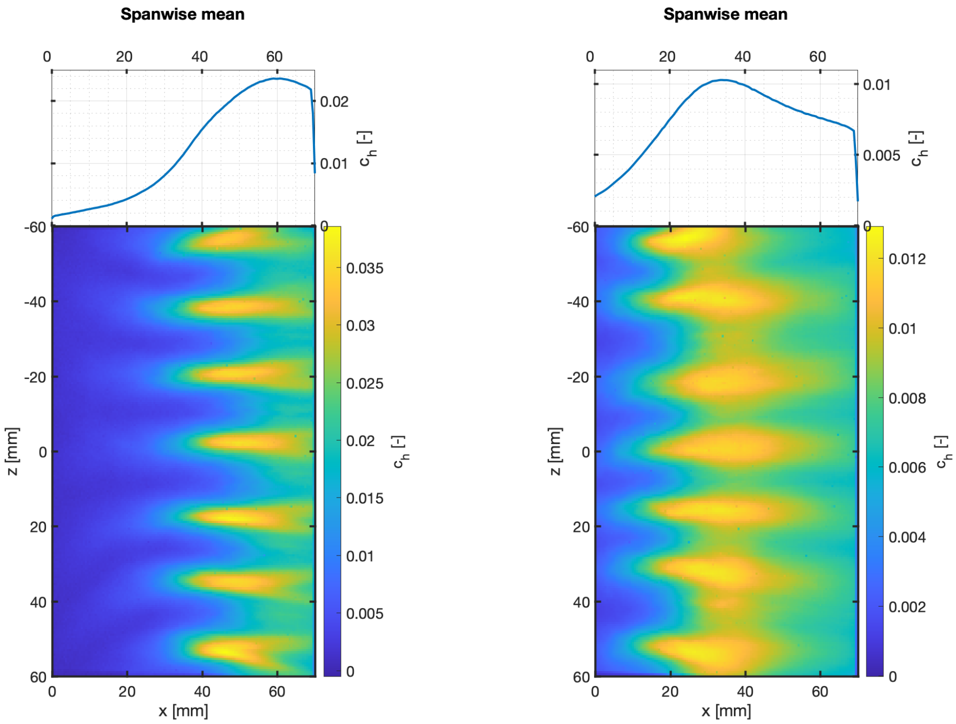

(a) $M_\infty = 7.5$; $Re = 9.2 \times 10^5$

(b) $M_\infty = 7.5$; $Re = 46.3 \times 10^5$

Figure E.20: **Nondimensional roughness strip wavelength:** $\lambda_\delta = 4.5$

E.2. RMS Results

E.2.1. Ramp angle of $15°$

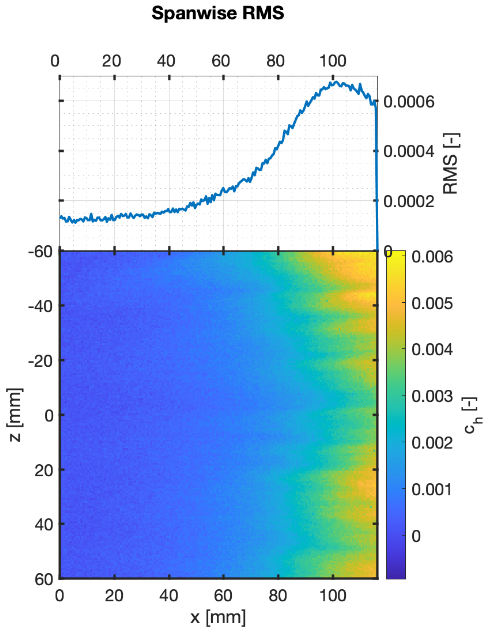

(a) $M_\infty = 7.5$; $Re = 9.2 \times 10^5$

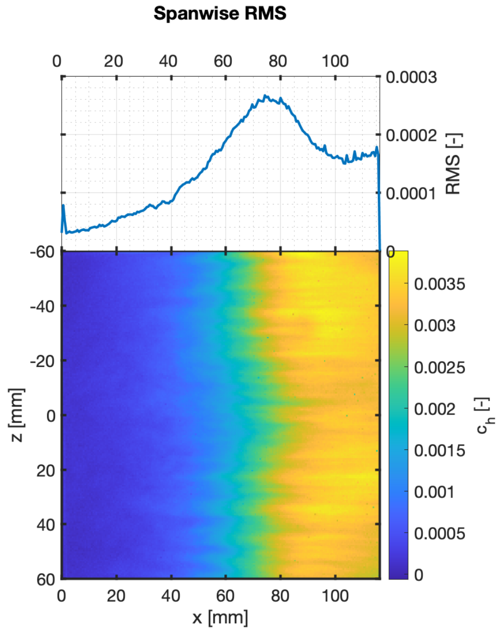

(b) $M_\infty = 7.5$; $Re = 46.3 \times 10^5$

Figure E.21: **No roughness strip.**

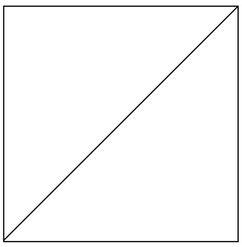

(a) $M_\infty = 7.5$; $Re = 9.2 \times 10^5$

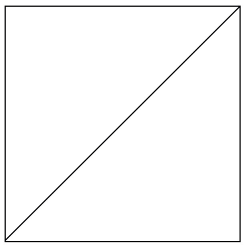

(b) $M_\infty = 7.5$; $Re = 46.3 \times 10^5$

Figure E.22: **Nondimensional roughness strip wavelength:** $\lambda_\delta = 1.8$

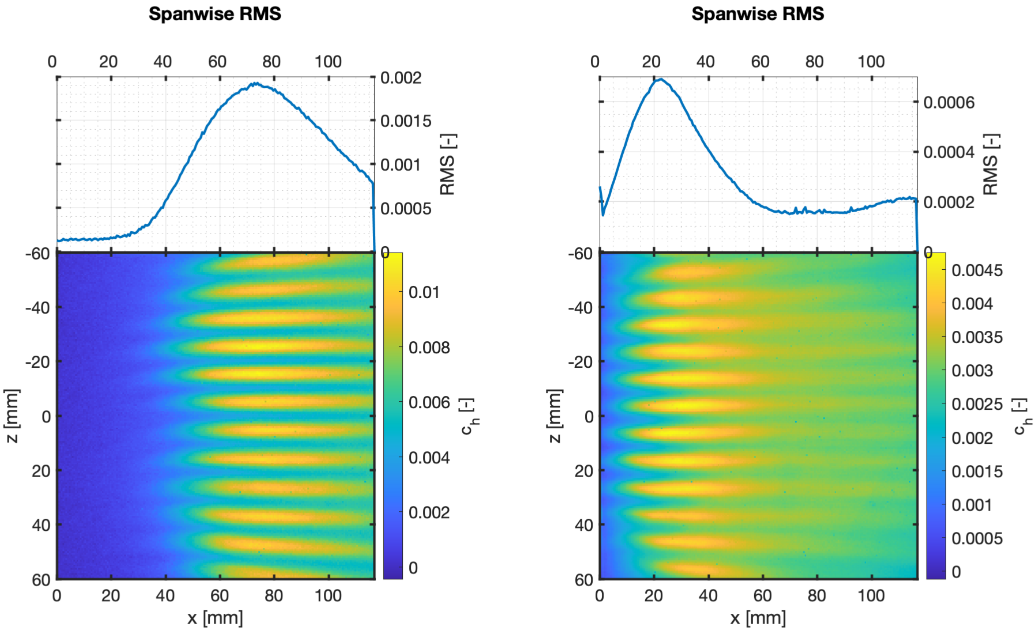

(a) $M_\infty = 7.5$; $Re = 9.2 \times 10^5$ (b) $M_\infty = 7.5$; $Re = 46.3 \times 10^5$

Figure E.23: **Nondimensional roughness strip wavelength:** $\lambda_\delta = 2.7$

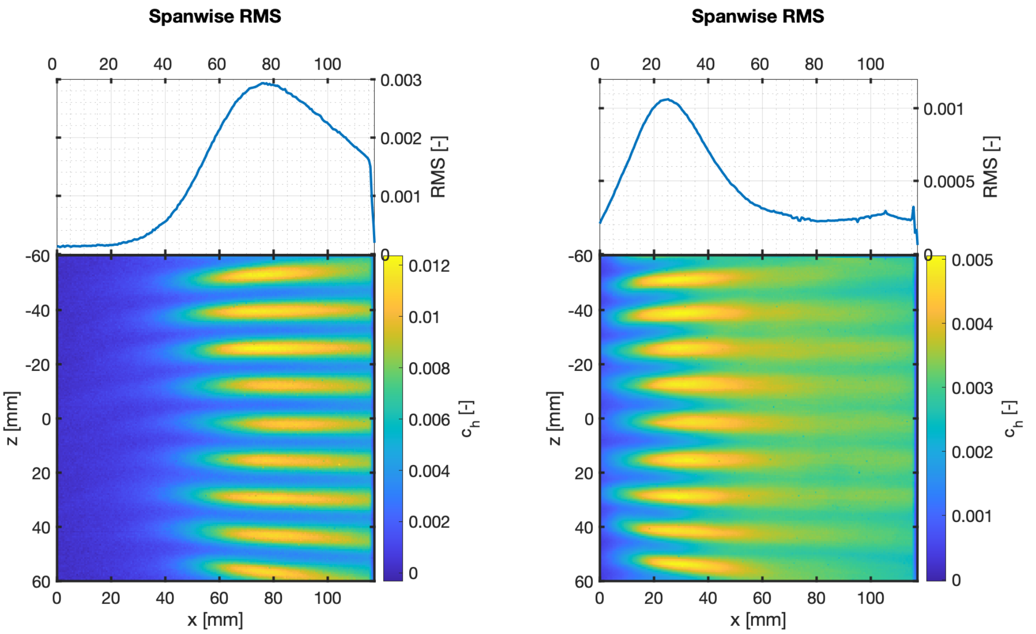

(a) $M_\infty = 7.5$; $Re = 9.2 \times 10^5$ (b) $M_\infty = 7.5$; $Re = 46.3 \times 10^5$

Figure E.24: **Nondimensional roughness strip wavelength:** $\lambda_\delta = 3.6$

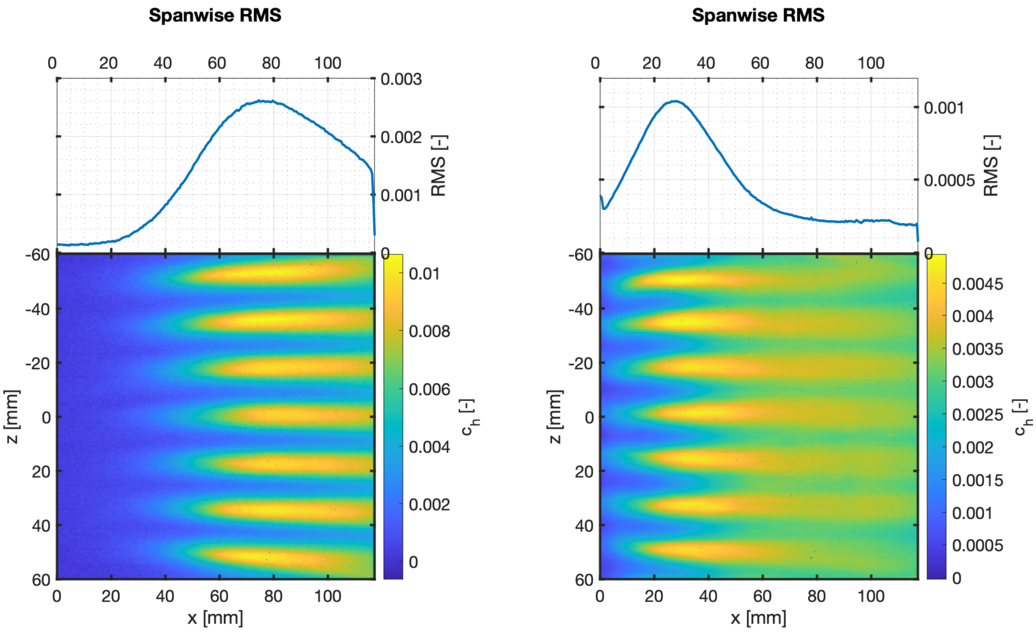

(a) $M_\infty = 7.5$; $Re = 9.2 \times 10^5$ (b) $M_\infty = 7.5$; $Re = 46.3 \times 10^5$

Figure E.25: **Nondimensional roughness strip wavelength:** $\lambda_\delta = 4.5$

E.2.2. Ramp angle of 20°

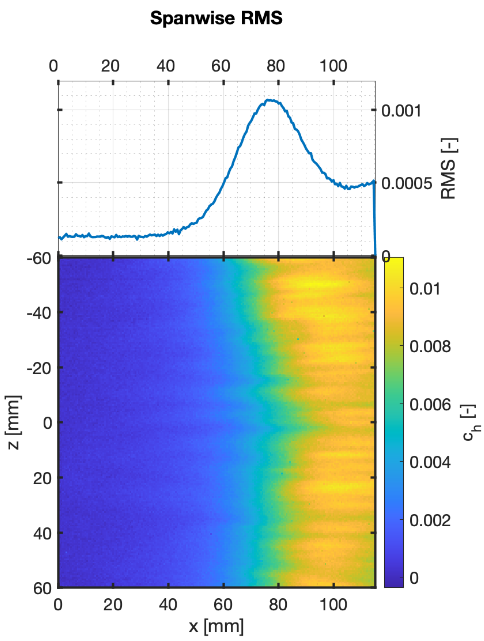

(a) $M_\infty = 7.5$; $Re = 9.2 \times 10^5$

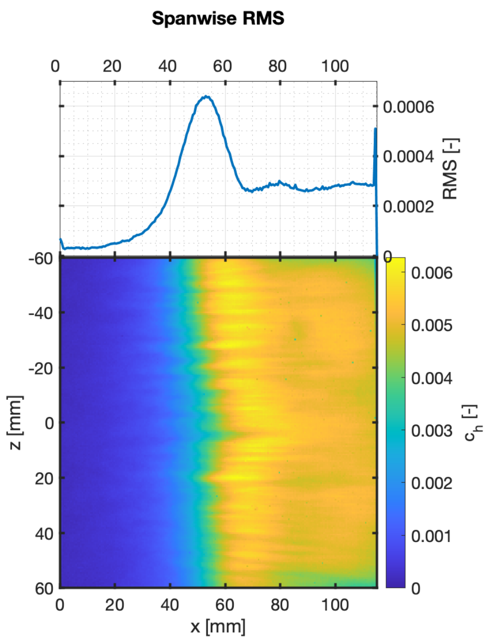

(b) $M_\infty = 7.5$; $Re = 46.3 \times 10^5$

Figure E.26: **No roughness strip.**

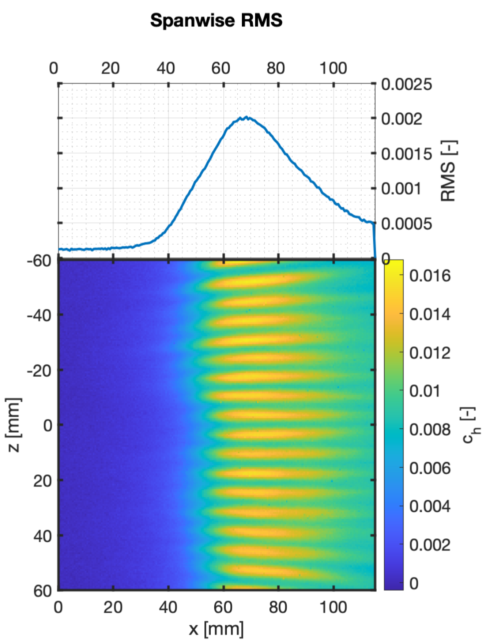

(a) $M_\infty = 7.5$; $Re = 9.2 \times 10^5$

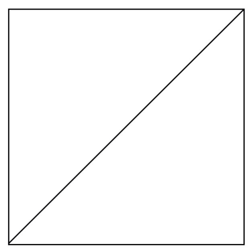

(b) $M_\infty = 7.5$; $Re = 46.3 \times 10^5$

Figure E.27: **Nondimensional roughness strip wavelength:** $\lambda_\delta = 1.8$

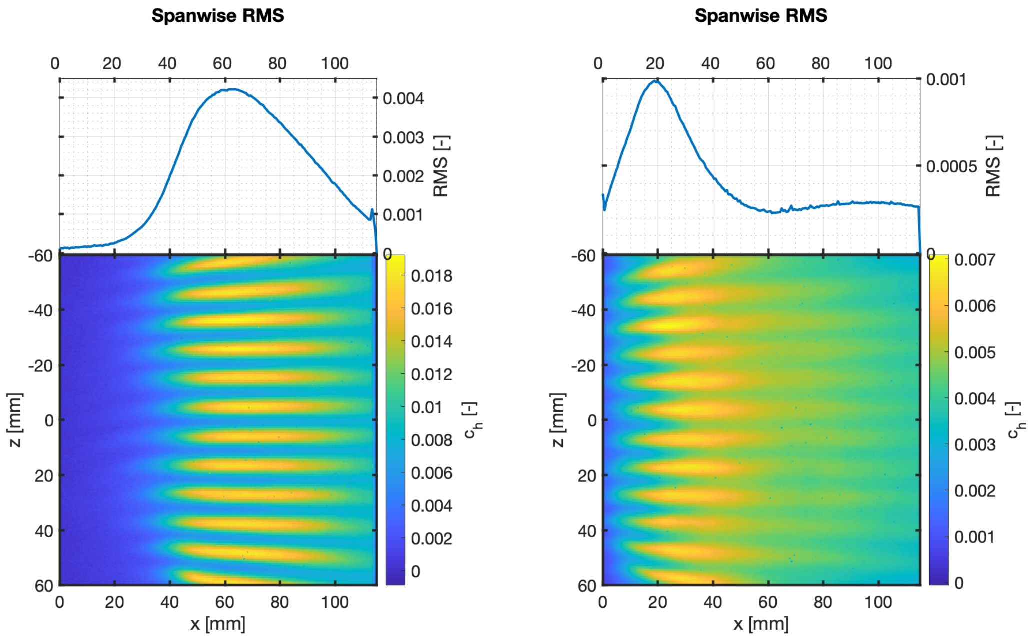

(a) $M_\infty = 7.5$; $Re = 9.2 \times 10^5$

(b) $M_\infty = 7.5$; $Re = 46.3 \times 10^5$

Figure E.28: **Nondimensional roughness strip wavelength:** $\lambda_\delta = 2.7$

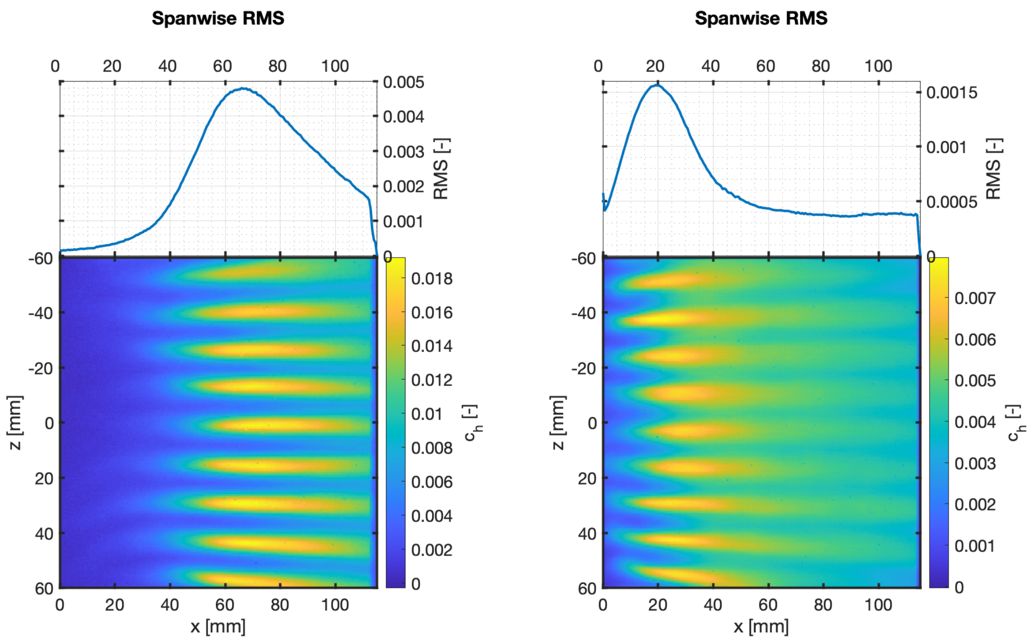

(a) $M_\infty = 7.5$; $Re = 9.2 \times 10^5$

(b) $M_\infty = 7.5$; $Re = 46.3 \times 10^5$

Figure E.29: **Nondimensional roughness strip wavelength:** $\lambda_\delta = 3.6$

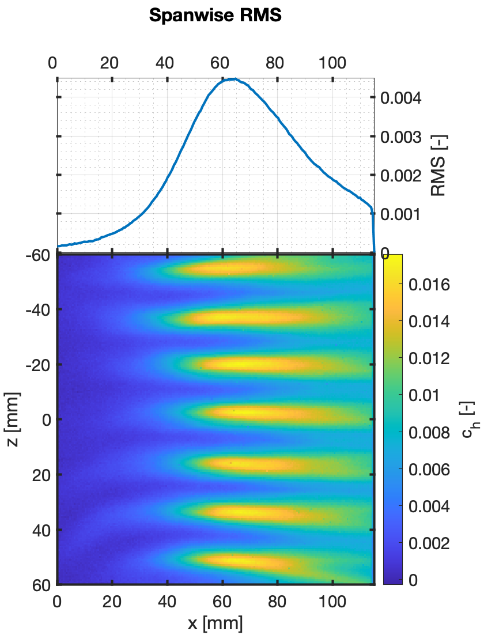

(a) $M_\infty = 7.5$; $Re = 9.2 \times 10^5$

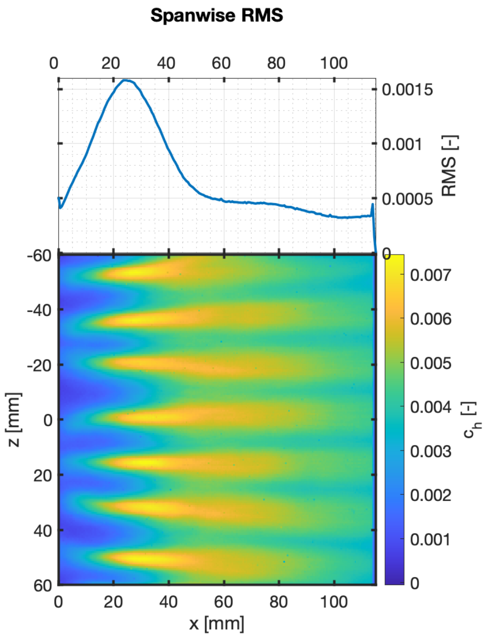

(b) $M_\infty = 7.5$; $Re = 46.3 \times 10^5$

Figure E.30: **Nondimensional roughness strip wavelength:** $\lambda_\delta = 4.5$

E.2.3. Ramp angle of 25°

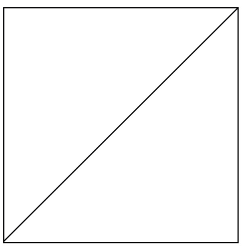

(a) $M_\infty = 7.5$; $Re = 9.2 \times 10^5$

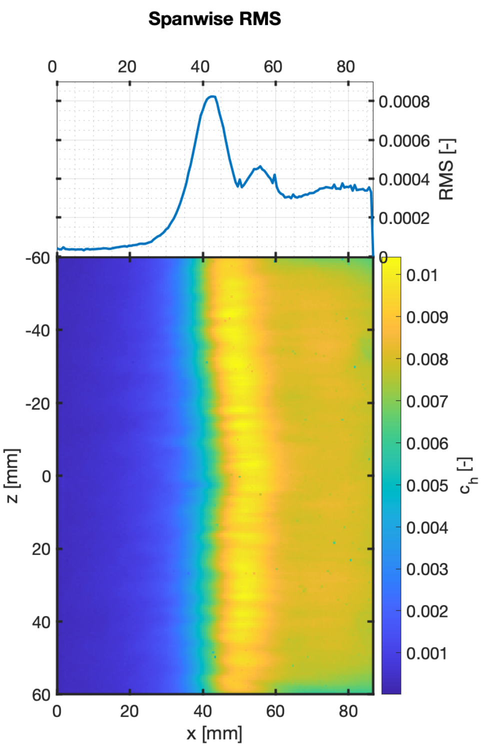

(b) $M_\infty = 7.5$; $Re = 46.3 \times 10^5$

Figure E.31: **No roughness strip.**

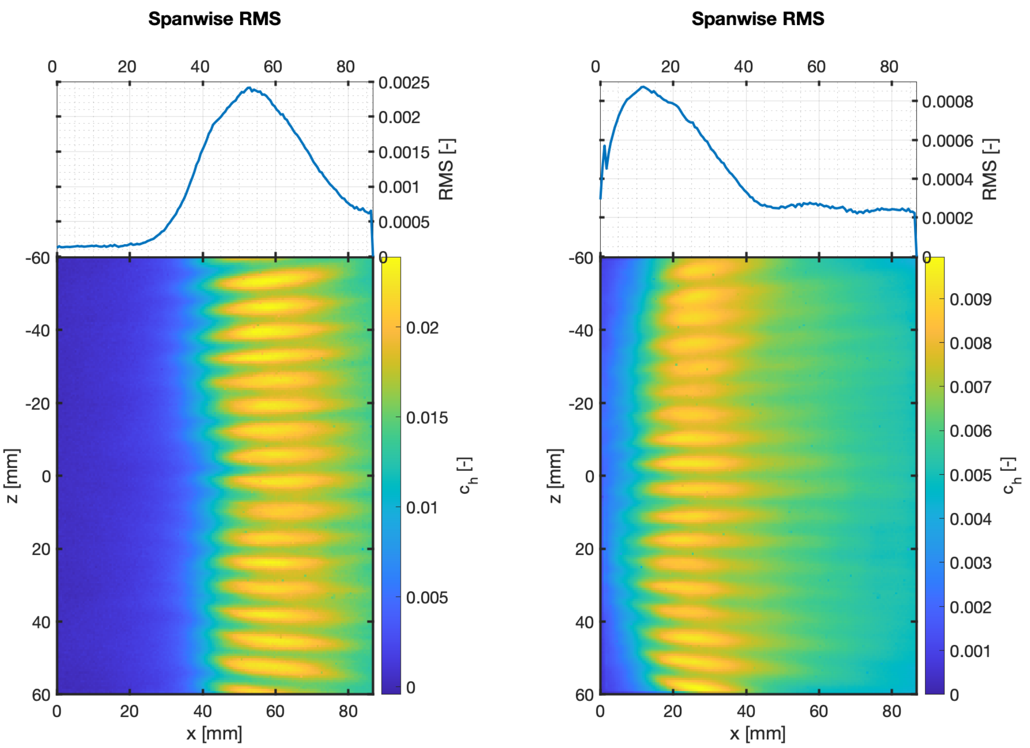

(a) $M_\infty = 7.5$; $Re = 9.2 \times 10^5$ (b) $M_\infty = 7.5$; $Re = 46.3 \times 10^5$

Figure E.32: **Nondimensional roughness strip wavelength:** $\lambda_\delta = 1.8$

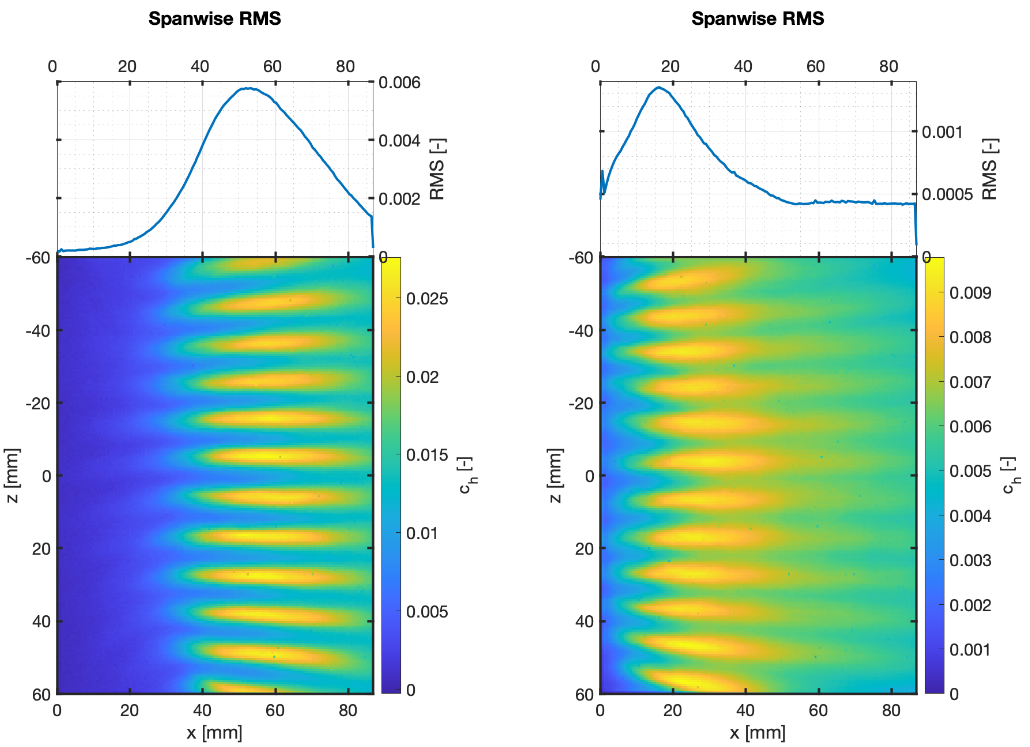

(a) $M_\infty = 7.5$; $Re = 9.2 \times 10^5$ (b) $M_\infty = 7.5$; $Re = 46.3 \times 10^5$

Figure E.33: **Nondimensional roughness strip wavelength:** $\lambda_\delta = 2.7$

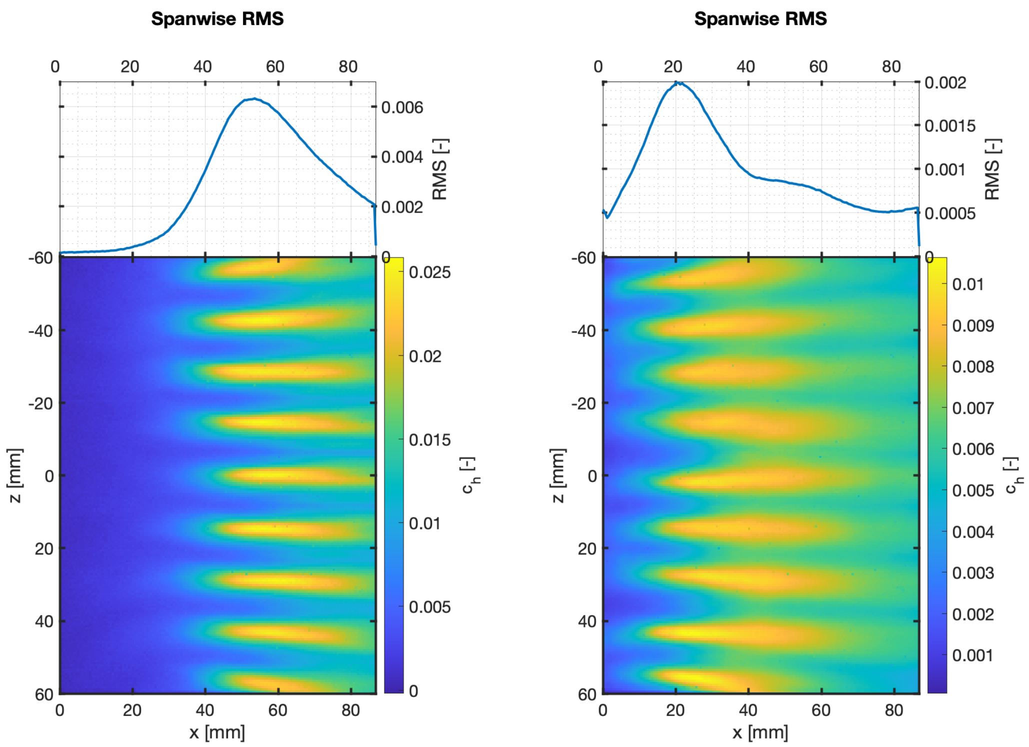

(a) $M_\infty = 7.5$; $Re = 9.2 \times 10^5$ (b) $M_\infty = 7.5$; $Re = 46.3 \times 10^5$

Figure E.34: **Nondimensional roughness strip wavelength:** $\lambda_\delta = 3.6$

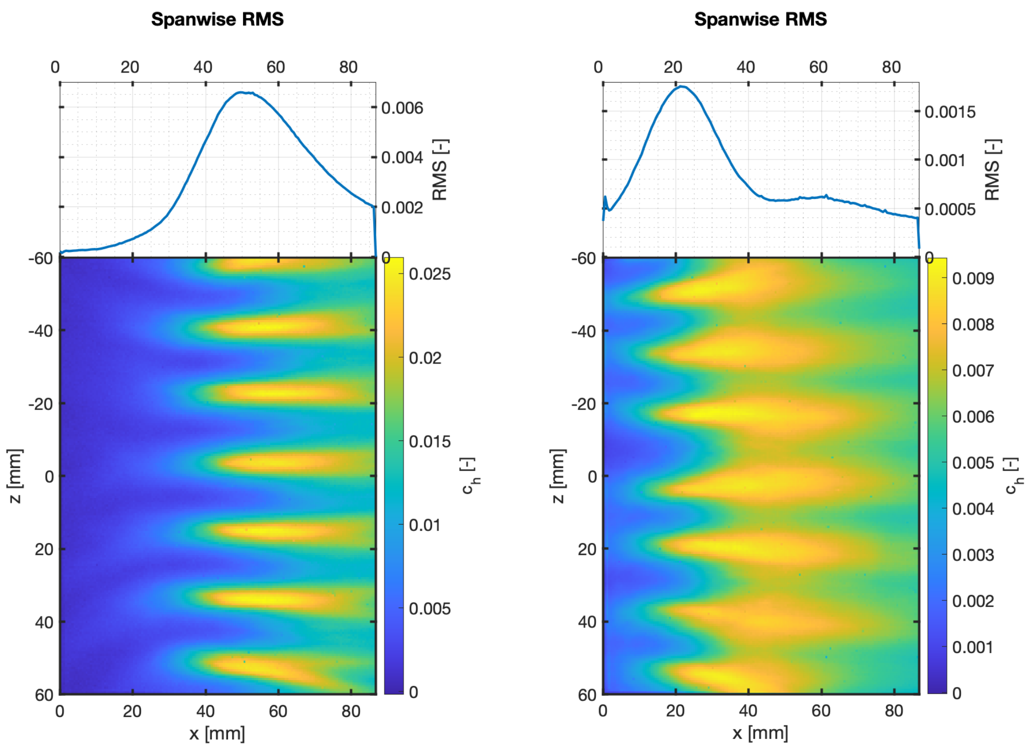

(a) $M_\infty = 7.5$; $Re = 9.2 \times 10^5$ (b) $M_\infty = 7.5$; $Re = 46.3 \times 10^5$

Figure E.35: **Nondimensional roughness strip wavelength:** $\lambda_\delta = 4.5$

E.2.4. Ramp angle of 30°

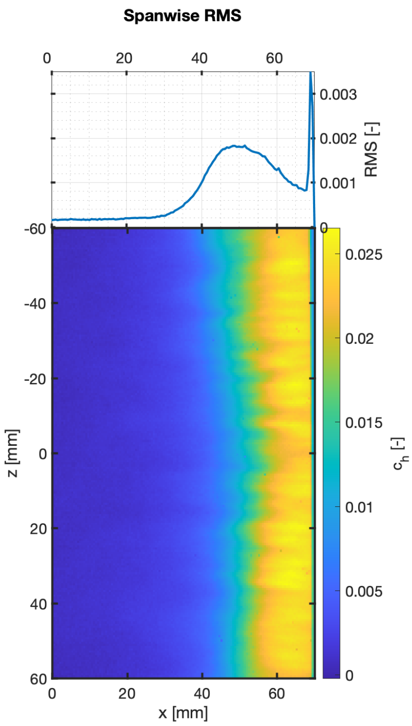

(a) $M_\infty = 7.5$; $Re = 9.2 \times 10^5$

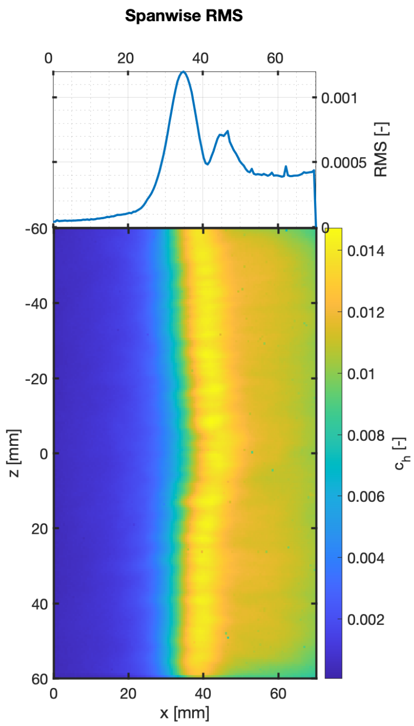

(b) $M_\infty = 7.5$; $Re = 46.3 \times 10^5$

Figure E.36: **No roughness strip.**

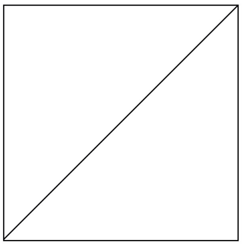

(a) $M_\infty = 7.5$; $Re = 9.2 \times 10^5$

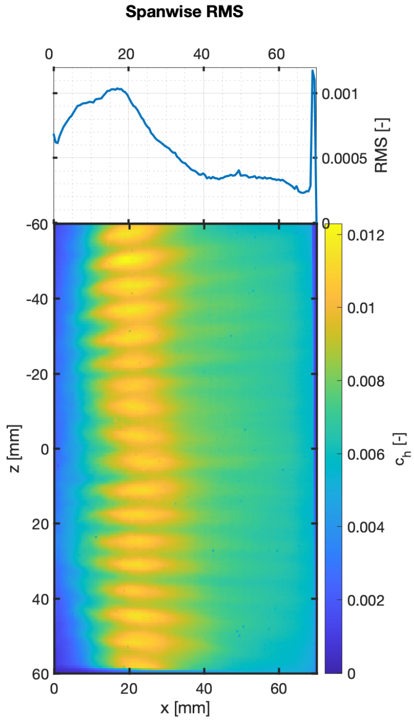

(b) $M_\infty = 7.5$; $Re = 46.3 \times 10^5$

Figure E.37: **Nondimensional roughness strip wavelength:** $\lambda_\delta = 1.8$

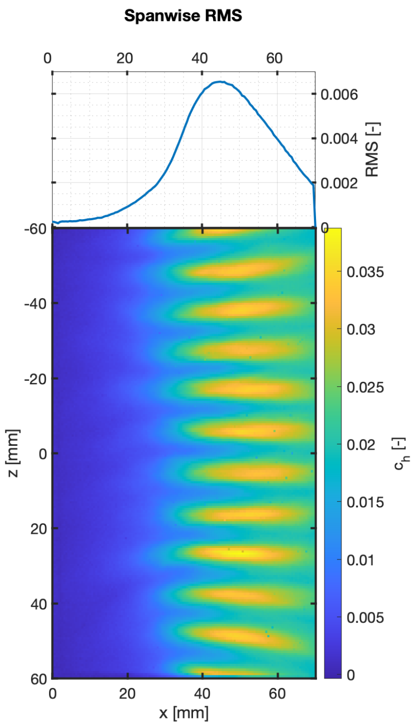

(a) $M_\infty = 7.5$; $Re = 9.2 \times 10^5$

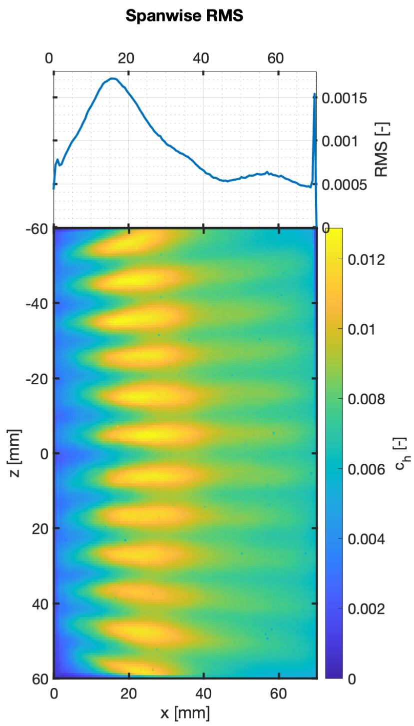

(b) $M_\infty = 7.5$; $Re = 46.3 \times 10^5$

Figure E.38: **Nondimensional roughness strip wavelength:** $\lambda_\delta = 2.7$

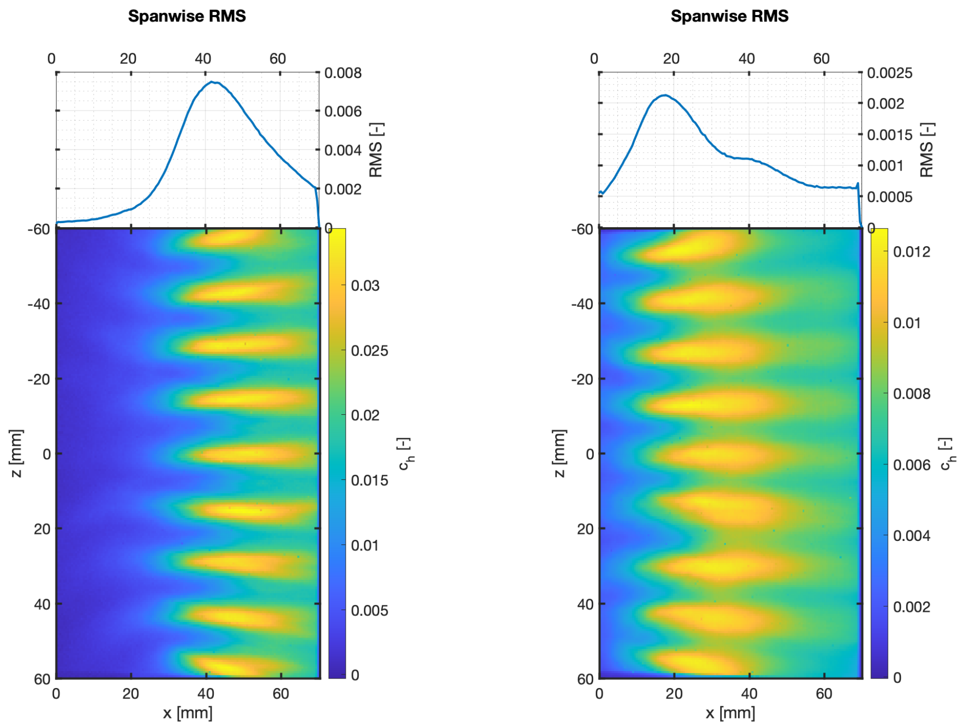

(a) $M_\infty = 7.5$; $Re = 9.2 \times 10^5$

(b) $M_\infty = 7.5$; $Re = 46.3 \times 10^5$

Figure E.39: **Nondimensional roughness strip wavelength:** $\lambda_\delta = 3.6$

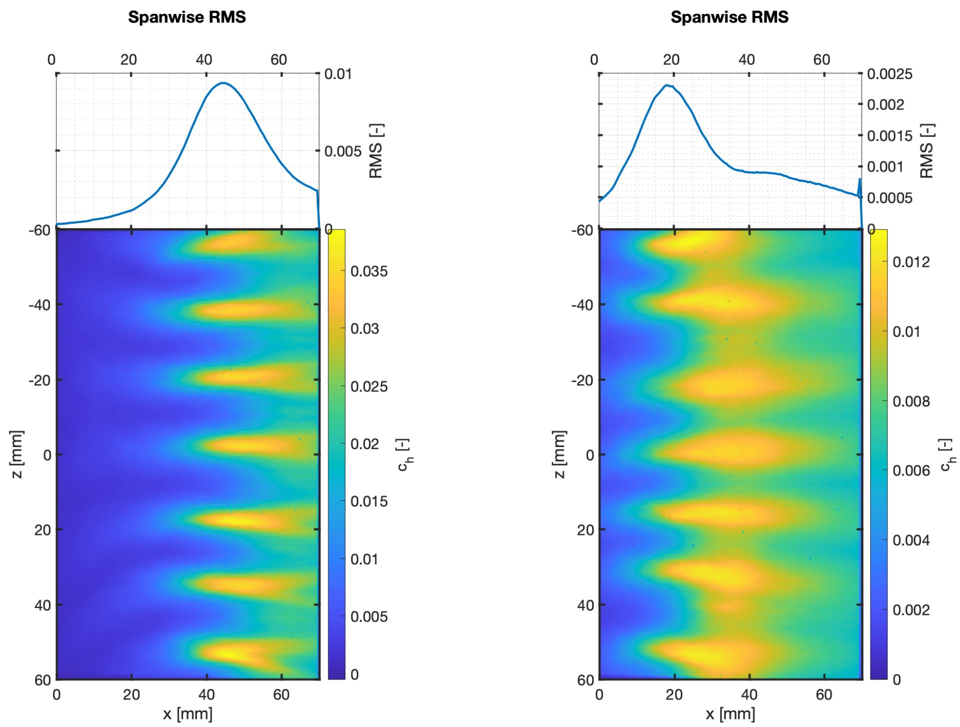

(a) $M_\infty = 7.5$; $Re = 9.2 \times 10^5$

(b) $M_\infty = 7.5$; $Re = 46.3 \times 10^5$

Figure E.40: **Nondimensional roughness strip wavelength:** $\lambda_\delta = 4.5$

F

QIRT Images: Image-Plot Comparison – Normal to Ramp Surface

The images adhere to the following specifications:

- Frame rate: $200\ Hz$
- Integration time: $250\ \mu s$
- Spatial resolution: $1.66\ px/mm$

F.1. Mean Results

F.1.1. Ramp angle of 15°

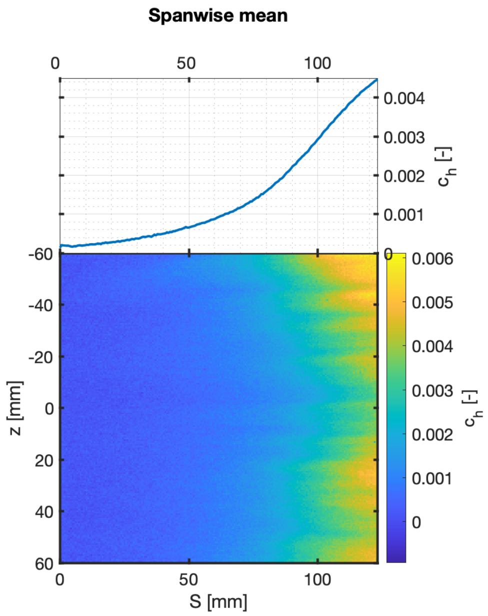

(a) $M_\infty = 7.5$; $Re = 9.2 \times 10^5$

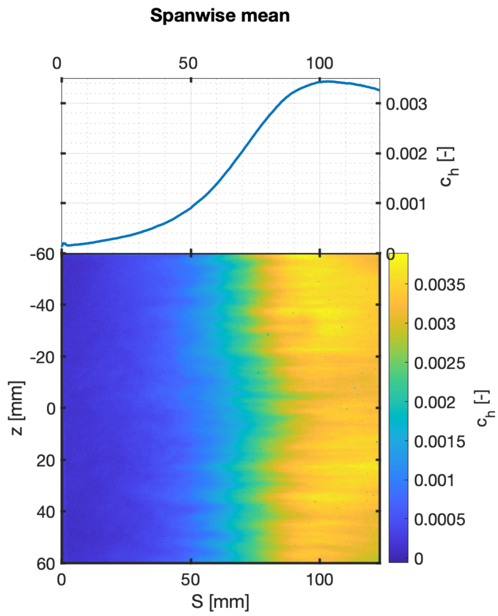

(b) $M_\infty = 7.5$; $Re = 46.3 \times 10^5$

Figure F.1: **No roughness strip.**

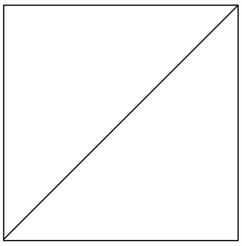

(a) $M_\infty = 7.5$; $Re = 9.2 \times 10^5$

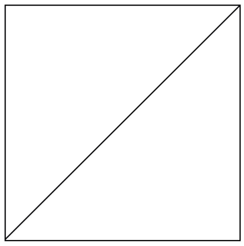

(b) $M_\infty = 7.5$; $Re = 46.3 \times 10^5$

Figure F.2: **Nondimensional roughness strip wavelength:** $\lambda_\delta = 1.8$

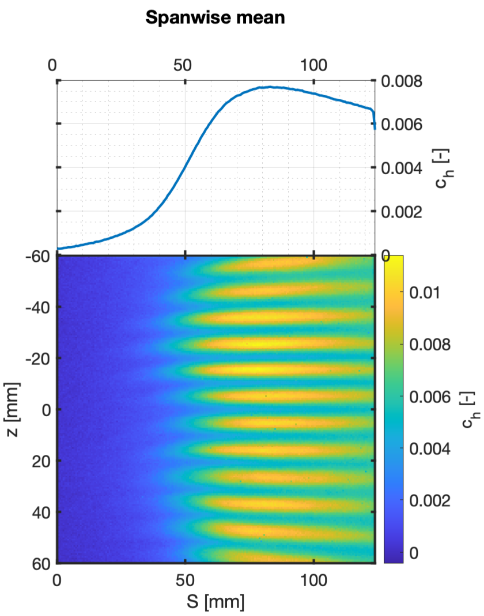

(a) $M_\infty = 7.5$; $Re = 9.2 \times 10^5$

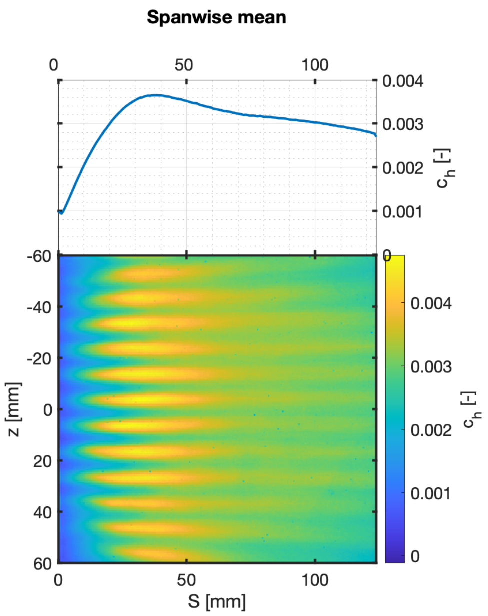

(b) $M_\infty = 7.5$; $Re = 46.3 \times 10^5$

Figure F.3: **Nondimensional roughness strip wavelength:** $\lambda_\delta = 2.7$

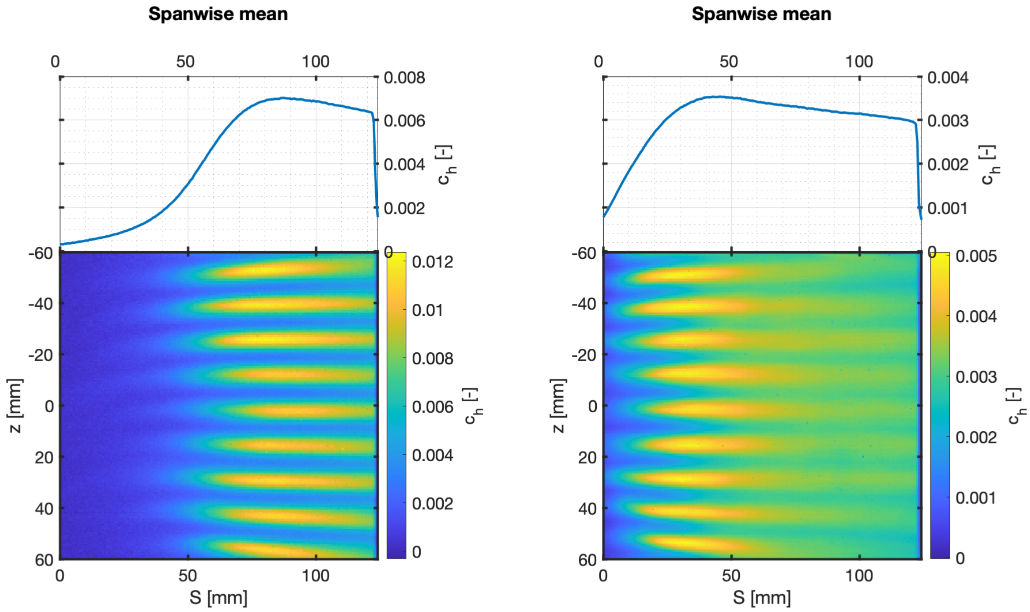

(a) $M_\infty = 7.5$; $Re = 9.2 \times 10^5$ (b) $M_\infty = 7.5$; $Re = 46.3 \times 10^5$

Figure F.4: **Nondimensional roughness strip wavelength:** $\lambda_\delta = 3.6$

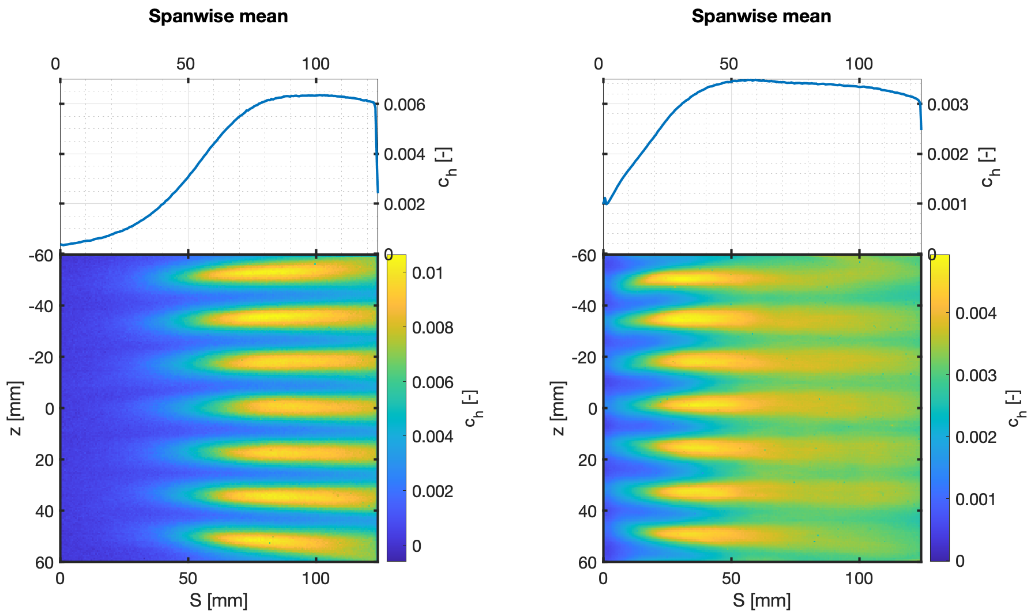

(a) $M_\infty = 7.5$; $Re = 9.2 \times 10^5$ (b) $M_\infty = 7.5$; $Re = 46.3 \times 10^5$

Figure F.5: **Nondimensional roughness strip wavelength:** $\lambda_\delta = 4.5$

F.1.2. Ramp angle of 20°

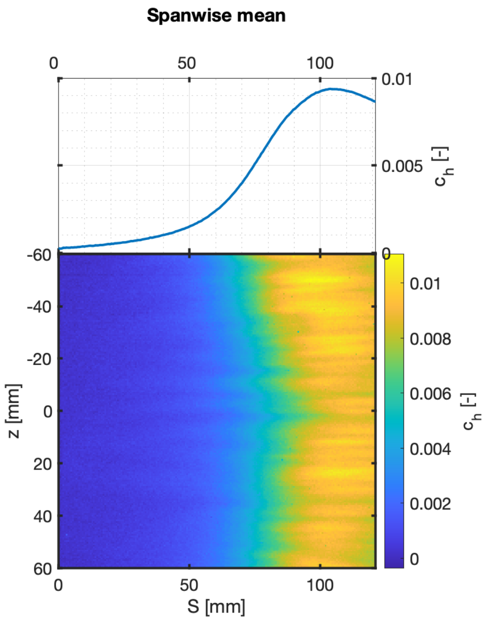

(a) $M_\infty = 7.5$; $Re = 9.2 \times 10^5$

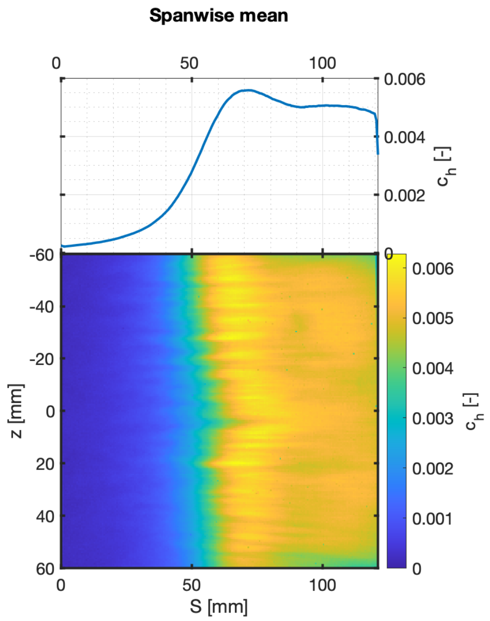

(b) $M_\infty = 7.5$; $Re = 46.3 \times 10^5$

Figure F.6: **No roughness strip.**

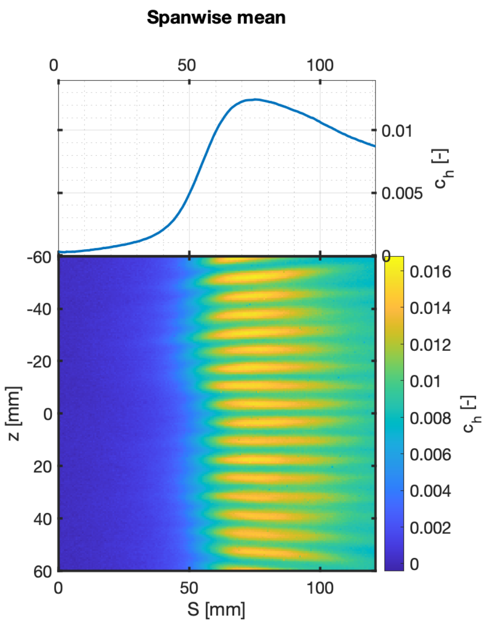

(a) $M_\infty = 7.5$; $Re = 9.2 \times 10^5$

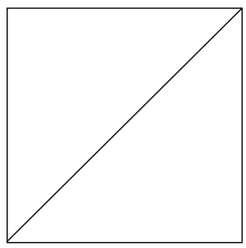

(b) $M_\infty = 7.5$; $Re = 46.3 \times 10^5$

Figure F.7: **Nondimensional roughness strip wavelength:** $\lambda_\delta = 1.8$

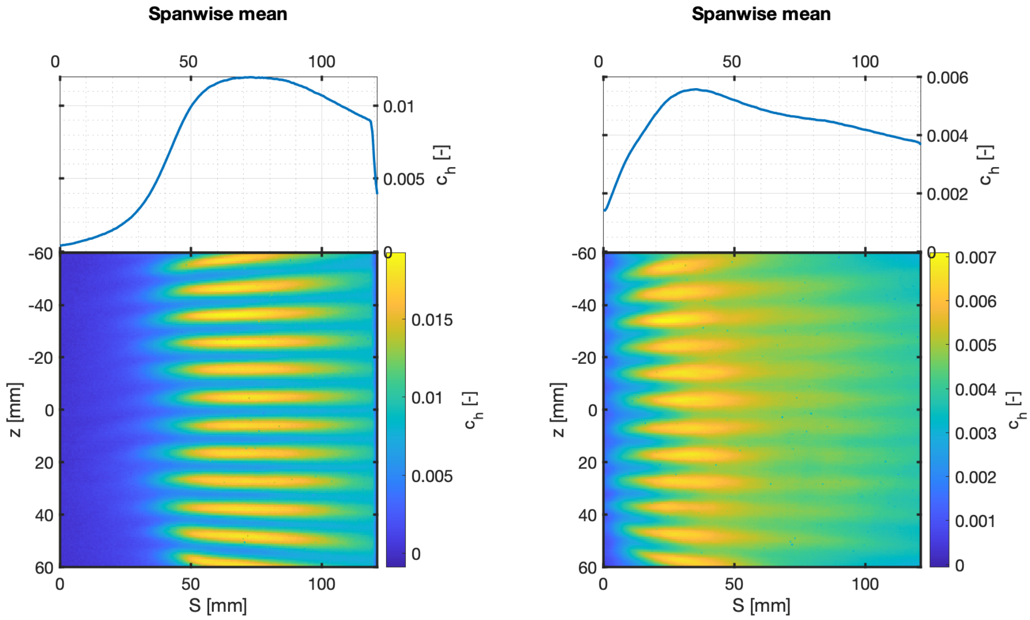

(a) $M_\infty = 7.5$; $Re = 9.2 \times 10^5$ (b) $M_\infty = 7.5$; $Re = 46.3 \times 10^5$

Figure F.8: **Nondimensional roughness strip wavelength:** $\lambda_\delta = 2.7$

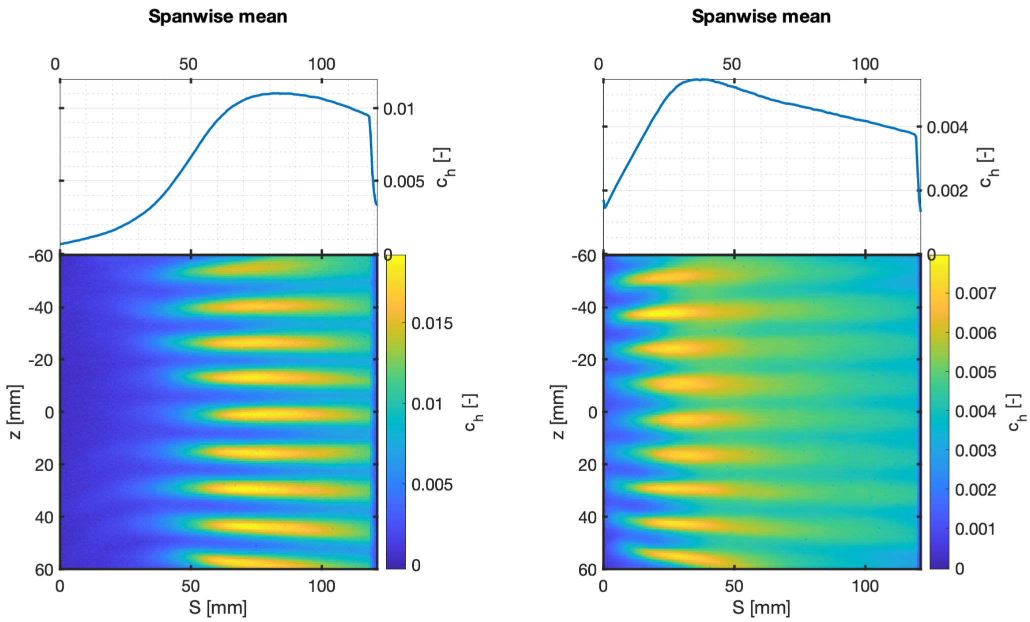

(a) $M_\infty = 7.5$; $Re = 9.2 \times 10^5$ (b) $M_\infty = 7.5$; $Re = 46.3 \times 10^5$

Figure F.9: **Nondimensional roughness strip wavelength:** $\lambda_\delta = 3.6$

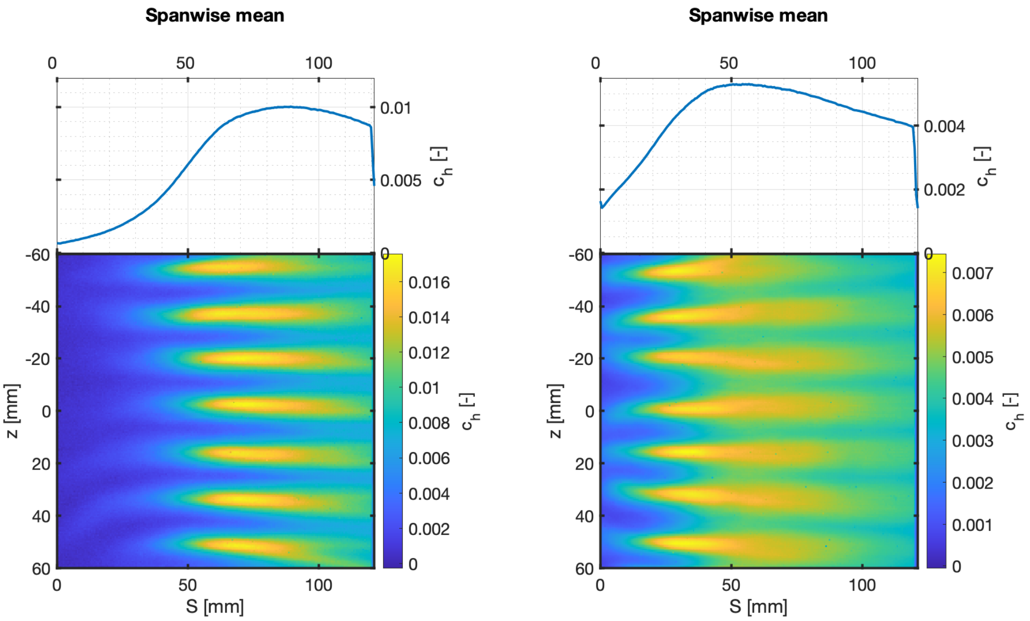

(a) $M_\infty = 7.5$; $Re = 9.2 \times 10^5$

(b) $M_\infty = 7.5$; $Re = 46.3 \times 10^5$

Figure F.10: **Nondimensional roughness strip wavelength:** $\lambda_\delta = 4.5$

F.1.3. Ramp angle of $25°$

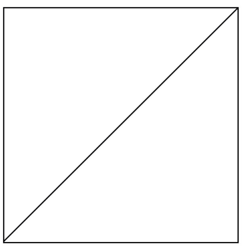

(a) $M_\infty = 7.5$; $Re = 9.2 \times 10^5$

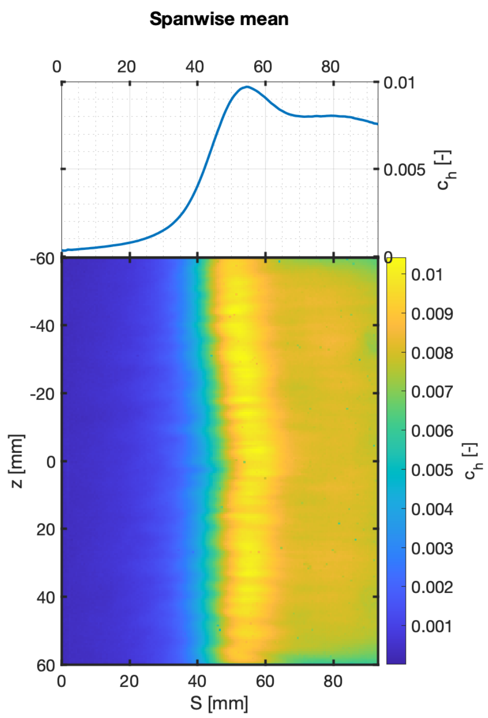

(b) $M_\infty = 7.5$; $Re = 46.3 \times 10^5$

Figure F.11: **No roughness strip.**

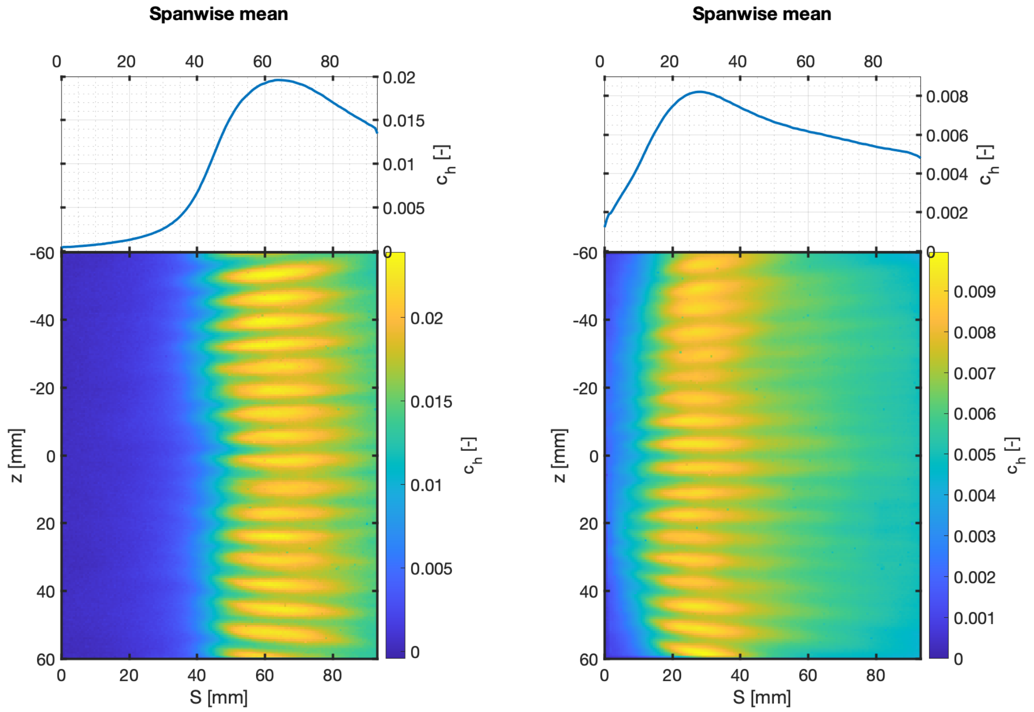

(a) $M_\infty = 7.5$; $Re = 9.2 \times 10^5$ (b) $M_\infty = 7.5$; $Re = 46.3 \times 10^5$

Figure F.12: **Nondimensional roughness strip wavelength:** $\lambda_\delta = 1.8$

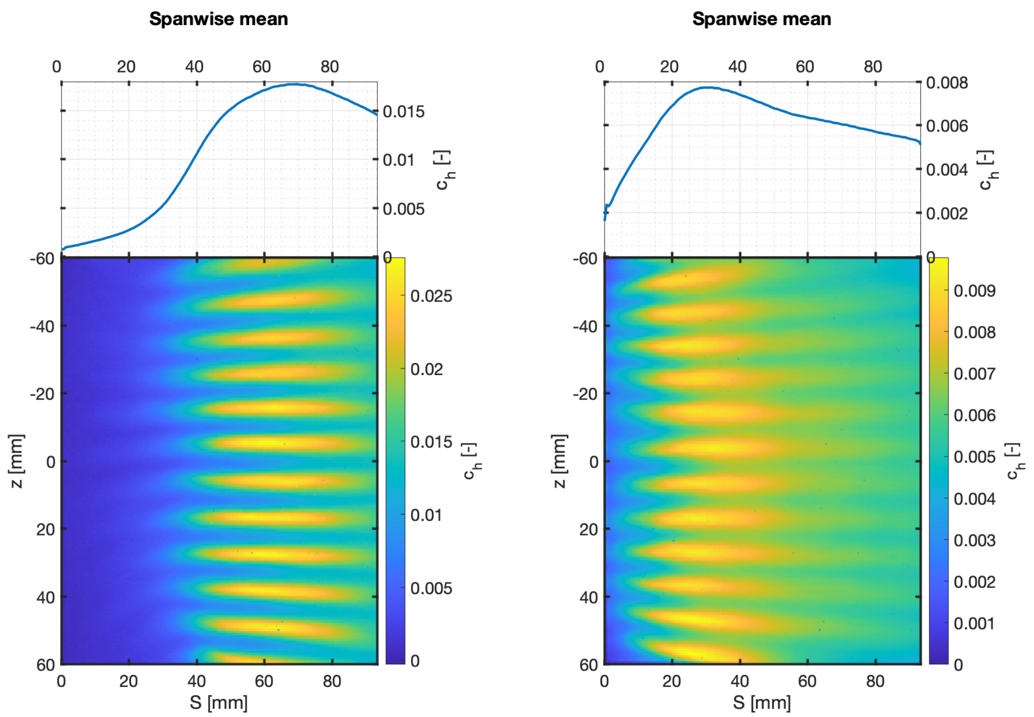

(a) $M_\infty = 7.5$; $Re = 9.2 \times 10^5$ (b) $M_\infty = 7.5$; $Re = 46.3 \times 10^5$

Figure F.13: **Nondimensional roughness strip wavelength:** $\lambda_\delta = 2.7$

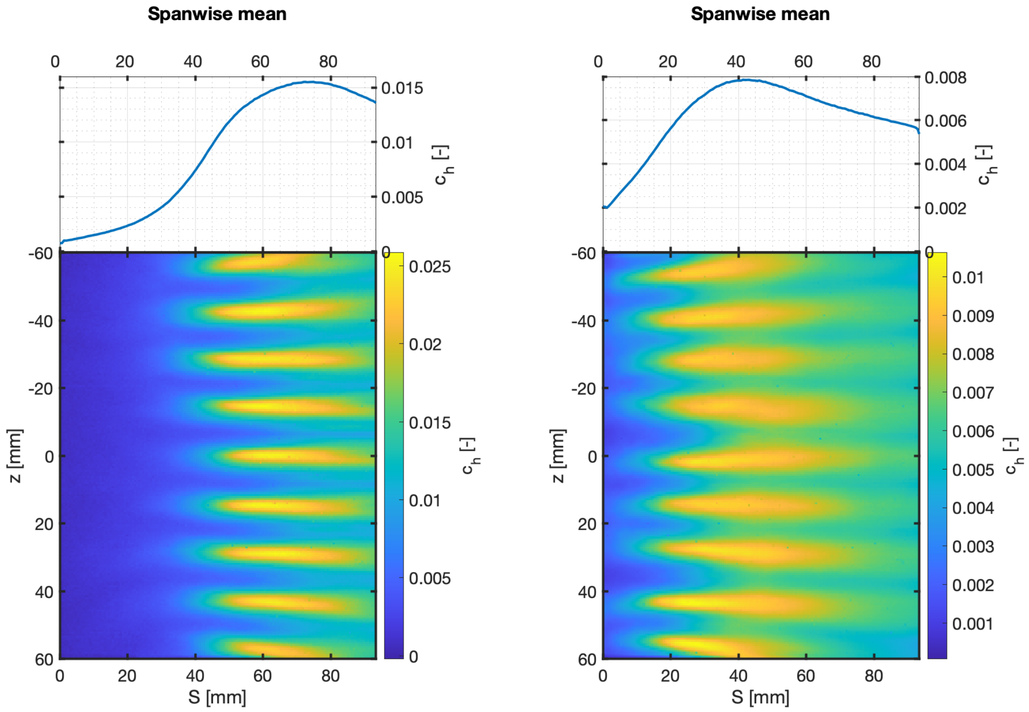

(a) $M_\infty = 7.5$; $Re = 9.2 \times 10^5$ (b) $M_\infty = 7.5$; $Re = 46.3 \times 10^5$

Figure F.14: **Nondimensional roughness strip wavelength:** $\lambda_\delta = 3.6$

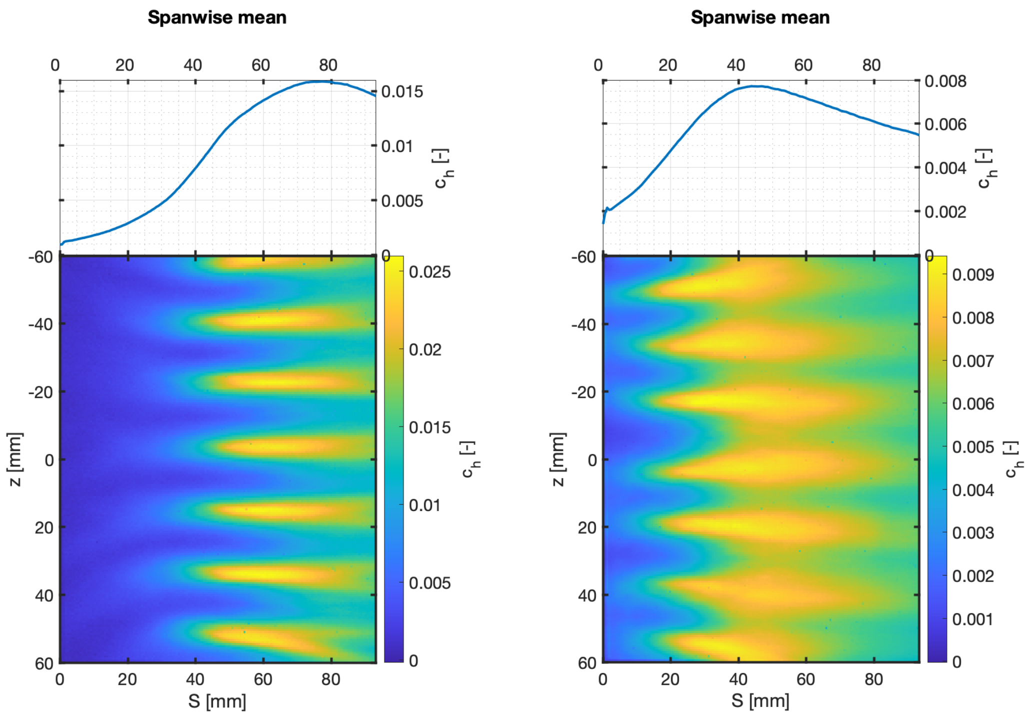

(a) $M_\infty = 7.5$; $Re = 9.2 \times 10^5$ (b) $M_\infty = 7.5$; $Re = 46.3 \times 10^5$

Figure F.15: **Nondimensional roughness strip wavelength:** $\lambda_\delta = 4.5$

F.1.4. Ramp angle of 30°

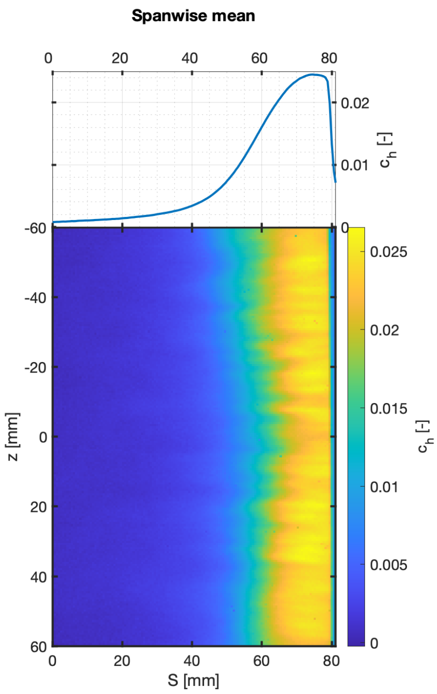

(a) $M_\infty = 7.5$; $Re = 9.2 \times 10^5$

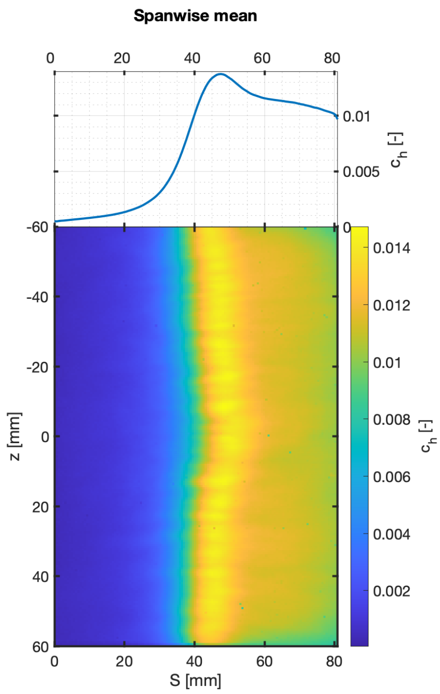

(b) $M_\infty = 7.5$; $Re = 46.3 \times 10^5$

Figure F.16: **No roughness strip.**

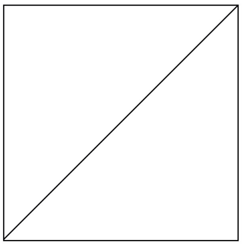

(a) $M_\infty = 7.5$; $Re = 9.2 \times 10^5$

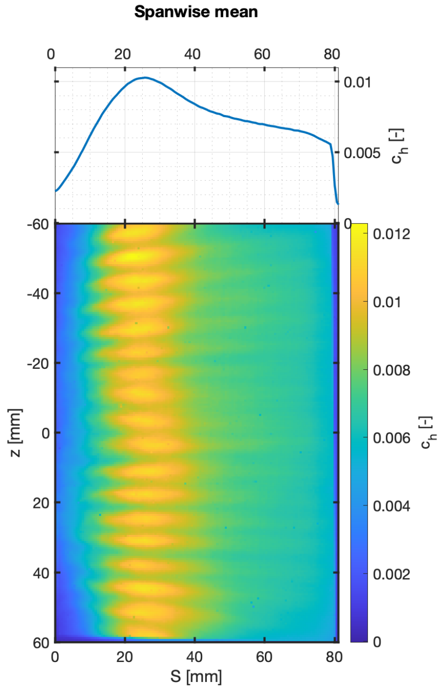

(b) $M_\infty = 7.5$; $Re = 46.3 \times 10^5$

Figure F.17: **Nondimensional roughness strip wavelength:** $\lambda_\delta = 1.8$

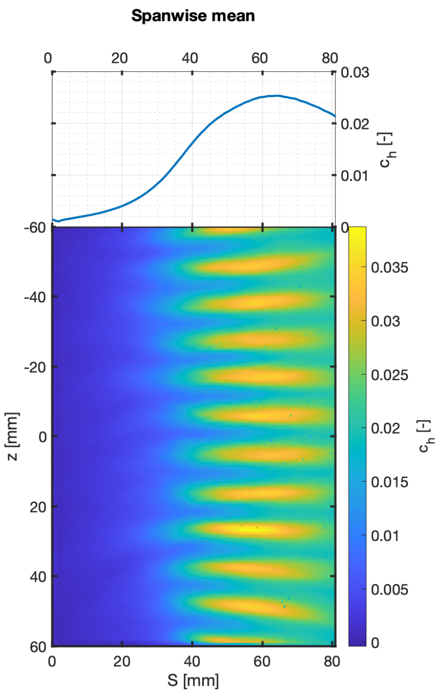

(a) $M_\infty = 7.5$; $Re = 9.2 \times 10^5$

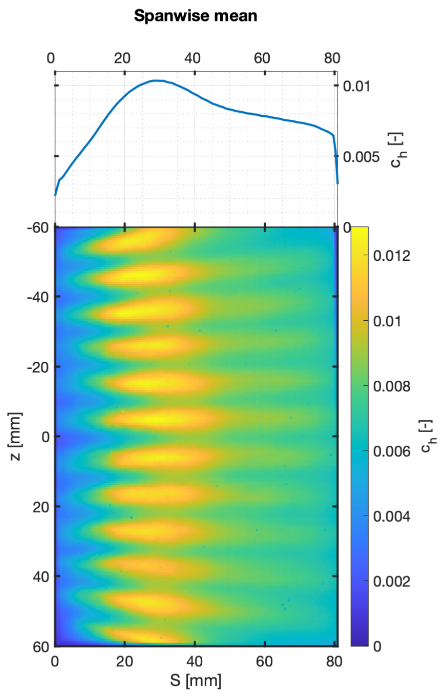

(b) $M_\infty = 7.5$; $Re = 46.3 \times 10^5$

Figure F.18: **Nondimensional roughness strip wavelength:** $\lambda_\delta = 2.7$

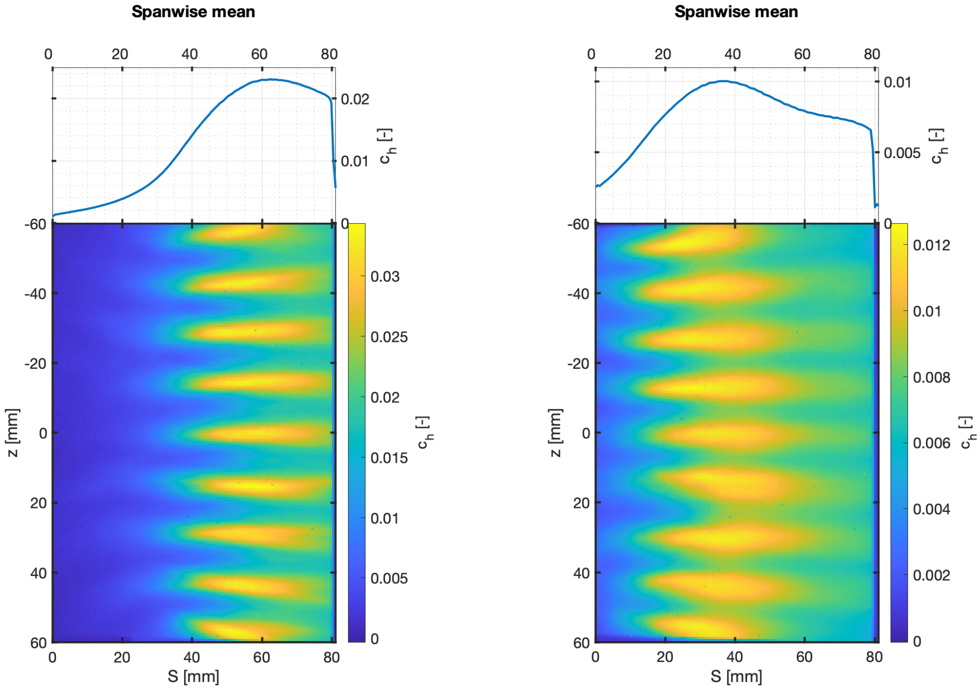

(a) $M_\infty = 7.5$; $Re = 9.2 \times 10^5$ (b) $M_\infty = 7.5$; $Re = 46.3 \times 10^5$

Figure F.19: **Nondimensional roughness strip wavelength:** $\lambda_\delta = 3.6$

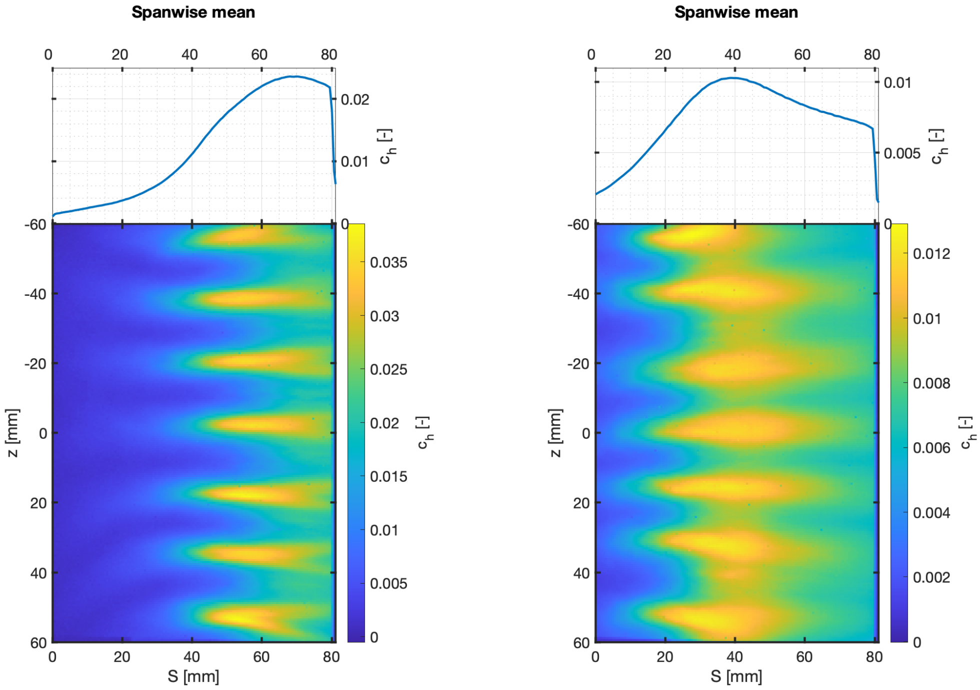

(a) $M_\infty = 7.5$; $Re = 9.2 \times 10^5$ (b) $M_\infty = 7.5$; $Re = 46.3 \times 10^5$

Figure F.20: **Nondimensional roughness strip wavelength:** $\lambda_\delta = 4.5$

F.2. RMS Results

F.2.1. Ramp angle of 15°

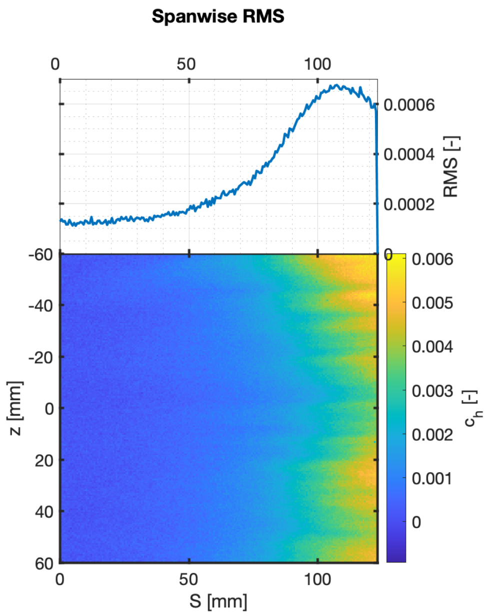

(a) $M_\infty = 7.5$; $Re = 9.2 \times 10^5$

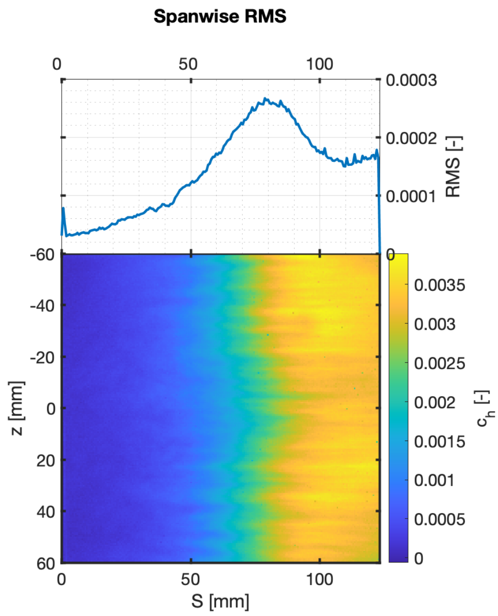

(b) $M_\infty = 7.5$; $Re = 46.3 \times 10^5$

Figure F.21: **No roughness strip.**

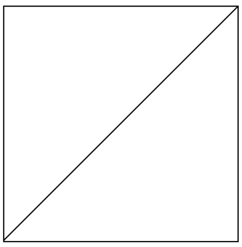

(a) $M_\infty = 7.5$; $Re = 9.2 \times 10^5$

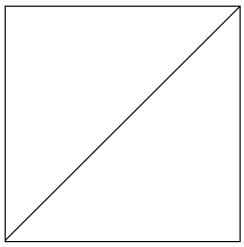

(b) $M_\infty = 7.5$; $Re = 46.3 \times 10^5$

Figure F.22: **Nondimensional roughness strip wavelength:** $\lambda_\delta = 1.8$

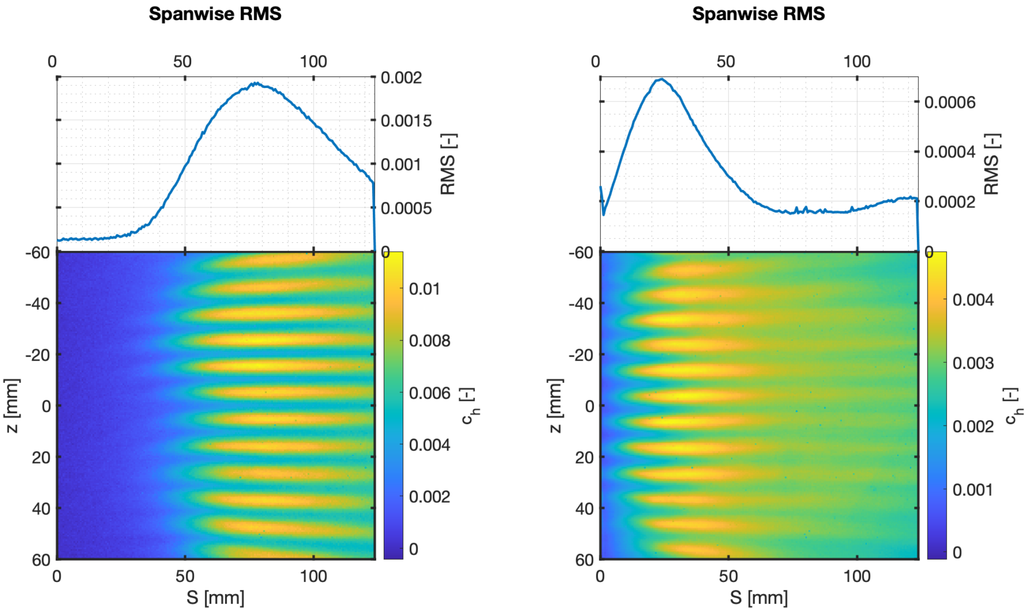

(a) $M_\infty = 7.5$; $Re = 9.2 \times 10^5$

(b) $M_\infty = 7.5$; $Re = 46.3 \times 10^5$

Figure F.23: **Nondimensional roughness strip wavelength:** $\lambda_\delta = 2.7$

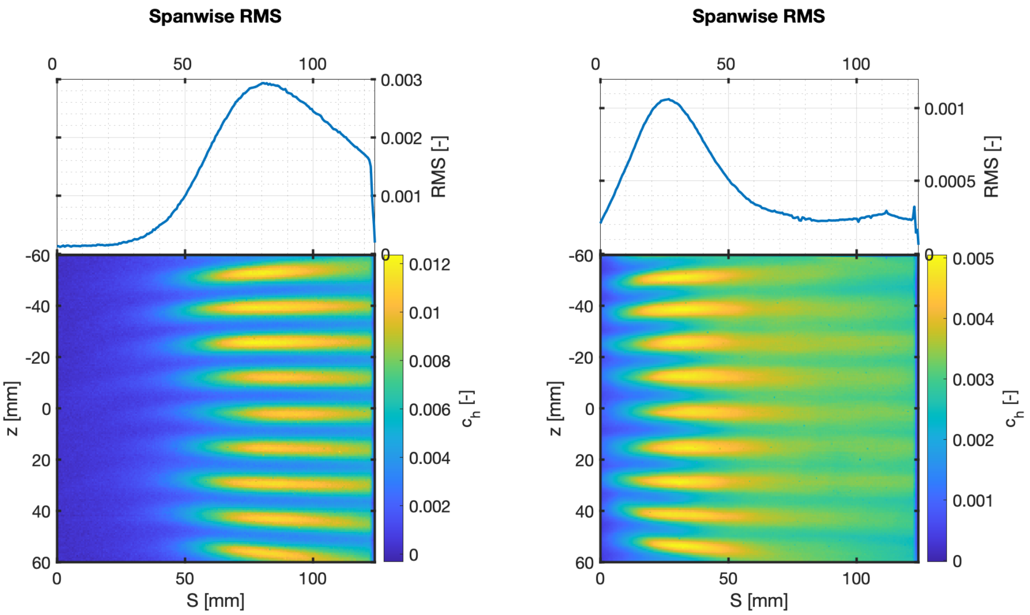

(a) $M_\infty = 7.5$; $Re = 9.2 \times 10^5$

(b) $M_\infty = 7.5$; $Re = 46.3 \times 10^5$

Figure F.24: **Nondimensional roughness strip wavelength:** $\lambda_\delta = 3.6$

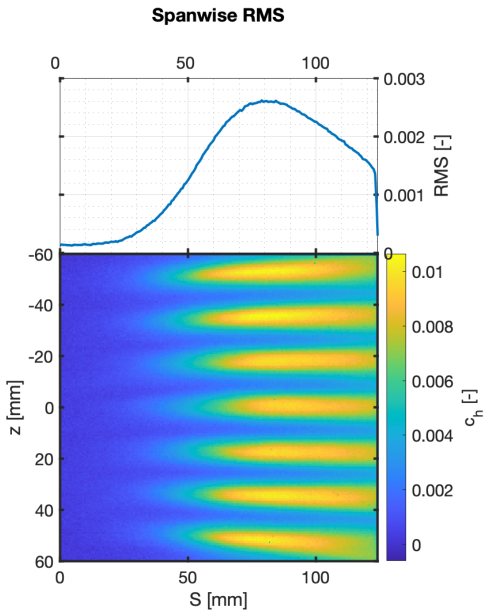

(a) $M_\infty = 7.5$; $Re = 9.2 \times 10^5$

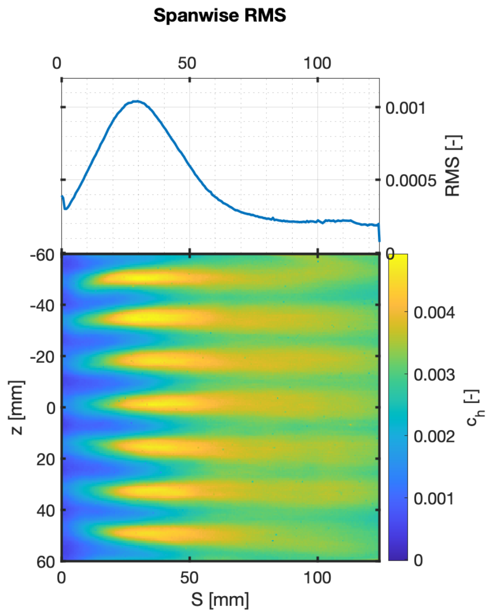

(b) $M_\infty = 7.5$; $Re = 46.3 \times 10^5$

Figure F.25: **Nondimensional roughness strip wavelength:** $\lambda_\delta = 4.5$

F.2.2. Ramp angle of 20°

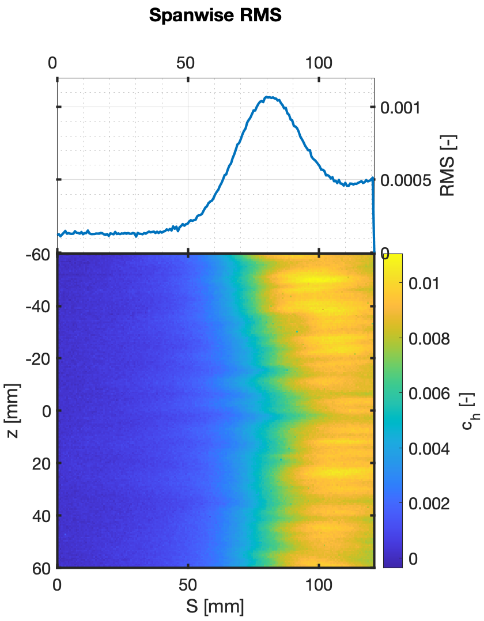

(a) $M_\infty = 7.5$; $Re = 9.2 \times 10^5$

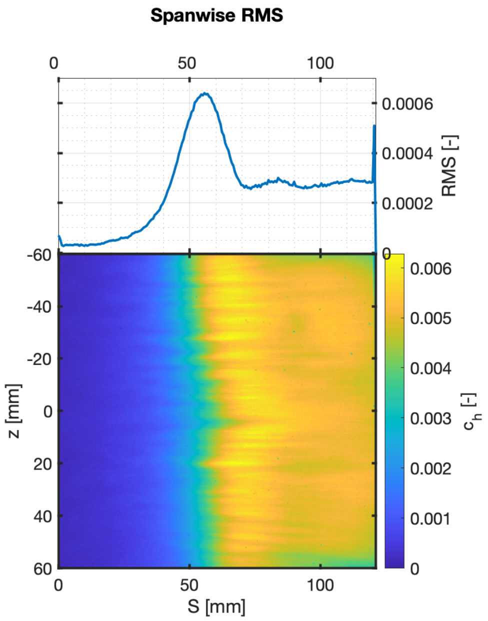

(b) $M_\infty = 7.5$; $Re = 46.3 \times 10^5$

Figure F.26: **No roughness strip.**

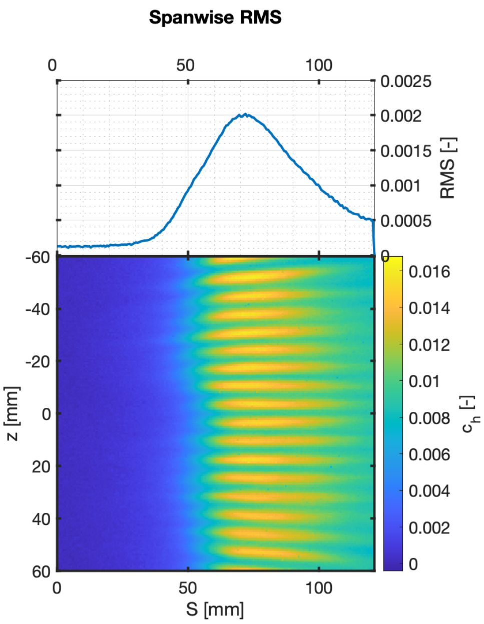

(a) $M_\infty = 7.5$; $Re = 9.2 \times 10^5$

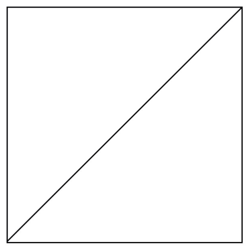

(b) $M_\infty = 7.5$; $Re = 46.3 \times 10^5$

Figure F.27: **Nondimensional roughness strip wavelength:** $\lambda_\delta = 1.8$

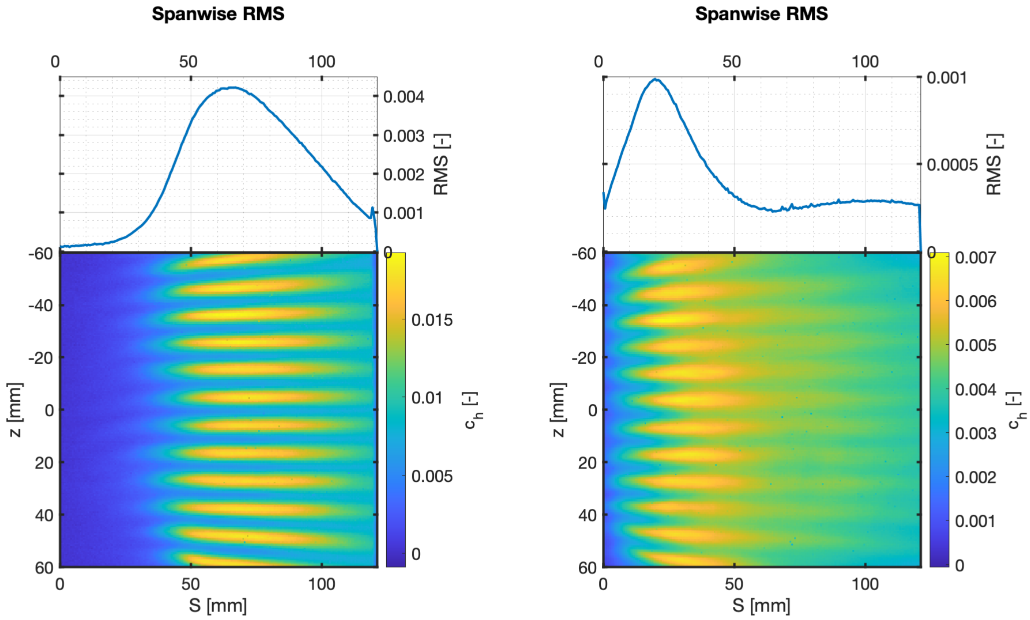

(a) $M_\infty = 7.5$; $Re = 9.2 \times 10^5$

(b) $M_\infty = 7.5$; $Re = 46.3 \times 10^5$

Figure F.28: **Nondimensional roughness strip wavelength:** $\lambda_\delta = 2.7$

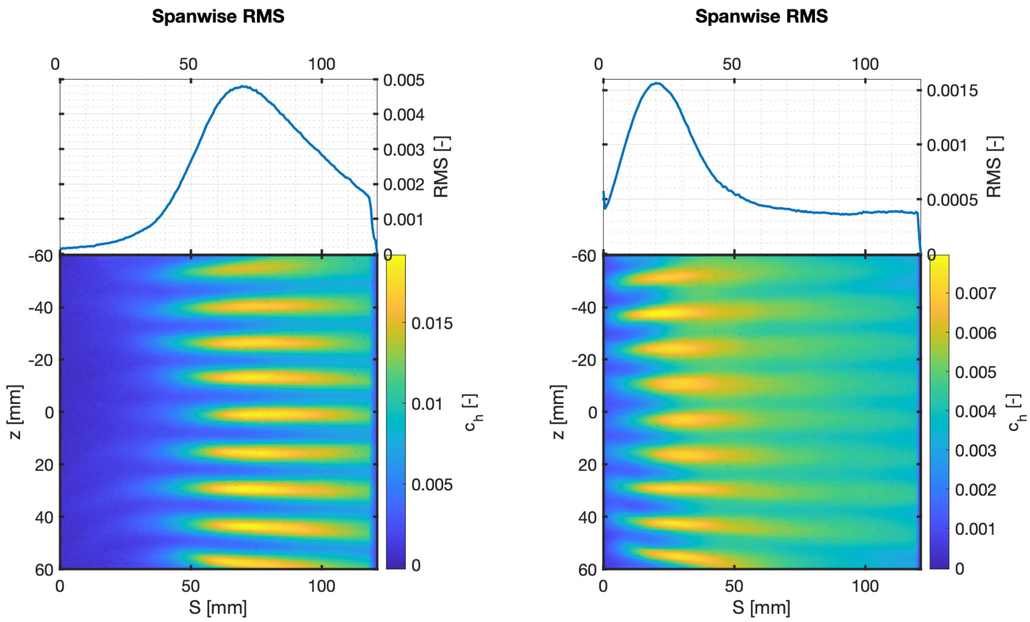

(a) $M_\infty = 7.5$; $Re = 9.2 \times 10^5$

(b) $M_\infty = 7.5$; $Re = 46.3 \times 10^5$

Figure F.29: **Nondimensional roughness strip wavelength:** $\lambda_\delta = 3.6$

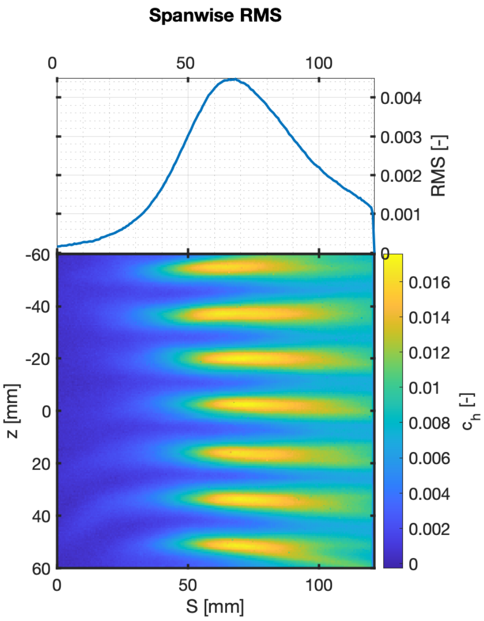

(a) $M_\infty = 7.5$; $Re = 9.2 \times 10^5$

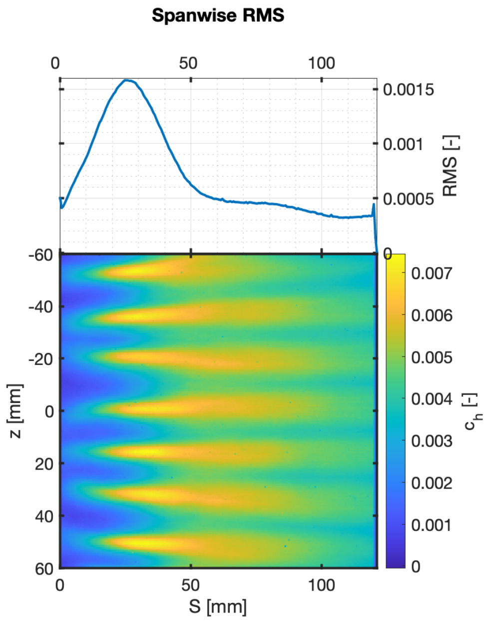

(b) $M_\infty = 7.5$; $Re = 46.3 \times 10^5$

Figure F.30: **Nondimensional roughness strip wavelength:** $\lambda_\delta = 4.5$

F.2.3. Ramp angle of $25°$

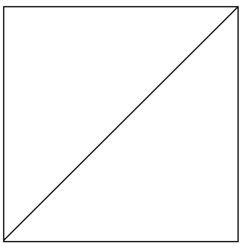

(a) $M_\infty = 7.5$; $Re = 9.2 \times 10^5$

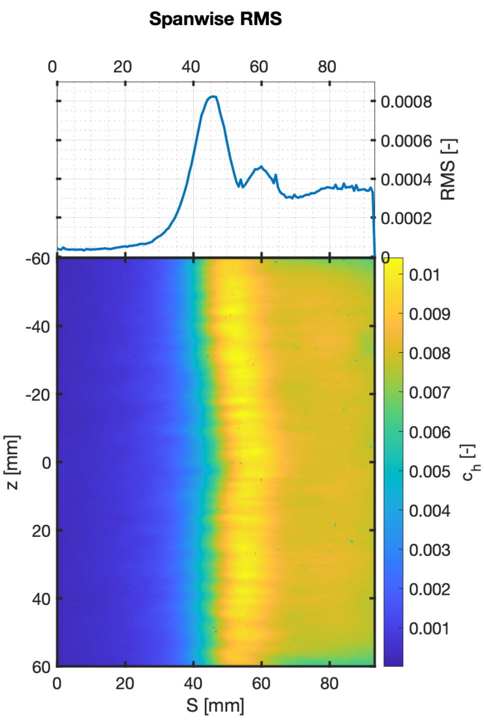

(b) $M_\infty = 7.5$; $Re = 46.3 \times 10^5$

Figure F.31: **No roughness strip.**

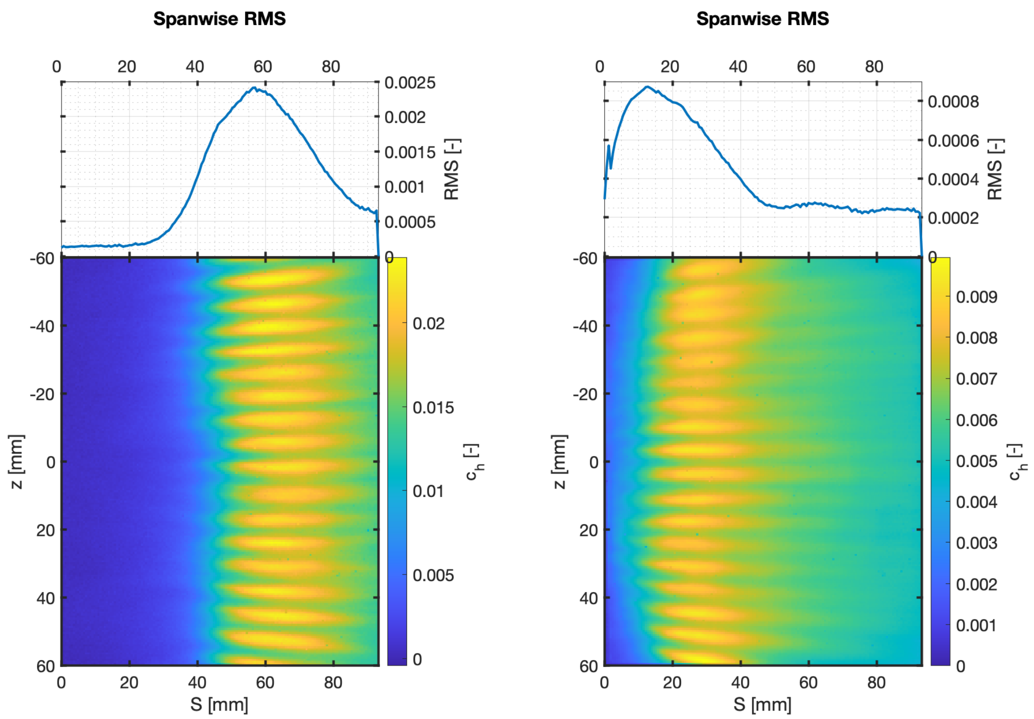

(a) $M_\infty = 7.5$; $Re = 9.2 \times 10^5$ (b) $M_\infty = 7.5$; $Re = 46.3 \times 10^5$

Figure F.32: **Nondimensional roughness strip wavelength:** $\lambda_\delta = 1.8$

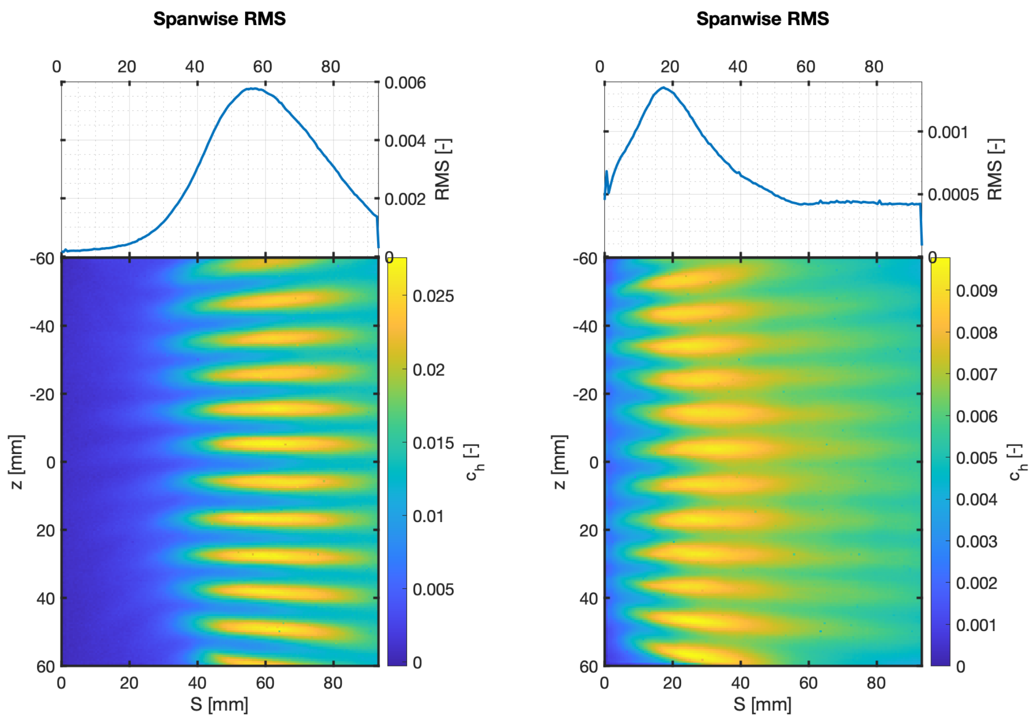

(a) $M_\infty = 7.5$; $Re = 9.2 \times 10^5$ (b) $M_\infty = 7.5$; $Re = 46.3 \times 10^5$

Figure F.33: **Nondimensional roughness strip wavelength:** $\lambda_\delta = 2.7$

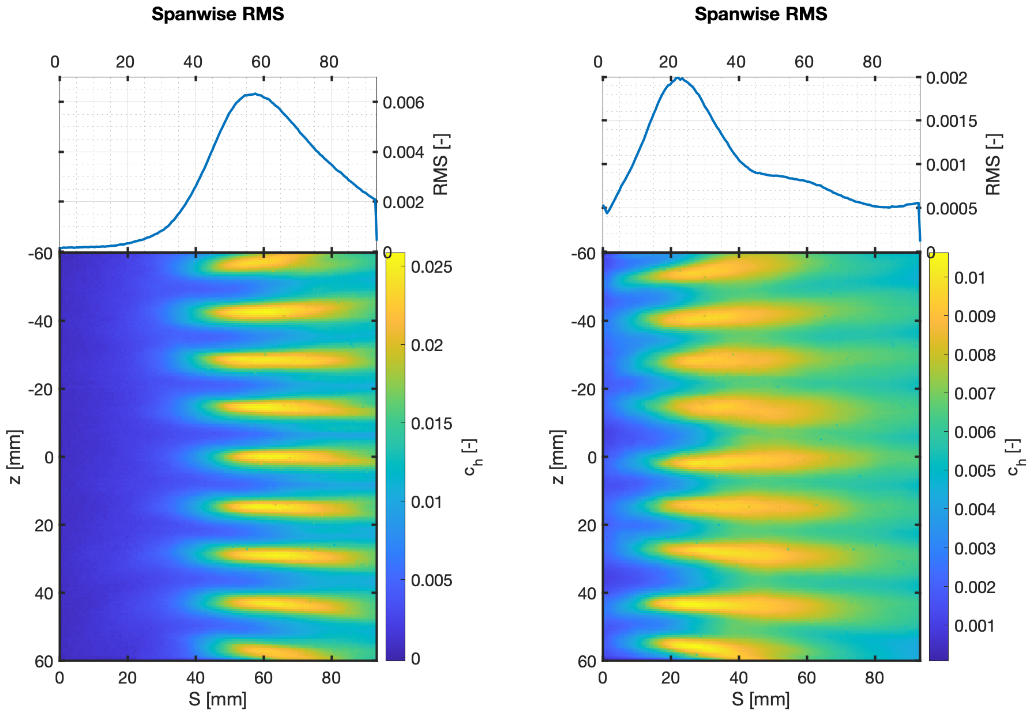

(a) $M_\infty = 7.5$; $Re = 9.2 \times 10^5$

(b) $M_\infty = 7.5$; $Re = 46.3 \times 10^5$

Figure F.34: **Nondimensional roughness strip wavelength:** $\lambda_\delta = 3.6$

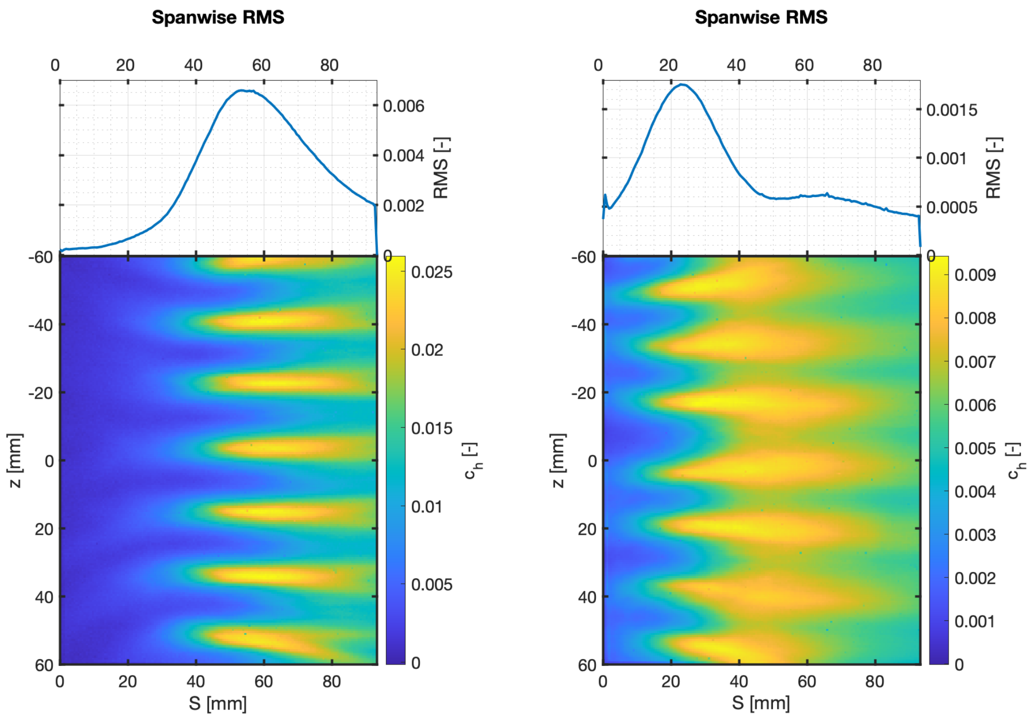

(a) $M_\infty = 7.5$; $Re = 9.2 \times 10^5$

(b) $M_\infty = 7.5$; $Re = 46.3 \times 10^5$

Figure F.35: **Nondimensional roughness strip wavelength:** $\lambda_\delta = 4.5$

F.2.4. Ramp angle of 30°

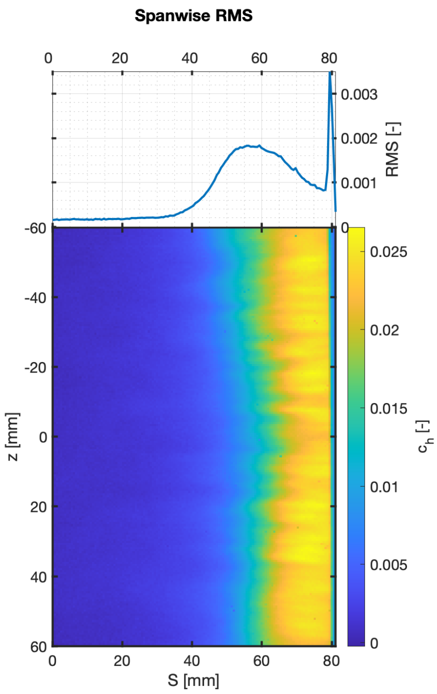

(a) $M_\infty = 7.5$; $Re = 9.2 \times 10^5$

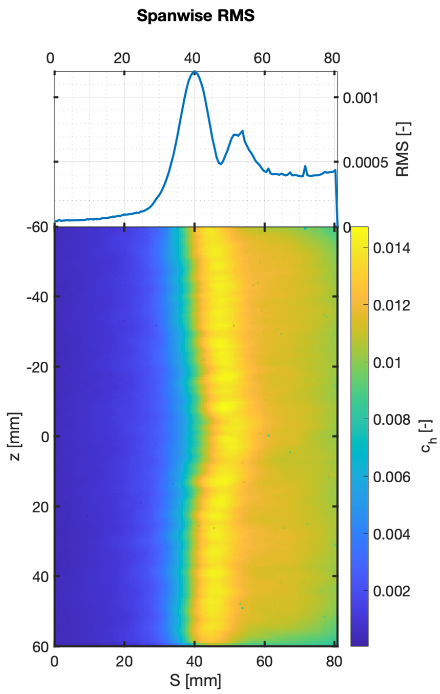

(b) $M_\infty = 7.5$; $Re = 46.3 \times 10^5$

Figure F.36: **No roughness strip.**

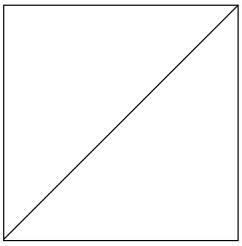

(a) $M_\infty = 7.5$; $Re = 9.2 \times 10^5$

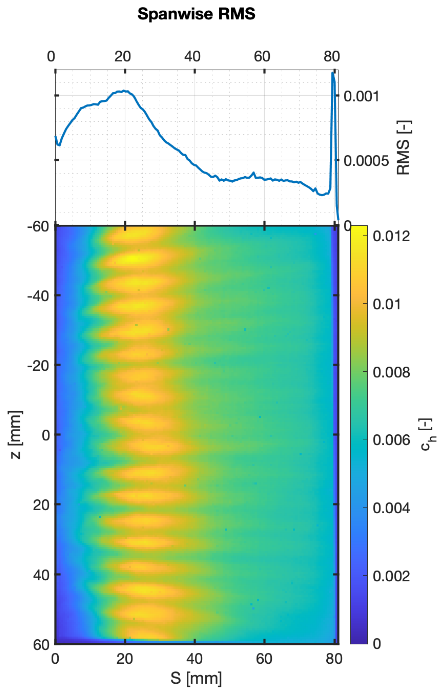

(b) $M_\infty = 7.5$; $Re = 46.3 \times 10^5$

Figure F.37: **Nondimensional roughness strip wavelength:** $\lambda_\delta = 1.8$

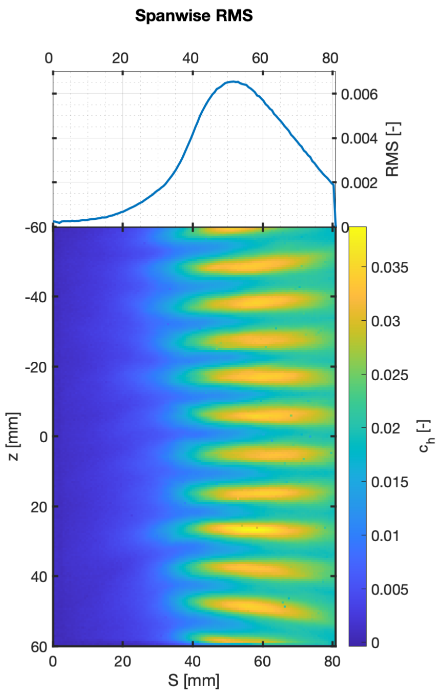

(a) $M_\infty = 7.5$; $Re = 9.2 \times 10^5$

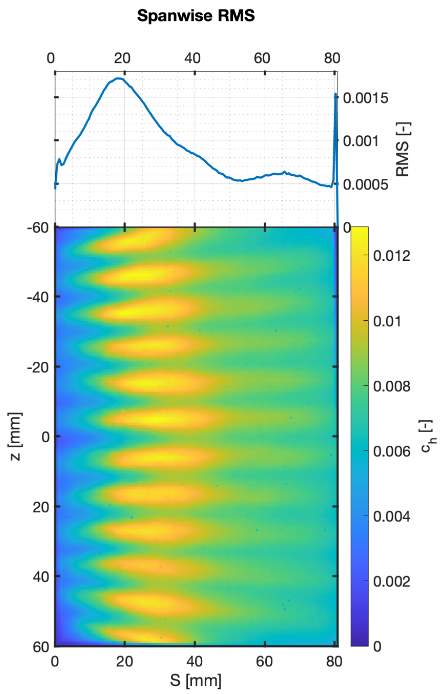

(b) $M_\infty = 7.5$; $Re = 46.3 \times 10^5$

Figure F.38: **Nondimensional roughness strip wavelength:** $\lambda_\delta = 2.7$

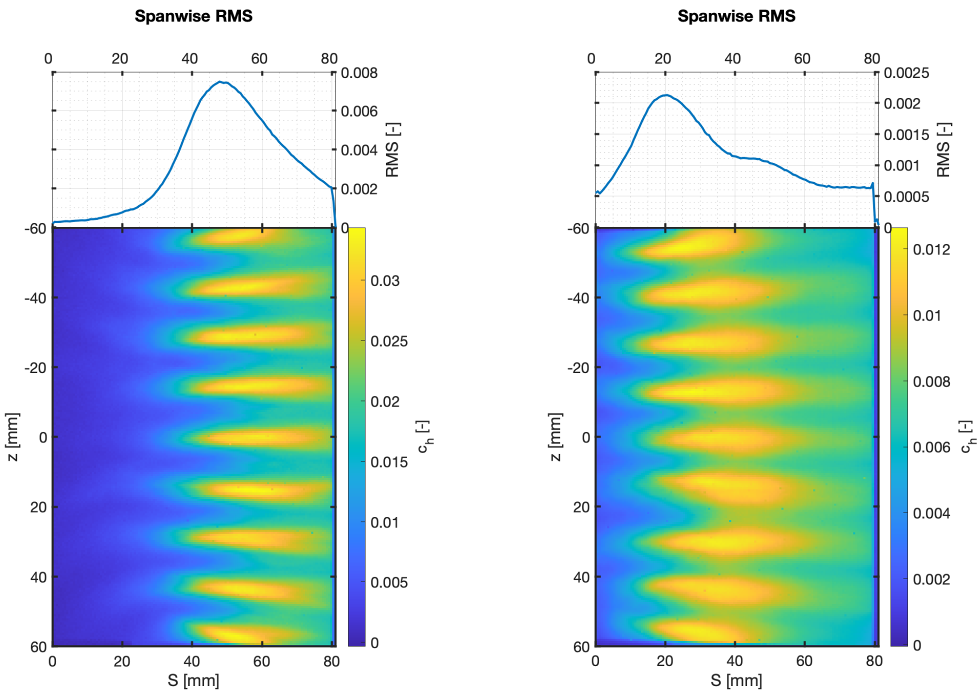

(a) $M_\infty = 7.5$; $Re = 9.2 \times 10^5$ (b) $M_\infty = 7.5$; $Re = 46.3 \times 10^5$

Figure F.39: **Nondimensional roughness strip wavelength:** $\lambda_\delta = 3.6$

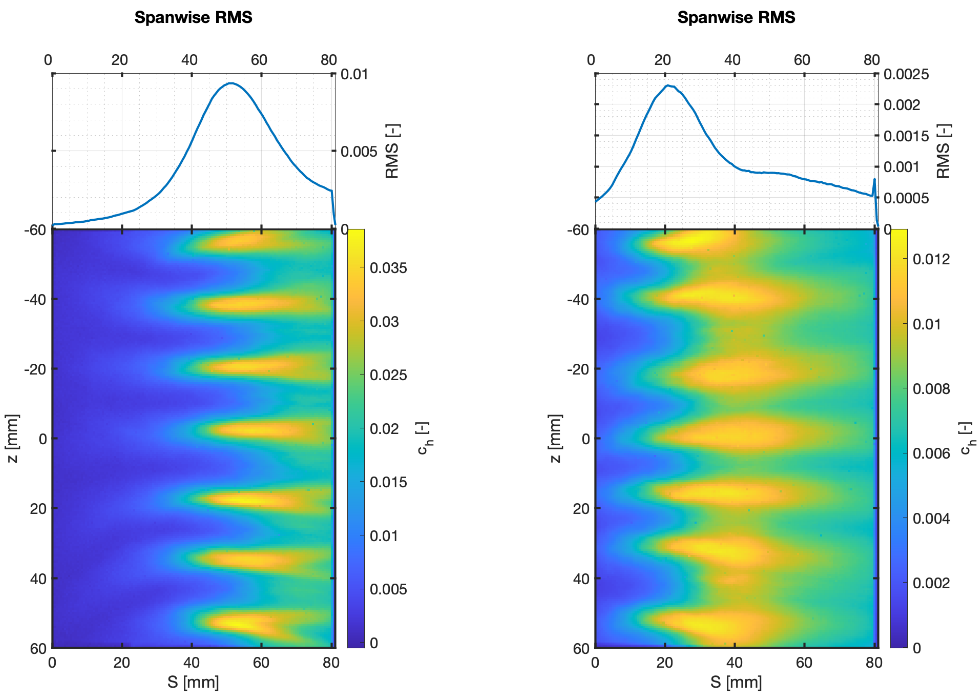

(a) $M_\infty = 7.5$; $Re = 9.2 \times 10^5$ (b) $M_\infty = 7.5$; $Re = 46.3 \times 10^5$

Figure F.40: **Nondimensional roughness strip wavelength:** $\lambda_\delta = 4.5$

G
QIRT Images: Maximum Spanwise Plots – Normal to Flat Plate

G.1. Mean Results

G.1.1. Compiled Results

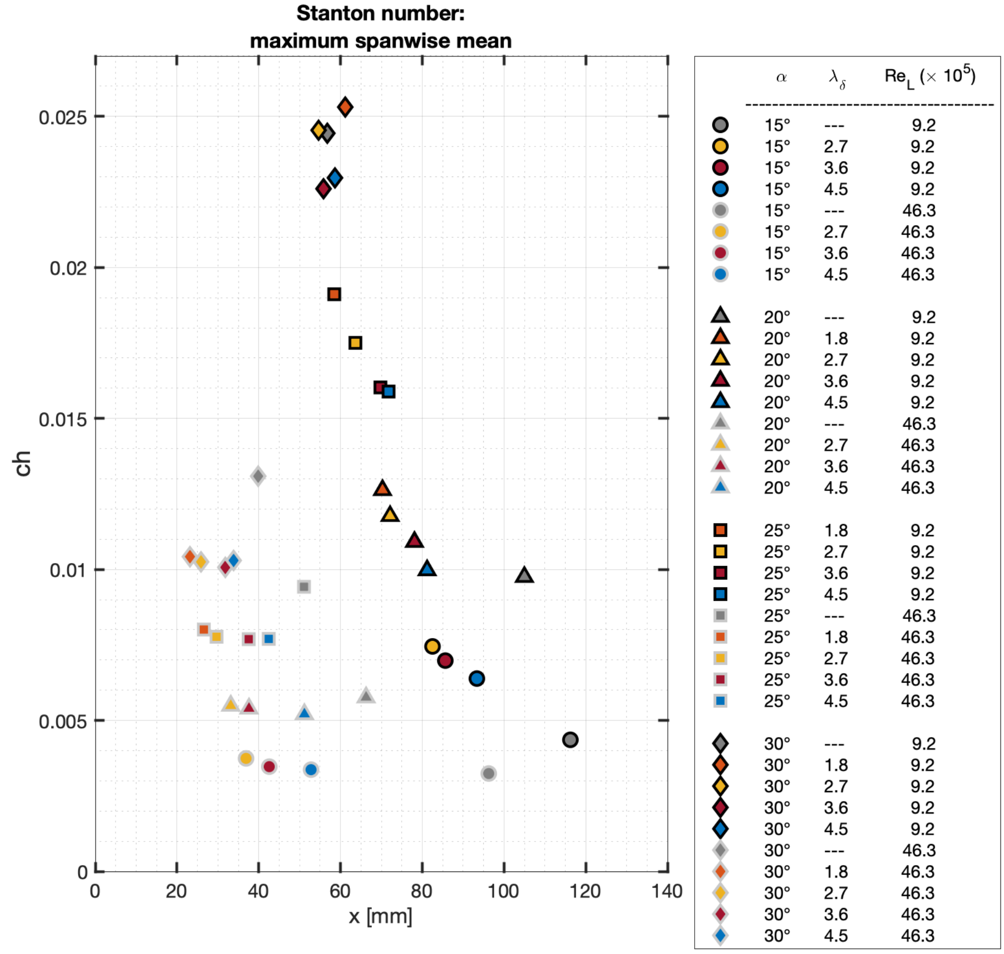

Figure G.1

G.1.2. Stanton Number versus x – Identified by Nondimensional Strip Wavelength λ_δ

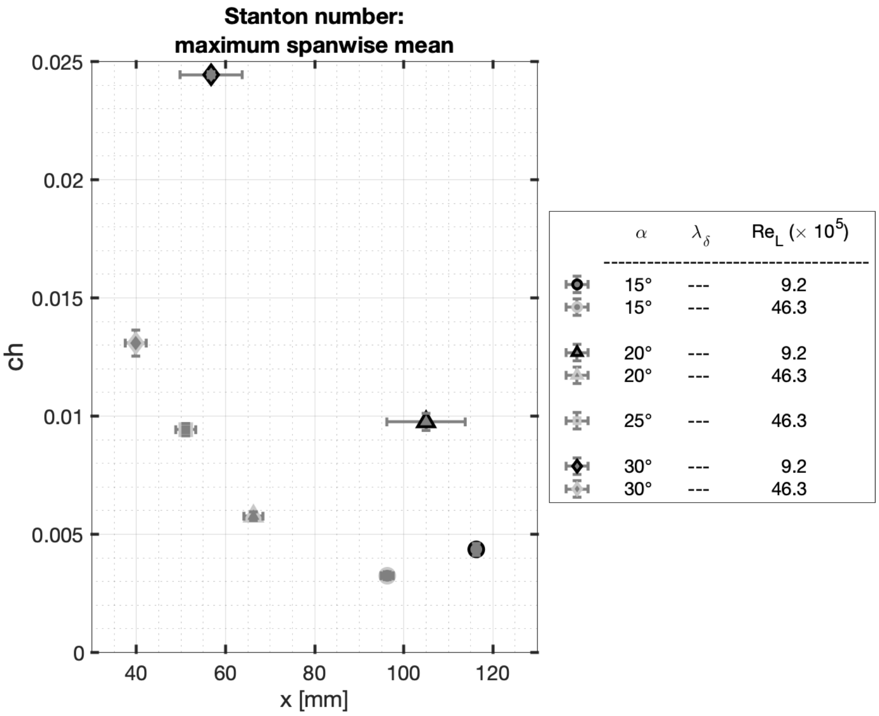

Figure G.2: **No roughness strip.**

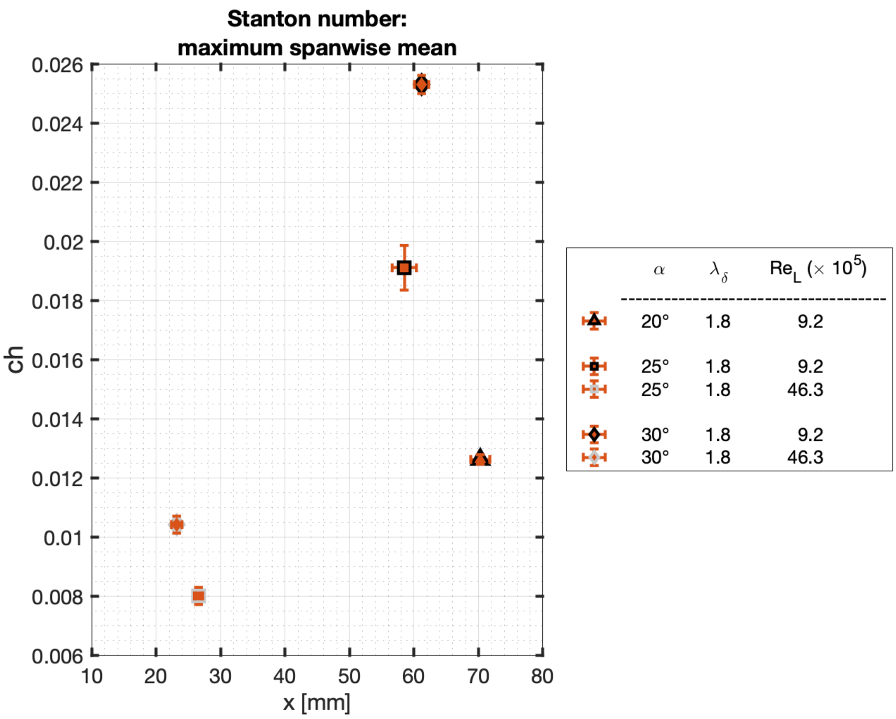

Figure G.3: **Nondimensional roughness strip wavelength:** $\lambda_\delta = 1.8$

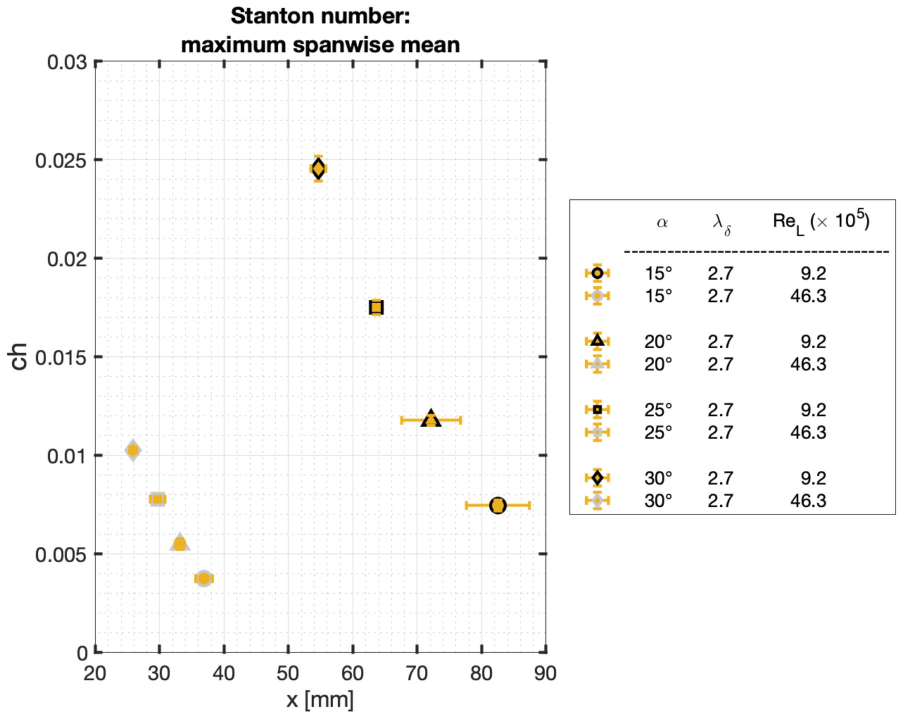

Figure G.4: **Nondimensional roughness strip wavelength:** $\lambda_\delta = 2.7$

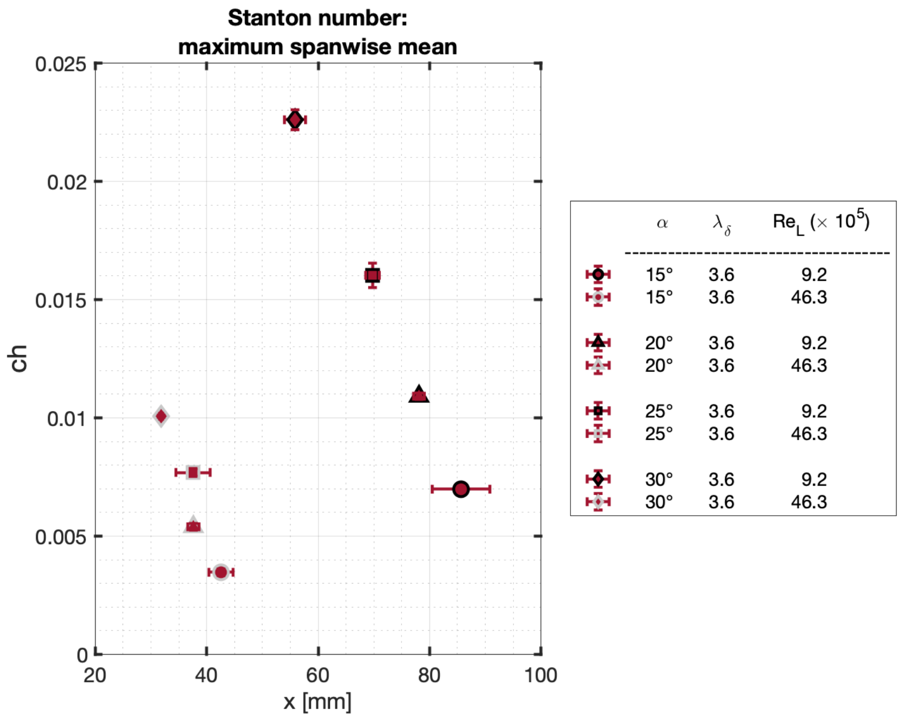

Figure G.5: **Nondimensional roughness strip wavelength:** $\lambda_\delta = 3.6$

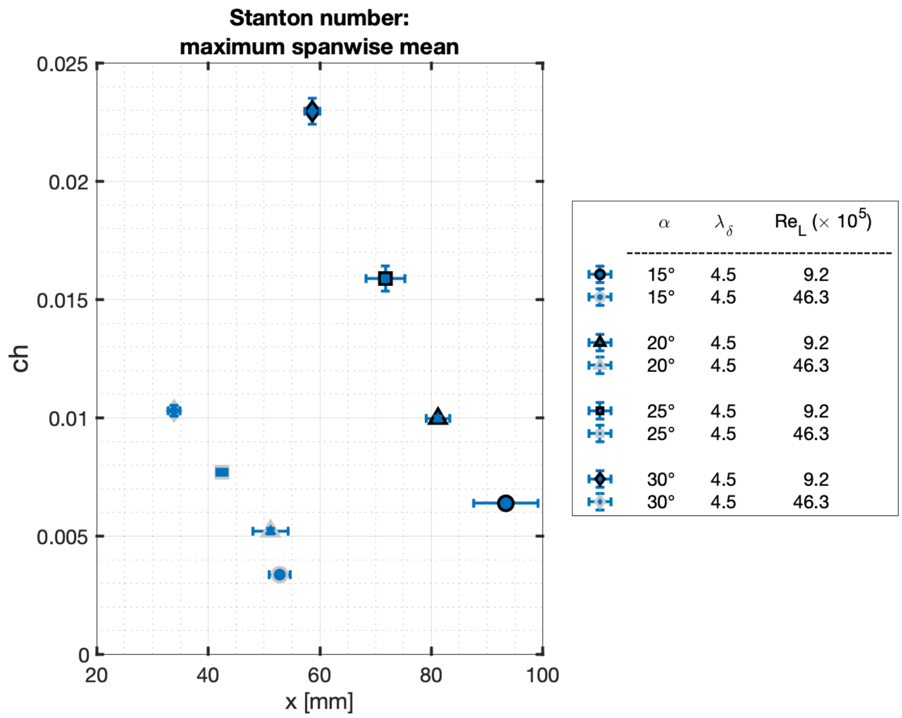

Figure G.6: **Nondimensional roughness strip wavelength:** $\lambda_\delta = 4.5$

G.1.3. Stanton Number versus x – Identified by Ramp Angle α

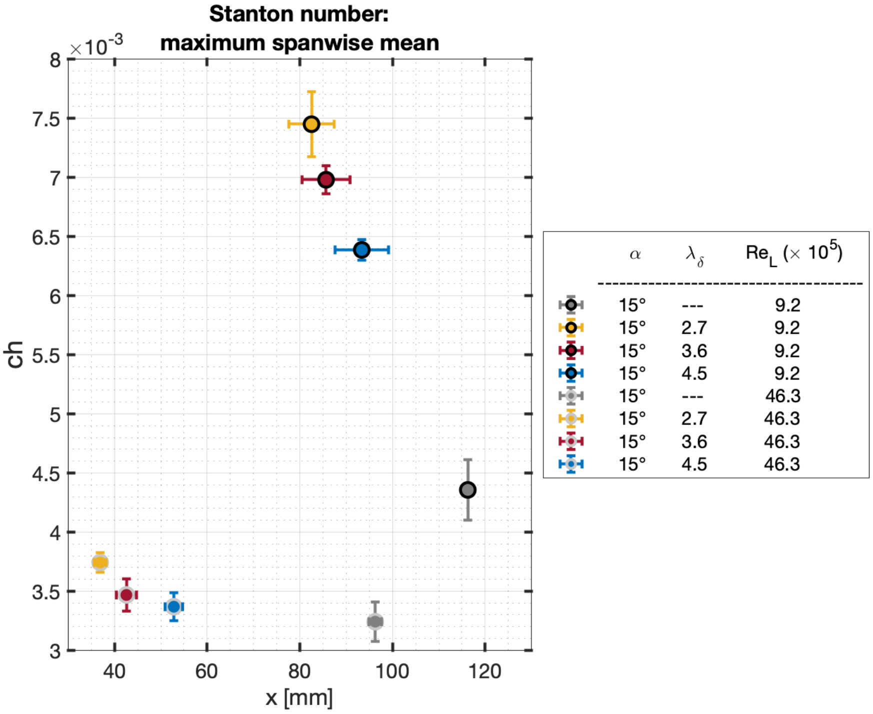

Figure G.7: **Ramp angle:** α = 15°

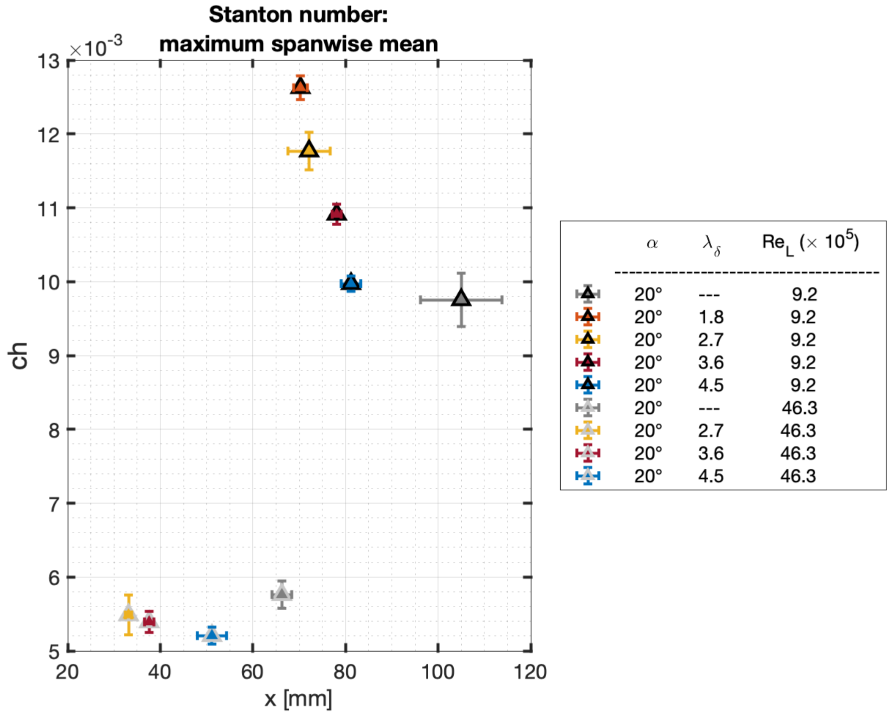

Figure G.8: **Ramp angle:** α = 20°

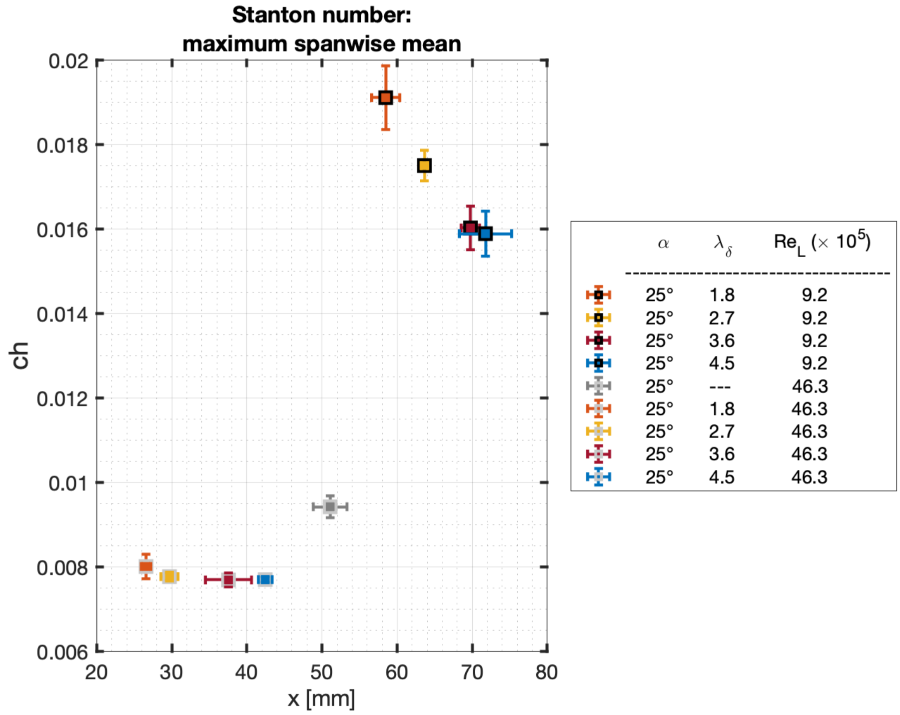

Figure G.9: **Ramp angle:** $\alpha = 25°$

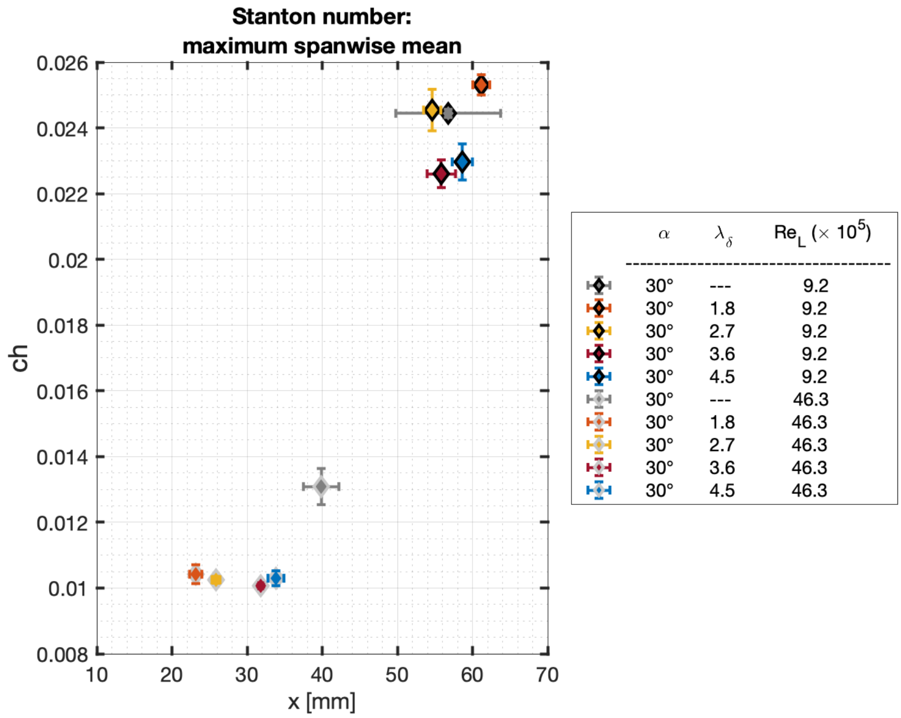

Figure G.10: **Ramp angle:** $\alpha = 30°$

G.1.4. Stanton Number versus Ramp Angle α

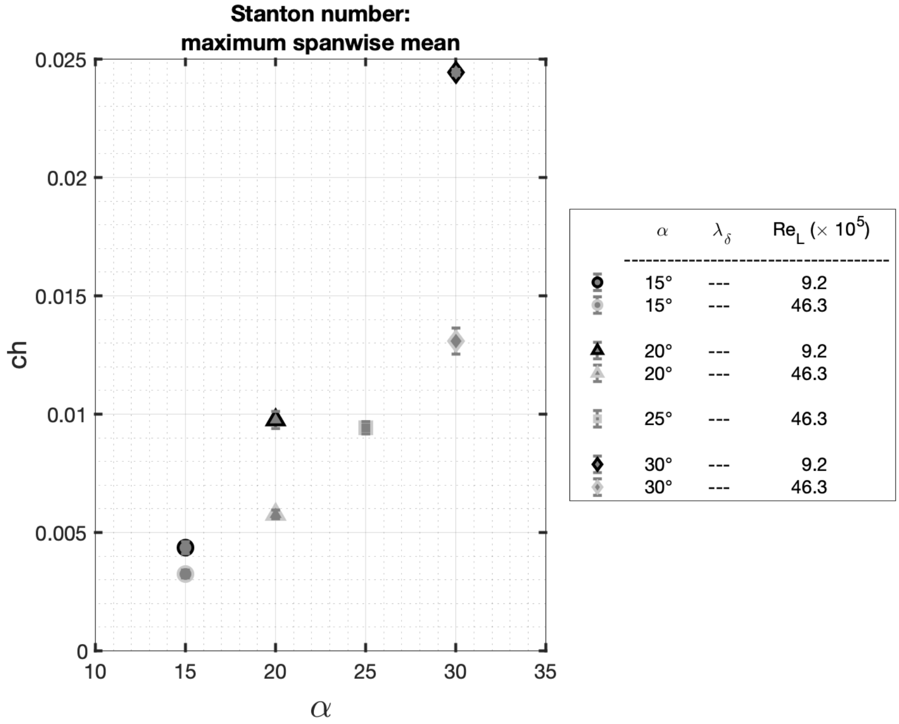

Figure G.11: **No roughness strip.**

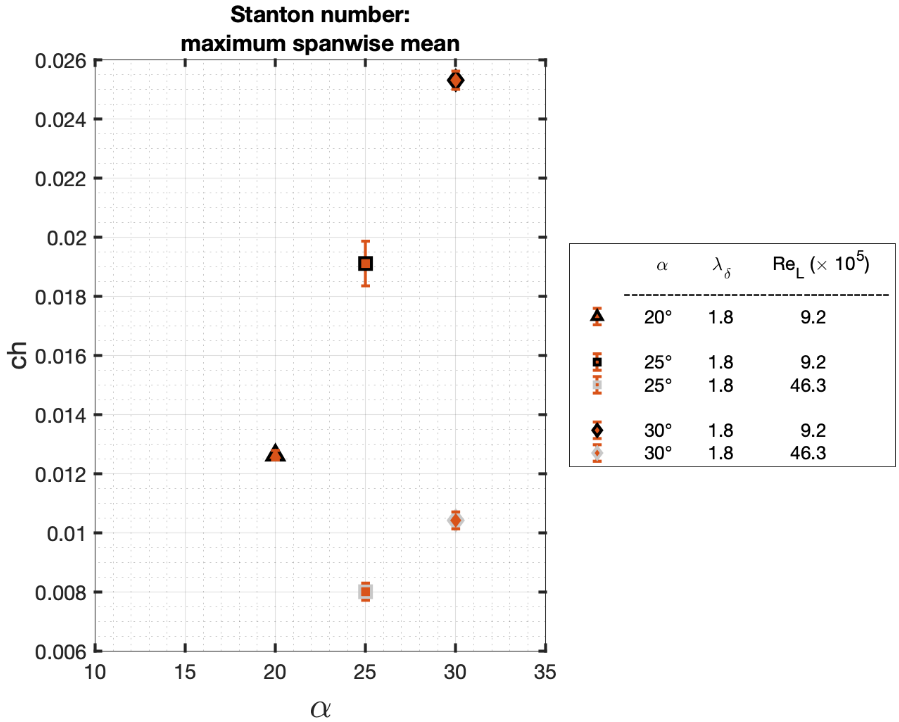

Figure G.12: **Nondimensional roughness strip wavelength:** $\lambda_\delta = 1.8$

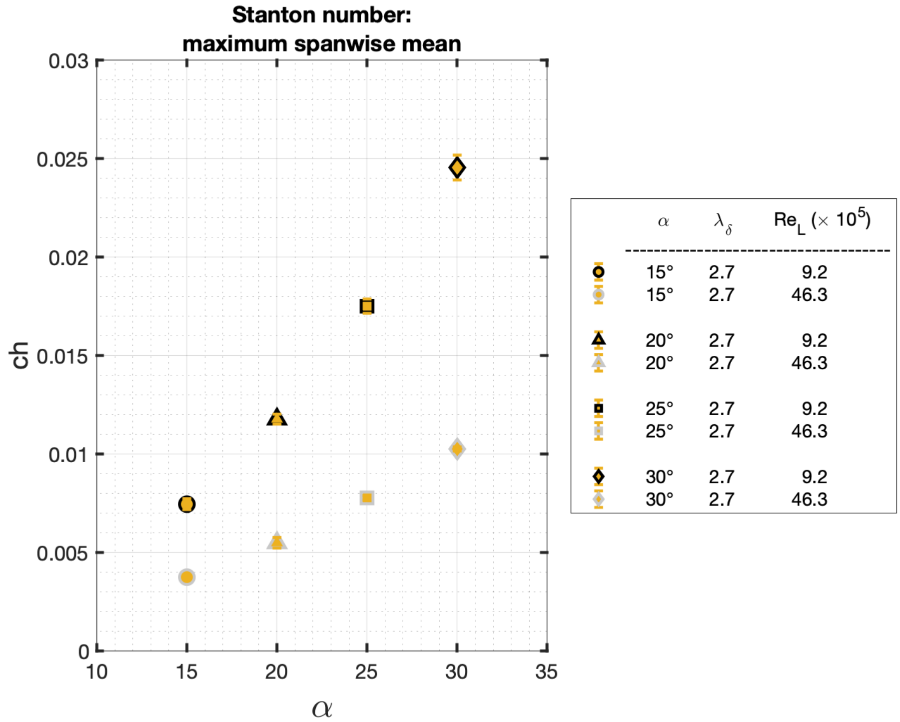

Figure G.13: **Nondimensional roughness strip wavelength:** $\lambda_\delta = 2.7$

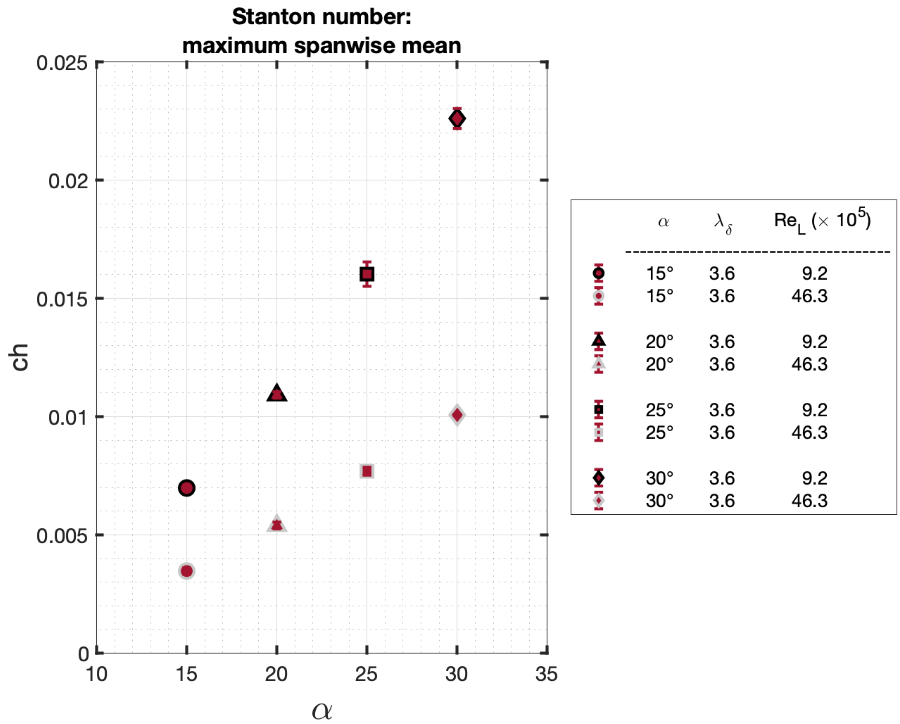

Figure G.14: **Nondimensional roughness strip wavelength:** $\lambda_\delta = 3.6$

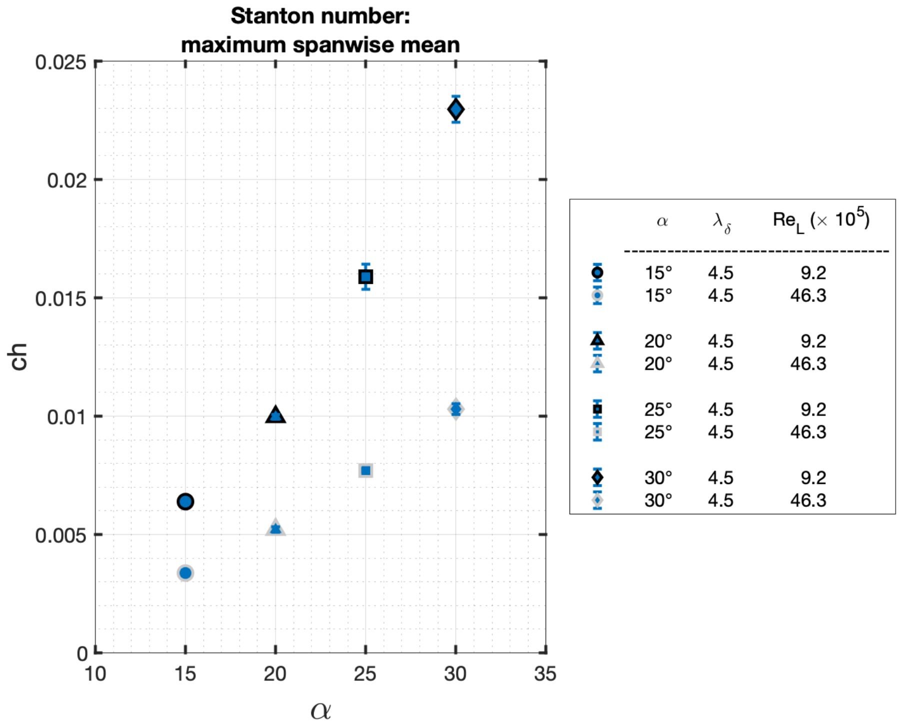

Figure G.15: **Nondimensional roughness strip wavelength:** $\lambda_\delta = 4.5$

G.1.5. Stanton Number versus Nondimensional Strip Wavelength λ_δ

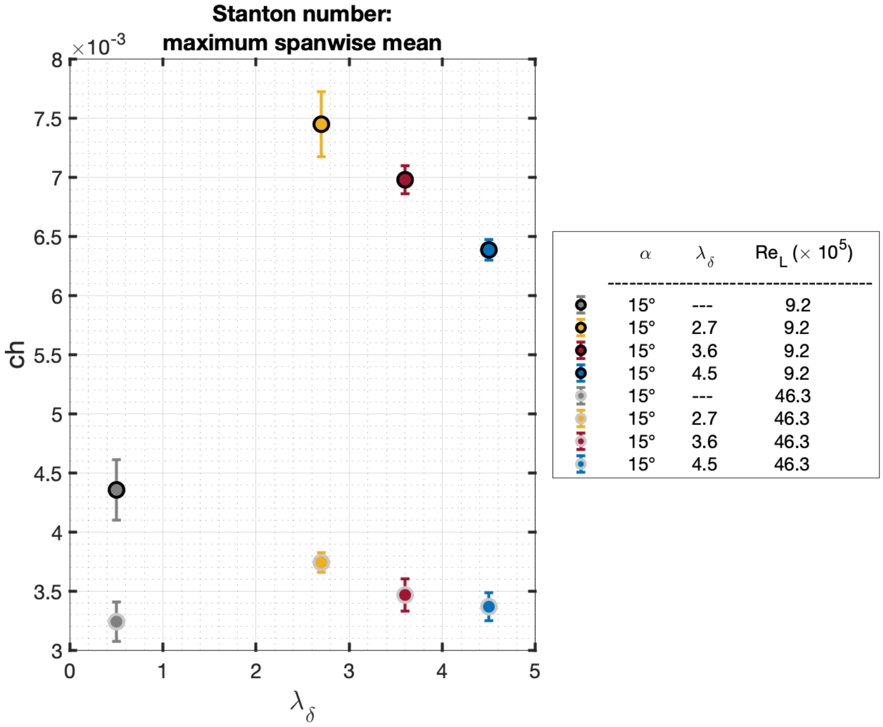

Figure G.16: **Ramp angle:** α = 15°

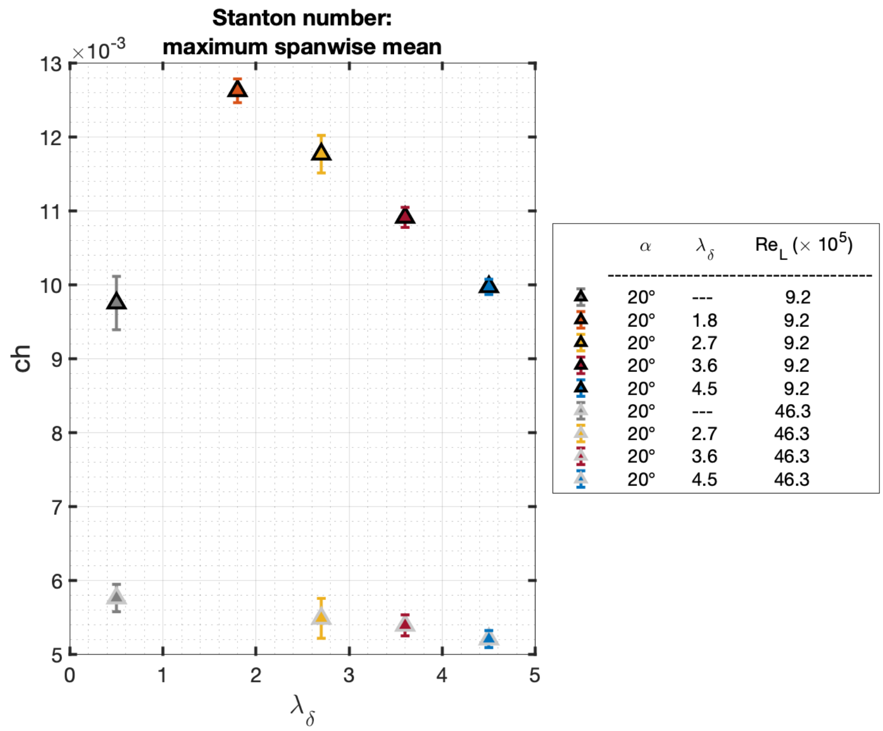

Figure G.17: **Ramp angle:** α = 20°

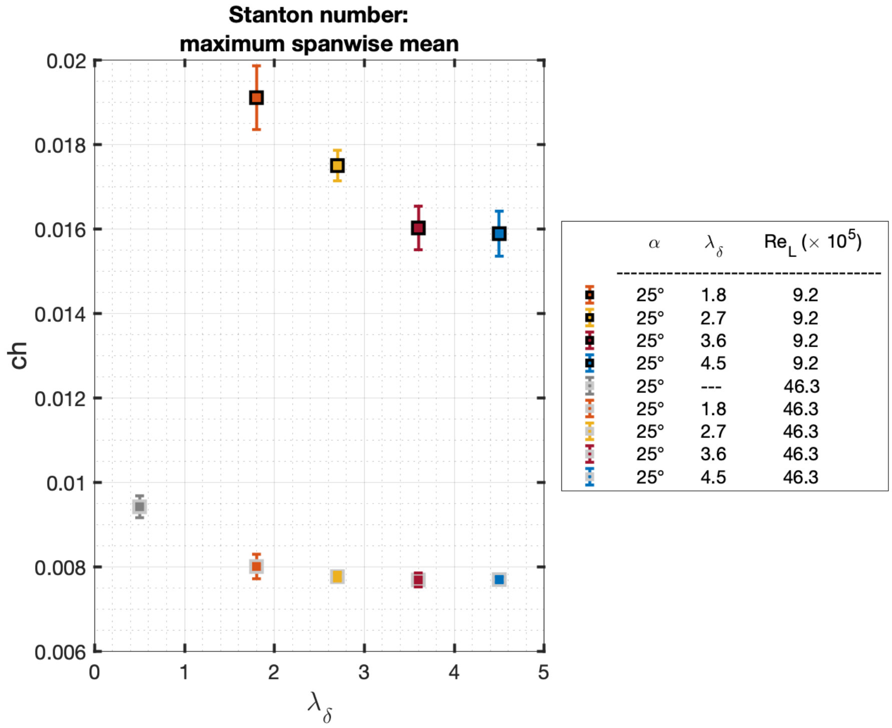

Figure G.18: **Ramp angle:** $\alpha = 25°$

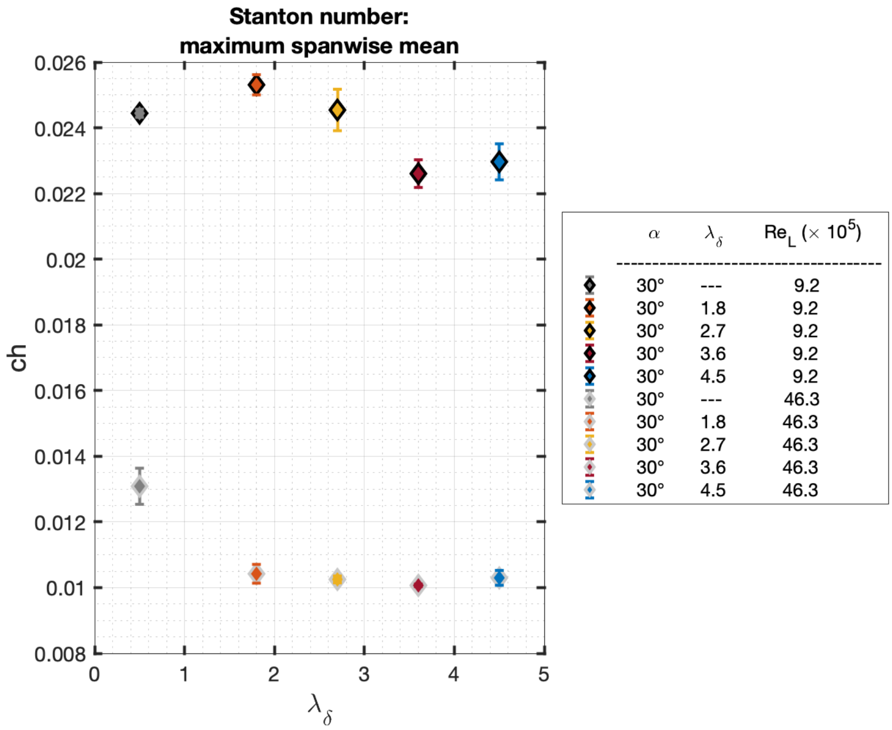

Figure G.19: **Ramp angle:** $\alpha = 30°$

G.2. RMS Results

G.2.1. Compiled Results

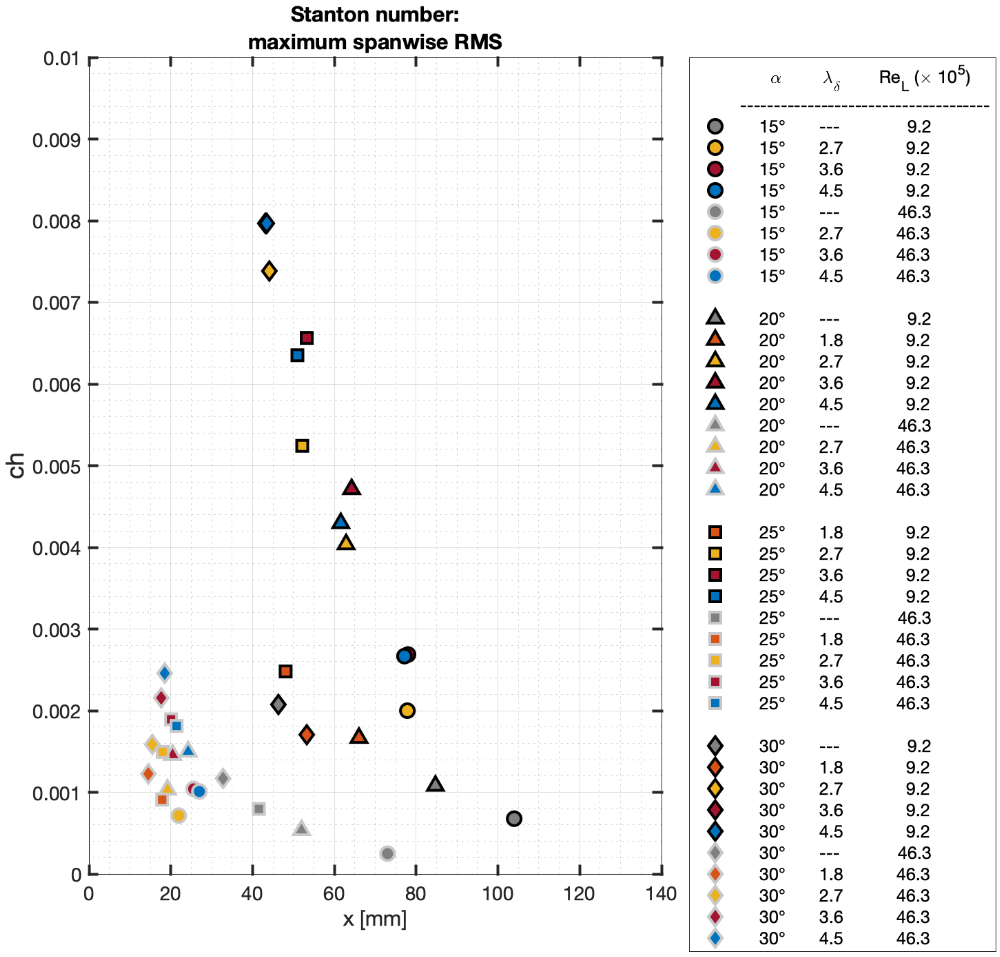

Figure G.20

G.2.2. Stanton Number versus x – Identified by Nondimensional Strip Wavelength λ_δ

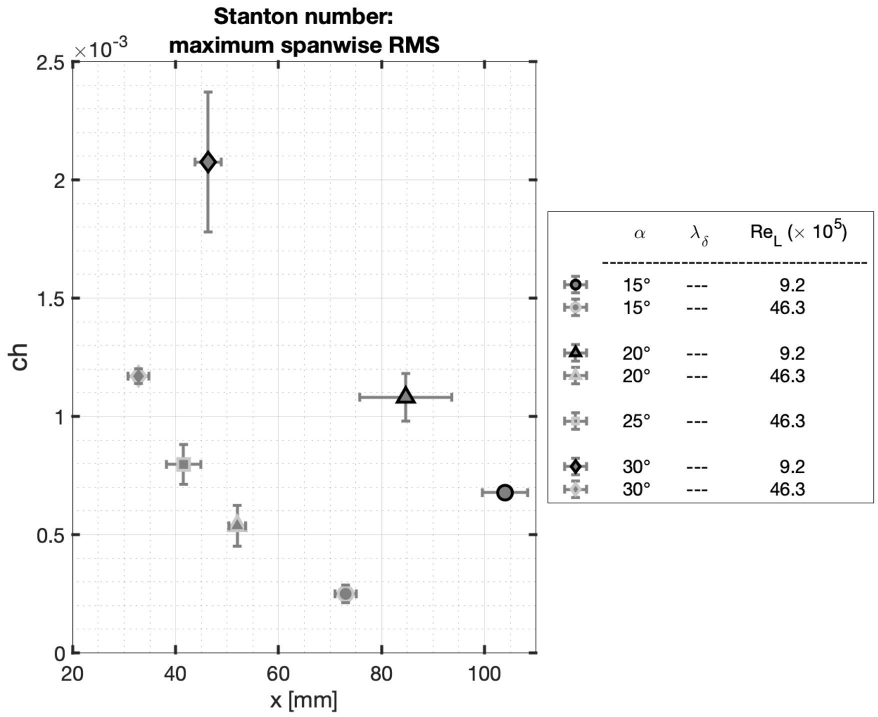

Figure G.21: **No roughness strip.**

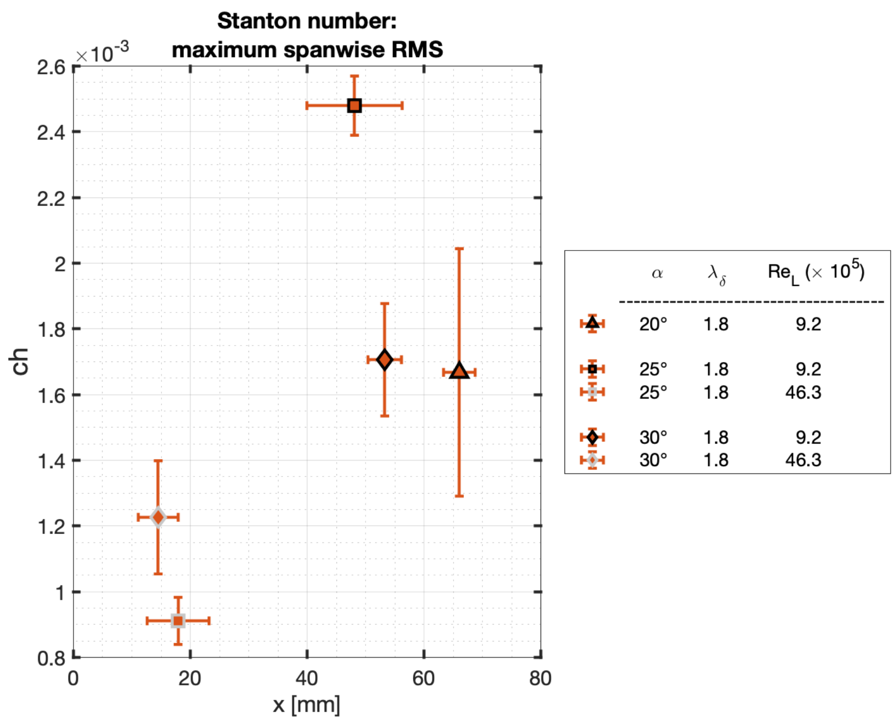

Figure G.22: **Nondimensional roughness strip wavelength:** $\lambda_\delta = 1.8$

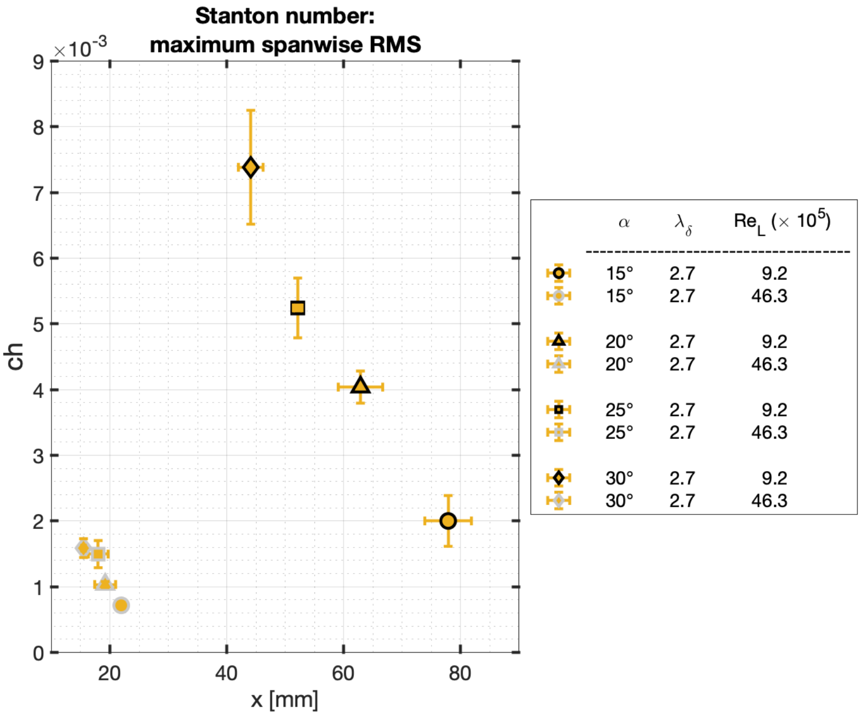

Figure G.23: **Nondimensional roughness strip wavelength:** $\lambda_\delta = 2.7$

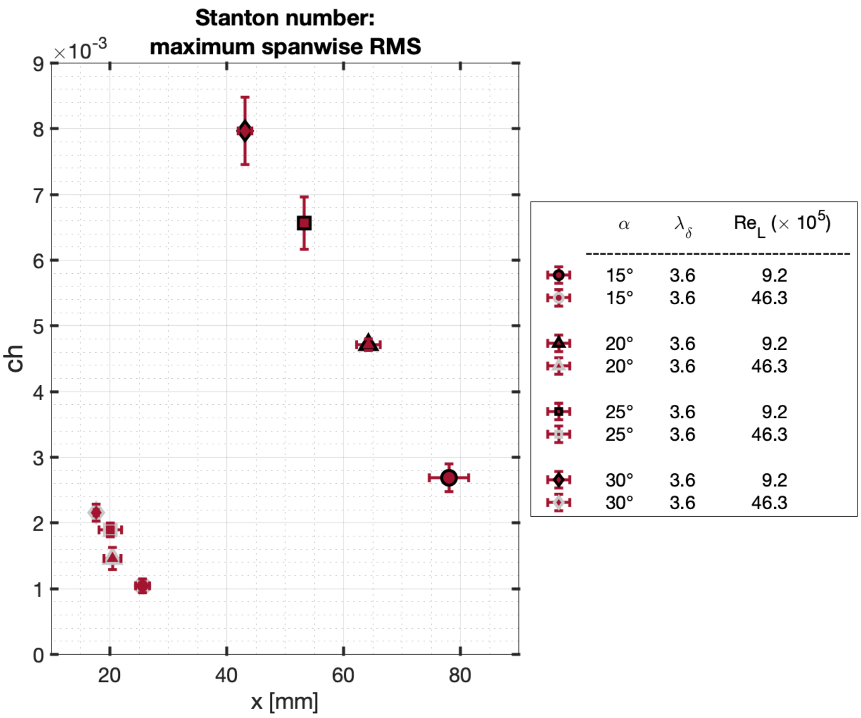

Figure G.24: **Nondimensional roughness strip wavelength:** $\lambda_\delta = 3.6$

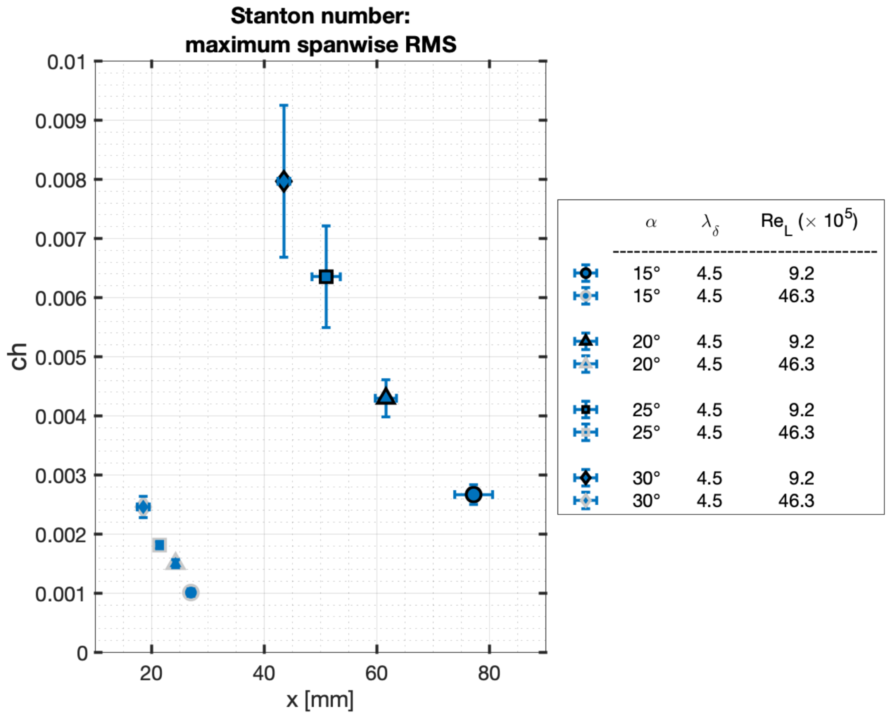

Figure G.25: **Nondimensional roughness strip wavelength:** $\lambda_\delta = 4.5$

G.2.3. Stanton Number versus x – Identified by Ramp Angle α

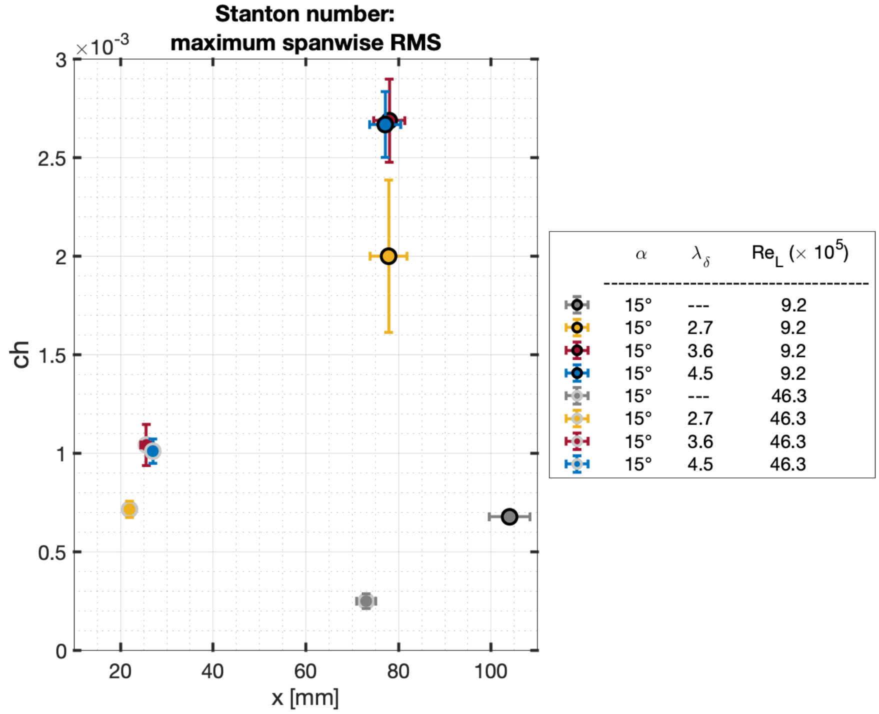

Figure G.26: **Ramp angle:** α = 15°

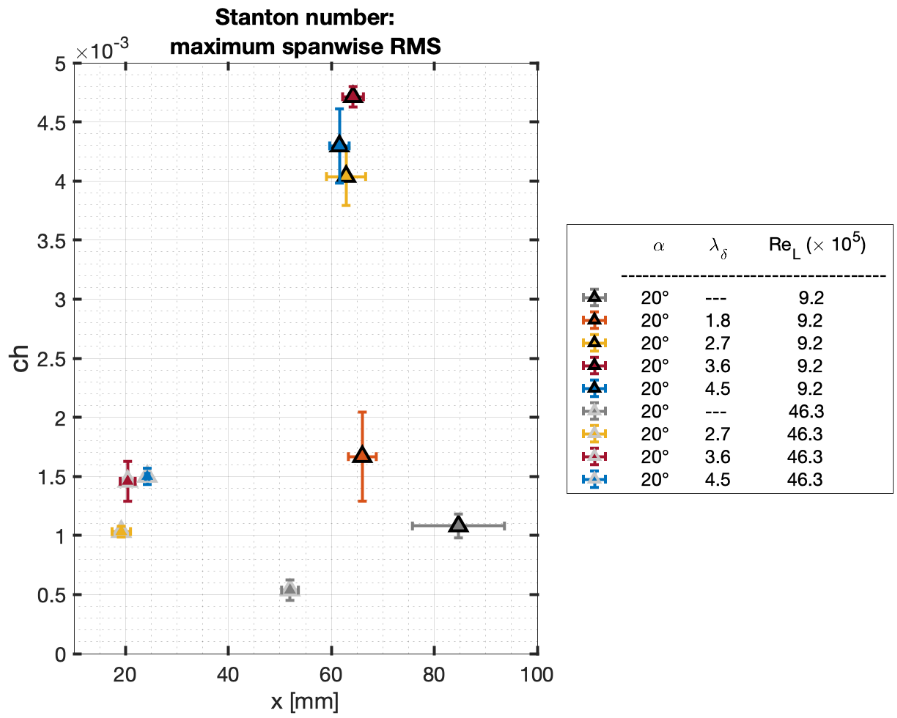

Figure G.27: **Ramp angle:** α = 20°

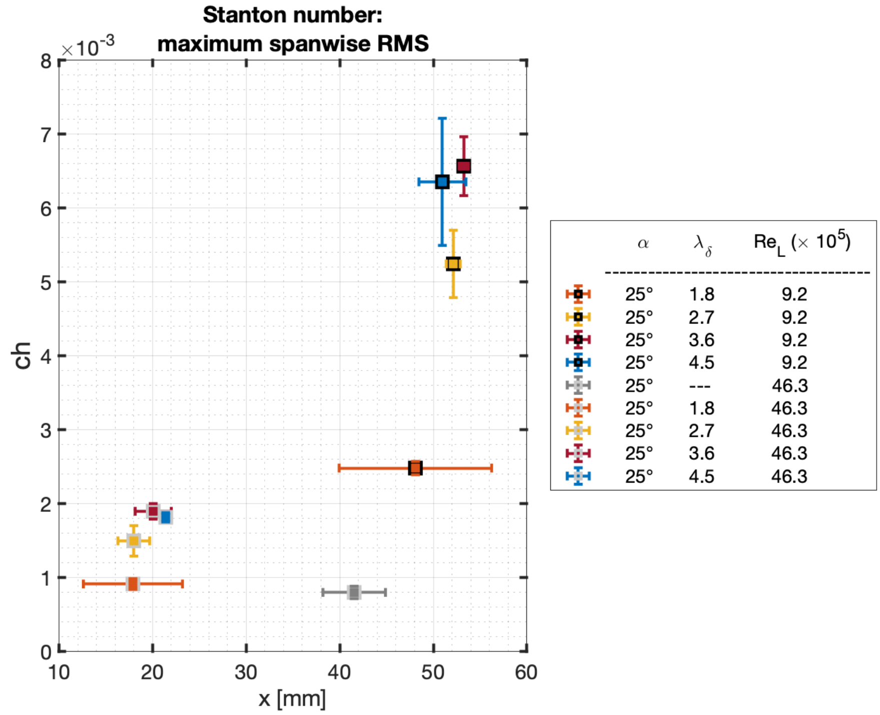

Figure G.28: **Ramp angle:** $\alpha = 25°$

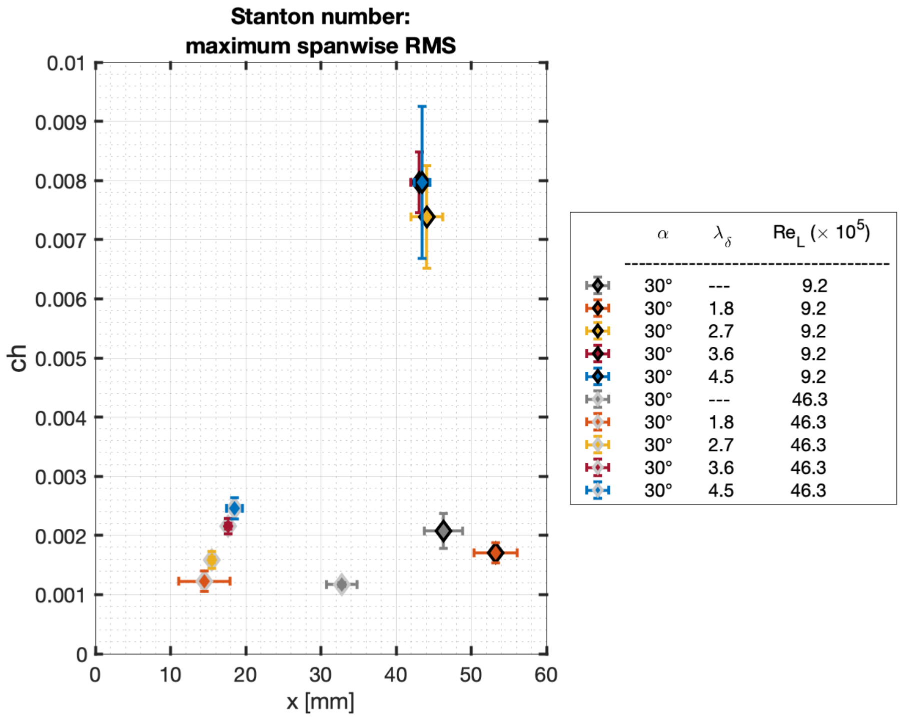

Figure G.29: **Ramp angle:** $\alpha = 30°$

G.2.4. Stanton Number versus Ramp Angle α

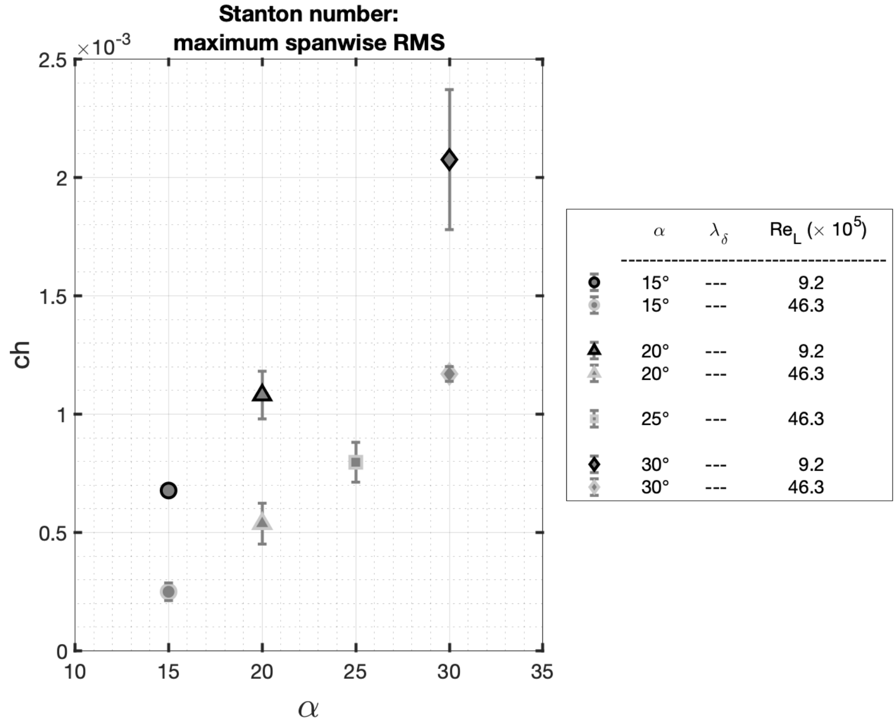

Figure G.30: **No roughness strip.**

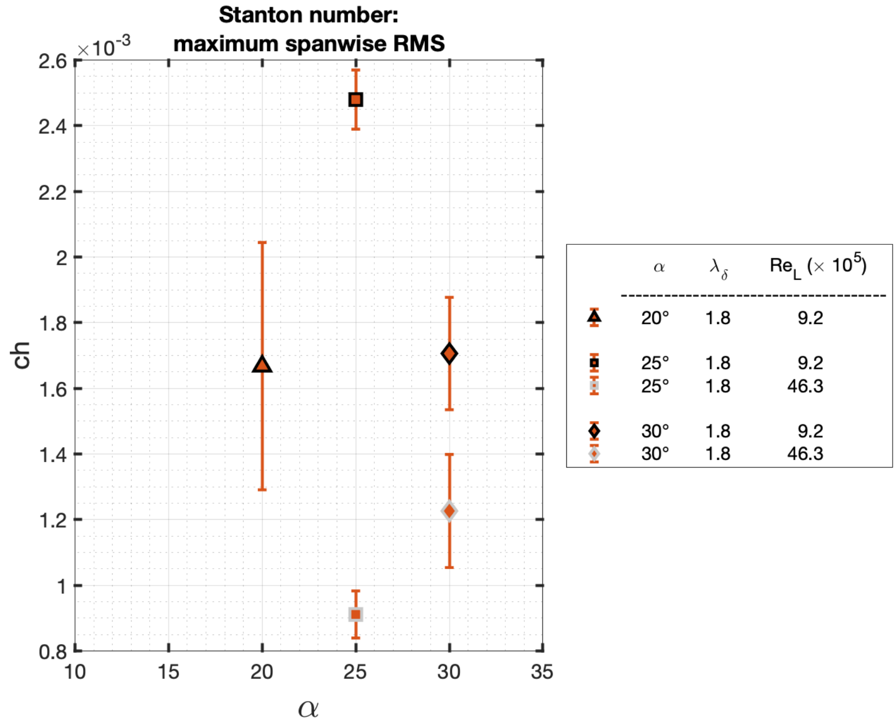

Figure G.31: **Nondimensional roughness strip wavelength:** $\lambda_\delta = 1.8$

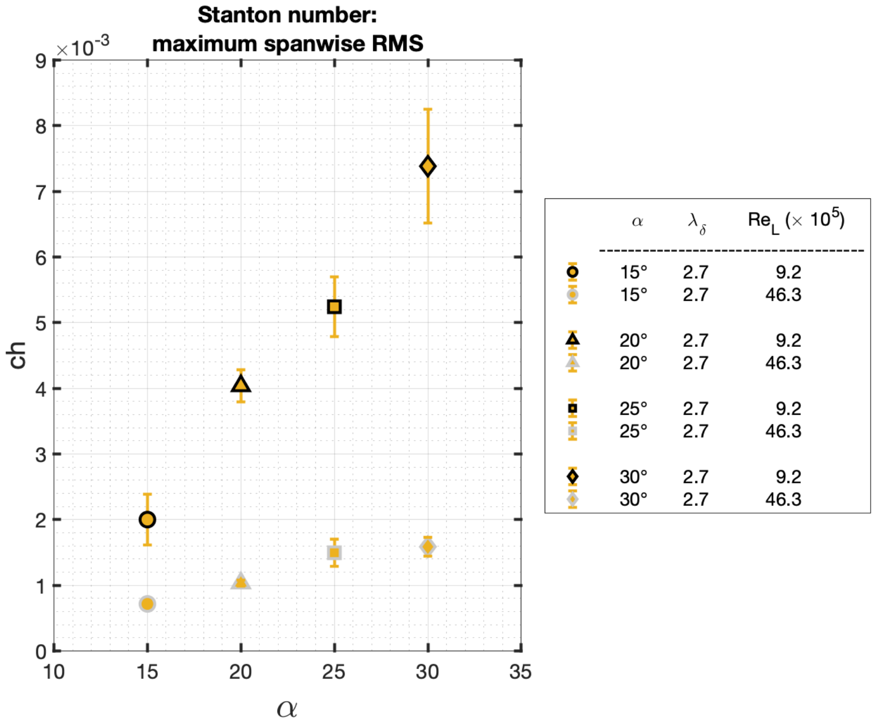

Figure G.32: **Nondimensional roughness strip wavelength:** $\lambda_\delta = 2.7$

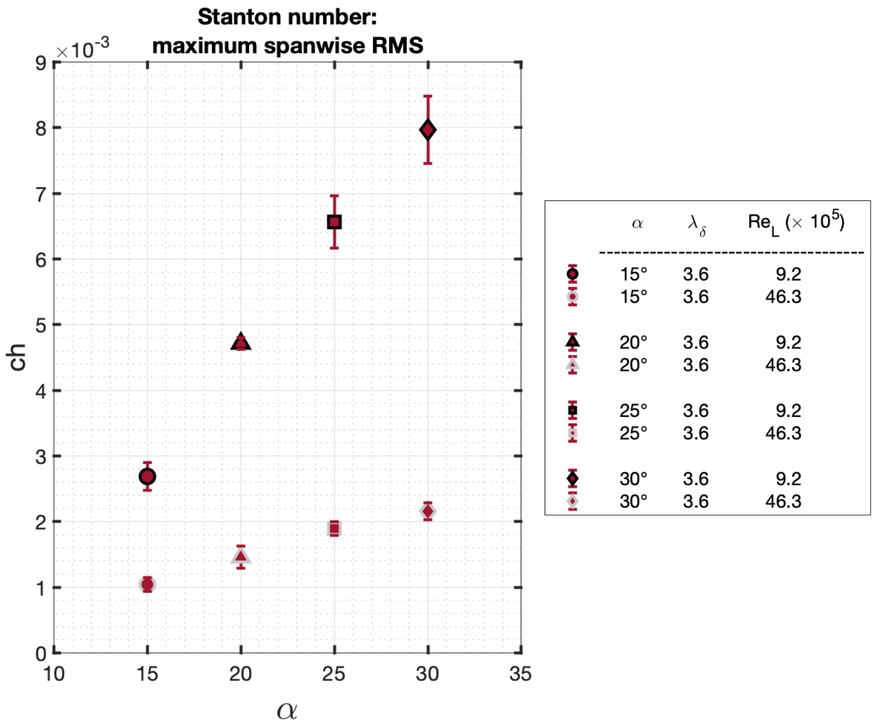

Figure G.33: **Nondimensional roughness strip wavelength:** $\lambda_\delta = 3.6$

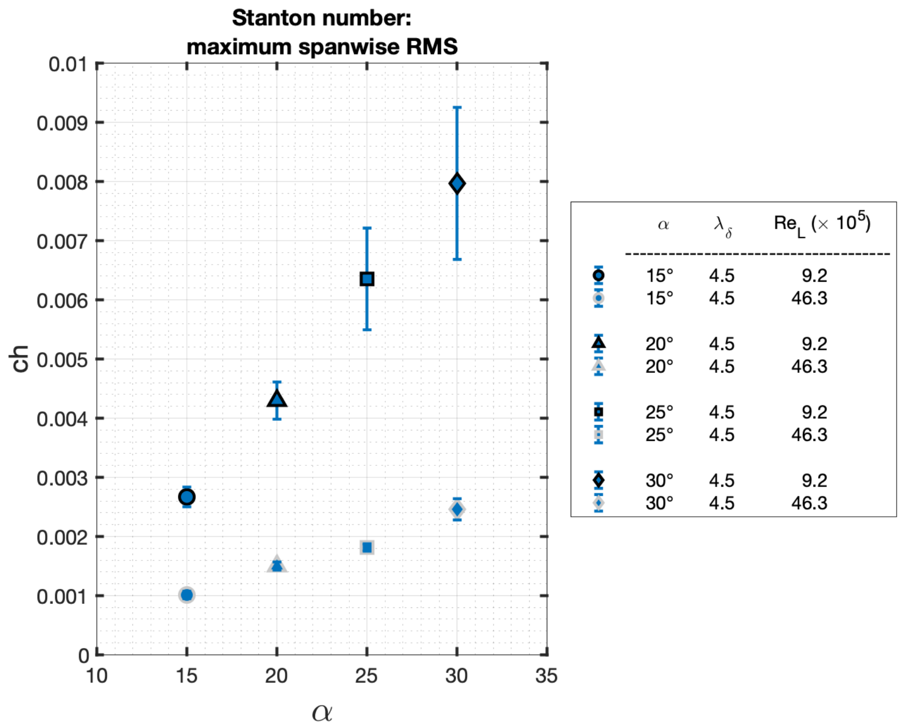

Figure G.34: **Nondimensional roughness strip wavelength:** $\lambda_\delta = 4.5$

G.2.5. Stanton Number versus Nondimensional Strip Wavelength λ_δ

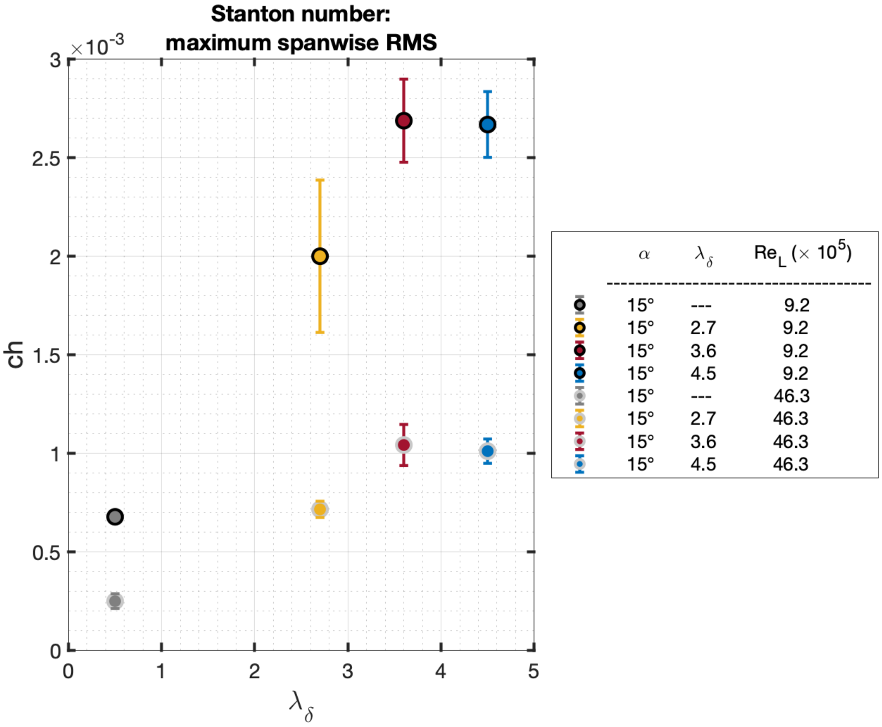

Figure G.35: **Ramp angle:** α = 15°

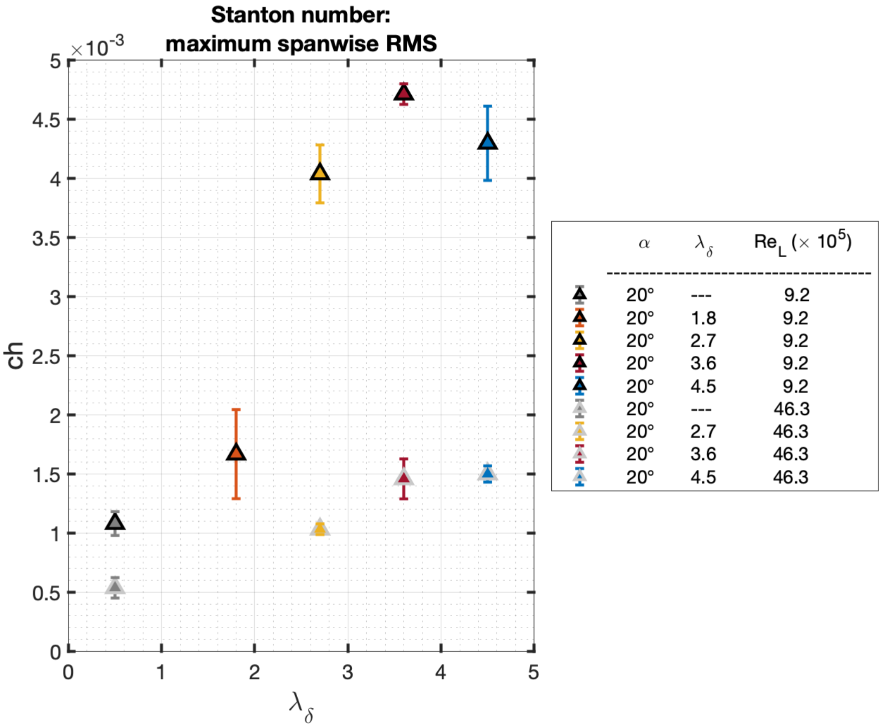

Figure G.36: **Ramp angle:** α = 20°

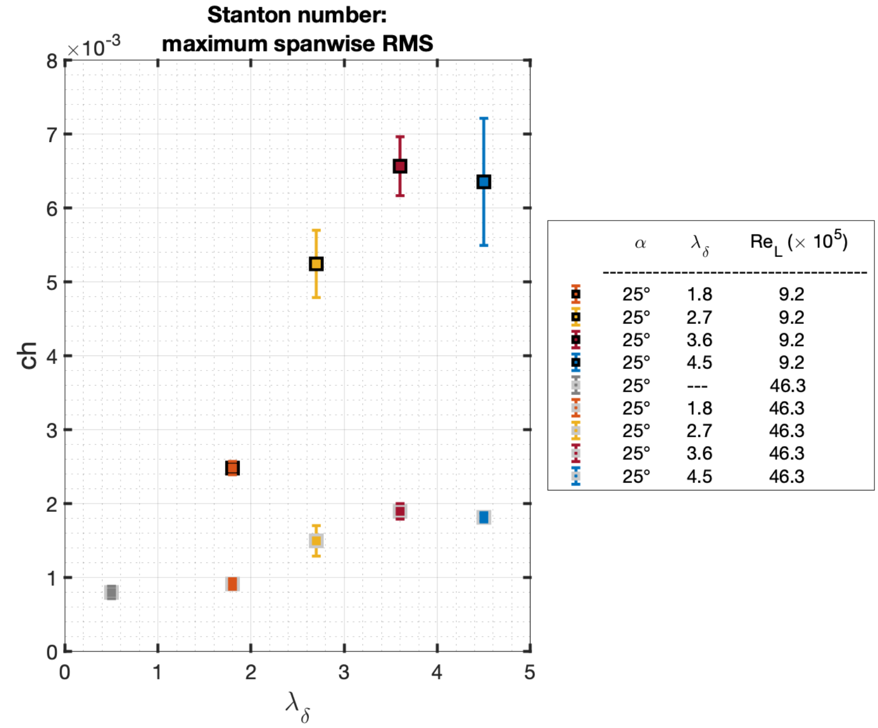

Figure G.37: **Ramp angle:** $\alpha = 25°$

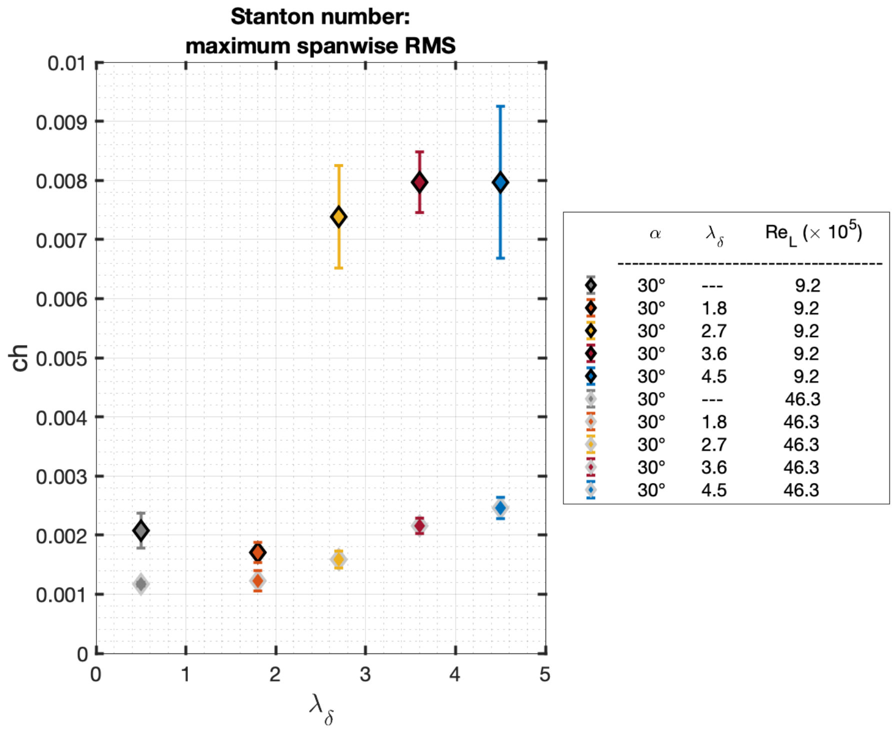

Figure G.38: **Ramp angle:** $\alpha = 30°$

H

QIRT Images: Maximum Spanwise Plots – Normal to Ramp Surface

H.1. Mean Results

H.1.1. Compiled Results

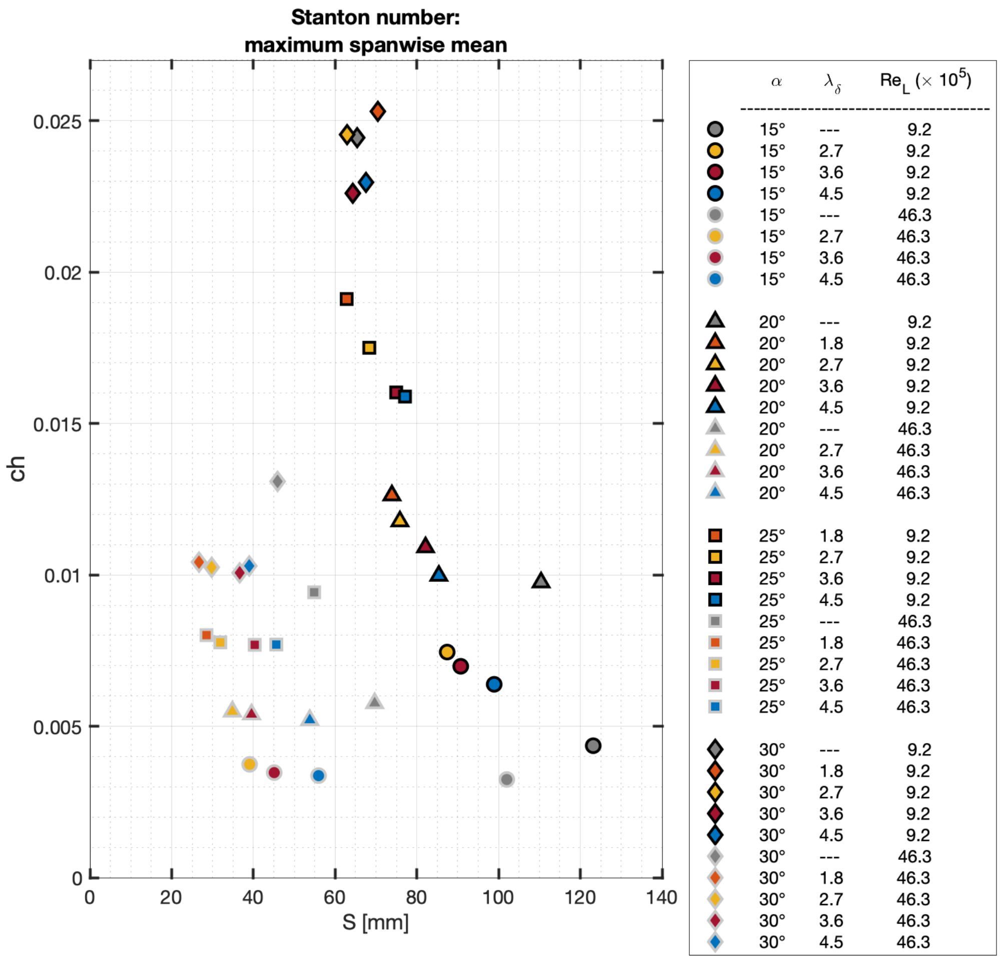

Figure H.1

H.1.2. Stanton Number versus S – Identified by Nondimensional Strip Wavelength λ_δ

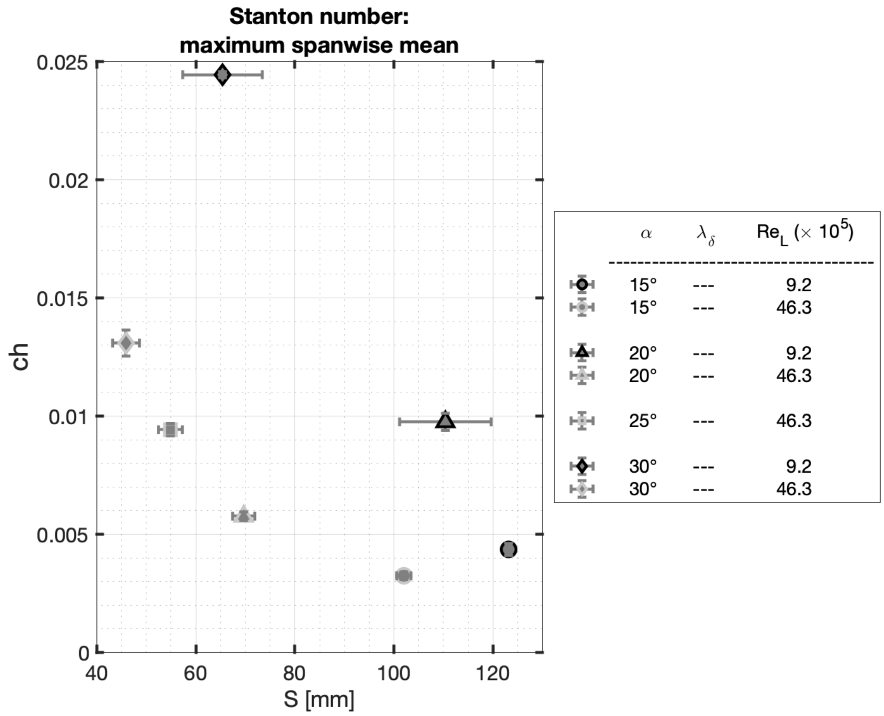

Figure H.2: **No roughness strip.**

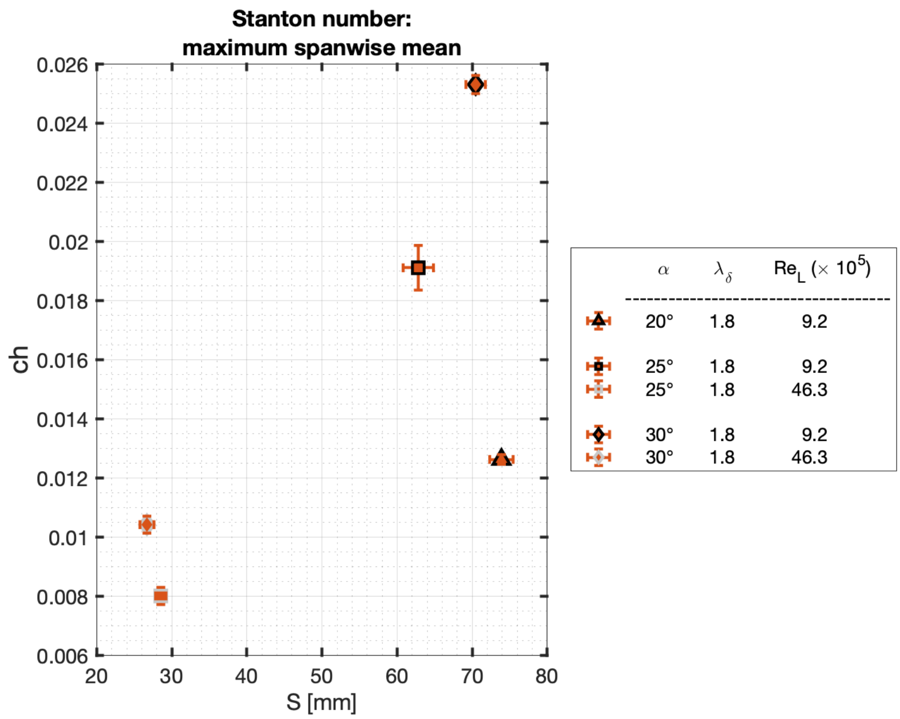

Figure H.3: **Nondimensional roughness strip wavelength:** $\lambda_\delta = 1.8$

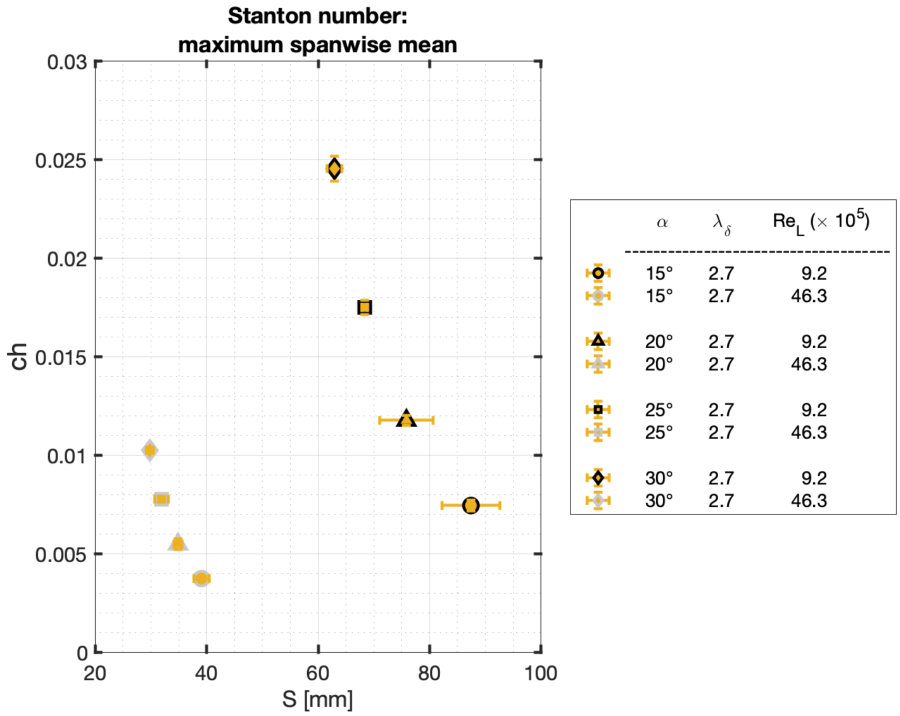

Figure H.4: **Nondimensional roughness strip wavelength:** $\lambda_\delta = 2.7$

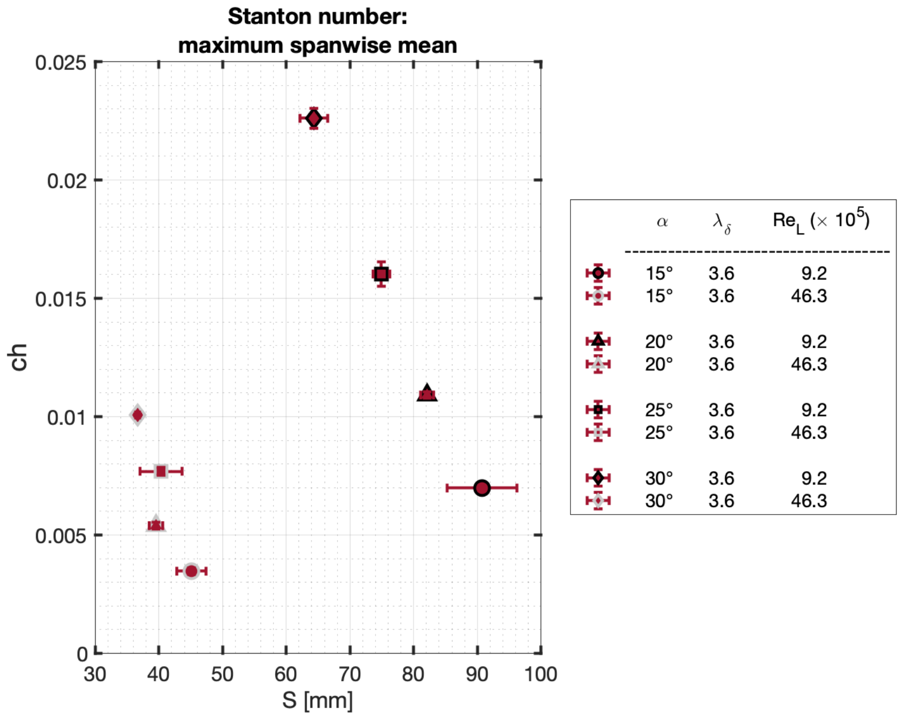

Figure H.5: **Nondimensional roughness strip wavelength:** $\lambda_\delta = 3.6$

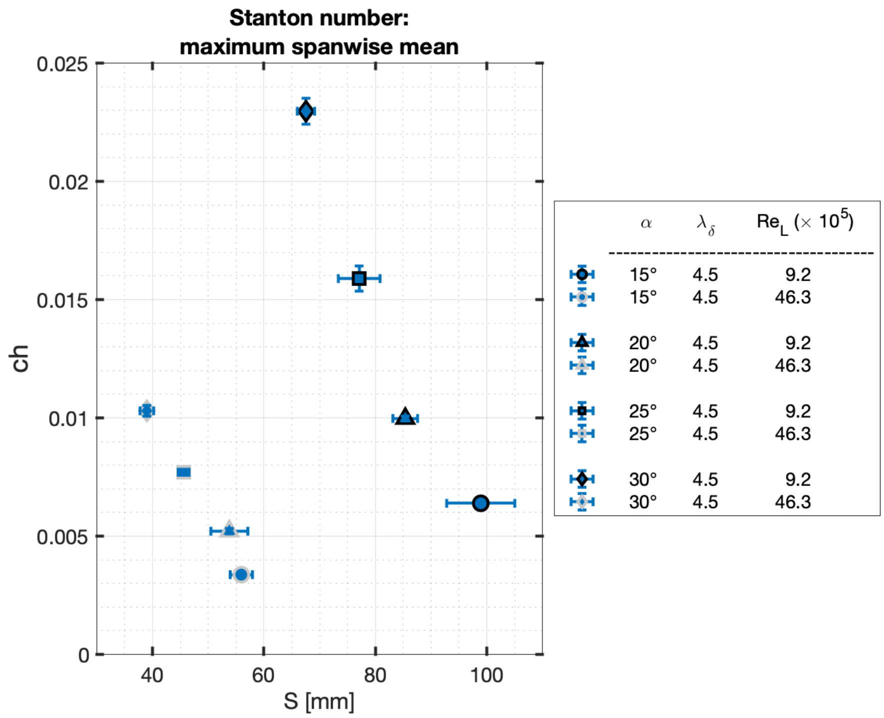

Figure H.6: **Nondimensional roughness strip wavelength:** $\lambda_\delta = 4.5$

H.1.3. Stanton Number versus S – Identified by Ramp Angle α

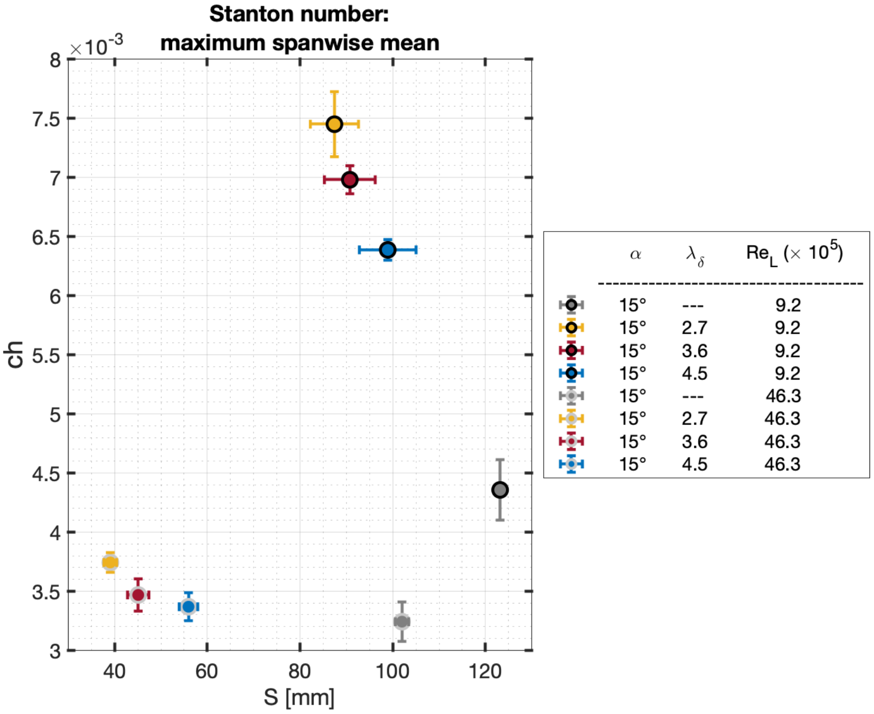

Figure H.7: **Ramp angle:** α = 15°

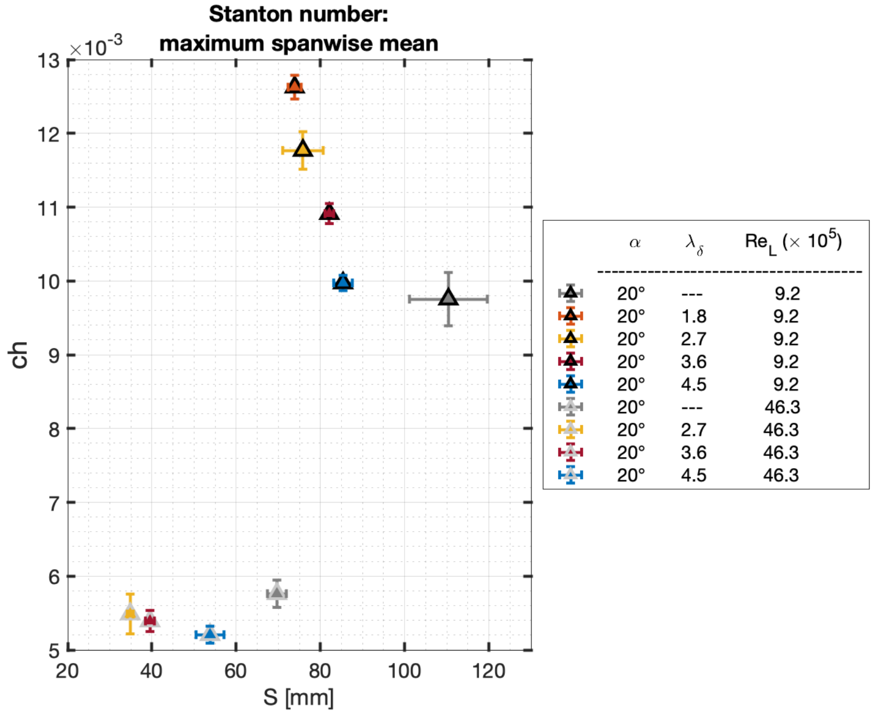

Figure H.8: **Ramp angle:** α = 20°

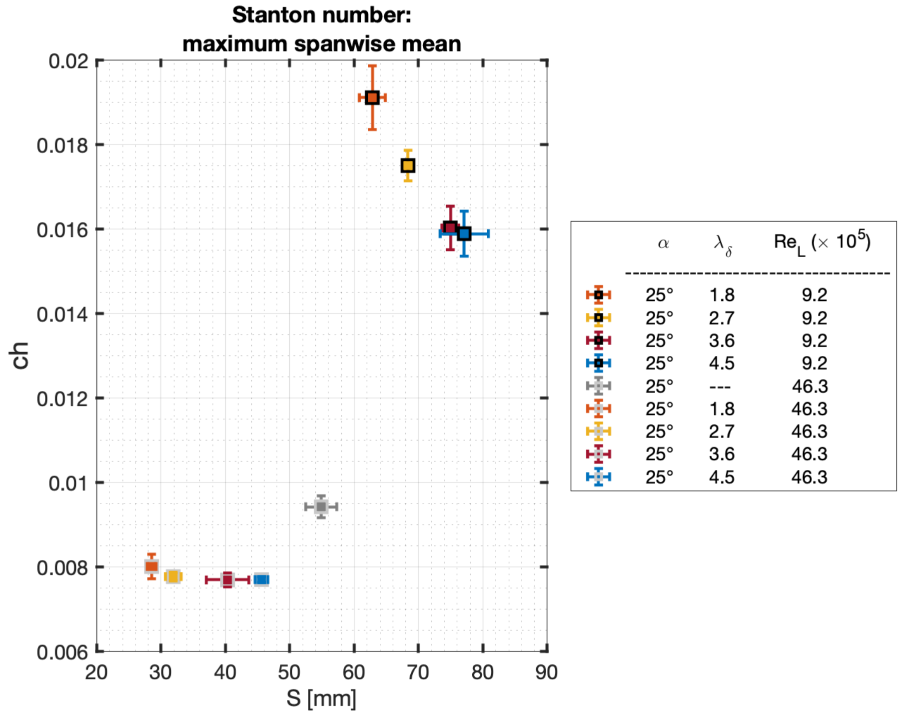

Figure H.9: **Ramp angle:** α = 25°

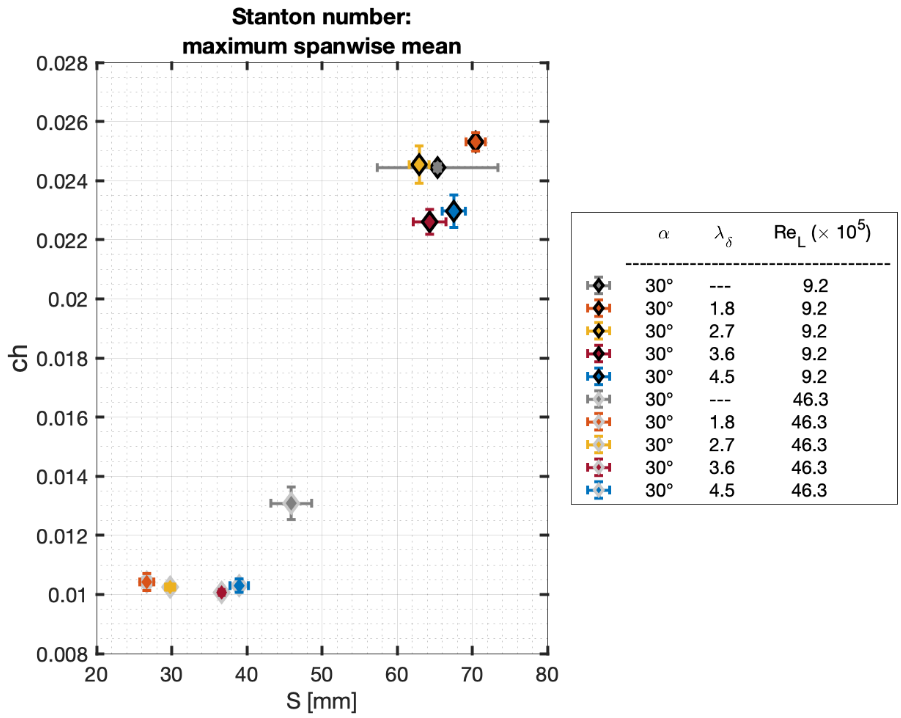

Figure H.10: **Ramp angle:** α = 30°

H.1.4. Stanton Number versus Ramp Angle α

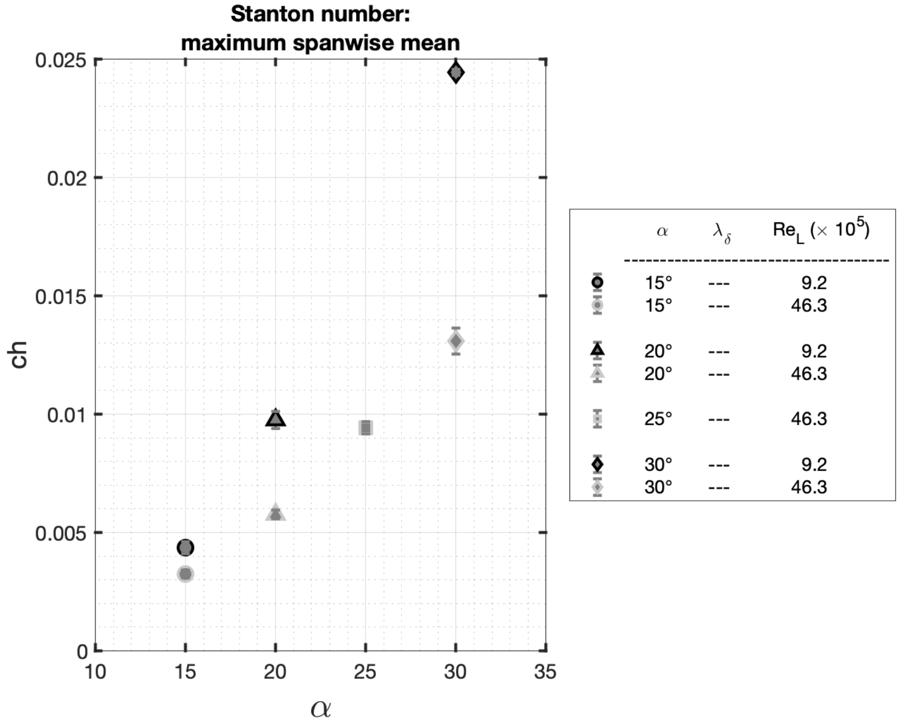

Figure H.11: **No roughness strip.**

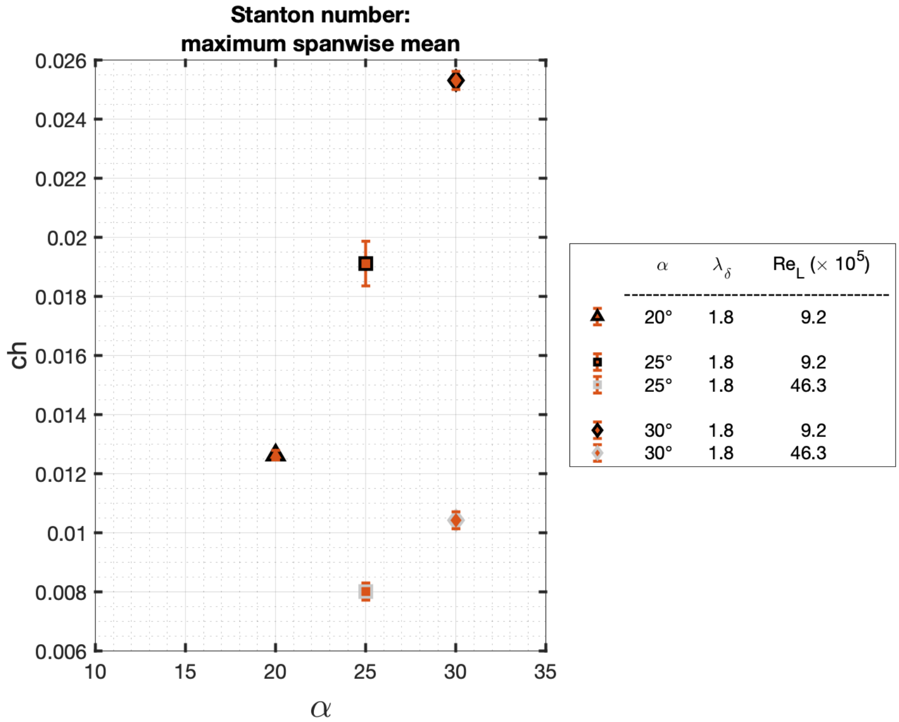

Figure H.12: **Nondimensional roughness strip wavelength:** $\lambda_\delta = 1.8$

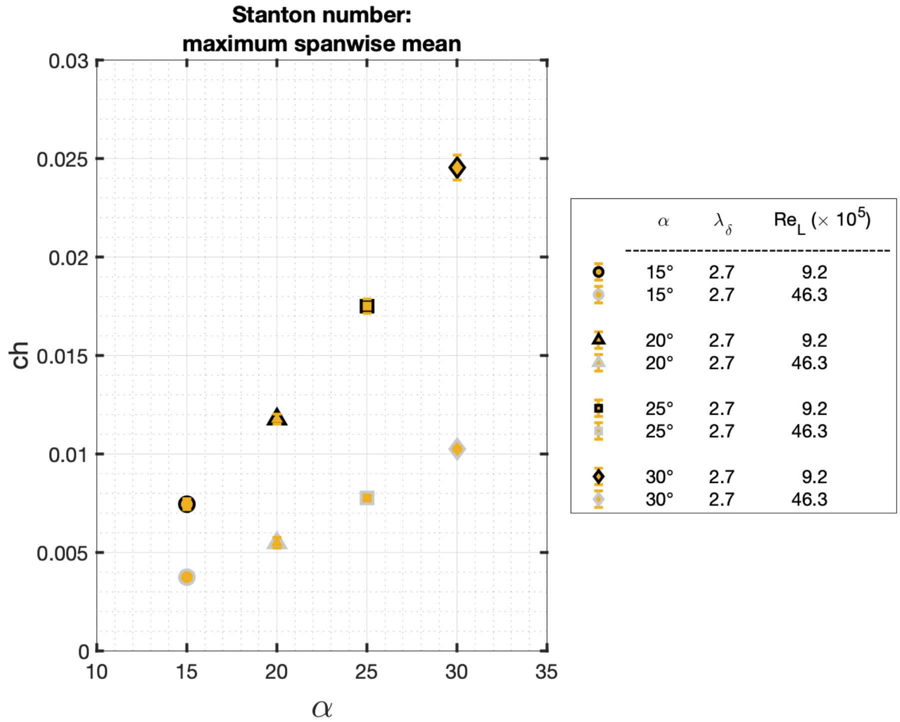

Figure H.13: **Nondimensional roughness strip wavelength:** $\lambda_\delta = 2.7$

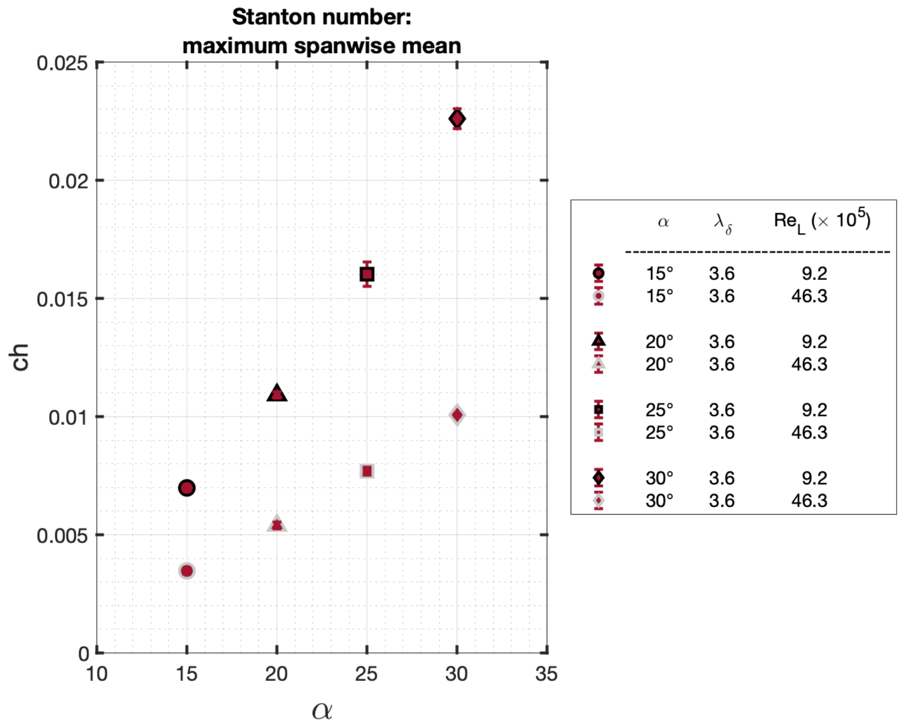

Figure H.14: **Nondimensional roughness strip wavelength:** $\lambda_\delta = 3.6$

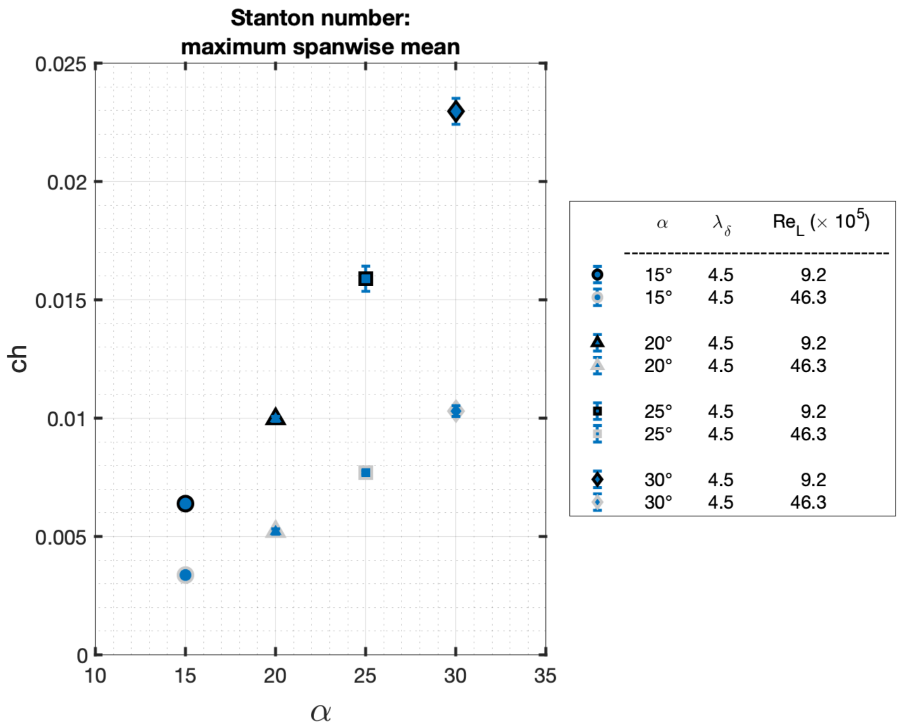

Figure H.15: **Nondimensional roughness strip wavelength:** $\lambda_\delta = 4.5$

H.1.5. Stanton Number versus Nondimensional Strip Wavelength λ_δ

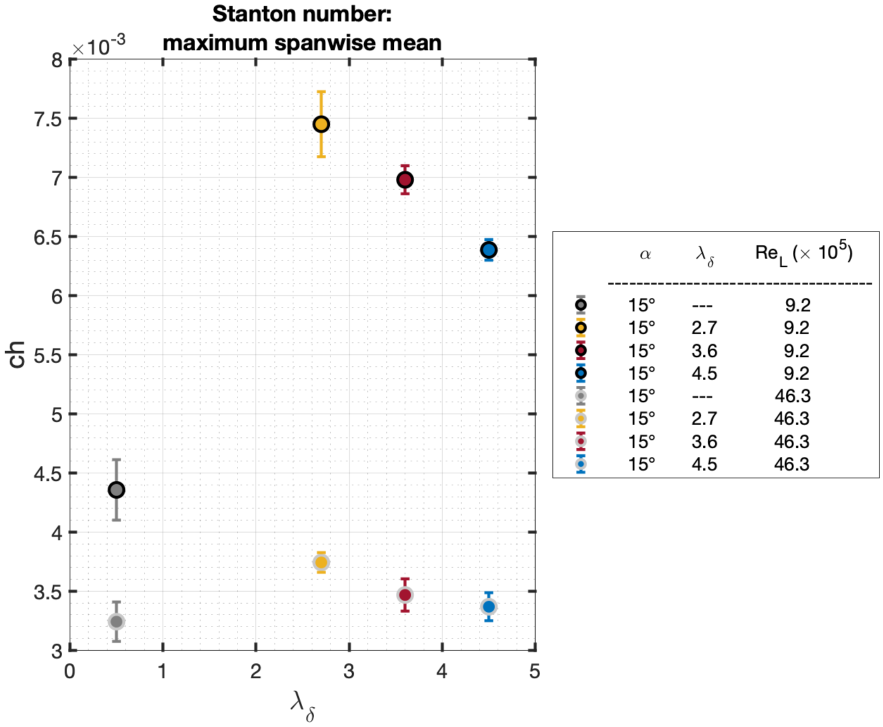

Figure H.16: **Ramp angle:** α = 15°

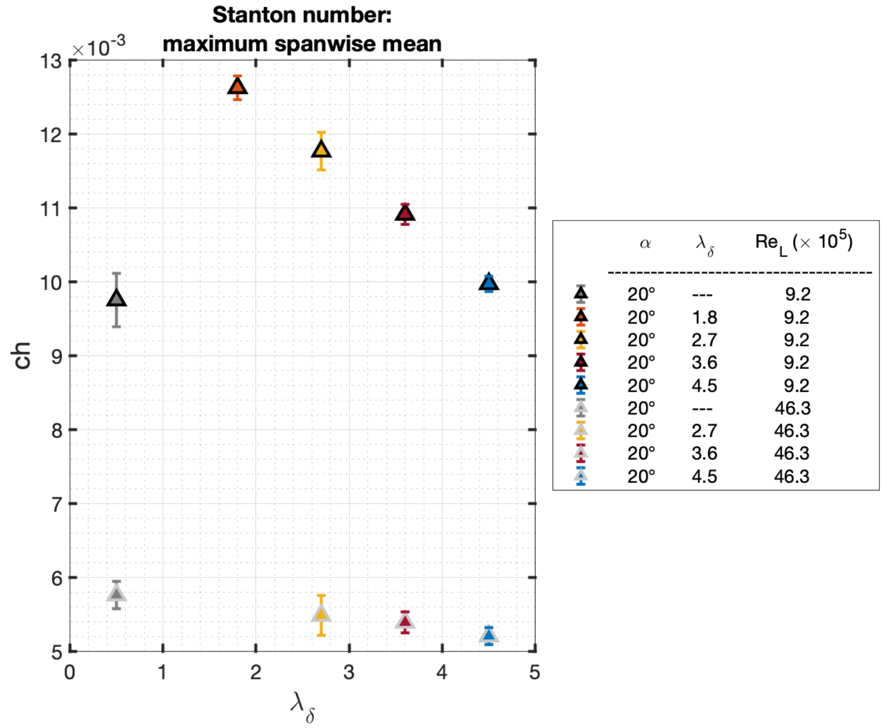

Figure H.17: **Ramp angle:** α = 20°

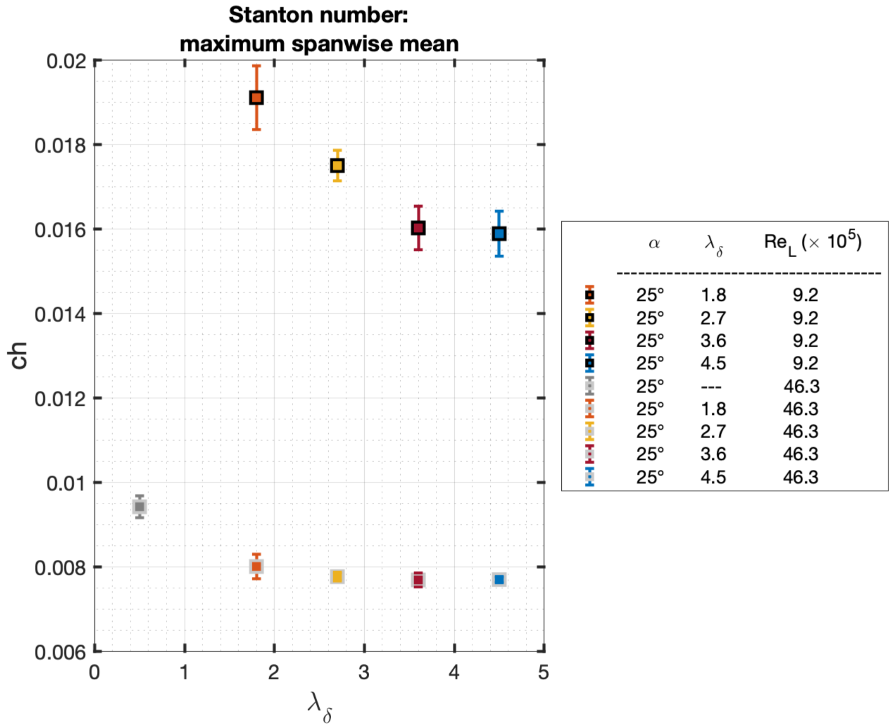

Figure H.18: **Ramp angle:** $\alpha = 25°$

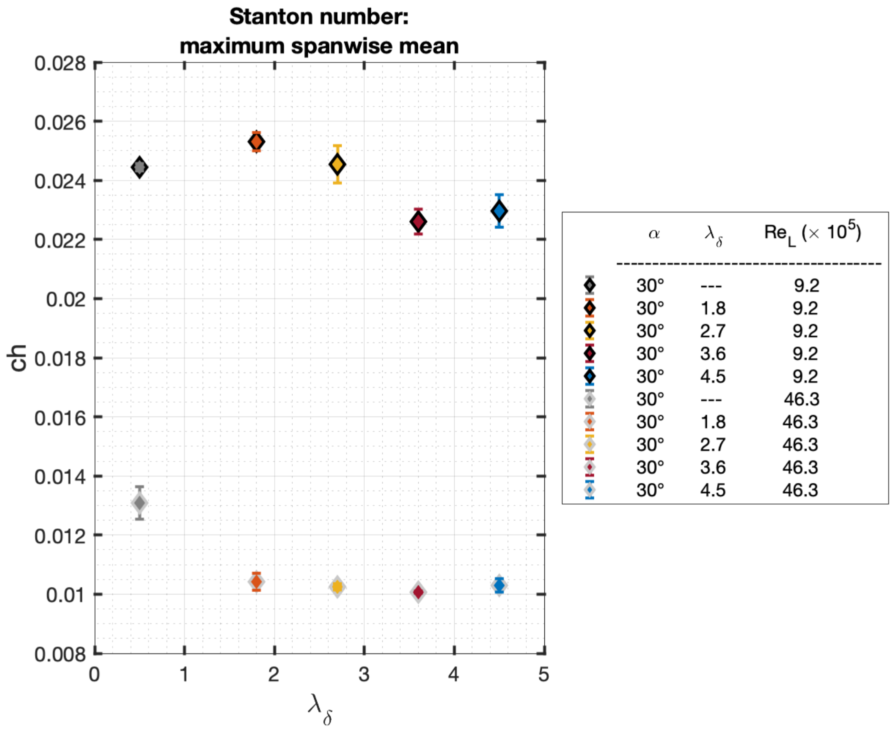

Figure H.19: **Ramp angle:** $\alpha = 30°$

H.2. RMS Results

H.2.1. Compiled Results

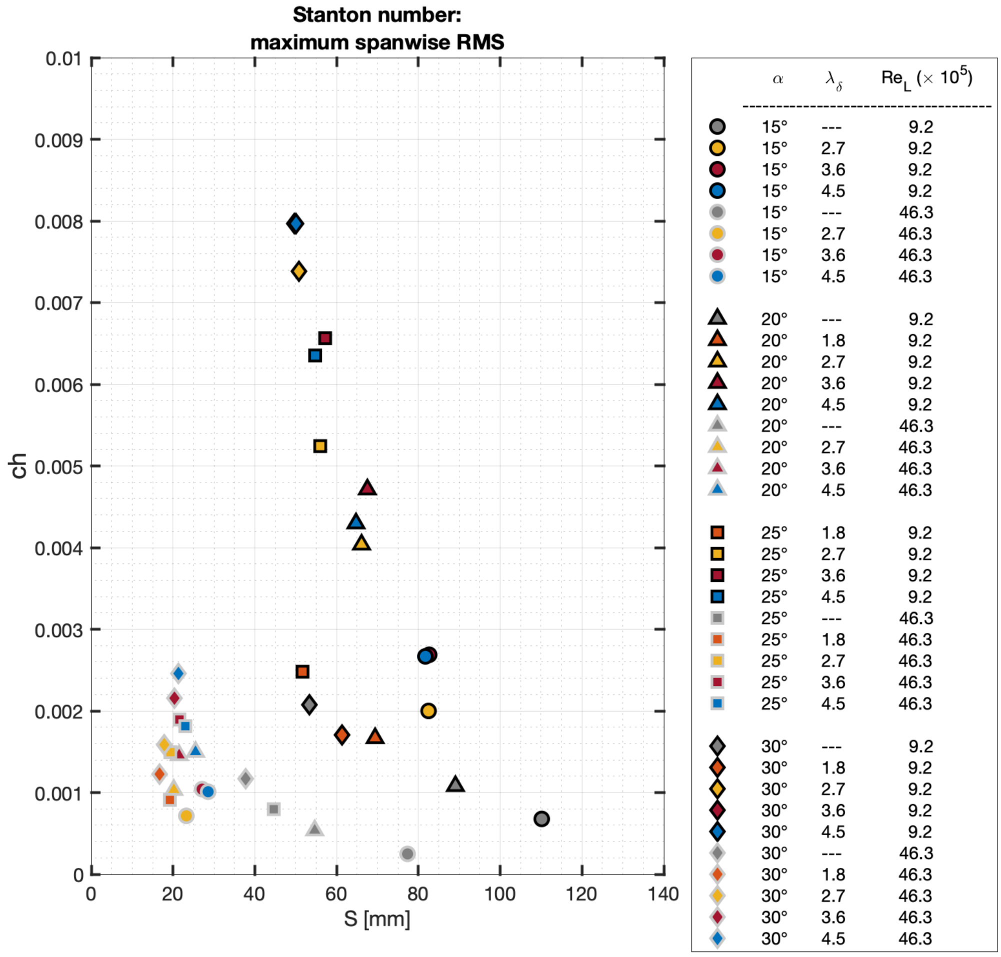

Figure H.20

H.2.2. Stanton Number versus S – Identified by Nondimensional Strip Wavelength λ_δ

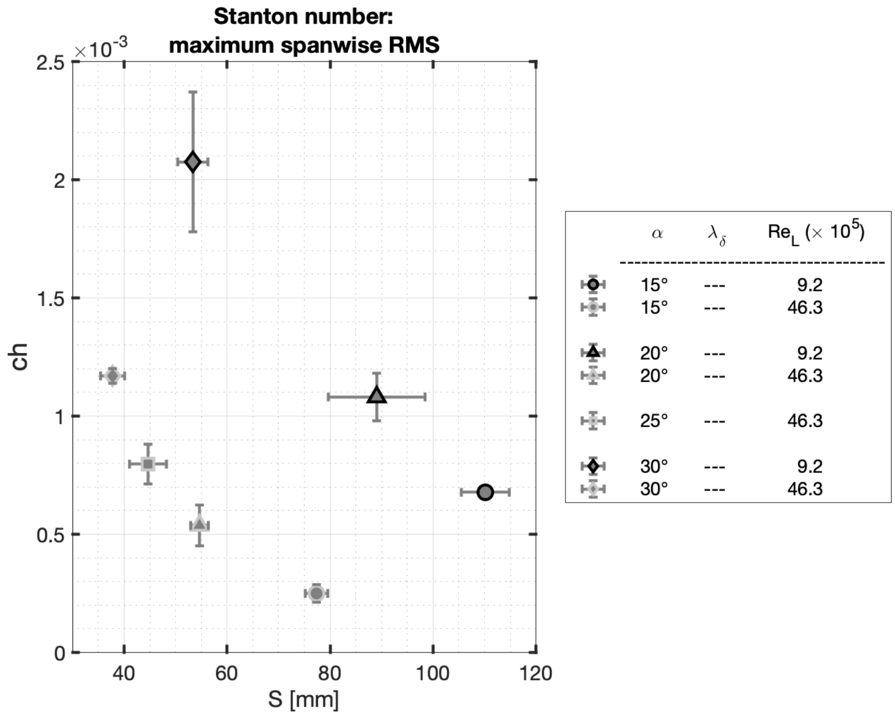

Figure H.21: **No roughness strip.**

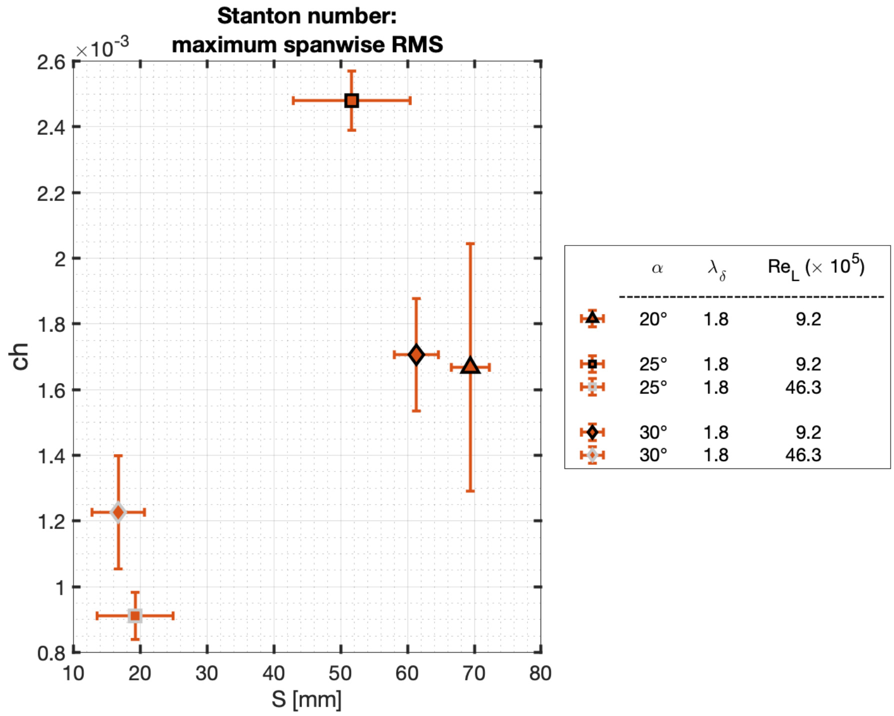

Figure H.22: **Nondimensional roughness strip wavelength:** $\lambda_\delta = 1.8$

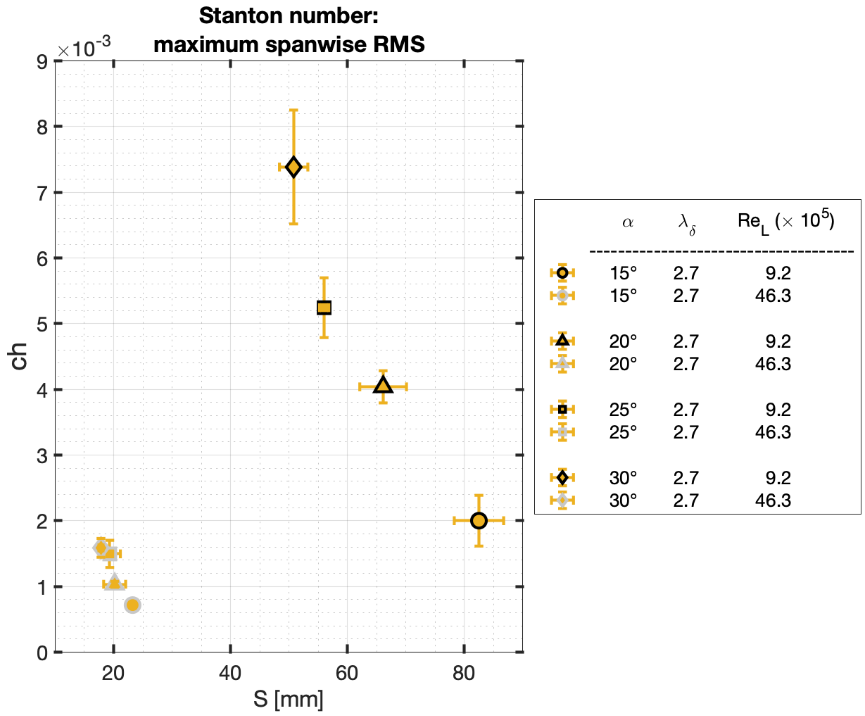

Figure H.23: **Nondimensional roughness strip wavelength:** $\lambda_\delta = 2.7$

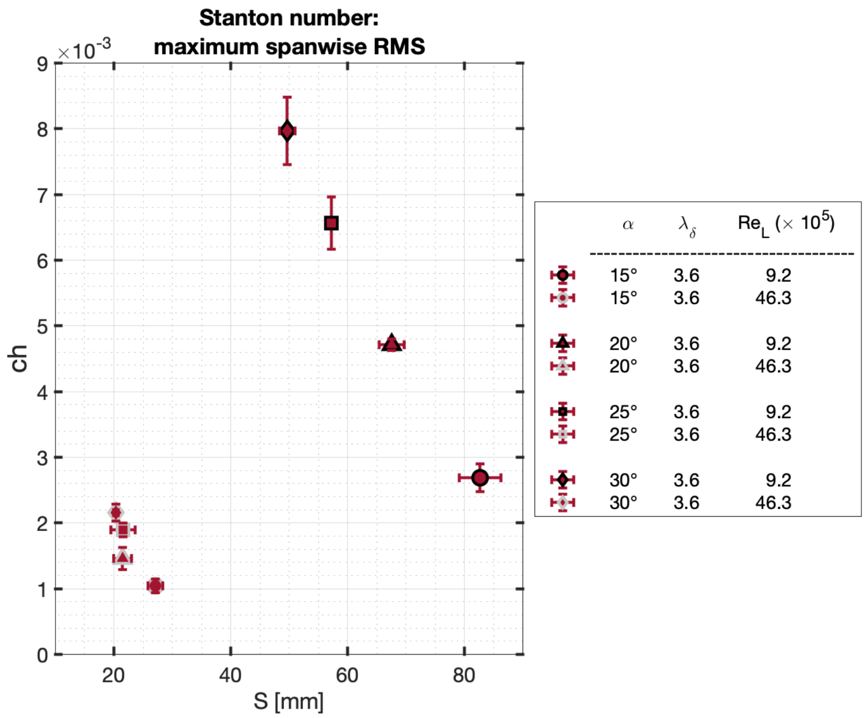

Figure H.24: **Nondimensional roughness strip wavelength:** $\lambda_\delta = 3.6$

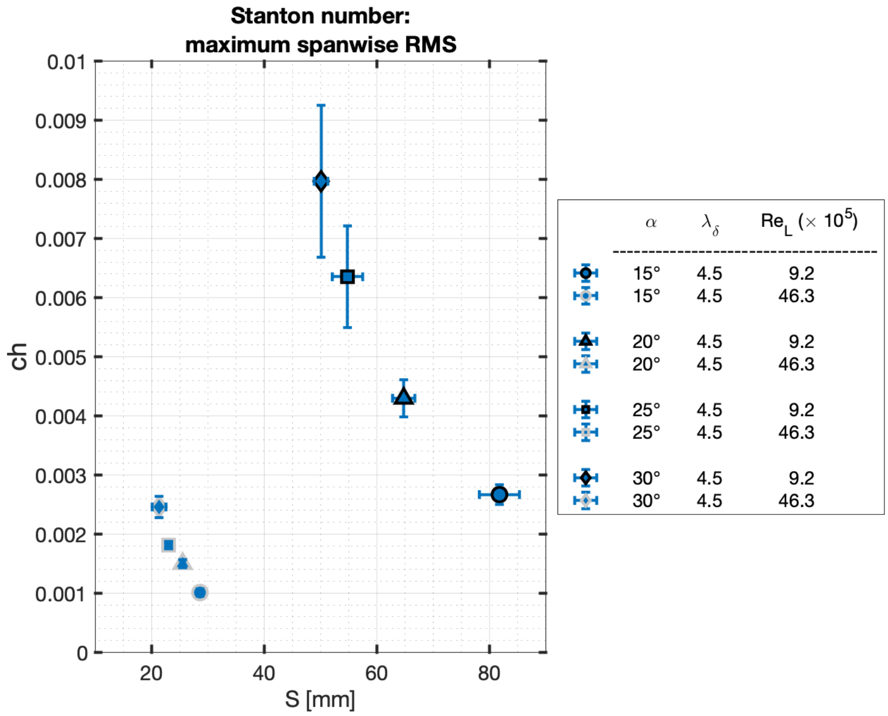

Figure H.25: **Nondimensional roughness strip wavelength:** $\lambda_\delta = 4.5$

H.2.3. Stanton Number versus S – Identified by Ramp Angle α

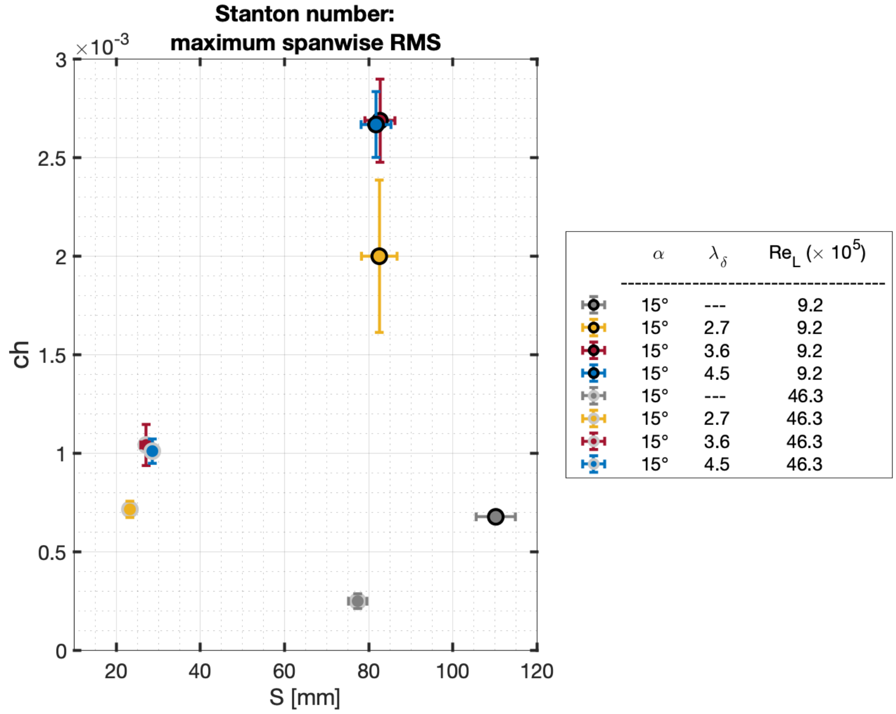

Figure H.26: **Ramp angle:** α = 15°

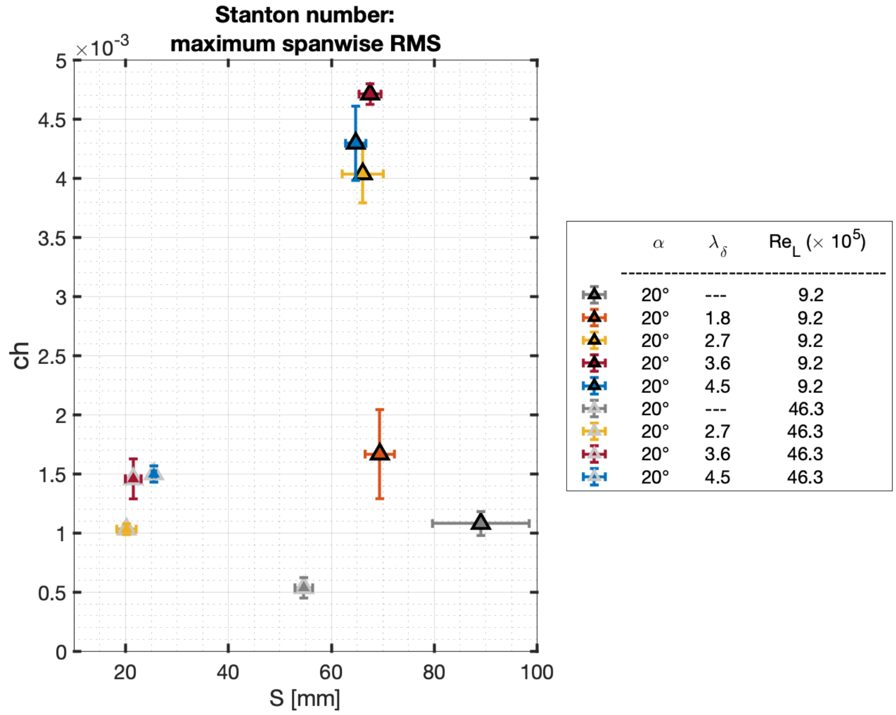

Figure H.27: **Ramp angle:** α = 20°

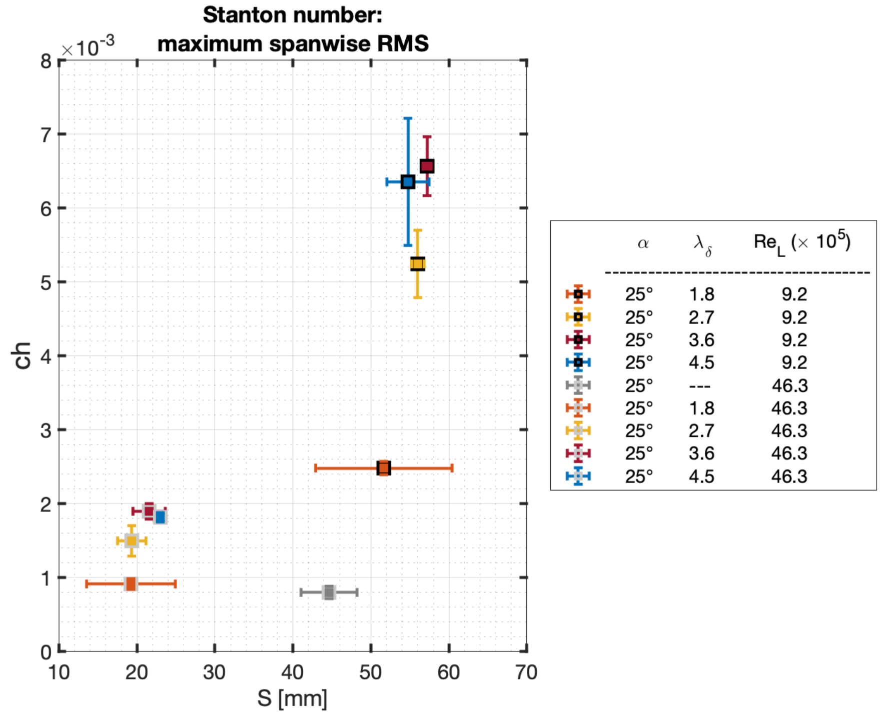

Figure H.28: **Ramp angle:** $\alpha = 25°$

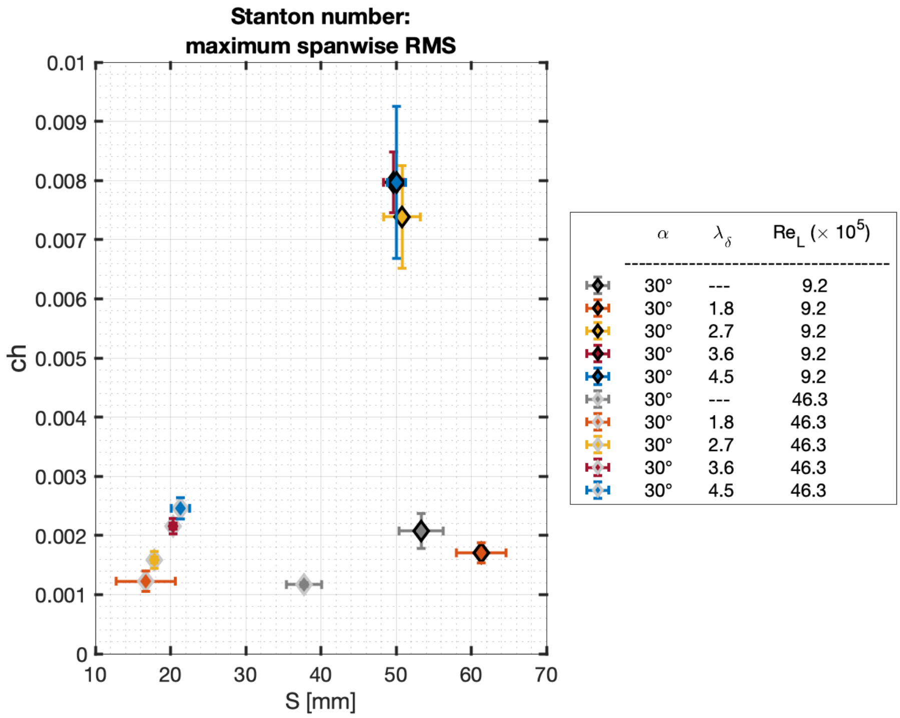

Figure H.29: **Ramp angle:** $\alpha = 30°$

H.2.4. Stanton Number versus Ramp Angle α

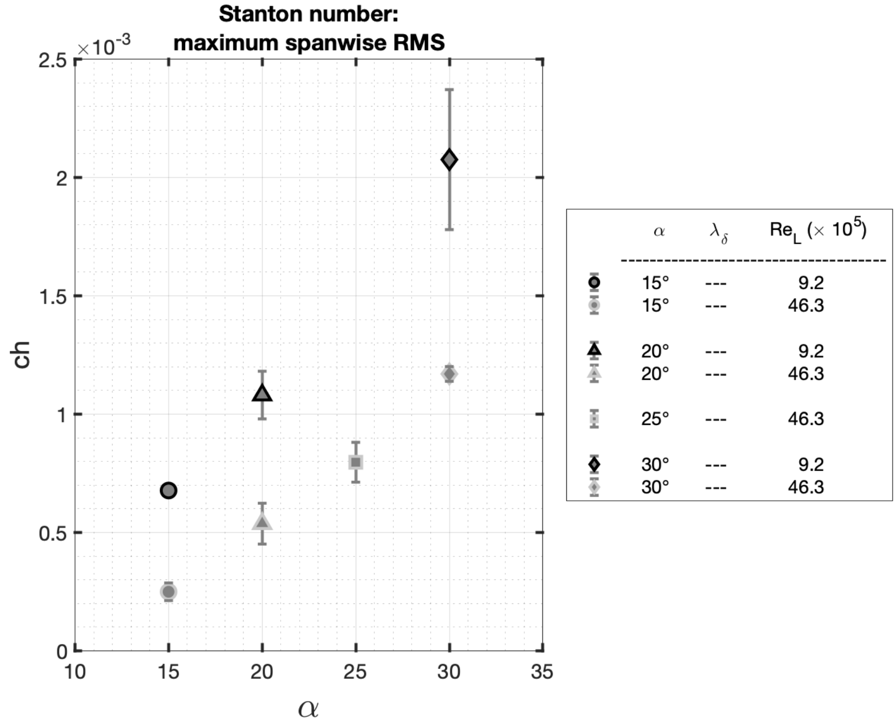

Figure H.30: **No roughness strip.**

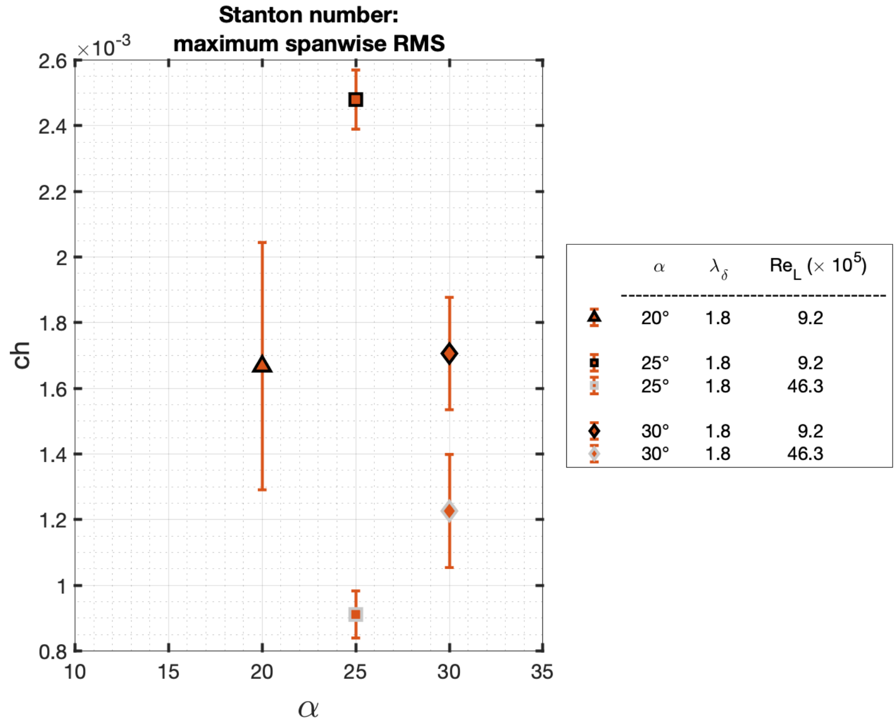

Figure H.31: **Nondimensional roughness strip wavelength:** $\lambda_{\delta} = 1.8$

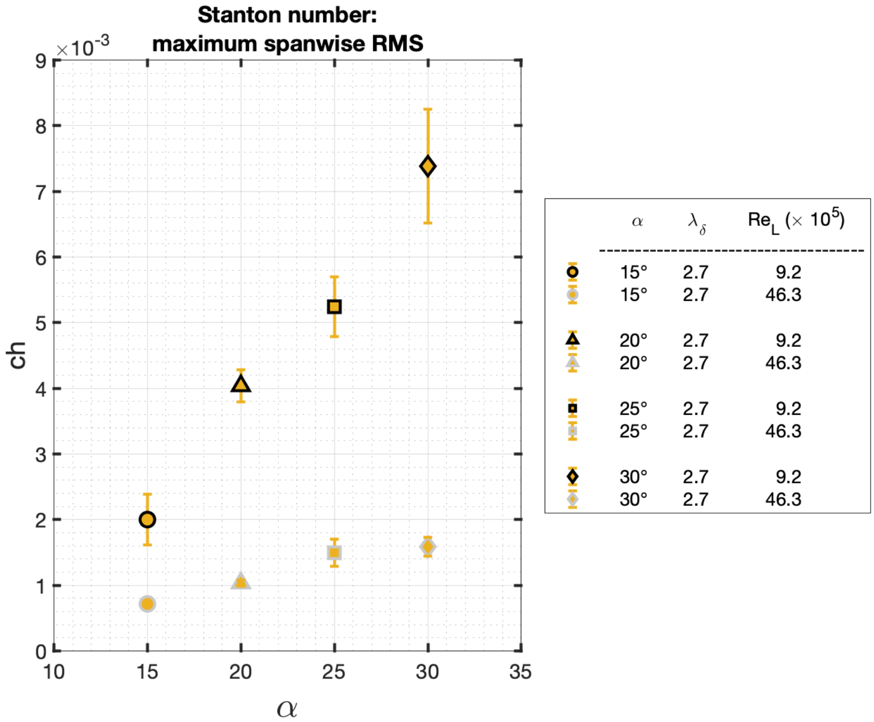

Figure H.32: **Nondimensional roughness strip wavelength:** $\lambda_\delta = 2.7$

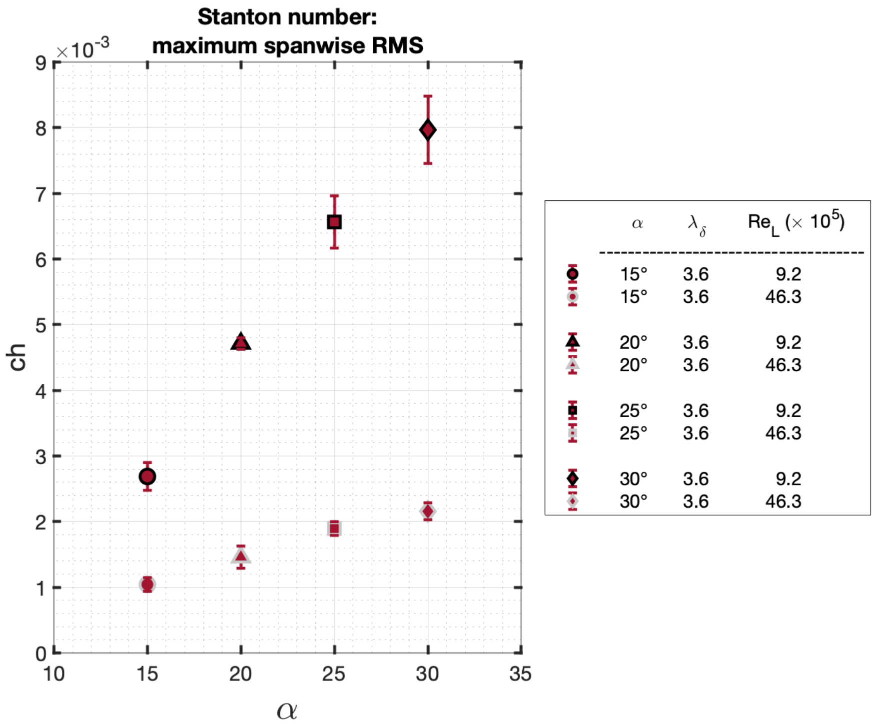

Figure H.33: **Nondimensional roughness strip wavelength:** $\lambda_\delta = 3.6$

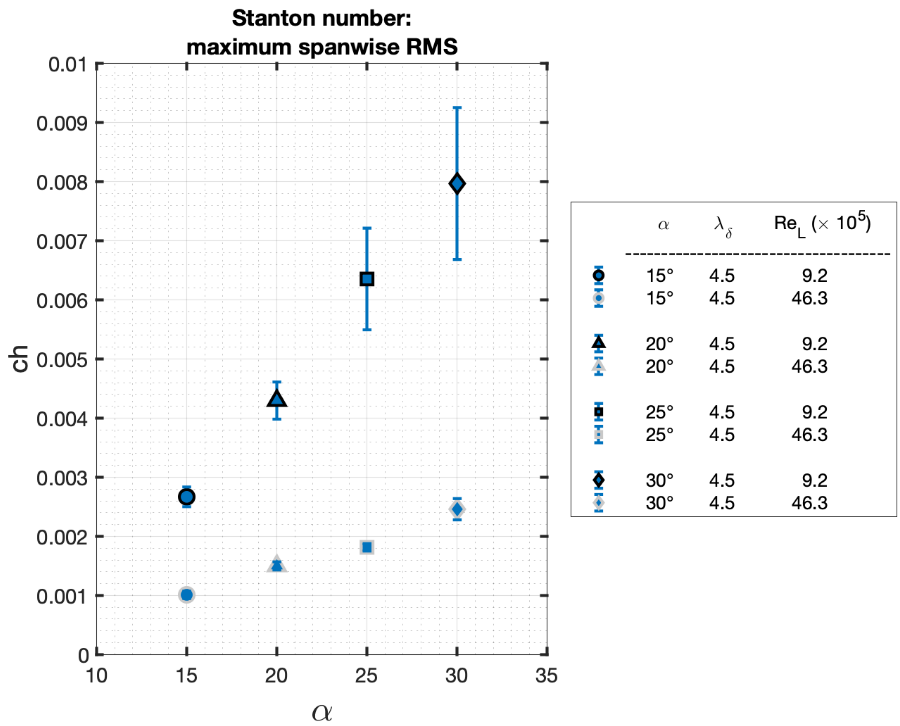

Figure H.34: **Nondimensional roughness strip wavelength:** $\lambda_\delta = 4.5$

H.2.5. Stanton Number versus Nondimensional Strip Wavelength λ_δ

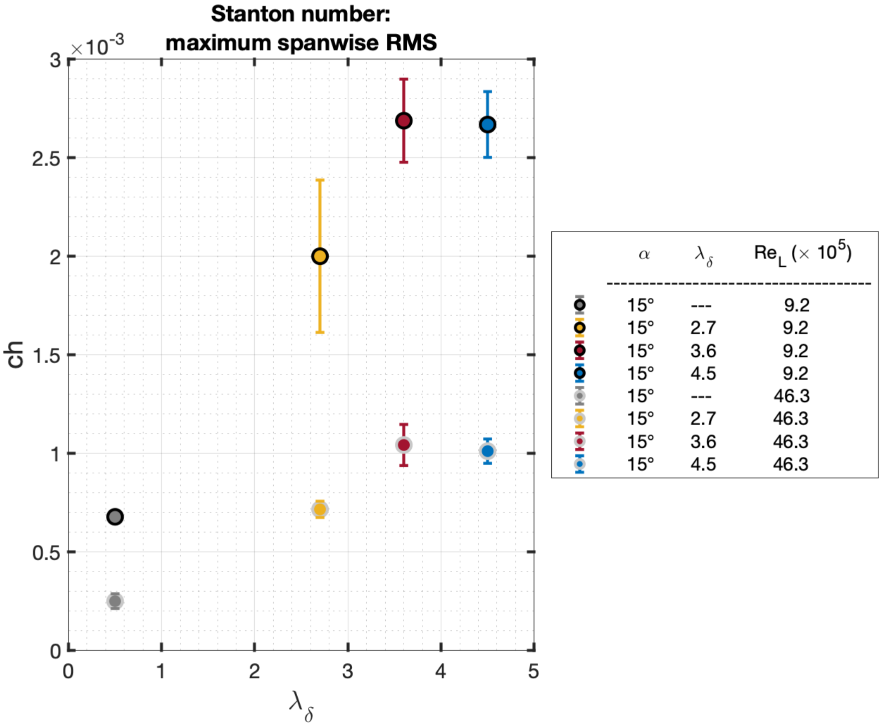

Figure H.35: **Ramp angle:** α = 15°

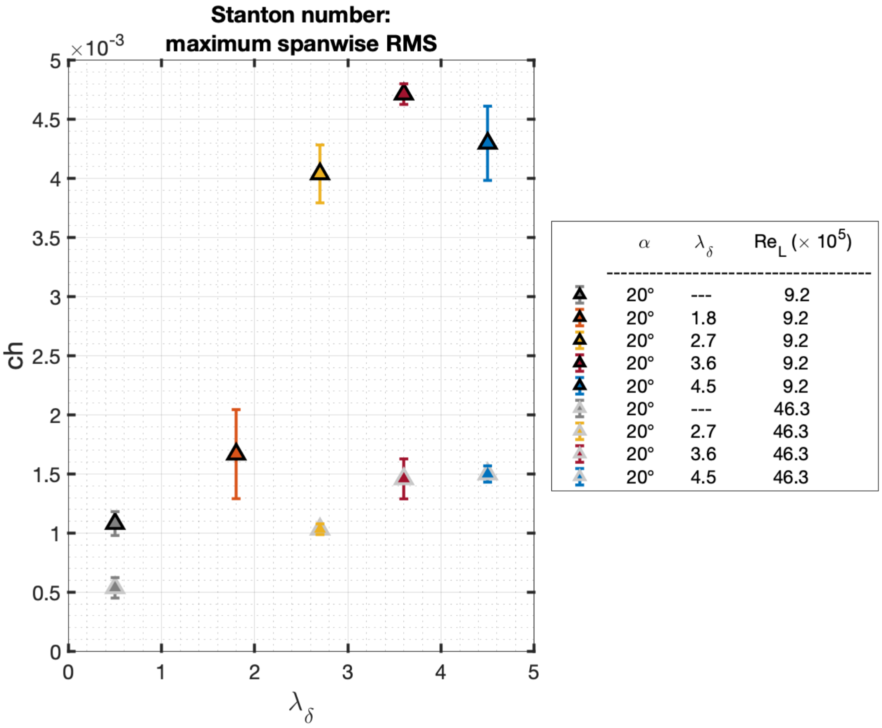

Figure H.36: **Ramp angle:** α = 20°

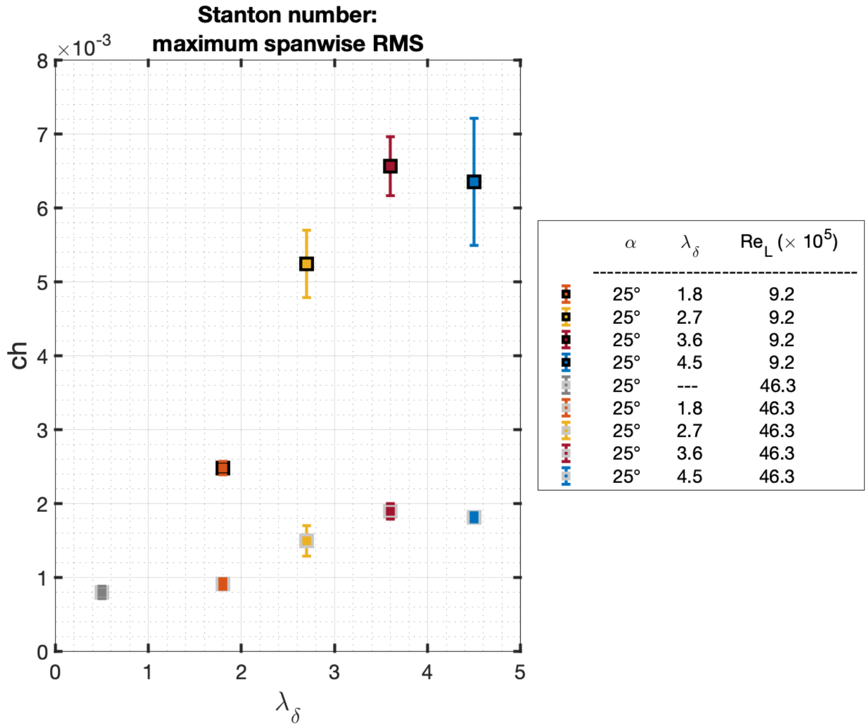

Figure H.37: **Ramp angle:** $\alpha = 25°$

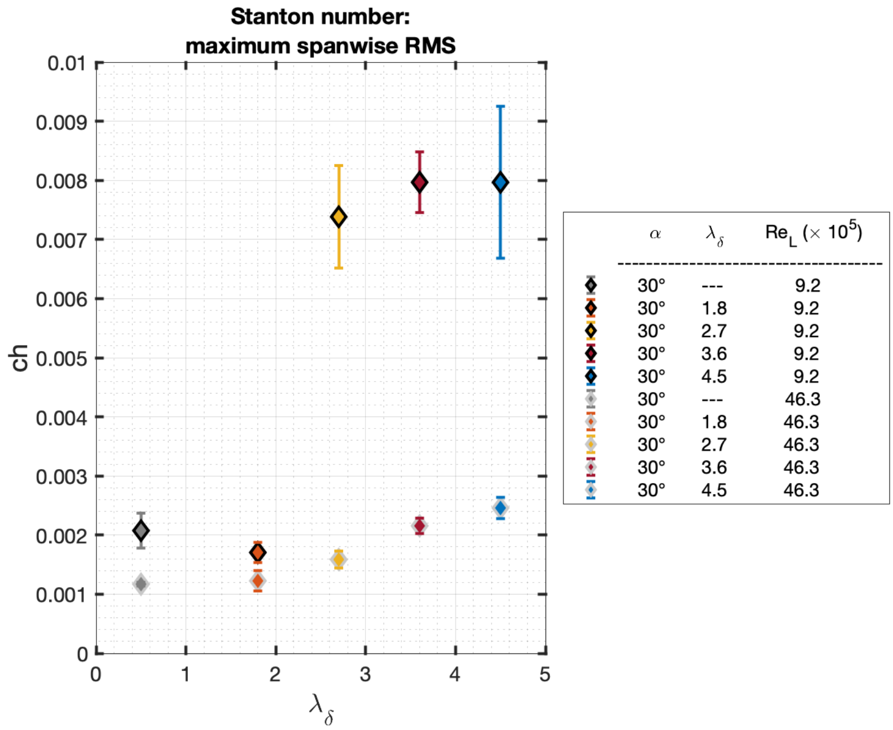

Figure H.38: **Ramp angle:** $\alpha = 30°$

Schlieren Images – Set A

This appendix presents schlieren images captured with the following specifications:

- Frame rate: 1.279 kHz
- Exposure time: $4.352\ \mu s$
- Spatial resolution: $9.52\ px/mm$
- Field of view: $212 \times 142\ mm^2$

These specifications yield a relatively large image window that includes nearly the entire span (i.e. diameter) of the test window, the entire inclined ramp, and the region of the flow that contains the bulk of the shock–boundary-layer interaction. For enhanced schlieren images of the shear layer and circulation region, the reader is referred to Appendix J.

I.1. Ramp angle of $15°$

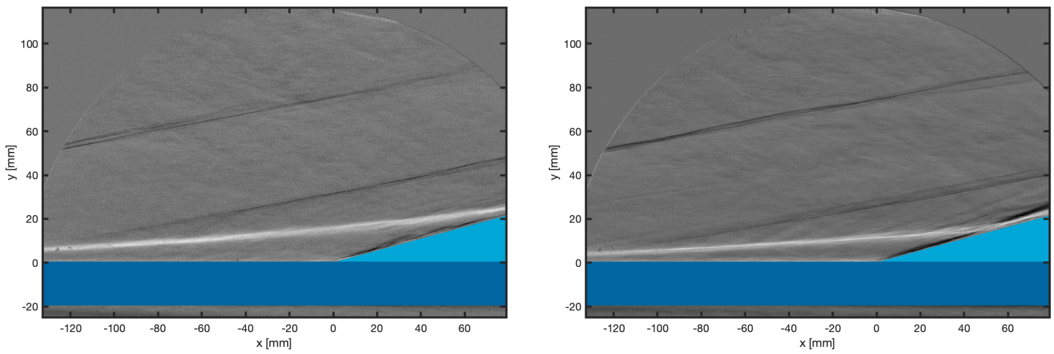

(a) $M_\infty = 7.5$; $Re = 9.2 \times 10^5$ (b) $M_\infty = 7.5$; $Re = 46.3 \times 10^5$

Figure I.1: **No roughness strip.**

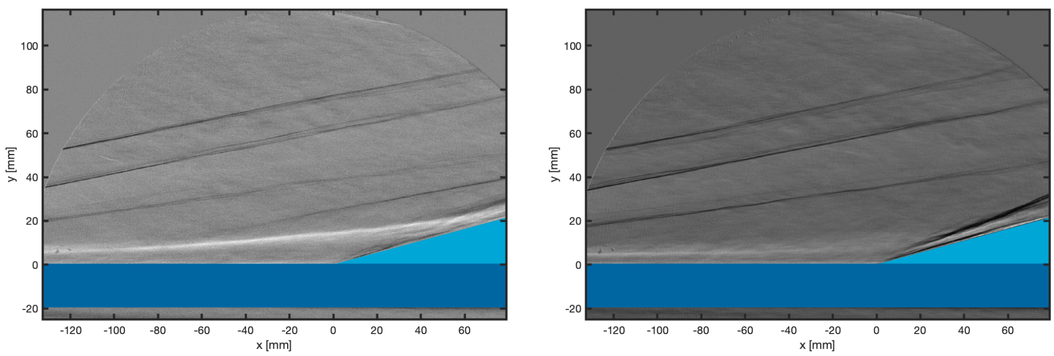

(a) $M_\infty = 7.5$; $Re = 9.2 \times 10^5$ (b) $M_\infty = 7.5$; $Re = 46.3 \times 10^5$

Figure I.2: **Nondimensional roughness strip wavelength:** $\lambda_\delta = 1.8$

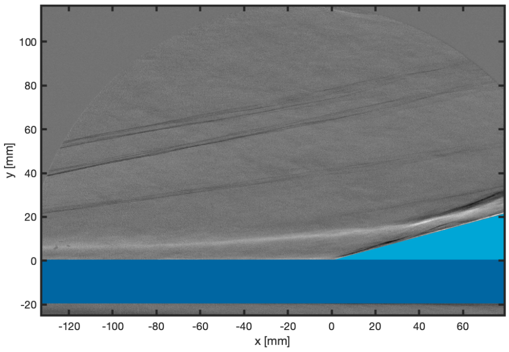

(a) $M_\infty = 7.5$; $Re = 9.2 \times 10^5$

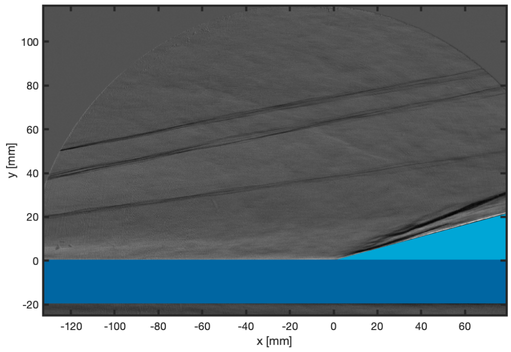

(b) $M_\infty = 7.5$; $Re = 46.3 \times 10^5$

Figure I.3: **Nondimensional roughness strip wavelength:** $\lambda_\delta = 2.7$

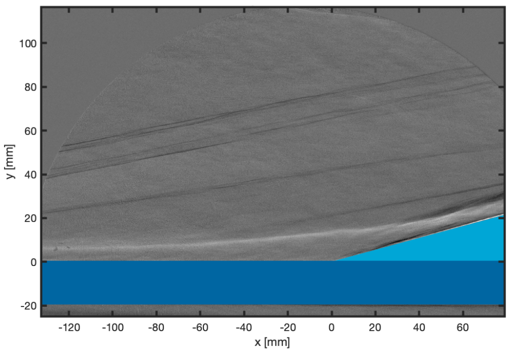

(a) $M_\infty = 7.5$; $Re = 9.2 \times 10^5$

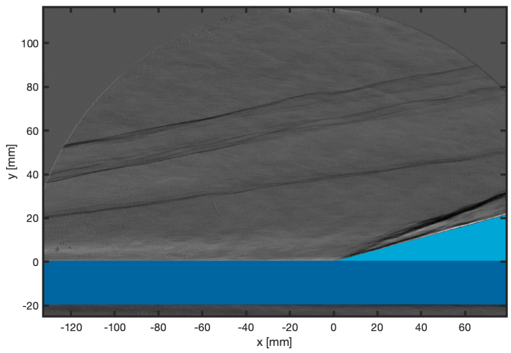

(b) $M_\infty = 7.5$; $Re = 46.3 \times 10^5$

Figure I.4: **Nondimensional roughness strip wavelength:** $\lambda_\delta = 3.6$

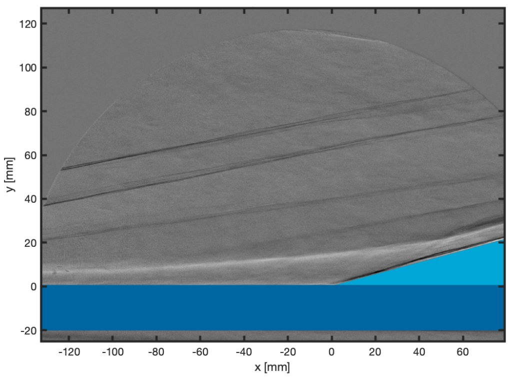

(a) $M_\infty = 7.5$; $Re = 9.2 \times 10^5$

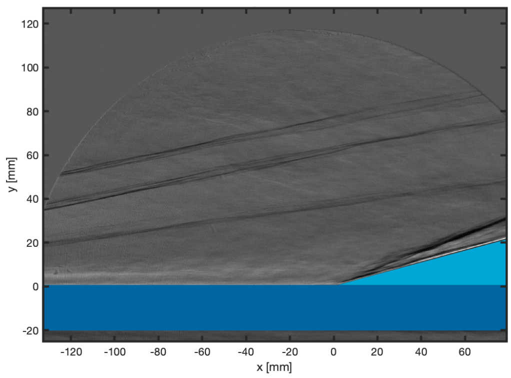

(b) $M_\infty = 7.5$; $Re = 46.3 \times 10^5$

Figure I.5: **Nondimensional roughness strip wavelength:** $\lambda_\delta = 4.5$

I.2. Ramp angle of $20°$

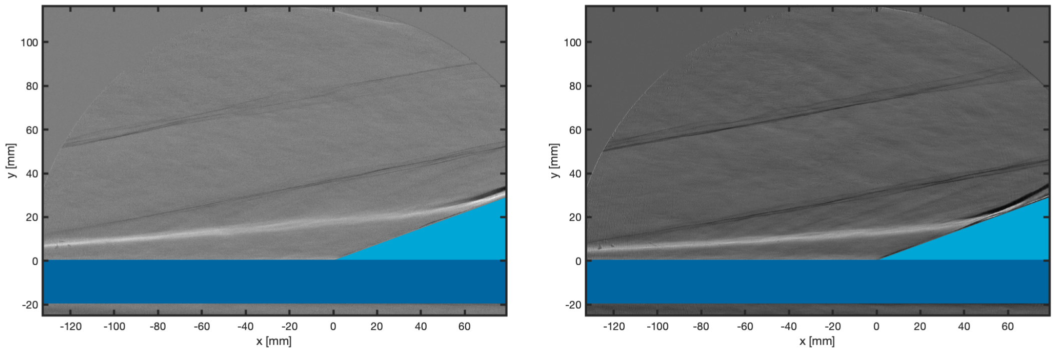

(a) $M_\infty = 7.5$; $Re = 9.2 \times 10^5$ (b) $M_\infty = 7.5$; $Re = 46.3 \times 10^5$

Figure I.6: **No roughness strip.**

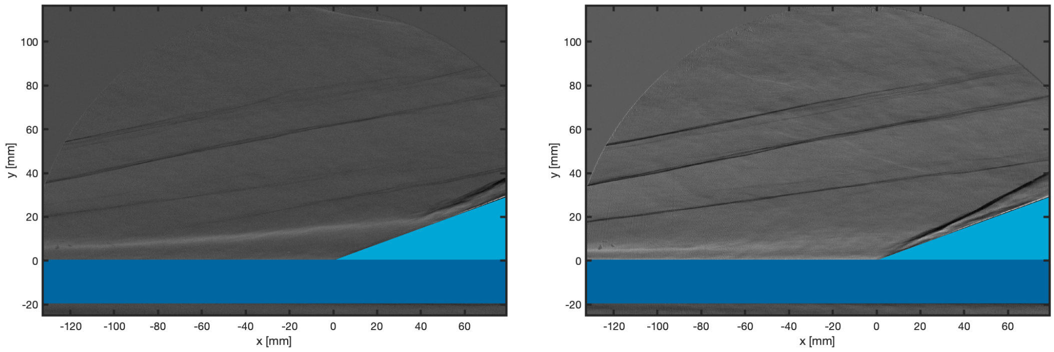

(a) $M_\infty = 7.5$; $Re = 9.2 \times 10^5$ (b) $M_\infty = 7.5$; $Re = 46.3 \times 10^5$

Figure I.7: **Nondimensional roughness strip wavelength:** $\lambda_\delta = 1.8$

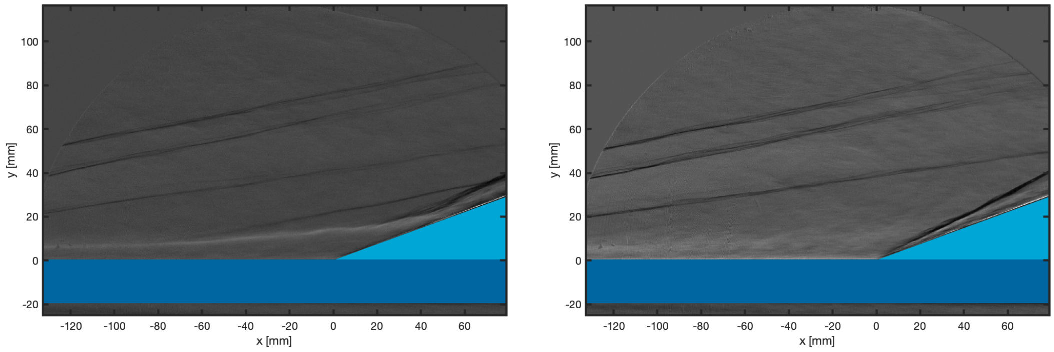

(a) $M_\infty = 7.5$; $Re = 9.2 \times 10^5$ (b) $M_\infty = 7.5$; $Re = 46.3 \times 10^5$

Figure I.8: **Nondimensional roughness strip wavelength:** $\lambda_\delta = 2.7$

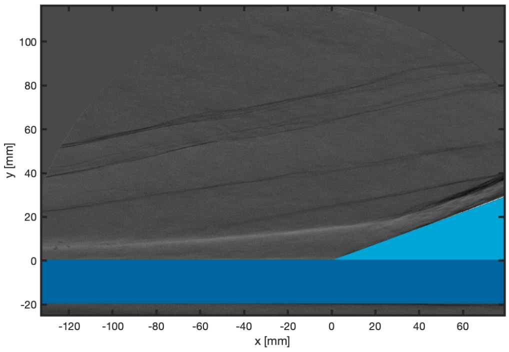

(a) $M_\infty = 7.5$; $Re = 9.2 \times 10^5$

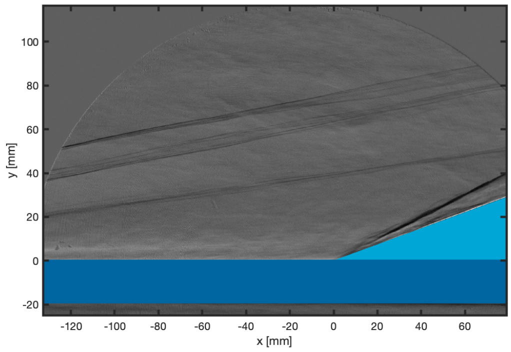

(b) $M_\infty = 7.5$; $Re = 46.3 \times 10^5$

Figure I.9: **Nondimensional roughness strip wavelength:** $\lambda_\delta = 3.6$

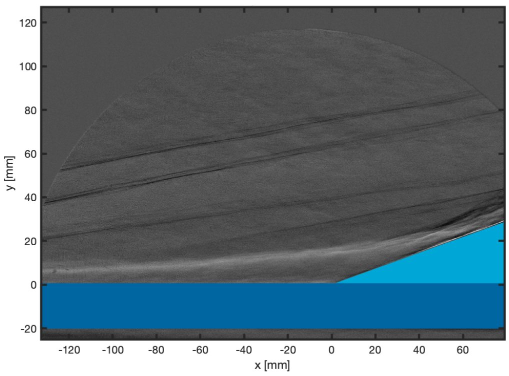

(a) $M_\infty = 7.5$; $Re = 9.2 \times 10^5$

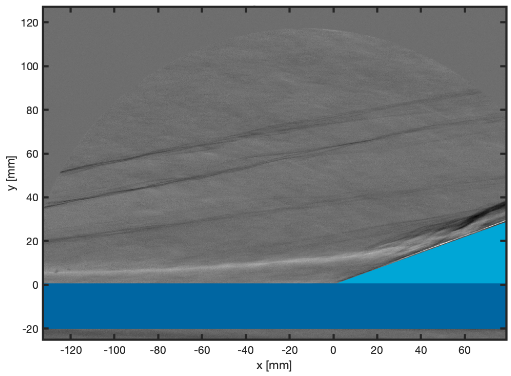

(b) $M_\infty = 7.5$; $Re = 46.3 \times 10^5$

Figure I.10: **Nondimensional roughness strip wavelength:** $\lambda_\delta = 4.5$

I.3. Ramp angle of $25°$

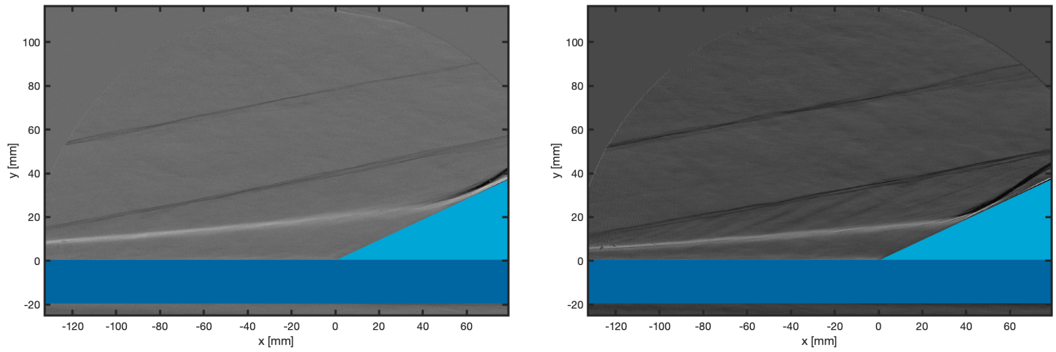

(a) $M_\infty = 7.5$; $Re = 9.2 \times 10^5$

(b) $M_\infty = 7.5$; $Re = 46.3 \times 10^5$

Figure I.11: **No roughness strip.**

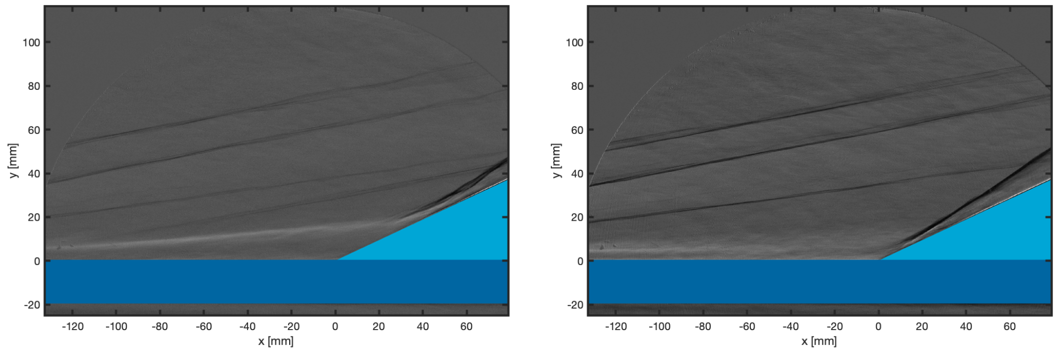

(a) $M_\infty = 7.5$; $Re = 9.2 \times 10^5$

(b) $M_\infty = 7.5$; $Re = 46.3 \times 10^5$

Figure I.12: **Nondimensional roughness strip wavelength:** $\lambda_\delta = 1.8$

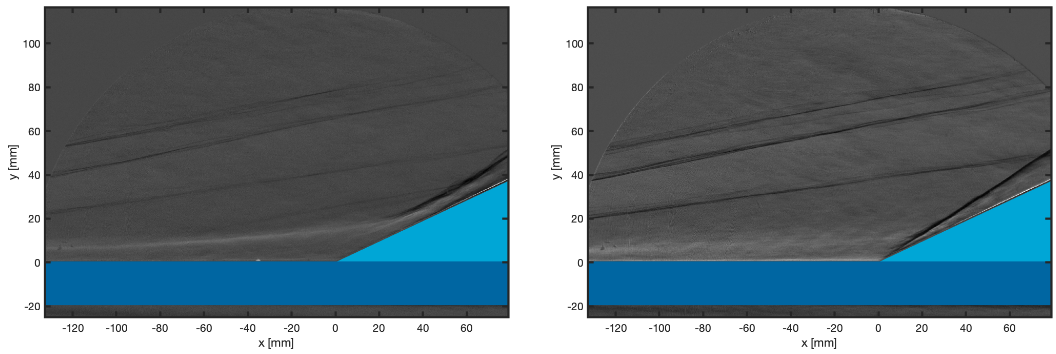

(a) $M_\infty = 7.5$; $Re = 9.2 \times 10^5$

(b) $M_\infty = 7.5$; $Re = 46.3 \times 10^5$

Figure I.13: **Nondimensional roughness strip wavelength:** $\lambda_\delta = 2.7$

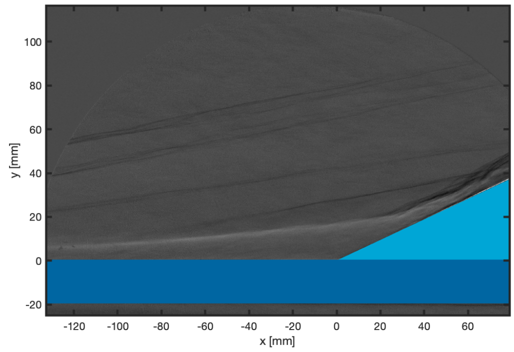

(a) $M_\infty = 7.5$; $Re = 9.2 \times 10^5$

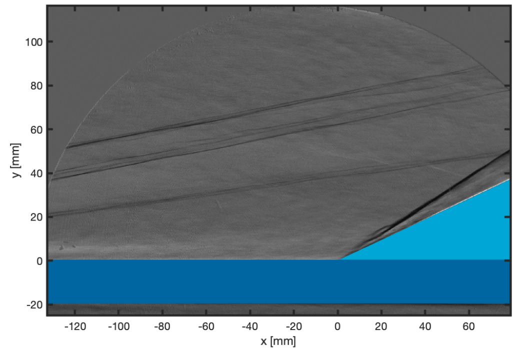

(b) $M_\infty = 7.5$; $Re = 46.3 \times 10^5$

Figure I.14: **Nondimensional roughness strip wavelength:** $\lambda_\delta = 3.6$

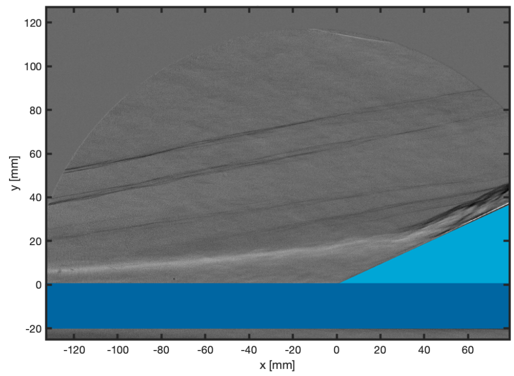

(a) $M_\infty = 7.5$; $Re = 9.2 \times 10^5$

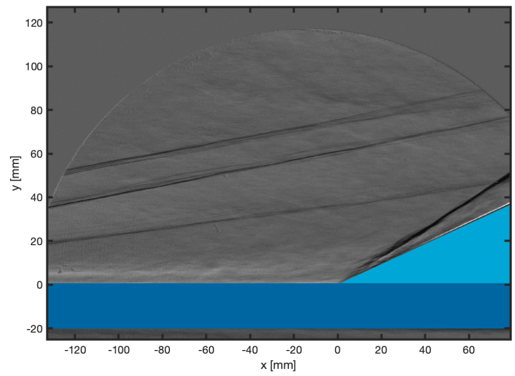

(b) $M_\infty = 7.5$; $Re = 46.3 \times 10^5$

Figure I.15: **Nondimensional roughness strip wavelength:** $\lambda_\delta = 4.5$

I.4. Ramp angle of 30°

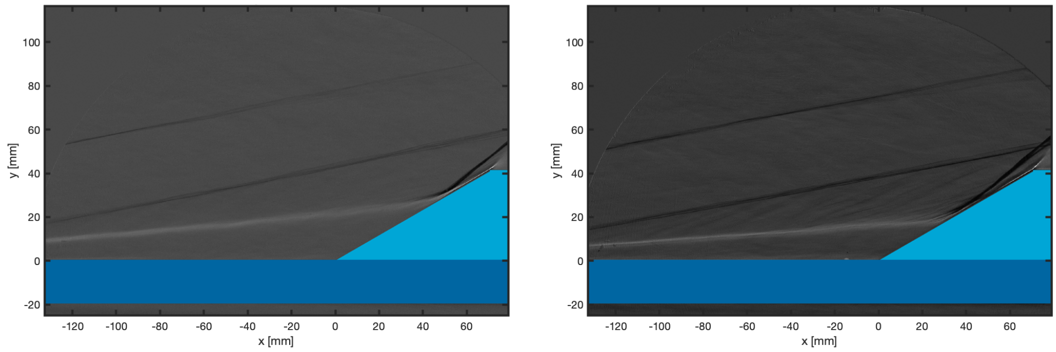

(a) $M_\infty = 7.5$; $Re = 9.2 \times 10^5$ (b) $M_\infty = 7.5$; $Re = 46.3 \times 10^5$

Figure I.16: **No roughness strip.**

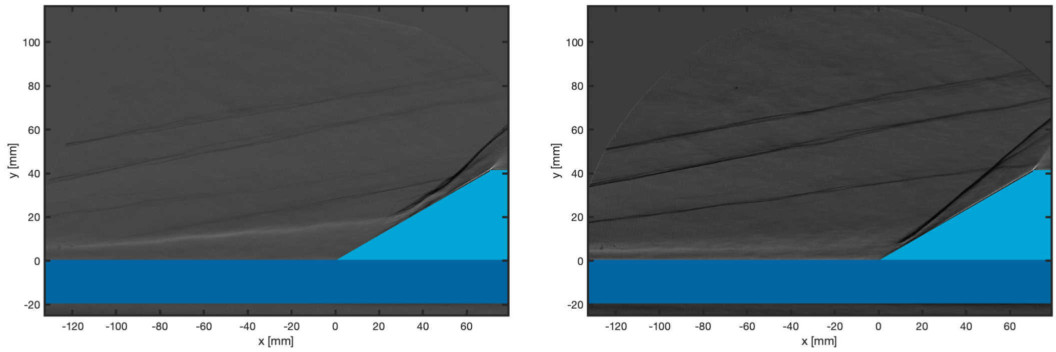

(a) $M_\infty = 7.5$; $Re = 9.2 \times 10^5$ (b) $M_\infty = 7.5$; $Re = 46.3 \times 10^5$

Figure I.17: **Nondimensional roughness strip wavelength:** $\lambda_\delta = 1.8$

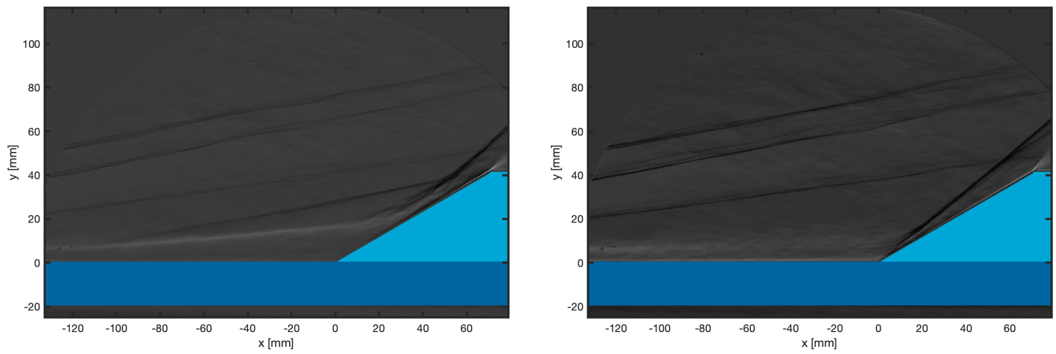

(a) $M_\infty = 7.5$; $Re = 9.2 \times 10^5$ (b) $M_\infty = 7.5$; $Re = 46.3 \times 10^5$

Figure I.18: **Nondimensional roughness strip wavelength:** $\lambda_\delta = 2.7$

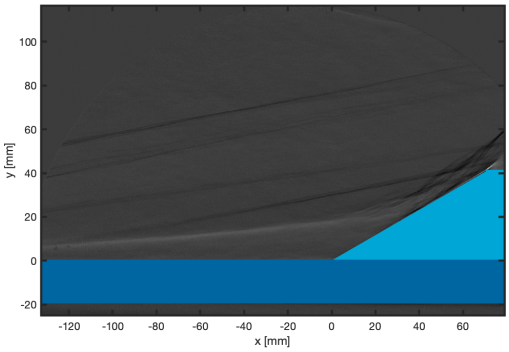

(a) $M_\infty = 7.5$; $Re = 9.2 \times 10^5$

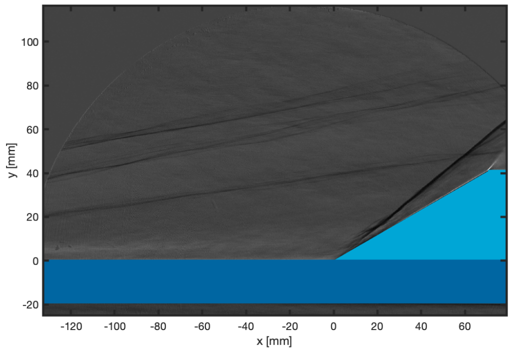

(b) $M_\infty = 7.5$; $Re = 46.3 \times 10^5$

Figure I.19: **Nondimensional roughness strip wavelength:** $\lambda_\delta = 3.6$

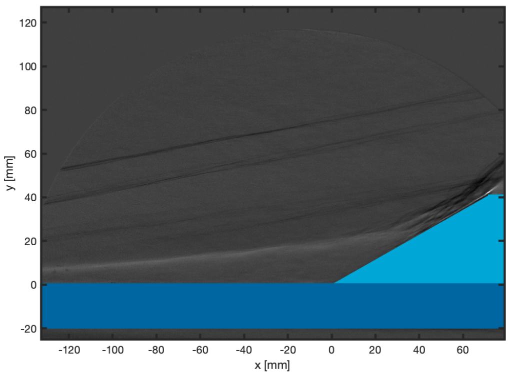

(a) $M_\infty = 7.5$; $Re = 9.2 \times 10^5$

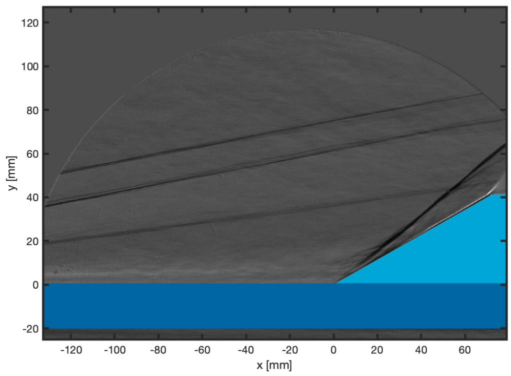

(b) $M_\infty = 7.5$; $Re = 46.3 \times 10^5$

Figure I.20: **Nondimensional roughness strip wavelength:** $\lambda_\delta = 4.5$

J
Schlieren Images – Set B

This appendix presents schlieren images captured with the following specifications:

- Frame rate = 28.975 kHz
- Exposure time = $1.28\ \mu s$
- Spatial resolution: $4.57\ px/mm$
- Field of view: $147 \times 39\ mm^2$

These specifications yield a smaller image window than those specified in Appendix I. The main purpose of capturing schlieren images under these specifications is to closely observe the overall behavior of the shear layer and circulation region of the shock–boundary-layer interaction.

J.1. Ramp angle of $15°$

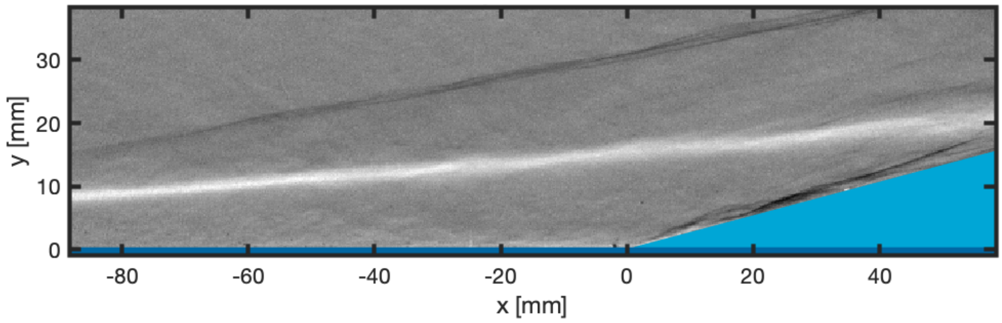

(a) $M_\infty = 7.5$; $Re = 9.2 \times 10^5$

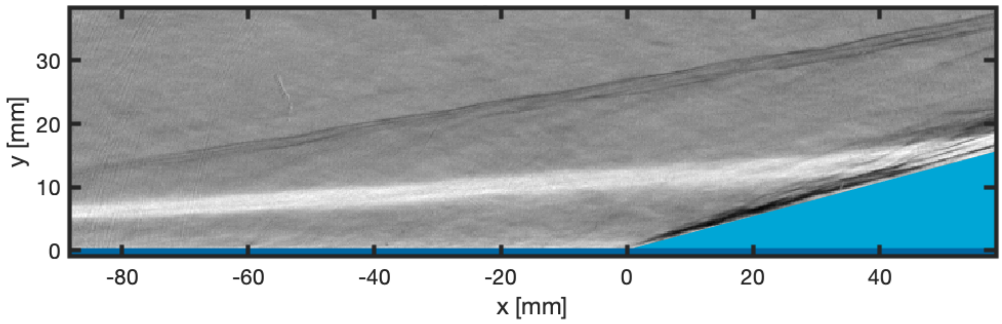

(b) $M_\infty = 7.5$; $Re = 46.3 \times 10^5$

Figure J.1: **No roughness strip.**

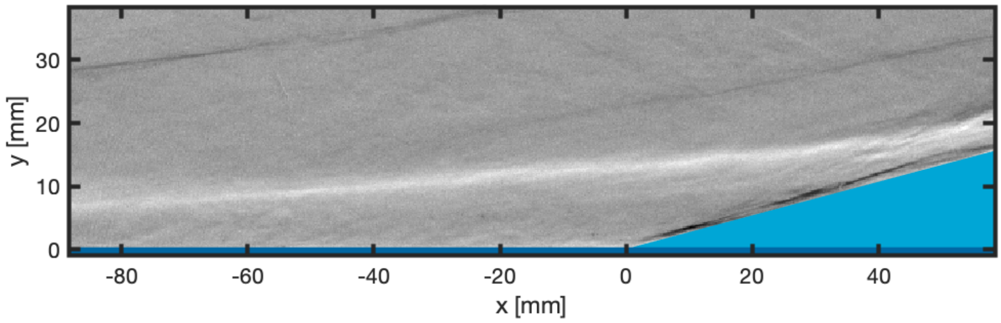

(a) $M_\infty = 7.5$; $Re = 9.2 \times 10^5$

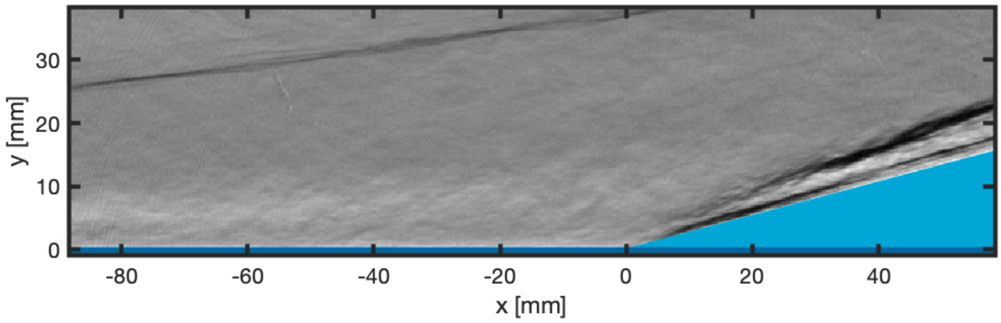

(b) $M_\infty = 7.5$; $Re = 46.3 \times 10^5$

Figure J.2: **Nondimensional roughness strip wavelength:** $\lambda_\delta = 1.8$

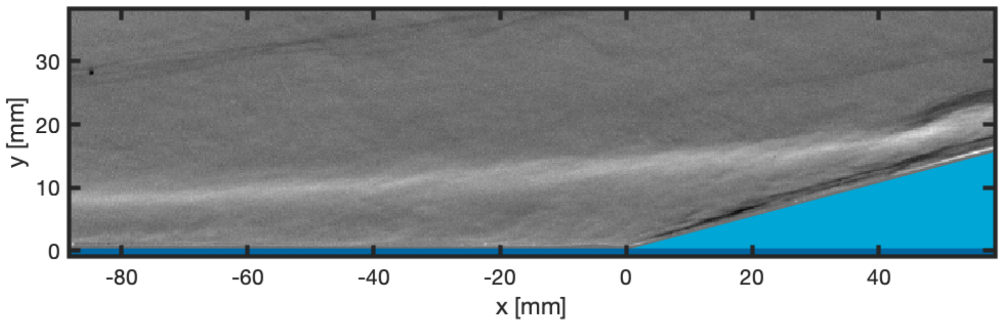

(a) $M_\infty = 7.5$; $Re = 9.2 \times 10^5$

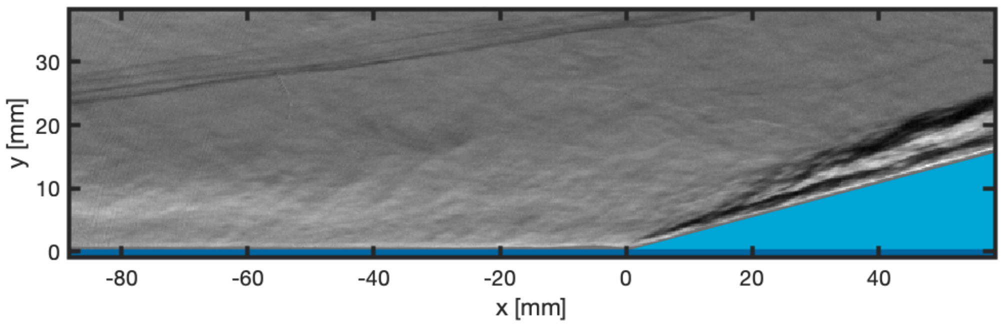

(b) $M_\infty = 7.5$; $Re = 46.3 \times 10^5$

Figure J.3: **Nondimensional roughness strip wavelength:** $\lambda_\delta = 2.7$

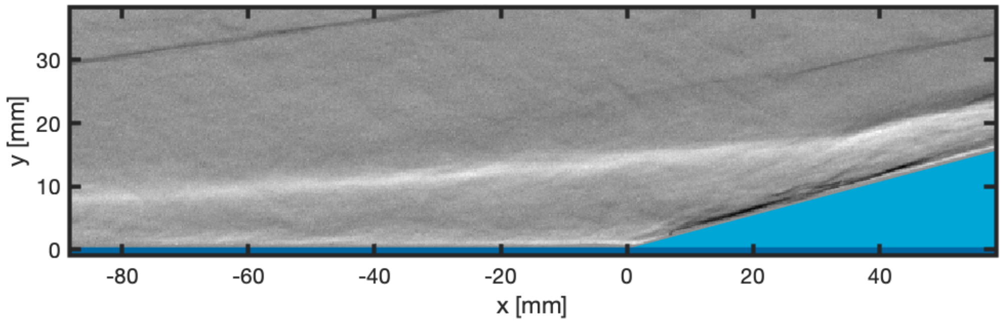

(a) $M_\infty = 7.5$; $Re = 9.2 \times 10^5$

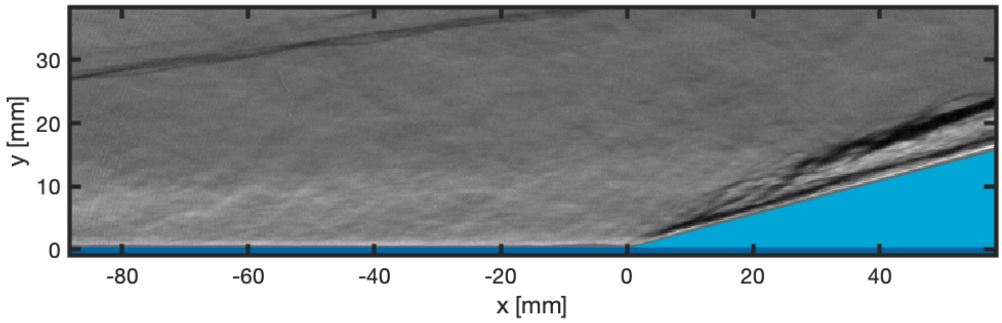

(b) $M_\infty = 7.5$; $Re = 46.3 \times 10^5$

Figure J.4: **Nondimensional roughness strip wavelength:** $\lambda_\delta = 3.6$

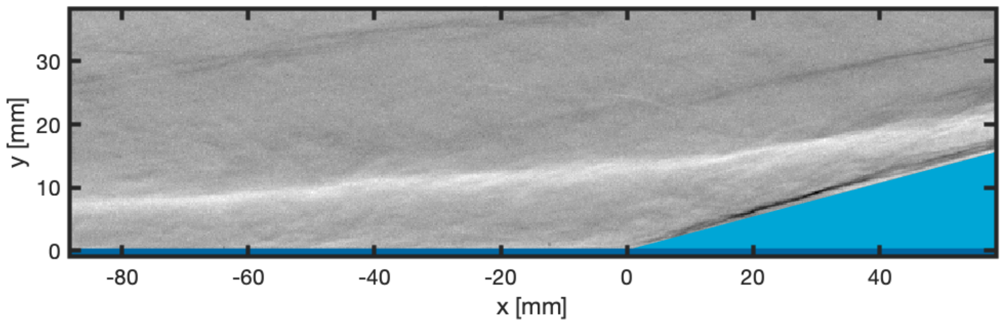

(a) $M_\infty = 7.5$; $Re = 9.2 \times 10^5$

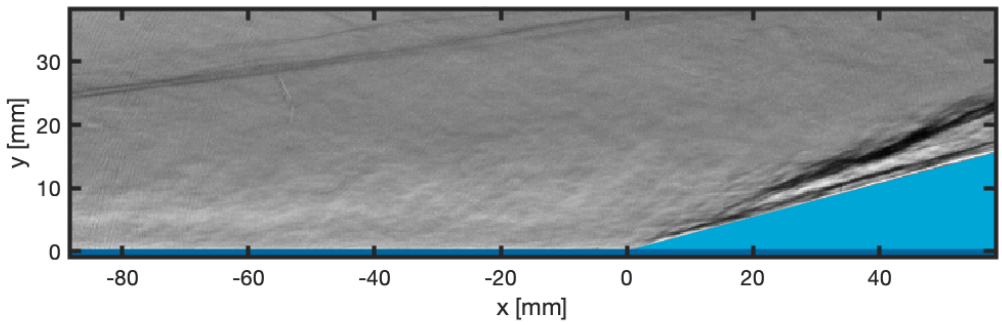

(b) $M_\infty = 7.5$; $Re = 46.3 \times 10^5$

Figure J.5: **Nondimensional roughness strip wavelength:** $\lambda_\delta = 4.5$

J.2. Ramp angle of $20°$

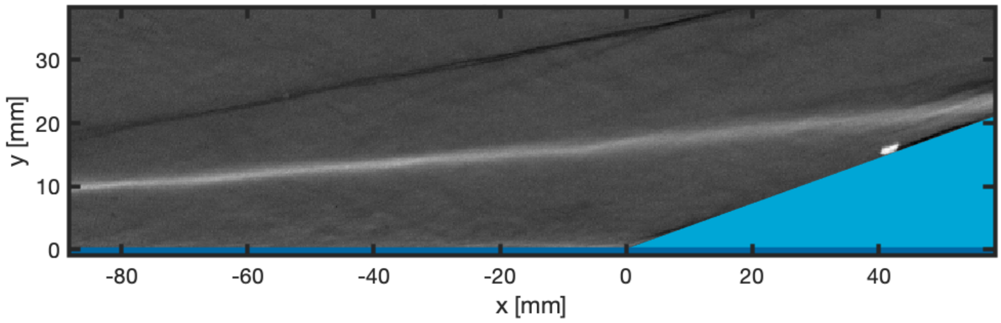

(a) $M_\infty = 7.5$; $Re = 9.2 \times 10^5$

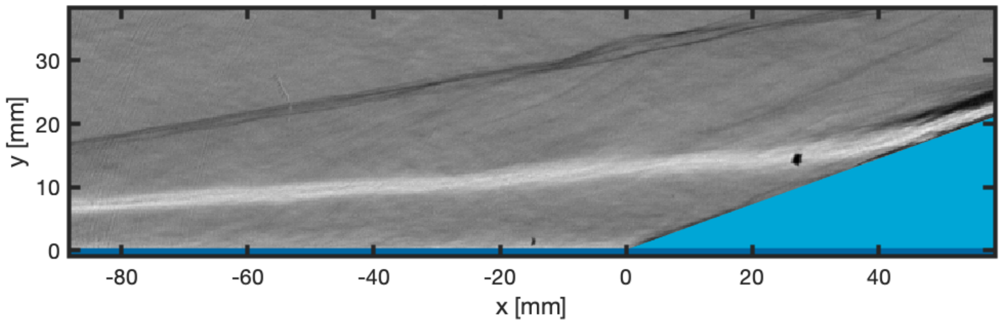

(b) $M_\infty = 7.5$; $Re = 46.3 \times 10^5$

Figure J.6: **No roughness strip.**

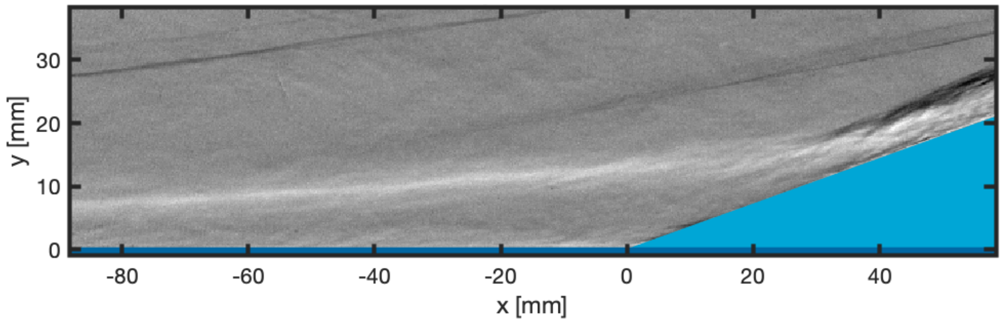

(a) $M_\infty = 7.5$; $Re = 9.2 \times 10^5$

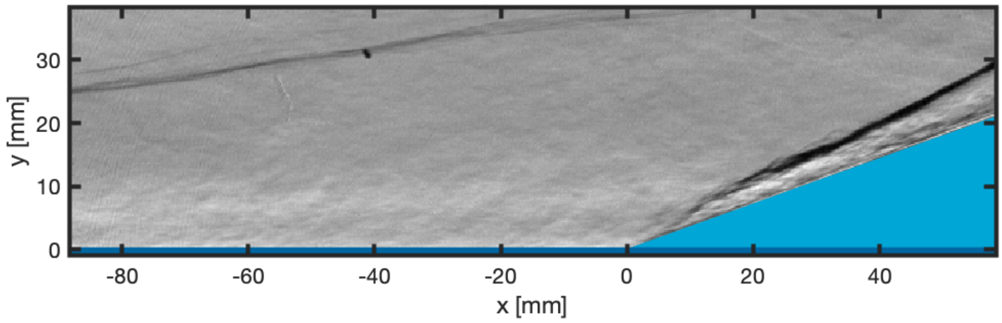

(b) $M_\infty = 7.5$; $Re = 46.3 \times 10^5$

Figure J.7: **Nondimensional roughness strip wavelength:** $\lambda_\delta = 1.8$

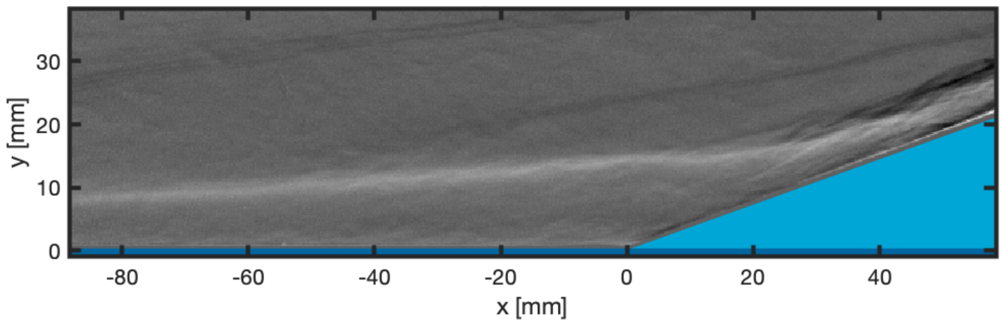

(a) $M_\infty = 7.5$; $Re = 9.2 \times 10^5$

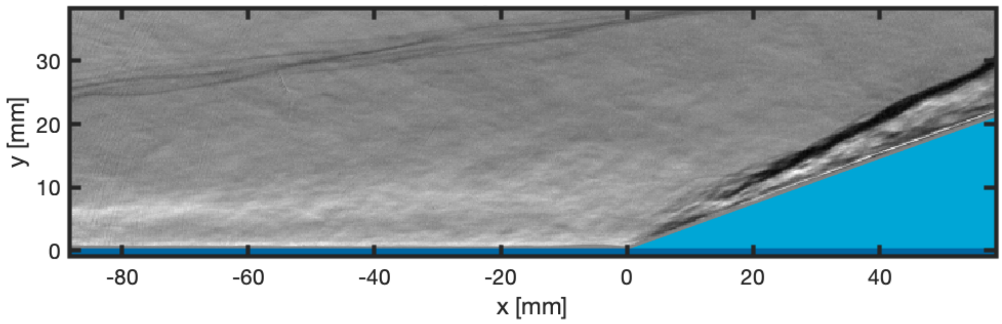

(b) $M_\infty = 7.5$; $Re = 46.3 \times 10^5$

Figure J.8: **Nondimensional roughness strip wavelength:** $\lambda_\delta = 2.7$

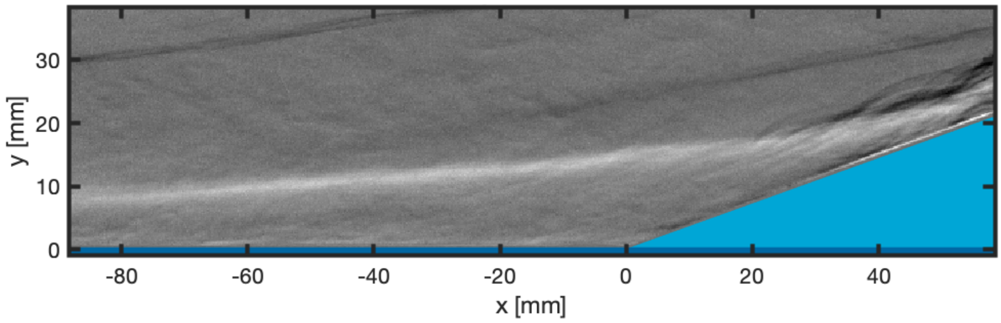

(a) $M_\infty = 7.5$; $Re = 9.2 \times 10^5$

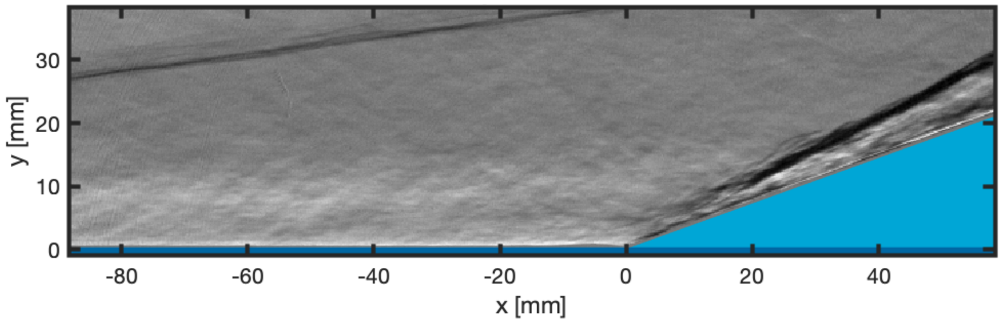

(b) $M_\infty = 7.5$; $Re = 46.3 \times 10^5$

Figure J.9: **Nondimensional roughness strip wavelength:** $\lambda_\delta = 3.6$

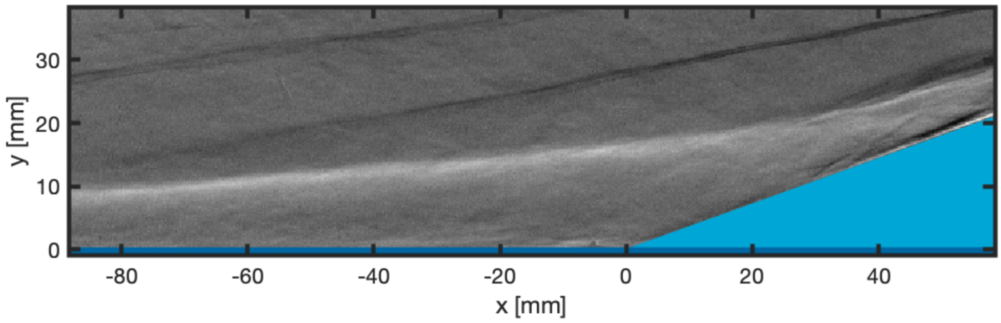

(a) $M_\infty = 7.5$; $Re = 9.2 \times 10^5$

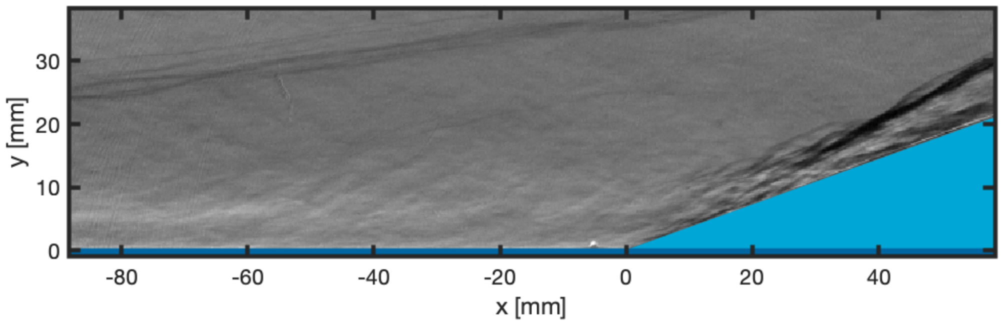

(b) $M_\infty = 7.5$; $Re = 46.3 \times 10^5$

Figure J.10: **Nondimensional roughness strip wavelength:** $\lambda_\delta = 4.5$

J.3. Ramp angle of $25°$

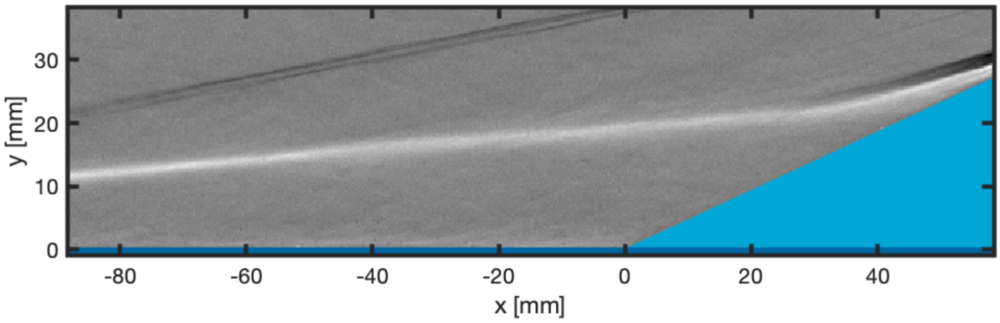

(a) $M_\infty = 7.5$; $Re = 9.2 \times 10^5$

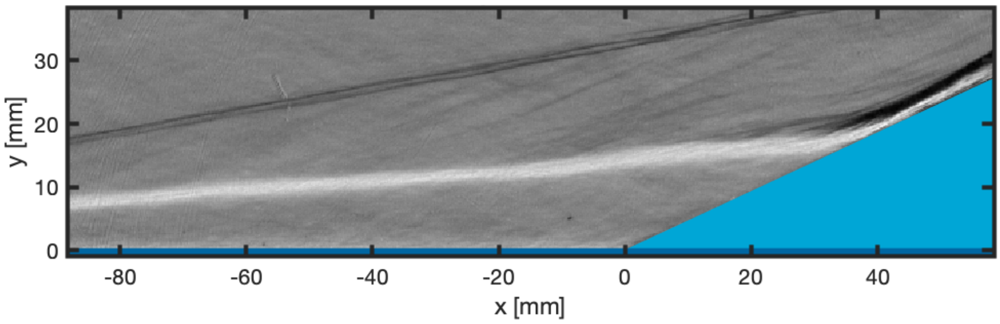

(b) $M_\infty = 7.5$; $Re = 46.3 \times 10^5$

Figure J.11: **No roughness strip.**

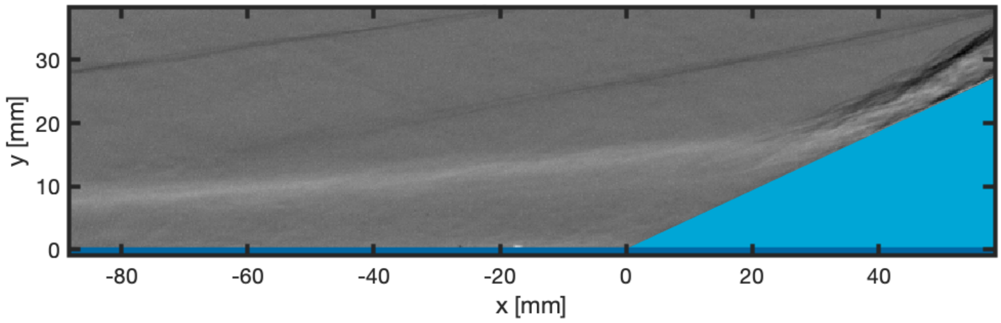

(a) $M_\infty = 7.5$; $Re = 9.2 \times 10^5$

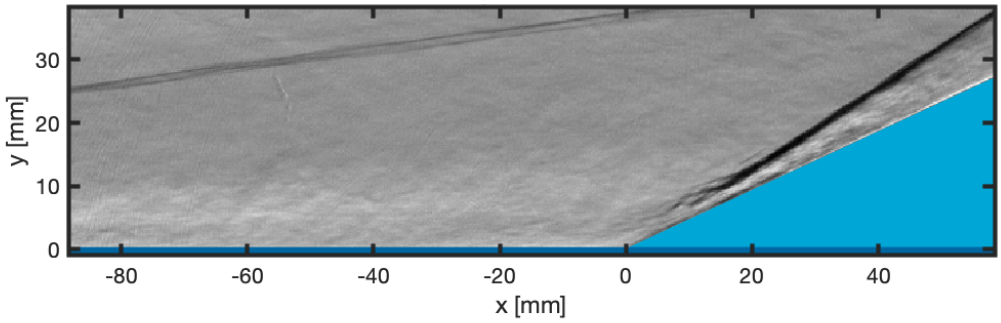

(b) $M_\infty = 7.5$; $Re = 46.3 \times 10^5$

Figure J.12: **Nondimensional roughness strip wavelength:** $\lambda_\delta = 1.8$

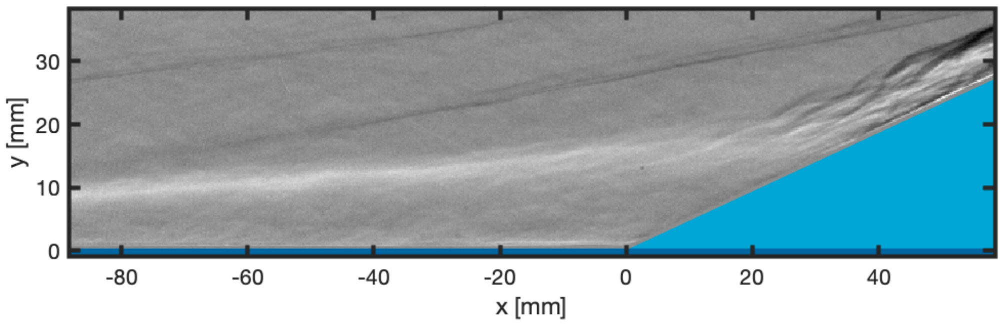

(a) $M_\infty = 7.5$; $Re = 9.2 \times 10^5$

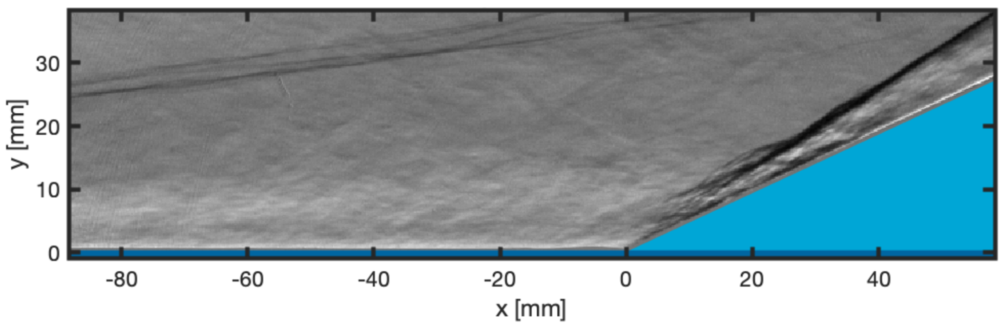

(b) $M_\infty = 7.5$; $Re = 46.3 \times 10^5$

Figure J.13: **Nondimensional roughness strip wavelength:** $\lambda_\delta = 2.7$

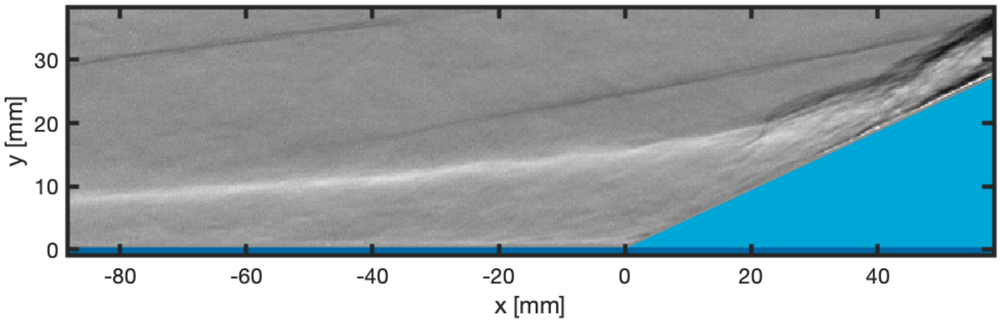

(a) $M_\infty = 7.5$; $Re = 9.2 \times 10^5$

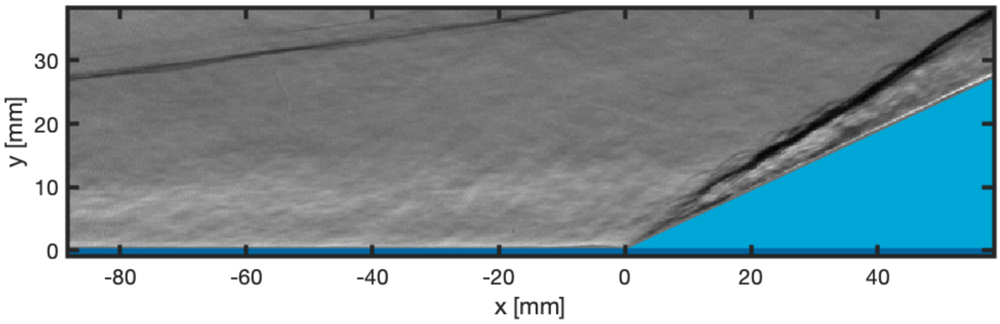

(b) $M_\infty = 7.5$; $Re = 46.3 \times 10^5$

Figure J.14: **Nondimensional roughness strip wavelength:** $\lambda_\delta = 3.6$

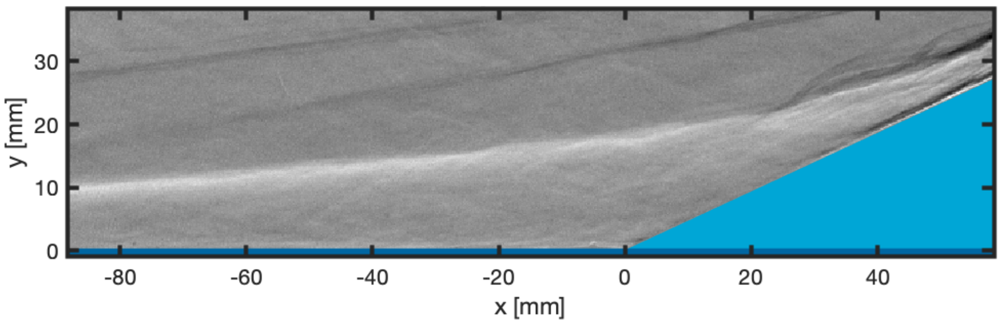

(a) $M_\infty = 7.5$; $Re = 9.2 \times 10^5$

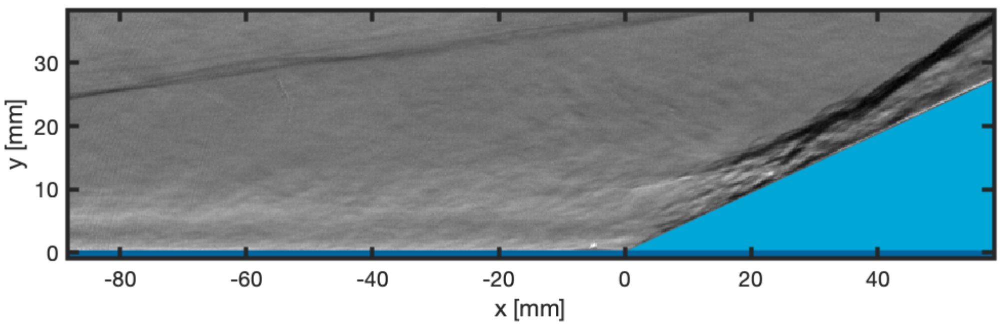

(b) $M_\infty = 7.5$; $Re = 46.3 \times 10^5$

Figure J.15: **Nondimensional roughness strip wavelength:** $\lambda_\delta = 4.5$

J.4. Ramp angle of $30°$

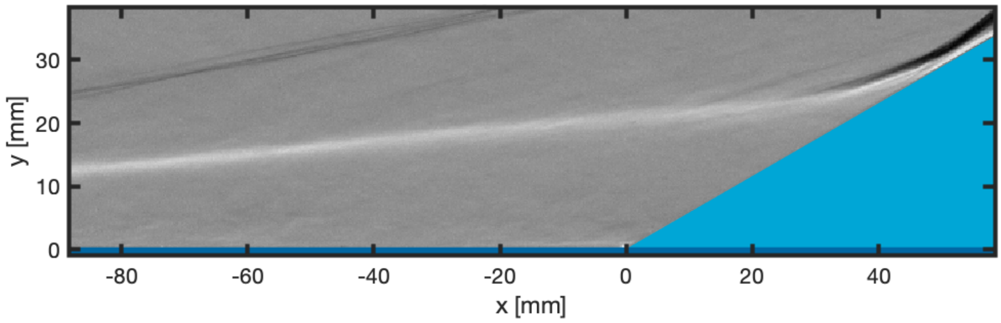

(a) $M_\infty = 7.5$; $Re = 9.2 \times 10^5$

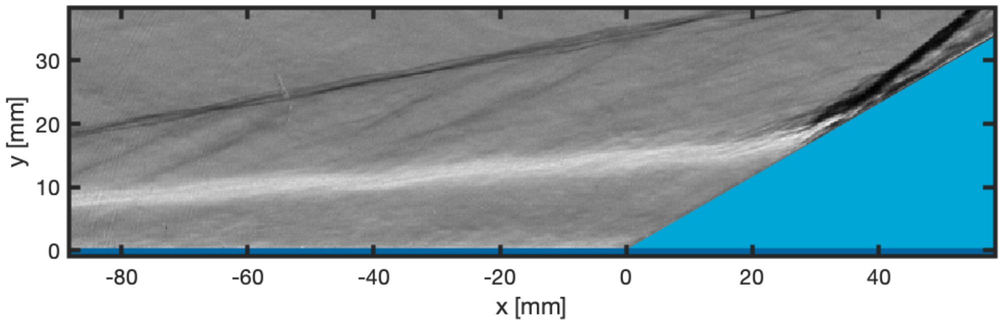

(b) $M_\infty = 7.5$; $Re = 46.3 \times 10^5$

Figure J.16: **No roughness strip.**

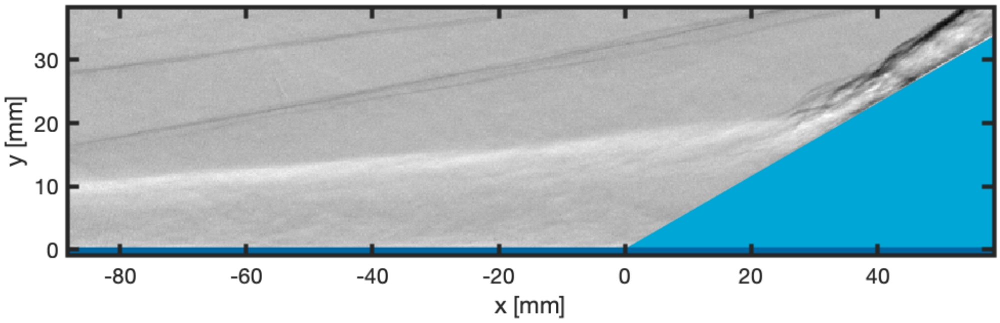

(a) $M_\infty = 7.5$; $Re = 9.2 \times 10^5$

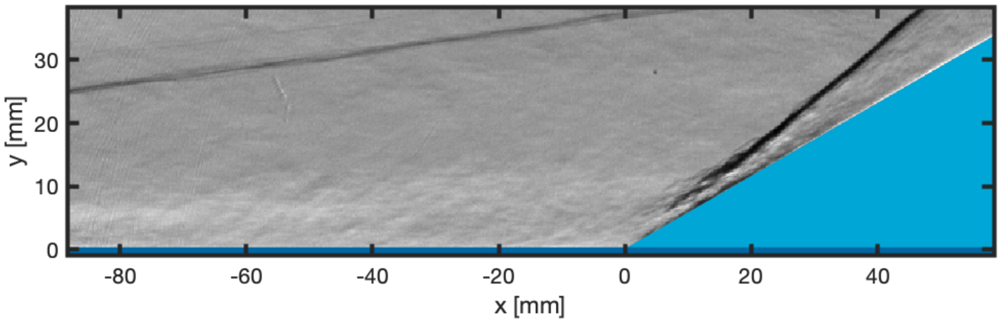

(b) $M_\infty = 7.5$; $Re = 46.3 \times 10^5$

Figure J.17: **Nondimensional roughness strip wavelength:** $\lambda_\delta = 1.8$

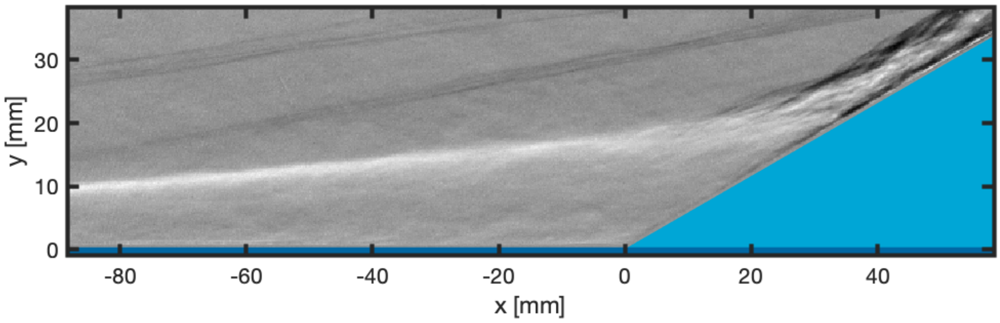

(a) $M_\infty = 7.5$; $Re = 9.2 \times 10^5$

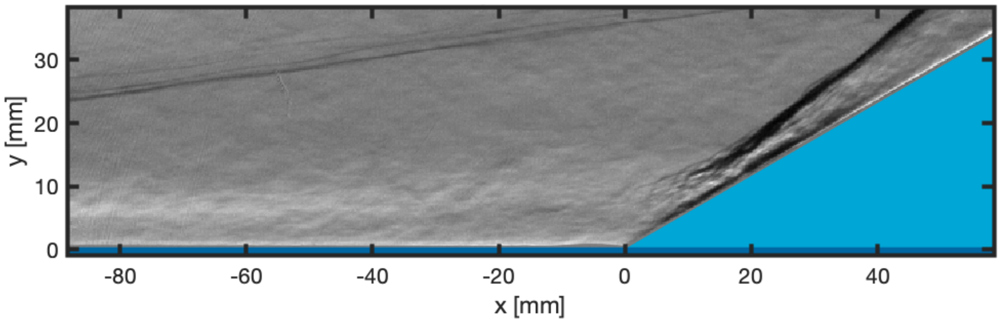

(b) $M_\infty = 7.5$; $Re = 46.3 \times 10^5$

Figure J.18: **Nondimensional roughness strip wavelength:** $\lambda_\delta = 2.7$

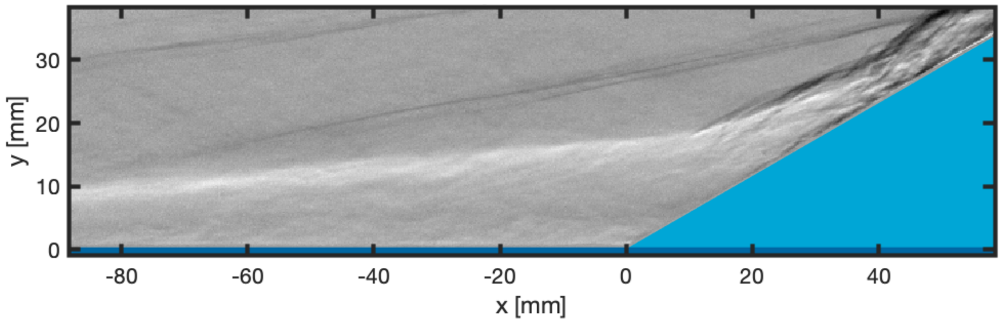

(a) $M_\infty = 7.5$; $Re = 9.2 \times 10^5$

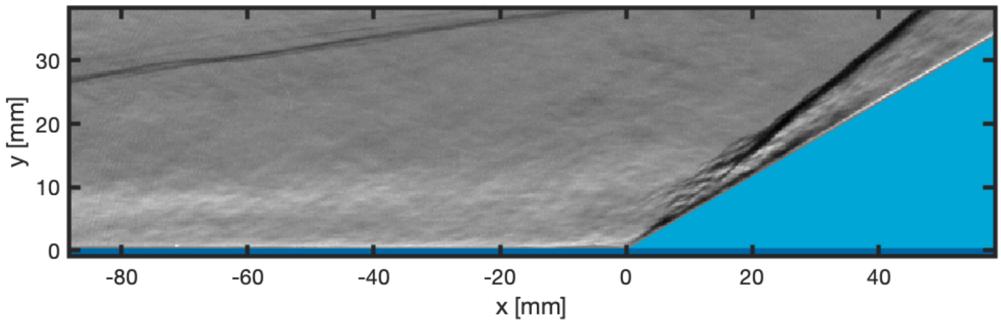

(b) $M_\infty = 7.5$; $Re = 46.3 \times 10^5$

Figure J.19: **Nondimensional roughness strip wavelength:** $\lambda_\delta = 3.6$

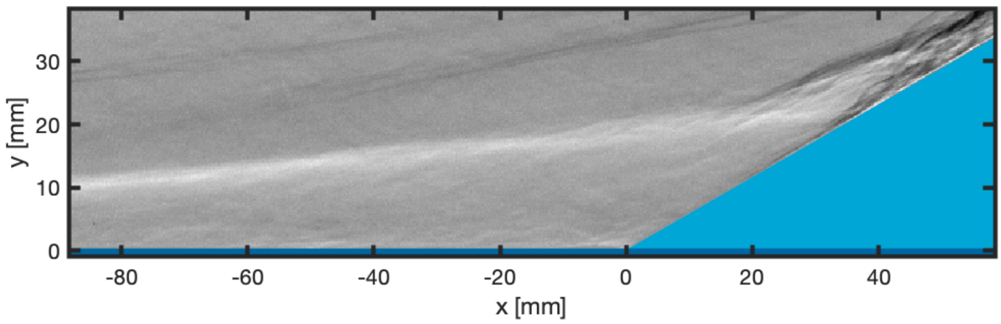

(a) $M_\infty = 7.5$; $Re = 9.2 \times 10^5$

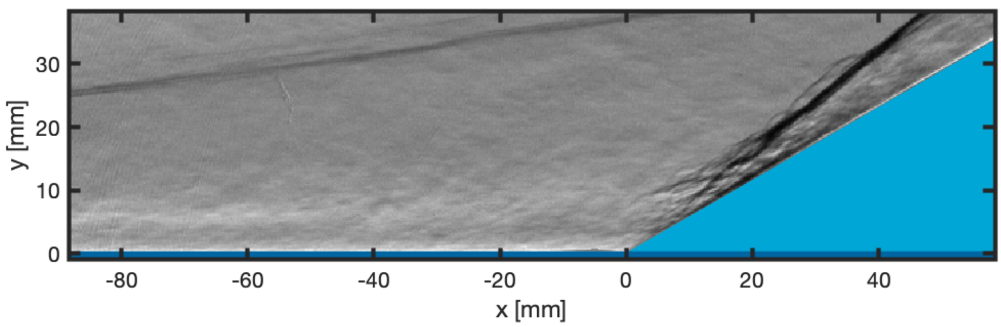

(b) $M_\infty = 7.5$; $Re = 46.3 \times 10^5$

Figure J.20: **Nondimensional roughness strip wavelength:** $\lambda_\delta = 4.5$

K
Schlieren Images – RMS

This appendix presents schlieren images captured with the following specifications:

- Frame rate = 28.975 kHz
- Exposure time = $1.28\ \mu s$
- Spatial resolution: $4.57\ px/mm$
- Field of view: $147 \times 39\ mm^2$

K.1. Ramp angle of $15°$

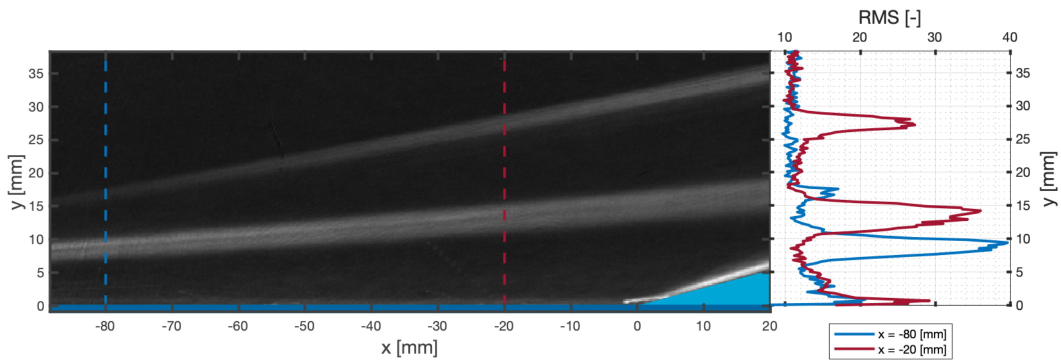

(a) $M_\infty = 7.5$; $Re = 9.2 \times 10^5$

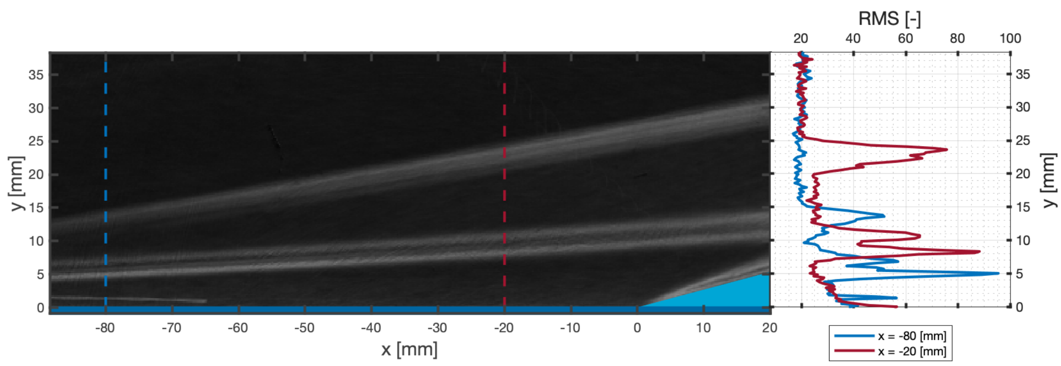

(b) $M_\infty = 7.5$; $Re = 46.3 \times 10^5$

Figure K.1: **No roughness strip.**

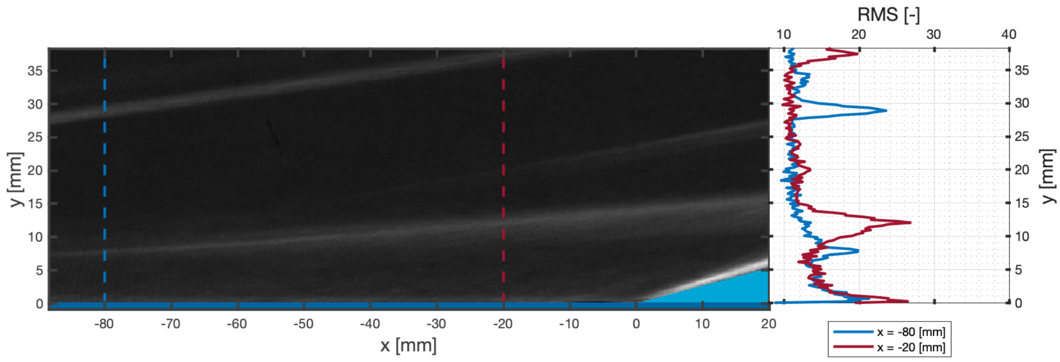

(a) $M_\infty = 7.5$; $Re = 9.2 \times 10^5$

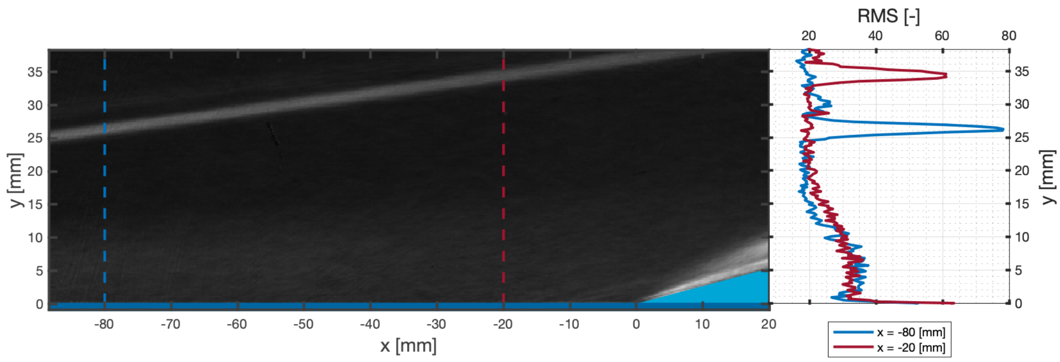

(b) $M_\infty = 7.5$; $Re = 46.3 \times 10^5$

Figure K.2: **Nondimensional roughness strip wavelength:** $\lambda_\delta = 1.8$

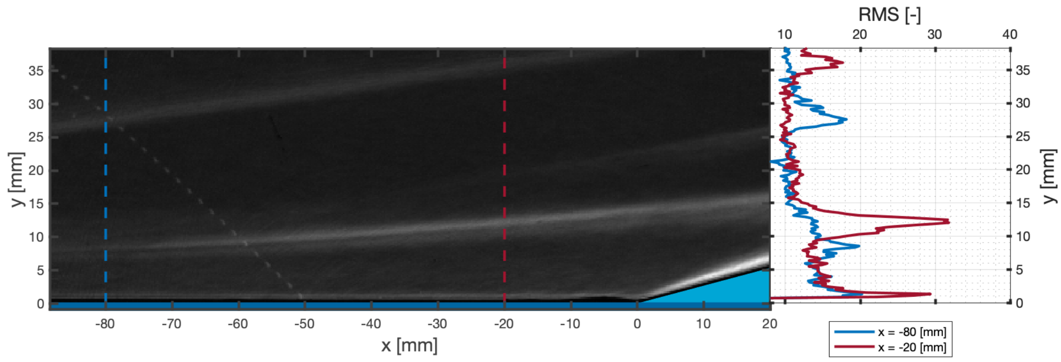

(a) $M_\infty = 7.5$; $Re = 9.2 \times 10^5$

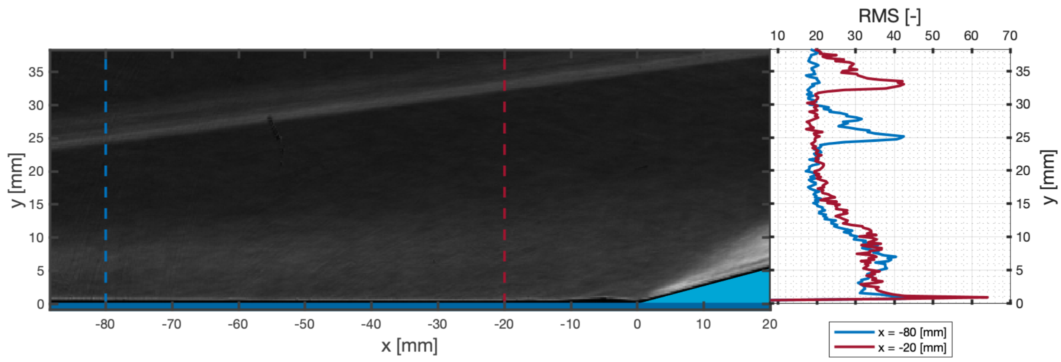

(b) $M_\infty = 7.5$; $Re = 46.3 \times 10^5$

Figure K.3: **Nondimensional roughness strip wavelength:** $\lambda_\delta = 2.7$

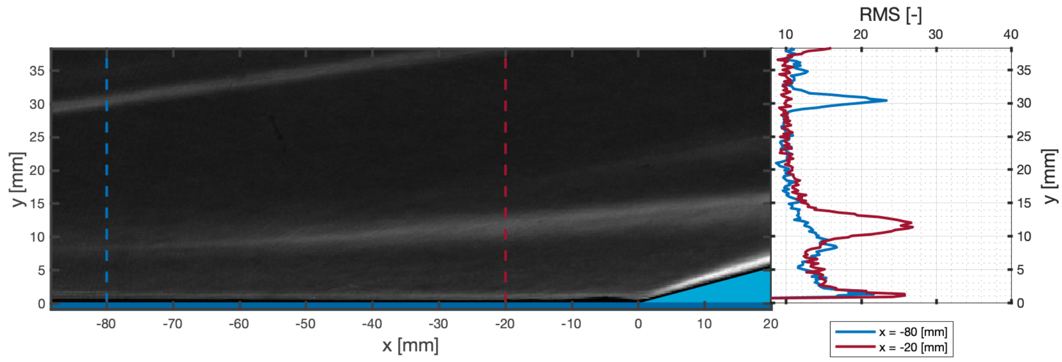

(a) $M_\infty = 7.5$; $Re = 9.2 \times 10^5$

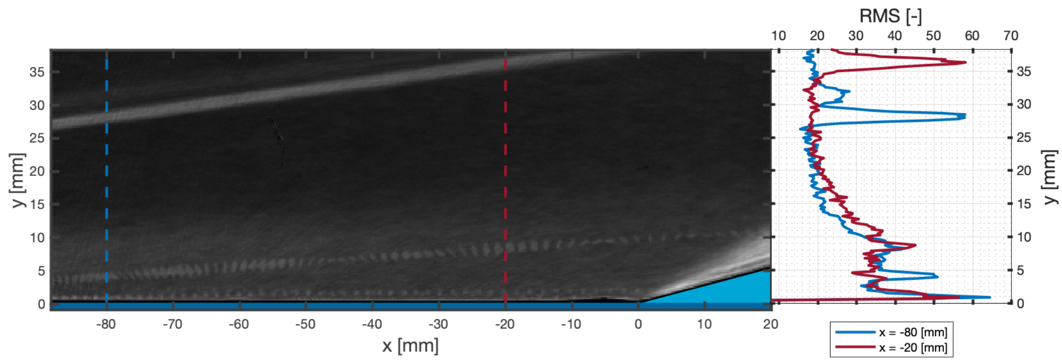

(b) $M_\infty = 7.5$; $Re = 46.3 \times 10^5$

Figure K.4: **Nondimensional roughness strip wavelength:** $\lambda_\delta = 3.6$

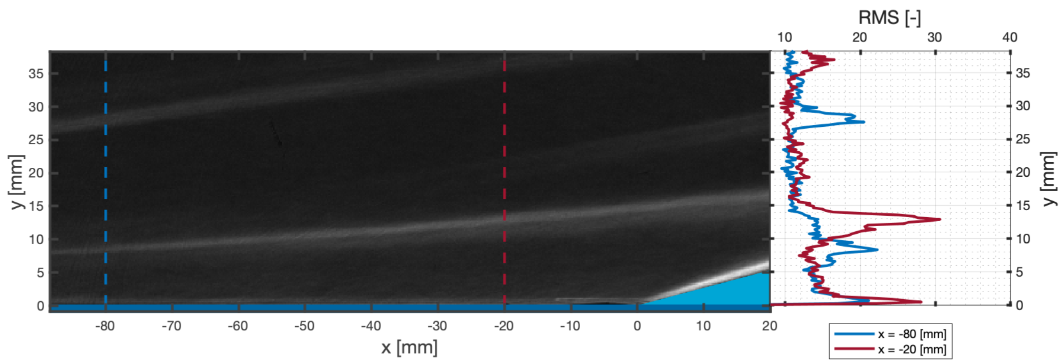

(a) $M_\infty = 7.5$; $Re = 9.2 \times 10^5$

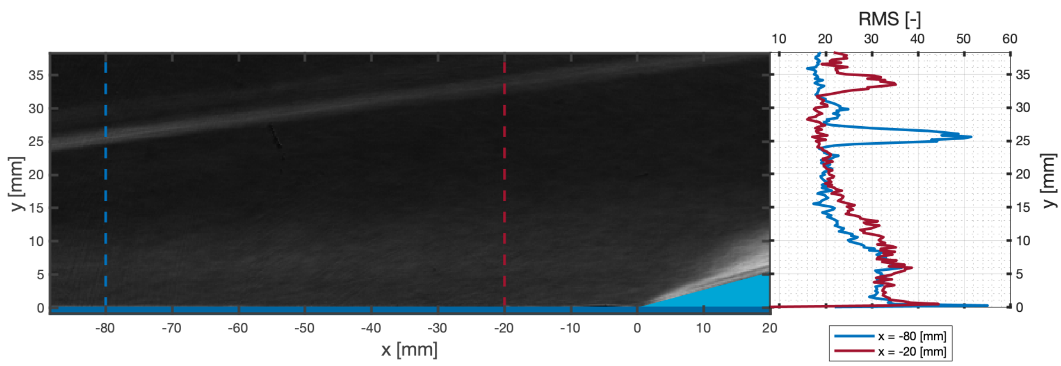

(b) $M_\infty = 7.5$; $Re = 46.3 \times 10^5$

Figure K.5: **Nondimensional roughness strip wavelength:** $\lambda_\delta = 4.5$

K.2. Ramp angle of $20°$

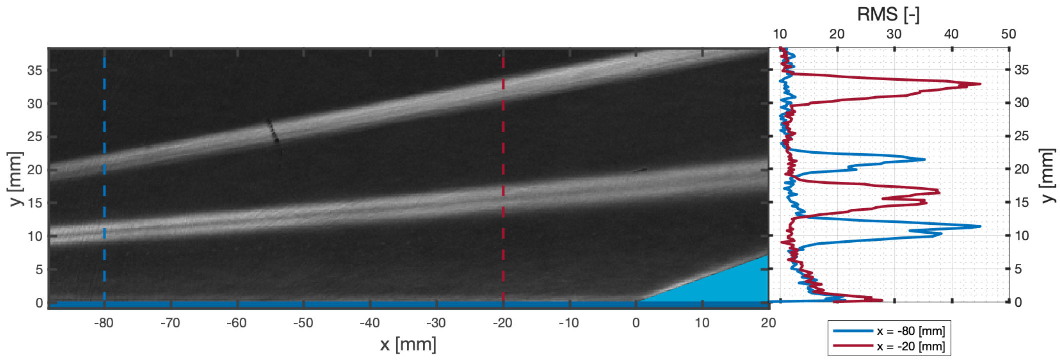

(a) $M_\infty = 7.5$; $Re = 9.2 \times 10^5$

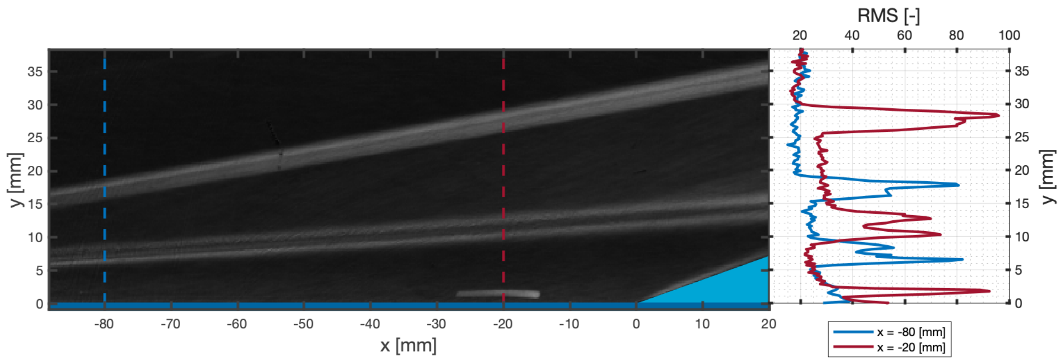

(b) $M_\infty = 7.5$; $Re = 46.3 \times 10^5$

Figure K.6: **No roughness strip.**

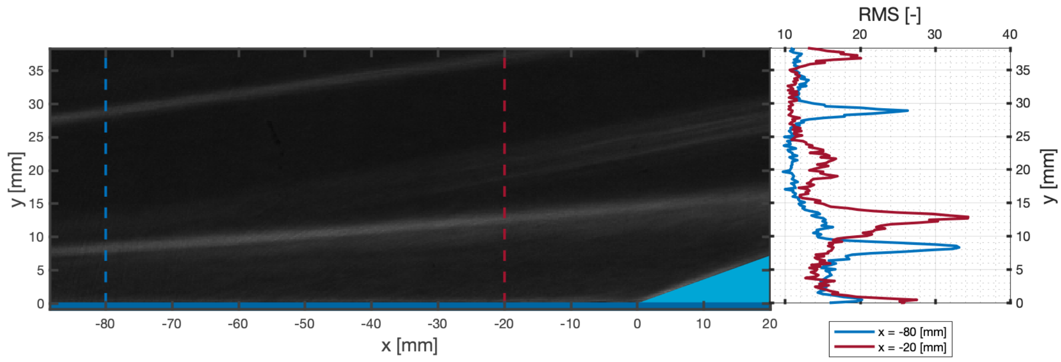

(a) $M_\infty = 7.5$; $Re = 9.2 \times 10^5$

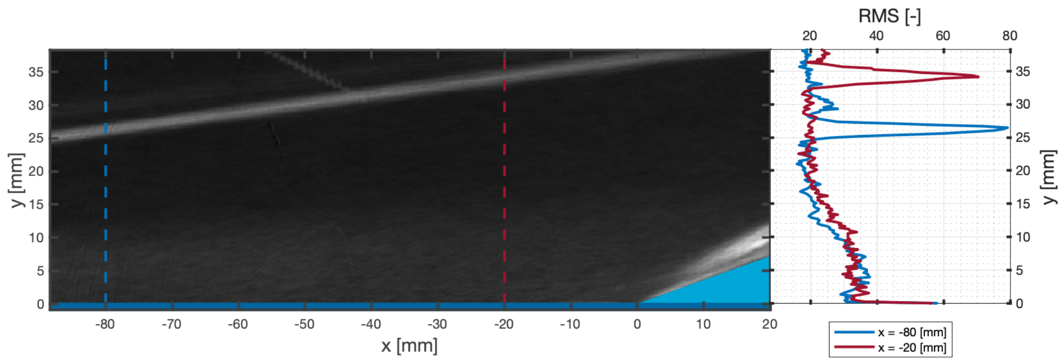

(b) $M_\infty = 7.5$; $Re = 46.3 \times 10^5$

Figure K.7: **Nondimensional roughness strip wavelength:** $\lambda_\delta = 1.8$

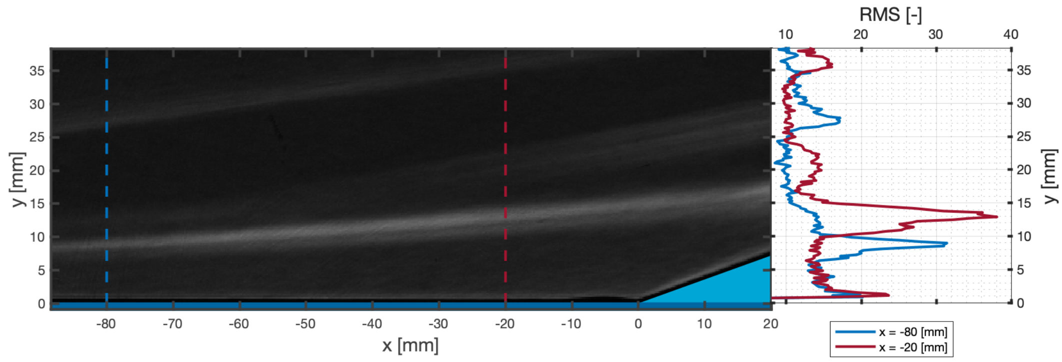

(a) $M_\infty = 7.5$; $Re = 9.2 \times 10^5$

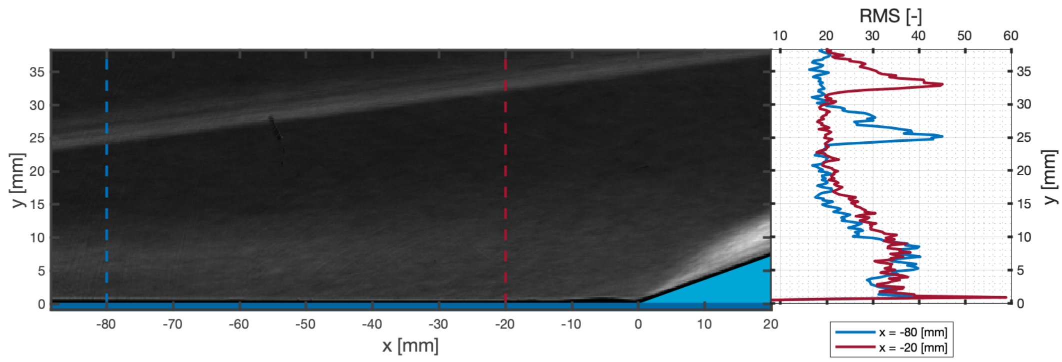

(b) $M_\infty = 7.5$; $Re = 46.3 \times 10^5$

Figure K.8: **Nondimensional roughness strip wavelength:** $\lambda_\delta = 2.7$

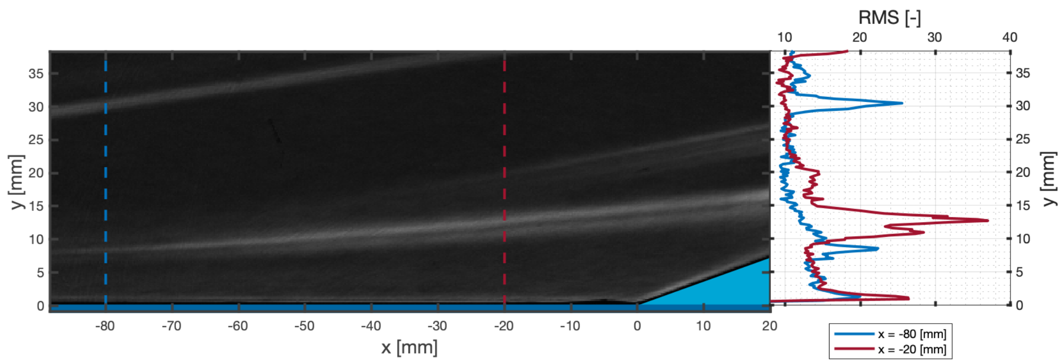

(a) $M_\infty = 7.5$; $Re = 9.2 \times 10^5$

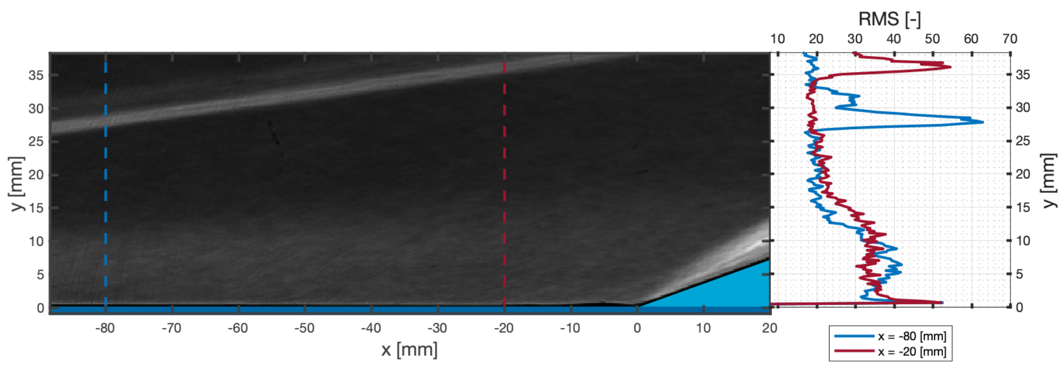

(b) $M_\infty = 7.5$; $Re = 46.3 \times 10^5$

Figure K.9: **Nondimensional roughness strip wavelength:** $\lambda_\delta = 3.6$

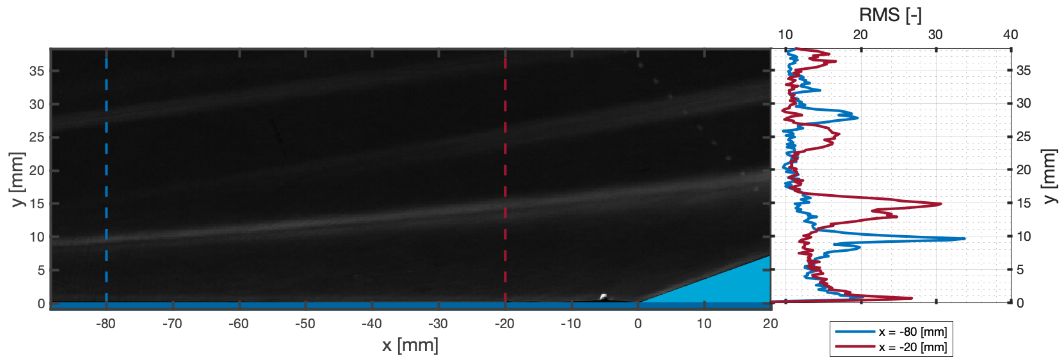

(a) $M_\infty = 7.5$; $Re = 9.2 \times 10^5$

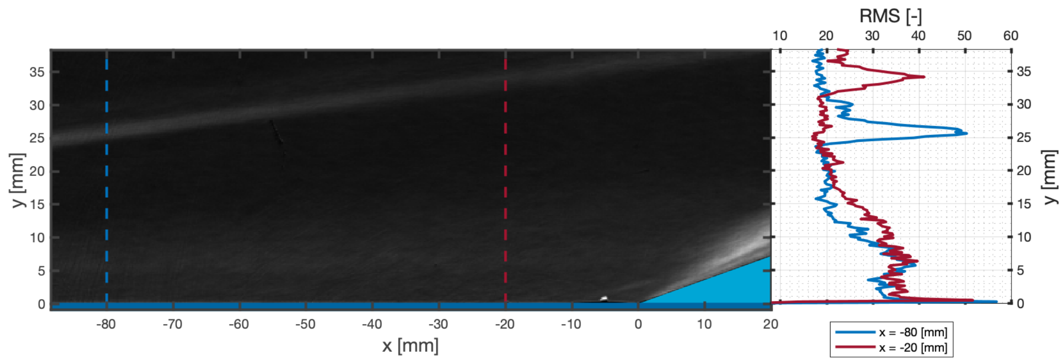

(b) $M_\infty = 7.5$; $Re = 46.3 \times 10^5$

Figure K.10: **Nondimensional roughness strip wavelength:** $\lambda_\delta = 4.5$

K.3. Ramp angle of 25°

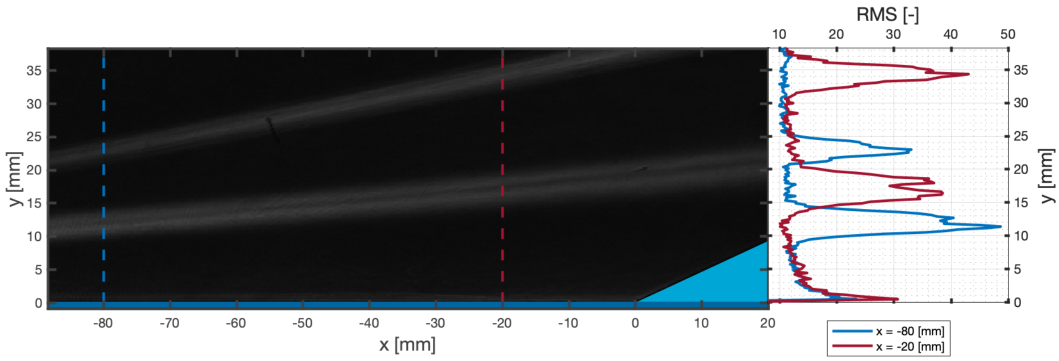

(a) $M_\infty = 7.5$; $Re = 9.2 \times 10^5$

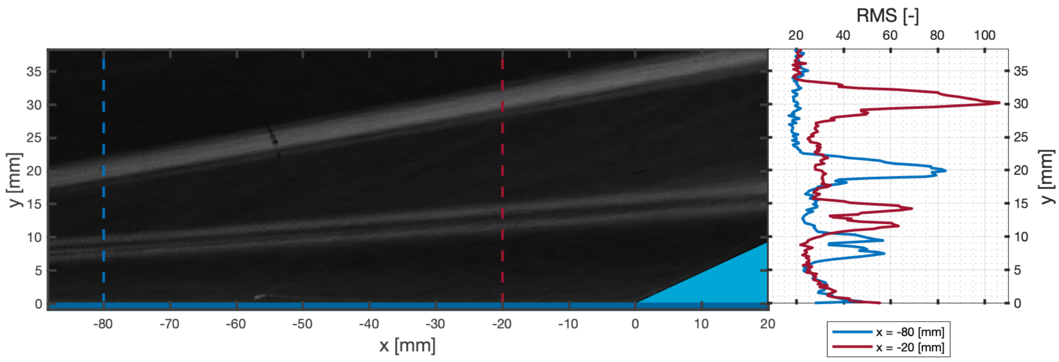

(b) $M_\infty = 7.5$; $Re = 46.3 \times 10^5$

Figure K.11: **No roughness strip.**

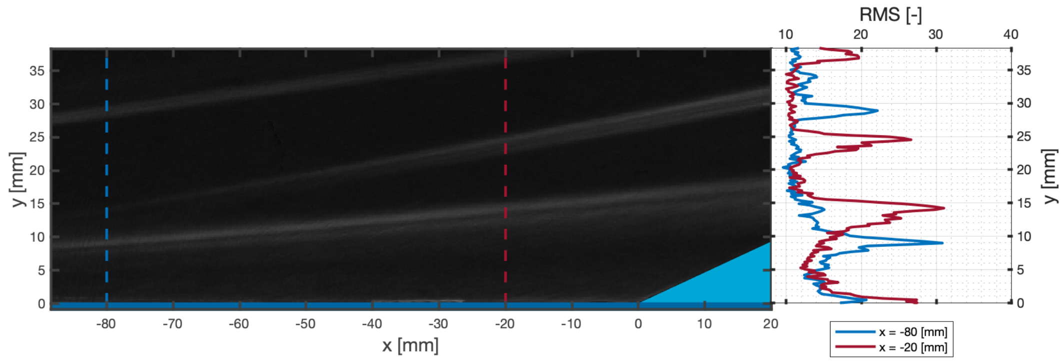

(a) $M_\infty = 7.5$; $Re = 9.2 \times 10^5$

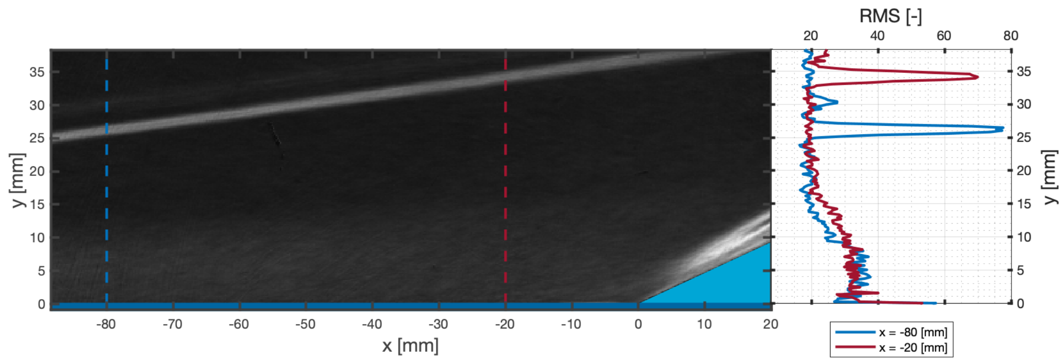

(b) $M_\infty = 7.5$; $Re = 46.3 \times 10^5$

Figure K.12: **Nondimensional roughness strip wavelength:** $\lambda_\delta = 1.8$

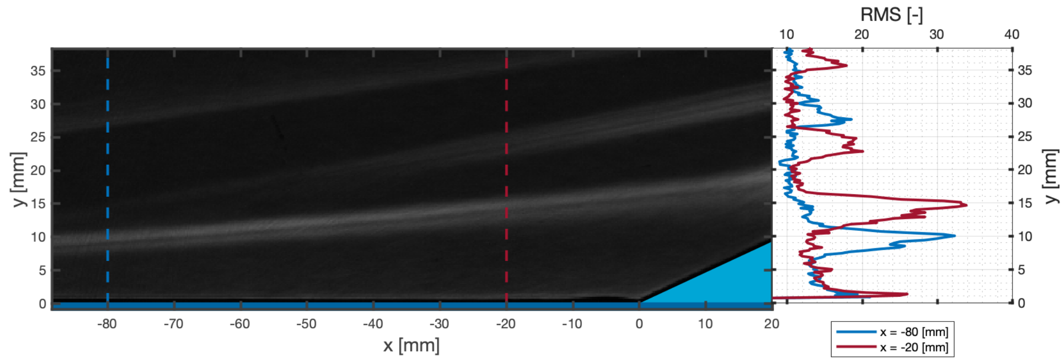

(a) $M_\infty = 7.5$; $Re = 9.2 \times 10^5$

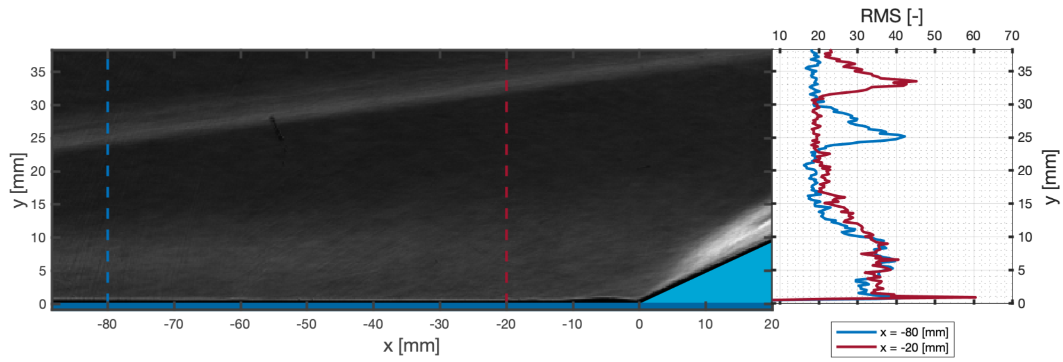

(b) $M_\infty = 7.5$; $Re = 46.3 \times 10^5$

Figure K.13: **Nondimensional roughness strip wavelength:** $\lambda_\delta = 2.7$

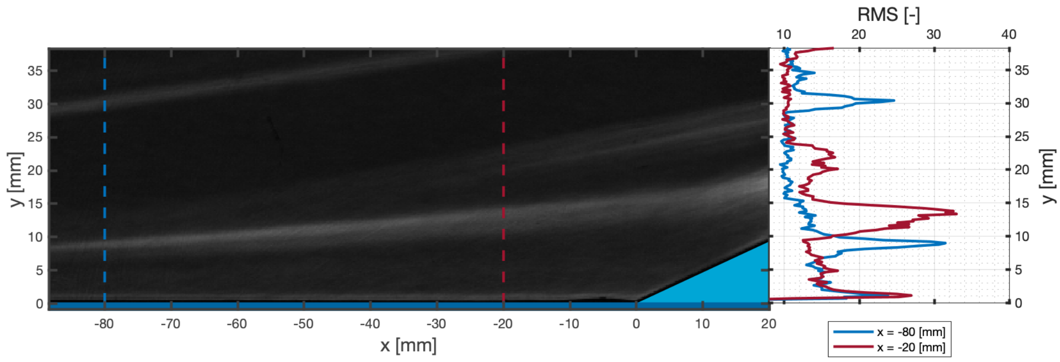

(a) $M_\infty = 7.5$; $Re = 9.2 \times 10^5$

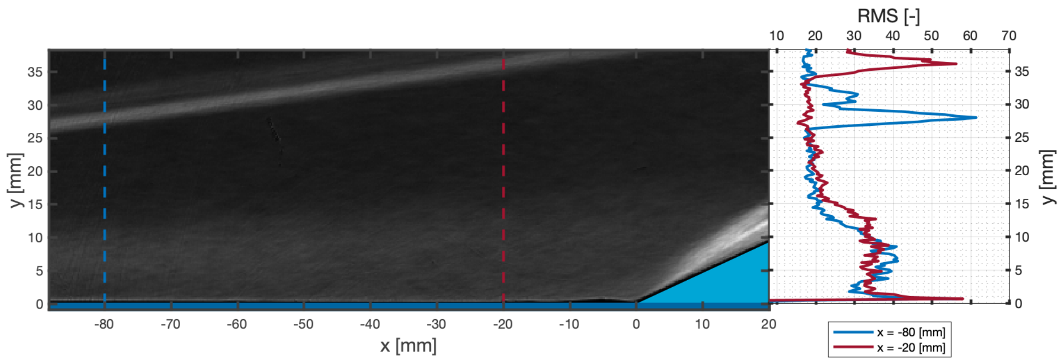

(b) $M_\infty = 7.5$; $Re = 46.3 \times 10^5$

Figure K.14: **Nondimensional roughness strip wavelength:** $\lambda_\delta = 3.6$

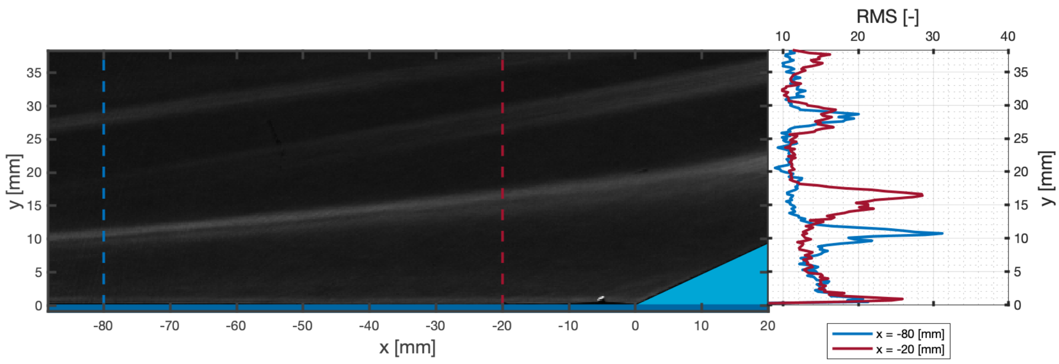

(a) $M_\infty = 7.5$; $Re = 9.2 \times 10^5$

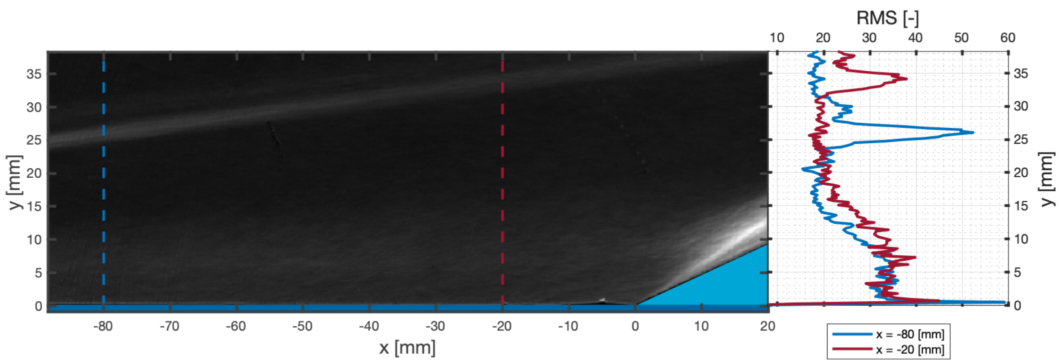

(b) $M_\infty = 7.5$; $Re = 46.3 \times 10^5$

Figure K.15: **Nondimensional roughness strip wavelength:** $\lambda_\delta = 4.5$

K.4. Ramp angle of 30°

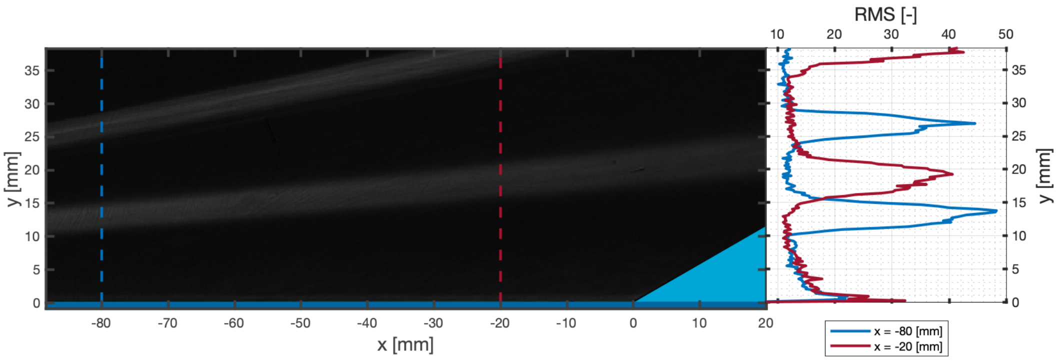

(a) $M_\infty = 7.5$; $Re = 9.2 \times 10^5$

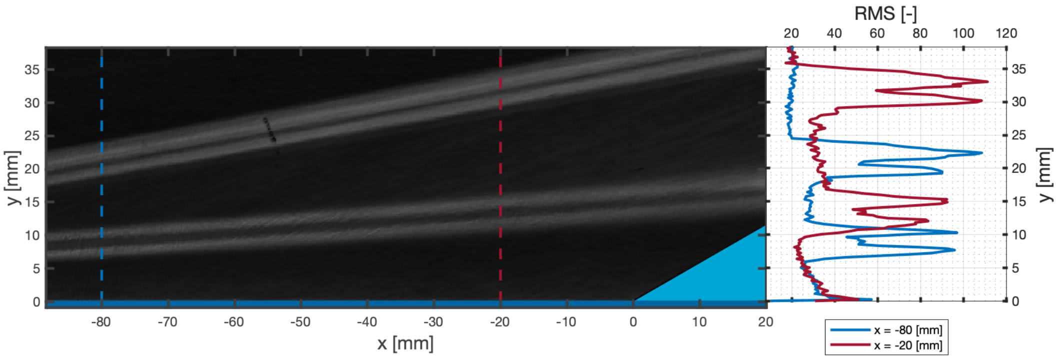

(b) $M_\infty = 7.5$; $Re = 46.3 \times 10^5$

Figure K.16: **No roughness strip.**

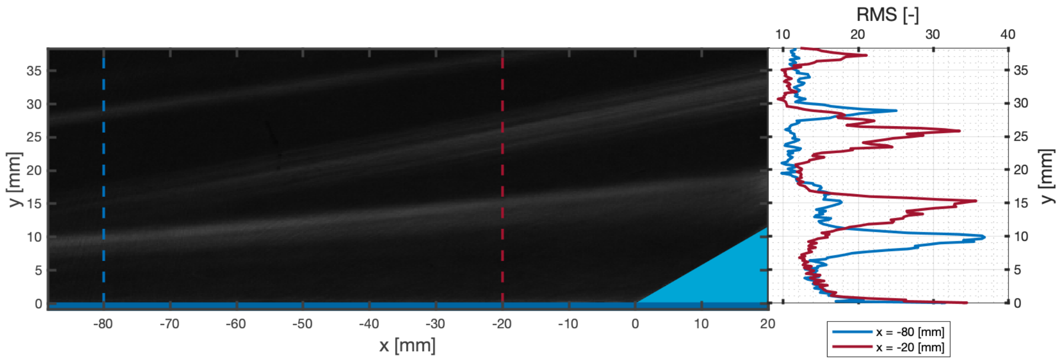

(a) $M_\infty = 7.5$; $Re = 9.2 \times 10^5$

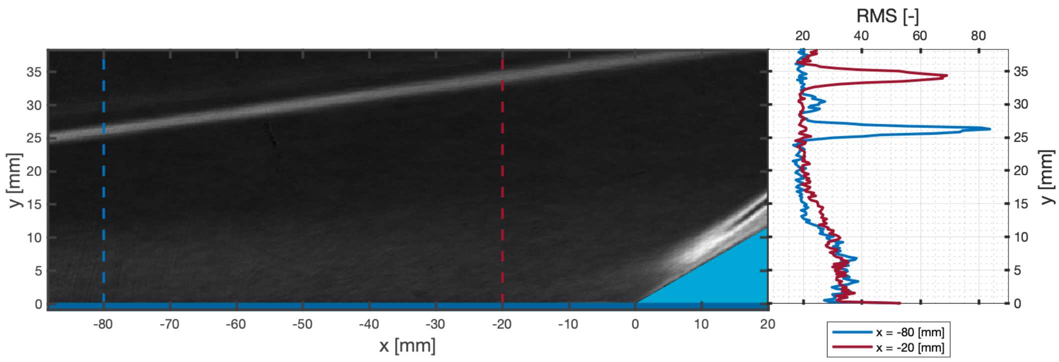

(b) $M_\infty = 7.5$; $Re = 46.3 \times 10^5$

Figure K.17: **Nondimensional roughness strip wavelength:** $\lambda_\delta = 1.8$

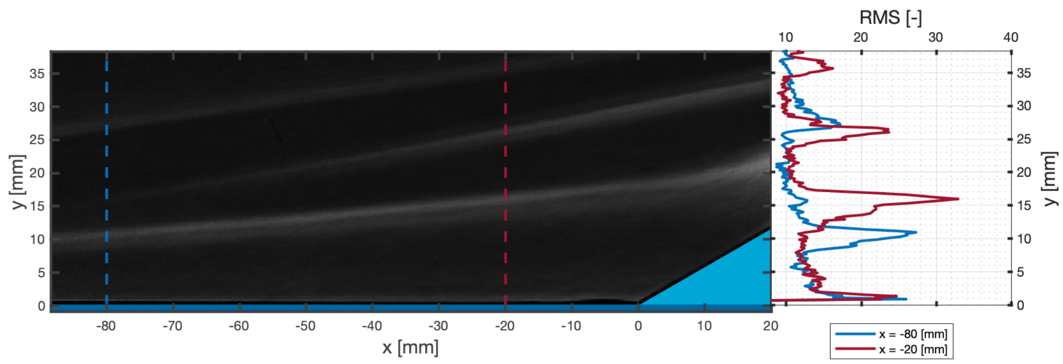

(a) $M_\infty = 7.5$; $Re = 9.2 \times 10^5$

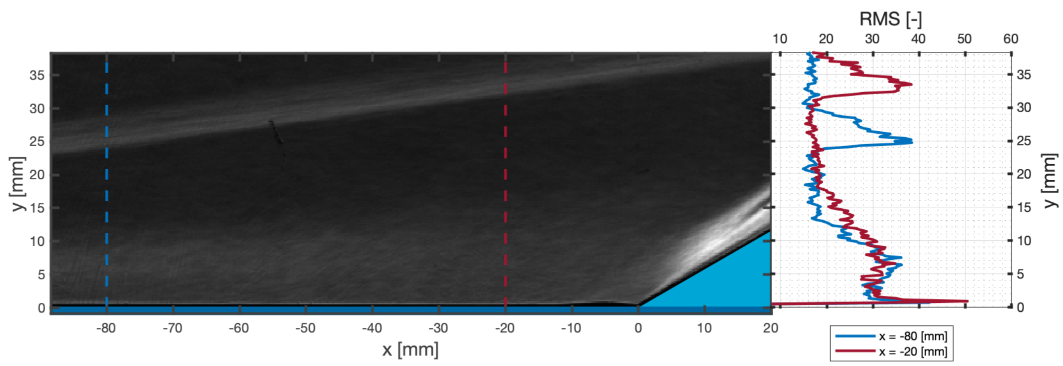

(b) $M_\infty = 7.5$; $Re = 46.3 \times 10^5$

Figure K.18: **Nondimensional roughness strip wavelength:** $\lambda_\delta = 2.7$

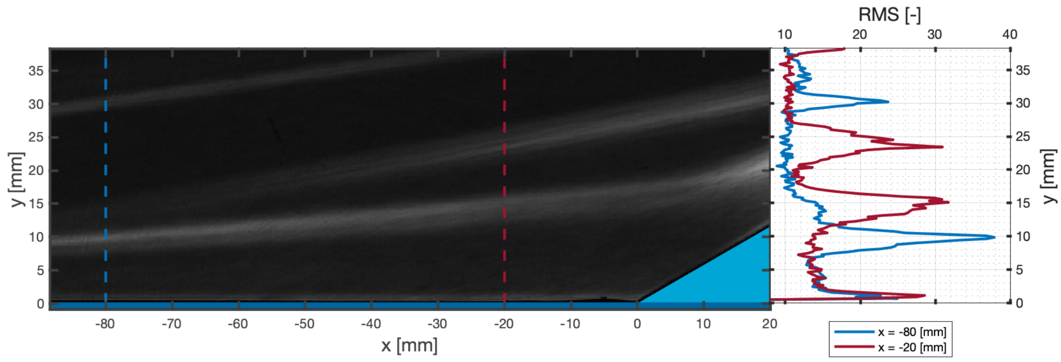

(a) $M_\infty = 7.5$; $Re = 9.2 \times 10^5$

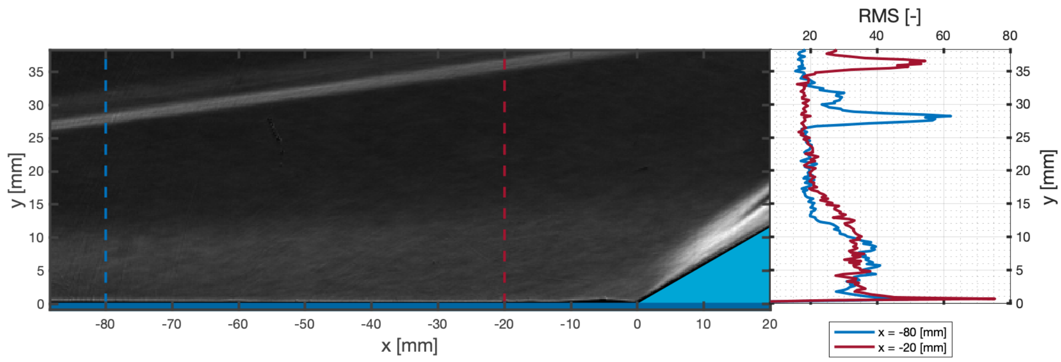

(b) $M_\infty = 7.5$; $Re = 46.3 \times 10^5$

Figure K.19: **Nondimensional roughness strip wavelength:** $\lambda_\delta = 3.6$

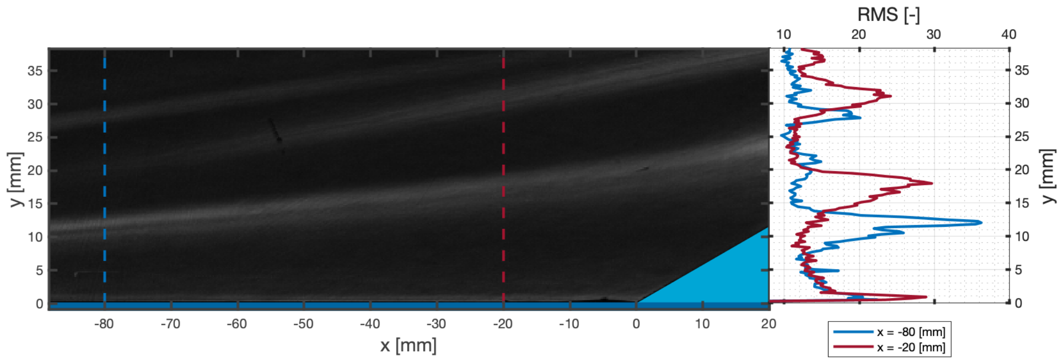

(a) $M_\infty = 7.5$; $Re = 9.2 \times 10^5$

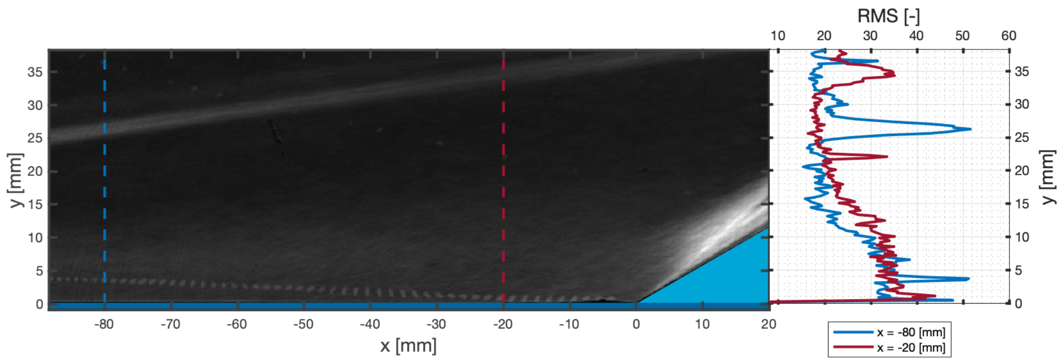

(b) $M_\infty = 7.5$; $Re = 46.3 \times 10^5$

Figure K.20: **Nondimensional roughness strip wavelength:** $\lambda_\delta = 4.5$

L
Oil Flow Images: Normal to Flat Plate Surface

This appendix chapter presents all valid oil flow results normal to the flat plate. These results present only the $30°$ ramp at the low and high Reynolds number conditions ($9.2{\times}10^5$ and $46.3{\times}10^5$, respectively) both with and without a roughness strip for a total of four images. For the cases with a strip, the strip is designated by its nondimensional wavelength as $\lambda_\delta = 1.8$. All results are of Mach 7.5 flow.

L.1. No Strip

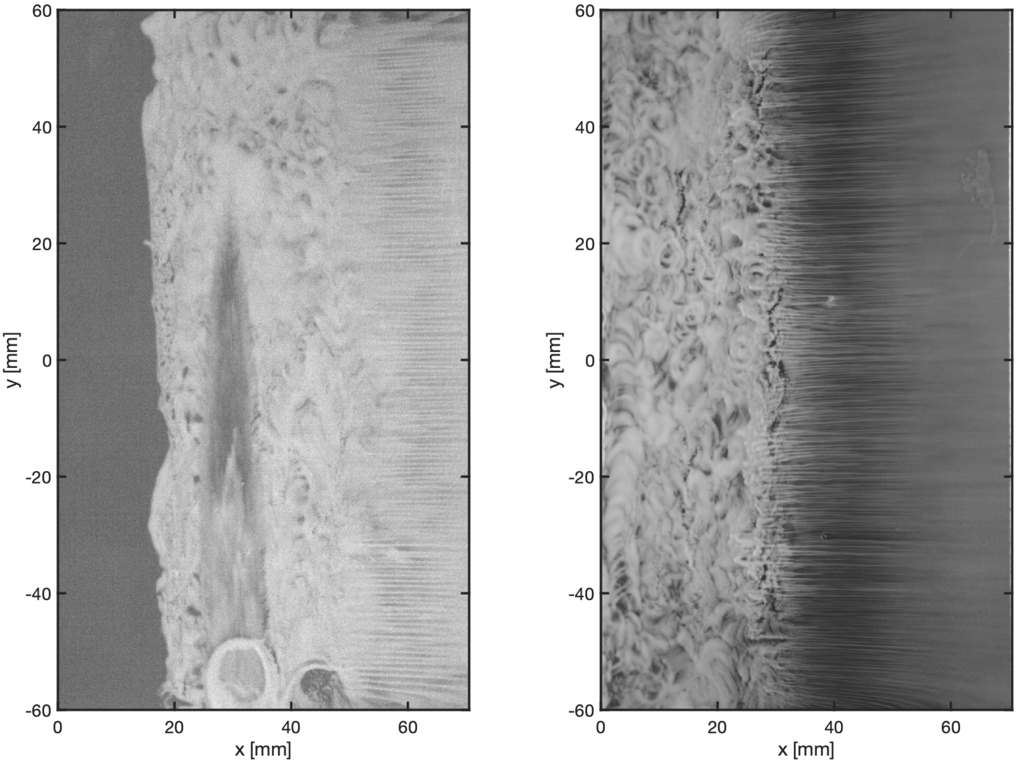

(a) $Re = 9.2 \times 10^5$ (b) $Re = 46.3 \times 10^5$

Figure L.1: **Left:** Section between $x = 0\ mm$ and $x = 20\ mm$ is not oiled prior to the run. Section between $x = 20\ mm$ and $x \approx 50\ mm$ is oiled prior to the run but is relatively unaffected. **Right:** Section between $x = 0\ mm$ and $x \approx 30\ mm$ is oiled prior to the run but is relatively unaffected.

L.2. Nondimensional Strip Wavelength: $\lambda_\delta = 1.8$

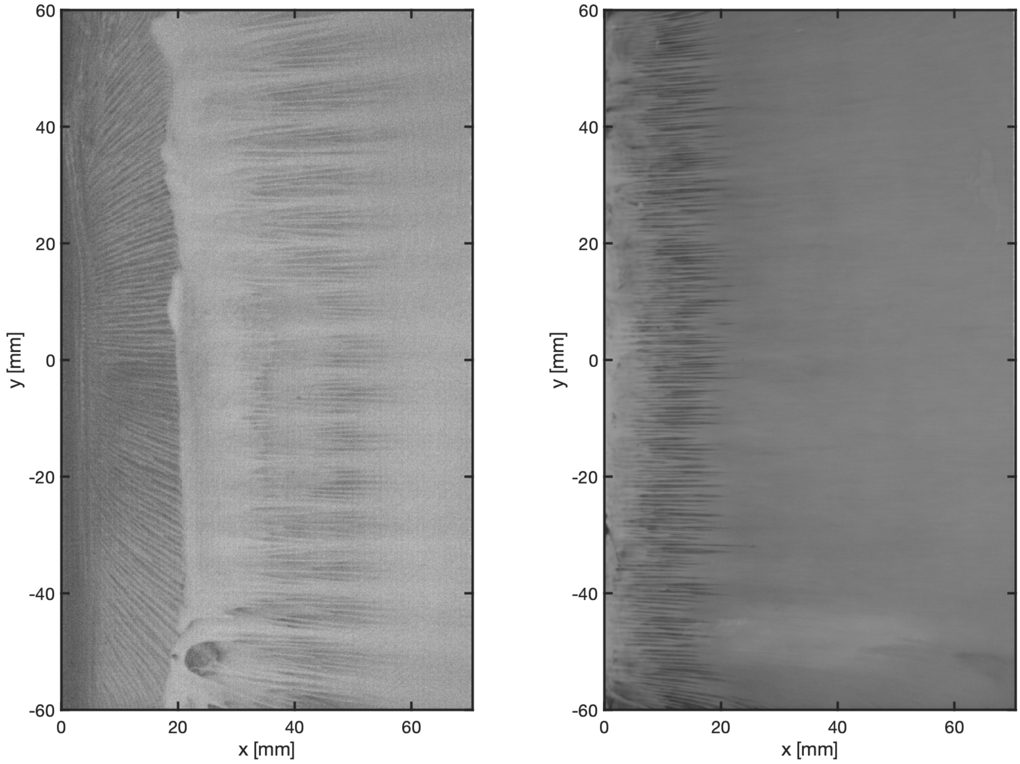

(a) $Re = 9.2 \times 10^5$ (b) $Re = 46.3 \times 10^5$

Figure L.2: **Left:** Section between $x = 0\ mm$ and $x = 20\ mm$ exhibits oil residue from previous run.

M
Oil Flow Images: Normal to Ramp Surface

This appendix chapter presents all valid oil flow results normal to the inclined ramp surface. These results present only the $30°$ ramp at the low and high Reynolds number conditions (9.2×10^5 and 46.3×10^5, respectively) both with and without a roughness strip for a total of four images. For the cases with a strip, the strip is designated by its nondimensional wavelength as $\lambda_\delta = 1.8$. All results are of Mach 7.5 flow.

M.1. No Strip

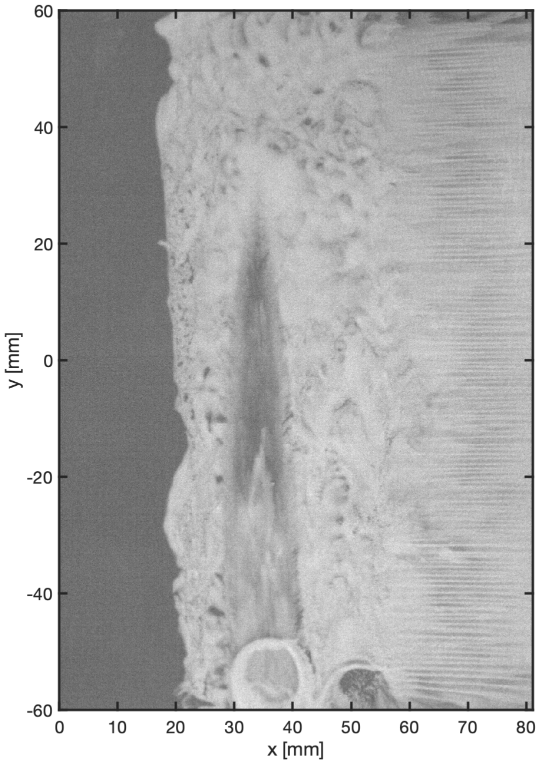

(a) $Re = 9.2 \times 10^5$

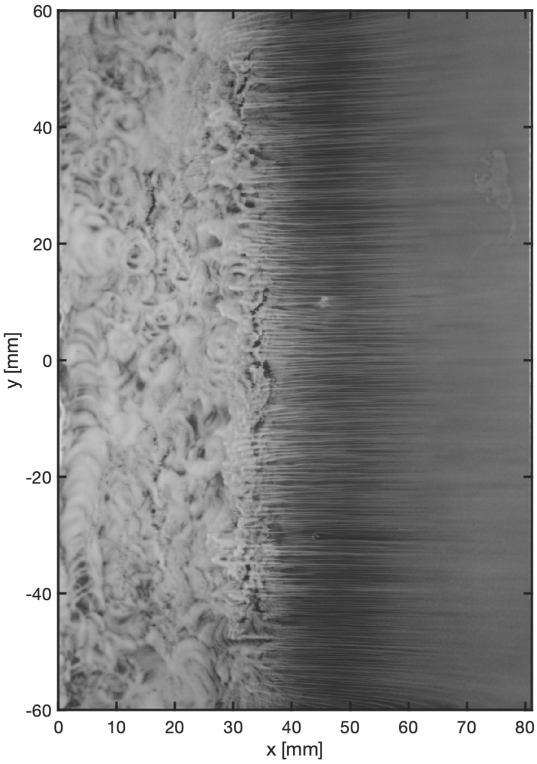

(b) $Re = 46.3 \times 10^5$

Figure M.1: **Left:** Section between $x = 0\ mm$ and $x = 20\ mm$ is not oiled prior to the run. Section between $x = 20\ mm$ and $x \approx 60\ mm$ is oiled prior to the run but is relatively unaffected. **Right:** Section between $x = 0\ mm$ and $x \approx 30\ mm$ is oiled prior to the run but is relatively unaffected.

M.2. Nondimensional Strip Wavelength: $\lambda_\delta = 1.8$

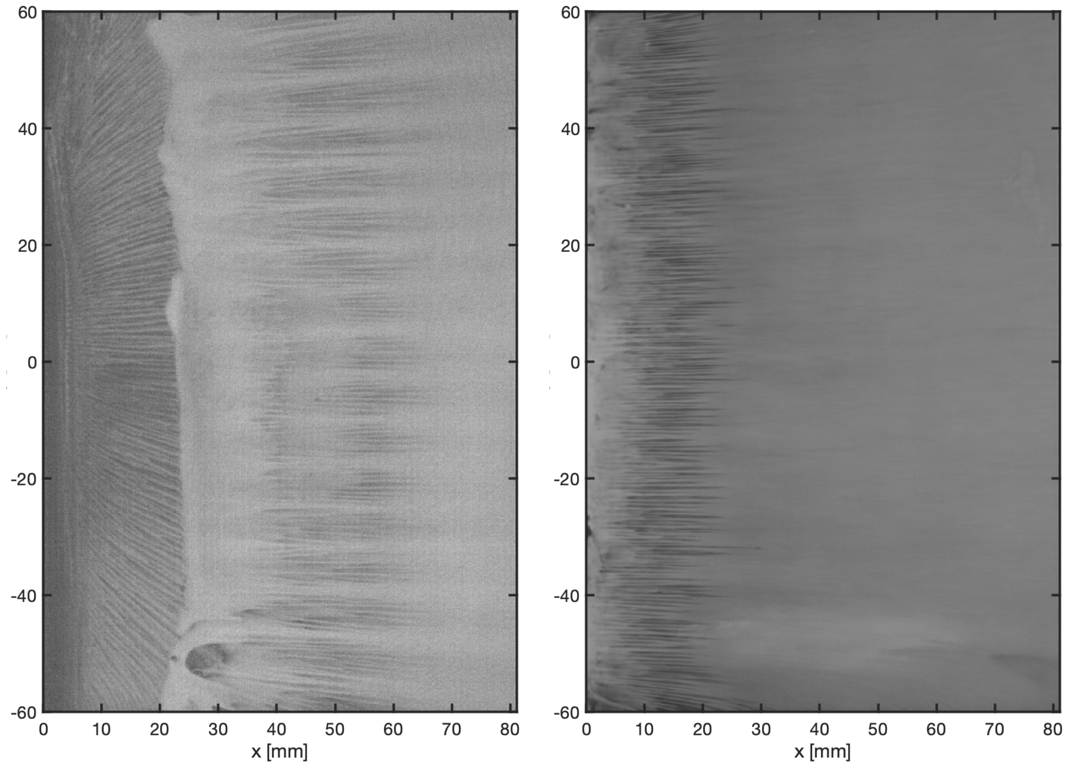

(a) $Re = 9.2 \times 10^5$ (b) $Re = 46.3 \times 10^5$

Figure M.2: **Left:** Section between $x = 0\ mm$ and $x = 20\ mm$ exhibits oil residue from previous run.

Bibliography

[1] John D Anderson Jr. *Hypersonic and high-temperature gas dynamics*. American Institute of Aeronautics and Astronautics, 2006.

[2] Daniel Arnal and Jean Délery. Laminar-turbulent transition and shock wave/boundary layer interaction. *Critical Technologies for Hypersonic Vehicle Development*, pages 10–14, 2004. URL `ftp://ftp.rta.nato.int/PubFullText/RTO/EN/RTO-EN-AVT-116/EN-AVT-116-04.pdf`.

[3] WJ Bannink. De hypersone test faciliteit delft (htfd). *Lezing: Najaarscolloquium JM Burgerscentrum*, 29, 1996.

[4] Gabi Ben-Dor and Gabi Ben-Dor. *Shock wave reflection phenomena*, volume 2. Springer, 2007.

[5] Richard Benay, Bruno Chanetz, and Jean Délery. Experimental aspects of code verification/validation application to internal and afterbody aerodynamics. Technical report, ONERA-MEUDON CENTRE MEUDON (FRANCE) FUNDAMENTAL/EXPERIMENTAL AERODYNAMICS DEPT, 2003.

[6] M Bleilebens and H Olivier. On the influence of elevated surface temperatures on hypersonic shock wave/boundary layer interaction at a heated ramp model. *Shock Waves*, 15(5):301–312, 2006.

[7] Laurie Brown, Russell Boyce, Neil Mudford, and Sean O'Byrne. Intrinsic three-dimensionality of laminar hypersonic shock wave/boundary layer interactions. In *16th AIAA/DLR/DGLR International Space Planes and Hypersonic Systems and Technologies Conference*, page 7205, 2009.

[8] Ruud Caljouw. An experimental investigation of a three-dimensional hypersonic flow on a double ramp geometry using stereo-PIV. Master's thesis, Delft University of Technology, 2007.

[9] Graham V Candler. Numerical simulation of hypersonic shock wave–boundary-layer interactions. *Shock Wave–Boundary-Layer Interactions, 1st edn. Cambridge University Press, Cambridge*, pages 314–335, 2011.

[10] Shibin Cao, Igor Klioutchnikov, and Herbert Olivier. Görtler vortices in hypersonic flow on compression ramps. *AIAA Journal*, pages 1–11, 2019.

[11] Ross S Chaudhry, Pramod K Subbareddy, Ioannis Nompelis, and Graham V Candler. Direct numerical simulation of roughness-induced transition in the vki mach 6 tunnel. In *53rd AIAA Aerospace Sciences Meeting*, page 0274, 2015.

[12] P. V. Chuvakhov, V. Ya Borovoy, I. V. Egorov, V. N. Radchenko, H. Olivier, and A. Roghelia. Effect of Small Bluntness on Formation of Görtler Vortices in a Supersonic Compression Corner Flow. *Journal of Applied Mechanics and Technical Physics*, 58(6):975–989, 2017. ISSN 15738620. doi: `10.1134/S0021894417060037`.

[13] WJ Cook and EJ Felderman. Reduction of data from thin-film heat-transfer gages – a concise numerical technique. *AIAA journal*, 4(3):561–562, 1966.

[14] D Aymer de la Chevalerie, A Fonteneau, L De Luca, and G Cardone. Görtler-type vortices in hypersonic flows: the ramp problem. *Experimental thermal and fluid science*, 15(2):69–81, 1997.

[15] Luigi De Luca, Gennaro Cardone, Dominique Aymer de la Chevalerie, and Alain Fonteneau. Viscous interaction phenomena in hypersonic wedge flow. *AIAA journal*, 33(12):2293–2298, 1995.

[16] J Délery and B Chanetz. Experimental aspects of code verification/validation (application to internal aerodynamics). *Tiré à part- Office national d'études et de recherches aerospatiales*, 2000.

[17] J Delery and M-C Coet. Experiments on shock-wave/boundary-layer interactions produced by two-dimensional ramps and three-dimensional obstacles. In *Hypersonic Flows for Reentry Problems*, pages 97–128. Springer, 1991.

[18] Jean Delery. Experimental investigation of the reflection of a shock wave on a heated surface in presence of a turbulent boundary layer. *La Recherche Aerospatiale(English Edition)*, (1):1–23, 1992.

[19] Jean Délery. Physical introduction. *Shock Wave–Boundary-Layer Interactions, 1st edn. Cambridge University Press, Cambridge*, pages 5–86, 2011.

[20] Dirk Ekelschot. Investigation of Görtler vortices in hypersonic flow using Quantitative Infrared Thermography (QIRT) and Tomographic Particle Image Velocimetry (Tomo-PIV). Master's thesis, Delft University of Technology, 2012.

[21] Alexander Fedorov. Transition and stability of high-speed boundary layers. *Annual review of fluid mechanics*, 43:79–95, 2011.

[22] Sidharth Gs, Anubhav Dwivedi, Graham V. Candler, and Joseph W. Nichols. Onset of three-dimensionality in supersonic flow over a slender double wedge. *Physical Review Fluids*, 3(9): 1–29, 2018. ISSN 2469990X. doi: 10.1103/PhysRevFluids.3.093901.

[23] P. Hall. The linear development of görtler vortices in growing boundary layers. *Journal of Fluid Mechanics*, 130:41–58, 1983. doi: 10.1017/S0022112083000968.

[24] Michael Holden. A study of flow separation in regions of shock wave-boundary layer interaction in hypersonic flow. In *11th Fluid and PlasmaDynamics Conference*, page 1169, 1978.

[25] Michael S Holden. Experimental studies of shock wave–boundary-layer interactions in hypersonic flows. *Shock Wave–Boundary-Layer Interactions, 1st edn. Cambridge University Press, Cambridge*, pages 259–313, 2011.

[26] F Hung and D Barnett. Shockwave-boundary layer interference heating analysis. In *11th Aerospace Sciences Meeting*, page 237, 1973.

[27] GR Inger. Three-dimensional heat-and mass-transfer effects across high-speed reattaching flows. *AIAA Journal*, 15(3):383–389, 1977.

[28] Doyle D Knight and Alexander A Zheltovodov. Ideal-gas shock wave–turbulent boundary-layer interactions (stblis) in supersonic flows and their modeling: Two-dimensional interactions. *Shock Wave–Boundary-Layer Interactions, 1st edn. Cambridge University Press, Cambridge*, pages 137–201, 2011.

[29] R Legendre et al. Lignes de courant d'un ecoulement permanent, decollement et separation. 1977.

[30] Lars Lodder. Investigation of Hypersonic Transitional Shock Wave Boundary-Layer Interactions. Master's thesis, Delft University of Technology, 2020.

[31] P R A Lyons and S L Gai. A method for the accurate determination of the thermal product (ρck) for thin film heat transfer or surface thermocouple gauges. *Journal of Physics E: Scientific Instruments*, 21(5):445–448, may 1988. doi: 10.1088/0022-3735/21/5/005.

[32] Shin Matsumura, Steven P Schneider, and Scott A Berry. Streamwise vortex instability and transition on the hyper-2000 scramjet forebody. *Journal of spacecraft and rockets*, 42(1):78–89, 2005.

[33] Mark V Morkovin. Recent insights into instability and transition to turbulence in open-flow systems, 1988.

[34] Suman Muppidi and Krishnan Mahesh. Direct numerical simulations of roughness-induced transition in supersonic boundary layers. *Journal of Fluid Mechanics*, 693(2):28–56, 2012.

[35] Herbert Olivier and Sangdi Gu. Vki lecture series - avt 325, flow characterization and modeling of hypersonic wind tunnels: Operation, capabilities and limitations of existing hypersonic facilities, December 2018.

[36] John D Reinert, Ioannis Nompelis, and Graham V Candler. Coupled conjugate heat transfer simulation for a scramjet inlet at mach 8. In *23rd AIAA Computational Fluid Dynamics Conference*, page 4502, 2017.

[37] John D. Reinert, G. S. Sidharth, Graham V. Candler, and Jérey R. Komives. Three-dimensional simulations of hypersonic double wedge flow experiments. *47th AIAA Fluid Dynamics Conference, 2017*, (June):1–16, 2017. doi: 10.2514/6.2017-4125.

[38] Eli Reshotko. Transition issues at hypersonic speeds. *Collection of Technical Papers - 44th AIAA Aerospace Sciences Meeting*, 12(January):8472–8480, 2006. doi: 10.2514/6.2006-707.

[39] Eli Reshotko. Transition issues for atmospheric entry. *Journal of Spacecraft and Rockets*, 45(2): 161–164, 2008.

[40] Amit Roghelia, Pavel V. Chuvakhov, Herber Olivier, and Ivan V. Egorov. Experimental investigation of Görtler vortices in hypersonic ramp flows behind sharp and blunt leading edges. *47th AIAA Fluid Dynamics Conference, 2017*, (June):1–14, 2017. doi: 10.2514/6.2017-3463.

[41] Amit Roghelia, Pavel V Chuvakhov, Herbert Olivier, and Ivan Egorov. Experimental investigation of görtler vortices in hypersonic ramp flows behind sharp and blunt leading edges. In *47th AIAA Fluid Dynamics Conference*, page 3463, 2017.

[42] Amit Roghelia, Herbert Olivier, Ivan Egorov, and Pavel Chuvakhov. Experimental investigation of Görtler vortices in hypersonic ramp flows. *Experiments in Fluids*, 58(10):1–15, 2017. ISSN 07234864. doi: 10.1007/s00348-017-2422-y.

[43] Fulvio Scarano. Experimental aerodynamics (first edition): Lecture notes in infrared thermography, February 2013.

[44] Fulvio Scarano and Andrea Sciacchitano. Lecture notes in quantitative infrared thermography, May 2015.

[45] Fulvio Scarano and Andrea Sciacchitano. Lecture notes in shadowgraphy and schlieren, May 2015.

[46] Hermann Schlichting and Klaus Gersten. *Boundary-layer theory*. Springer, 2016.

[47] Steven P Schneider. Effects of roughness on hypersonic boundary-layer transition. *Journal of Spacecraft and Rockets*, 45(2):193–209, 2008.

[48] Steven P Schneider. Summary of hypersonic boundary-layer transition experiments on blunt bodies with roughness. *Journal of Spacecraft and Rockets*, 45(6):1090–1105, 2008.

[49] Steven P Schneider. Developing mechanism-based methods for estimating hypersonic boundary-layer transition in flight: the role of quiet tunnels. In *43rd AIAA Fluid Dynamics Conference*, page 2608, 2013.

[50] Ferry FJ Schrijer and Willem J Bannink. Description and flow assessment of the delft hypersonic ludwieg tube. *Journal of Spacecraft and Rockets*, 47(1):125–133, 2010.

[51] FFJ Schrijer. *Experimental investigation of re-entry aerodynamic phenomena – Development of non-intrusive flow diagnostics in a Ludwieg tube*. PhD thesis, PhD thesis, Technological University Delft, The Netherlands, 2010.

[52] FFJ Schrijer. Experimental investigation of re-entry aerodynamic phenomena. In *48th aiaa aerospace sciences meeting. AIAA Paper*, volume 1251, 2010.

[53] Gary S Settles. *Schlieren and shadowgraph techniques: visualizing phenomena in transparent media*. Springer Science & Business Media, 2012.

[54] GS Settles. Schlieren and shadowgraph techniques- visualizing phenomena in transparent media(book). *Berlin, Germany: Springer-Verlag GmbH, 2001.*, 2001.

[55] Prakash Shrestha and Graham V Candler. Direct numerical simulation of high-speed transition due to roughness elements. *Journal of Fluid Mechanics*, 868:762–788, 2019.

[56] G. Simeonides, W. Haaset, and M. Manna. Experimental, analytical, and computational methods applied to hypersonic compression ramp flows. *AIAA Journal*, 32(2):301–310, 1994. ISSN 00011452. doi: 10.2514/3.11985.

[57] Pramod K Subbareddy, Matthew D Bartkowicz, and Graham V Candler. Direct numerical simulation of high-speed transition due to an isolated roughness element. *Journal of Fluid Mechanics*, 748:848–878, 2014.

[58] F Ulrich and C Stemmer. Comparison of chemical modeling for high-temperature gas effects with direct numerical simulations of roughness-induced transition in a re-entry scenario of a hemispherical capsule. In *ESA International Confe-rence on Flight Vehicles, Aerothermodynamics and Re-rentry Missions and Engi-neering*, 2019.

[59] Nick Voogt. Investigation on supersonic, large wall roughness elements using QIRT and PIV. Master's thesis, Delft University of Technology, 2017.

[60] Qingqing Ye. *Mechanisms of boundary layer transition induced by isolated roughness*. PhD thesis, PhD thesis, Technological University Delft, The Netherlands, 2017.

[61] Yi Zhuang, Hui-jun Tan, Ya-zhou Liu, Yu-chao Zhang, and Yu Ling. High resolution visualization of görtler-like vortices in supersonic compression ramp flow. *Journal of Visualization*, 20(3):505–508, 2017.